**The Dissertation Committee for Vishal Timal Maharaj Certifies that this is the approved version of the following dissertation:**

# The Effects of Confining Minibasin Topography on Turbidity Current Dynamics and Deposit Architecture

**Committee:**

Lesli J. Wood, Supervisor

David Mohrig

Ronald J. Steel

William L. Fisher

Erik D. Scott

# The Effects of Confining Minibasin Topography on Turbidity Current Dynamics and Deposit Architecture

**by**

**Vishal Timal Maharaj, B.S.; M.S.Geo.Sci.**

**Dissertation**

Presented to the Faculty of the Graduate School of

The University of Texas at Austin

in Partial Fulfillment

of the Requirements

for the Degree of

**Doctor of Philosophy**

**The University of Texas at Austin**

**December 2012**

# Dedication

For Melissa, Mom, Dad, Dalini and Ravi

# Acknowledgements

The following paragraphs represent my humble attempt to formally thank each person who made this dissertation possible. Due to the numerous individuals who assisted me in the completion of my degree, I apologize if your name is not explicitly included, but know that I appreciate your contributions.

First, I thank my advisor, Lesli Wood for her friendship. I also thank her for providing an ocean of opportunities that extend past my first day as a graduate student. Her support for both my academic-and non-academic pursuits is greatly appreciated. To my Examining Committee members, David Mohrig, Ronald Steel, William Fisher, and Erik Scott, thanks for your support and taking the time to evaluate my work.

One summer's day in 2010, I approached the folks at the UT Morphodynamics Laboratory for assistance with my research. Very soon, the experience turned out to be one of the most insightful phases of my research. I express my gratitude particularly to Jim Buttles for all the moments spent helping me get up to speed with an unfamiliar field, and for his continued support until the very end. I also thank Elizabeth Rinehart and Evan Wagner for their assistance with setting up experiments and data processing in the lab.

I thank friends and staff at both the Jackson School of Geosciences and the Bureau of Economic Geology for providing a home away from home for the past four years, and for all their continued support and encouragement. In no particular order, these persons include, Sharon Mosher, Philip Guerrero, Candace Sandefur, Debra Sue Trinque, Dennis Trombatore, Alejandra Bernal, Scott Tinker, Jay Kipper, Eric Potter, Michael Young, William Ambrose, Peter Eichhubl, David Carr, Bob Hardage, Martin Jackson, Lorena Moscardelli, Ramon Treviño, Chris Zahm, Paula Beard, Aaron Everett, Amelia

Bridges, Cathy Brown, Sharon Campos, Claudia Gerardo, Lana Dieterich, Shirley Dutton, Tucker Hentz, Dallas Dunlap, Reuben Reyes, Kenneth Edwards, Jennifer Edwards, Jenny Turner, Amelia Bridges, Julie Duiker, Melissa Garcia, Carlos Garza, Anselmo Jacobo, Ron Russell, Joseph Yeh, Amanda Masterson and Sigrid Clift. To the innumerable friends I have made during my time as a graduate student in Austin, thanks for your friendship and support.

Funding of this dissertation was made possible by several entities. I thank present and past member companies at the Quantitative Clastics Laboratory consortium, including Anadarko, BG Group, BHPBilliton, Cairn, Chevron, Cobalt International Energy, ConocoPhillips, EcoPetrol, ENI, ExxonMobil, Hess, IMP, KerrMcGee, Marathon Oil Corporation, Noble Energy, Saudi Aramco, Schlumberger, Shell, Statoil, Talisman, Total, Woodside and YPF. Also, I thank AAPG, ConocoPhillips, ExxonMobil, GCAGS and GCSSEPM for providing external grants and scholarships during my time as a graduate student.

I thank my parents, Deosaran and Sandra, and siblings, Ravi and Dalini for their support, and for allowing me to be ambitious. Finally, and most importantly, I thank my wife, Melissa. Her support, encouragement, patience, tolerance and unwavering love were the bedrock upon which the past four years of my life have been built.

# The Effects of Confining Minibasin Topography on Turbidity Current Dynamics and Deposit Architecture

Vishal Timal Maharaj, Ph.D.

The University of Texas at Austin, 2012

Supervisor: Lesli J. Wood

This dissertation advances our understanding of how turbidity currents interact with three-dimensional (3-D) minibasin topography and the resulting deposits that form. Conceptual Gulf of Mexico-centric models of minibasin fill development have become the foundation for exploring and identifying strategic deep-water hydrocarbon reserves on continental slopes around the world. Despite the abundance of subsurface data, significant questions remain about the 3-D physical processes through which minibasins fill and the relationship between these processes and the topography of the basin. To overcome this problem, I utilize techniques in physical laboratory modeling to query established models of the role that turbidity currents play in minibasin fill development, and observe the relationships between fill from the Lobster minibasin located in a proximal continental slope position in the Gulf of Mexico and from the Safi Haute Mer (SHM) minibasin located in the distal continental slope of offshore western Morocco. First, existing published literature are reviewed and assessed for the known state of minibasin development and fill processes, and the strengths and weaknesses of our current knowledge base. Second, results are presented from two series of experiments that document the interaction between steady, depletive turbidity currents and 3-D minibasin topography. Experimental results suggest that turbidity currents produce

deposits that are more likely to drape pre-flow topography than pond within it. Turbidity current velocity data show a strong 3-D physical component in minibasin fill sedimentation that also influences extra-basinal sedimentation patterns. Details of these results provide insight into processes that have not been previously considered in published conceptual models of minibasin fill. Third, a comparison of the two subsurface datasets show that the types and abundance of architectural elements vary depending on the location of the minibasin on the continental slope (i.e. proximal vs. distal), and suggests key differences in the processes responsible for their infilling. Finally, a comparison of experimental results to preserved deposit architectures in the Lobster and SHM datasets suggest a more complex relationship of process-driven sedimentation than that derived primarily from suspension fallout. This improved understanding of minibasin fill is applicable to industry for increasing confidence in subsurface interpretations and reducing risk while exploring for quality reservoirs in deepwater regions.

# Table of Contents

# List of Tables

# List of Figures

# Chapter 1 – Introduction, Objectives and Overview

## PROBLEM AND HYPOTHESIS

Gulf of Mexico-centric models of minibasin development have become the foundation for exploring and identifying strategic deep-water hydrocarbon reserves. Despite the abundance of subsurface data, little is documented about the three-dimensional (3-D) physical processes through which minibasins fill relative to the topography created by underlying mobile salt. A review of current literature elaborates on key aspects that highlight this gap in knowledge that relates the depositional architecture observed from various data sources (outcrop, physical and numerical modeling, and industry-grade subsurface data such as seismic reflection, well-log and core data) with physical processes on various scales.

In this research, it is my objective to address minibasin development using techniques in physical modeling to investigate minibasin fill architecture as observed in subsurface datasets from offshore Gulf of Mexico and Morocco. Through this process, I will address established models of minibasin development, including positive aspects, negative paradigms and possible pitfalls of current knowledge. This dissertation seeks to test four hypotheses:

1. The *fill and spill* model (Booth et al., 2000) is inadequate for explaining sediment delivery to minibasins on complex slopes.
2. Confinement of minibasin deposits is not exclusively related to ponded accommodation and confined turbidity current conditions.

3. Differences in minibasin configuration and input turbidity current conditions will result in significant differences in the character of deposit geometry, architecture and grain size distribution.
4. The paleo-topographic state of a minibasin can be reconstructed based on resultant fill character and geometry.

## RESEARCH GOALS

Research goals will be met by applying a detailed qualitative and quantitative analysis of minibasin fill in three phases of research. These phases include (1) physically modeling flow behavior under conditions of varying topographic relief; (2) examining deep water fills in the Lobster salt basin of the proximal Gulf of Mexico shelf that underwent a transition from low topographic relief to high topographic relief; and (3) examining deep water fills in the Safi Haute Mer (SHM) minibasin from the distal shelf of offshore Morocco that underwent extremely rapid subsidence.

To test my hypothesis and address the aforementioned limitations and discrepancies in past studies, I attempt to revisit the existing but limited and mostly older models of minibasin fill evolution by combining observations from experimental models with preserved geometries and lithologies recorded in 3D seismic, and well-log data. In so doing, I intend to create a broader understanding of the influence of local and regional tectonics on fill timing, architecture and sedimentology, especially as it applies to reservoir distribution in provinces of regional substrate instability. This improved understanding of minibasin fill is applicable to industry for increasing confidence in subsurface interpretations and reducing risk while exploring deepwater regions.

## SIGNIFICANCE OF STUDY

Minibasin provinces are economically relevant as focal points for the deposition of siliciclastic sediment in deepwater slope settings. Some of these sandy deposits in turn serve as excellent reservoirs for hydrocarbons. Through an improved understanding of the sediment fill histories within minibasins we can improve our knowledge of how these basins form and the processes that influence their fill, as well as improve our estimates of the timing and the volumes of sediment which make their way to the deep ocean seafloor. More specifically, by using the methodology outlined in this study, a better understanding of the process by which minibasins fill with mud and sand will substantially improve:

- The understanding of the spatial and temporal relationships between turbidity currents and the confining topography they encounter as they make their way to the ocean floor.
- The understanding of the stratigraphic distribution of these sediments within confined minibasin settings, and the nature by which hydrocarbon reservoir-quality rock terminate on basin margins.
- The ability to identify the location of such reservoirs in deepwater locations with sparse subsurface data, as well as frontier deepwater locations.

This improved understanding of minibasin formation and fill is applicable for industry use in that it can be used as a predictive tool to increase confidence in subsurface interpretation and reduce risk while exploring deep-water regions that provide vital conventional energy resources.

## AN INTRODUCTION TO MINIBASINS

Minibasins are important morphological features on many continental slopes, and are especially prevalent along slope characterized by underlying mobile substrates (Fig.

1.1) (Pratson and Ryan, 1994; Lamb et al., 2006). These slopes are economically relevant in that these minibasins constitute focal points for the deposition of reservoir-quality sand, some of which contain significant volumes of hydrocarbons. As a result, minibasins have been intensely studied in the past two decades because of giant oil discoveries in minibasins on the Gulf of Mexico slope (e.g., Holman and Robertson, 1995; Mahaffie, 1994; McGee et al., 1994; Sullivan et al., 2004; Sawyer et al., 2007).

Minibasins are usually associated with the deformation of a mobile substrate due to the buoyant instability of a mobile substrate (e.g., salt body) overlain by a load of denser sediment. As their name implies, minibasins are much smaller than sedimentary basins – typically only a few tens of kilometers in diameter. Minibasins are analogous to crustal basins, since subsidence is accommodated by the flow of an underlying viscous fluid, but their confinement to the upper lithosphere renders the effects of magmatism, heat flow, flexural loading and compositional heterogeneity negligible (Hudec et al, 2009). Additionally, minibasin subsidence exceeds crustal basin subsidence by several orders of magnitude. Subsidence rates of > 1 km /m.y. can be sustained for several million years and produce fill strata up to 8 km thick in late Pliocene to Pleistocene minibasins (Hudec et al., 2009). Minibasins also form supra-mobile substrate topography that controls how sediment volumes are transferred from shelf edges to ultimate sinks in the deep ocean.

Although the concept of minibasins was conceived in the 1930's, the term, *minibasin* was first published by Worrall and Snelson (1989). The global occurrence of minibasins have been summarized by Hudec et al., (2009) and include the following: minibasins have been described in the Aptian salt basins of Brazil (e.g., Demercian et al., 1993; Cobbold et al., 1995; Roberts et al., 2004) and West Africa (e.g., Duval et al., 1992; Marton et al., 2000; Hudec and Jackson, 2004), the Pricaspian Basin (e.g., Barde et

al., 2002; Volozh et al., 2003; Ismail-Zadeh et al., 2004), Sverdrup Basin (Jackson and Harrison, 2006), Canadian Maritime basins (e.g., Balkwill and Legall, 1989; Shimeld, 2004), Zechstein salt basin (e.g., Stewart and Clark, 1999; Baldschuhn et al., 2001; Mohr et al., 2005), Flinders Ranges (e.g., Dyson, 1999; Rowan and Vendeville, 2006), Paradox Basin (Hudec and May, 1998; Prochnow et al., 2005, 2006; Matthews et al., 2007), the Red Sea (Heaton et al., 1995), and in several Mesozoic salt basins of northwest Africa (e.g., Tari et al., 2003).

Salt withdrawal minibasins are some of the most complex basin types because of the mobilization of underlying salt substrate and the effect that syn-tectonic and post-tectonic deformation have on the overlying sedimentary strata. However, the sedimentary fill in these minibasins is a function of the balance of sedimentation and available accommodation space for those sediments. Therefore, it stands to reason that the phases of local and regional structural-induced accommodation development (i.e., salt inflation and deflations, compression, extension, etc.) should be accompanied by a unique expression in the geomorphic framework of the basin fills.

## MINIBASIN SUBSIDENCE MECHANISMS

Conventional understanding of minibasin subsidence has always alluded to the theory of density inversion to explain the primary mechanism that drives the subsidence of salt to create supra-salt topography. Hudec et al., (2009), however show that for a phenomena to occur, 2300 m (7500 ft) of siliciclastic fill will be needed to create a scenario where the average density of the basin fill exceeds the density of the underlying salt. However, it is usually observed that most minibasins begin subsiding when their fill thickness is significantly less than 2300 m. Hudec et al. (2009) identify five mechanisms of minibasin subsidence that are alternative to the classic density-driven subsidence

mechanism (Fig. 1.2). These alternatives include: 1) during diapir shortening, the squeezed diapirs inflate, leaving the intervening minibasin as a bathymetric depression; (2) in extensional diapir fall, stretching of a diapir causes it to sag, producing a minibasin above its subsiding crest; (3) during decay of salt topography, a dynamic salt bulge subsides as upward flow of salt slows, which lowers the salt surface below the regional sediment surface; (4) during sedimentary topographic loading, sediments accumulate as a bathymetric high above salt; and (5) subsalt deformation affecting the base of salt may produce relief at the top of salt. Each mechanism (including density-driven subsidence) produces a different bathymetry, which interacts with sediment transport to produce different facies patterns in the associated minibasins. The particular mechanism responsible for minibasin subsidence depends on the tectonic environment, regional bathymetry, and sedimentation rate.

## MINIBASINS AND THE CONCEPT OF ACCOMMODATION

The concept of *accommodation* describes the amount of space that is available for sediments to fill, and is measured by the distance between base level and the depositional surface (Fig. 1.3) (Jervey, 1988; Catuneanu, 2006). Base level (of deposition or erosion) is generally regarded as a global reference surface to which long-term continental denudation and marine aggradation tend to proceed (Catuneanu, 2006). The surface is dynamic – moving upward and downward through time relative to the center of the Earth in parallel with esustatic rises and falls in sea level. Usually, base level is often approximated with sea level, but in deepwater settings, the role of sea level in affecting sedimentation can become less pronounced.

It is generally accepted that the ultimate, large-scale, controls influencing deepwater depositional systems on continental margins are sediment supply, regional

basin tectonics and relative changes in sea level (Mutti & Normark, 1991; Posamentier et al., 1988; Posamentier & Vail, 1988; Reading & Richards, 1994; Vail et al., 1977). The interplay among these controls results in an infinite amount of scenarios for deepwater fill and the degree of influence of the individual components are complex. Moreover, the relative contribution of each component is difficult to use predictively toward characterizing the sedimentary record of deepwater deposits. For the case of minibasins located on the slopes of continental margins with underlying mobile substrate (e.g. salt, shale), the sedimentary delivery system and the receiving basin configuration are the primary factors that govern fill morphology and lithofacies distribution (Steffens et al., 2003).

Slopes can be divided into graded slope and above-graded slope on the basis of topography (Prather, 2000; 2003; Ross et al., 1994) and its relationship to the slope equilibrium profile. Gravity structural movement tends to produce a rough surface and thus an above-graded slope, while deep-water deposition and erosion tend to create gentle topography and consequently a graded slope. Mobile substrates with relatively large amounts of ponded-basin and healed-slope accommodation space across the mid-slope are termed to be above-grade slopes (Fig. 1.4).

Implicit in the discussion of deepwater accommodation in minibasin settings are the processes responsible for the space created and the types of accommodation that exist along the irregular slope profile. Shelf and slope minibasins form when an underlying salt sheet is loaded by an advancing shelf margin (Sumner et al., 1991; Shoup and Karlo, 1999). Sediments from the advancing deltas load and mobilize the underlying salt, causing it to flow up section, both laterally and in the downdip direction. The evacuating salt leaves a topographic low that traps sediments from the advancing deltas. New accommodation space is created as the salt migrates from the center of the minibasin.

After the salt has evacuated from beneath the minibasin, creation of new accommodation space ceases.

Prather et al., (1998) defined three types of accommodation in the Gulf of Mexico continental slope profile (Fig. 1.4): (1) ponded-basin accommodation, (2) slope accommodation, and (3) healed-slope accommodation. Ponded-basin accommodation develops in association with localized salt withdrawal and minibasin formation. This space is usually circular to semicircular and increases into the distal part of most basins. Slope accommodation is the space between a typical graded-slope profile pinned at the shelf-slope break and the stepped equilibrium profile at the top of the ponded-basin accommodation. Healed-slope accommodation, in the northern Gulf of Mexico is the space between a lower gradient profile near the crest of the Sigsbee Escarpment with the shelf/slope break and the depositional surface at the top of the combined ponded-basin and slope accommodation space. Each type of accommodation is associated with specific deposits (and thus, on seismic, distinct seismic facies). The spatial distribution of these deposits i.e. fill pattern, is usually complex due to changes in local gradients within the slope and the delicate balance between accommodation and slope gradient. Further study of selected deep-water clastic margins by Steffens et al. (2003) shows that there are significant differences in receiving basin configurations between salt-based and shale-based continental margins.

In this study, I refer to accommodation in the context of minibasins based on the methods presented by Prather et al. (1998) and Steffens et al., (2003), and not the general form of the concept first introduced by Jervey (1988).

## MODELS OF MINIBASIN FILL

Although several global examples of minibasin provinces exist, models of minibasin development are dominated by Gulf of Mexico examples, principally the Booth et al. (2000) model, also known as the "fill and spill" model. This model suggests a process dominated by sediment-driven-subsidence accommodation tied to eustatic sea-level changes along the margin. In this model, developed principally through work in the Auger and Macaroni basins in the Gulf of Mexico, Booth et al., (2000) define five phases of minibasin development. These include (a) healing phase in intra-slope sinks; (b) ponded phase sheets in distal sinks; (c) bypass of channel and overbanks; (d) gorge system development and bypass to more distal sinks; and e) normal faulting in proximal slope with footwall fills. Similarly, Sinclair and Tomasso (2002) attempted to define a simplistic model for confined turbidite basins by incorporating outcrop data from upper slope Tertiary Alpine basins with subsurface data from the Gulf of Mexico. They conclude that the progressive infill of confined turbidite basins can be characterized by four phases: (a) flow ponding, where incoming flows are totally trapped; (b) flow stripping, where the finer, more dilute portion of the flow is able to escape over the confining topography; (c) flow bypass, either by flows traversing over the filled basin or by switching of feeder channels away from the basin; and (d) blanketing, of the basin and surrounding topography with fine-grained sediment due to base-level rise.

DeVay et al. (2000) suggest that the process of filling and spilling works best in relatively low sediment input scenarios in which the basin fill rate is equal to or less than the rate of salt displacement, otherwise sediments will be able to reach the abyssal plain with relatively little obstruction. In another scenario, Wood (2006) suggests that the processes presented by the Booth et al., (2000) model might vary dramatically in the more distal minibasin systems of the Gulf of Mexico, where basins are farther removed

from the influences of eustatically-driven shelf edge sediment supply changes (Fig. 1.5). Montoya and Hudec (2007) and Madof et al., (2009) also acknowledge this point, in that complex accommodation scenarios in distal slope settings generate more complex accommodation and sedimentation histories, and require more robust models to understand the dynamics and 3-D evolution of minibasins.

## SEDIMENT GRAVITY FLOWS

The term, *sediment gravity flow* was introduced by Middleton and Hampton (1973) to describe major flow types involved in sedimentation processes. Sediment gravity flows are defined as the flow of sediments or sediment-fluid mixtures in which the interstitial fluid is driven by the grains moving under the action of gravity. There are fifteen conceptually distinct processes that are part of the process gravity flow process continuum (a continuum of mechanical behavior), ranging from elastic through plastic viscous fluid and viscous settling (Stow 1986; Fig. 1.6). The transition from slides to sediment gravity flows involves a change in the physical state of the sediment mass from a state of aggregation to internal disaggregation and the incorporation of a fluid phase (Fig. 1.7). The transition from debris flows to liquefied or fluidized flows and turbidity currents involves further remolding and dilution of the flow. The extreme member of sediment gravity flows; a very low-concentration, low-velocity turbidity current is deflected by the Coriolis force from its downslope path and grades into a normal current known as a contour current. During deposition, five main parameters of a sediment gravity flow determine its laminar or turbulent behavior according to Bingham and Reynolds dimensionless numbers: (1) velocity, (2) density, (3) cohesive strength, (4) flow thickness, and (5) apparent viscosity of the fluid (Postma, 1986). The experimental portion of this research is focused on turbidity-current generated gravity flows.

## TURBIDITY CURRENTS

Turbidity currents are particle-laden, gravity-driven underflows of Newtonian rheology in which the particles are largely or wholly suspended by fluid turbulence (Meiburg and Kneller, 2009). Turbidity currents transport particles from a few hundred meters or less, up to thousands of kilometers on the ocean floor (e.g. the Amazon Channel, Pirmez and Imran, 2003; and the north Atlantic Mid-Ocean Channel, Klaucke et al., 1998). The sedimentary deposit formed by a single turbidity current is commonly referred to as a turbidite (Bouma, 1962). The link between turbidity currents and their deposits are the topic of several investigations, both qualitative and quantitative.

The action of turbulence is a key component that separates turbidity currents from other types of sediment gravity flows, and is generated due to the forward motion of the current along a basal boundary (usually defined by the interface between the sediment surface and ambient fluid). The motion along the basal boundary is driven due to the action of gravity on the density difference between the particle-fluid mixture in the current and the ambient fluid. This density difference is usually referred to as the excess density.

The ambient fluid is generally of similar composition to the fluid within the turbidity current, although temperature and salinity differences may temporarily hinder their mixing rate. In most natural cases on the Earth's surface, this fluid is water. Particles within the current usually contain rock or mineral fragments that have been eroded from terrigenous sources, as well as both transported and reworked flora and fauna material that are useful tools for dating sedimentary successions.

Although there is uncertainty in estimating particle concentrations in natural cases, it is generally assumed that particle-particle interactions play a negligible role in maintaining suspension (Bagnold, 1954) since documented particle volume

concentrations in natural cases are relatively low (0.1 – 7% by volume). For those concerned with hydrocarbon exploration in deepwater environments, turbidity currents are considered to be important agents that deliver large volumes of reservoir-quality sediments (up to millions of $km^3$) into subaqueous environments (e.g. Lamb et al., 2006). These deposits may consist of a variety of submarine fans, channels and related systems that accumulate over periods of $10^4$ to $10^6$ years (Meiburg and Kneller, 2009).

This research is concerned only with the response of low-density turbidity currents to varying degrees of current confinement and minibasin configuration. Low-density turbidity currents carry largely clay- and silt-sized particles up to fine-grained sands in low concentrations and at relatively low velocities. They are probably much more common in the deep sea than high-density currents (Piper, 1978; Stow and Bowen, 1980), and occur in different forms, generated by several different processes. The processes involved are for high-density turbidity currents, however the caliber of sediments being transported in high-density turbidity currents contains a lower concentration of finer-grained material (mud and silts). Creeps, slumps, debris flows and high-density turbidity currents may all develop into low-density currents. The duration of both high-and low-density turbidity currents are relatively short (the order of hours to days), when compared to normal bottom currents that are of considerably longer duration.

***Flow Morphology and Duration***

Turbidity currents can be characterized by a well-defined front, also known as a head, followed by a layer known as the body of the current (Fig. 1.8). Even with steady inflow conditions, Normark (1989) and Best et al., (2005) have documented the development of pulsing flow with periods of a few minutes. The motion of the fluid behind the head can be approximated with a modified form of the Chezy equation for

flow in open channels, using the reduced gravity (Middleton 1993), and is slope dependent. Consequently, the buoyancy flux into the head increases with increasing slope, resulting in a concomitant effect on mixing (see below). Finite-volume releases ('surge-type' currents) may be dominated by the properties of the front (Hacker et al. 1996), in contrast to sustained or continuous underflows.

***Flow Structure (Velocity, Turbulence, Density and Entrainment)***

Stacey and Brown (1988) analyze the vertical structure of turbidity currents. The analysis of velocity distribution within turbidity currents in the literature varies depending on application and comprises instantaneous (real-time) and mean (time-averaged) analyses. For purposes of graphic representation, the mean velocity structure consists of an inner region with a positive velocity gradient, and an outer region (shear layer), which is generally five- to ten-times thicker than the inner region, with a negative velocity gradient (Fig. 1.8b) (Parker et al., 1987; Kneller and Buckee, 2000; Gray et al., 2005; Leeder et al., 2005).

Turbulent kinetic energy profiles are close to zero at the height of the downstream velocity maximum at the fluid-sediment interface, and reflect the dominance of turbulence production by shear related to the mean stream-wise velocity profile. The density structure within turbidity currents is determined by the distribution of suspended sediment (Parker et al., 1987; Kneller and Buckee, 2000). These authors also show that the highest suspended sediment concentrations occur immediately above the bed. Baas et al., (2005) demonstrate that the suspended sediment distribution is unsteady and controlled by the ratio of particle settling velocity to the upward-directed component of local turbulent velocity. Entrainment of ambient fluid into the head of gravity currents is shown by Parsons and Garcia (1998) to be dependent on a Reynolds number based on the

cube root of the buoyancy flux into the head. Entrainment into the body is a function of the overall Richardson number (Ellison and Turner, 1959).

***Turbidity Currents and Minibasin Topography***

Researchers have long recognized that topography and related sediment accommodation space can significantly affect the dynamics and initiation of turbidity currents (Prather et al., 1998; Winker, 2000; Kneller and Buckee, 2000; Lamb et al., 2006). Chapter 3 reviews the state of current literature in more detail, and addresses the various types of investigations that determine the influence of confining topography on turbidity currents and their deposits. It is reasonable to hypothesize that if the confining topography is sufficiently high, turbidity currents will either be deflected or completely contained within the confining limits. On the other hand, if confining topography is not sufficiently high to contain the flows, the manner in which they move from one basin to another and the resulting stratigraphy have been points of great discussion.

Some studies have noted that when basins are filled to their topographic spill point with an onlap-fill succession, these onlap-fill packages are incised by an overlying channel system which bypassed sediment to the next basin(s) (Winker, 1996; Badalini et al., 1999; Beaubouef and Friedman, 2000). Other authors have noted experimental results suggesting that turbidity current run-out up topography may be up to 4.5 times the height of the flow thickness (Lane-Serff et al., 1995) and that the body of a flow will surmount topography less than 2.5 times the body thickness (Rottman et al., 1985), or 1.5 times the head height (Kneller and McCaffrey, 1999; Muck and Underwood, 1990). These authors advocate that while turbidity currents can overcome relative low relief and transport sediments to downstream locations, some material in the lower part of the flow may be left behind as the flow surmounts the relief. These two different ideas, incision and

remobilization of older onlap deposits versus flows bypassing the basins entirely, have implications for the character, distribution and architectures of the resultant sand bodies.

## TURBIDITES

Turbidites are commonly referred to sediments that are transported and deposited by turbidity currents (turbulent suspension flows), and are usually not associated with tractional or frictional flow. Bouma (1962) first described the type sequence for turbidite deposits from the Grès d'Annot Formation of southeastern France, from which the internal deposit structures have been linked to waning flow conditions. The interpretation of turbidites in the sedimentary record through time has however shown to be increasingly difficult, especially considering the existence of other deep-water bottom currents (e.g. thermohaline, wind-driven, tidal and baroclinic currents). Turbidite facies models have been established using guiding principles of flow processes and the associated sedimentary structures due to sediment detrainment from turbidity currents. They are outlined in the following section. This research only considers deposits laid down under turbid flow conditions and the variability associated with confined minibasin topography, and not hybrid deposits that result from flow transformation on the slope.

### *Turbidite Facies Models*

Extensive debate exists on the interpretation of how sediments from turbidity currents are preserved in the rock record, and the link between deposit structures and the processes that formed them. Models range from simplistic turbidite facies associations that have been widely utilized in the past four decades, to more recent models that incorporate the complexities associated with flow transformation and the associated internal structure of deposits as a result of the transformation.

Examples of simplistic models are shown in Figure 1.9, each of which contains their own distinctive standard sequence of sedimentary structures within a bed. They are; (1) the coarse-grained turbidite model (Lowe, 1982); (2) the medium-grained turbidite model (Bouma, 1962); and (3) The fine-grained turbidite model (Stow and Piper, 1984). Although each model postulates a distinct set of facies order and sequence, very rarely do complete sequences of each model appear in the real world. The idealized sequences also can be interpreted hydrodynamically as resulting from a single resedimentation event with waning flow, and by consequence, a reduction in carrying capacity.

The coarse-grained turbidite facies model represents both organized and disorganized facies from the coarse-grained facies classes (see Stow, 1985). The main process of long-distance transport is considered to be high-density turbidity currents, and many of the preserved sedimentary structures are considered to be a result of grain flow, fluidized or liquefied flow mechanisms during the final stages of deposition. The lower part of the sequence can comprise gravel, pebbly sand or sand, overlying a sharp, scoured base. Characteristic structures include negatively-graded lower division ($R_1$) overlain by massive ($R_2$), stratified ($S_1$), graded-stratified ($S_2$) and finally by dish and pipe structured ($S_3$) divisions. The top is commonly sharp and flat (Walker, 1978; Lowe, 1979, 1982). It is postulated that some of the facies in classes A and B may be a result of traction processes rather than turbidity currents.

The medium-grained turbidite facies model is commonly referred to as the Bouma (1962) sequence. The turbidite sequence comprises some of Lowe's facies class B, most of facies class C (sand-mud couplets and muddy sands), and some of facies class D (silts, silty muds and silt-mud couplets). Overlying a sharp, erosive or loaded base are five sedimentary divisions of the Bouma sequence: a massive to graded sand ($T_a$), parallel-

laminated sand ($T_b$), cross-laminated and convolute sand ($T_c$), parallel-laminated fine sand and silt (Td), and massive to bioturbated mud ($T_d$).

The fine-grained turbidite facies model (after Stow and Piper, 1984) represents much of facies classes D and E (muds and clays). A graded silt-laminated mud division (E1) can be further subdivided into a thick, often lenticular basal silt laminae with fading ripples at the top ($T_0$), a relatively thick mud layer with convolute silt laminae ($T_1$), low-amplitude ripples ($T_2$), parallel distinct ($T_3$), parallel indistinct ($T_4$), and wispy silt laminae ($T_5$). These are overlain by graded muds ($T_6$), non-graded mud ($T_7$) and a thin microbioturbated zone ($T_8$). (Rupke and Stanley, 1974; Normark et al., 1978; Stow and Shanmugam, 1980; Kelts and Arthur, 1981).

Proponents of the dynamic nature of flow transformation on the slope commonly refer to a model of hybrid sediment gravity flow deposits (e.g. Haughton et al., 2009, Fig. 1.10). These authors recognize that the deposits from sediment gravity flows can show evidence for changes in flow behavior that can make it difficult to ascribe them to a single flow type. Often they show evidence of having been deposited under a range of conditions from poorly cohesive and turbulent flows to increasingly cohesive deposition with suppressed turbulence. These hybrid sediment gravity flow deposits may contain up to five internal divisions, two of which relate to turbidity currents. These include structureless sandstones related to (a) high-density turbidity currents (H1) that record longitudinal and lateral heterogeneity in flow structure and the development of turbulent, transitional and laminar flow heterogeneity in flow behavior in different parts of the same flow; and b) well-structured and graded mud-sand couplet related to a trailing low-density turbulent cloud (H4) and mud suspension fallout (H5). Progressive bed aggradation results in the deposits of the different flow components that stack vertically in the final bed.

## ARRANGEMENT OF DISSERTATION CHAPTERS

Chapter one (this chapter) introduces the research presented in this dissertation.

Chapter 2 describes the components of research applied in this dissertation. For each component, I describe the data used, the geological setting (in the case of the GOM and SHM localities), and previously accomplished work by other authors in each field/ locality. A summary of observations and interpretations in each locality gives insight into the more detailed work presented in Chapters 4-8.

Chapter 3 is a literature review that addresses the state of existing work on confined deposits in margins with underlying mobile substrate. The review aims to clarify some of the misconceptions about how confinement is interpreted in the geological record, as well as the limitations in models used to describe the processes that are responsible for creating confined deposits.

Chapter 4 present results from the first of two series of experiments that documents the interaction of unconfined turbidity currents in 3-D minibasin topography space, and investigates the character of deposits as the basin fills.

Chapter 5 presents results from the second series of experiments that documents the interaction of steady, depletive turbidity currents and a subsiding 3-D minibasin. This paper describes an attempt to investigate the influence of 3-D minibasin topography and current confinement on turbidity current dynamics, deposit geometry, intra-basinal sediment distribution and the influence of these factors in the extra-basinal delivery of sediment. Results are compared to ancient deposits from the Lobster minibasin of the Gulf of Mexico, and implications for applying existing models of minibasin fill development are discussed.

Chapter 6 incorporates observations and results from experimental work in Chapter 5, and delivers a set of quantitative tools that attempts to link the preserved

deposits from the Lobster minibasin of the Gulf of Mexico to the processes responsible for its infilling.

Chapter 7 proposes a methodology to reconstruct the tectonic evolution of an isolated minibasin in the deep water of offshore Morocco by implementing observations from geomorphological and structural analysis using 3D seismic data. Seismic cross-section and attribute analysis is used to investigate the change in character of the fill through time, and the influence of regional structural features developed during the evolution of the Moroccan continental slope is combined with observations to develop a model for a minibasin's evolution in the context of extremely rapid subsidence.

Chapter 8 reviews the conclusions of Chapters 3-8 and discusses the validity of the hypotheses introduced in Chapter 1. The limitations of the three components are also addressed and the implications are summarized as a starting point for future work.

## FIGURES

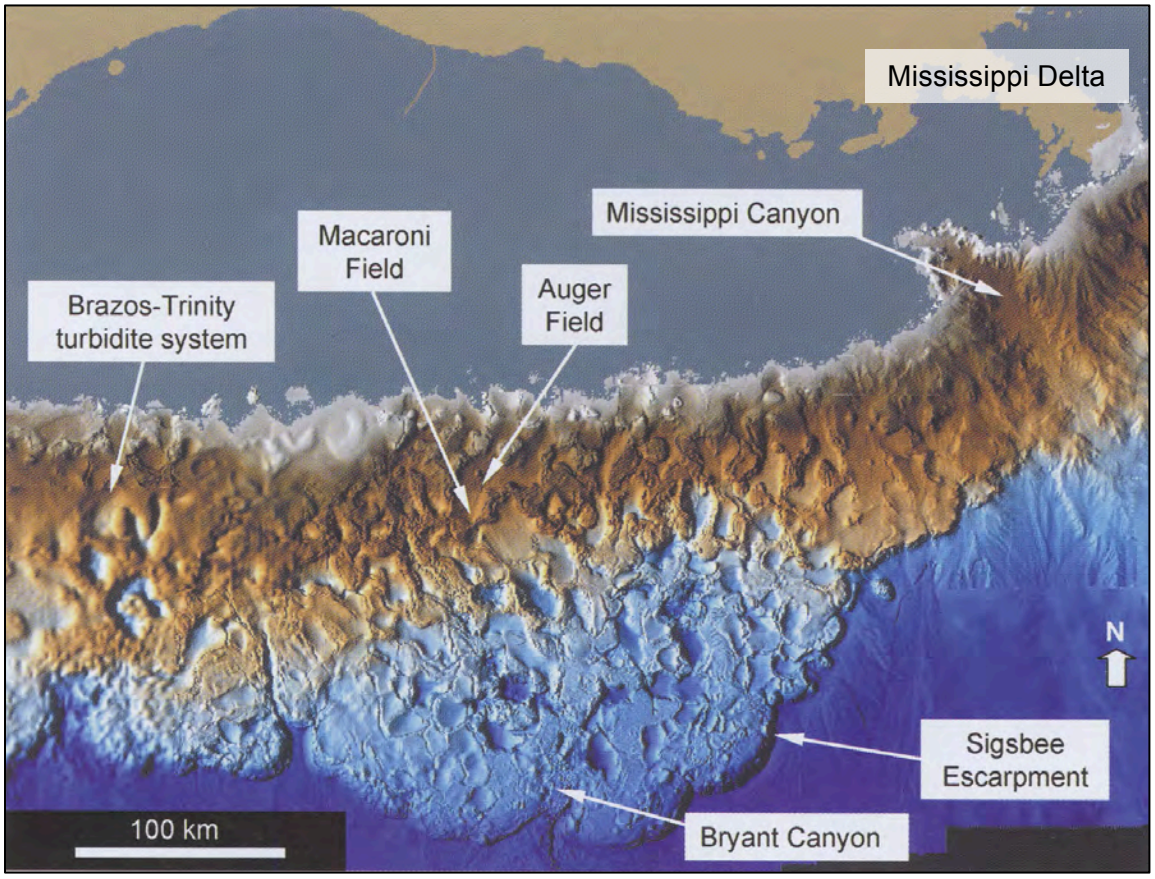


Figure 1.1: Rendered seafloor image of the Gulf of Mexico salt-based slope (modified from Smith, 2004) showing circular to elliptical salt-withdrawal intraslope basins or "minibasins" with diameters ranging between approximately 5 and 20 km. Well studied modern and subsurface localities are labeled in white. Note the location of the minibasins in relation to the modern Mississippi delta.

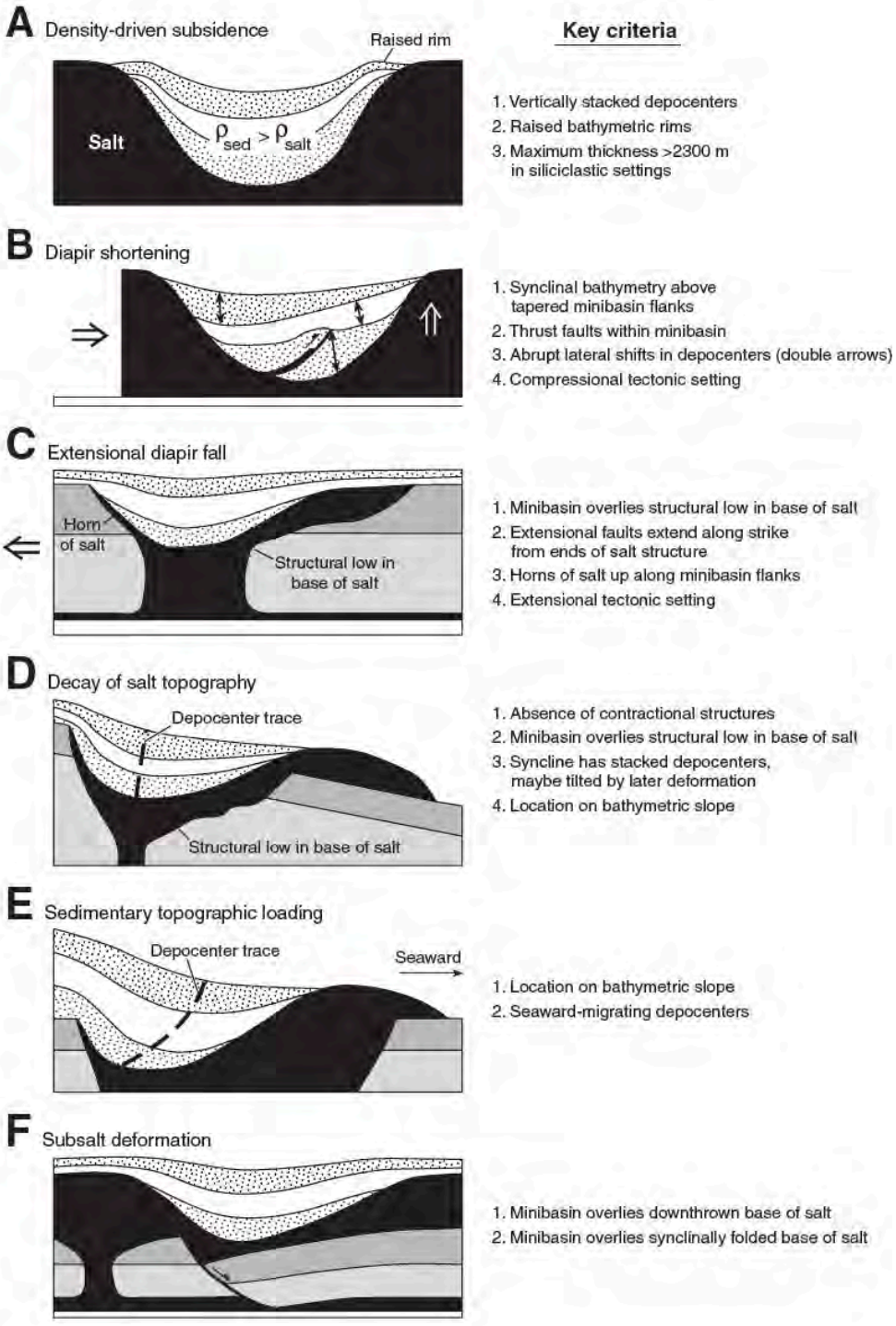


Figure 1.2: Summary of minibasin subsidence models and criteria used to distinguish them (from Hudec et al., 2009).

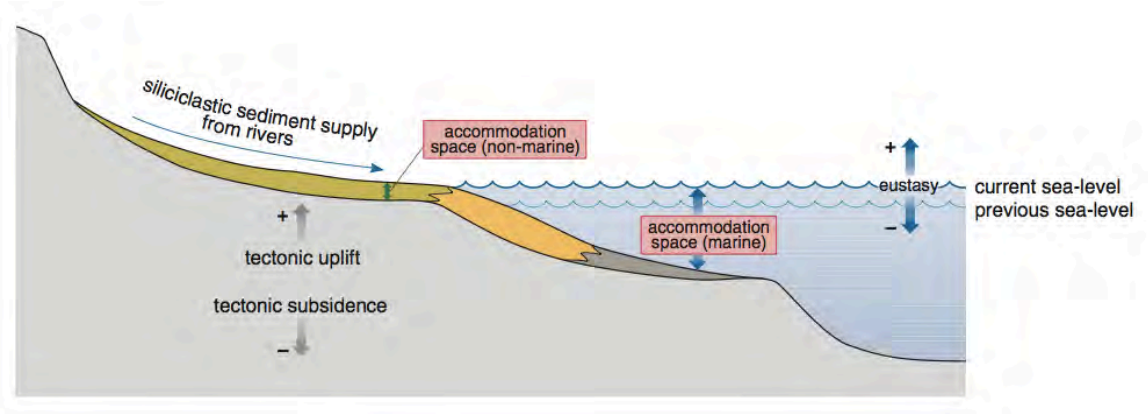


Figure 1.3: Sediment accommodation space and its relationship to eustatic sea level, tectonic uplift and subsidence (Modified from Coe, 2003). Marine accommodation space created during a rise in relative sea level has been particlly filled with sediment (yellow and dark grey), whereas the non-marine accommodation space created during the rise in relative sea level has been completely filled with sediment (green).

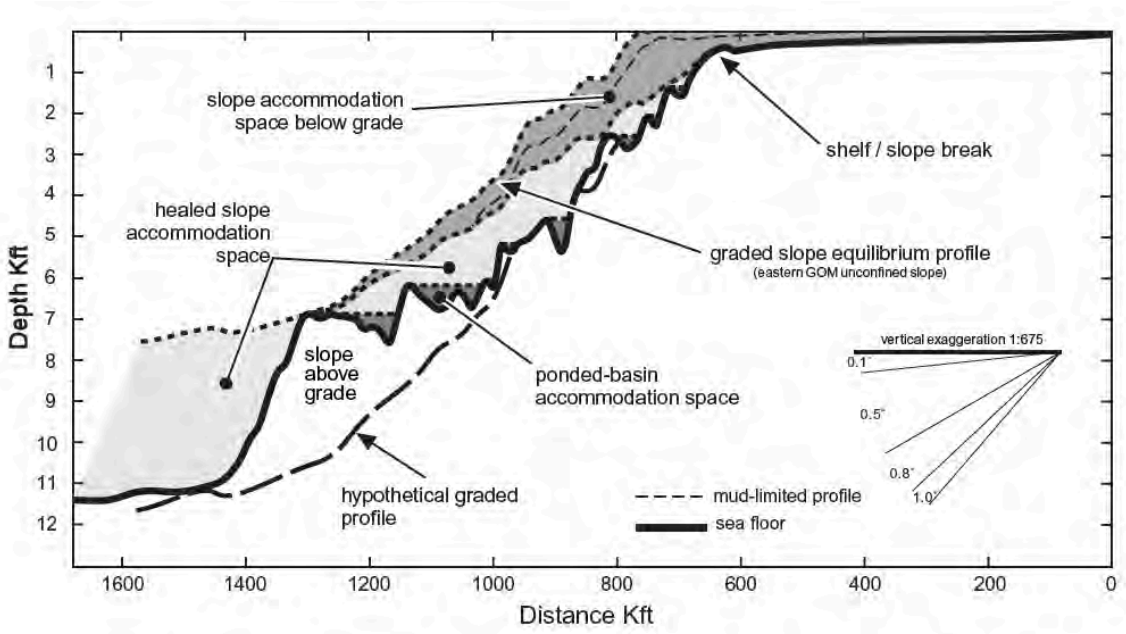


Figure 1.4: A seafloor profile across central Gulf of Mexico (GOM) shows the distribution of accommodation on a typical above-grade slope profile: (1) ponded basin accommodation; (2) slope accommodation; and (3) healed-slope accommodation (modified from Prather et al., 1998). The graded slope profile comes from the present-day unconfined slope of the eastern GOM where it dips to the south at about $0.8^{o}$.

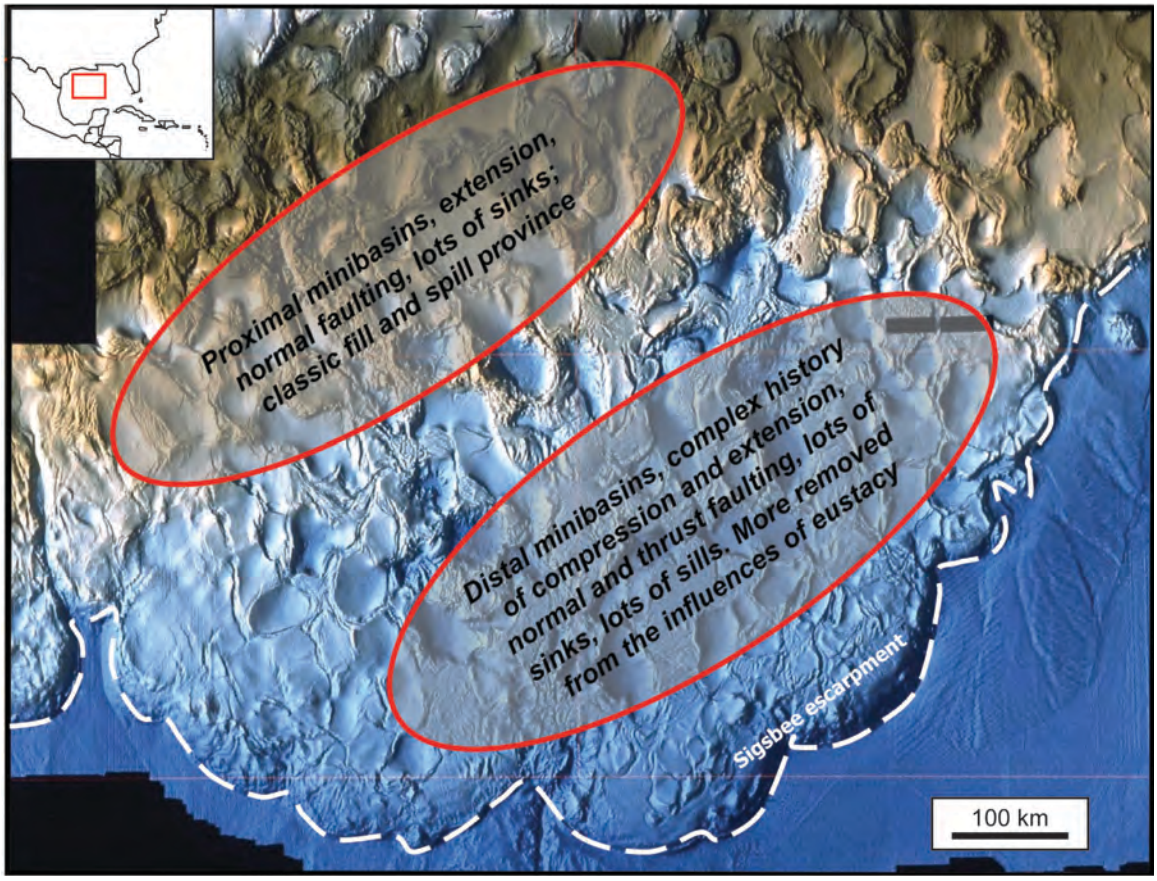


Figure 1.5: Shaded relief map of the present-day seafloor of the Gulf of Mexico basin. Minibasins exist in the area influenced by mobile salt substrate, and can be described as proximal and distal relative to the coastline. The extent of the basin affected by underlying salt substrate terminates at the Sigsbee Escarpment (white dashed line) in the south of the basin.

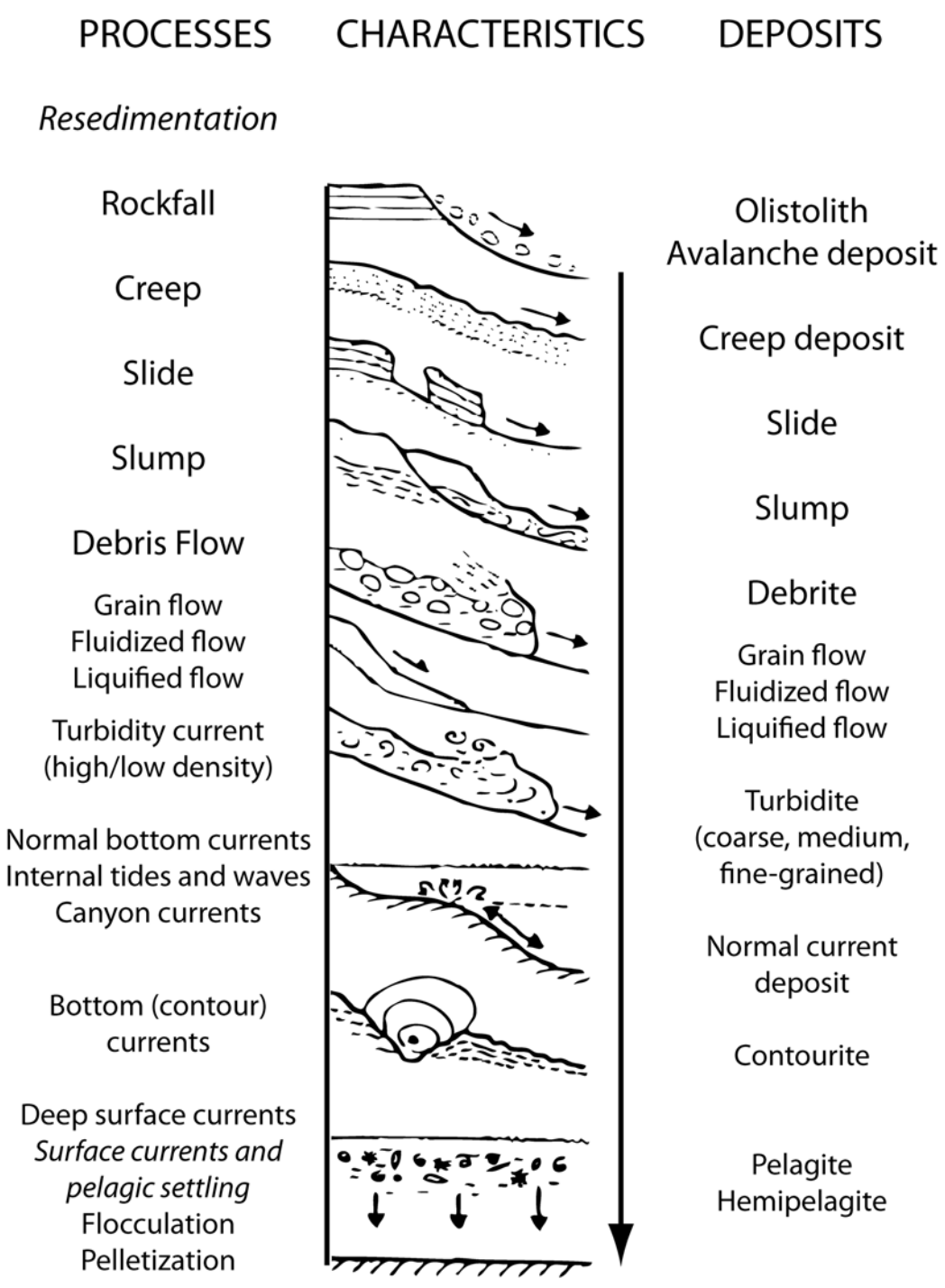


Figure 1.6: Process continuum of the main transport and depositional processes in the deep sea (modified from Stow, 1986).

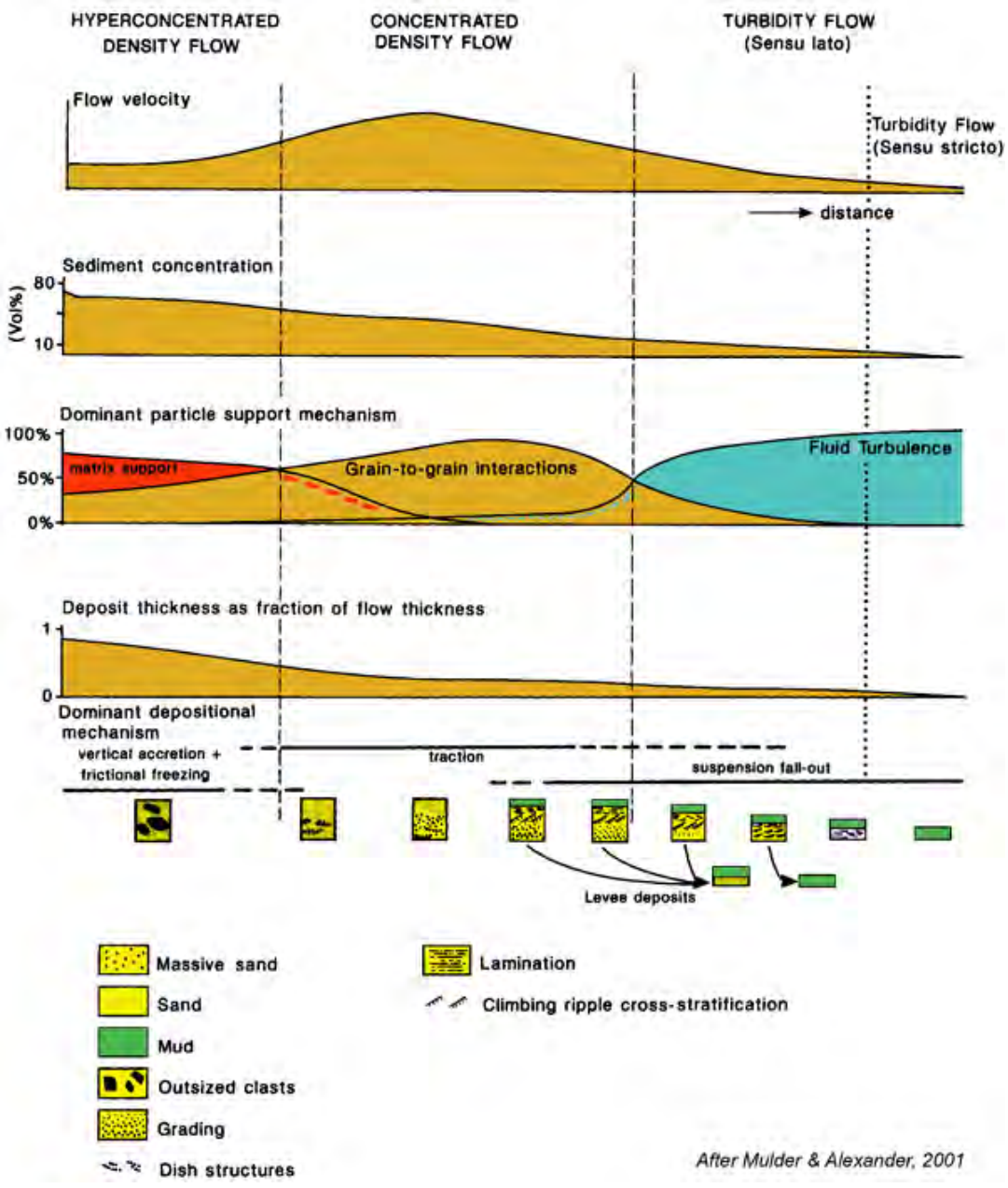


Figure 1.7: Illustration of changes during subaqueous flow transformation (Modified from Mulder and Alexander, 2001). Flows range from hyperconcentrated density flows to concentrated density flows, and then to surge-like turbidity flow. Sediment concentration decreases progressively with distance. Major particle-support mechanisms are shows and demonstrates part of the basis for distinguishing between flow types.

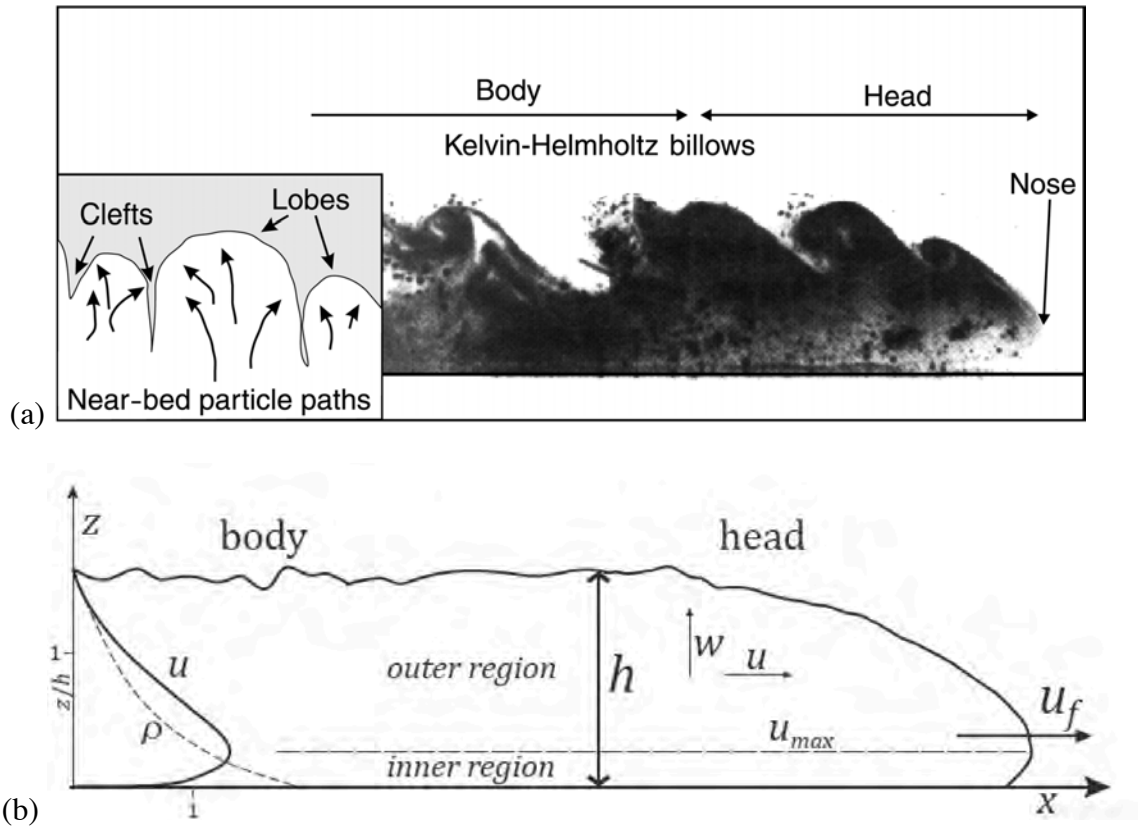


Figure 1.8: (a) Quasi two-dimensional image of an experimental turbidity current illustrating the overhanging 'nose' that corresponds to the height of the stream-wise velocity maximum. Also shown are well-developed Kelvin-Helmholtz billows associated with fluid turbulence (from Kneller and Buckee, 2000; modified from Simpson, 1969). Inset shows schematic view of lobes and clefts seen from below; (b) schematic diagram of the head and body of a gravity current, showing generalized velocity and density profiles based on an integral length scale for current thickness.

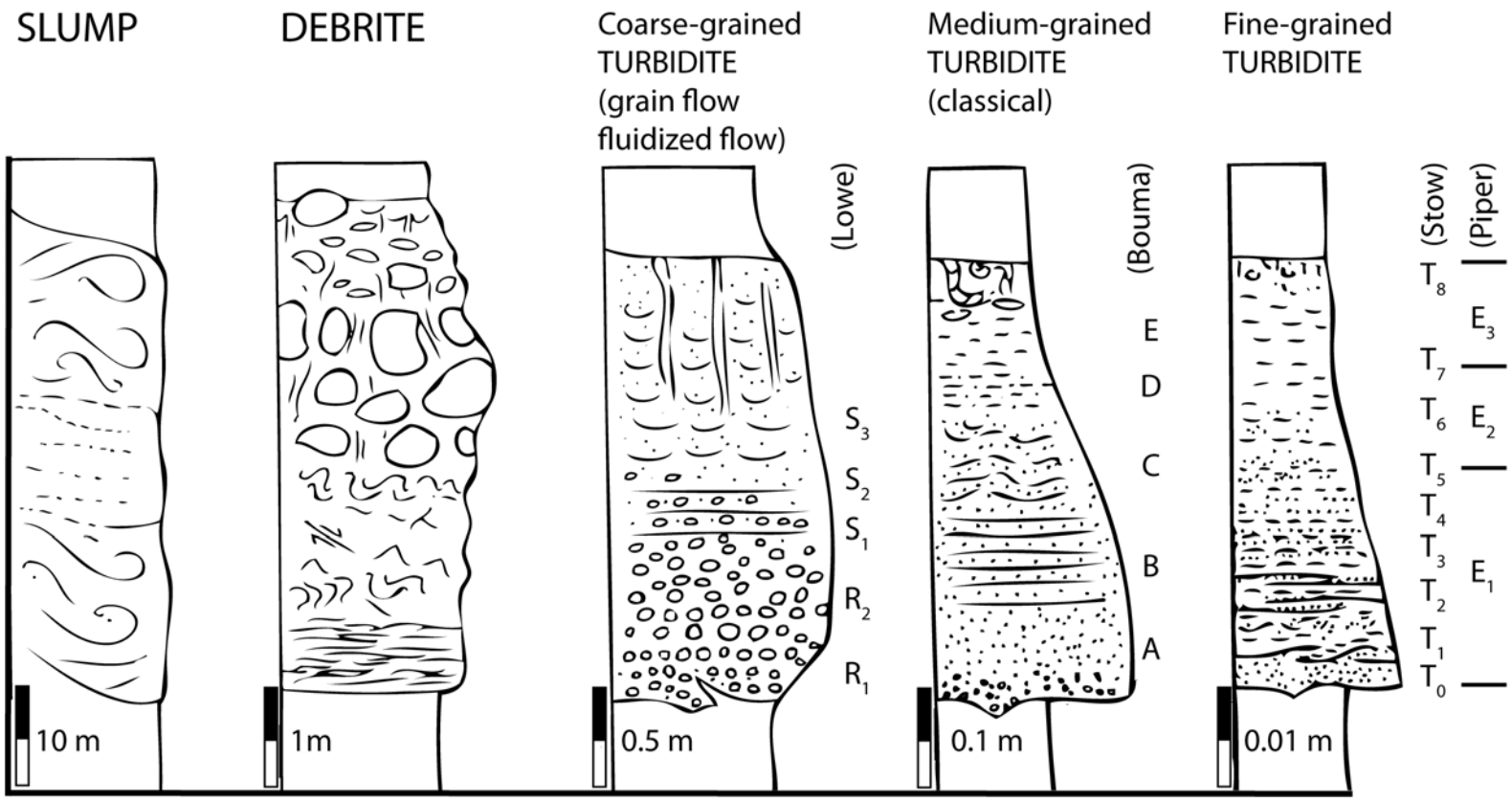


Figure 1.9: Deepwater clastic facies models for slumps, debrites and turbidites, showing the idealized sedimentary structure sequences. The scale bars give an indication only of typical unit thickness, which may vary widely in practice. Grain size increases to the left of each column (from Stow, 1986).

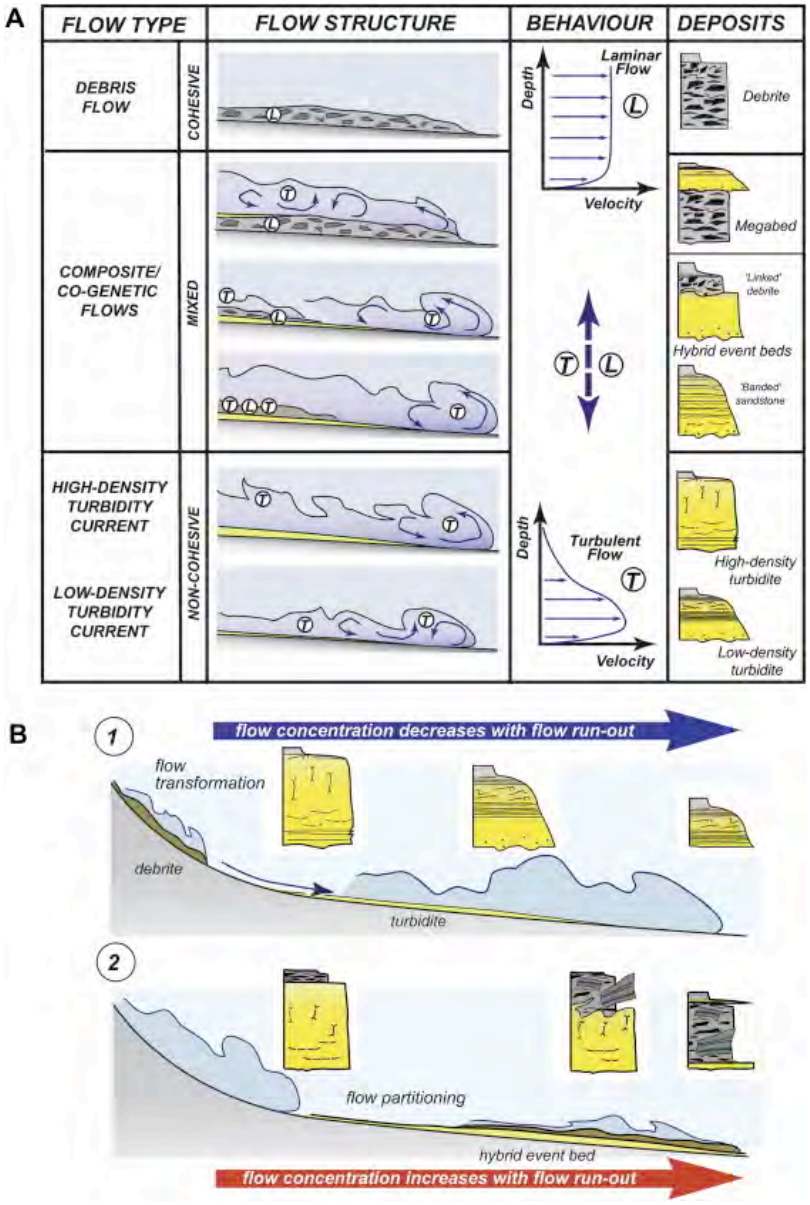


Figure 1.10: Summary of the link between subaqueous sediment gravity flow processes and their corresponding deposits (modified from Haughton et al., 2009). (A) Classification scheme for event beds emplaced by sediment gravity flows. (B) Whereas stand-alone debrites and turbidites dominate the record of many deep-water systems, other systems show a down-dip progression for non-cohesive flows to flows that are partitioned into sections with different rheology and the deposits of cohesive slow components increasingly dominating in distal parts.

## REFERENCES


Baas, J. H., W. D. McCaffrey, P. D. W. Haughton, and C. Choux, 2005, Coupling between suspended sediment distribution and turbulence structure in a laboratory turbidity current: J. Geophys. Res., v. 110, p. 20.

Badalini, G., B. Kneller, and C. D. Winker, 1999, Late Pleistocene Trinity-Brazos turbidite system; depositional processes and architectures in a ponded mini-basin system, Gulf of Mexico continental slope: AAPG Bulletin, v. 83, p. 1297-1298.

Bagnold, R.A., 1954, Experiments on gravity free dispersion of large solid spheres in a Newtonian fluid under stress, in Proceedings of Royal Society of London, Sem. A: Math and Phys, v. 225.

Baldschuhn, R., Binot, F., Frisch, U., and Kockel, F., 2001, Geotektonischer Atlas von Nordwest-Deutschland und dem Deutschen Nordsee-Sektor: Geologisches Jahrbuch, v. A153, 3 CD-ROM, 88 p.

Balkwill, H.R., and Legall, F.D., 1989, Whale Basin, offshore Newfoundland: Extension and salt diapirism, in Tankard, A.J., and Balkwill, H.R., eds., Extension Tectonics and stratigraphy of the North Atlantic margins: American Association of Petroleum Geologists Memoir 46, p. 233–245.

Barde, J.P., Gralla, P., Harwijanto, J., and Marsky, J., 2002, Exploration at the eastern edge of the Precaspian basin: Impact of data integration on Upper Permian and Triassic prospectivity: American Association of Petroleum Geologists Bulletin, v. 86, p. 399–415.

Beaubouef, R. T., and S. J. Friedmann, 2000, High resolution seismic/sequence stratigraphic framework for the evolution of Pleistocene intra slope basins, western Gulf of Mexico; depositional models and reservoir analogs: Program and Abstracts - Society of Economic Paleontologists. Gulf Coast Section. Research Conference, v. 20, p. 40-60.

Best, J. L., R. A. Kostaschuk, J. Peakall, P. V. Villard, and M. Franklin, 2005, Whole flow field dynamics and velocity pulsing within natural sediment-laden underflows: Geology [Boulder], v. 33, p. 765-768.

Booth, J. R., A. E. DuVernay, III, D. S. Pfeiffer, and M. J. Styzen, 2000, Sequence stratigraphic framework, depositional models, and stacking patterns of ponded and slope fan systems in the Auger Basin; central Gulf of Mexico slope: Program and Abstracts - Society of Economic Paleontologists. Gulf Coast Section. Research Conference, v. 20, p. 82-103.

Catuneanu, O., 2006, Principles of Sequence Stratigraphy: Developments in Sedimentology: Amsterdam, Elsevier.

Cobbold, P.R., Szatmari, P., Demercian, L.S., Coelho, D., and Rossello, E.A., 1995, Seismic and experimental evidence for thin-skinned horizontal shortening by

convergent radial gliding on evaporites, deep-water Santos Basin, Brazil, in Jackson, M.P.A., Roberts, D.G., and Snelson, S., Salt tectonics: A global perspective: American Association of Petroleum Geologists Memoir 65, p. 305–321.

Coe, A. L., D. W. J. Bosence, K. D. Church, S. S. Flint, J. A. Howell, and R. C. L. Wilson, 2003, The sedimentary record of sea-level change: United Kingdom, Cambridge University Press : Cambridge, United Kingdom.

Demercian, S., Szatmari, P., and Cobbold, P.R., 1993, Style and pattern of salt diapirs due to thin-skinned gravitational gliding, Campos and Santos Basins, offshore Brazil: Tectonophysics, v. 228, p. 393–433.

DeVay, J. C., D. Risch, E. D. Scott, and C. Thomas, 2000, A Mississippi-sourced middle Miocene (M4), fine-grained abyssal plain fan complex, northeastern Gulf of Mexico: AAPG Memoir, v. 72, p. 109-118.

Duval, B., Cramez, C., and Jackson, M.P.A., 1992, Raft tectonics in the Kwanza Basin, Angola: Marine and Petroleum Geology, v. 9, p. 389–404.

Dyson, I.A., 1999, The Beltana Diapir—A salt withdrawal minibasin in the northern Flinders Ranges: Mines and Energy South Australia Journal, v. 15, p. 40–46.

Ellison, T. H., and J. S. Turner, 1959, Turbidity entrainment in stratified flows: J. Fluid Mech., v. 6, p. 423-448.

Gray, T. E., J. Alexander, and M. R. Leeder, 2005, Quantifying velocity and turbulence structure in depositing sustained turbidity currents across breaks in slope: Sedimentology, v. 52, p. 467-488.

Hacker, J., P. F. Linden, and S. B. Dalziel, 1996, Mixing in lock-release gravity currents: Dyn. Atmos. Oceans, v. 24, p. 183-195.

Haughton, P., C. Davis, W. McCaffrey, and S. Barker, 2009, Hybrid sediment gravity flow deposits – Classification, origin and significance: Marine and Petroleum Geology, v. 26, p. 1900-1918.

Heaton, R.C., Jackson, M.P.A., Bamahmoud, M., and Nani, A.S.O., 1995, Superposed Neogene extension, contraction, and salt canopy emplacement in the Yemeni Red Sea, in Jackson, M.P.A., Roberts, D.G., and Snelson, S., eds., Salt tectonics: A global perspective: American Association of Petroleum Geologists Memoir 65, p. 333–351.

Holman, W. E., and S. S. Robertson, 1995, Field development, depositional model and production performance of the turbiditic 'J' Sands at Prospect Bullwinkle, Green Canyon 65 Field outer-shelf Gulf of Mexico: Annual Meeting Expanded Abstracts - American Association of Petroleum Geologists, v. 4, p. 42.

Hudec, M.R., and Jackson, M.P.A., 2004, Regional restoration across the Kwanza Basin, Angola: Salt tectonics triggered by repeated uplift of a metastable passive margin: American Association of Petroleum Geologists Bulletin, v. 88, p. 971–990,

Hudec, M. R., M. P. A. Jackson, and D. D. Schultz-Ela, 2009, The paradox of mini-basin subsidence into salt; clues to the evolution of crustal basins: Geological Society of America Bulletin, v. 121, p. 201-221.

Hudec, M.R., and May, S.R., 1998, The Courthouse syncline: A Gulf of Mexico–style minibasin exposed in the Paradox Basin, Utah [abs.]: American Association of Petroleum Geologists Annual Convention Official Program, v. 7, CD-ROM.

Ismail-Zadeh, A., Tsepelev, I., Talbot, C., and Korotkii, A., 2004, Three-dimensional forward and backward modeling of diapirism: Numerical approach and its applicability to the evolution of salt structures in the Pricaspian basin: Tectonophysics, v. 387, p. 81–103.

Jackson, M.P.A., and Harrison, J.C., 2006, An allochthonous salt canopy on Axel Heiberg Island, Sverdrup Basin, Arctic Canada: Geology, v. 34, no. 12, p. 1045–1048.

Jervey, M. T., 1988, Quantitative geological modeling of siliciclastic rock sequences and their seismic expression: Special Publication - Society of Economic Paleontologists and Mineralogists, v. 42, p. 47-69.

Kelts, K., and M. A. Arthur, 1981, Turbidites after ten years of deep-sea drilling; wringing out the mop?: Special Publication - Society of Economic Paleontologists and Mineralogists, p. 91-127.

Klaucke, I., R. Hesse, and W. B. F. Ryan, 1998, Seismic stratigraphy of the Northwest Atlantic Mid-Ocean Channel; growth pattern of a mid-ocean channel-levee complex: Marine and Petroleum Geology, v. 15, p. 575-585.

Kneller, B., and C. Buckee, 2000, The structure and fluid mechanics of turbidity currents; a review of some recent studies and their geological implications: Sedimentology, v. 47, p. 62-94.

Kneller, B., and W. McCaffrey, 1999, Depositional effects of flow nonuniformity and stratification within turbidity currents approaching a bounding slope; deflection, reflection, and facies variation: Journal of Sedimentary Research, v. 69, p. 980-991.

Lamb, M. P., T. Hickson, J. G. Marr, B. Sheets, C. Paola, and G. Parker, 2004, Surging versus continuous turbidity currents; flow dynamics and deposits in an experimental intraslope mini-basin: Journal of Sedimentary Research, v. 74, p. 148-155.

Lamb, M. P., H. Toniolo, and G. Parker, 2006, Trapping of sustained turbidity currents by intraslope mini-basins: Sedimentology, v. 53, p. 147-160.

Lane-Serff, G. F., L. M. Beal, and T. D. Hadfield, 1995, Gravity current flow over obstacles: J. Fluid Mech., v. 292, p. 39-53.

Leeder, M. R., T. E. Gray, and J. Alexander, 2005, Sediment suspension dynamics and a new criterion for the maintenance of turbulent suspensions: Sedimentology, v. 52, p. 683-691.

Liu, J. Y., and W. R. Bryant, 2000, Sea floor morphology and sediment paths of the northern Gulf of Mexico deepwater, in A. H. Bouma, and C. G. Stone, eds., Fine-grained turbidite systems, v. 72: Tulsa, OK, United States, American Association of Petroleum Geologists p. 13.

Madof, A. S., N. Christie-Blick, and M. A. Anders, 2009, Stratigraphic controls on a salt-withdrawal intraslope minibasin, north-central Green Canyon, Gulf of Mexico: Implications for misinterpreting sea level change: AAPG Bulletin, v. 93, p. 535-561.

Mahaffie, M.J., 1994, Reservoir classification for turbidite intervals at the Mars discovery, Mississippi Canyon 807, Gulf of Mexico, in Weimer, P., Bouma, A.H., and Perkins, B.F., eds., Submarine fans and turbidite systems—Sequence stratigraphy, reservoir architecture and production characteristics, 14th Annual Research Conference Proceedings: Houston, Texas, Society of Economic Paleontologists and Mineralogists, Gulf Coast Section, p. 233–244.

Marton, L.G., Tari, G.C., and Lehmann, C.T., 2000, Evolution of the Angolan passive margin, West Africa, with emphasis on post-salt structural styles, in Mohriak, W.U., and Talwani, M., eds., Atlantic rifts and continental margins: American Geophysical Union Geophysical Monograph 115, p. 129–149.

Matthews, W.J., Hampson, G.J., Trudgill, B.D., and Underhill, J.R., 2007, Controls on fluiviolacustrine reservoir distribution and architecture in passive salt-diapir provinces: insights from outcrop analogs: American Association of Petroleum Geologists Bulletin, v. 91, p. 1367–1403.

McGee, D.T., Bilinski, P.W., Gary, P.S., Pfeiffer, D.S., and Sheiman, J.L., 1994, Geologic models and reservoir geometries of Auger Field, deepwater Gulf of Mexico, in Weimer, P., Bouma, A.H., and Perkins, B.F., eds., Submarine fans and turbidite systems—Sequence stratigraphy, reservoir architecture and production characteristics, 14th Annual Research Conference Proceedings: Houston, Texas, Society of Economic Paleontologists and Mineralogists, Gulf Coast Section, p. 245–256.

Meiburg, E., and B. Kneller, 2009, Turbidity currents and their deposits: Annual Review of Fluid Mechanics, v. 42, p. 135-156.

Middleton, G. V., 1993, Sediment deposition from turbidity currents: Annual Review of Earth and Planetary Sciences, v. 21, p. 89-114.

Mohr, M., Kukla, P.A., Urai, J.L., and Bresser, G., 2005, Multiphase salt tectonic evolution in NW Germany: Seismic interpretation and retro-deformation: International Journal of Earth Sciences, v. 94, p. 917– 940.

Montoya, P., and M. R. Hudec, 2007, Active salt tectonics and its effect on the internal architecture and connectivity between mini-basins near the Sigsbee Escarpment, Gulf of Mexico: Abstracts: Annual Meeting - American Association of Petroleum Geologists, v. 2007, p. 96.

Moscardelli, L., L. Wood, and P. Mann, 2006, Mass-transport complexes and associated processes in the offshore area of Trinidad and Venezuela: AAPG Bulletin, v. 90, p. 1059-1088.

Muck, M. T., and M. B. Underwood, 1990, Upslope flow of turbidity currents: A comparison among field observations, theory, and laboratory models: Geology, v. 18, p. 54-57.

Mulder, T., and J. Alexander, 2001, The physical character of subaqueous sedimentary density flows and their deposits: Sedimentology, v. 48, p. 269-299.

Mutti, E., and W. R. Normark, 1991, An integrated approach to the study of turbidite systems Frontiers in sedimentary geology: United States, Springer-Verlag : New York, NY, United States, p. 75-106.

Normark, W. R., 1989, Observed parameters for turbidity-current flow in channels, Reserve Fan, Lake Superior: Journal of Sedimentary Petrology, v. 59, p. 423-431.

Normark, W. R., G. R. Hess, and F. N. Spiess, 1978, Mapping of small scale (outcrop-size) sedimentological features on modern submarine fans: Proceedings - Offshore Technology Conference, p. 593-598.

Parker, G., M. Garcia, Y. Fukushima, and W. Yu, 1987, Experiments on turbidity currents over an erodible bed: Journal of Hydraulic Research = Journal de Recherches Hydrauliques, v. 25, p. 123-147.

Parsons, J. D., and M. H. Garcia, 1998, Similarity of gravity current fronts: Physics of Fluids, v. 10, p. 3209-3213.

Piper, D. J. W., 1978, Turbidite muds and silts on deep sea fans and abyssal plains, *in* D. J. Stanley, and G. Kelling, eds., Sedimentation in submarine canyons, fans and trenches: Stroudsburg, PA, Dowden, Hutchinson and Ross, p. 163-175.

Pirmez, C., and J. Imran, 2003, Reconstruction of turbidity currents in Amazon Channel: Marine and Petroleum Geology, v. 20, p. 823-849.

Posamentier, H. W., M. T. Jervey, and P. R. Vail, 1988, Eustatic controls on clastic deposition; I, Conceptual framework: Special Publication - Society of Economic Paleontologists and Mineralogists, v. 42, p. 109-124.

Posamentier, H. W., and P. R. Vail, 1988, Eustatic controls on clastic deposition; II, Sequence and systems tract models: Special Publication - Society of Economic Paleontologists and Mineralogists, v. 42, p. 125-154.

Prather, B. E., 2000, Calibration and visualization of depositional process models for above-grade slopes; a case study from the Gulf of Mexico, Marine and Petroleum Geology, United Kingdom, Elsevier : Oxford, United Kingdom, p. 619-638.

Prather, B. E., 2003, Controls on reservoir distribution, architecture and stratigraphic trapping in slope settings, Marine and Petroleum Geology, United Kingdom, Elsevier : Oxford, United Kingdom, p. 529-545.

Prather, B.E., Booth, J.R., Steffens, G.S., and Craig, P.A., 1998, Classification, lithologic calibration, and stratigraphic succession of seismic facies of intraslope basins, deep-water Gulf of Mexico: American Association of Petroleum Geologists Bulletin, v. 82, p. 701– 728.

Pratson, L. F., and W. B. F. Ryan, 1994, Pliocene to Recent infilling and subsidence of intraslope basins offshore Louisiana: AAPG Bulletin, v. 78, p. 1483-1506.

Prochnow, S.J., Nordt, L.C., Atchley, S.C., Hudec, M., and Boucher, T.E., 2005, Triassic paleosol catenas associated with a salt-withdrawal minibasin in southeastern Utah, U.S.A.: Rocky Mountain Geology, v. 40, p. 25–49

Reading, H. G., and M. Richards, 1994, Turbidite systems in deep-water basin margins classified by grain size and feeder system: AAPG Bulletin, v. 78, p. 792-822.

Roberts, M.J., Metzgar, C.R., Liu, J., and Lim, S.J., 2004, Regional assessment of salt weld timing, Campos Basin, Brazil, in Post, P.J., Olson, D.L., Lyons, K.T., Palmes, S.L., Harrison, P.F., and Rosen, N.C., eds., Salt-sediment interactions and hydrocarbon prospectivity: Concepts, applications, and case studies for the 21st Century, 24th Annual Research Conference Proceedings: Houston, Texas, Society of Economic Paleontologist and Mineralogists, Gulf Coast Section, p. 371–389.

Ross, W. C., B. A. Halliwell, J. A. May, D. E. Watts, and J. P. M. Syvitski, 1994, Slope readjustment; a new model for the development of submarine fans and aprons: Geology [Boulder], v. 22, p. 511-514.

Rottman, J. W., J. E. Simpson, J. C. R. Hunt, and R. E. Britter, 1985, Unsteady gravity current flows over obstacles: Some observations and analysis related to the phase II trials: Journal of Hazardous Materials, v. 11, p. 325-340.

Rowan, M.G., and Vendeville, B.C., 2006, Foldbelts with early salt withdrawal and diapirism: Physical model and examples from the northern Gulf of Mexico and the Flinders Ranges, Australia: Marine and Petroleum Geology, v. 23, p. 871–891.

Sawyer, D.E., Flemings, P.B., Shipp, R.C., and Winker, C.D., 2007, Seismic geomorphology, lithology, and evolution of the late Pleistocene Mars-Ursa

turbidite region, Mississippi Canyon area, northern Gulf of Mexico: American Association of Petroleum Geologists Bulletin, v. 91, p. 215–234.

Stow, D. A. V., and G. Shanmugam, 1980, Sequence of structures in fine-grained turbidites; comparison of Recent deep-sea and ancient flysch sediments: Sedimentary Geology, v. 25, p. 23-42.

Shimeld, J., 2004, A comparison of salt tectonic subprovinces beneath the Scotian slope and Laurentian fan, in Post, P.J., Olson, D.L., Lyons, K.T., Palmes, S.L., Harrison, P.F., and Rosen, N.C., eds., Salt-sediment interactions and hydrocarbon prospectivity: Concepts, applications, and case studies for the 21st Century, 24th Annual Research Conference Proceedings: Houston, Texas, Society of Economic Paleontologist and Mineralogists, Gulf Coast Section, p. 502–532.

Shoup, R. C., and J. F. Karlo, 1999, Classification of syndepositional structural systems, northern Gulf of Mexico: AAPG Bulletin, v. 83, p. 1339-1340.

Sinclair, H. D., and M. Tomasso, 2002, Depositional evolution of confined turbidite basins: Journal of Sedimentary Research, v. 72, p. 451-456.

Stacey, M. W., and A. J. Brown, 1988, Vertical structure of density and turbidity currents: Theory and observations: J. Geophys. Res., v. 93, p. 3528-42.

Steffens, G. S., E. K. Biegert, H. Scott Sumner, and D. Bird, 2003, Quantitative bathymetric analyses of selected deepwater siliciclastic margins: receiving basin configurations for deepwater fan systems: Marine and Petroleum Geology, v. 20, p. 547-561.

Stewart, S.A., and Clark, J.A., 1999, Impact of salt on the structure of the central North Sea hydrocarbon fairways, in Fleet, A.J., and Boldy, S.A.R., eds., Petroleum geology of northwest Europe: Proceedings of the 5th Conference: London, Geological Society of London, p. 179–200.

Stow, D. A. V., 1986, Deep Clastic Seas, *in* H. G. Reading, ed., Sedimentary Environments and Facies, Blackwell Scientific Publications, p. 399-444.

Stow, D. A. V., and A. J. Bowen, 1980, A physical model for the transport and sorting of fine-grained sediment by turbidity currents: Sedimentology, v. 27, p. 31-46.

Sullivan, M.D., Foreman, J.L., Jennette, D.C., Stern, D., Jensen, G.N., and Goulding, F.J., 2004, An integrated approach to characterization and modeling of deepwater reservoirs, Diana field, western Gulf of Mexico, in Grammer, G.M., Harris, P.M., and Eberli, G.P., eds., Integration of outcrop and modern analogs in reservoir modeling: American Association of Petroleum Geologists Memoir 80, p. 215–234.

Sumner, H. S., B. A. Robison, W. K. Dirks, and J. C. Holliday, 1991, Structural style of salt/mini-basin systems; lower shelf and upper slope, central offshore Louisiana: Transactions - Gulf Coast Association of Geological Societies, v. 41, p. 582-582.

Tari, G., Molnar, J., and Ashton, P., 2003, Examples of salt tectonics from West Africa: A comparative approach, in Arthur, T.J., MacGregor, D.S., and Cameron, N.R., eds., Petroleum Geology of Africa: New themes and developing technologies: Geological Society of London Special Publication 207, p. 85–104.

Vail, P. R., R. M. Mitchum, Jr., and S. Thompson, III, 1977, Seismic stratigraphy and global changes of sea level; Part 3, Relative changes of sea level from coastal onlap: Memoir - American Association of Petroleum Geologists, p. 63-81.

Volozh, Y., Talbot, C., and Ismail-Zadeh, A., 2003, Salt structures and hydrocarbons in the Pricaspian basin: American Association of Petroleum Geologists Bulletin, v. 87, p. 313–334.

Winker, C. D., 1996, High-resolution seismic stratiraphy of a late Pleistocene submarine fan ponded by salt-withdrawal minibasins on the Gulf of Mexico continental slope: Proceedings - Offshore Technology Conference, v. 28, Vol. 1, p. 619-628.

Winker, C.D., and Booth, J.R., 2000, Sedimentary dynamics of the salt-dominated continental slope, Gulf of Mexico: Integration of observations from the seafloor, near-surface, and deep subsurface, in Weimer, P., Slatt, R.M., Coleman, J., Rossen, N.C., Nelson, H., Bouma, A.H., Styzen, M.J., and Lawrence, D.T., eds., Deepwater reservoirs of the world, 20th Annual Research Conference Proceedings: Houston, Texas, Society of Economic Paleontologists and Mineralogists, Gulf Coast Section, p. 1059–1086.

Wood, L. J., S. Sullivan, and P. Mann, 2004, Influence of mobile shales in the creation of successful hydrocarbon basins: Program and Abstracts - Society of Economic Paleontologists. Gulf Coast Section. Research Conference, v. 24, p. 38-38.

Wood, L. J., 2006, Source-to-sink sediment movements in structurally complex setting: the role of gateway basins (abs.): American Association of Petroleum Geologists Annual Convention, v. 15, p. 115.

Worrall, D.M., and Snelson, S., 1989, Evolution of the northern Gulf of Mexico, with emphasis on Cenozoic growth faulting and the role of salt, in Bally, A., and Palmer, A., eds., The geology of North America—An overview: Boulder, Colorado, Geological Society of America, v. A, p. 97–138.

# Chapter 2: Data and Methods

## Overview

To meet the study objectives, this research comprises three phases: (1) examining the current state of the literature that explain how minibasins fill relative to the topography created by the displacement of mobile salt substrate; (2) physically modeling flow behavior under conditions of varying topographic relief; and (3) examining deepwater fill in salt withdrawal minibasins from the Gulf of Mexico shelf and the distal Morocco shelf. Observations from each phase will be integrated to determine the influence of minibasin topography on sediment distribution and the significance of the input delivery systems relative to the minibasin position on the slope. Implications for predicting potential deposit facies distribution to assess hydrocarbon reservoir potential within minibasin provinces are also discussed.

## Literature Review

In the first phase, an extensive literature review outlines key studies that focus on confinement as it relates to deep-water depositional systems in minibasin settings and the implications for interpreting the sediment gravity flow processes from which they originate.

## Experimental Modeling

The second phase of experimental modeling flow behavior under conditions of varying topographic relief incorporates an investigation of turbidite flows into a model minibasin through varying conditions of controlled subsidence and sediment supply in a simplified configuration (Fig. 2.1). Recent field studies (e.g. Badalini et al., 2000; Beaubouef and Friedman, 2000; Pirmez et al., 2000) have revealed much information

about the processes by which GOM minibasins fill with sediment. To make further strides in this area, more knowledge is needed of the 3-D flow dynamics of turbidity currents and how they deposit sediment in a confined 3-D space.Since the direct observation and documentation of turbidity currents in the field has remained difficult, physical modeling of turbidity currents fill this gap in knowledge. Physical laboratory experiments also allow the study of steady states and responses to changes in a single variable that would otherwise be difficult to control in natural systems.

**Previous Work**

A literature search shows that experimental modeling of turbidity currents into minibasins topography has been almost exclusively two-dimensional (2-D) (e.g. Toniolo, 2002; Lamb et al., 2004). Although these 2-D experiments have been useful in quantifying flow processes and modes of deposition in minibasin topography, there are two important variables that limit the applicability of these experimental results. These variables are: (1) the lack of a dynamic basin floor (varying the topography and geometry of the accommodation space) and (2) the 2-D nature of the experiments limit the integration of affects from the third dimension such as lateral flow spreading (and hence, the establishment of 3-D current vorticity fields), compensational stacking of depositional lobes, and the self-formation of channels.

Violet et al., (2005) attempted to overcome the 2-D restrictions of most studies by initiating an experimental laboratory study of a 3-D minibasin undergoing subsidence. Three types of turbidity currents were studied, and include: 1) continuous-feed; being currents of relatively long durations (> 30 minutes) 2) small-pulse; being currents of relatively short durations (< 2 minutes) and 3) large-pulse events; being of short durations, but longer then short pulse events (2-4 minutes). The researchers observed that

continuous flow events produced depocenters that were more proximally situated than the pulse events. Additionally, continuous flow events tended to drape topography more broadly than surge events. The depocenters of events did not coincide with the zone of maximum subsidence in the minibasin. Violet et al., (2005) compared the morphology and pattern of depositional stratigraphy in their experimental basins to that documented in Basin 4 from the Brazos-Trinity intraslope basin system of the Gulf of Mexico (Beaubeouf et al., 2003). While the successful attempt of Violet et al. (2005) yielded valuable observations on the quantitative link between turbidity current flow dynamics and deposit geometry, three-dimensional stratal architecture within an experimental minibasin still remained poorly understood.

**Data and Methods**

The experiments described in the research documented in the following chapters were performed at the University of Texas Morphodynamics Lab (UTML) facility at the J.J. Pickle Research Campus, University of Texas of Austin (Fig. 2.1). The flume is a rectangular structure with dimensions of 8 m (length; L) x 4 m (width; W) x 2 m (height; H). Water and sediment were fed into the basin from a constant head tank using scaled-process parameters. Both processes and deposits were analyzed using a series of measuring and recording equipment that capture their dynamics and give insight into the link between them. The experimental minibasins were set up on a 10-degree ramp within the deep basin flume to overcome the increased friction in the experimental submerged environment (*sensu* Paola et al., 2009).

Two series of experiments were conducted in this research; each modeling scaled turbidity currents into basins with different structural configurations. The spatial characteristics of the experimental basin for each series experiments was scaled based on

morphometric data collected by Pratson and Ryan (1994) of intraslope basins of the present day seafloor of the Gulf of Mexico (Table 2.1). These data provided some relative ratios of width, depth and length for minibasins subsiding over salt. Although it was impossible to simulate the dimensions of a real-world minibasin, it was the desire to keep the relative ratios of dimensions similar to real-world settings. In the first experiment (Series 1), a series of scaled unconfined turbidity current flows was issued into a deep 3-D basin to investigate the evolving character of the deposits as a basin fills under fixed input current conditions. In the second series (Series 2), an incremental subsidence and fill approach is implemented to investigate the effect of varying degrees of 3-D confining topography and scaled turbidity currents of fixed dimensions. Continuous (long-duration) unconfined flows were modeled in Series 1 experiments while both continuous and surge (short-duration) flows were modeled throughout the duration of Series 2. An extensive dataset of bathymetric scans, current velocity, current concentration and grain size data were collected to characterize the dynamics of the turbidity currents and the resulting deposits.

In the analysis of minibasin fill, stratigraphic geometries on various scales were used to calculate a 2-D Ponding index. The principle of mass conservation was applied to experimental turbidity currents to investigate the sediment trapping in minibasins.

***Series 1 Experiments***

For Series 1 experiments, the submerged bed was allowed to subside to accentuate the bowl-shaped pattern of the initial basin, representing a configuration of maximum subsidence (Fig. 2.2). The results of these experiments are documented in Chapter 4. Subsidence was facilitated by controlled drainage of a water-filled plastic bladder that was packed in the submerged gravel basement. The gravel basement was

first made sufficiently thick to allow the maximum subsidence planned during the experiment. The withdrawal of water from the bladder allowed the basement to deform on a 10-degree slope, and the resulting cross-sectional shape of the basin was asymmetric due to the effect of gravity on the slope (Fig. 2.2). The dimensions of the basin measured 50 cm (L) x 50 cm (W) x 12cm (H). The 10-degree slope is a universal application applied to overcome the internal frictional effects of experimental flows (e.g. Toniolo et al., 2001; 2002; Violet et al., 2005).

Eighteen unconfined turbidity current flow events were issued into the Series 1 minibasin, all with an average inlet discharge of 200 $cm^3/s$, lasting 60 minutes. Characteristic current properties of these flows are shown in Table 2.2, and characteristic velocity and concentration profiles are shown in Figure 2.3. Following each event, the sediment was allowed to settle for 180 minutes, then laser mapping of each bed was performed. The map resolution produced by the laser was 2 mm (streamwise) x 2mm (cross-streamwise) x 200 μm (vertical). One unintended aspect of the run was the creation of bubble escape "craters and pockmarks" within the basin area due to air escape from the gravel basement. The spatial coverage of these features, however, was insignificant relative to the overall basin dimensions and turbidity current dynamics. There was no method to alleviate these features once the first series of experiments was initiated, but a plastic membrane was put between the gravel basement and top sediment layer for Series 2 experiments to avoid air escape while the experiment was running.

***Series 2 Experiments***

Series 2 experiments comprised three basin configurations into which currents of fixed spatial properties were issued (Fig. 2.4). Unlike Series 1, current durations varied among configurations. The results of these experiments are documented in Chapter 5.

The main objective of this series was to investigate the influence of basin confinement on the deposit (geometry, architecture, grain size distribution) and the current flow field (within and around the basin). For all configurations, a confining inlet channel guided the turbidity current into the basin. Characteristic current properties for Series 2 experiments are shown in Table 2.2, and characteristic velocity and concentration profiles are shown in Figure 2.3.

The first basin configuration (Config. 1) at maximum (initial) subsidence measured 35 cm (L) x 35 cm (W) x 3.5 cm (D), and represents the smallest relative current width to basin width ratio (Fig. 2.4). Five continuous flow events (events 1-5) of 15 minutes each were issued into Config. 1 basin. During each event, near-bed current velocities were recorded using ADV equipment along a centerline (dip-oriented) transect. Like the procedure described for Series 1, the sediment was allowed to settle for 180 minutes following each event in the series, and laser mapping of each bed was performed. After this phase of experiments were completed, the Config. 1 basin was then subsided over a period of five hours to form the second structural configuration (Config. 2).

The Config. 2 initial basin dimensions at maximum subsidence (Fig. 2.4) measured 55 cm (W) x 55 cm (L) x 6 cm (D). Nine continuous flows (events 6–14) were issued into the basin, their durations ranging from 15 minutes to 60 minutes. Near-bed current velocities were also recorded for each event using ADV equipment. Longer experiment durations facilitated the collection of more current velocity data beyond the centerline axis. Turbidity current profile data were also collected in certain experiments using ADV equipment. The procedure of controlled subsidence was then repeated to create the third structural configuration (Config. 3).

The initial basin dimensions for Config. 3 (Fig. 2.4) represent both the largest structural configuration and the highest relative current width to basin width ratio for

Series 2 experiments. The basin's dimensions measured 60 cm (L) x 65 cm (W) x 8 cm (H). Flows of varying durations were issued into the experimental basin, and included five surge events lasting 15 seconds each; and 25 continuous events with durations ranging from 15 to 120 minutes. An extensive database of current velocity data was collected using both 3-D ADV and 3-D Profiling Acoustic Doppler Velocimeter (PADV) equipment. Following the experiment, the flume was drained over a two-week period and the deposit was allowed to dry for an additional week. A hollow, thin, metal rod was submerged in liquid nitrogen, and pushed into the drained and dried surface to sample the deposit. Each core sample was divided vertically into proportional thirds. Each 1/3$^{rd}$ sample was then processed using a Laser Particle Size Analyzer (LPSA) to determine grain size distributions within that portion of the deposit.

In the analysis of the data collected, individual and cumulative deposits captured within the experimental minibasin were characterized by using indices that determine the geometry of the deposit relative to the basin's structural configuration (e.g. ponding index and taper rate) and the ability for the basin to trap sediment from incoming turbidity currents (e.g. capture efficiency). Coring and sectioning the final deposit provided a database of sediment grain size distributions captured in the basin. These data were quantitatively analyzed to determine relationships among turbidity current characteristics and the resulting preserved bed geometries, as well as the nature of stratigraphic terminations in the basin fill as it relates to grain size distribution.

## LOBSTER AREA, EWING BANK 873, GULF OF MEXICO

### Regional Setting

Formation of the Gulf of Mexico basin was initiated in the late Middle to early Late Jurassic as a consequence of continental rifting, crustal thinning, and subsequent oceanic spreading associated with the breakup of the super-continent Pangea (Pindell and Dewey, 1982; Salvador, 1987). During the Middle to Late Jurassic, up to several kilometers of salt were deposited as a result of the evaporation of sea water in restricted embayments (Diegel et al., 1995). The accumulation of thick Mesozoic- and Cenozoic-age sediments subsequently mobilized the salt. Subsequent Oligocene-to-Miocene time differential loading of the upper- to mid-slope salt massif by deepwater sediments formed the complex array of intraslope minibasins located beneath the present continental slope (Prather, 2000). These minibasins exhibits pronounced paleo-topographic relief, circular to elliptical map view and simple symmetric to asymmetric internal structure (Prather et al., 1998).

The northern deep Gulf of Mexico is a geologically complex province consisting of Neogene-age intraslope minibasins created by sediment loading onto and evacuation of allochthonous salt (Villamil et al., 1998). Sedimentary fill in the minibasins consists of bathyal turbidite systems with highly variable facies distribution related to channelization, mass wasting and individual lobe deposition. Neogene-age turbidite systems of the northern Gulf of Mexico basin form the primary reservoirs in the deepwater and subsalt hydrocarbon plays (Weimer et al., 1998). Several publications have described the stratigraphic variations or the three-dimensional geometries of these turbidite systems in detail (e.g. Beaubouef et al., 1999; Sullivan et al., 2000); hence, an understanding of the stratigraphic characteristics of the producing sands is important for

successful deepwater energy exploration in the Gulf of Mexico basin and similar basins worldwide. Intrinsic to this understanding is the topography created by underlying autochthonous and allochthonous salt. The regional stratigraphic setting beyond the study area is summarized by Weimer et al., (1998) and the structural setting by Rowan (1995).

Approximately 50% of the drainage area of North America delivered sediment to the northern Gulf of Mexico (GOM) region during the Pliocene and Pleistocene (Fig. 2.5; Pulham, 1993; Galloway, 2011). Up to 7600 m (25,000 ft) of sediments accumulated in northern Green Canyon and Ewing Bank areas during the past 5.5 m.y., indicating relatively high rates of deposition (Villamil et al., 1998). By comparison, Hudec et al., (2009) have reported subsidence rates exceeding 1 km per million years for certain GOM minibasins. Sediment deposition occurred primarily through the action of turbidite systems on the lower to upper slope for most of the Pliocene and Pleistocene, although the influence of halokinesis in remobilizing sediment and supplying it to distally located minibasins have been found to be volumetrically significant (e.g. Giles and Lawton, 2002; Rowan et al., 2003). Galloway et al., (1998; 2000; 2004; 2005; 2008; and 2011) show that there were significant shifts in the shallow marine depocenters that fed the slope turbidite systems during the Pliocene and Pleistocene, thus affecting local rates of deposition, as well as influencing the nature of sediments delivered to the basin. One such Pliocene turbidite system is documented in the Lobster Field of the Gulf of Mexico basin.

**The Lobster Field**

The Lobster Field (Lobster) was first discovered in 1991 by Marathon Oil Company, and is located in Ewing Bank 873 (EW 873), 130 miles southwest of New Orleans in 235 m (775 ft) of water (Fig. 2.6). The Lobster minibasin is shelf proximal and was subject to eustatic influences during its evolutionary development. The producing

field contains all the depositional elements of a confined, deepwater basin including lobes, mass failure deposits and confined channel deposits composed of axis, off-axis, channel margin sediments and channel drapes. Structural elements include salt diapirism, normal and reactivated counter-normal faulting. The field is a prolific hydrocarbon producer where stratigraphic trapping of reservoirs predominates.

To date, the Lobster Field has cumulatively produced an excess of 137 million barrels of oil equivalent (MMBOE), with total reserves estimated at 181 MMBOE. Since the discovery of the Lobster Field, Marathon drilled four infill wells in the middle Pliocene *Buliminella 1 (Bul. 1)* sandstones due to their hydrocarbon resource capacity. As a result, subsurface well-log and seismic data made available for this study provide constraints for lithological interpretations.

**Data and Methods**

This integrated subsurface analysis of the Lobster minibasin dataset from Ewing Bank 873, Gulf of Mexico, incorporates a 3-D seismic dataset and multiple well logs from 24 wells (some with sidetracks). The dataset covers an area of 177 $km^2$ (68.2 $mi^2$), and is located 210 km (130 mi) southwest of New Orleans (Fig. 2.6). The legacy 3-D seismic dataset is provided through the *Research Partnership to Secure Energy for America (RPSEA),* a joint industry-academic effort. Permissions were granted by Petroleum Geo-Services (PGS) and Marathon Oil to work on the data and show results of this work. Although a more recent, higher-resolution dataset exists, it was not made available for this study.

The wells drilled in the area are linked to a 30-slot platform, which was set in 1994. The platform is located ~1.3 km (0.8 mi) southeast from the center of the seismic dataset (Figure 2.7). The minibasin's clastic sedimentary fill within the 3-D seismic data

extends to a two-way travel time (TWT) depth of 5 seconds, while the deepest fill within the minibasin penetrated by wells has been recorded at 5195 m (17,045 ft). The sample rate of the 3-D seismic data is 4 milliseconds. Two major allochthonous salt bodies and laterally extensive welds in the dataset are responsible for poor imaging and seismic resolution degradation at depth.

Usually, seismic tools are used for check shot surveys to obtain a depth-travel time relation and zero-offset vertical seismic profile (VSP) experiments to obtain seismograms at the site. These seismograms are used to correlate well depths with the seismic data. Additionally, the depth-travel time relation can be derived from the sonic velocity log which together with the density log and seismic source wavelet, combine to make a synthetic seismogram. In the case of this data, time-depth tables have been provided for each well, which positions the well logs relatively accurately in the two-way travel time space of the 3-D seismic volume.

The most useful logs for lithological discrimination are resistivity, P wave velocity, and gamma ray logs because they have a greater depth of investigation and are the least sensitive to poor borehole conditions. However, of the 40 wells present in the dataset only 22 contain gamma ray well-log data, while none contain resistivity, velocity or velocity-log data. Gamma-ray well log data are therefore the principal lithological discriminator, to which seismic reflection amplitudes are compared to determine the degree of lithological continuity beyond the borehole.

**Previous Work**

Rowan et al. (1998) integrated sequence stratigraphic interpretations of 2-D seismic and well data from northern Green Canyon and Ewing bank to evaluate how salt deformation influenced the distribution of Pliocene-Pleistocene facies in time and space.

Their results show that both structural and sedimentological variables influenced lithofacies development, while external factors influenced the volume and type of clastic input to the area. They interpreted that local factors, including the thickness of underlying salt, influenced minibasin evolution on three scales: 1) a broad transition from sand-rich ponded settings to shale-dominated bypass settings during the Plio-Pleistocene; 2) fluctuations in input conditions over periods of several sequences that created highly variable stacking patterns; and 3) a progression from ponded to bypass facies within individual sea level cycles.

Weimer et al., (1998) investigated the sequence stratigraphy of the Pliocene-Pleistocene turbidite systems of the Northern Green Canyon and Ewing Bank areas in more detail, integrating 2-D seismic lines, 185 well logs and biostratigraphy from 180 wells. Their geologic evolution of the area is indicated by the seismic and geologic facies, depositional rates, nature of turbidite systems and sand content. Results from their analysis show that basin fans were deposited at the base of Pliocene sequences and that their geometry and nature were greatly influenced by salt topography. In Pleistocene sequences, salt withdrawal rates were significantly lower, and smaller, thinner fans were deposited.

Burk et al., (1999) describe the geological evolution of the Lobster area, partly using data made available to this study (Fig. 2.8). Reconstruction of the basin formation was done through the use of regional 2-D seismic lines, high-resolution 3-D seismic data and well penetration data through the life of exploration and early development. They suggest that a massive salt canopy was emplaced at approximately the end of the Miocene. Onto the salt canopy, large basin floor fans were deposited in the early Pliocene in a moderately confined structural setting. During the middle Pliocene, basin floor fan deposition into the Lobster minibasin included the major *Bul. 1* reservoirs, as well as

other time-equivalent reservoirs identified from paleontological data. Basin loading resulted in the development of salt highs and increased the degree of structural confinement of the minibasin. The salt highs developed on the southeastern edge of the basin blocked sand flow into the next down dip basin. Extensive basin rim normal and tear-faulting then began to develop. The final phase of middle Pliocene deposition was a channel/overbank complex on the eastern side of the *Bul. 1* reservoirs. Well logs show that sand delivery to the basin soon dwindled and isolated channel/ overbank systems prevailed. As the degree of structural confinement increased, faulting accelerated and welding at the base of the basin may have occurred during the late Pliocene. At the end of the late Pliocene, a major depositional hiatus occurred, and 60 m (200 ft) of marl accumulated over a period of approximately 1.9 million years. During the Pleistocene, the sediment source shifted from northwest to northeast. Large canyon systems were responsible for delivering sediment load to more distal locations on the slope. Graben fault systems that are still presently active are suggested to relate to salt highs during the Pleistocene.

## SAFI HAUTE MER AREA, OFFSHORE MOROCCO

### Geologic Setting

The offshore basins of Morocco's Atlantic margin represent the westernmost exploration frontier area in North Africa (Tari et al., 2000). Morocco contains the largest offshore exploration area in North Africa, covering an area over 300,000 $km^2$ (115, 831 $mi^2$) on both the continental margin and deepwater provinces. The study area is located in the northern offshore portion of the Essaouira Basin, also referred to as the Safi sub-basin (Fig. 2.9; Tari et al., 2003). The physiographic setting of the study area puts it the base of

the Moroccan continental rise, near the western termination of the Atlas fold-belt. The width of the Moroccan continental shelf ranges between 40 to 60 km (25 to 37 mi), and the shelf break usually occurs at water depths of 110 to 150 m (361 to 492 ft) (Seibold, 1982). The complex geological history of the margin has been responsible for several large-scale events, all of which include the mobilization of Jurassic salt, regional-scale mass-wasting deposits and reworking of strata. The resulting morphology makes the Moroccan continental margin topographically complex and influences the sedimentary processes that occur in the study area. The continental slope exhibits a range in gradient between 1-6 degrees, and transitions into the continental rise at water depths of 1500 to 4000 m (4921 to 13123 ft) (Seibold, 1982).

Prominent bathymetric features near the study area include the Essaouira Canyon immediately north of the 3-D seismic survey used in this study, the Tafelney Plateau to the southeast, and the Agadir Canyon to the south. The Essaouira Canyon empties onto the Seine Abyssal Plain and is one of the many canyons dissecting the continental slope. Because of its proximity to the study area, the Essaouira Canyon has likely transported sediments eroded from the survey area. The Tafelney Plateau is interpreted as a high-relief accommodation zone inherited from the rifting stage of the central Atlantic basin (Tari et al., 2002). The topographic high has a tectonic history involving Mesozoic extension, Late Cretaceous inversion and Late Tertiary doming (Fig. 2.10; Hedley and Warburton, 1999). The Agadir canyon extends from the shelf break to the upper rise to a water depth of at least 3200 m and separates the Tafelney Plateau from the North Tarfaya margin to the south (Seibold, 1982).

## Data

The 3-D seismic dataset used for this study is the result of re-processing two overlapping surveys in the offshore Safi Haute Mer (SHM) block, offshore Morocco. The seismic data is industry-collected and processed data, and has been provided by Vanco Energy of Morocco. One survey covering 3025 $km^2$ (1168 $mi^2$) was acquired in 2001 in the SHM and Ras Tafelney permit areas. The northern 400 $km^2$ (154 $mi^2$) of that survey was reprocessed and merged with a second, more recently acquired 3-D survey shot in 2005 that covers 719 $km^2$ (278 $mi^2$). The 3-D seismic survey used in this study covers an area of 1064 $km^2$ (411 $mi^2$) in the lower continental slope between 31.99682° N and 31.41798° N and between 11.30082° W and 10.54431° W (Figure 2). The extent of the survey ranges in water depths of 1200 m (3937 ft) in the southeast to 2800 m (9186 ft) in the northwest (Fig. 2.11).

Although the dataset contains a variety of structures attractive to hydrocarbon exploration, the area still remains relatively unexplored when compared to onshore activity. Consequently, the lithological control of seismic data is virtually non-existent due to the lack of wells drilled in offshore Morocco. Deep Sea Drilling Project (DSDP) data from the deep offshore, however, shows the Early-Jurassic to Early-Cretaceous strata to be carbonates, while the strata younger than Early Cretaceous are dominantly siliciclastic.

## Previous Work

Few publications specific to the study area exist with the exception of those done in recent years using data available through recent industry activity. Publications by Tari et al. (2000, 2001, 2003) use the 3-D survey acquired in 2000 to compare styles of salt tectonics of Morocco with those of other basins along West Africa and the Gulf of

Mexico. Weisenburger (2007) provided an excellent overview of the existing work done within the study area, and documents the author's own sub-regional-scale analysis of the morphology of the lower continental slope. He primarily focused on determining the emplacement history of allochthonous salt structures and examines regional-scale temporal changes in the interaction of structure and sedimentation. Structural restorations and isopach maps of Jurassic through Tertiary strata proved to be key elements in demonstrating the evolution of the margin. Exploration drilling in the Essaouria Basin has been limited to on-shelf shallow water and to the active onshore program in the eastern part of the basin. Therefore, no deterministic well control exists for defining the age of the section of interest or relationships between seismic data and lithology (Dunlap et al., 2010). Access to data from DSDP boreholes from leg 50 drilled in 1976, however, provide insight into the overall stratigraphy within the abyssal plains near the study area. DSDP Borehole 416 in a water depth of 4191 m (13750 ft) (Lancelot and Winterer, 1980) is located approximately 100 km north-northwest of the study area. The maximum depth achieved at site 416 is 1624 m (5328 ft) sub-bottom and the oldest strata encountered were Upper Jurassic (Kimmeridgian–Tithonian) distal turbidites. The stratigraphy encountered at this drill site comprised deepwater turbidite sands, gravels and siltstones, and pelagic muds, marls and chalk. DSDP Borehole 415 in a water depth of 2794 m (9167 ft) (Lancelot and Winterer, 1980) is located approximately 85 km (53 mi) southwest of the study area. The maximum depth achieved at site 415 is 1080 m (3543 ft) sub-bottom, and the oldest strata encountered were Albian in age. These wells both show that sandy turbidites were moving through the more eastward slope minibasins during the Tertiary.

## DATA SYNTHESIS

Observations and interpretations from the physical modeling phase of this research will be combined with deterministic observations from data interpretations in the ancient fills to determine the significance of the input sediment delivery systems relative to the position of the minibasin on the slope, the preserved cross-sectional geometries and implications for predicting potential facies distribution to assess hydrocarbon reservoir potential within minibasin provinces.

**TABLES**

| Basin | Length (km) | Width (km) | Perimeter (km) | Area (km) | Volume (km3) | Relief (m) | Stratal Geometry |
|---|---|---|---|---|---|---|---|
| Stewart | 17.6 | 9.3 | 21.8 | 31.3 | 175.2 | 80 | bowl |
| Harrison | 12.5 | 4.3 | 34.8 | 41.8 | 60.3 | 85 | bowl |
| Longhorn | 16.7 | 6.3 | 54 | 93.9 | 142.7 | 227 | box |
| Tiger | 21.6 | 8.3 | 55.6 | 120.2 | 207.1 | 159 | barrier |
| Leipper | 4 | 1.8 | 9.9 | 5.5 | 5.6 | 75 | |
| Tambalier | 7.2 | 3.8 | 21.4 | 24.5 | 35 | 155 | box |
| Tamu | 17.2 | 9.8 | 50.4 | 125 | 188.6 | 166 | barrier |
| Hancock | 17.5 | 9.3 | 51.8 | 131.3 | 209.8 | 346 | barrier |
| Ship | 13.9 | 8.8 | 44.8 | 113.4 | 189.6 | 158 | barrier |
| West Tamu | 8.3 | 4.3 | 24.2 | 27.9 | 39.2 | 78 | barrier |
| Cat | 7.6 | 5.3 | 20.6 | 30.7 | 45.2 | 101 | bowl |
| Pigmy | 28.7 | 9.8 | 86.3 | 226.1 | 452.7 | 521 | box |
| Camerson | 5 | 3.3 | 14.5 | 12.3 | 20 | 53 | barrier |
| Tison | 15.3 | 5.3 | 42.6 | 60.9 | 108.5 | 270 | box |
| Saint Tammany | 17.6 | 8.3 | 55.5 | 109.9 | 210.8 | 305 | barrier |
| Researcher | 9.1 | 8.3 | 28.5 | 61.2 | 105.7 | 174 | bowl |
| Vermillion | 13.5 | 5.3 | 35.6 | 51.9 | 86.8 | 200 | bowl |
| Green | 12.9 | 6.8 | 36.4 | 65.8 | 112.7 | 57 | bowl |
| West Pigmy | 5.5 | 3.3 | 16 | 14.1 | 25.6 | 106 | box |
| Orleans | 11.3 | 7.3 | 32 | 64.3 | 127.2 | 150 | barrier |
| North Terrebonne | 16.3 | 5.3 | 44.6 | 56.2 | 119.5 | 247 | box |
| Orca | 26.5 | 12.8 | 83.2 | 311.8 | 684.1 | 466 | box |
| Pilsbury | 10.3 | 7.3 | 30.8 | 61.6 | 117.2 | 166 | bowl |
| Saint Mary | 25.7 | 8.3 | 75.4 | 156.3 | 289.1 | 194 | bowl |
| Jefferson | 14.9 | 7.3 | 44.3 | 80.4 | 165.8 | 228 | box |
| Terrebonne | 33.3 | 11.3 | 114.4 | 295 | 626.1 | 281 | box |
| Aggasiz | 23.7 | 8.3 | 66.9 | 146.3 | 299.5 | 301 | box |
| Mitchell | 19.2 | 9.8 | 53.2 | 148.5 | 289.3 | 216 | bowl |
| Saint Bernard | 6.5 | 4.8 | 20.5 | 26.2 | 53 | 93 | barrier |
| Lafourche | 8.1 | 6.3 | 23 | 38.2 | 70.9 | 51 | |
| Choctaw | 25.5 | 12.8 | 68.6 | 242.7 | 550.5 | 443 | box |
| Mattison | 7.8 | 5.8 | 21.8 | 33.3 | 68.1 | 75 | |
| Natchez | 11.2 | 9.3 | 35.1 | 84.8 | 169.1 | 227 | |

| | | | | | | | |
|---|---|---|---|---|---|---|---|
| Hydrographer | 13.8 | 7.3 | 38.9 | 85.4 | 192.1 | 212 | bowl |
| Plaquemines | 9.6 | 6.3 | 26.4 | 45 | 93.2 | 75 | bowl |
| West Chitimacha | 24.1 | 13.3 | 92.8 | 251.9 | 584.6 | 442 | box |
| East Chitimacha | 23.7 | 13.3 | 68.2 | 214.5 | 495.5 | 282 | bowl |
| Atakapa | 21.6 | 9.8 | 74 | 175.6 | 404.4 | 366 | box |
| Arellano | 9.7 | 2.3 | 22.4 | 18.6 | 40.2 | 77 | |
| Dorantes | 16.4 | 9.3 | 47.7 | 119.9 | 267.5 | 242 | barrier |
| Karanka | 15.9 | 6.8 | 43.9 | 84.8 | 193.5 | 324 | barrier |
| Desoto | 7.9 | 5.3 | 21.6 | 29.6 | 64 | 66 | bowl |
| Castillo | 8.9 | 5.3 | 24.1 | 38.5 | 84.1 | 106 | |
| Estavanico | 14.2 | 9.3 | 40.2 | 101.1 | 231.4 | 126 | bowl |
| Iberia | 9 | 2.3 | 21 | 14.6 | 34.9 | 200 | box |
| Vaca | 22.9 | 12.8 | 72.3 | 241.7 | 594.2 | 412 | bowl |
| **Minimum** | 4 | 1.8 | 9.9 | 5.5 | 5.6 | 51 | |
| **Maximum** | 33.3 | 13.3 | 114.4 | 311.8 | 684.1 | 521 | |
| **Average** | 15 | 7.4 | 43.7 | 98.1 | 202.8 | 204 | |
| **Standard Deviation** | 7.1 | 3 | 23.6 | 80.4 | 181.2 | 123.6 | |

Table 2.1: Simple geometry data for present-day Gulf of Mexico minibasins (n=46) compiled by Pratson and Ryan (1994).

**(a) Sediment-Fluid Mixture Properties (Initial Conditions)**

| | | |
|---|---|---|
| Water temperature | 23 | $^{o}C$ |
| Ambient fluid density, $r_w$ | 0.998 | kg/L, g/cm$^3$ |
| Density of solution $r_{salt+H2O}$ | 1.006 | kg/L, g/cm$^3$ |
| Specific gravity of solution, $SG_{salt+H2O}$ | 1.007 | |
| Density of solution $r_{salt+H2O}$ | 1.005 | kg/L, g/cm$^3$ |
| Density of sediment, $r_s$ | 2.65 | kg/L, g/cm$^3$ |
| Volume concentration, $C_{s+salt+H2O}$ | 2.3 | % |
| Density of solution and sediment mixture, $r_{s+salt+H2O}$ | 1.048 | kg/L, g/cm$^3$ |
| Excess density | 5.1 | % |
| Number of flows – Series 1 | 18 | flows |
| Average flow duration | 60 | mins |
| Number of flows – Series 2 | 27 | flows |
| Flow duration (1-8) | 15 | mins |
| Flow duration (8-19, 21, 23, 24, 27) | 60 | mins |
| Flow duration (20a, 20b, 20c, 22a, 22b) | 15 | sec |
| Flow duration (25-26) | 120 | mins |

**(b) Input Turbidity Current Dynamics**

| | | |
|---|---|---|
| Input current velocity range | 4.75-10.00 | cm/s |
| Discharge | 200-500 | cm$^3$/s |
| Reynolds Number, Re | 3000-5000 | |
| Froude Number, Fr | 0.5-0.8 | |
| Current width (Series 1) | Unconfined (Approximately equal to basin width) | |
| Current width (Series 2) | 10 | cm |
| Current thickness | 2.0-4.0 | cm |

Table 2.2: (a) shows density properties of materials used for creating the experimental turbidity current mixture, followed by the number of flows and their durations for each series of mini-basin experiments; (b) lists the turbidity current fluid dynamics properties that characterize flows for Series 1 and 2 experiments.

## FIGURES

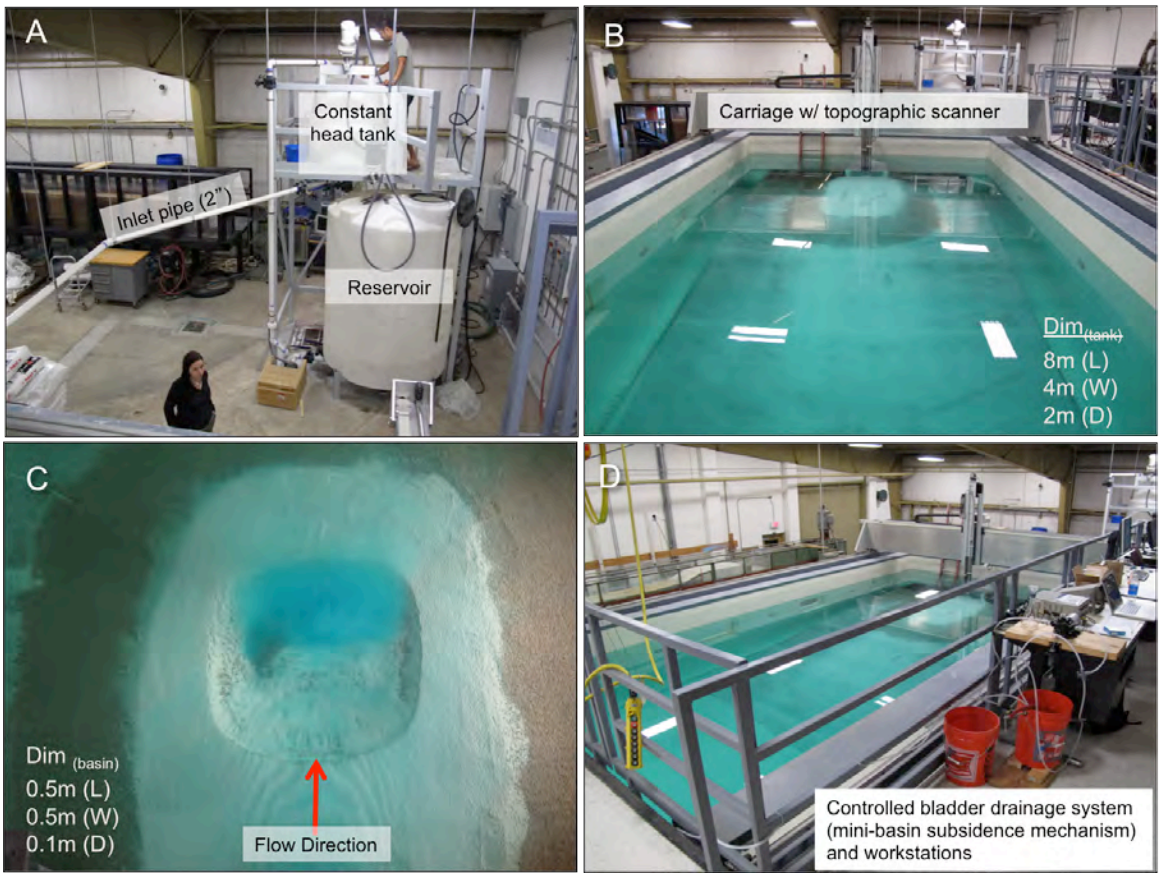


Figure 2.1: Minibasin experiment setup in the UT Morphodynamics Laboratory. (A) Shows the reservoir mixing tank where salt, sediment and water are combined to form the turbidity current slurry. The slurry is pumped to the constant head tank, and released through the inlet pipe to the experimental tank shown in (B). Attached to the motorized carriage is a laser topographic scanner, onto which other measuring equipment can be placed for measuring turbidity current properties (e.g. Acoustic Doppler Velocimeter (ADV), siphons and sonar equipment). (C) Shows a plan view of a fully subsided minibasin from Series 1 experiments, and (D) shows the controlled bladder drainage system used to subside the experimental minibasin.

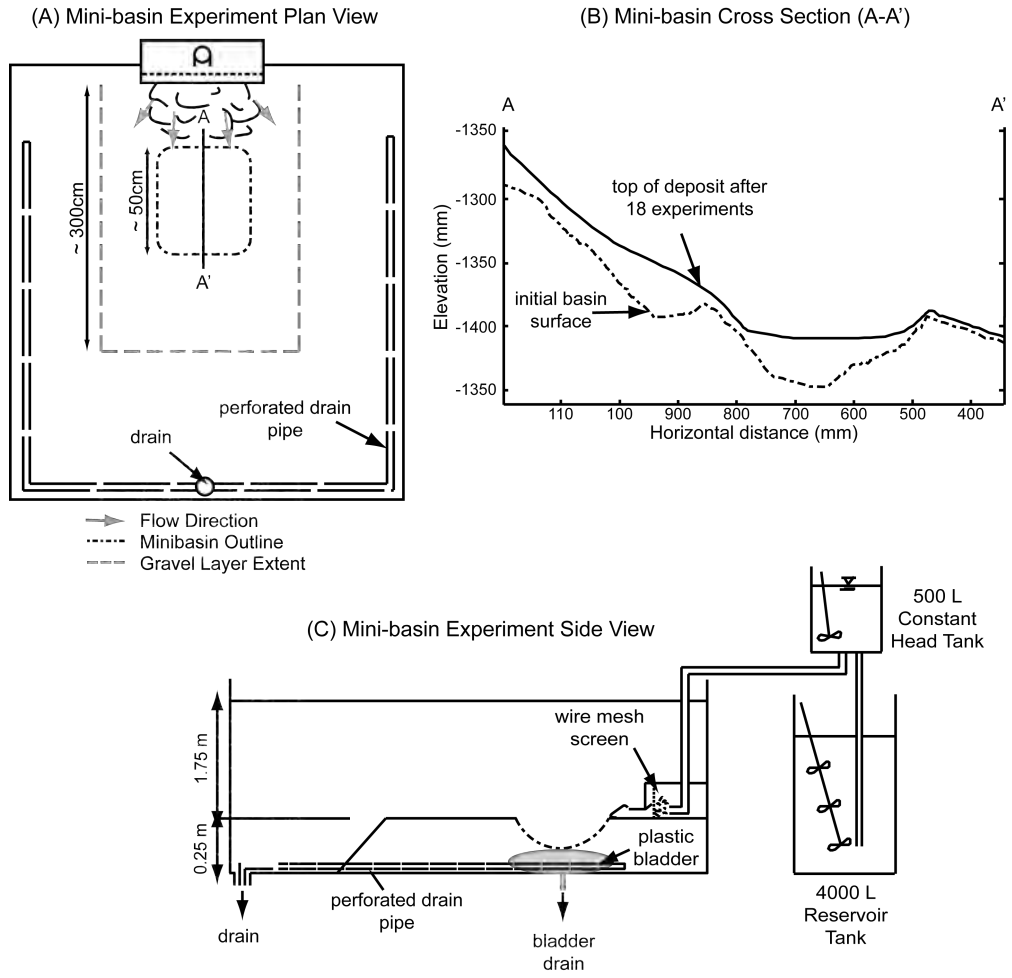


Figure 2.2: Schematic figure for Series 1 of the minibasin experiments and current generation conditions. Plan view of the basin tank (A) with the completely subsided minibasin configuration. The bold outline represents the extent of the false floor, and the dashed red outline represents the extent of the minibasin. Dimensions of the minibasin cross-section are shown in (B). Side View (C) shows the reservoir tank where sediment, water and salt are mixed and then pumped to the upper constant head tank. Currents are generated by releasing the mixed fluid from the head tank into the basin tank/ minibasin through a wire mesh screened entrance box. As the currents move over the edge of the false floor they are drained away by a system of perforated pipes in order to minimize basin tank wall reflections. The minibasin cross-sectional shape was established by controlled drainage of a water filled bladder that was buried in a gravel basement, shown in (B). The dimensions of the bladder were 40 cm (L) x 40 cm (W) x 15 cm (D). The inlet box configuration for the minibasin was oriented parallel to the long axis of the basin tank.

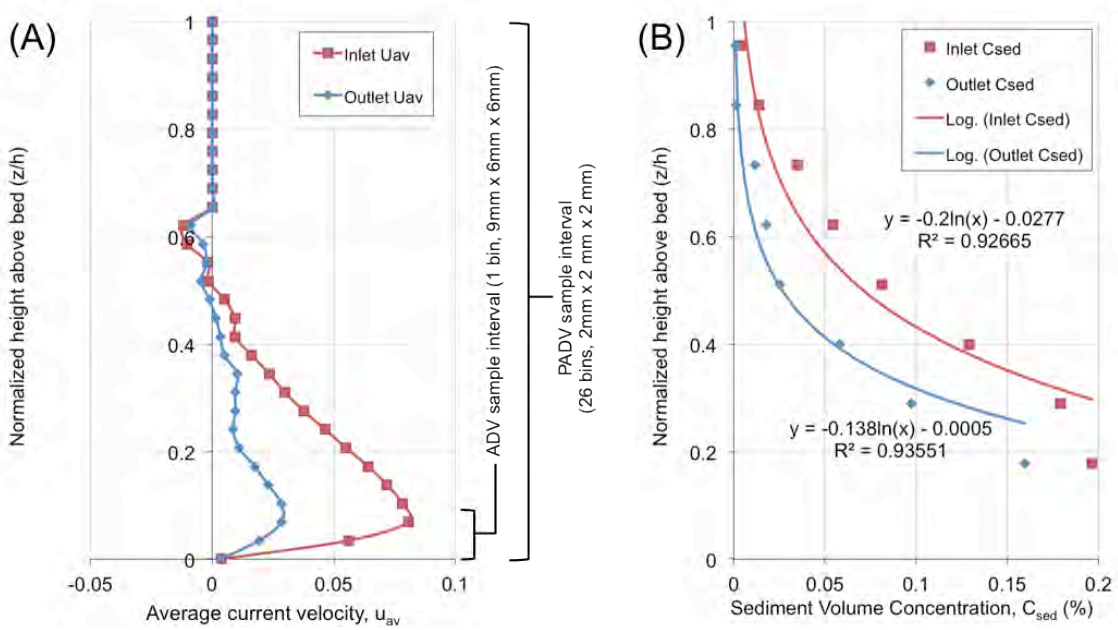


Figure 2.3: Characteristic input (red) and output (blue) velocity and sediment concentration profiles from a flow. (A) Shows a time averaged (t=15 s) velocity profile for a turbidity current entering the minibasin collected using an Acoustic Doppler Velocimeter Profiler (PADV) and plotted with dimensionless height, z/h with h = 56mm (h=measured current depth from PADV equipment where there was no measured current velocity disturbance in the fluid column). Profile sampling dimensions and their relative locations are shown for both ADV and PADV equipment. (B) Shows typical turbidity current concentration data from an 8-component siphon rack. An exponential function is fit to the data and forward and backward extrapolated for visualization. The equation is shown on the figure.

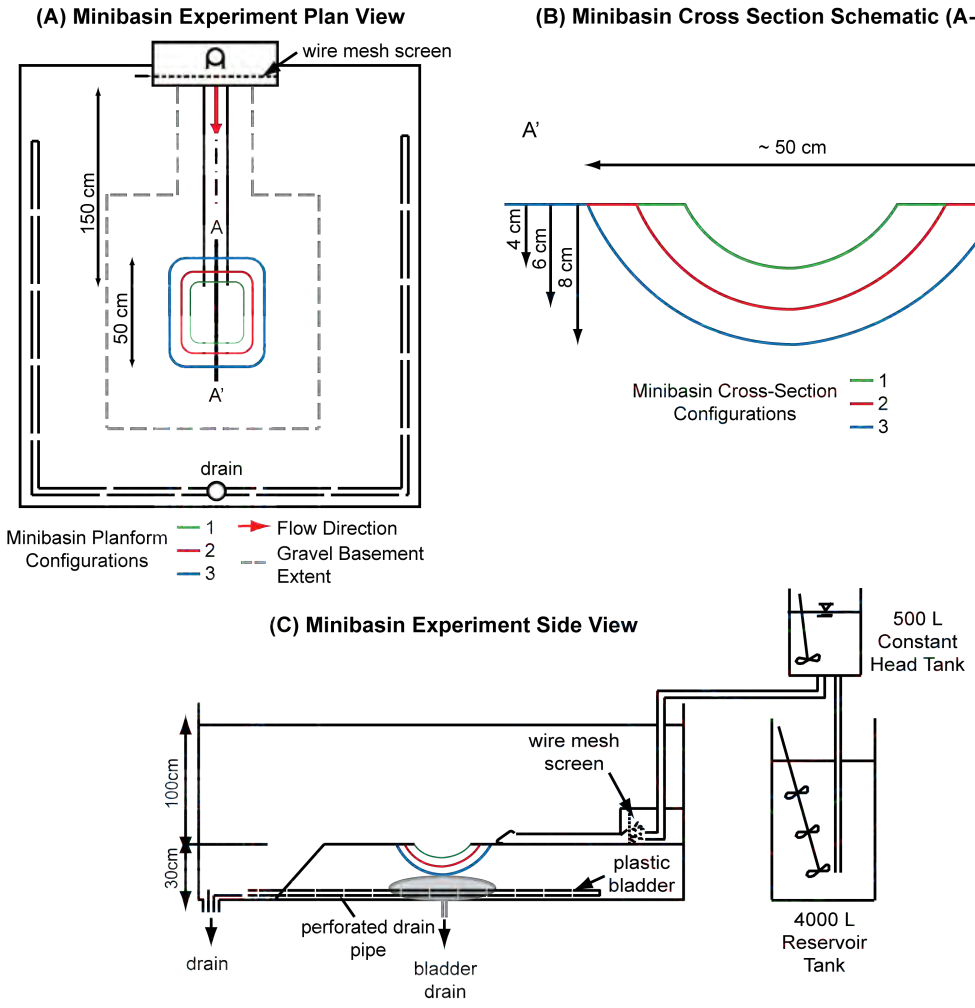


Figure 2.4: Idealized schematic figure for Series 2 of the minibasin experiments and current generation conditions. Plan view of the basin tank (A) with the three subsided minibasin configurations 1 (smallest) to 3 (largest). The bold outline represents the extent of the false floor. Dimensions of the minibasin configurations in cross-section are shown in (B). Side View (C) shows the reservoir tank where sediment, water and salt are mixed and then pumped to the upper constant head tank. Currents are generated by releasing the mixed fluid from the head tank into the basin tank/ minibasin through a wire mesh screened entrance box. As the currents move over the edge of the false floor they are drained away by a system of perforated pipes in order to minimize basin tank wall reflections. The minibasin cross-sectional shape was established by controlled drainage of a water filled bladder that was buried in a gravel basement, shown in (B). The dimensions of the bladder were 40 cm (L) x 40 cm (W) x 15 cm (D). The inlet box configuration for the minibasin was oriented parallel to the long axis of the basin tank.

(A)

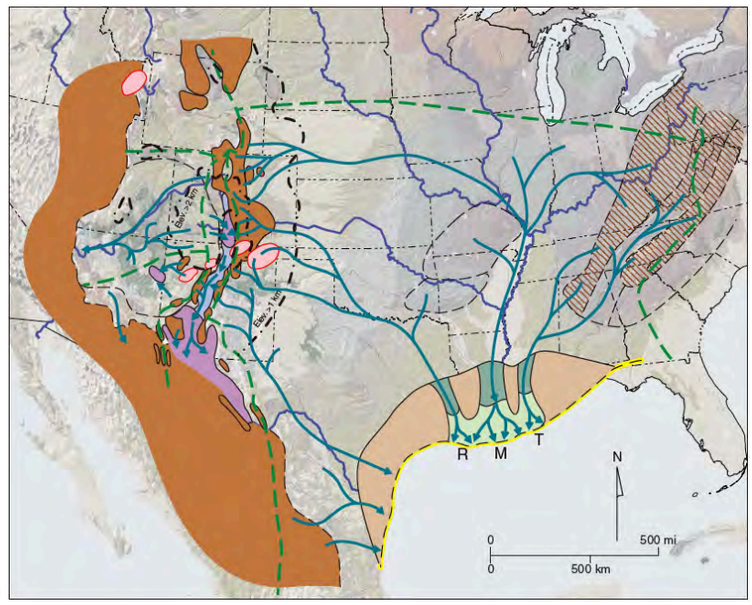


(B)

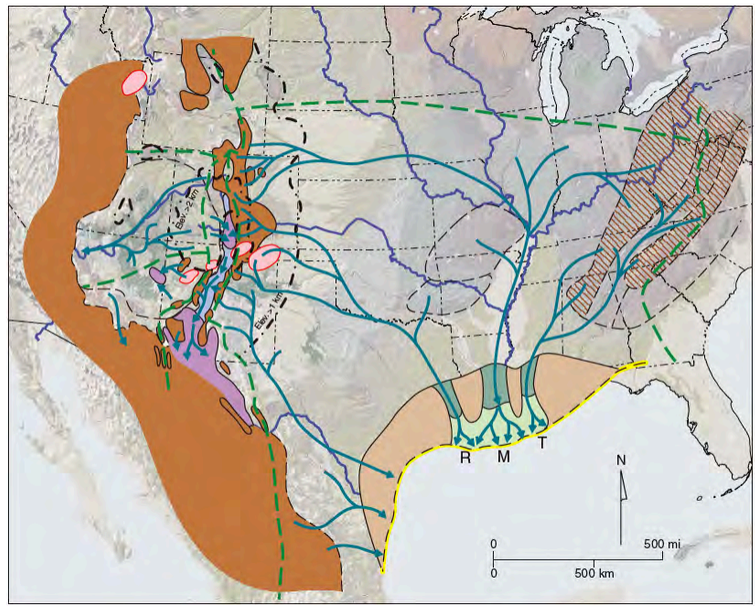


(C)

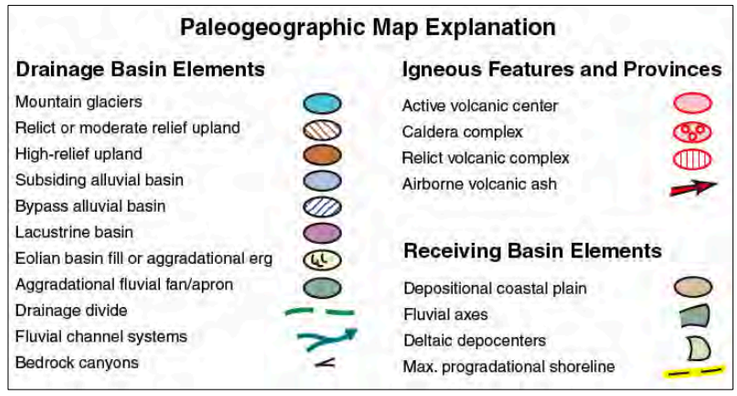


Figure 2.5: (A) Pliocene paleogeography of the United States and northern Gulf of Mexico (from Galloway et al., 2011). Main receiving basin elements are the Red (R), Mississippi (M), and Tennessee (T) Rivers. (B) Pleistocene paleogeography of the United States and northern Gulf of Mexico. The Rio Grande (RG) River becomes an additional receiving basin element; (C) is the key to A and B.

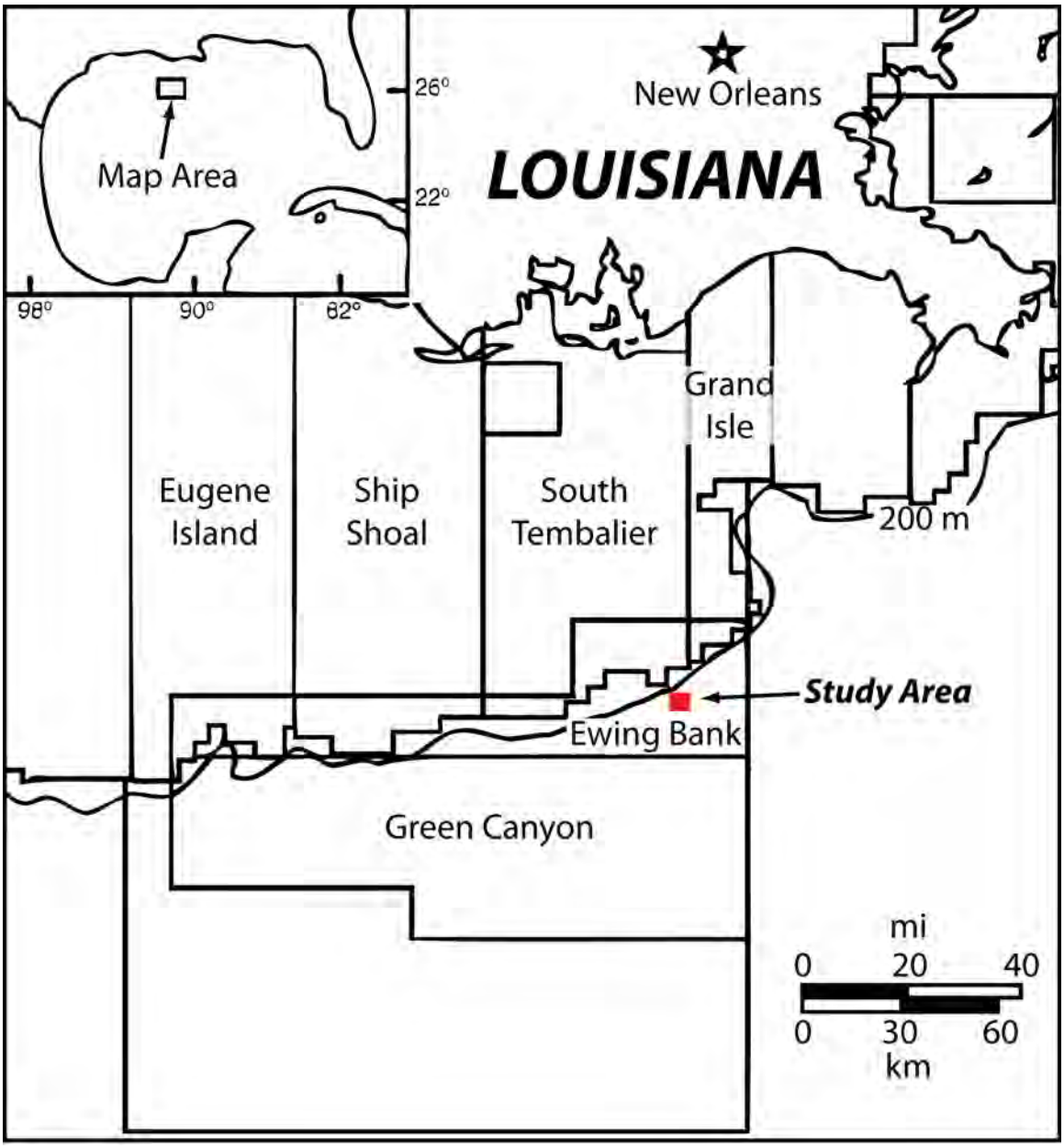


Figure 2.6: Map of the Gulf Coast near Louisiana showing the location of the Lobster dataset (red polygon) in relation to the city of New Orleans (red polygon).

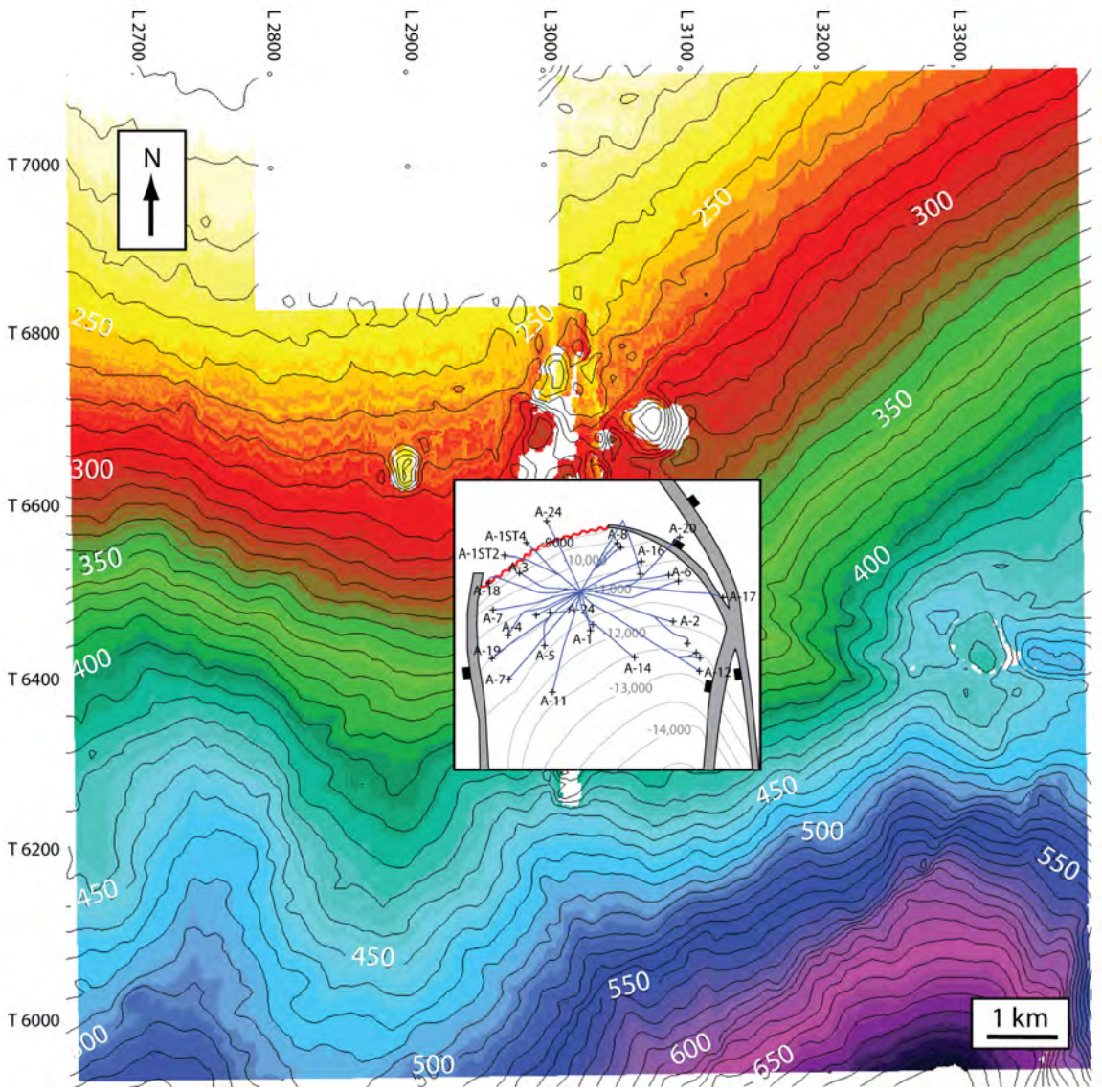


Figure 2.7: Map view extent of Lobster data coverage and location of well penetrations. Two mapped horizons are shown: (a) the horizon covering the extent of the dataset is ta structural map of the present-day seafloor. Elevation contours are shown in two-way travel time (ms), where smaller numbers correspond to shallow depths and vice versa; (b) and the inset map is a structure map of the main producing *Bul. 1* reservoir interval (modified from Burke et al., 1999), located at approximately 3,050 m (10,000 ft) below sea level. Depth elevation contours are true vertical depth sub-sea (ft). Bounding faults at depth are shown by shaded grey polygons, and are generally oriented N-S.

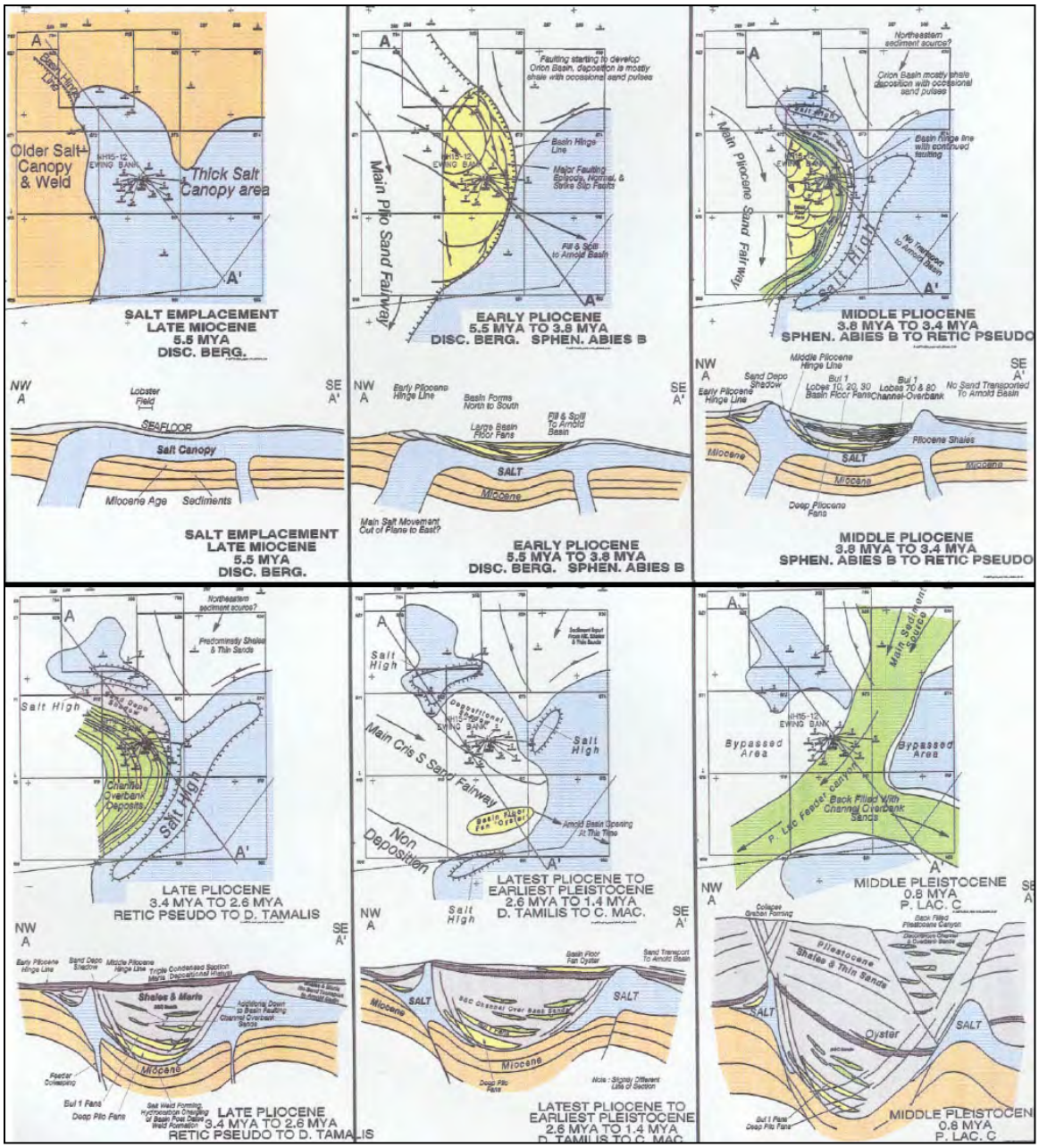


Figure 2.8: Evolutionary model of the Lobster minibasin, located in the Ewing Bank Block 873, Gulf of Mexico (From Burk et al., 1999). Topographic confinement due to salt diapirism increases from the Late Miocene to the Middle Pliocene, and has implications for sediment partitioning as accommodation is developed.

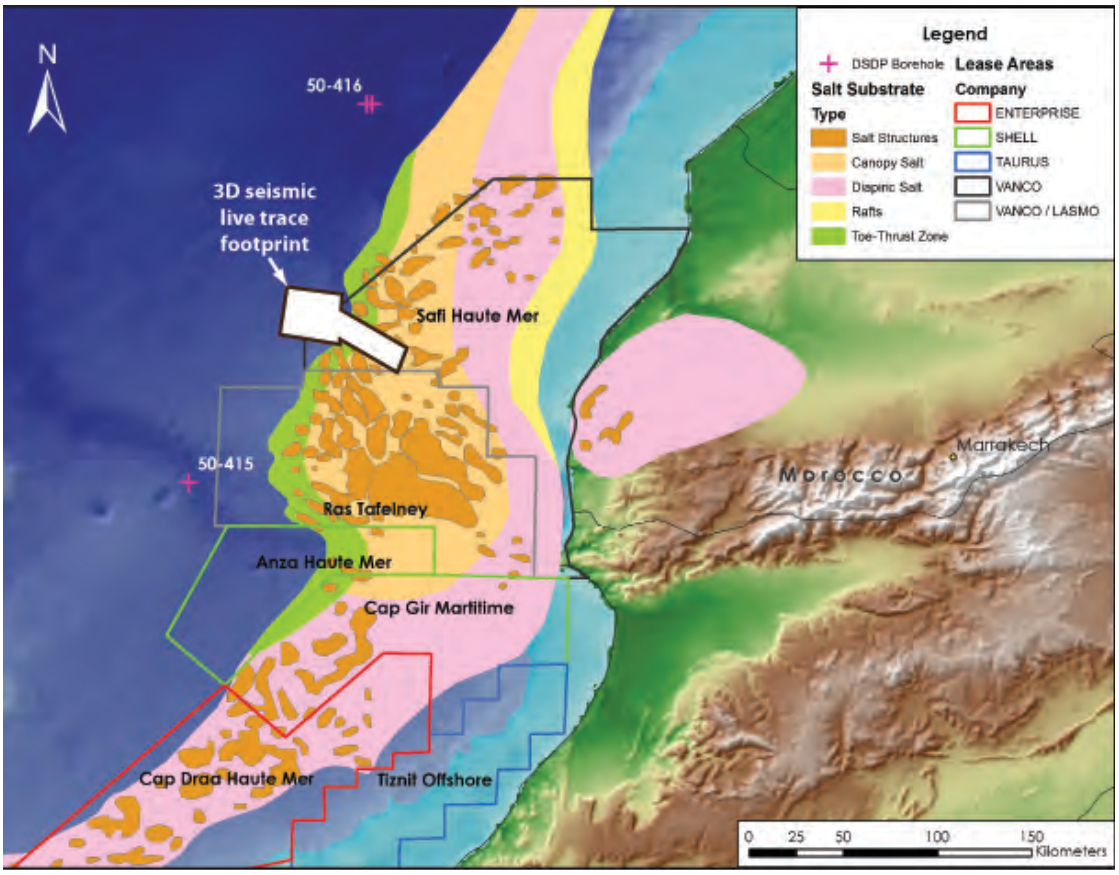


Figure 2.9: Shaded relief profile of the Moroccan continental margin showing the extent of the study area (grey filled polygon) relative to the Moroccan coastline. Location of the Safi Haute-Mer 3D seismic dataset is highlighted in white. Variability in structural controls is mainly due to the types of salt substrate present. Offshore permit areas are outlined by hollow polygons.

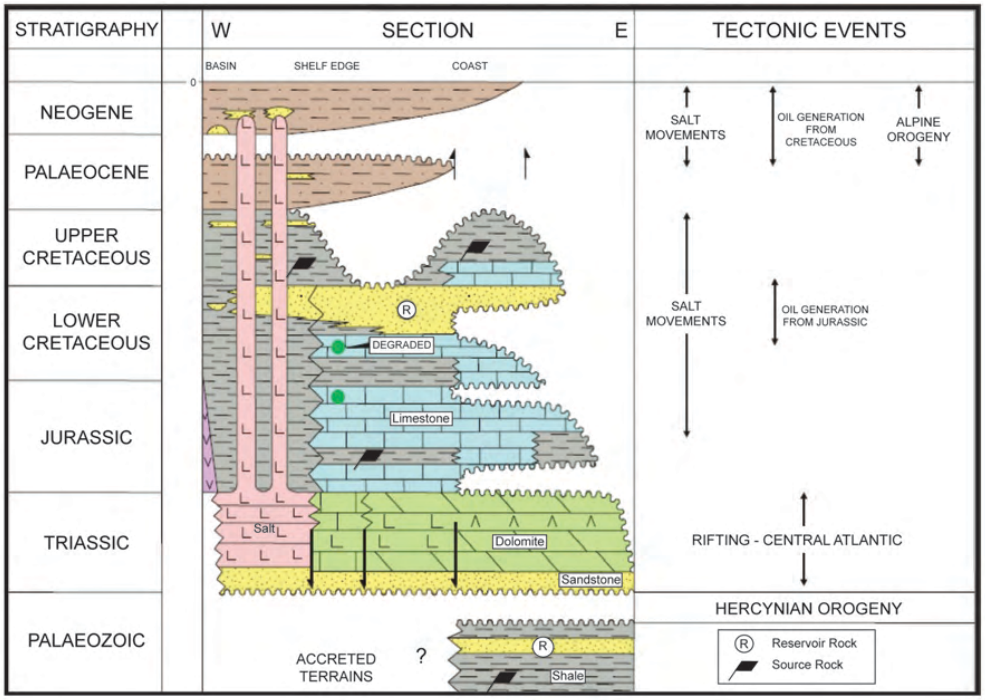


Figure 2.10: Chronostratigraphic chart for the Atlantic Margin of Morocco (modified from Davison, 2005).

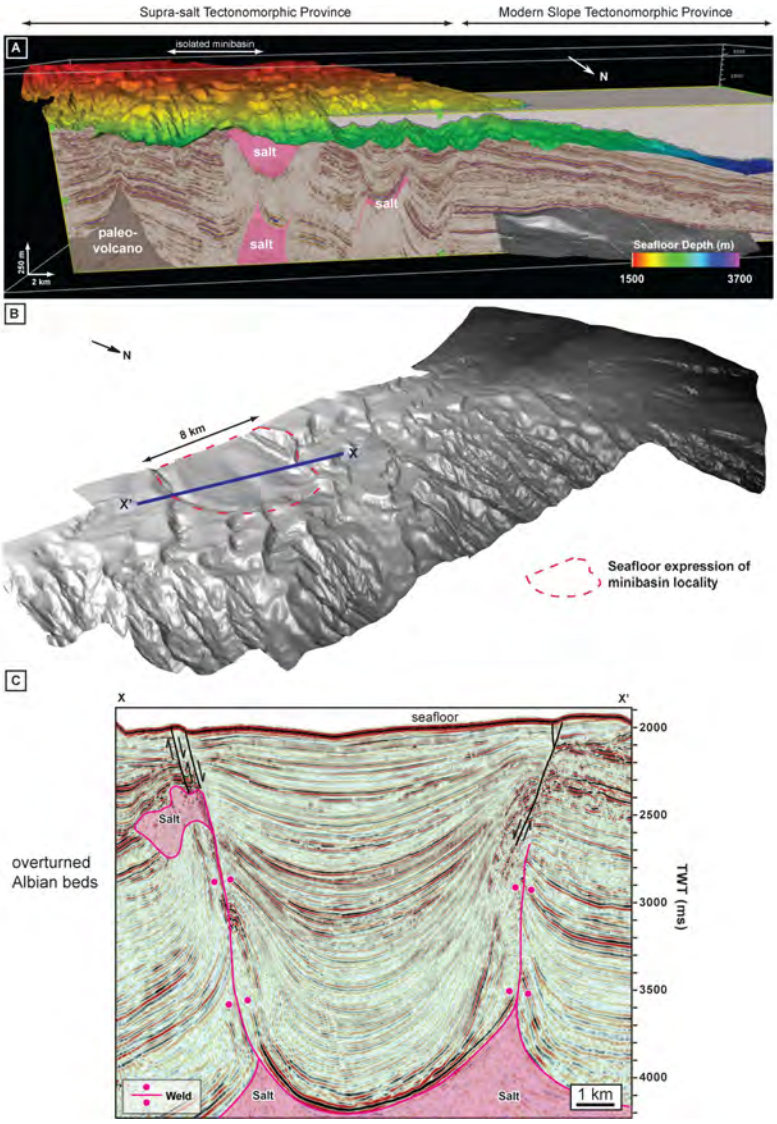


Figure 2.11: (a) Seismic dip section of the study area with superimposed structure map of the seafloor. The seismic section illustrates the Triassic to Recent stratigraphy preserved in the study area. Irregularly deformed features shaded in pink is interpreted as mobile salt substrate, and the conical feature shaded in brown within the proximal portion of the dataset is interpreted as a paleovolcano; (b) a structure map, shown in three dimensions, completed on the Moroccan seafloor illustrates the relationship between the isolated minibasin under investigation (outlined in red) and the rest of the 3D seismic volume; and (c) an arbitrary seismic cross section (X-X') shows the 3 kilometers of stratigraphy preserved within the subsiding minibasin. Interpreted underlying present-day salt structures are outlined and shaded pink.

## REFERENCES


Badalini, G., B. Kneller, and C. D. Winker, 2000, The late Pleistocene Trinity-Brazos turbidite system; new insights for deep turbidite reservoir interpretation: Annual Meeting Expanded Abstracts - American Association of Petroleum Geologists, v. 2000, p. 8-8.

Beaubouef, R. T., C. Rossen, F. B. Zelt, M. D. Sullivan, D. C. Mohrig, and D. C. Jennette, 1999, Deep-water sandstones,Brushy Canyon Formation, West Texas: Field Guide, AAPG Hedberg Field Research Conference.

Beaubouef, R. T., V. Abreu, and J. C. Van Wagoner, 2003, Basin 4 of the Brazos-Trinity slope system, western Gulf of Mexico; the terminal portion of a late Pleistocene lowstand systems tract: Program and Abstracts - Society of Economic Paleontologists. Gulf Coast Section. Research Conference, v. 23, p. 45-66.

Beaubouef, R. T., and S. J. Friedmann, 2000, High resolution seismic/sequence stratigraphic framework for the evolution of Pleistocene intra slope basins, western Gulf of Mexico; depositional models and reservoir analogs: Program and Abstracts - Society of Economic Paleontologists. Gulf Coast Section. Research Conference, v. 20, p. 40-60.

Burk, M. K., G. L. Brown, and D. R. Petro, 1998, Evolution of the geological model, Lobster Field (Ewing Bank 873): AAPG Discovery Series, v. 1.

Burk, M. K., G. L. Brown, and D. R. Petro, 1999, Evolution of the geological model, Lobster Field (Ewing Bank 873): AAPG Bulletin, v. 83, p. 1350-1350.

DeVay, J. C., D. Risch, E. D. Scott, and C. Thomas, 2000, A Mississippi-sourced middle Miocene (M4), fine-grained abyssal plain fan complex, northeastern Gulf of Mexico: AAPG Memoir, v. 72, p. 109-118.

Diegel, F. A., J. F. Karlo, D. C. Schuster, R. C. Shoup, and P. R. Tauvers, 1995, Cenozoic structural evolution and tectono-stratigraphic framework of the northern Gulf Coast continental margin: AAPG Memoir, v. 65, p. 109-151.

Dunlap, D. B., L. J. Wood, C. Weisenburger, and H. Jabour, 2010, Seismic geomorphology of offshore Morocco's east margin, Safi Haute Mer area: AAPG Bulletin, v. 94, p. 28.

Galloway, W. E., 1998, Siliciclastic slope and base-of-slope depositional systems; component facies, stratigraphic architecture, and classification: AAPG Bulletin, v. 82, p. 569-595.

Galloway, W. E., 2005, Gulf of Mexico basin depositional record of Cenozoic North American drainage basin evolution: Special Publication of the International Association of Sedimentologists, v. 35, p. 409-423.

Galloway, W. E., 2008, Depositional evolution of the Gulf of Mexico sedimentary basin Sedimentary basins of the world, v. 5: Netherlands, Elsevier : Amsterdam, Netherlands, p. 505-549.

Galloway, W. E., P. E. Ganey-Curry, X. Li, and R. Buffler, 2000, Cenozoic depositional history of the Gulf of Mexico basin: AAPG Bulletin, v. 84, p. 1743-1774.

Galloway, W. E., S. Mentemeier, M. Rowan, and L. M. Gochioco, 2004, Plumbing the depths of the Gulf of Mexico; recent understanding of Cenozoic sand dispersal systems and ultradeep reservoir potential: Leading Edge [Tulsa, OK], v. 23, p. 44-51.

Galloway, W. E., T. L. Whiteaker, and P. Ganey-Curry, 2011, History of Cenozoic North American drainage basin evolution, sediment yield, and accumulation in the Gulf of Mexico Basin: Geosphere, v. 7, p. 938-973.

Giles, K. A., and T. F. Lawton, 2002, Halokinetic sequence stratigraphy adjacent to the El Papalote Diapir, northeastern Mexico: AAPG Bulletin, v. 86, p. 823-840.

Hedley, R., and J. Warburton, 1999, The structural evolution of the Tafelney Plateau, offshore Morocco: AAPG Bulletin, v. 83, p. 1316.

Lamb, M. P., T. Hickson, J. G. Marr, B. Sheets, C. Paola, and G. Parker, 2004, Surging versus continuous turbidity currents; flow dynamics and deposits in an experimental intraslope minibasin: Journal of Sedimentary Research, v. 74, p. 148-155.

Lamb, M. P., H. Toniolo, and G. Parker, 2006, Trapping of sustained turbidity currents by intraslope minibasins: Sedimentology, v. 53, p. 147-160.

Lancelot, Y., 1980, Evolution of the Moroccan oceanic basin and adjacent continental margin; a synthesis, *in* E. L. Winterer, ed., Initial Reports of the Deep Sea Drilling Project, United States, Texas A & M University, Ocean Drilling Program : College Station, TX, United States, p. 801-821.

Paola, C., K. Straub, D. C. Mohrig, and L. Reinhardt, 2008, The 'unreasonable effectiveness' of stratigraphic and geomorphic experiments: Eos, Transactions, American Geophysical Union, v. 89, p. @AbstractV33F-05.

Pindell, J., and J. F. Dewey, 1982, Permo-Triassic reconstruction of western Pangea and the evolution of the Gulf of Mexico/Caribbean region: Tectonics, v. 1, p. 179-211.

Pirmez, C., R. T. Beaubouef, S. J. Friedmann, and D. C. Mohrig, 2000, Equilibrium profile and baselevel in submarine channels; examples from late Pleistocene systems and implications for the architecture of deepwater reservoirs: Program and Abstracts - Society of Economic Paleontologists. Gulf Coast Section. Research Conference, v. 20, p. 782-805.

Pirmez, C., B. E. Prather, G. Mallarino, W. W. O'Hayer, and A. W. Droxler, 2012, Chronostratigraphy of the Brazos–Trinity Depositional System, Western Gulf of

Mexico: Implications For Deepwater Depositional Models: SEPM Special Publication, v. 99, p. 111-143.

Prather, B. E., 1998, A Gulf of Mexico based depositional process model for above-grade slopes: AAPG Bulletin, v. 82, p. 1953-1953.

Pratson, L. F., and W. B. F. Ryan, 1994, Pliocene to Recent infilling and subsidence of intraslope basins offshore Louisiana: AAPG Bulletin, v. 78, p. 1483-1506.

Rowan, M. G., 1995, Structural styles and evolution of allochthonous salt, central Louisiana outer shelf and upper slope: AAPG Memoir, v. 65, p. 199-228.

Rowan, M. G., T. F. Lawton, K. A. Giles, and R. A. Ratliff, 2003, Near-salt deformation in La Popa Basin, Mexico, and the northern Gulf of Mexico; a general model for passive diapirism: AAPG Bulletin, v. 87, p. 733-756.

Salvador, A., 1987, Late Triassic-Jurassic paleogeography and origin of Gulf of Mexico Basin: AAPG Bulletin, v. 71, p. 419-451.

Seibold, E., and D. Fuetterer, 1982, Sediment dynamics on the Northwest African continental margin: United Kingdom, John Wiley & Sons : Chichester, United Kingdom, 147-163 p.

Sullivan, M., G. Jensen, F. Goulding, D. Jennette, L. Foreman, and D. Stern, 2000, Architectural analysis of deepwater outcrops: implications for exploration and production of the Diana sub-basin, western Gulf of Mexico, *in* P. Weimer, R. M. Slatt, J. L. Coleman, N. Rosen, C. H. Nelson, A. H. Bouma, M. Styzen, and D. T. Lawrence, eds., Global Deep-Water Reservoirs: Gulf Coast Section-SEPM Foundation 20th Annual Bob F. Perkins Research Conference, p. 1010-1031.

Tari, G., 2000, Salt tectonics in the Atlantic margin of Morocco, *in* J. Molnar, P. Ashton, and R. Hedley, eds., Leading Edge [Tulsa, OK], United States, Society of Exploration Geophysicists : Tulsa, OK, United States, p. 1074.

Tari, G. C., 2001, Examples of deep-water salt tectonics from West Africa; are they analogs to the deep-water salt-cored fold belts of the Gulf of Mexico?: Program and Abstracts - Society of Economic Paleontologists. Gulf Coast Section. Research Conference, v. 21, p. 251-270.

Tari, G. C., 2002, Expression of the Atlas inversion tectonics in deep-water offshore Morocco; implications for hydrocarbon exploration, *in* P. R. Ashton, J. S. Molnar, and P. Thompson, eds., Annual Meeting Expanded Abstracts - American Association of Petroleum Geologists, United States, American Association of Petroleum Geologists and Society of Economic Paleontologists and Mineralogists (AAPG) : Tulsa, OK, United States, p. 174-174.

Tari, G., 2003, Examples of salt tectonics from West Africa; a comparative approach, *in* J. Molnar, and P. Ashton, eds., Geological Society Special Publications, United Kingdom, Geological Society of London : London, United Kingdom, p. 85-104.

Toniolo, H., 2003, Depositional turbidity currents in diapiric minibasins on the continental slope; theory, experiments and numerical simulation, *in* P. Gary, ed., Annual Meeting Expanded Abstracts - American Association of Petroleum Geologists, United States, American Association of Petroleum Geologists and Society of Economic Paleontologists and Mineralogists : Tulsa, OK, United States, p. 171-171.

van Andel, T. H., and P. D. Komar, 1969, Ponded sediments of the Mid-Atlantic ridge between 22 degrees and 23 degrees north latitude: Geological Society of America Bulletin, v. 80, p. 1163-1190.

Villamil, T., C. Arango, P. Weimer, A. Waterman, M. G. Rowan, P. Varnai, A. J. Pulham, and J. R. Crews, 1998, Biostratigraphic techniques for analyzing benthic biofacies, stratigraphic condensation, and key surface identification, Pliocene and Pleistocene sediments, northern Green Canyon and Ewing Bank (offshore Louisiana), northern Gulf of Mexico: AAPG Bulletin, v. 82, p. 961-985.

Violet, J., B. Sheets, L. Pratson, C. Paola, R. Beaubouef, and G. Parker, 2005, Experiment on turbidity currents and their deposits in a model 3D subsiding minibasin: Journal of Sedimentary Research, v. 75, p. 820-843.

Weisenburger, C. M., 2007, Salt Tectonics, Sedimentation, and Basin Development in Safi Haute Mer, offshore Morocco: M.S. thesis, University of Texas at Austin, Austin, TX, 106 p.

# Chapter 3: Literature Review – Confinement of Turbidity Currents and the Deposits they Form

## INTRODUCTION

Deep-water sedimentation in both confined and unconfined settings has been a major focus of academic and industry research, however an understanding of flow processes and how they interact with 3-D topography still remains elusive. In addition, the deposits themselves are complex and remain poorly characterized, not to mention the lack of understanding regarding fluid flow within the resulting deposits. Such limited advance in understanding the nature of these systems and deposits is caused by no single reason, but entails many issues. The issues include (1) modern deep-water processes are difficult to study, occurring in often hostile environments where monitoring is untenable or incredibly expensive; (2) deep water processes tend to be episodic and often catastrophic in nature meaning that it can be difficult to catch nature in action, (3) high-resolution three-dimensional geophysical datasets are required to study detailed architecture, and such data are expensive; (4) outcrop analogues of deep water deposits from different settings lack fully three-dimensional representation, (5) core and log data, while providing detailed temporal information are often spatially not pervasive and the cost and maturity of drilling in deep water environments limit the amount of well and core data available, and (6) submarine gravity-driven processes are difficult to model in physical experiments, more so than subaerial processes such as rivers. In addition, models must be scaled down to accommodate the logistics of model building, a process that can render the observations difficult at best to apply to the modern real world systems.

The main factors controlling deposition in the deep-water environment include the sediment source area, wave action, basin physiography, grain size distribution, slope physiography, relative sea level and the morphology and bathymetry of the receiving deep-water basin (Mutti, 1979; Kneller, 1995; Winker, 1996; Prather et al., 1998; Kneller and McCaffrey, 1999; Mutti et al., 1999; Talling, 2001; Carlson et al., 2001; Sinclair and Tomasso, 2002; Sinclair and Cowie, 2003; Lomas and Joseph, 2004; and Smith, 2004; Kneller et al., 2009). The evolutionary growth and development of deep-water sedimentary elements in both unconfined and confined settings has been widely studied during the past two decades, and takes into account different combinations of the aforementioned variables responsible for deep-water sedimentation (e.g. Bouma et al., 1985; Pickering et al., 1989; Weimer and Link, 1991; Weimer et al., 1994; Reading and Richards, 1994; Shanmugam, 1999). The overall system morphology related to the caliber and total volume of sediment supplied and receiving-basin geometry is referred to as *the turbidite-system growth pattern* (Covault and Romans, 2009). Normark's (1970) seminal work introduced *the turbidite-system growth-pattern* concept, which was defined as the overall system morphology related to the origin and recent history of canyons and channels on the present seafloor.

Sequence stratigraphic concepts (Mitchum, 1985; Mutti, 1985; Vail, 1987; Posamentier et al., 1988; Normark et al., 1993; 1998) add further emphasis to the study of turbidite systems and highlight the relationships between eustasy and any associated secondary affects and turbidite deposition. Other authors downplay the role of sequence stratigraphic concepts in confined-slope, deep-water sedimentation, where local influences predominate (e.g. earthquakes, tectonic/depositional over-steepening, depositional/hydrostatic/glacial loading, cyclones, tsunamis, volcanic activity, salt/ shale movement, etc.).

Studies have shown (e.g. Smith, 2004) that the modern deep marine seafloor topography is structurally complex making it difficult to image and interpret. By consequence, it can be inferred that flows moving over such topography will be equally complex. The behavior of a turbidity current over even a static surface will change depending on the nature of that current - their relative size, composition and duration. Therefore, the complexity and variability of such a current moving will only increase over a topographically complex surface. Topography which might completely confine a flow of a particular set of properties, may have little effect on a flow characterized by different properties than the first. This issue has resulted in development of a sliding scale defining "confined" and "unconfined" settings for currents (Fig. 3.1). The resulting deposit architectures that are observed in well logs, core and outcrop only tell us part of the story. To add to the missing pieces in the puzzle, little is known about the size and characteristics of the input turbidity current conditions relative to the topography that they encounter on complex slopes. This lack of knowledge is encountered both in ancient and modern systems.

Recent studies have emphasized the fundamental influence of seafloor topography on the growth and morphology of submarine 'fans'. However, little attention is paid to the relationship between morphology of the submarine flows and the topography they interact with. In many turbidite systems and turbidite hydrocarbon reservoirs, depositional system development is interpreted to have been moderately to strongly confined by pre-existing bounding slopes (Lomas and Joseph, 2004). It has been established that the interaction of turbidity currents with basin topography can have complex effects upon deposit geometry (e.g. Edwards, 1993; 1994; Apps, 1994; Kneller, 1995a; Kneller and McCaffrey, 1995; Kneller and McCaffrey, 1999, Amy et al., 2000).

In this review, I outline key studies that focus on confinement as it relates to deep-water depositional systems and the implications for interpreting the sediment gravity flow processes from which they originate. I first address the concept of confinement, as it is understood in the present-day literature. Second, I introduce the concept of flow efficiency and the factors that contribute to the ability for a sediment gravity flow to transport sediment in the deep-water environment. Third, I cover the fundamentals of both unconfined and confined deep-water depositional systems and process models from a historical perspective, and outline the merits and weaknesses where applicable. Finally, I relate the described models to experimental and subsurface work that examine and characterize the processes involved with turbidity currents in confined settings and their deposits. Where applicable, I refer to a spectrum of published studies involving observations made through physical modeling experiments, high-resolution studies on the modern seafloor as well as observations and interpretations from ancient deep-water systems from outcrops and subsurface geophysical data.

As it pertains to this research, the limited number of 3-D quantitative studies, the lack of spatial and vertical resolution, the difficulties in recreating three-dimensional depositional topography from preserved segments and the question of how representative the published literature are of these deepwater systems, highlight the need for detailed modeling of processes influenced by 3-D deepwater minibasin topography. This need is addressed in subsequent chapters.

## THE CONCEPT OF CONFINEMENT

Many modern and ancient studies focus on the worldwide occurrence of turbidite systems where sediment dispersal patterns and the geometries of depositional bodies have been affected by local basin topography. Confinement is a term that has been historically

associated with the relationship between deep-water currents and the topography with which they interact, and the origin of the term possessed variants that described unique interactions between the two. Confinement has also been discussed in regards to currents in deepwater channel settings (e.g. Mohrig and Buttles, 2007; Straub, 2007; Straub et al. 2008; Straub and Mohrig, 2009). In this dissertation, I apply the concepts of confinement as it relates to minibasin topography.

*Ponding* was first proposed by Van Andel and Komar (1969) to describe situations where turbidity currents of sufficiently large volume were fully contained by enclosed bathymetry. The term however implies a component of flow process that remains unclear from distinguishing flow process from the resulting deposit. Pickering and Hiscott (1985) used the term, *contained turbidites,* to describe beds deposited by turbidity currents that were confined within a basin that was too small to permit sustained unidirectional flow. However, their explanation of quantitative relationships between flow height and basin topography was insufficient to support their interpretation of complete deposit containment relative to basin size and paleoflow conditions. In each case, variants of these terms therefore imply that the confining topography was sufficient to retain the flow so as to promote complete sediment detrainment and no further downdip transport. Although possible, such a case of sediment capture by basin topography has not been proven in modern settings, nor have existing models been adequate to explain the transport of relatively coarser grained fractions of sediment to distal locations on complex slopes.

In response to these complex relationships between turbidity current flow processes and the topography with which they interact, Lomas and Joseph (2004) define confinement as, "*…situations where sediment gravity flows and their deposits are appreciably affected by the presence of significant basin-floor topography, but without*

*the connotation of complete containment*." They recognize that implicit to the discussion of confinement is the relationship of flow magnitude to the size of the receiving basin. Flow magnitude can be considered to be associated with components of flow size and the total energy within the flow. Various factors contribute to flow magnitude and are related to the concept of flow efficiency, which is "…*the ability for a flow to deliver sediment to a downstream location"* (e.g. Mutti, 1979, Al-Ja'Aidi, 2000; Al-Ja'Aidi et al., 2004). More importantly, associated with this definition is a primarily qualitative measure that researchers have used to describe the degree of structural confinement in a particular setting. What appears to be poorly understood and not adequately addressed in published work is a quantitative measure between the magnitude of 3-D basin confinement relative to the size and efficiency of currents supplying sediment to the basin, and the implications for distributing sediment within and beyond the margins of the confining topography.

In subsurface and outcrop studies, interpretations of the degree of confinement of a flow is traditionally linked to relationships among the preserved volume of the deposits (from isopach maps), the morphology of the deposits (from outcrop/core or seismic attribute analysis), and the paleotopography responsible for guiding and containing the flow (constructed from paleontological and/or tectonic/stratigraphic relationships). For the case of shelfal drainage systems that are strongly influenced by guiding submarine canyons and "deep" channels, there has been documented impact on the degree of transport of coarse-grained materials and the morphology of the deposits produced in the receiving basin (e.g. Winker, 1996; Prather et al., 1998). On the other hand, for drainage pathways not subject to confining topography, low-concentration turbidity currents tend to spread laterally on the shelf, which potentially has an impact on the transport of coarse-grained materials and the morphology of deposits in receiving basins.

When considering the geometry and architecture of the deposit from turbidity currents, sedimentologists and stratigraphers often use the nature of accommodation development, the geometry and nature of stratigraphic terminations as a primary characteristic for classifying the deposit as "confined" or "unconfined." In some cases, this classification is usually based on an interpretation of the flow transport processes using lithological data from samples or outcrop analogs (e.g. Winker, 1996, Prather at al., 1998). A key component to the classification of deposits as being confined or not usually depends on the relationship between the termination styles of the deposit relative to the 3-D geometry of the receiving basin. Additionally, confining topography characterized by both the delivery system (e.g. submarine channels, canyons) and the receiving basin impacts the ability for the turbidity current to transport reservoir-grade sediment from source to sink (i.e. the flow efficiency). In this research, priority is therefore placed on investigating these relationships to grasp a better handle on how the degree of current containment affects the geometry and character of deposits.

**Morphology of Turbidity Currents and Confining Topography**

The morphology of turbidity currents is discussed in Chapter 1 of this dissertation. Chapter 1 also addresses the influence of topography on disrupting the flow structure of an input current, and the associated studies that address this phenomenon. In an obstacle-free setting, a turbidity current leaves a deposit were the thickness and grain size generally decrease away from its source as it loses kinetic energy through flow expansion and results in grain deposition (e.g Middleton, 1967; Scheidegger and Potter, 1971; Garcia, 1994) This process usually forms predictable deposit successions. Examples of these relationships have been documented from innumerable outcrop examples, with two of the best being documented in the Permian Brushy Canyon

outcrops in west Texas (e.g. Beaubouef et al., 1999; Gardner et al., 2003), and the Permian Skoorsteenberg Formation in the Tanqua depocenter, southwest Karoo Basin, South Africa (e.g. Hodgson et al., 2006; van der Werff, 2003). When topography is introduced, these progressive trends in deposit character can be interrupted.

When turbidity currents encounter confining topography, there are two possible scenarios that occur that are variants of the standard trend (Brunt et al., 2004). If the confining topography is sufficiently high to capture or entirely contain the incoming current, the current may be contained entirely within this topography. Alternatively, if topography exists but is not substantial enough to entirely capture the current, inherent kinetic and potential energy may enable a portion (or all) of the current to surmount the topography and escape.

Deposition resulting from the interaction of turbidity currents with topography is further complicated because of vertical flow stratification. Studies show that turbid gravity flows develop vertical gradients in suspended sediment concentrations, which results in a stratification of density and grain size (Middleton and Southard, 1984; Middleton, 1993; Kneller and McCaffrey, 1999). The greatest concentrations occur at the lowest point in the flow, where the high shear velocities are sufficient to keep coarser fractions suspended in the flow, while finer materials are relatively more uniformly distributed throughout the flow (Kneller and Buckee, 2000). Usually the degree of influence exerted by topography on the flow is directly related to the height of the topographic obstacle relative to the flow's head thickness, where most of the energy, and by association, most of the momentum of the flow is concentrated (Fig. 3.2). Early 2-D experimental studies show that turbidity currents are able to surmount obstacles whose height is up to 2.5 times the body thickness (Fig. 3.2) of the flow (Rottman et al., 1985), or 1.5 times the head thickness (Muck and Underwood, 1990; Kneller and McCaffrey,

1999). These experiments are however insufficient for understanding flow dynamics on a complex slope, at the least due to effects of lateral spreading and variable topography. Mohrig and Buttles (2007) show that currents and their associated sedimentation patterns are influenced by even the smallest relative topography, since the kinetic energy of a current is concentrated in the lowest portions of the flow where the current velocity is highest in the profile (Fig. 3.2). Where currents are able to overcome confining topography Piper and Normark (1983) proposed the concept of flow stripping, where obstacles on the seafloor obstruct the higher-energy, lower portions of the flow while upper portions of the flow continue their downslope trajectory with minimal disturbance

Although it can be inferred that topography from mobile substrates present a significant obstacle to flow bypass, recent exploration in confined ultra deep-water settings show significant accumulations of sand with net to gross values of twenty percent or more. Such high net to gross sands have been seen for example, in offshore Brazil (e.g. Bruhn, 1998), offshore Angola (e.g. Alexander et al., 2001), offshore Equatorial Guinea (e.g. Schwans et al., 2007); and offshore Gulf of Mexico (e.g. Clemenceau and Colbert, 1999; Meckel, 2004; Wagner, 2006; Sweet and Sumpter, 2007). Topography is clearly not entirely inhibiting the movement of coarse-grained sediments in most deep marine settings.

### FLOW EFFICIENCY AND CONFINEMENT

Mutti (1979) introduced the idea of flow efficiency, which is defined as "*...the ability of the flow to move its sand-sized load in a basinward direction*." It is generally accepted that flow efficiency plays a major role in controlling the distribution and geometry of reservoir-quality sand deposited from turbidity currents. Flow efficiency is controlled by the rate of momentum-loss of a flow. Several authors have discussed the

factors that determine the efficiency of turbidity currents (e.g. Normark 1978; Mutti 1980, 1992; Mutti & Normark 1987; Laval et al. 1988; Normark & Piper 1991; Nilsen et al. 1994; Gladstone et al. 1998; Bouma 2000). On the basis of field observations, Mutti (1979, 1992) concluded that the geometry of individual beds or groups of beds is not exclusively determined by the slope and basin configuration, but also by the flow efficiency. Mutti (1992) distinguished high-efficiency from low-efficiency flows. High-efficiency flows are flows of large volumes and/or those that transport a considerable amount of fines, while low-efficiency flows are of relatively smaller volumes, and/or are those flows loaded mainly with coarse sediment. Although this definition for flow efficiency provides some insight into the relative sizes of the flows, little mention is made of the nature of topographical interaction and its implications for affecting the ability of the flow to transport sediment and did not serve as a useful classification. High efficiency flows are important for the case of confined deep-water systems because for currents transporting sediment, a flow gradually loses its density excess when progressive sediment fallout occurs in the downstream direction. This loss of density will reduce the flow's buoyancy and this reduction will eventually cause the flow to detach from the seabed.

Three factors that contribute to flow efficiency include (a) the suspended sediment grain size distribution; (b) flow volume; and (c) suspension density (Al-Ja'Aidi, 2000, 2004), each of which have a characteristically different effect upon the volume, geometry and the stacking patterns of resultant deposits. The presence of considerable amounts of suspended fine material reduces the density difference between coarser grains within the flow and the interstitial fluid that consists of fines and water. Associated with this reduced density contrast are reduced rates of momentum loss due to low mud deposition rates and friction reduction. The combination of these actions effectively

reduces the settling velocities of the coarser grains (Lowe 1982; Middleton and Southard, 1984; Gladstone et al., 1998), and by consequence the rate of sedimentation of particles within the flow. Suspension density affects flow efficiency primarily due to its impact on flow momentum, and suspension volume affects flow efficiency principally by affecting shear velocities (Al-Ja'aidi, 2000). Al Ja'Aidi et al. (2004) found that increases in the initial flow density, volume and proportion of fines in turbidity currents each resulted in an increased flow efficiency, which were attributed to an increase in potential energy and maintenance of negative buoyancy in the flow. They also found that both the proportion of sediment reaching obstructing topography and the proportion able to surmount the topography increased as flow efficiency increased.

## DEEP-WATER DEPOSITIONAL MODELS

The importance of deep-water reservoirs in hydrocarbon exploration and exploitation, and their confounding complexity, high development cost and sometimes low success rates have led to a proliferation of models to explain deep-water depositional processes, systems and characteristics. Elements within the deepwater system may include canyons, channels, levees, lobes (channelized and depositional), slumps and slides. Studies published on in the geoscience literature seek to understand the geometry, continuity and stacking patterns of sediment gravity flow deposits on a range of scales – from pore, bed and bedset properties (reservoir scale) to complexes and complex sets (seismic-scale). However, two key concerns arise when describing and interpreting the associated models that have been introduced into the field of deep-water sedimentology and stratigraphy: (1) spatial and temporal scale of facies development and distribution, that is to say are conceptual models applicable to understanding deep-water sedimentary facies development and distribution on various spatial and temporal scales and (2) how

well are the 3-D physical processes responsible for deep-water clastic sedimentation understood and do we truly understand their influence on facies distribution and architecture. This research hopes to shed some light on these two issues.

**Unconfined Basin Depositional Models**

The early 1970's marked the introduction of deep-water fan models, which attempted to interpret turbidite deposits within the framework of deep-sea fan depositional systems. These were formulated from work in unconfined basin settings. Normark (1970) presented the first widely used model of submarine-fan growth from the California Borderland and offshore Baja California (Fig. 3.3), which inspired subsequent studies regarding the development of modern and ancient turbidite systems (e.g., Mutti and Ricci Lucchi, 1972; Walker, 1978; Normark, 1978; Normark et al., 1979; Normark and Hess, 1980; Nilsen, 1980; Nardin, 1983; Mutti, 1985; Mutti and Normark, 1991; Fildani and Normark, 2004). Normark's (1970) groundbreaking turbidite-system growth-pattern concept, related the overall system morphology to the origin and recent history of canyons and channels on the present seafloor. He emphasized the importance of depositional bulges or suprafans developed at the terminus of fan valleys (Fig. 3.3). Suprafans were described as "*…convex-upward depositional features with proximal shallow and ephemeral distributary channels, which grade to progressively smoother zones that comprise finer-grained sediments*."

Mutti and Ghibaudo (1972) and Mutti and Ricci Lucchi (1972) proposed a model for unconfined ancient turbidite systems where, for the first time facies associations were interpreted in terms of specific deep-water fan environments. They emphasized what they interpreted to be depositional similarities between fluvial-dominated deltas and deep-water fans, by suggesting a direct comparison between deltaic channels and their

resultant mouth bars, and turbidite channels and their resultant lobes. They also offered a more comprehensive model of unconfined systems where turbidite facies associations were interpreted in terms of slope, fan and basin plain environments, and specific facies associations were interpreted to be diagnostic of inner, middle and outer deep-water fan environments. Emphasis was placed on the overall progradational character of many ancient submarine fan systems, and emphasized the thinning- and fining-upward nature of channel-fill sequences, in contrast to the thickening- and coarsening-upward character of turbidite sand lobes.

Walker (1978) attempted to combine the models of Normark (1970) and Mutti and Ricci Lucchi (1972), into a single model for unconfined systems, which eventually became popular among the sedimentology community. Later, Chan and Dott (1983) and Heller and Dickinson (1985) proposed a ramp model for turbidite systems that expounded on the classic point-sourced (canyon-fed) systems but further introduced the concept of a line-sourced (multiple deltaic distributary channel-fed) unconfined deepwater system. As more and more detailed models were proposed for deep-water unconfined systems, Normark et al. (1993) commented that *"…it seemed that the number of fan models began to approach the number of turbidite systems that had been studied*." Such is always the danger in trying to explain a very complex depositional system with multiple embellishments of a single generic model. Growing evidence from outcrop and marine geology studies, show that application of existing models to describe and interpret various modern and ancient turbidite systems in a range of tectonic and physiographic settings is limited.

The adverse reaction by the geologic community against the single-point source submarine fan model (e.g. Normark, 1970) was based on the premise that there should not be more than one fan model to explain fundamental differences between different

types of fans; and that deep-water systems are not exclusively fed by point-sourced systems. Much of the negative reaction to the single-point source submarine fan model of Normark (1970) stems from the widely held belief that deep-water systems are not fed by single point-source systems. As observations increased, so thoughts from original deepwater stratigraphers matured. Mutti and Normark (1987) expanding on some of their original work, recognized four main types of turbidite basins. They emphasized that the volume of sediment and the long-term stability of the receiving basin primarily control the morphology and internal facies associations of submarine fans. Thus, along with eustasy and tectonism, Mutti and Normark's more recent 1991 paper emphasizes the composition and volume of turbidity currents as well as the basin type and configuration as primary factors controlling the geometry and facies patterns of turbidite systems. Ross et al. (1994) introduced a slope readjustment model, suggesting that depositional and erosional processes on continental slopes tend towards maintaining graded, steady state profiles.

Reading and Richards (1994) continuing to split hairs, sub-divide continental slopes into 12 classes based on grain size (mud-rich, mud/ sand-rich, sand-rich and gravel-rich) and feeder system configuration (point-sourced, line-source and multiple sourced). Richards et al. (1998) ascribe predictive value to this classification scheme and describe a method for reservoir description and prediction in three investigative stages that include basin screening, fan delineation and fan characterization. Richards and Bowman (1998) further describe a predictive arrangement of architectural elements that form the basic building blocks of each system from wireline logs. All together these papers describe a conceptual framework for the classification of fan types based on slope characteristics.

Antithesis to the concept of deepwater systems as arranged predictable successions, Anderton (1995) suggested that such organization was not the case with deepwater systems. He instead championed stochastic techniques for modeling deep-water depositional systems. It was his belief that parts of some fans behave in such a way that they leave behind sequences that can be used to define bed geometry, but a significant proportion of the fan sands found in hydrocarbon reservoirs are deposited in unstable mid-fan environments that produce chaotic vertical successions making prediction of vertical sequences suspect at best.

Despite Anderton's (1995) attempt to steer geoscientists away from belief in a well-defined, organized deepwater system, many authors in the late 1990's proposed models which relate facies patterns in submarine channel and overbank deposits to their position on a slope-to-basin profile. One such author, Gardner et al. (2000) proposed the "build-cut-fill-and-spill" model, developed from extensive outcrop study of the West Texas Brushy Canyon Formation. The preservation of each stage in the Gardner model is related to the position on the depositional profile or in the depositional cycle that records migration of the cycle. It is these types of organizational models that provide geoscientists the most comfort in trying to understand these complex systems, however may be misleading in their simplicity. Complexity can only grow when one adds topography that can inhibit the downslope movement of gravity flows, creating various states of flow confinement.

**Confined Basin Depositional Models**

The growth and morphologies of turbidite systems in confined receiving basins, such as the western Gulf of Mexico and South Atlantic margins, are greatly influenced by the relatively meager volumes of sediment supplied the receiving basin, and the

receiving-basin confinement. These basin fills are distinctly different from larger systems in unconfined ocean basins which enjoy large volumes of sediment supplied from extensive terrestrial drainages (Covault and Romans, 2009). In theory, sedimentation in confined deep-water depositional systems is governed by either eustasy or steady-state bathymetry (Madof et al., 2009). The eustatic-driven model for deepwater fan development asserts a correlation between sea level and facies assemblages (Weimer, 1990; Posamentier and Kolla, 2003), where sediment is derived primarily from shelfal cyclicity that relates to the frequency of eustatic cycles. Still further, the bathymetric model for fan development proposes an association between antecedent physiography and instantaneous patterns of sedimentation (Prather at el., 1998; Winker and Booth, 2000). Each model developed as a function of observations in a variety of structural and sedimentological regimes, emphasizing the difficulty for development of universally applicable models for deepwater systems.

Typical characteristics influencing confined deep water sedimentation include substantial sea-floor topography, syn-sedimentary tectonism or halokinesis, unstable oversteepened slopes and relatively high sedimentation rates (Hurst et al., 2000). The main influence that confinement has on deep-water clastic deposition is that turbidity currents are obstructed (deflected or diverted) by topography and limited in lateral extent by basin margin geometry. Sediment ponds against topography, heals topographic irregularities and may be remobilized later by reactivation of tectonically controlled topography (Haughton, 2000).

The nature of margin destabilizations influences the nature of accommodation and thus seafloor topography that strongly influences the resultant patterns of deepwater sedimentation. A quantitative bathymetric analysis of selected deep-water clastic margins by Steffens et al. (2003) shows that there are significant differences in receiving basin

configurations between salt-based and shale-based continental margins. Salt-based systems are shown to contain more "ponded" accommodation with isolated deposit geometries, while shale-based systems are found to be more susceptible to extensive bypass with elongate, connected deposit geometries. Additionally, Steffens et al. (2003) demonstrate that salt-based above-grade slopes have significantly more volume of ponded accommodation (25% across the central GOM mid-slope) than lower mobility salt-based stepped profiles such as the Lower Congo Slope and shale-based stepped profiles such as where the amount of ponded accommodation is generally less than 2%. Combining Reading and Richards (1994) concepts of sediment supply and concepts for submarine accommodation shows that the majority of deep-water hydrocarbon discoveries occur in reservoirs from muddy, above-grade slope settings with confined basins. Characteristics of these margins have potential impact on deep-water sedimentation patterns and associated fan development, which are inherently unique compared to graded (unconfined) slope settings.

Smith (2004), building upon the work of Steffens et al., (2003), describes two end members of topographically-complex slopes as either cascades of silled sub-basins, or connected, tortuous corridors. In the first scenario, a downslope sill hinders downslope flow, or at least the basal, sandy portions of sediment gravity flows until deposition reduces the relief sufficiently to facilitate downslope "spilling." For the second scenario, flows tend to avoid bathymetric obstacles, and follow a laterally confined, continuous tortuous path down the slope. He proposes that fill patterns and reservoir architecture are controlled by the volume and flow properties of the sediment supply, the relative scale of the receiving basin space and the flows, the relative rates of basin subsidence, and the infilling depositional processes.

### *Gulf of Mexico-Centric Models*

Subsurface data from the Gulf of Mexico has given insight to the characteristic stratigraphic history of numerous salt withdrawal basins on the continental slope (Winker, 1996; Prather at al., 1998; Sinclair and Tomasso, 2002). Satterfield and Behrens (1990) and Winker (1996) describe in detail the Trinity/Brazos fan system in the Gulf of Mexico that progressively filled- and spilled-through the topography of four intra-slope basins, depositing various seismic facies in each basin, often referred to as the *fill and spill* model. Further analysis by Beaubouef and Friedmann (2000) led to the interpretation of the progressive downslope filling of these longitudinally-linked basins and the systematic vertical and lateral arrangement of mass transport, distributary channel-lobe, and leveed-channel complexes in each of the basins. Similar processes and stacking patterns are documented for the shallow Auger Basin in the Central Gulf of Mexico as well (McGee et al. 1994; Prather et al. 1998; Booth et al., 2000; Winker and Booth, 2000).

To elaborate on the fill and spill model in more detail, Prather at al. (1998) suggested the evolution of an idealized ponded depositional sequence (Fig. 3.4). They assumed a static initial topographical profile, with sedimentation patterns tied to sea level. This involves the capture of submarine sediments in ponded accommodation space created by salt withdrawal. As the fans progressively fill the accommodation space, turbidity currents spill downslope as the sill separating the upslope basin from the downslope basin is overtopped. Associated with the overspill process is a localized truncation surface that forms from erosion of the upslope basin margin as the equilibrium profile adjusts to the downslope basin. Backfill of the space above the truncation surface then occurs as the downslope basin fills and the slope profile between the two basins aggrades to a local equilibrium. Finally, muddy turbidites or hemipelagic deposits drape

the basins after the slope grades to the equilibrium profile, or there is a decrease in sediment influx resulting from either a rise in eustatic sea level or slope system avulsion.

Although this model has been widely applied in the stratigraphic studies of intra-slope minibasins in the Gulf of Mexico, it is currently debated due to several limitations. These limitations include (1) the stratigraphic development of initial sediment deposition that fills local accommodation and subsequent spilling of sediment into subsequent basins equates the degree of flow process confinement to resulting deposit architecture, which has not been verified in laboratory conditions nor in the natural environment; (2) the model is two-dimensional, and does not account for the 3-D nature of flow dispersal in the natural environment; (3) the model suggests a process dominated by sediment-driven subsidence accommodation tied to eustatic sea-level changes along the margin, which may vary dramatically in more distal minibasin systems as well as other margins across the globe (e.g. Madof and Christie-Blick, 2007). Implicit in this discussion is the degree of connectivity among confined basins in nature, which has been suggested to be a function of massif uplift rate and the rate of sedimentation in updip confined basins (Montoya and Hudec, 2007).

The debate concerning the process mechanism of filling and subsequent spilling spans a range of scenarios with two end members (Toniolo et al., 2004). On one end is the possibility of large sustained turbidity currents that cascade from one basin to the next, simultaneously sculpting the channel during each event. At the other end is the possibility that small, pulse-like events must substantially fill each minibasin before enough overflow occurs to initiate erosion through the ridge at the downdip end and start the process of filling the next basin. In between these two end members, currents may be "stripped," with the updip basin containing the high-energy portion of the turbidity

current retaining coarser grains while the upper portions of the flow column flows to the downslope basin(s), transporting fine-grained suspended particles.

Badalini et al., (2000) introduced a model where basins could fill coevally, but with partitioning of sand and mud among basins due to flow stratification. Their hypothesis was based on the premise that the coarser fraction of sediments was transported lower in the flow, which was then stripped from the upper flow when basin confining basin topography was encountered, but not pronounced enough to contain the entire vertical section of the flow. As a result, the coarser sediments were retained in the proximal basin, while finer suspended sediment in the upper flow was transported further downdip into successive basins. Sinclair and Tomasso (2002) outlined this process in more detail in their static depositional model for confined intraslope basins on based on observations from a combination of Alpine outcrop studies and the Gulf of Mexico rock record. The characteristic basin morphology for the model is of two basins perched one above another on a submarine slope, separated by an interbasin high (Fig. 3.5). They used observations from flume and outcrop studies to interpret the link between process and deposit characteristics. The four phases that comprise this model are (1) flow ponding, where flows are completely contained in the basin, depositing thick sheets of sand and mud couplets; (2) flow stripping, where upper (finer) portions of the flow surmount the confining topography; (3) flow bypass, where flows can either (a) traverse the filled basin and incise a channel; or (b) switch the position of feeder channels, leading to abandonment; and finally (4) blanketing of the basin and surrounding topography during base level rise. It is suggested that the resulting confined basin sequences may be stacked during the episodic growth of the confining topography to a basin, and may appear similar to depositional sequences associated with sea level change.

## DEEP-WATER PROCESS MODELS

Submarine sediment-laden flows are considered to be two-phase phenomena, since their initial acceptance over fifty years ago (e.g. Natland and Kuenen, 1951), as fundamental agents of sediment transport and deposition in the oceans (Amy et al. 2009, e.g. Heezen and Ewing, 1952). The variable character of submarine sediment-gravity flows is reflected in existing, well-established facies schemes. Many of these schemes describing downstream changes in facies resulting from flow dilution. These facies transition from relatively proximal concentrated flow deposits of slides, slumps and debris flows to those of high-concentration turbidity currents and subsequently low-concentration turbidity currents in the most distal reaches of submarine systems (e.g., Mutti, 1992). These dynamic flows can develop internal heterogeneity in velocity, concentration, sediment particle size and composition and hence rheology and fluid dynamical state. By consequence, flows are able to have multiple depositional regimes in operation in different parts of the flow at the same time, as well as through time at a single position in the flow. Individual events may therefore produce complex deposits characterized by lateral and vertical successions of facies apparently deposited under differing physical regimes.

Confined deep-water environments are inherently unique, and are affected by a combination of factors that significantly affect the ability for sediment to be transported and distributed on complex slopes. On many occasions it has been argued that a published model cannot capture the unique combination of factors that influence each confined locality. It is therefore suggested that a process-based approach be employed to understand and describe these systems, one which discusses the principal factors that are responsible for deposit geometries and architectures observed in a range of settings.

Unconfined turbidity currents have been well characterized by the experimental and theoretical analyses of Luthi (1981) and Choi and Garcia (1996), while experimental analyses of turbidity currents and confining 3-D topography has yet to be fully understood in the scientific community. Since the direct measurements of natural currents in the deep-water environment still remain unobtained (Hay, 1987; Khripounoff et al., 2003; Xu et al., 2004), there is a gap in the knowledge of the development of fill in confined space evolution models. This knowledge gap limits the ability to reconstruct past environmental states using deep-water stratigraphy. However, interactions between turbidity currents and confined basins can be studied in the laboratory at reduced scales, which form the basis for determining the influence of variables on process transformation within the deep-water environment.

## CHARACTERIZATION OF CURRENT PROCESSES AND ASSOCIATED DEPOSITS IN CONFINED BASIN SETTINGS

Despite much work on the fluid dynamics of turbidity currents, their sedimentary deposits and architectures are still relatively poorly understood with limited linkage to physical processes. One of the drawbacks to investigating modern environments is the in situ measurement deep-water systems, and observations are rare because of unpredictability and destructive nature of turbidity currents. In this section I show the application of (1) physical and numerical modeling, (2) modern, (3) outcrop, and (4) geophysical studies for characterizing deep-water processes and describe the implications for interpreting processes.

**Experimental Studies**

Documented analyses of minibasin physical models have exploited 2-D experimental setups and resultant observations provided critical insight into the relationship between turbidity currents and how they are affected by seafloor topography. Physical models provide an avenue for investigating these relationships in a laboratory setting, where the physical setting and flow characteristics of turbidity currents are scaled to natural systems through the applications of the Reynolds-averaged Navier-Stokes equations. Numerical models provide an alternative avenue for investigating flows and their deposits in confined settings. Like physical experiments, numerical models are used to study flow processes and the deposit architecture, but can be efficiently employed to incorporate a wide range of flow conditions and scales, and the subject of scaling flows associated with physical models is easily overcome. The main limitation to both physical and numerical models is that the simulation of flow processes tends to be both time- and depth-averaged, therefore sedimentary architecture at fine reservoir scale is difficult to reproduce.

Experimental work on minibasins was pioneered by Hickson et al (2000), where high-resolution bathymetric data from the Gulf of Mexico was used to derive a "typical" intraslope basin topographic profile that was used to construct a scale model of (1) a single basin and (2) two basins in succession into which sustained (long-duration) turbidity currents were run. The experiments revealed different depositional architectures that depend on the duration of the current events and their ability to create a fully ponded turbidity current within the minibasins. Additionally, these experiments revealed two characteristics of sustained turbidity currents, and include an internal hydraulic jump and a settling interface. These two phenomena have been reported in subsequent work by Toniolo (2002), Lamb et al. (2004), Lamb et al. (2006) and Toniolo et al. (2006a). For all

these experiments, turbidity currents were generated from dilute suspensions containing various combinations of sediment material with various grain size distributions.

Toniolo et al. (2006a,b) investigated these documented relationships in theory and related the process of filling and spilling of turbidity currents to the geometry of the basin, particularly the basin length and the height of the downdip barrier to flow using physical and numerical models. The resultant depth-averaged numerical model can be useful for simulating change in bed level, current thickness, and other depth-averaged properties, but these models are unable to replicate the vertical structure of a flow field. They proposed that if the "ponded" zone of the minibasin is sufficiently long, there may be no outflow of the current across the downdip barrier, even with continuous inflow. Additionally, their estimates of the effect of detrainment at field scale indicated that even with the influx of a succession of large, quasi-continuous events, there may be relatively little outflow from a minibasin until the relief has been reduced substantially. The three main assumptions to their model included (1) the barrier is significant enough to force a sharp hydraulic jump, effectively reducing the potential energy of the flow, (2) the hydraulic jump invokes vertical mixing, which (3) implies that water detrains across the interface over the ponded zone.

Lamb et al. (2004) focused on the dynamics and deposits of both surging and continuous turbidity currents flowing into a model minibasin. In their analysis, they employed the use of a Ponding Index to quantitatively illustrate the differences between the deposits formed from each type of event (Fig. 3.6). They suggested that the differences between the deposits are likely due to the relative proportion of head to body of the flows, where (1) the continuous flows led to the establishment of a quasi-steady dammed turbidity current, which resulted in uniform deposition with a low ponding index, while (2) the surge events were sufficiently small to be contained by the basin, and

deposited “ponded” deposits that were characterized by relatively higher ponding indices. Further implications for interpreting the ability of a basin to trap sediment from each type of flow are discussed, and the implications for interpreting the deposit geometries of single events versus cumulative events are described in Lamb et als. work.

Lamb et al. (2006) described a simple model to predict the trapping of sediment in an experimental basin based on the relative magnitudes of the input discharge of turbid water and the detrainment discharge of water across a settling interface. Their model shows a limiting case, whereby a basin captures 100 % of the sediment from a ponded turbidity current until sediment deposition raises the settling interface above the downstream lip of the minibasin. They therefore postulate that the mechanism is similar for minibasins filling in nature, and that the trap efficiency of sediment can be expected to be high until the minibasin is substantially filled with sediment.

Khan and Imran (2008) apply a 2-D numerical investigation of the dynamics of turbidity currents flowing through a series of minibasins. The resultant vertical-structure model reveals the velocity as well as the suspended-sediment concentration profiles, which was deficient in the previously described study of Toniolo et al (2006). The simulation result of Khan and Imran show that the sediment deposition pattern, as well as the vertical distributions of concentration profiles predicted by the model is in reasonably close agreement with the documented results of Lamb et al. (2004) and Lamb et al. (2006). The model successfully captures draping of sediment over initial bed irregularities. Their subsequent field-scale investigation of flows into two successive minibasins showed that the inflow condition of a continuous-feed turbidity current can strongly influence the bed morphology of the minibasin. Results showed that larger sediment particles in the inflow caused overall deposition while smaller sediment particles led to erosion.

Violet et al. (2005) recognized that while 2-D experiments such as those previously described above are useful, there are two limitations to their applicability. These limitations in the experimental conditions were (1) their basin floors were rigid and therefore did not subside, and (2) 3-D flows and deposits were not reproduced. The main implication to these limitations is that the modeling of compensationally stacked lobes and the self-formation of channels were impossible. Such stacking of lobes and self-formation of channels are important ways by which minibasins construct their sediment fill. To address these limitations, Violet et al. designed an experiment performed on a 3-D subsiding model minibasin into which varying durations of turbidity currents were run. Results from their analysis show that continuous turbidity current events formed depocenters that were more proximal than surge events. Additionally, in no case did the thickest portion of the deposit from a flow coincide with the deepest portion of the basin (zone of maximum subsidence/ accommodation). When currents were run during a subsidence event, it was found that the resulting deposit was relatively insensitive to this movement (i.e. the pattern of sedimentation was insensitive to tectonic subsidence). Erosion and lobe switching in the medial zone of the basin coincided with current ripples and post-depositional sediment deformation.

**Modern Studies**

Modern turbidite systems offer several advantages over study of ancient reservoir analogues: a) they can be imaged over large areas with sonar systems at relatively low cost (compared to 3-D seismic surveys) and large areas have already been mapped (e.g., Gardner et al., 1996; Damuth et al., 1988), and in some cases sampled extensively (e.g., Flood et al., 1995); b) because of their young age, the interaction of structural deformation (if any) and sedimentation can be evaluated more precisely than for deeply

buried or ancient outcrop systems; c) a higher-frequency (higher-resolution) end of the acoustic spectrum can be used to image them; and d) they are exposed at the seafloor and can usually be imaged from source to sink (Pirmez, 2000). By imaging entire systems from shelf to basin (i.e., source to sink), individual elements can be placed within a morphological context, which is often difficult to determine in highly deformed subsurface examples and rarely possible to demonstrate in outcrop studies.

Van Andel & Komar (1969) speculated that the rebound of turbidity currents off the bounding slopes was responsible for repeated grading profiles seen in their piston cores. Nelson (2004) described basic types of turbidite systems found in active margins (Cascadia Basin), rift basins (Lake Baikal), and continental slopes (Gulf of Mexico). The Cascadia Basin along the active subduction zone margin contains aprons, mixed fans, tectonically confined bypass channels from 20 to 2000 km and unusual turbidite systems with plunge pools, sediment waves, channels and lobes; the Lake Baikal rift basin contains aprons on the border fault footwalls, sand-rich fans on the ramp hanging walls, and elongate mud-rich fans in axial basins drained by axial fault-confined channels; and the Gulf of Mexico slopes contain ponded minibasins and bypass channels that sometimes traverse the slope to feed mixed fans in the Sigsbee Abyssal Plain where small sand-rich fans and large mud-rich fans also are found.

Gervais et al. (2004) describe the modern sandy Golo turbidite system, developed in a partly confined setting on the eastern margin of Corsica. They found that although the setting remains adjacent to a tectonically active margin, the dominant influences on depositional patterns appear to have been the antecedent basin-floor morphology, sediment source characteristics and eustasy. In a subsequent study, Gervais et al (2006) described the latest Pleistocene distal lobe of a confined turbidite system from which they built a comprehensive model for the interrelationship of various architectural elements

within a lobe complex. They demonstrate that the 3-D geometry of the lobe is directly controlled by the degree of confinement of gravity currents, which has a significant impact on reservoir petrophysical properties.

Covault and Romans (2009) compared turbidite-system gross morphologies from the California Borderland, and compared them to other types of confined and unconfined settings using published data to study the nature of deposits relative to the sizes of receiving basins. They characterized turbidite systems according to volume, area, maximum thickness, length and width. They interpreted that turbidite systems that were supplied a large enough volume of sediment to be confined by their basin margins were unable to areally expand and, subsequent turbidite deposition thickened the systems. Thinner deposits resulted where sediment volumes were insufficient to extend systems to their receiving-basin margins. Turbidite systems appeared to exhibit progressively smaller maximum thickness-to-area ratios (i.e. system areas increased more than maximum thicknesses during successive growth phases) as a basin filled. This was attributed to progressive turbidite deposition "healing" relatively high-relief bathymetry until a proximal basin was filled to its bounding ridges and subsequent turbidity currents spilled into a distal basin. They suggested that the growth and morphologies of turbidite systems in confined receiving basins, such as California borderland and the western Gulf of Mexico slope, are greatly influenced by relatively smaller volumes of sediment supplied and receiving-basin confinement. They are distinctively different from voluminous, finer-grained, unconfined systems that are unrestricted by basin margins. As a result, these fine-grained, unconfined systems grow to be distinctively areally extensive in large ocean basins. Areal characteristics (e.g. length-to-width and length-to-area ratios) of turbidite systems were generally similar as a result of sediment-gravity-flow processes and larger-scale autogenic behavior (e.g., channel avulsion, lobe switching, etc.).

Although Covault and Romans insights provided an excellent comparison of deposit morphologies from settings with varying degrees of confinement and sediment supply, their interpretation of processes responsible for filling basins were limited, with observations based on existing models of fill, particularly the fill and spill model.

**Outcrop Studies**

Since the interaction of turbidity currents with basin topography can have a complex effect upon deposit geometry, outcrop studies designed to investigate the controls upon sedimentary architecture must take into account the effects of local basin topography. Pickering & Hiscott (1985) recognized containment of turbidity currents in the Ordovician Cloridorme Formation of Québec from recognition of palaeocurrent reversals, which they interpreted to result from deflection and reflection of part of large-volume turbidity currents from confining slopes. Similar evidence of divergent palaeoflow indicators has subsequently been recognized at outcrop in various other successions representing depositional systems where turbidity currents have interacted with basin bounding or intrabasinal slopes (e.g. Kneller et al 1991; Smith, 2004).

Hodgson & Haughton (2004) detail the interplay between deep-water sedimentation and syn-depositional faulting in the Neogene fill of the Tabernas-Sorbas Basin, SE Spain, documenting the effects of a fault which appears to have propagated through to the sea-bed during turbidite deposition. They found that characteristic sedimentation in the fault-controlled ponded depocenter involved distinctive thick sheet-like sandstone-mudstone couplets, interpreted as the deposits of large volume turbidity currents that were entirely confined within the structurally defined minibasin.

McCaffrey and Kneller (2001) studied the character of deposit terminations in the from the confining slopes of the Annot and Peira Cava sub-basins of the lower Tertiary

turbidite system of the Alpine foreland basin (Annot Sandstone and the correlative Champsaur Sandstone). The location provided an ideal system in which to characterize sandstone geometries developed against confining slopes, because the basin floor was bathymetrically complex, being divided into a series of discrete sub-basins. They describe the geometry of deposits associated with systems confined by lateral or oblique frontal slopes, and interpret the processes responsible for their formation. Their study formulates a continuum between two geometries of pinch-out configuration. For the "type A" configuration, deposits thin onto the confining surface (commonly abruptly), and individual beds tend to not erode into earlier deposits. For the "type B" configuration, turbidite sandstones commonly thicken toward the confining slope, and beds may incise into earlier deposits. The two types are however not mutually exclusive in outcrop. Their analysis suggests that the principal control in determining pinch-out character is flow magnitude, with smaller, "confined" flows producing type A pinch-outs, and larger "unconfined" flows producing type B. The analysis is compared to Haughton's (1994) work on the Sorbas Basin in southeast Spain. Emphasis is placed on previous work (e.g. Kneller, 1995; Mulder and Syvitski, 1995; Kneller and Branney, 1995) to characterize the paleoflow conditions (e.g. size, duration, grain size distribution), and the application to subsurface data analysis in confined settings.

Sinclair and Cowie (2003) investigate thickness distributions and the geometrical features of the turbidite beds, using data from the Annot and Taveyannaz Sandstones of the Alpine foreland basin. In their analysis, they find that flow ponding causes dramatic thickening of beds. Flow stripping counteracts this, especially for thicker beds, and accounts for a very large proportion of the input volume of sediment bypassing the basin even before the basin is filled. For the base-of-slope setting, erosion and non-deposition of beds results in the preferential preservation of thicker beds.

Most recently, Pyles and Jennette (2009) and Pyles et al. (2011) document the geometry, architectural association and paleogeographic occurrence of co-genetic debrite-turbidite beds in the Carboniferous Ross Sandstone. They describe longitudinal changes in stratigraphic architecture from the basin floor to the distal basin margin. The channels and lobes on the basin floor laterally transfer into lobes that laterally transfer into co-genetic debrite–turbidite beds, locally derived slumps, and laminated shale.

**Subsurface Studies**

Subsurface studies have been the foundation of our current understanding of confined deep-water systems and the basis for many existing models. Key publications describe how minibasins on complex slopes fill with sediment are Gulf-of Mexico centric (e.g. Winker, 1996; Prather et al., 1998; Badalini et al., 2000; Booth et al., 2000; Beaubouef and Friedmann, 2000; Booth et al., 2002; among others), but other studies incorporate observations from margins across the globe (Steffens et al., 2003; Smith, 2004; Steffens et al, 2004).

Prather et al. (1998), one of the most popular subsurface based model for minibasin filling, published their hallmark classification scheme of seismic facies from an integrated Gulf of Mexico dataset, which is widely used for characterizing subsurface deposits and interpreting deep-water processes in proximal intraslope minibasins. Their classification scheme is based on geometric relationships that comprise bounding surface type, external geometry of surface-bounded seismic facies, event geometry internal to bounding surfaces, seismic reflectivity, and event continuity. Their analysis suggests that three primary seismic facies categories exist: (1) convergent, (2) draping, and (3) chaotic. They further subdivide the three primary facies categories into nine individual facies based on internal reflection configuration and reflectivity characteristics (Fig. 3.7) and

link them to process. They suggest that baselapping seismic events of the $C_{bh}$ facies reflect filling of ponded accommodation space with submarine fans. Non-baselapping, convergent thinning $C_{th}$ (high-reflectivity) and $C_{tl}$ (low-reflectivity) seismic facies formed as slope accommodation space was filled to grade by overbanking muddy turbidite and leveed channel processes. Draping D and E facies resulted from hemipelagic to pelagic processes as reduced sediment supply occurred during eustatic sea level rise, or followed filling of intraslope basins to their local equilibrium profile. Chaotic A and $B_l$ (low-reflectivity) facies formed as slopes built due to progradation or tilt above the at-grade slope angle in response to local or regional subsidence, producing slumps, submarine slides, and debris flows. Chaotic $B_h$ (high-reflectivity) facies formed as discontinuous channelized sand bodies filled incised valleys, canyons, and gorges on the paleoslope. They suggest that with the progressive infilling of a minibasin, the nine facies form two facies assemblages, namely the ponded facies assemblage (PFA) and bypass facies assemblage (BFA). BFA is generally the more proximal facies assemblage and PFA the more distal. In basin-fill successions BFA nearly always overlies PFA. Huang et al (2009) argue the point that these facies assemblages can be somewhat misleading, as "ponding" can occur within BFA and bypass within PFA (Booth et al., 2003; Winker, 2000). Additionally, Huang et al. (2009) suggest that the classification of PFA and BFA seems too simple to properly describe such a complicated setting.

A subsequent study by Booth (2003) reports results that focus on the main controls for reservoir distribution, architecture and stratigraphic trapping in various slope settings. He found that for above-grade slopes with ponded accommodation, sheet sand deposition occurs preferentially near the base of healed-slope accommodation as a result of "fill and spill" processes. In such a scenario, the pinchout of ponded sands into slope drapes deposited around ponded basins tend to form lateral seals for onlap traps.

## SUMMARY

In this chapter, I first introduced the concept of confinement of deep-water systems from a historical perspective, as it is understood from various published works. For confined basins, it is suggested that deposition from sediment gravity flows is strongly controlled by the interactions among flow magnitude and/or duration, flow efficiency, grain size distribution, and the size and morphology of the depocenters. Second, the concept of flow efficiency is emphasized as a key factor that contributes to turbidite deposition in confined basin settings that are removed from the shelf, as it is heavily dependent on the other mentioned factors. Third, I addressed the spectrum of studies that focus on depositional models and process models for confined basin settings that are encountered in the literature. Finally, I addressed the characterization of current processes and their associated deposits in confined basin settings by showing that the application of (1) physical and numerical modeling, (2) modern and (3) outcrop, and (4) geophysical studies for characterizing deep-water processes and described the implications for interpreting turbidity current flow processes.

The discussion above focused on components that collectively represent the state of the current literature on the topographical confinement of turbidity currents and the effect of changing basin and current property characteristics on influencing sediment geometry and distribution, but there are remaining gaps in knowledge that will be addressed in this research. Despite the abundance of subsurface data and the multitude of interpretations derived from them, little is documented about the three-dimensional (3-D) physical processes through which minibasins fill relative to the topography created by underlying mobile salt. While real world data provide a practical approach to investigating minibasin fill, an understanding of how turbidity currents physically interact with minibasin topography is limited since direct field observation of turbidity currents is

problematic. A better understanding of the flow dynamics of turbidity currents and how they deposit sediment in confined basins is therefore achieved through the application of experimental models, from which predictive relationships can be ascribed to real world data to gain a better handle on sediment distribution on complex slopes.

## FIGURES

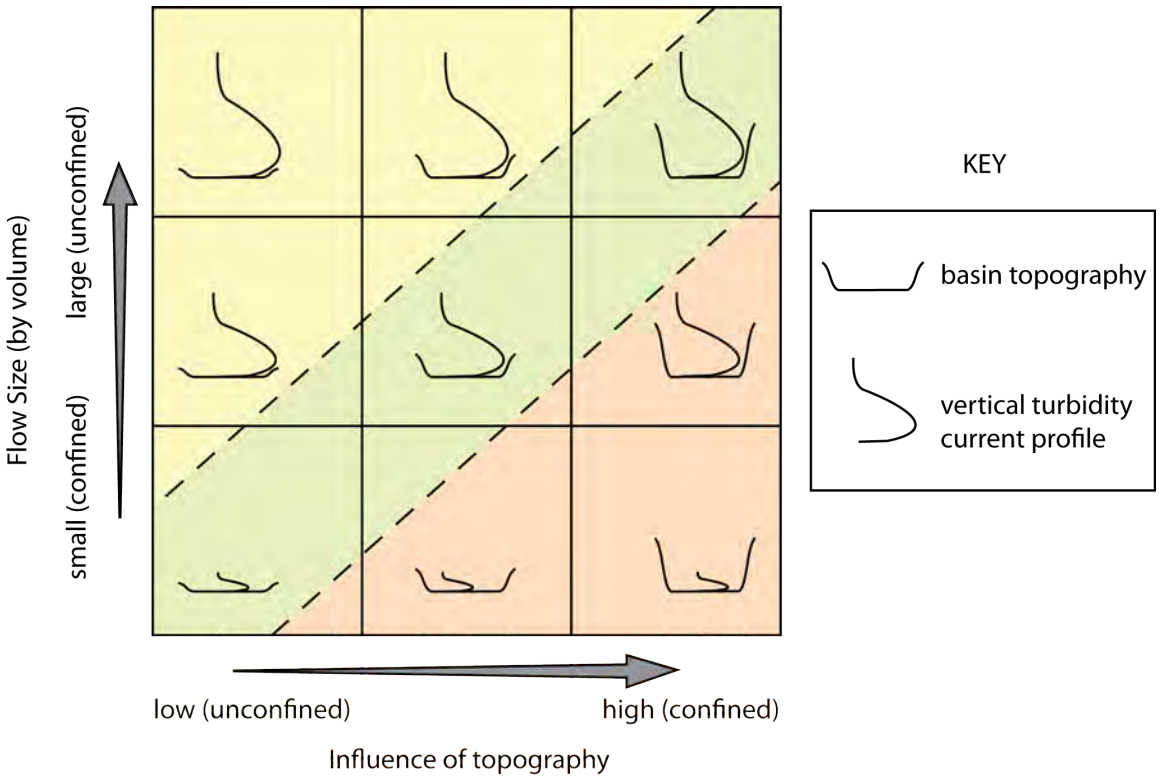


Figure 3.1: Simplified illustration of distinct possibilities that qualitatively describe the degree of confinement by comparing the relative size of the turbidity current to the accommodation of the receiving basin. Concepts gleaned from Mohrig and Buttles (2007), but are not to scale.

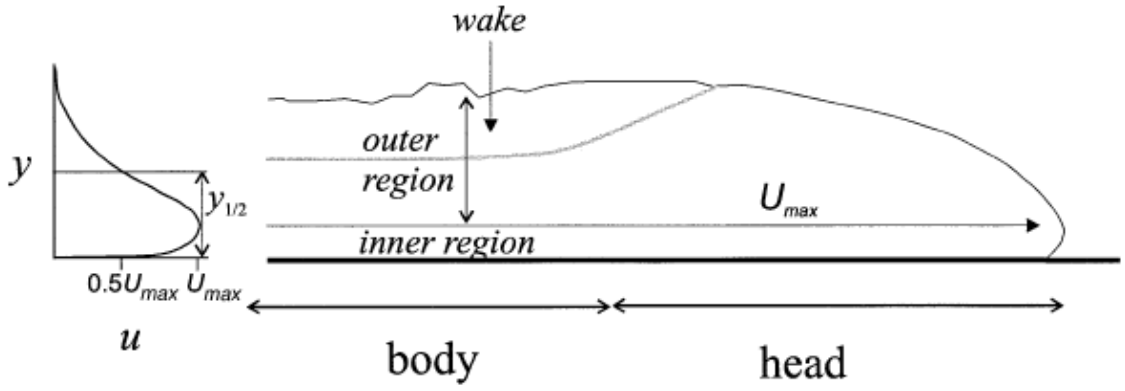


Figure 3.2: Schematic diagram of the head and body of a gravity current, showing a typical downstream velocity profile (modified from Kneller and Buckee, 2000; Meiburg and Kneller, 2000). The head of the flow is usually associated with the initial surge and is capable of eroding the bed on which the current traverses.

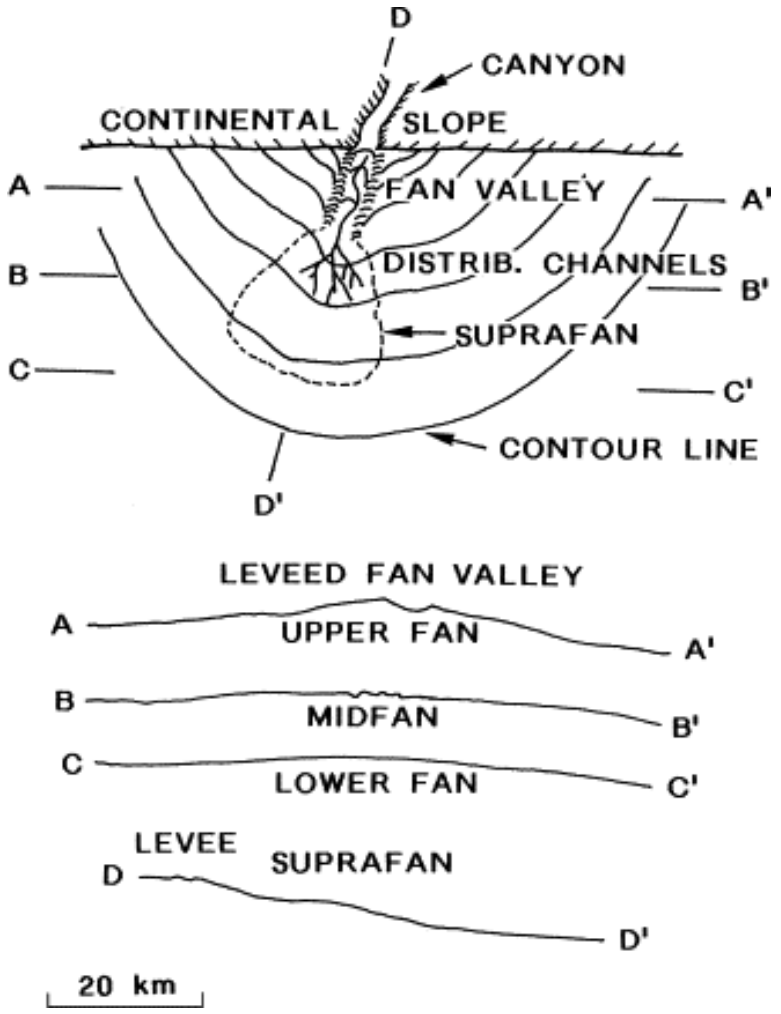


Figure 3.3: Model of a modern, sand-rich fan (modified from Normark, 1970), with distinct zones that characterize specific depositional facies.

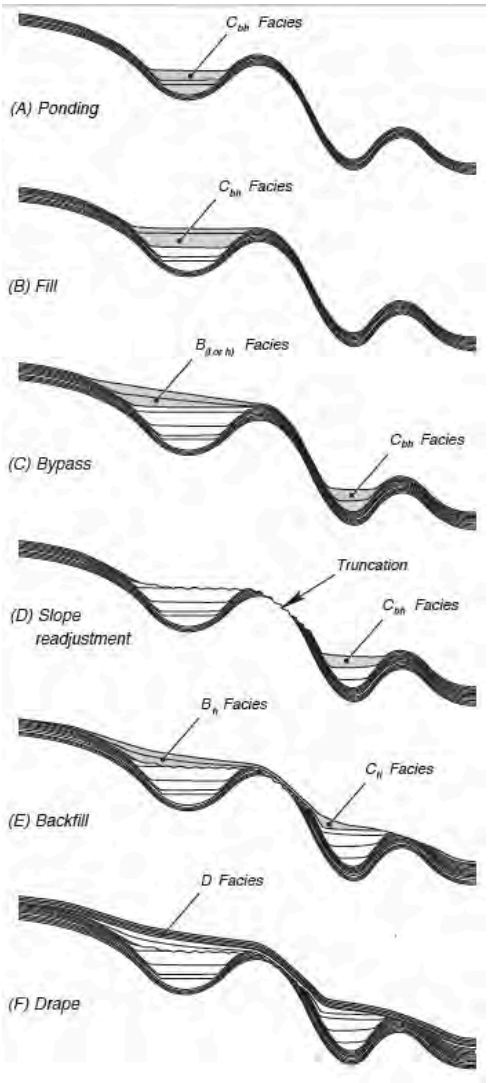


Figure 3.4: Evolution of the idealized ponded depositional sequence (after Prather et al., 1998). (A) Fans first fill ponded accommodation space in proximal basin (B) complete fill occurs. (C) Turbidites spill downslope into the distal basin. (D) Formation of a truncation surface from erosion of the upslope basin with the readjustment of the equilibrium profile (E) Backfill of the space above the truncation surface occurs as the downslope basin fills and the slope between the two basins aggrades to a local equilibrium profile. (F) Hemipelagic deposits drape the basins after the slope grades to the equilibrium profile, or a decrease in sediment influx from sea level rise or system avulsion.

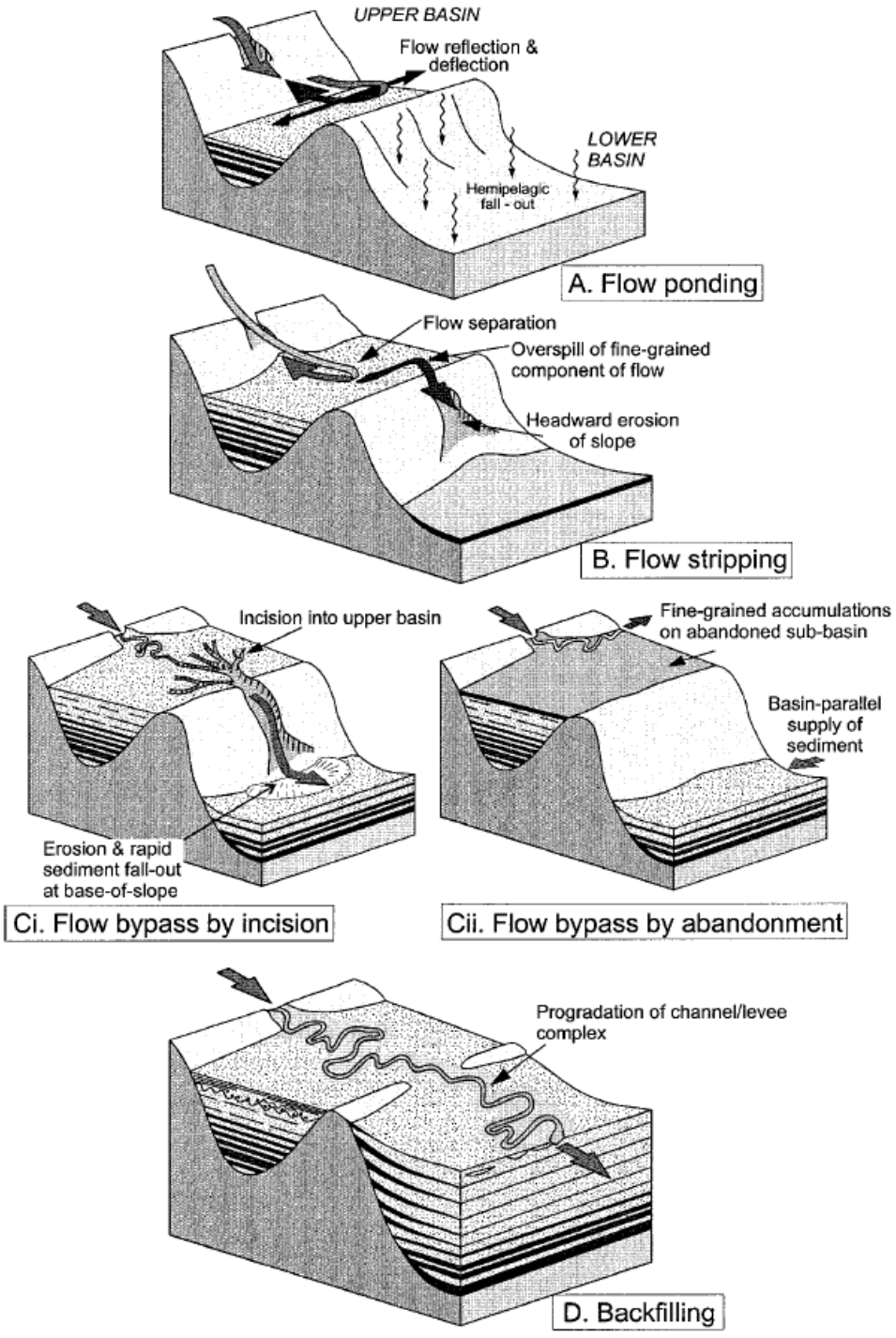


Figure 3.5: Depositional model for the progressive infill of a confined turbidite basin and associated deposits at the base of the slope of a lower basin (from Sinclair and Tomasso, 2002). See text for description.

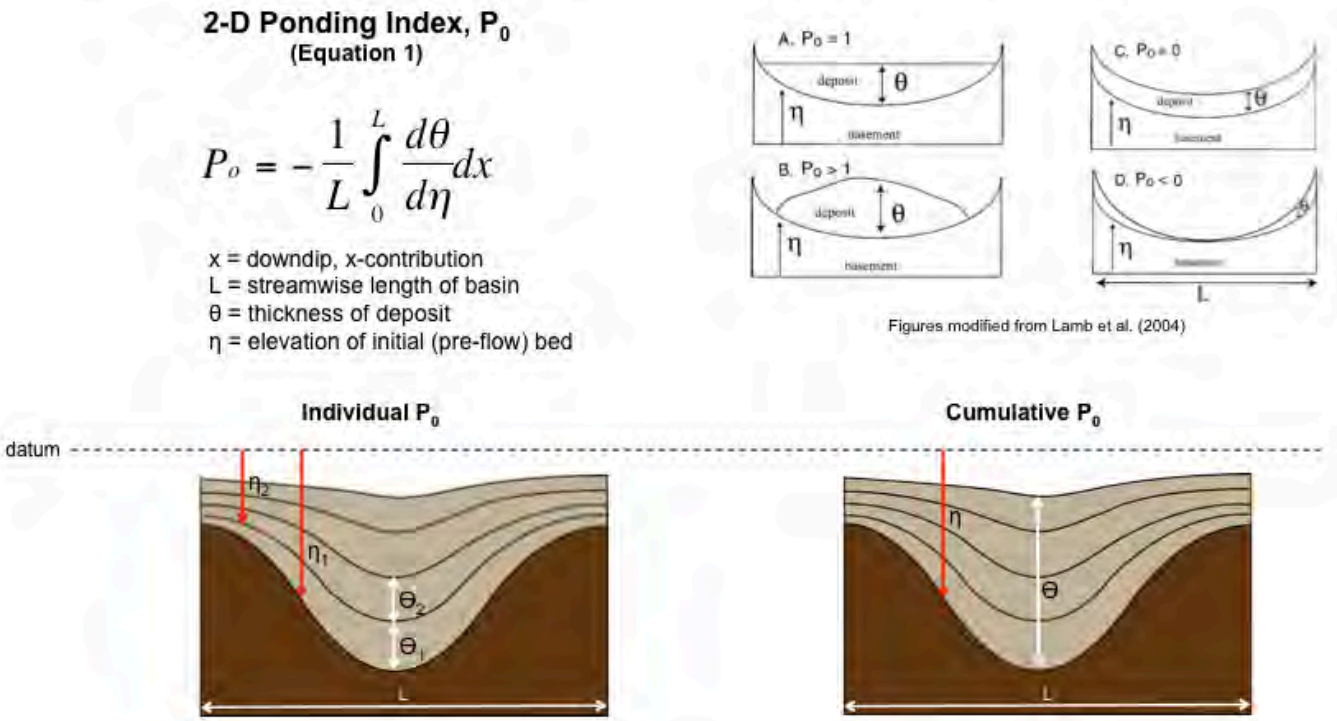


Figure 3.6: A dimensionless 2-D Ponding Index number ($P_o$) is used to describe the experimental deposits. The index is a number that compares the change in thickness of the deposit relative to the change in basin elevation over a given length (L). A deposit ponding index equal to one represents a completely ponded deposit (A, upper right figure), a deposit ponding index greater than one represents a mounded deposit (B, upper right figure), and a deposit ponding index equal to zero represents a draped deposit (C, upper right figure). A deposit with accentuated highs, meaning that the flow deposits preferentially on the slopes rather than the center of the basin, would have a negative deposit ponding index (D, upper right figure). The individual Ponding Index characterizes the geometry of a single bed relative to a prior basin deposit surface (lower left figure). The cumulative Ponding Index characterizes the geometry of a number of beds relative to the initial basin surface (lower right figure)

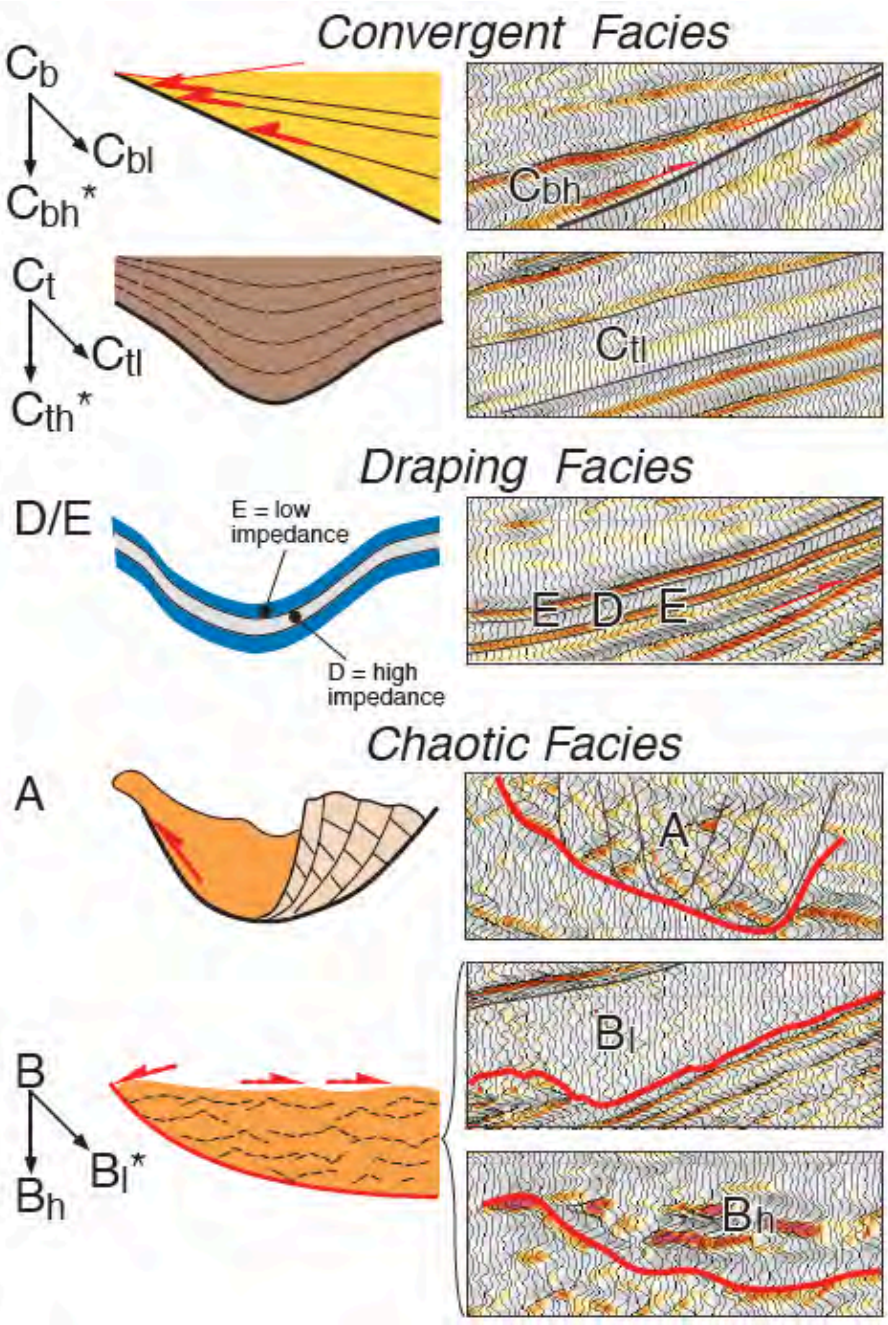


Figure 3.7: Idealized external and internal geometries that characterize seismic facies (from Prather et al., 1998). Facies marked with an asterisk are the more common of the two sub-facies. See text for facies and sub-facies descriptions.

## REFERENCES


Al-Ja'aidi, O., 2000, The influence of topography and flow efficiency on the deposition of turbidites, University of Leeds.

Al-Ja'Aidi, O. S., W. D. McCaffrey, and B. C. Kneller, 2004, Factors influencing the deposit geometry of experimental turbidity currents: implications for sand-body architecture in confined basins: Geological Society, London, Special Publications, v. 222, p. 45-58.

Alexander, C. S., L. M. Rumelhart, A. Raposo, and J. Dominey, 2001, The Plutonio discovery, Block 18, Angola; a 3-D visualization and multiattribute approach to exploration success: Leading Edge [Tulsa, OK], v. 20, p. 1393.

Amy, L., B. Kneller, and W. McCaffrey, 2000, Evaluating the links between turbidite characteristics and gross system architecture; upscaling insights from the turbidite sheet-system of Peira Cava, SE France: Program and Abstracts - Society of Economic Paleontologists. Gulf Coast Section. Research Conference, v. 20, p. 1-15.

Amy, L. A., W. D. McCaffrey, and P. J. Talling, 2009, Special Issue Introduction: Sediment gravity flows, Recent insights into their dynamic and stratified/composite nature: Marine and Petroleum Geology, v. 26, p. 1897-1899.

Anderton, R., 1995, Sequences, cycles and other nonsense: are submarine fan models any use in reservoir geology?: Geological Society, London, Special Publications, v. 94, p. 5-11.

Apps, G. M., F. J. Peel, C. J. Travis, and C. A. Yeilding, 1994, Structural controls on Tertiary deep water deposition in the northern Gulf of Mexico: Papers presented at the Gulf Coast Section, Society of Economic Paleontologists and Mineralogists Foundation Annual Bob F. Perkins Research Conference, v. 15, p. 1-7.

Badalini, G., B. Kneller, and C. D. Winker, 2000, The late Pleistocene Trinity-Brazos turbidite system; new insights for deep turbidite reservoir interpretation: Annual Meeting Expanded Abstracts - American Association of Petroleum Geologists, v. 2000, p. 8-8.

Beaubouef, R. T., C. Rossen, F. B. Zelt, M. D. Sullivan, D. C. Mohrig, and D. C. Jennette, 1999, Deep-water sandstones,Brushy Canyon Formation, West Texas: Field Guide, AAPG Hedberg Field Research Conference.

Beaubouef, R. T., and S. J. Friedmann, 2000, High resolution seismic/sequence stratigraphic framework for the evolution of Pleistocene intra slope basins, western Gulf of Mexico; depositional models and reservoir analogs: Program and Abstracts - Society of Economic Paleontologists. Gulf Coast Section. Research Conference, v. 20, p. 40-60.

Booth, J. R., A. E. DuVernay, III, D. S. Pfeiffer, and M. J. Styzen, 2000, Sequence stratigraphic framework, depositional models, and stacking patterns of ponded and slope fan systems in the Auger Basin; central Gulf of Mexico slope: Program and Abstracts - Society of Economic Paleontologists. Gulf Coast Section. Research Conference, v. 20, p. 82-103.

Booth, J. R., M. C. Dean, A. E. DuVernay, III, and M. J. Styzen, 2003, Paleo-bathymetric controls on the stratigraphic architecture and reservoir development of confined fans in the Auger Basin; central Gulf of Mexico slope: Marine and Petroleum Geology, v. 20, p. 563-586.

Bouma, A. H., 1985, Introduction to submarine fans and related turbidite systems Frontiers in sedimentary geology, v. 1: United States, Springer-Verlag: New York, NY, United States, p. 3-5.

Bouma, A. H., 2000, Fine-grained, mud-rich turbidite systems; model and comparison with coarse-grained, sand-rich systems: AAPG Memoir, v. 72, p. 9-20.

Bruhn, C. H. L., 1998, Major types of deep-water reservoirs from the eastern Brazilian rift and passive margin basins: AAPG Bulletin, v. 82, p. 1896-1897.

Brunt, R. L., W. D. McCaffrey, and B. C. Kneller, 2004, Experimental modeling of the spatial distribution of grain size developed in a fill-and-spill minibasin setting: Journal of Sedimentary Research, v. 74, p. 438-446.

Carlson, J., and J. P. Grotzinger, 2001, Submarine fan environment inferred from turbidite thickness distributions: Sedimentology, v. 48, p. 1331-1351.

Chan, M. A., and R. H. Dott, Jr., 1983, Shelf and deep-sea sedimentation in Eocene forearc basin, western Oregon; fan or non-fan?: AAPG Bulletin, v. 67, p. 2100-2116.

Choi, S., and M. H. Garcia, 1996, Arbitrary Lagrangian-Eulerian approach for finite element modeling of two-dimensional turbidity currents: Water International, v. 21, p. 175-182.

Clemenceau, G. R., and J. Colbert, 1999, Levee-overbank turbidite production from Ram/Powell Field, deepwater Gulf of Mexico: AAPG Bulletin, v. 83, p. 1305-1305.

Covault, J. A., 2009, Growth patterns of deep-sea fans revisited; turbidite-system morphology in confined basins, examples from the California Borderland, *in* B. W. Romans, ed., Marine Geology, Netherlands, Elsevier: Amsterdam, Netherlands, p. 51-66.

Damuth, J. E., R. D. Flood, R. O. Kowsmann, R. H. Belderson, and M. A. Gorini, 1988, Anatomy and growth pattern of Amazon deep-sea fan as revealed by long-range side-scan sonar (GLORIA) and high-resolution seismic studies: AAPG Bulletin, v. 72, p. 885-911.

Damuth, J. E., C. H. Nelson, and H. C. Olson, 2008, Bryant Canyon/Fan and Rio Grande Fan turbidite systems; shelf to basin modern analogues for productive Tertiary minibasin systems: Abstracts: Annual Meeting - American Association of Petroleum Geologists, v. 2008.

Edwards, D. A., 1993, Turbidity currents; dynamics, deposits and reversals, Lecture Notes in Earth Sciences, Federal Republic of Germany, Springer-Verlag : Berlin-Heidelberg-New York, Federal Republic of Germany.

Edwards, D. A., M. R. Leeder, J. L. Best, and H. M. Pantin, 1994, On experimental reflected density currents and the interpretation of certain turbidites: Sedimentology, v. 41, p. 437-461.

Fildani, A., and W. R. Normark, 2004, Late Quaternary evolution of channel and lobe complexes of Monterey Fan: Marine Geology, v. 206, p. 199-223.

Flood, R. D., D. J. W. Piper, A. Klaus, S. J. Burns, W. H. Busch, S. M. Cisowski, A. Cramp, J. E. Damuth, M. A. Goni, S. G. Haberle, F. R. Hall, K.-U. Hinrichs, R. N. Hiscott, R. O. Kowsmann, J. D. Kronen, Jr., D. Long, M. Lopez, D. K. McDaniel, P. L. Manley, M. A. Maslin, N. Mikkelsen, F. Nanayama, W. R. Normark, C. Pirmez, J. R. dos Santos, R. R. Schneider, W. J. Showers, W. Soh, and J. Thibal, 1995, Introduction: Proceedings of the Ocean Drilling Program, Part A: Initial Reports, v. 155, p. 5-16.

Garcia, M. H., 1994, Depositional turbidity currents laden with poorly sorted sediment: Journal of Hydraulic Engineering, v. 120, p. 1240-1263.

Gardner, J. V., R. G. Bohannon, M. E. Field, and D. G. Masson, 1996, The morphology, processes, and evolution of Monterey Fan; a revisit: United Kingdom, Cambridge University Press: Cambridge, United Kingdom, p. 193-220.

Gardner, M. H., J. M. Borer, M. Dechesne, and R. Wagerle, 1998, Cut, fill and spill; a new look at the overbank paradigm for sandy deep water systems: Annual Meeting Expanded Abstracts - American Association of Petroleum Geologists, v. 1998.

Gardner, M. H., and J. M. Borer, 2000, Submarine channel architecture along a slope to basin profile, Brushy Canyon Formation, West Texas: AAPG Memoir, v. 72, p. 195-213.

Gardner, M. H., J. M. Borer, J. J. Melick, N. Mavilla, M. Dechesne, and R. N. Wagerle, 2003, Stratigraphic process-response model for submarine channels and related features from studies of Permian Brushy Canyon outcrops, West Texas: Marine and Petroleum Geology, v. 20, p. 757-787.

Gervais, A., B. Savoye, D. J. W. Piper, T. Mulder, M. Cremer, and L. Pichevin, 2004, Present morphology and depositional architecture of a sandy confined submarine system: the Golo turbidite system (eastern margin of Corsica): Geological Society, London, Special Publications, v. 222, p. 59-89.

Gervais, A., B. Savoye, T. Mulder, and E. Gonthier, 2006, Sandy modern turbidite lobes; a new insight from high resolution seismic data: Marine and Petroleum Geology, v. 23, p. 485-502.

Gladstone, C., J. C. Phillips, and R. S. J. Sparks, 1998, Experiments on bidisperse, constant-volume gravity currents; propagation and sediment deposition: Sedimentology, v. 45, p. 833-843.

Haughton, P. D. W., 1994, Deposits of deflected and ponded turbidity currents, Sorbas Basin, Southeast Spain: Journal of Sedimentary Research, Section A: Sedimentary Petrology and Processes, v. 64, p. 233-246.

Haughton, P. D. W., 2000, Evolving turbidite systems on a deforming basin floor, Tabernas, SE Spain: Sedimentology, v. 47, p. 497-518.

Hay, A. E., 1987, Turbidity currents and submarine channel formation in Rupert Inlet, British Columbia; 1, Surge observations: Journal of Geophysical Research, v. 92, p. 2875-2881.

Heezen, B. C., and W. M. Ewing, 1952, Turbidity currents and submarine slumps, and the 1929 Grand Banks [Newfoundland] earthquake: American Journal of Science, v. 250, p. 849-873.

Hickson, T. A., and D. R. Lowe, 2002, Facies architecture of a submarine fan channel-levee complex; the Juniper Ridge Conglomerate, Coalinga, California: Sedimentology, v. 49, p. 335-362.

Hodgson, D. M., and P. D. W. Haughton, 2004, Impact of syndepositional faulting on gravity current behaviour and deep-water stratigraphy; Tabernas-Sorbas Basin, SE Spain: Geological Society Special Publications, v. 222, p. 135-158.

Hodgson, D. M., S. S. Flint, D. Hodgetts, N. J. Drinkwater, E. P. Johannessen, and S. M. Luthi, 2006, Stratigraphic evolution of fine-grained submarine fan systems, Tanqua depocenter, Karoo Basin, South Africa: Journal of Sedimentary Research, v. 76, p. 20-40.

Hurst, A., B. Cronin, and A. Hartley, 2000, Reservoir modelling sand-rich deep-water clastics; the necessity of down-scaling: Petroleum Geoscience, v. 6, p. 67-76.

Khan, S. M., and J. Imran, 2008, Numerical investigation of turbidity currents flowing through minibasins on the continental slope: Journal of Sedimentary Research, v. 78, p. 245-257.

Khripounoff, A., A. Vangriesheim, N. Babonneau, P. Crassous, B. Dennielou, and B. Savoye, 2003, Direct observation of intense turbidity current activity in the Zaire submarine valley at 4000 m water depth: Marine Geology, v. 194, p. 151-158.

Kneller, B., 1995, Beyond the turbidite paradigm: physical models for deposition of turbidites and their implications for reservoir prediction: Geological Society, London, Special Publications, v. 94, p. 31-49.

Kneller, B., 1995, Topographic controls on turbidite sandstone reservoirs; facies models with a physical basis: AAPG Bulletin, v. 79, p. 1227-1227.

Kneller, B. C., and M. J. Branney, 1995, Sustained high-density turbidity currents and the deposition of thick massive sands: Sedimentology, v. 42, p. 607-616.

Kneller, B., D. Edwards, W. McCaffrey, and R. Moore, 1991, Oblique reflection of turbidity currents: Geology [Boulder], v. 19, p. 250-252.

Kneller, B., and W. D. McCaffrey, 1995, Modelling the effects of salt-induced topography on deposition from turbidity currents: Papers presented at the Gulf Coast Section, Society of Economic Paleontologists and Mineralogists Foundation Annual Bob F. Perkins Research Conference, v. 16, p. 137-145.

Kneller, B., and W. McCaffrey, 1999, Depositional effects of flow nonuniformity and stratification within turbidity currents approaching a bounding slope; deflection, reflection, and facies variation: Journal of Sedimentary Research, v. 69, p. 980-991.

Kneller, B., and C. Buckee, 2000, The structure and fluid mechanics of turbidity currents; a review of some recent studies and their geological implications: Sedimentology, v. 47, p. 62-94.

Kneller, B., and B. McCaffrey, 2001, Flow parameters and stratigraphic architecture in turbidite systems: Annual Meeting Expanded Abstracts - American Association of Petroleum Geologists, v. 2001, p. 106-107.

Kneller, B., O. J. Martinsen, and B. McCaffrey, 2009, External controls on deep-water depositional systems, Special Publication - Society for Sedimentary Geology, United States, Society for Sedimentary Geology (SEPM) : Tulsa, OK, United States.

Lamb, M. P., T. Hickson, J. G. Marr, B. Sheets, C. Paola, and G. Parker, 2004, Surging versus continuous turbidity currents; flow dynamics and deposits in an experimental intraslope minibasin: Journal of Sedimentary Research, v. 74, p. 148-155.

Lamb, M. P., H. Toniolo, and G. Parker, 2006, Trapping of sustained turbidity currents by intraslope minibasins: Sedimentology, v. 53, p. 147-160.

Lane-Serff, G. F., L. M. Beal, and T. D. Hadfield, 1995, Gravity current flow over obstacles: J. Fluid Mech., v. 292, p. 39-53.

Laval, A., M. Cremer, P. Beghin, and C. Ravenne, 1988, Density surges; two-dimensional experiments: Sedimentology, v. 35, p. 73-84.

Lomas, S. A., and P. Joseph, 2004, Confined turbidite systems: Geological Society, London, Special Publications, v. 222, p. 1-7.

Lowe, D. R., 1982, Sediment gravity flows; II, Depositional models with special reference to the deposits of high-density turbidity currents: Journal of Sedimentary Petrology, v. 52, p. 279-297.

Luthi, S., 1981, Some new aspects of two-dimensional turbidity currents: Sedimentology, v. 28, p. 97-105.

Madof, A. S., N. Christie-Blick, and M. A. Anders, 2009, Stratigraphic controls on a salt-withdrawal intraslope minibasin, north-central Green Canyon, Gulf of Mexico: Implications for misinterpreting sea level change: AAPG Bulletin, v. 93, p. 535-561.

McCaffrey, W., and B. Kneller, 2001, Process controls on the development of stratigraphic trap potential on the margins of confined turbidite systems and aids to reservoir evaluation: AAPG Bulletin, v. 85, p. 971-988.

Meckel, L. D., III, 2004, Linking shelf-edge deltas to deepwater sheet sand and channel turbidite reservoirs; examples from the Miocene-Pleistocene, Gulf of Mexico: NOGS Log, v. 44, p. 7-7.

Middleton, G. V., 1967, The orientation of concavo-convex particles deposited from experimental turbidity currents: Journal of Sedimentary Petrology, v. 37, p. 229-232.

Middleton, G. V., 1993, Sediment deposition from turbidity currents: Annual Review of Earth and Planetary Sciences, v. 21, p. 89-114.

Middleton, G. V., and J. B. Southard, 1984, Mechanics of sediment movement, SEPM Short Course, United States, Society of Sedimentary Geology : Tulsa, OK, United States.

Mitchum, R. M., Jr., 1985, Seismic stratigraphic expression of submarine fans: AAPG Memoir, v. 39, p. 117-136.

Mohrig, D., and J. Buttles, 2007, Deep turbidity currents in shallow channels: Geology [Boulder], v. 35, p. 155-158.

Montoya, P., and M. R. Hudec, 2007, Active salt tectonics and its effect on the internal architecture and connectivity between minibasins near the Sigsbee Escarpment, Gulf of Mexico: Abstracts: Annual Meeting - American Association of Petroleum Geologists, v. 2007, p. 96-96.

Mulder, T., and J. P. M. Syvitski, 1995, Turbidity currents generated at river mouths during exceptional discharges to the world oceans: Journal of Geology, v. 103, p. 285-299.

Mutti, E., 1972, Examples of ancient deep-sea fan deposits from circum-Mediterranean geosynclines: United States, Univ. Wis.-Madison--Natl. Sci. Found., Madison, p. 20-21.

Mutti, E., 1979, Turbidites et cones sous-marins profonds: Sedimentation Detritique (Fluvial, Littoral et Marin): Institut de Géologie, Univerité de Fribourg (Suisse).

Mutti, E., 1980, Turbidites and deep-sea fans, Canada.

Mutti, E., 1985, Turbidite systems and their relations to depositional sequences: NATO Advanced Study Institutes Series. Series C: Mathematical and Physical Sciences, v. 148, p. 65-93.

Mutti, E., 1992, Turbidite sandstones: Italy, AGIP, Italy.

Mutti, E., 1977, Distinctive thin-bedded turbidite facies and related depositional environments in the Eocene Hecho Group (South-central Pyrenees, Spain): Sedimentology, v. 24, p. 107-131.

Mutti, E., 1985, Turbidite systems and their relations to depositional sequences: NATO Advanced Study Institutes Series. Series C: Mathematical and Physical Sciences, v. 148, p. 65-93.

Mutti, E., and G. Ghibaudo, 1972, Un esempio di torbiditi di conoide sottomarina esterna: le Arenarie di San Salvatore (Formazione di Bobbio, Miocene): Matematiche e Naturali, v. 4, 40 p.

Mutti, E., and F. Ricci Lucchi, 1972, Le torbiditi dell'Appennino settentrionale: Introduzione all' analisi di facies: Societa Geologica Italiana, v. 11, p. 161-199.

Mutti, E., and W. R. Normark, 1987, Comparing examples of modern and ancient turbidite systems; problems and concepts: United Kingdom, Graham and Trotman : London, United Kingdom, p. 1-38.

Mutti, E., and W. R. Normark, 1991, An integrated approach to the study of turbidite systems Frontiers in sedimentary geology: United States, Springer-Verlag: New York, NY, United States, p. 75-106.

Mutti, E., E. Remacha, R. Tinterri, N. Mavilla, S. Angella, and L. Fava, 1999, Facies tracts of highly-efficient turbidity currents in large and elongate foreland basins, and their implications for basin analysis and exploration: Giornale di Geologia, v. 61, Serie 3C, p. 187-190.

Nardin, T. R., 1983, Late Quaternary depositional systems and sea level change; Santa Monica and San Pedro basins, California continental borderland: AAPG Bulletin, v. 67, p. 1104-1124.

Natland, M. L., and P. H. Kuenen, 1951, Sedimentary history of the Ventura Basin, California, and the action of turbidity currents: Special Publication - Society of Economic Paleontologists and Mineralogists, v. 2, p. 76-107.

Nelson, C. H., 2002, Basic types of turbidite systems based on modern sea floor images: Annual Meeting Expanded Abstracts - American Association of Petroleum Geologists, v. 2002, p. 130-130.

Nilsen, T. H., R. G. Walker, and W. R. Normark, 1980, Modern and ancient submarine fans; discussion and replies: AAPG Bulletin, v. 64, p. 1094-1112.

Nilsen, T. H., D. P. Imperato, and D. W. Moore, 1994, Reservoir geometry and architecture of productive Upper Cretaceous mud-rich and sand-rich submarine-fan systems, Sacramento Basin, California: Papers presented at the Gulf Coast Section, Society of Economic Paleontologists and Mineralogists Foundation Annual Bob F. Perkins Research Conference, v. 15, p. 269-280.

Normark, W. R., 1970, Growth patterns of deep-sea fans: American Association of Petroleum Geologists Bulletin, v. 54, p. 2170-2195.

Normark, W. R., 1978, Fan Valleys, channels, and depositional lobes on modern submarine fans; characters for recognition of sandy turbidite environments: AAPG Bulletin, v. 62, p. 912-931.

Normark, W. R., 1983, Quaternary development of channels, levees, and lobes on middle Laurentian Fan, *in* D. J. W. Piper, and D. A. V. Stow, eds., AAPG Bulletin, United States, American Association of Petroleum Geologists : Tulsa, OK, United States, p. 1400-1409.

Normark, W. R., G. R. Hess, and F. N. Spiess, 1978, Mapping of small scale (outcrop-size) sedimentological features on modern submarine fans: Proceedings - Offshore Technology Conference, p. 593-598.

Normark, W. R., and G. R. Hess, 1980, Quaternary growth patterns of California submarine fans: Pacific Coast Paleogeography Symposium, p. 201-210.

Normark, W. R., and D. J. W. Piper, 1991, Initiation processes and flow evolution of turbidity currents; implications for the depositional record: Special Publication - Society of Economic Paleontologists and Mineralogists, v. 46, p. 207-230.

Normark, W. R., H. Posamentier, and E. Mutti, 1993, Turbidite systems; state of the art and future directions: Reviews of Geophysics, v. 31, p. 91-116.

Normark, W. R., D. J. W. Piper, and R. N. Hiscott, 1998, Sea level controls on the textural characteristics and depositional architecture of the Hueneme and associated submarine fan systems, Santa Monica Basin, California: Sedimentology, v. 45, p. 53-70.

Peakall, J., K. J. Amos, G. M. Keevil, P. W. Bradbury, and S. Gupta, 2007, Flow processes and sedimentation in submarine channel bends: Marine and Petroleum Geology, v. 24, p. 470-486.

Pickering, K. T., and R. N. Hiscott, 1985, Contained (reflected) turbidity currents from the Middle Ordovician Cloridorme Formation, Quebec, Canada; an alternative to the antidune hypothesis: Sedimentology, v. 32, p. 373-394.

Pickering, K. T., R. N. Hiscott, and F. J. Hein, 1989, Deep marine environments; clastic sedimentation and tectonics: United Kingdom, Unwin Hyman: London, United Kingdom.

Piper, D. J. W., and W. R. Normark, 1983, Turbidite depositional patterns and flow characteristics, Navy submarine fan, California Borderland: Sedimentology, v. 30, p. 681-694.

Posamentier, H. W., M. T. Jervey, and P. R. Vail, 1988, Eustatic controls on clastic deposition; I, Conceptual framework: Special Publication - Society of Economic Paleontologists and Mineralogists, v. 42, p. 109-124.

Posamentier, H. W., and V. Kolla, 2003, Anatomy of a deep-water channel avulsion; example from the basin floor of the Desoto Canyon area, Gulf of Mexico: Annual Meeting Expanded Abstracts - American Association of Petroleum Geologists, v. 12, p. 140-140.

Pickering, K. T., R. N. Hiscott, and F. J. Hein, 1989, Deep marine environments; clastic sedimentation and tectonics: United Kingdom, Unwin Hyman: London, United Kingdom.

Prather, B. E., 1998, Classification, lithologic calibration, and stratigraphic succession of seismic facies of intraslope basins, deep-water Gulf of Mexico; errata, *in* J. R. Booth, G. S. Steffens, and P. A. Craig, eds., AAPG Bulletin, United States, American Association of Petroleum Geologists : Tulsa, OK, United States, p. 707R-707R.

Pyles, D. R., and D. C. Jennette, 2009, Geometry and architectural associations of co-genetic debrite-turbidite beds in basin margin strata, Carboniferous Ross Sandstone (Ireland); applications to reservoirs located on the margins of structurally confined submarine fans: Marine and Petroleum Geology, v. 26, p. 1974-1996.

Pyles, D. R., J. P. M. Syvitski, and R. M. Slatt, 2011, Defining the concept of stratigraphic grade and applying it to stratal (reservoir) architecture and evolution of the slope-to-basin profile: An outcrop perspective: Marine and Petroleum Geology, v. 28, p. 675-697.

Reading, H. G., and M. Richards, 1994, Turbidite systems in deep-water basin margins classified by grain size and feeder system: AAPG Bulletin, v. 78, p. 792-822.

Richards, M., and M. Bowman, 1998, Submarine fans and related depositional systems; II, Variability in reservoir architecture and wireline log character: Marine and Petroleum Geology, v. 15, p. 821-839.

Richards, M., M. Bowman, and H. Reading, 1998, Submarine-fan systems; I, Characterization and stratigraphic prediction: Marine and Petroleum Geology, v. 15, p. 689-717.

Ross, W. C., B. A. Halliwell, J. A. May, D. E. Watts, and J. P. M. Syvitski, 1994, Slope readjustment; a new model for the development of submarine fans and aprons: Geology [Boulder], v. 22, p. 511-514.

Rottman, J. W., J. E. Simpson, J. C. R. Hunt, and R. E. Britter, 1985, Unsteady gravity current flows over obstacles: Some observations and analysis related to the phase II trials: Journal of Hazardous Materials, v. 11, p. 325-340.

Satterfield, W. M., and E. W. Behrens, 1988, Intraslope basin evolution, Northwest Gulf of Mexico: AAPG Bulletin, v. 72, p. 244-244.

Satterfield, W. M., and E. W. Behrens, 1990, A late Quaternary canyon channel system, Northwest Gulf of Mexico continental slope: Marine Geology, v. 92, p. 51-67.

Scheidegger, A. E., and P. E. Potter, 1971, Downcurrent decline of grain size and thickness of single turbidite beds; a semi-quantitative analysis: Sedimentology, v. 17, p. 41-49.

Schwans, P., M. Cohen, K. Zauderer, S. D. Knapp, and T. C. Lukas, 2007, High-resolution reservoir modeling of a deepwater channel complex with thin beds, Zafiro Field, Equatorial Guinea: Abstracts: Annual Meeting - American Association of Petroleum Geologists, v. 2007, p. 125-125.

Shanmugam, G., 1999, Deep-water processes and facies models; a paradigm shift for the 21st century: Program and Abstracts - Society of Economic Paleontologists. Gulf Coast Section. Research Conference, v. 19.

Sinclair, H. D., and P. A. Cowie, 2003, Basin-floor topography and the scaling of turbidites: Journal of Geology, v. 111, p. 277-299.

Sinclair, H. D., and M. Tomasso, 2002, Depositional evolution of confined turbidite basins: Journal of Sedimentary Research, v. 72, p. 451-456.

Smith, R., 2004, Silled sub-basins to connected tortuous corridors: sediment distribution systems on topographically complex sub-aqueous slopes: Geological Society, London, Special Publications, v. 222, p. 23-43.

Steffens, G. S., R. C. Shipp, B. E. Prather, J. A. Nott, J. L. Gibson, and C. D. Winker, 2004, The use of near-seafloor 3D seismic data in deepwater exploration and production: Memoirs of the Geological Society of London, v. 29, p. 35-43.

Sweet, M. L., and L. T. Sumpter, 2007, Genesis Field, Gulf of Mexico; recognizing reservoir compartments on geologic and production time scales in deep-water reservoirs: AAPG Bulletin, v. 91, p. 1701-1729.

Talling, P. J., 2001, On the frequency distribution of turbidite thickness: Sedimentology, v. 48, p. 1297-1329.

Toniolo, H. A., 2002, Debris flows and turbidity current deposition in the deep sea and reservoirs, United States.

Toniolo, H., P. Harff, J. Marr, C. Paola, and G. Parker, 2004, Experiments on reworking by successive unconfined subaqueous and subaerial muddy debris flows: Journal of Hydraulic Engineering, v. 130, p. 38-48.

Toniolo, H., M. Lamb, and G. Parker, 2006, Depositional turbidity currents in diapiric minibasins on the continental slope; formulation and theory: Journal of Sedimentary Research, v. 76, p. 783-797.

Toniolo, H., G. Parker, V. Voller, and R. T. Beaubouef, 2006, Depositional turbidity currents in diapiric minibasins on the continental slope; experiments-numerical simulation and upscaling: Journal of Sedimentary Research, v. 76, p. 798-818.

Vail, P. R., 1987, Seismic stratigraphy interpretation using sequence stratigraphy; Part 1, Seismic stratigraphy interpretation procedure: AAPG Studies in Geology, v. 27, p. 1-10.

van Andel, T. H., and P. D. Komar, 1969, Ponded sediments of the Mid-Atlantic ridge between 22 degrees and 23 degrees north latitude: Geological Society of America Bulletin, v. 80, p. 1163-1190.

van der Werff, W., and S. Johnson, 2003, High resolution stratigraphic analysis of a turbidite system, Tanqua Karoo Basin, South Africa: Marine and Petroleum Geology, v. 20, p. 45-69.

Violet, J., B. Sheets, L. Pratson, C. Paola, R. Beaubouef, and G. Parker, 2005, Experiment on turbidity currents and their deposits in a model 3D subsiding minibasin: Journal of Sedimentary Research, v. 75, p. 820-843.

Wagner, J. B., R. L. Blythe, and P. F. Rush, 2006, Reservoir characteristics and architectural elements associated with production from a localized slump deposit, deepwater Gulf of Mexico: Abstracts: Annual Meeting - American Association of Petroleum Geologists, v. 15, p. 111-111.

Walker, R. G., 1978, Deep-water sandstone facies and ancient submarine fans; models for exploration for stratigraphic traps, AAPG Bulletin, United States, American Association of Petroleum Geologists: Tulsa, OK, United States, p. 932-966.

Weimer, P., 1990, Sequence stratigraphy, facies geometries, and depositional history of the Mississippi Fan, Gulf of Mexico: AAPG Bulletin, v. 74, p. 425-453.

Weimer, P., and M. H. Link, 1991, Seismic facies and sedimentary processes of ancient submarine fans and turbidite systems; introduction Frontiers in sedimentary geology: United States, Springer-Verlag: New York, NY, United States, p. 193-196.

Weimer, P., A. H. Bouma, and B. F. Perkins, 1994, Submarine fans and turbidite systems; sequence stratigraphy, reservoir architecture and production characteristics, Gulf of Mexico and international; papers presented at the Gulf Coast Section Society of Economic Paleontologists and Mineral: Papers presented

at the Gulf Coast Section, Society of Economic Paleontologists and Mineralogists Foundation Annual Bob F. Perkins Research Conference.

Winker, C. D., 1996, High-resolution seismic stratigraphy of a late Pleistocene submarine fan ponded by salt-withdrawal minibasins on the Gulf of Mexico continental slope: Proceedings - Offshore Technology Conference, v. 28, Vol. 1, p. 619-628.

Winker, C. D., and J. R. Booth, 2000, Sedimentary dynamics of the salt-dominated continental slope, Gulf of Mexico; integration of observations from the seafloor, near-surface, and deep subsurface: Annual Meeting Expanded Abstracts - American Association of Petroleum Geologists, v. 2000, p. 158-158.

Xu, J., M. Noble, and L. Rosenfeld, 2004, In-situ measurements of turbidity currents in Monterey submarine canyon: Eos, Transactions, American Geophysical Union, v. 85.

# Chapter 4: Modeling Unconfined Flows in a 3-D Experimental Minibasin: Investigating Relationships of Fill Process and Deposit Architecture


## ABSTRACT

Results from the first of two series of experiments document the interaction of unconfined turbidity currents with 3-D minibasin topography. Initial minibasin topography was created through controlled drainage of a water-filled bladder that was overlain by loose gravel. As the bladder drained, the overlying gravel collapsed, resulting in a large basin with two internal subbasins (subbasins 1 and 2). The initial, asymmetric basin measured 50×50 ×8 cm. A total of 18 unconfined turbidity currents were released into the basin. All currents had a Froude number of 0.7 and an initial height of approximately 3 cm at the inlet. An automated laser-mapping system was used to record bed topography after each flow event.

Observations and analyses of the fill process and sediment trapping were made. For all flows, minibasin accommodation was insufficient to retain them. Coeval filling of two spatially successive subbasins was possible under conditions of high current-efficiency and/or low sediment-trapping rates. Sediment trapping within the minibasin remained consistent over time but remained less than 0.2% of the total sediment flux to the system. Sediment partitioning between the two subbasins suggests that flow stripping is more likely a process by which sediments are moving across minibasin topography; however, caution should be taken in applying a 2-D flow-stripping model to a 3-D setting. A quantitative analysis of deposit geometry using a dimensionless ponding index (Lamb et al., 2004) showed that ponded deposits can occur in two scenarios: (1) throughout episodic, high-concentration gravity failure events and (2) through the

cumulative stacking of individual-event deposits in a minibasin fill. Also, the geometry of individual deposits can change dramatically, depending on the orientation of the stratigraphic section taken through the fill, and is ultimately related to the source of the current and its primary transport direction. Principles and relationships presented in this research can be used to enhance interpretations of subsurface deep-water stratigraphy and reservoir characterization as it applies to minibasin provinces.

## INTRODUCTION

Diapiric intraslope basins, or minibasins, are important morphological features on many continental slopes (Lamb et al., 2006) with an underlying mobile substrate because their sedimentary fill contains reservoirs that are a prolific source of hydrocarbons. Minibasins are thought to be infilled by turbidity currents, which transport the siliciclastic material from which hydrocarbon reservoirs are composed. Unfortunately, direct measurements of natural turbidity currents in minibasin settings are still rare, and measurements defining how natural currents interact with topography and modify associated fill architectures are infrequent. This paucity of observations hampers the development of seascape evolution models and limits the researcher's ability to reconstruct past environmental states using deep-water stratigraphy. However, interactions between turbidity currents and minibasins can be studied in the laboratory at reduced scales.

Salt basins are some of the most complex basin types because of the mobilization of underlying salt substrate and the effect that syn-tectonic and post-tectonic deformation has on the overlying sedimentary strata (Fig. 4.1). Sedimentary fill in these minibasins is a function of the balance of sedimentation supply and tectonic-driven accommodation, the latter being able to be treated as a static condition on a turbidity-current event scale.

Therefore, the phases of local and regional, structurally induced accommodation development (i.e., salt inflation and deflations, compression, extension, etc.) should be accompanied by a unique expression in the stratigraphy of the basin fills.

Many minibasins are thought to fill by deposition from turbidity currents through a process of fill and spill. Satterfield and Behrens (1990) and Winker (1996) initially, and later Beaubouef and Friedmann (2000), suggested a model in which minibasins infilled progressively from source to sink (Pirmez et al., 2012). Although this model has been applied widely in the stratigraphic studies of intraslope minibasins in the Gulf of Mexico (GOM), it is currently being debated owing to its several limitations: (1) stratigraphic development of initial sediment deposition that fills local accommodation and subsequent spilling of sediment into successive basins equates the degree of flow-process confinement to resulting deposit architecture, which has not been verified in the natural environment; (2) the model is two-dimensional and does not account for the 3-D nature of flow dispersal and sedimentation in the natural environment; (3) the model suggests a process dominated by sediment-driven subsidence accommodation tied to eustatic sea-level changes along the margin, which may vary dramatically in more distal minibasin systems (e.g., Madof and Christie-Blick, 2007).

In a second hypothetical fill situation, Badalini et al. (2000) and Sinclair and Tomasso (2002) suggested that minibasins could fill coevally, but with partitioning of sand and mud between basins because of the interaction between the stratified flows and minibasin topography. The model has commonly been referred to as a *flow-stripping model*. In this case, coarser grains are carried lower in the flow and are retained within proximal basins, while finer, suspended material higher in the current profile is transported to the next downstream basin. This process occurs until proximal basin

topography is sufficiently infilled to facilitate the transport of coarser fractions of sediment farther downdip.

Processes whereby scaled turbidity currents flow into minibasins have been well documented by both 2-D physical experiments (e.g., Toniolo, 2002; Brunt et al., 2004; Lamb at al., 2004, 2006; Toniolo et al., 2006a, b; Sequeiros et al., 2009) and 3-D physical experiments (e.g., Violet et al., 2005). Flow processes have also been interpreted from minibasin-deposit geometries and architectures from high-resolution subsurface data (e.g., Winker, 1996; Prather et al., 1998, 2000, 2003; Badalini et al., 2000; Beaubouef and Friedmann, 2000; Booth et al., 2002). Despite these attempts to fill the gap in understanding, little is documented about the 3-D physical processes by which minibasins fill or the relationship between these processes and the topography created by its underlying mobile substrate.

The objective of this study is to improve understanding of the interaction of dilute turbidity currents using 3-D minibasin topography and to gain insight into the geometry and character of subsequent deposits. In this study, a static minibasin setup is considered as an initial condition into which a series of 18 continuous, unconfined turbidity currents of equal durations and properties were flowed. The trapping potential of the basin was used to determine the extent of sediment trapping relative to the degree of sediment bypass for individual flows. Geometrical observations of both individual (single) and cumulative (stacked) deposits were quantified using a dimensionless ponding index, and an investigation of interpreting deposit geometry on (1) an event and (2) a cumulative-event scale was made. Results from these analyses were then linked to the flow behavior and evolution of unconfined turbidity currents. Finally, implications for applying existing models of minibasin-fill development are discussed herein.

## THEORY

### Model Scaling

The appeal of physical laboratory experiments for modeling deep-water sedimentation stems from the ability to study steady states and response to changes in controlled variables that would otherwise be difficult to observe in the natural seascape. Although it is virtually impossible to recreate the unique morphology and dynamics of minibasins and the associated depositional processes that occur within them, it is possible to scale minibasins relative to modern examples to glean useful information from physical experiments so as to help us better understand the nature by which they fill (Table 4.1). The experiments reported herein were geometrically scaled on the basis of present-day minibasin morphometric data collected by Pratson and Ryan (2004) from high-resolution, gridded, multibeam bathymetry of 46 intraslope basins of the present-day seafloor of the GOM (Fig. 4.2).

Dynamic scaling offers a rigorous and well-defined method of imposing experimental conditions that not only match the prototype system in appearance, but also reproduce it dynamically (Paola et al., 2009). Subaqueous gravity flows can be characterized by three dimensionless variables derived from the Navier-Stokes equations that describe the motion of fluids: (1) densimetric Froude number, $Fr$; (2) bulk Reynolds number, $Re$; and (3) Rouse number, $p$. The densimetric Froude number of a turbidity current, defined as the ratio of inertial forces to gravitational forces, is used to determine the resistance of a density current moving through an ambient fluid.

$$Fr_d = \frac{U}{\sqrt{g'h}},$$

where $U$ is depth-averaged current velocity, reduced gravity, $g' = RCg$, and $R = (\rho_s/\rho_a - 1)$ is submerged specific density of sediment particles, where $\rho_s$ is density of salt and sediment mixture, $\rho_a$ is density of fresh water, $C$ is volumetric concentration of particles in the flow, and $h$ is current thickness. Typical values of $Fr_d$ applied in experiments ranged between 0.7 and 0.8 (Table 4.1).

The Reynolds number, $Re$, is a dimensionless number providing a measure of the ratio of inertial forces to viscous forces.

$$Re = \frac{UL}{v},$$

where $U$ and $L$ are velocity and length scales, respectively; $g$ is acceleration due to gravity; and $v$ is kinematic viscosity. Typical values of $Re$ applied in experiments ranged from 3,000 to 5,000 (Table 4.1).

In the case of turbidity-current scaling, model and prototype Froude numbers are the same; however, the model Reynolds number is reduced to the prototype Reynolds number. But for experimental-scale Reynolds numbers greater than 2,000, the model turbidity currents are sufficiently turbulent (Parsons and Garcia, 1998). Experimental studies of sediment-laden turbidity currents are also scaled to the natural system using a dimensionless Rouse number, $p$.

$$p = \frac{w_s}{\kappa u_*},$$

where $w_s$ is terminal settling velocity, $\kappa$ is von Karman's constant, and $u_*$ is dimensionless shear velocity.

## EXPERIMENTAL SETUP

The experiments described in this study were performed in The University of Texas at Austin Morphodynamics Laboratory deep-water basin. The basin tank is 8 × 4 × 2 m (Fig. 4.3), equipped with a mixing tank and a constant-head tank-feeder system (Fig. 4.3), and outfitted with a fixed platform set to a slope of 8°. A 25-cm-tall gravel layer was built on the platform, into which the minibasin subsidence mechanism was placed (Fig. 4.3). A 2-cm-thick layer of 300-$\mu$m and finer silica flour was draped on top of the gravel layer to reduce rugosity of the initial depositional surface. At the upstream end, the gravel layer measured 0.7 m in width, whereas at the downstream end past the minibasin, the gravel layer was 1.5 m wide. The surface of the gravel layer maintained the same slope as that of the fixed platform and was made sufficiently wide beyond the minibasin margins so as not to interfere or influence turbidity-current dynamics within and around the minibasin area.

The model minibasin was created inside the tank by means of a controlled, water-filled-bladder drainage system that was emplaced within the gravel layer and allowed to lie flat on the sloped surface. The bladder was drained using a water-pump system that was controlled by varying the supply voltage. Water was pumped from the bladder into a bucket. The rising water level in the bucket was monitored using a MassaSonic™ M-*5000* acoustic sensor to monitor the subsidence rate. At maximum subsidence, the minibasin measured 60 ×45 ×8 cm (Fig. 4.3). The average inlet slope of the minibasin was 20°, and its average outlet slope was 25°.

To create the mixture for the turbidity current, we filled the mixing tank with sediment, calcium chloride salt, and fresh water. The sediment consisted of moderately sorted silica flour (specific gravity of 2.65), with a geometric median grain size of 11.4 $\mu$m and a standard deviation of 8.5 $\mu$m (Fig. 4.4). For every 1,000 L of water, 11.34 kg

(25 lb) of salt and 63.52 kg (140 lb) of sediment were added. The resulting volumetric concentration and dimensionless excess density of the mixture were 2.3% and 5.1%, respectively (Table 4.1). Salt was added to increase the excess density of the mixture. Both the mixing tank and constant-head tank were equipped with mixers to keep sediment suspended in the mixture.

To produce a turbidity current, water and sediment were fed into the basin tank via an external constant-head tank system supplied by the mixing tank. During an experimental run, the drainage pipe was opened while fresh water was supplied to the tank to maintain the water depth (Table 4.1). During an experiment, a valve was open to release the mixture into the basin tank, which entered the minibasin tank through a momentum-reduction box that restricted the vertical-flow thickness of the turbidity current to 3 cm. The current was allowed to flow on the sloped surface for a distance of 50 cm before encountering minibasin topography. A perimeter drainage system within the basin tank acted to minimize wall reflections.

A Keyence™ LK-G502 displacement laser was used to record initial basin topography and topography at the end of each event. The laser was mounted to a three-axis, computer-controlled cart over the basin. The laser system mapped each surface on a 2 ×2 mm grid, at approximately 200-$\mu$m vertical resolution. The bathymetric scanning area was 1.5 ×1.0 m. Throughout the series of experiments, 19 bathymetric maps were recorded following each experiment, which were used to create slope maps and deposit-thickness maps from which interpretations of fill process and deposit geometry were made.

## EXPERIMENTAL APPROACH

For the experiments reported, the bladder was filled to capacity and emplaced within the gravel layer. Once the gravel-layer topography was smoothed to mimic the slope of the ramp, the tank was filled with fresh water. Afterward, the plastic bladder was drained completely in the gravel layer at a rate of 16 mm/h to achieve maximum subsidence. Associated with basin subsidence was the reconfiguration and minor collapse of the gravel layer, which breached the silica flour layer and became exposed (Fig. 4.5). Reconfiguration of the gravel layer during the experiment resulted in the establishment of two subbasins. These subbasins are herein referred to as subbasins 1 and 2, subbasin 1 being the more proximally situated of the two relative to the current inlet area (Fig. 4.5). Subbasin 1's initial dimensions measured 30 ×45 × 8 cm, subbasin 2's initial dimensions were 30 ×45 ×5 cm, and the overall basin's initial dimensions measured 60 ×45 ×8 cm (Table 4.1). Basin height is measured as the deepest point in the basin relative to the basin spill point at its downstream end. Between the two subbasins was a topographic high, formed as a result of gravel collapse, and is herein referred to as the *intrabasinal high*.

A total of 18 continuous turbidity currents of equal duration were released into the minibasin, each lasting 1 h (60 min), with a cumulative duration of 18 h (1,080 min). The currents were released from a submerged head gate attached to a momentum-reduction box. At the current source area, the box constricted the current to a flow depth of approximately 3 cm and a width of approximately 40 cm. The flow outlet from the momentum box was adjustable so as to compensate for any bed aggradation at the source zone. At the end of each flow, the deposit surface was mapped using a displacement laser.

## CURRENT-BASIN INTERACTION AND DEPOSIT MORPHOLOGY

Observations of current processes and fill morphology are described on the basis of zones relative to basin topography and its subdivisions (Fig. 4.5) and include (1) the inlet zone—a sloping, flat, gravel layer between the turbidity-current inlet area and the break of the inlet slope of subbasin 1; (2) the basin accommodation zone, which comprises (a) subbasin 1 (b) the intrabasinal high, and (c) subbasin 2; and (3) the exit zone—a sloping, flat, gravel layer downdip from the exit point of the minibasin.

In these experiments, turbidity currents were unconfined as they entered the minibasin (Fig. 4.6). Average turbidity-current input velocities measured from the ADV were 5 cm/s, minimizing reworking by bedload transport. At the inlet zone, currents spread and thinned and became wider than the minibasin as they entered. Nonuniform thinning at the current front resulted in local variations in thickness and momentum on the subbasin 1 inlet slope, causing spatially variable accelerations as the current entered the basin. Flows decelerated as they encountered the intrabasinal high. Some currents displayed a process of flow stripping as they traversed the topographical barrier, whereas the rest were deflected around the obstacle. Downstream bypassing of the flow beyond the basin accommodation zone was common, and at no time did the current form a stable zone of "ponded" flow, with a uniform settling interface within the minibasin (Fig. 4.6).

Throughout the experiments, sediment fallout at the turbidity-current inlet zone created a sedimentary wedge between the momentum box and the break of the minibasin entry slope (Fig. 4.7a). For individual flows, the sedimentary wedge was generally between two and four times thicker than deposits within the basin-accommodation zone. Deposits in the basin accommodation were similar in that they were rarely confined to the lowest point in the basin, despite the relatively steep basin slopes modeled in the experiment exceeding $20^0$ (Fig. 4.5b). Exceptions occurred in the last two flows of the

experiments, in which short-lived surge events were generated from remobilization of sediment owing to steep slopes on the aggrading sedimentary wedge at the inlet slope (Fig. 4.7c). Corresponding cross sections from subbasins 1 and 2 are shown in Figure 4.8. In subsequent sections, both trapping of sediments and geometry of deposits within the basin are quantified and further analyses performed to explain how deposits evolved as the basin filled.

## DATA ANALYSIS

### Sediment Trapping

The volume of sediment trapped within the experimental basin was compared with that supplied to determine basin-trapping efficiency, $T_e$ (from Lamb et al., 2006). The equation used to calculate event trapping efficiency in the experimental basin is as follows:

$$T_e = \frac{100 * V_B}{V_T - V_P}$$

where $V_B$ is the volume of sediment captured in the basin, $V_T$ is the total sediment supplied to the system via the constant head tank, and $V_P$ is the volume of sediment deposited on the platform before the basin entry point. Each variable was calculated from deposit thickness maps. Input turbidity-current properties, including flow velocity, sediment concentration, and flow height–width measurements (Table 4.1), were used to calculate the sediment volume supplied to the basin. Assuming a completely efficient system where sediment delivery is exclusive to the basin, initial basin volume is approximately five times greater than the cumulative volumetric discharge at t = 60 s (Fig. 4.9). Cumulative sediment discharge to the basin equals the initial basin volume after 5 min (300 s) (Fig. 4.9). For a 60-min experiment, the cumulative sediment flux to

the basin would be 11.9 times greater than the initial volume of the basin, and by the end of the experiments, cumulative sediment flux to the basin would be 214 times greater than the initial volume of the basin (Fig. 4.9).

Despite the considerable amount of sediment being supplied to the basin, only a fraction is trapped within it. Sediment loss due to deposition on the proximal platform slope relative to the entry point was calculated to be approximately 10% of the total sediment supplied to the system. Individual-event trapping efficiency, $T_{ei}$, is a measure of the volume of sediment trapped within the basin for individual flows, whereas cumulative-event trapping efficiency, $T_{ec}$, is a measure of the cumulative volume of sediment trapped relative to the total sediment flux for the duration of the experiments (Fig. 4.9b). Results show a relatively high degree of variability in the ability of the minibasin to trap sediment among individual events, which is confirmed by a low $R^2$ value of 0.01 for the linear regression applied. Average $T_{ei}$ is approximately 1.6 % of the input-event sediment volume supplied to the basin (Fig. 4.9b). $T_{ec}$ is, however, more consistent as the basin fills, with an $R^2$ value of 0.44 for the linear regression applied. Average $T_{ec}$ was found to be 1.5 %. In both cases, regression lines are similar, showing that the cumulative and individual deposits fill at a rate within an order of magnitude of one another.

$T_{ei}$ data (Figure 4.9b) suggest that $T_{ei}$ is highly variable and may be due to a response to local changes in basin topography and turbidity-current conditions. Although not quantified, deposit remobilization during flows may have also contributed to the high variability in $T_{ei}$. Despite the existence of this high-frequency variability, the basin's ability to trap sediment remained fairly consistent with a slight positive trend as it filled. The low trapping-efficiency magnitudes for the mini-basin suggest that turbidity currents are efficient at transporting sediment through the basin, most of which was transported

beyond the downstream margin of the basin. The argument for low $T_e$ and bypass of sediment can, however, be partly explained by experimental studies that show how turbidity currents are able to surmount obstacles whose height is as much as 2.5 times the body thickness of the flow (Rottman et al., 1985), or 1.5 times the head thickness (Muck and Underwood, 1990; Kneller and McCaffrey, 1999). For this experiment, thickness of minibasin topography was approximately 2.5 times greater than turbidity-current body thickness at the beginning of the experiment and appeared to have little effect on containing the flow or trapping large volumes of sediment.

**Subbasin Sediment Partitioning**

Partitioning of the total volume of sediment trapped in the minibasin into individual subbasins was considered and compared with hypothetical scenarios of sediment partitioning derived from the two existing models of minibasin-fill development (Fig. 4.10). A graph (Fig. 4.10a) shows the percentage of sediment trapped by each subbasin relative to the duration of flow events, and two polynomial lines were fitted to the distributions from each subbasin. Experimental results show a reverse trend in the relationship between percentages of sediment trapped in subbasin 1 relative to percentages of sediment trapped in subbasin 2 (Fig. 4.10a). At the beginning of the experiment, subbasin 2 trapped a higher percentage of sediment than did subbasin 1. After flow-event 2, trapping distribution between the two subbasins is similar at 50%. Between events 2 and 14, partitioning of sediment favors subbasin 1, which attains a partition maximum of 70% of the sediment trapped following flow-event 9. Partitioning between both subbasins converges once again to 50% following flow-event 15, after which sediment partitioning favors subbasin 2 (Fig. 4.10a).

If the subbasin system were thought to represent two individual minibasins, in which subbasin 1 was proximal relative to subbasin 2, results suggest that sedimentation would be occurring simultaneously in both subbasin systems at varying rates. The relative proportion of sediment deposited in each basin, however systematically varied, and the nature of filling are unlike those of hypothetical partitioning scenarios derived from existing published models (Fig. 4.10b, c). Although a case can be made for greater proportions of sediment being partitioned in subbasin 1 for most experiments, maximum sediment partitioning in subbasin 1 did not occur until later in the series (flow-event 9). Even then, sedimentation was not contained exclusively within subbasin 1. The partitioning scenario modeled in this experiment therefore most likely incorporates a third dimension of length not previously considered in the two existing models of minibasin-fill development. Despite the divergence between results in these experiments and the existing models, flow stripping and flow deflection relative to the intrabasinal high appears to be a more likely process by which sediments move across minibasin topography within turbidity currents, given the presence of coeval filling and the flow disturbance that occurs when the current interacts with the intrabasinal high. The 2-D flow-stripping model appears, however, to be insufficient for describing basin infilling because flows could deflect around obstacles internal to the minibasin.

**Characterizing Deposit Geometry**

The 2-D deposit geometry is analyzed in each subbasin using a dimensionless ponding index, $P_o$. The ponding index, first applied by Lamb et al. (2004) for their 2-D experiment, is applied in this study to determine the spatial and temporal variability in deposit geometry. This index compares the change in thickness of the deposit with the

change in basin elevation over a given length and is used to quantify the geometry of experimental deposits (Fig. 4.11).

$$P_o = -\frac{1}{L_{1,2}} \int_0^L \frac{d\theta_{1,2}}{d\eta_{1,2}} dx_{1,2},$$

where $L$ is the integrated length of the basin, $\theta$ is the thickness of the deposit, $\eta$ is the elevation of the existing bed, $dx$ is the interval length from which deposit-thickness and bed-elevation changes are derived, and subscripts $_{1,2}$ represent downdip and strike orientations, respectively. A deposit ponding index equal to one ($P_o = 1$) represents a completely ponded deposit (Fig. 4.11a), an index greater than one ($P_o > 1$) represents a convex-up, mounded deposit (Fig. 4.11b), an index equal to zero ($P_o = 0$) represents a draped deposit (Fig. 4.11c), and a deposit with accentuated highs (deposit is emplaced preferentially in the confining slopes rather than in the center of the basin) would have a ponding index of less than zero ($P_o < 0$) (Fig. 4.11d). A hybrid case of deposit geometry is also examined in which $0 < P_o < 1$ and is considered a wedged deposit herein. In ponding-index analyses, two metrics of deposit geometries are applied: (1) individual and (2) cumulative (Fig. 4.12). The individual ponding index characterizes the geometry of a single bed relative to a prior basin-deposit surface (Fig. 4.12a), whereas the cumulative-deposit ponding index characterizes the geometry of a number of beds relative to the initial basin surface (Fig. 4.12b).

The effect of various horizontal-interval scales on deposit ponding indices can be quantified by varying the horizontal-interval length, $dx_{1,2}$. The horizontal interval length represents the measurement length from which deposit-thickness and basin-elevation changes are recorded and applied in the ponding index equation (Fig. 4.13). For small horizontal scales of investigation ($dx_{1,2} \ll L$), relative changes in magnitudes of both $x$

and $\theta$ favor the rugosity associated with small-scale topography, whereas the contributions of topography change relative to the overall shape of the basin are reduced (Fig. 4.13a). When the interval length is increased ($dx_{1,2} < L$), the new investigational surface tends toward the original depositional surface because of the coarser data resolution. Here, finer-scale topographical and local deposit thickness contributions become less important, whereas topographical and deposit changes associated with overall basin geometry become weightier in ponding-index calculation (Fig. 4.13b). If the interval length is large and begins to resemble the integrated length ($L \geq dx_{1,2}$), the aliased surface coarsens too much to provide accurate contributions of both deposit thickness and basin elevation and may output erroneous ponding-index data.

Ponding-index data from both the centerline-dip (D440) and strike sections (X600 and X900) of subbasins 1 and 2, respectively, were compiled so that the spatial distribution of both individual- and cumulative-deposit geometries within the zone of basin accommodation (shown in Fig. 4.5) could be analyzed. These three cross sections were selected because they intersect points of deepest bathymetry in subbasins 1 and 2 (Fig. 4.8).

***Individual-Deposit Geometry***

Individual ponding-index values were calculated for deposits within subbasins 1 and 2 along dip-section D440 (Fig. 4.8a) so that how deposit geometry varied along dip as each subbasin filled could be investigated. Integrated dip length, $L$, of each subbasin along section D440 was approximately 30 cm (Fig. 4.8a). Results from each subbasin show that individual-deposit ponding-index values are lower than cumulative ponding index values (Figs. 4.14, 4.15). Linear regressions applied to individual ponding-index values in each subbasin section show that magnitudes generally decrease with time in the

case of subbasin 1 (Fig. 4.14a, b), whereas they increase with time in the case of subbasin 2 (Fig. 15a, b). For both subbasins, the impact of an increased interval length (dx = 100 mm) affects the ponding-index magnitude of individual events but does not affect the overall trend in deposit geometry from events 1 through 16. Also, calculated individual ponding-index values for the deposits from flows 17 and 18 in subbasin 2 increased relatively little when short and long interval lengths were applied in the ponding-index calculation. Ponding indices were calculated for individual deposits along the strike sections of each subbasin (X600 and X900). In both cases, integrated strike basin lengths were approximately 45 cm, approximately 50% more than the integrated dip length of each subbasin (Fig. 4.8b, c). Despite the greater integrated length of the strike sections, individual ponding-index magnitudes and temporal trends that resulted along strike were similar to those along dip.

Individual ponding-index trends along both dip sections from subbasin 1 therefore suggest that deposits from low-concentration, unconfined flows from flows 1 through 16 produce deposit geometries that are more likely to drape over 3-D topography, and the potential for draped geometries increases as the basin fills ($P_o \rightarrow 0$). In the topographically lower subbasin 2, individual deposits, however, showed a trend of increasing individual ponding-index magnitude over time, albeit small. This increase was also associated with the contribution of high individual ponding-index values at the end of the experiments, which resulted in individually ponded deposits being confined to subbasin 2.

Because individual deposits generally displayed small thickness variations relative to changes in preflow basin elevation, interval length was found to have little effect on individual ponding-index outcomes. In cases where fill from flows 1 through 16 produced deposits that were primarily a result of suspension fallout from turbidity

currents, most of the deposit volumes in subbasin 2 from flows 17 and 18 were associated with short-duration "surge" events in the form of high-concentration gravity flows that originated from upstream remobilization of deposits.

***Cumulative-Deposit Geometry***

Calculated cumulative ponding-index values show trends that are different from those of individual ponding-index values and vary according to section of observation (Figs. 4.14, 4.15). For dip-section D440, a departure from individual-deposit ponding indices is evident as the basin fills and the cumulative deposit thickens relative to the original basin surface (Fig. 4.14). The linear regression trends toward higher ponding-index values as the basin fills with sediment, attaining a more ponded geometry. For subbasin 1, cumulative-deposit ponding-index values decreased for deposits from flow events 17 and 18, whereas they continued to increase for subbasin 2. Associated with the contributions from deposits 17 and 18 were high-concentration surge events generated as a result of the remobilization of deposit material away from the sedimentary wedge near the inlet zone into distally located subbasin 2 (Fig. 4.7c).

Larger interval lengths in the cumulative ponding index may increase or decrease the rate at which cumulative-deposit ponding indices rise as the subbasins fill (Figs. 4.14, 4.15). This observation is demonstrated by the gradient characteristics of linear regressions and final cumulative ponding-index magnitude at the end of the series of experiments. Along dip (D440), cumulative deposits from subbasin 1 may be interpreted as becoming more ponded in geometry ($P_o \rightarrow 1$) for low interval-length applications, whereas they may be interpreted to have accentuated thicks along the basin margin ($P_o \rightarrow -1$) for high interval-length applications (Fig. 4.14a, b). The dip-oriented section of subbasin 2, however, produced only cumulative deposits that became more ponded in

geometry ($P_o \rightarrow 1$) at both interval-length applications. Along strike, the cumulative deposit in subbasin 1 (X600) assumes a more mounded geometry ($P_o > 1$), with higher interval lengths, whereas the cumulative deposit in subbasin 2 (X900) assumes a more ponded geometry ($P_o \rightarrow 1$), with higher interval lengths.

Vast departures in magnitudes of cumulative-deposit ponding-index values occur that depend on the length scale used and deposit section orientation. Interval length therefore greatly influences the quantification of cumulative-deposit geometry and the interpretation of flow process from them, as shown in dip and cross-basin examples. Results show that as basin topography is progressively filled, cumulative deposits from low-concentration, unconfined turbidity currents become more ponded for small-interval-length applications, whereas for high-interval-length applications, cumulative deposits can be interpreted to have accentuated thicks along dip, or they can be interpreted to either mound (subbasin 1) or pond (subbasin 2) along strike. As a result, ponding and/or mounding of cumulative deposits along strike may influence or induce the lateral stacking of individual deposits because flow can become more variable within and around morphological features. The application of interval lengths can therefore have a great impact on the interpretation of such possibilities. The experiments reported herein thus show that a combination of interpretations along dip and strike are crucial to establishing deposit geometry and are more variable than suggested from the published 2-D models of minibasin-fill development.

**Spatial Distribution of Deposit Geometry**

The spatial distribution of deposit geometry is analyzed using frequency distributions of individual and cumulative ponding-index values for each subbasin and is presented relative to cross-section orientation (Fig. 4.16). Ponding-index-frequency data

include data calculated for various interval-length scales (2, 4, 10, 20, 50, and 100 mm), and the total number of observations from both subbasins is 192. Ponding-index calculations from events 17 and 18 were excluded owing to the nature of deposit emplacement, which significantly affected their ponding-index magnitudes relative to the rest of the fill.

***Individual-Deposit Geometries***

Individual ponding-index-frequency data along dip (Fig. 4.16a) show that both subbasins have similar individual ponding-index distributions. The individual ponding-index-frequency distribution for subbasin 1 ranges from -0.2 to 0.9 and peaks at a value of 0 along dip. For subbasin 2, the individual ponding-index-frequency distribution along dip ranges from 0 to 0.6 and peaks at a value of 0.1. Individual ponding-index-frequency distributions between the two subbasins are, however, less similar along strike (Fig. 4.16b). The individual ponding-index-frequency distribution for subbasin 1 is broad and ranges from -0.5 to 0.8, peaking at a value of 0.1 along strike section. For subbasin 2, the individual ponding-index-frequency distribution along dip ranges from -0.5 to 0.1 and peaks at a value of -0.4 along strike section.

For each subbasin, individual-deposit geometries are therefore interpreted to drape along dip, whereas deposits favor a slight degree of wedging along the strike section. For subbasin 2, observations of individual-deposit frequency show that deposits also favor draping along dip section and are accentuated along margins in the strike section.

### *Cumulative-Deposit Geometries*

For cumulative deposits, frequency data (Fig. 4.16c, d) show a range in ponding-index values that is wider than that for individual ponding-index values. Cumulative ponding-index-frequency data along dip (Fig. 4.16c) show that both subbasins have similar cumulative ponding-index distributions. The cumulative ponding-index-frequency distribution for subbasin 1 ranges from -1 to 0.5 and peaks at a value of 0.4 along dip. For subbasin 2, the cumulative ponding-index-frequency distribution along dip ranges from 0 to 0.5 and peaks at a value of 0.2. Cumulative ponding-index-frequency distributions between the two subbasins are less similar along strike section (Fig. 4.16d). The cumulative ponding-index-frequency distribution for subbasin 1 is broad and uniformly distributed, with a range of from -0.4 to 1.5 along strike section. A peak frequency occurs at a cumulative ponding-index value of 1.1, but it is less weighted because of the broad distribution of the data. For subbasin 2, the cumulative ponding-index-frequency distribution along dip ranges from 0 to 0.8 and peaks at a value of 0.4 along strike section.

Cumulative-deposit geometries from both basins are characterized by slightly higher ponding-index values and ranges along strike than along dip, which suggests a higher degree of ponding and mounding along strike than what occurs along dip. Additionally, the distribution of cumulative ponding-index values that is higher than that of individual ponding-index values along dip and strike in both subbasins confirms the previous interpretation that thicker stacked deposits appear to be more ponded or mounded than do the individual deposits that compose them. For subbasin 1, the broader distribution of cumulative ponding-index data along strike shows that mounding of deposits is possible and perhaps related to the proximity of the subbasin relative to the source.

## DISCUSSION

Results presented herein model the effect of unconfined, low-concentration turbidity currents on deposit geometry and trapping in a minibasin setting. Sediment-gravity flows are dynamic on complex slopes, and their physical character evolves as they interact with complex topography and may result in entirely different outcomes from the results reported herein. Consequently, the modeled scenario presented herein represents a small fraction of possibilities of interactions between natural currents and 3-D minibasins and should be interpreted accordingly.

For interpretations of the fill process, sediment-trapping data show that the basin captured less than 2 % of the total sediment supplied to the basin, highlighting a high potential for sediment transport in a turbidity current able to overcome minibasin topography. Event-trapping data, however, show that the basin was able to capture more sediment as it filled, albeit a very small percentage (less than 0.5% of the sediment supplied to the basin). Sediment partitioning between subbasins 1 and 2 shows that the coeval filling of two spatially successive basins is possible. These occurred under conditions of high current efficiency (high velocity or high fraction of suspended fines) and/or low basin capture rates (low topography or possibly short flow run-up lengths). In a comparison of these results with hypothetical sediment-partitioning scenarios presented by the existing models of minibasin fill development, no direct resemblance in the fill patterns derived from the published models seems to occur, and is attributed primarily to the 3-D nature of turbidity current interactions with topography in distributing sediment within the basin space.

The ponding index is a useful tool for both calculating deposit geometry and investigating the effect of scale in resolving interpretations of deposit geometry. Application of differing interval lengths in ponding-index calculation has shown that the

ponding index is a scale-dependent metric, especially when applied to cumulative deposits. Despite the scale dependence of the equation, the ponding index may be useful in discerning fill phases linked to structural episodes within a basin (e.g., Buddin et al., 2002; Haddad et al., 2003; Pyles, 2008), in which significant departures in incremental changes in fill geometry can be identified. Additionally, these data can be compared with deposit and morphological architecture data extracted from subsurface data to support interpretations. Notable differences in cumulative ponding-index data relative to deposit cross-section orientation suggest that both primary transport direction and basin morphology are primary factors that influence individual- and cumulative-deposit morphology. The ability of sustained, low-density currents to create truly ponded deposits is also unlikely.

Fill and spill models may be too simplistic for explaining how minibasins fill with sediment. For example, such a model proposes that sediment fallout from a turbidity current is confined to the topographically deepest areas of the basin. However, such was not observed in the experiments. Additionally, for a minibasin that is progressively shallowing and narrowing to fill completely prior to spilling into the next downslope basin, sediment detrainment needs to balance the energy of the incoming turbidity current (Toniolo, 2002). One way to create such a scenario is through smaller-scale, surge-type flows that are volumetrically smaller than the minibasin into which they flow and that do not possess the energy necessary to surmount confining topography. Although this process was not tested in these experiments, results suggest that deposits are more likely to drape the topography that they interact with, as opposed to pond within it.

Flow stripping appears to be a more likely process by which sediments are transported across minibasin topography because of the nature of the physical processes observed in the basin, as well as the coeval filling of successive downslope basins.

Caution must, however, be taken in applying a 2-D-flow-stripping model to a three-dimensional setting because we observed that flows can deflect around obstacles internal to the minibasin, thus potentially affecting sediment detrainment within the basin and the resulting deposit geometry.

The link to flow types and deposit geometry shows that ponded deposits from low-concentration turbidity currents could occur in two scenarios. First, individual fills tended to drape the entire experimental minibasin topography. Although individual deposits show indiscernible thickness changes, giving each individual event a draped shape, the cumulative effect of these topographical and thickness irregularities is to, over time, create a deposit that appears ponded in geometry. Therefore, when viewed in seismic data, these fills may appear ponded, highlighting the importance of observation scale in interpreting deposit geometry. Second, the only true ponded deposits that were preserved in these series of experiments resulted from surge deposits in the form of high-concentration gravity flows originating from remobilization of sediment on the inlet slope. Therefore, ponding of individual deposits, as depicted in published literature models of minibasin fill, may not necessarily reflect the dynamics of low-density turbidity currents, but instead may be the result of higher-concentration sediment-gravity flows. Generation of such flows depends on local controls not limited to flow transformation on complex 3-D topography, mass wasting, or sediment remobilization due to halokinesis.

Morphologic information from modern environments can provide insight into the duration of flow events filling minibasins. Moderately deep-water, sinuous channels and their associated levees and erosional potential are generally considered to be the products of a longer-duration, sustained turbidity current, rather than shorter-duration surges (e.g., Inman et al., 1976; Hay, 1987; Prior and Bornhold, 1990; Twichell et al., 1991; Pirmez,

1994; Mulder and Syvitski, 1995; Puig et al., 2003). Results reported from these experiments are therefore useful for highlighting the sediment-transport capacity of turbidity currents on a complex slope, where topographical obstacles are thought to be a considerable limiting factor. Although the physical size of turbidity currents are, for the most part, unknown, Mohrig and Buttles (2007) showed that the small density contrast between a dilute turbidity current and the surrounding water helps to promote turbidity-current heights that can be much greater than relief of the topography with which they interact.

Although results documented from these experiments show systematic variation in the nature of sediment trapping and deposit geometry within a minibasin fill, the introduction of more complex topography and various types of sediment-gravity flows may produce entirely different deposit geometries and sediment-trapping efficiencies than those reported herein.

## CONCLUSIONS

The experiments reported in this study encapsulate results from a series of 18 continuous, unconfined flows into a static, 3-D minibasin setting and document the evolution of fill through time. Analysis of the fill process shows that (1) total sediment trapping within the minibasin remained fairly consistent over time, with a slight positive trend; (2) deposits from turbidity currents were more likely to drape topography; (3) coeval filling of two spatially successive basins is possible, especially under conditions of high current-efficiency and/or low basin-trapping rates; and (4) flow stripping is a more likely process by which sediments are moving across minibasin topography but is insufficient for describing fill evolution within a 3-D minibasin environment. Analysis of deposit geometries produced from modeled turbidity currents shows that ponded deposits

can occur in two scenarios: (1) throughout episodic, high-concentration gravity failure events and (2) through cumulative stacking of small-scale thickness changes of individual-event deposits in a minibasin fill. The only true ponded deposits that were preserved in these series of experiments resulted from surge deposits in the form of high-concentration gravity flows originating from remobilization of sediment on the inlet slope. Therefore, event-scale ponding of deposits, as depicted in published literature models of minibasin fill, may not necessarily reflect the dynamics of low-density turbidity currents, but instead may be the result of higher-concentration sediment-gravity flows. The relationship between geometries produced from individual vs. cumulative events therefore highlights the importance of observation scale in resolving event-scale processes and stratigraphy. Observations of fill architecture showed that (1) the thickest part of an individual fill deposit does not always lie in the topographic low of the basin at the time of deposition and (2) the geometry of individual deposits can change dramatically, depending on the orientation of the stratigraphic section taken through the fill. Principles and relationships presented in this research can be used to enhance interpretations of subsurface deep-water stratigraphy and reservoir characterization as they apply to minibasin provinces.

## TABLES

**(A) Sediment-Fluid Mixture Properties (Initial Conditions)**

| | | |
|---|---|---|
| Water temperature | 23 | °C |
| Ambient fluid density, $r_w$ | 0.998 | kg/L, g/cm$^3$ |
| Density of solution, $r_{salt+water}$ | 1.006 | kg/L, g/cm$^3$ |
| Specific gravity of solution, $SG_{salt+water}$ | 1.007 | |
| Density of solution, $r_{salt+water}$ | 1.005 | kg/L, g/cm$^3$ |
| Density of sediment, $r_{sed}$ | 2.65 | kg/L, g/cm$^3$ |
| Volume concentration, $C_{sed+water}$ | 2.3 | % |
| Density of solution and sediment mixture, $r_{sed+salt+water}$ | 1.048 | kg/L, g/cm$^3$ |
| Excess density | 5.1 | % |
| Number of flows – Series 1 | 18 | flows |
| Average flow duration | 60 | minutes |

**(B) Input Turbidity-Current Properties**

| | | |
|---|---|---|
| Input current-velocity range | 5–8 | cm/s |
| Discharge | 200–500 | cm$^3$/s |
| Reynolds number, Re | 3000–5000 | |
| Froude number, Fr | 0.5–0.8 | |
| Current width | > 60 | cm |
| Current thickness | 2.0–4.0 | cm |

**(C) Minibasin Container Properties**

| | | |
|---|---|---|
| Length (centerline) | 60 | cm |
| Width (centerline) | 50 | cm |
| Maximum depth (centerline) | 8 | cm |
| Inlet slope, $s_{i(av)}$ (initial condition) | 20 | degrees |
| Outlet slope, $s_{o(av)}$ (initial condition) | 25 | degrees |

Table 4.1: Initial and boundary conditions for minibasin experiments. (A) Density properties of materials used for creating turbidity-current (solution and sediment) mixture, followed by number of flows and their durations; (B) turbidity-current fluid dynamics properties that characterize flows for series 1 experiments; and (C) initial basin dimensions following controlled subsidence prior to turbidity-current flow events. Averaged inlet and outlet slopes annotated as $s_{i(av)}$ and $s_{o(av)}$, respectively.

## FIGURES

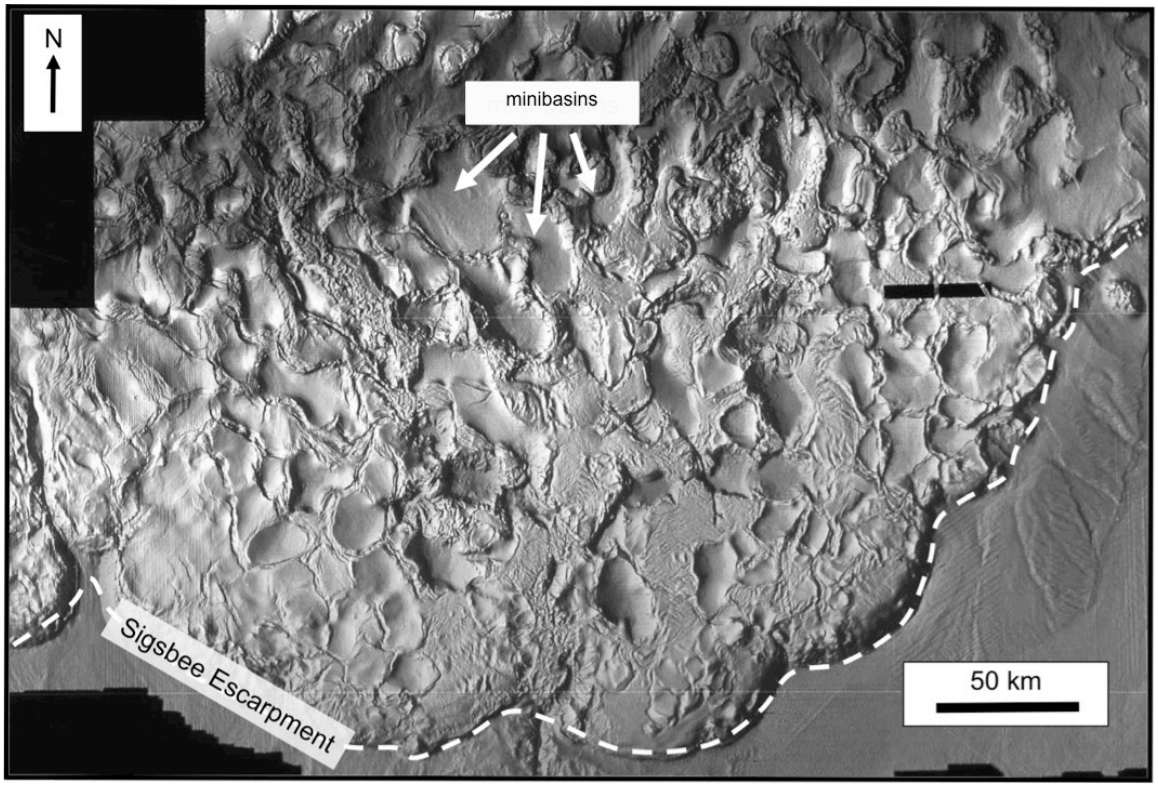


Figure 4.1: Shaded relief map of present-day seafloor of the Gulf of Mexico (GOM) basin (modified from Liu and Bryant, 2000). Minibasins in area influenced by mobile salt substrate form a complex array of depocenters on the continental slope. These basins extend to Sigsbee Escarpment (white dashed line) in south of basin.

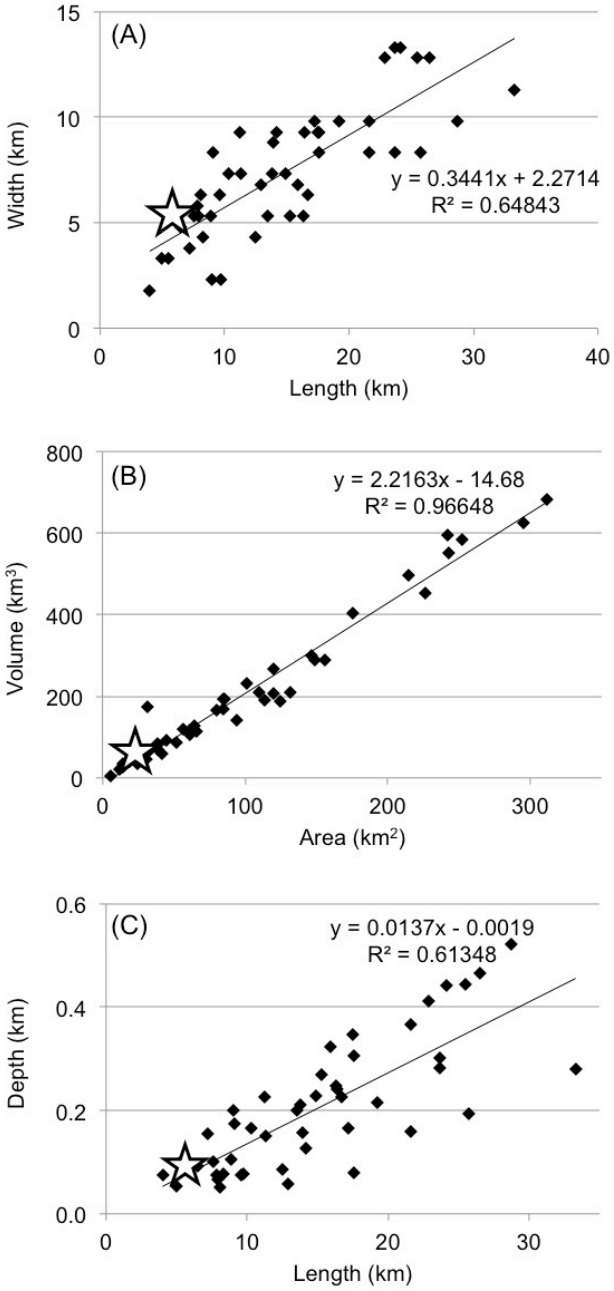


Figure 4.2: Modern GOM minibasin morphological data (from Pratson and Ryan, 2004) plotted and compared with scaled minibasin. (A) Graph shows distribution of GOM minibasin length vs. width ($R^2 = 0.648$); (B) graph shows distribution of area vs. volume ($R^2 = 0.966$); (C) graph shows distribution of length vs. relief ($R^2 = 0.613$). Superimposed on plots are scaled minibasin data represented by star for series 1 experimental basin.

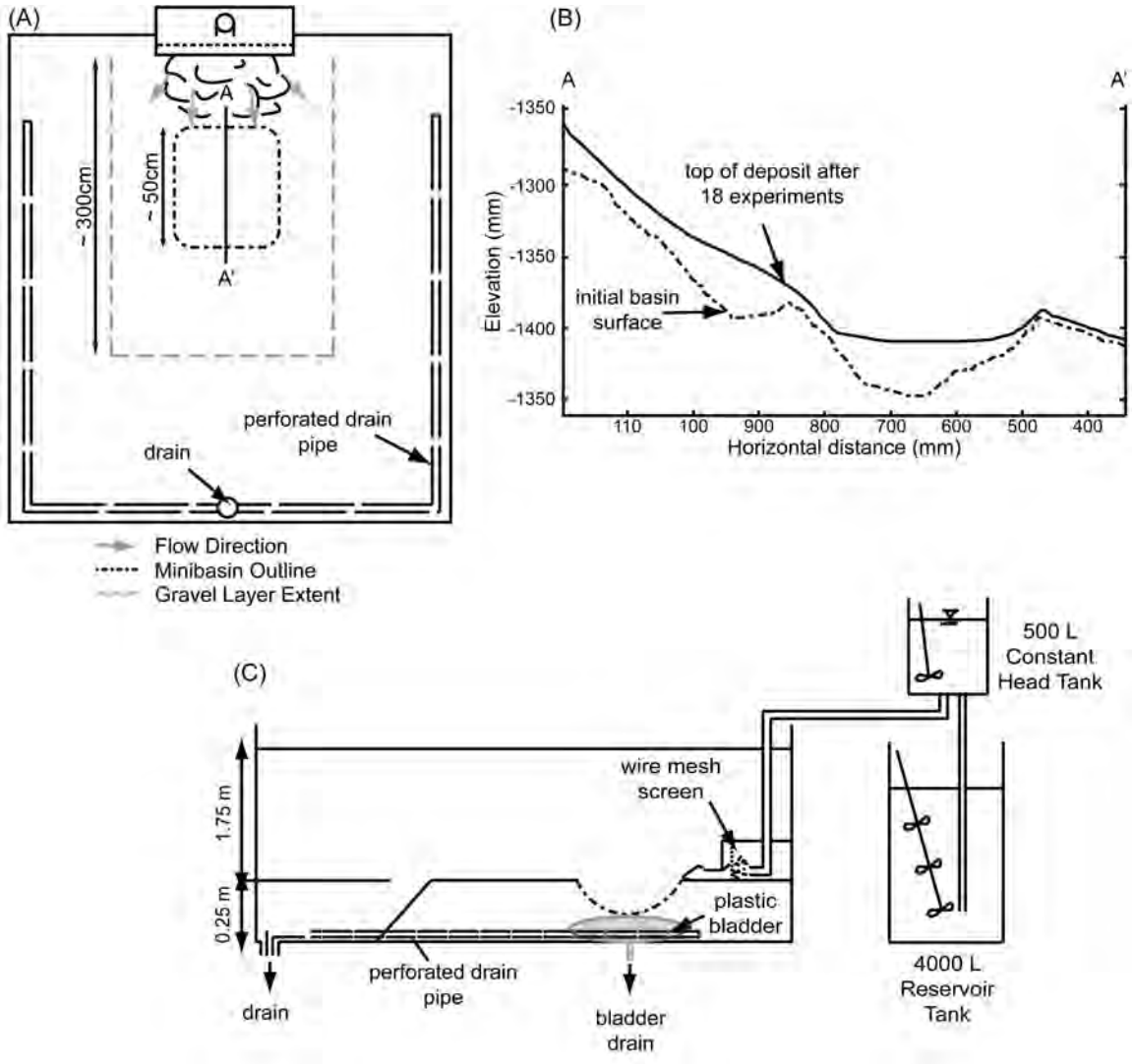


Figure 4.3: Schematic figure for series 1 of minibasin experiments and current generation conditions. (A) Plan view of basin tank with completely subsided minibasin configuration. bold outline represents extent of false floor, and dashed red outline represents extent of minibasin. (B) Dimensions of minibasin cross section. (C) Side view shows reservoir tank where sediment, water, and salt are mixed and then pumped to upper constant-head tank. Currents generated by releasing mixed fluid from head tank into basin tank/minibasin through wire-mesh-screened entrance box. As currents move over edge of false floor, they are drained away by a system of perforated pipes so as to minimize basin-tank wall reflections. Minibasin cross-sectional shape established by controlled drainage of water-filled bladder buried in a gravel basement, shown in B. Dimensions of bladder 40 × 40 × 15 cm. Inlet box configuration for minibasin oriented parallel to long axis of basin tank.

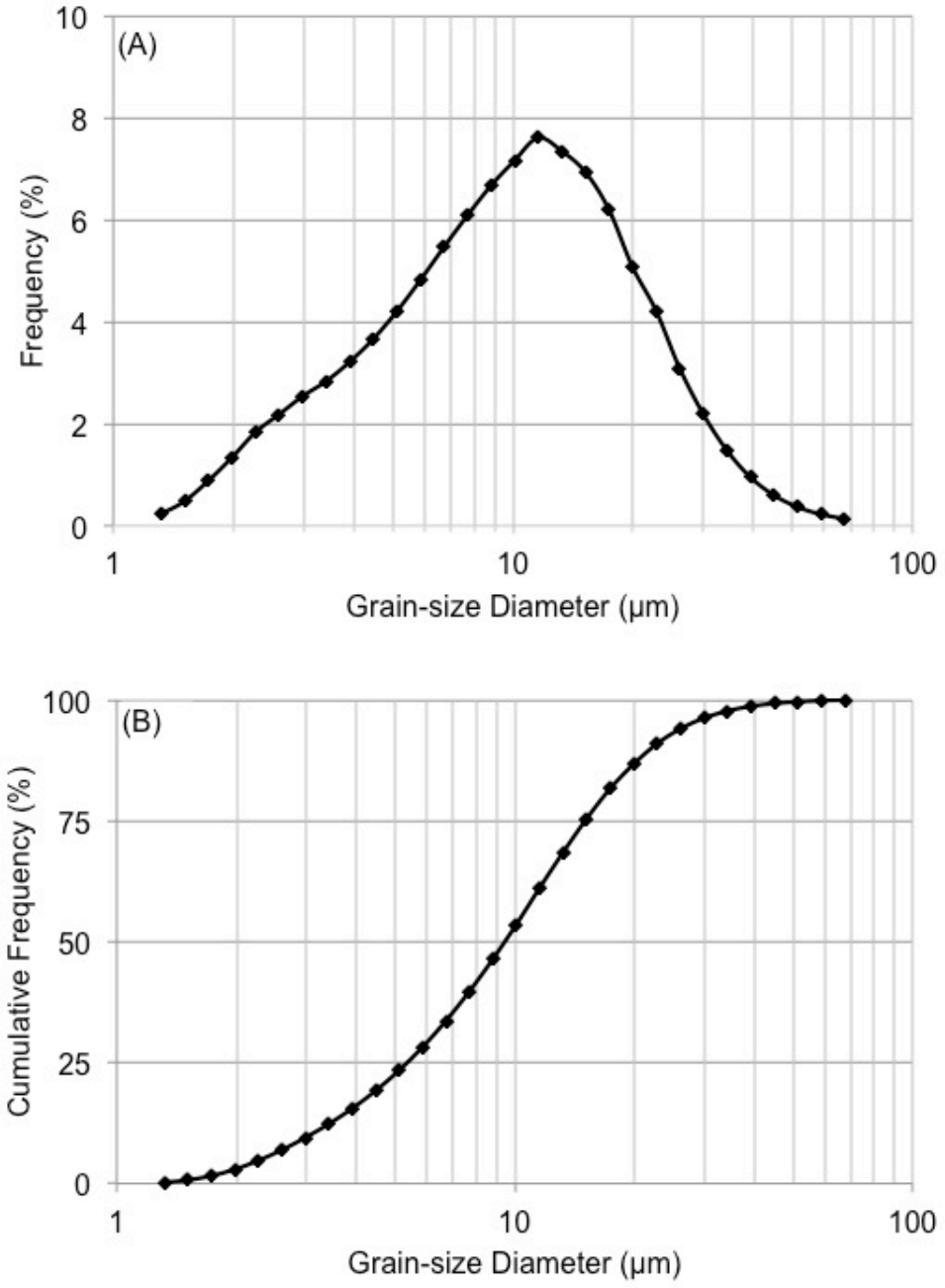


Figure 4.4: Measured grain size distribution data for silica flour used in turbidity current solution and sediment mixture. Data graphically illustrated in (A) frequency-distribution plot and (B) cumulative-frequency plot.

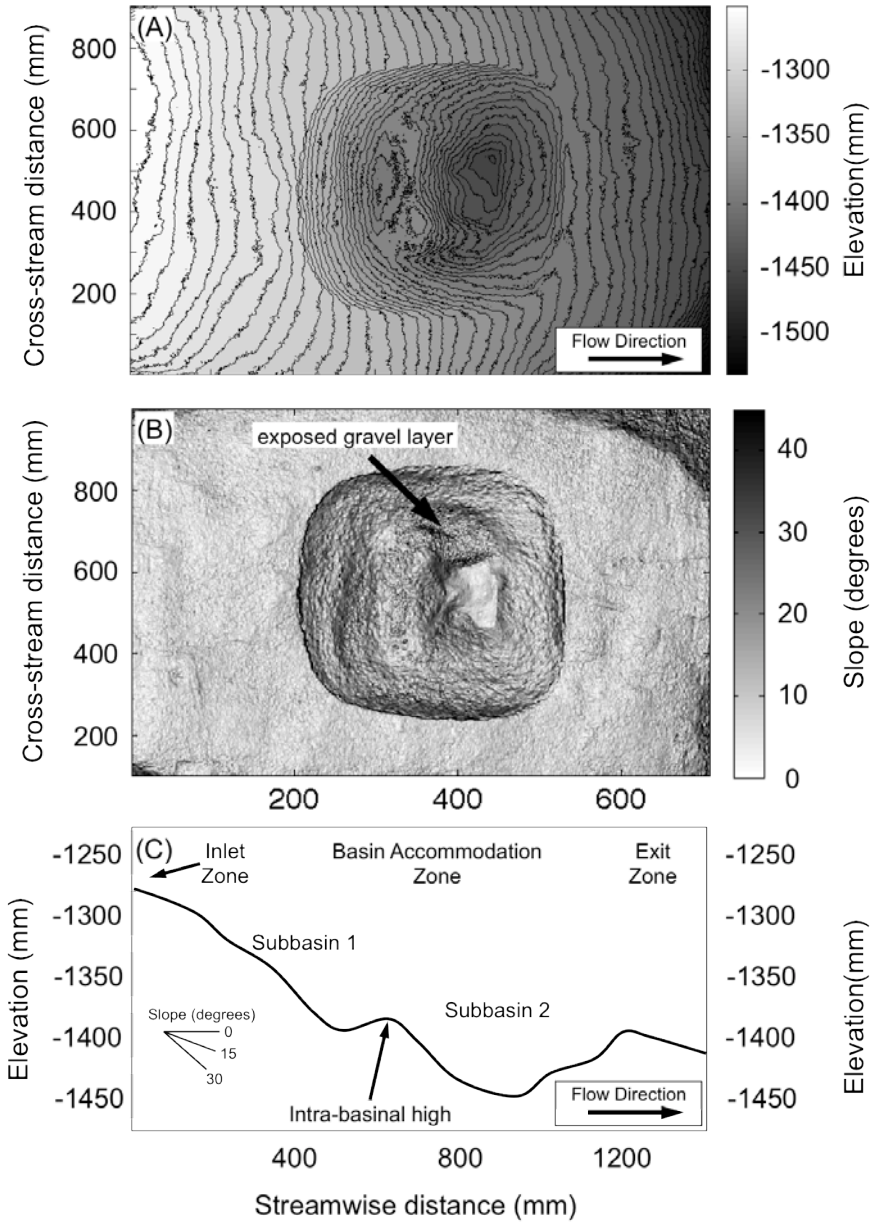


Figure 4.5: Bathymetry contour map, corresponding slope map, and minibasin dip cross section at t=0. Surface at t=0 represents initial basin configuration at maximum basin subsidence. (A) Bathymetry contour map illustrating topographical basin zonation; (B) slope map highlighting rugose basin topography associated with gravel exposure; and (C) in cross section, inlet zone is sloping flat basement between turbidity current inlet area and break of inlet slope of subbasin 1; ponded accommodation zone comprises subbasins 1 and 2; and exit zone is sloping basement downdip from exit point of minibasin.

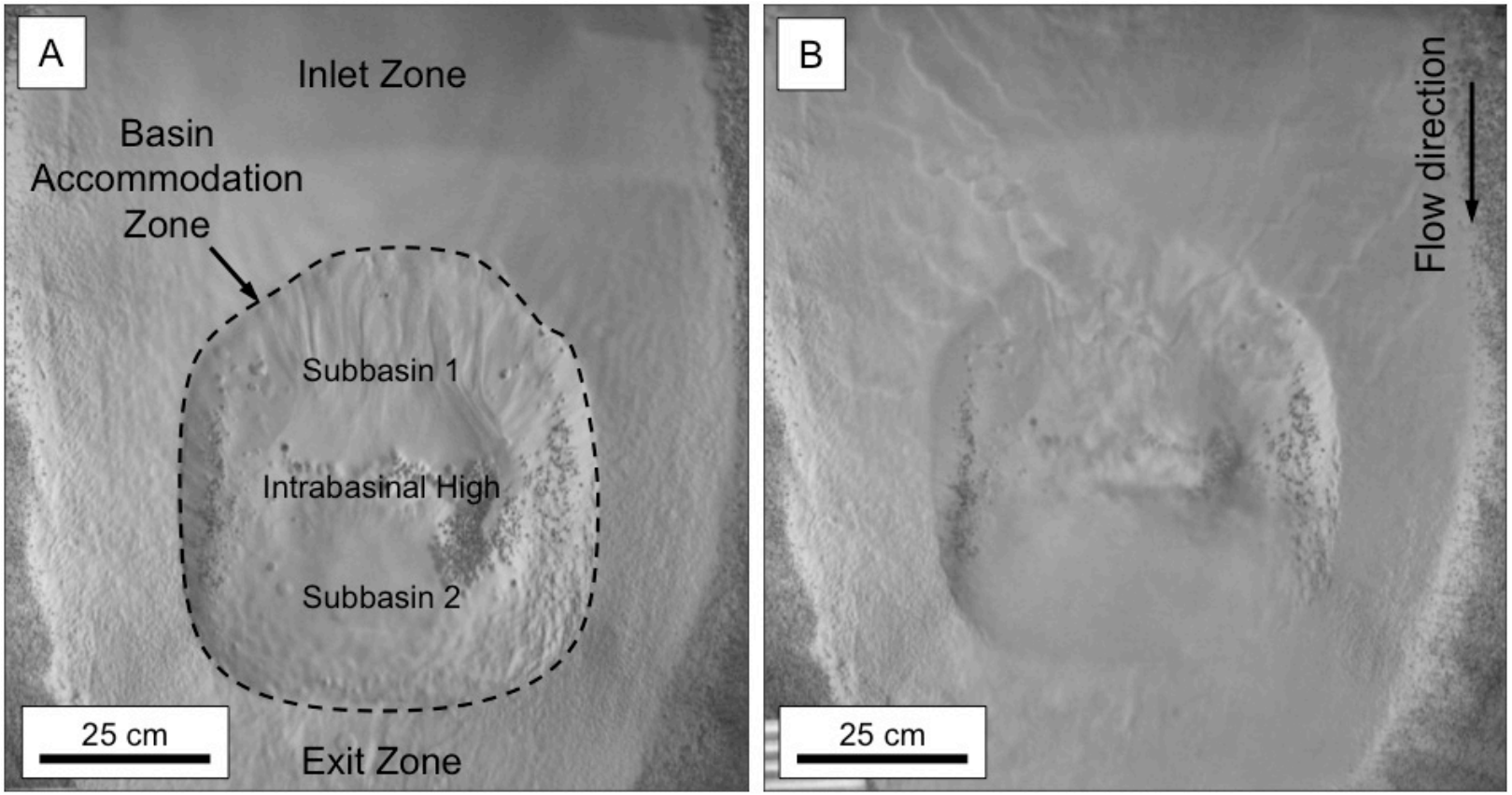


Figure 4.6: Overhead photographs of (A) minibasin before flow event and (B) during flow event. Turbidity currents introduced at top (upstream) end of basin through momentum-reduction box, and current interacted with subtle topography to dissociate into series of individual flows within larger turbidity current system.

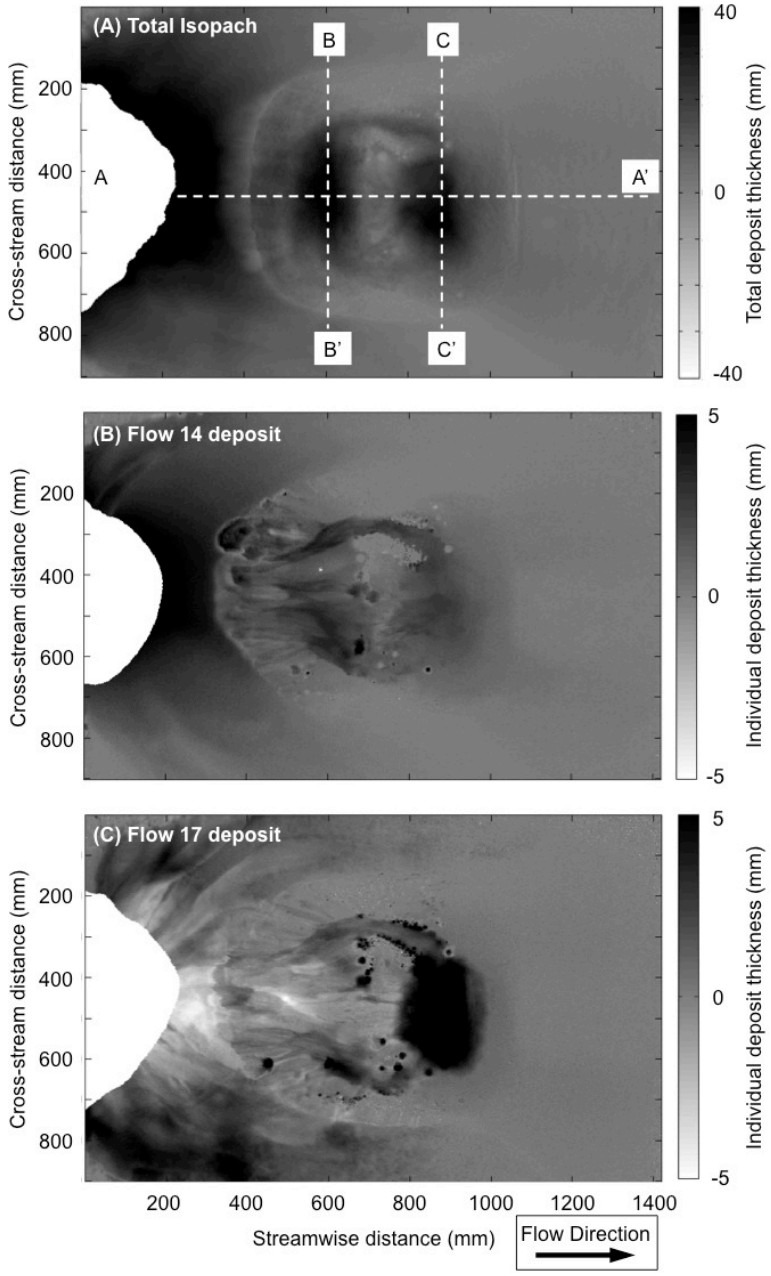


Figure 4.7: (A) Total isopach map of complete fill sequence from 18 unconfined, continuous turbidity currents; (B) isopach map of flow 14 deposit fill showing typical turbidity current deposit over minibasin surface; and (C) isopach map of flow 17 deposit fill showing ponded deposit from high-concentration surge flow. Deposit thickness calculated by subtracting preevent bathymetry from postevent bathymetry.

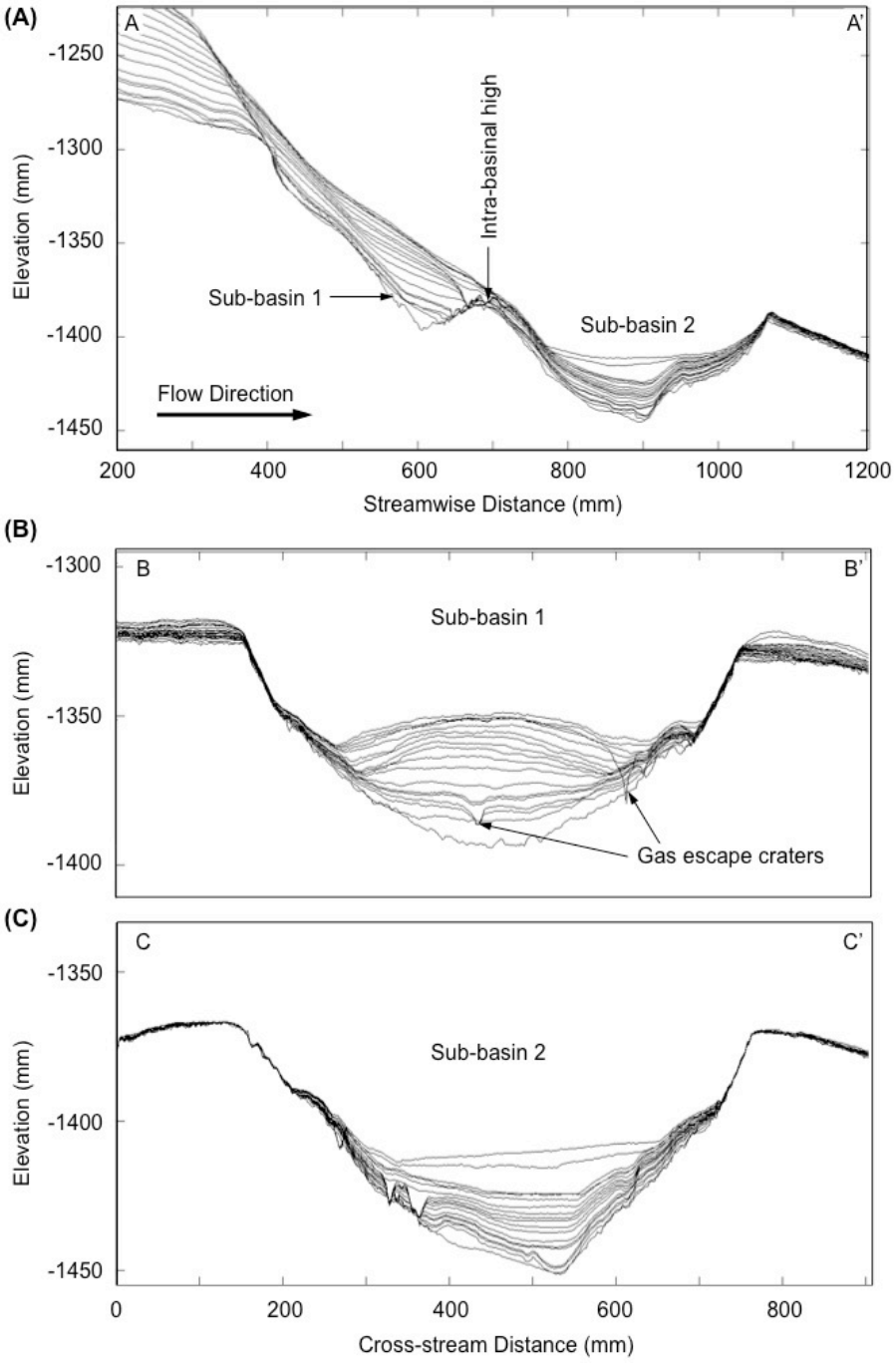


Figure 4.8: Cross-sectional basin fill architecture (see Fig. 7a) from (A) dip cross section A-A′ (D440); (B) strike cross section B-B′ (X600); and (C) strike cross section C-C′ (X900). Note v-shaped gas escape craters located at intrabasinal high.

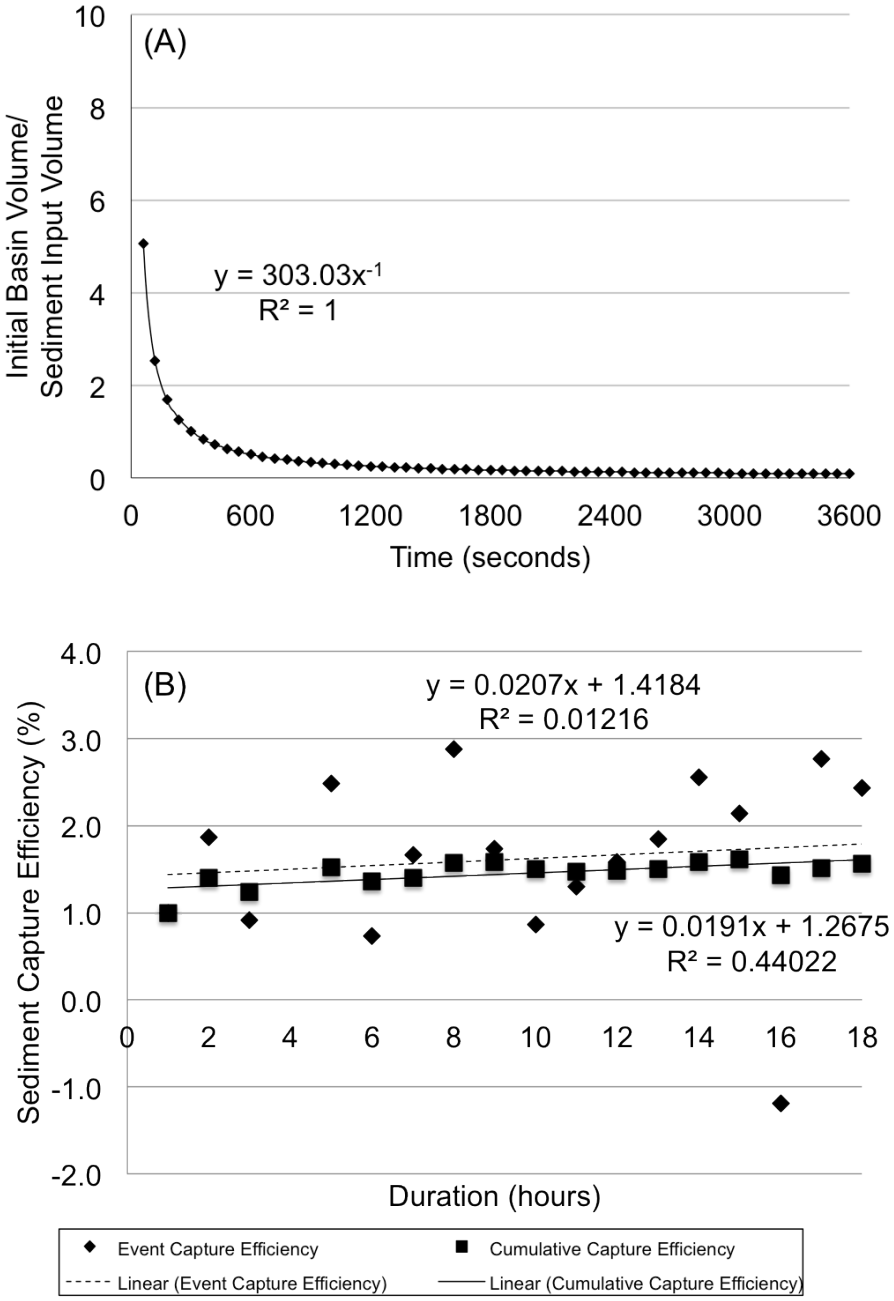


Figure 4.9: (A) Graph of experiment duration versus ratio of initial basin volume and (B) graph of experiment duration vs. total basin sediment capture efficiency. Diamond data points depict individual deposit contributions, and square data points depict cumulative deposit contributions. Linear regressions show that sediment capture is similar for both individual and cumulative sediment volumes and increases with time.

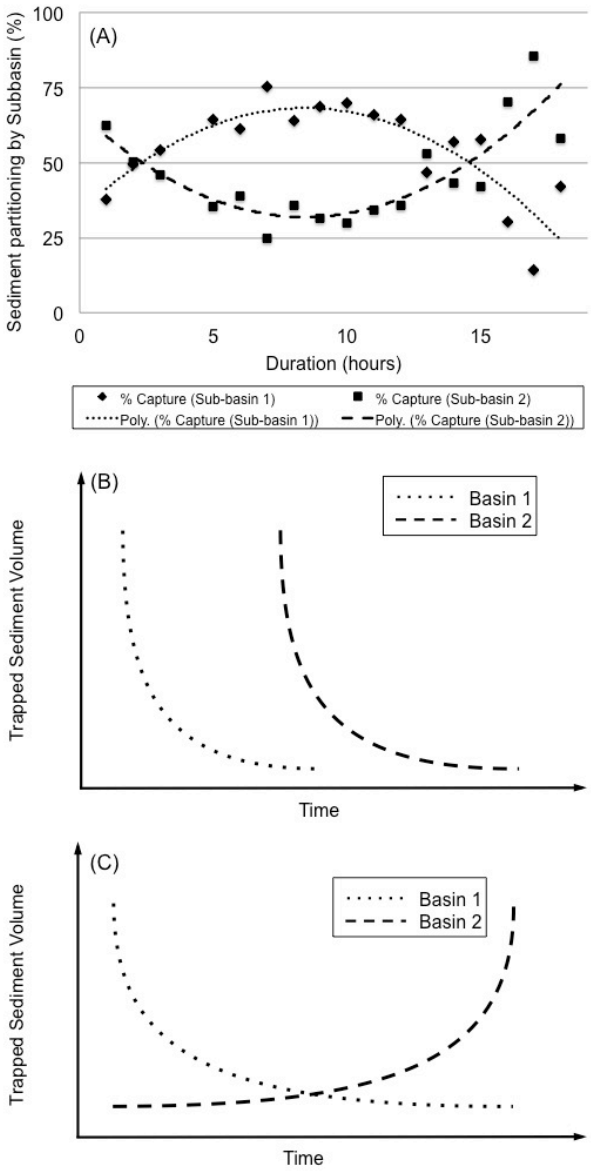


Figure 4.10: (A) Graph of experiment duration vs. sediment partitioning from experiments. Diamond and square data points depict contributions from subbasins 1 and 2, respectively; (B) graph of hypothetical sediment capture scenario for two successive basins using concepts from fill and spill model; and (C) graph of hypothetical flow stripping model sediment capture scenario for two successive basins using concepts from flow stripping model. Results from experiments show that sediment capture does not conform to any of the models, but coeval filling is possible as proposed in C.

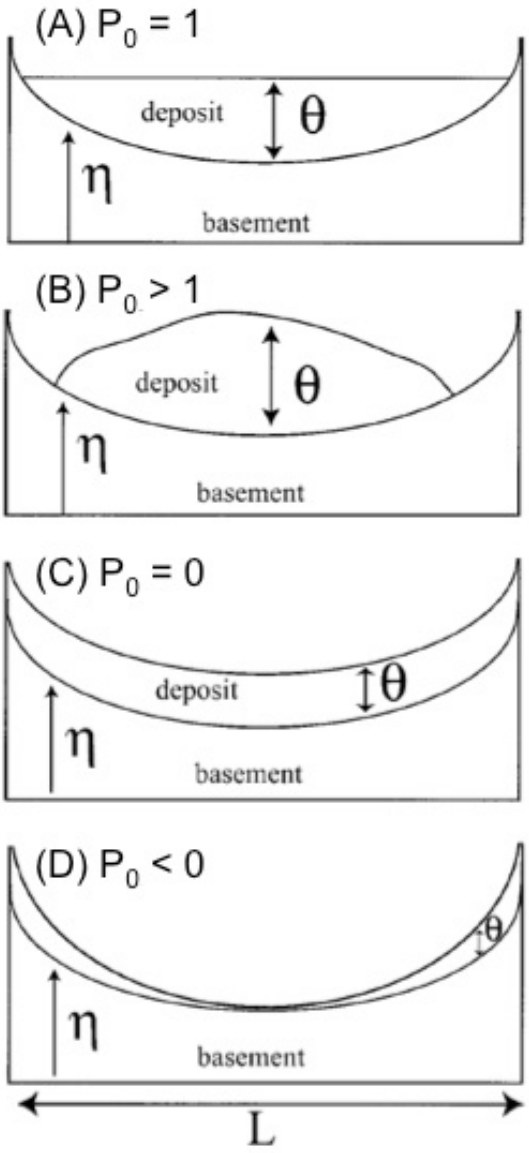


Figure 4.11: Dimensionless ponding index used to describe experimental deposits (modified from Lamb et al., 2004). Index is number that compares change in thickness of deposit relative to change in basin elevation over given length (L). (A) Deposit ponding index equal to one represents completely ponded deposit; (B) deposit ponding index greater than one represents mounded deposit, and (C) deposit ponding index equal to zero represents draped deposit (upper right). Deposit with accentuated highs (flow deposits preferentially on slopes rather than center of basin) would have (D) negative deposit ponding index.

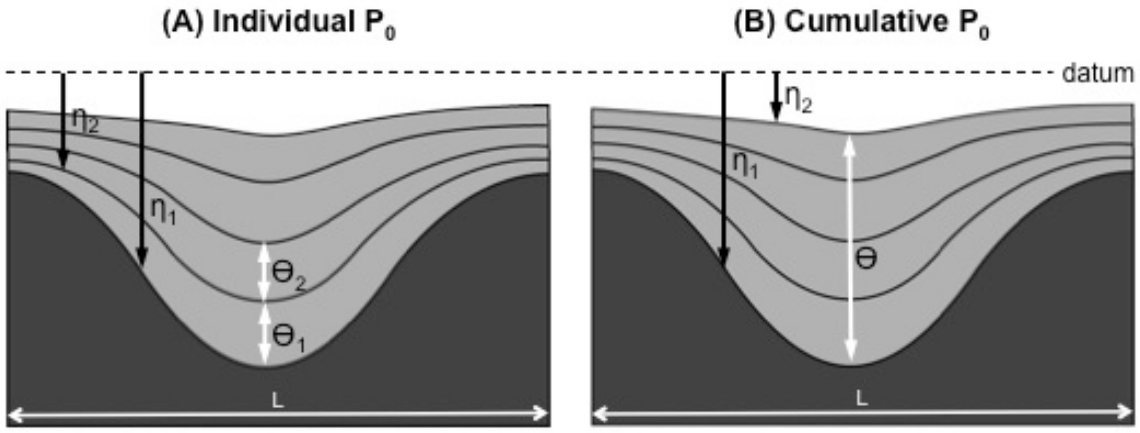


Figure 4.12: Ponding-index calculations performed for (A) individual deposits and (B) cumulative deposits that compose basin fill. Individual ponding index characterizes geometry of single bed relative to prior basin deposit surface (A). Cumulative ponding index characterizes geometry of number of beds relative to initial basin surface (B).

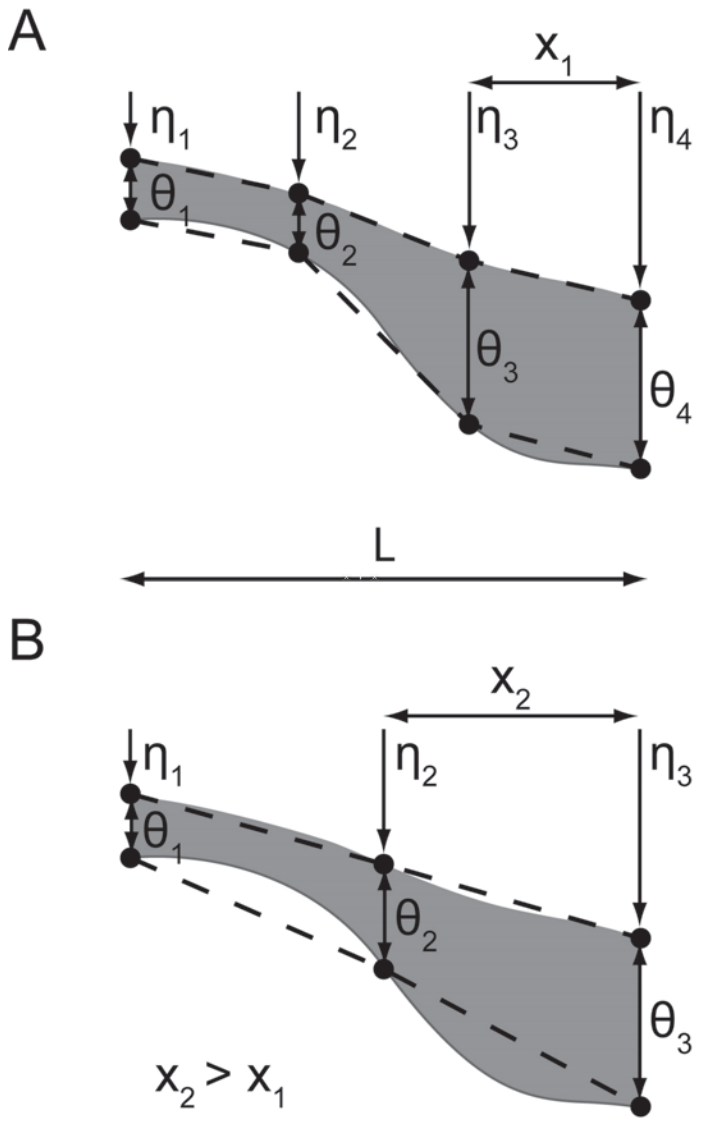


Figure 4.13: Effect of interval length on ponding-index calculations. Here, $x_2 > x_1$ and $L_2 = L_1$. (A) For small horizontal scales of investigation ($x \ll L$), relative changes in magnitudes of both $x$ and $\theta$ favor small-scale morphological features (local); (B) when interval length is increased ($x < L$), relative changes in magnitudes of both $x$ and $\theta$ favor large-scale morphological features (regional).

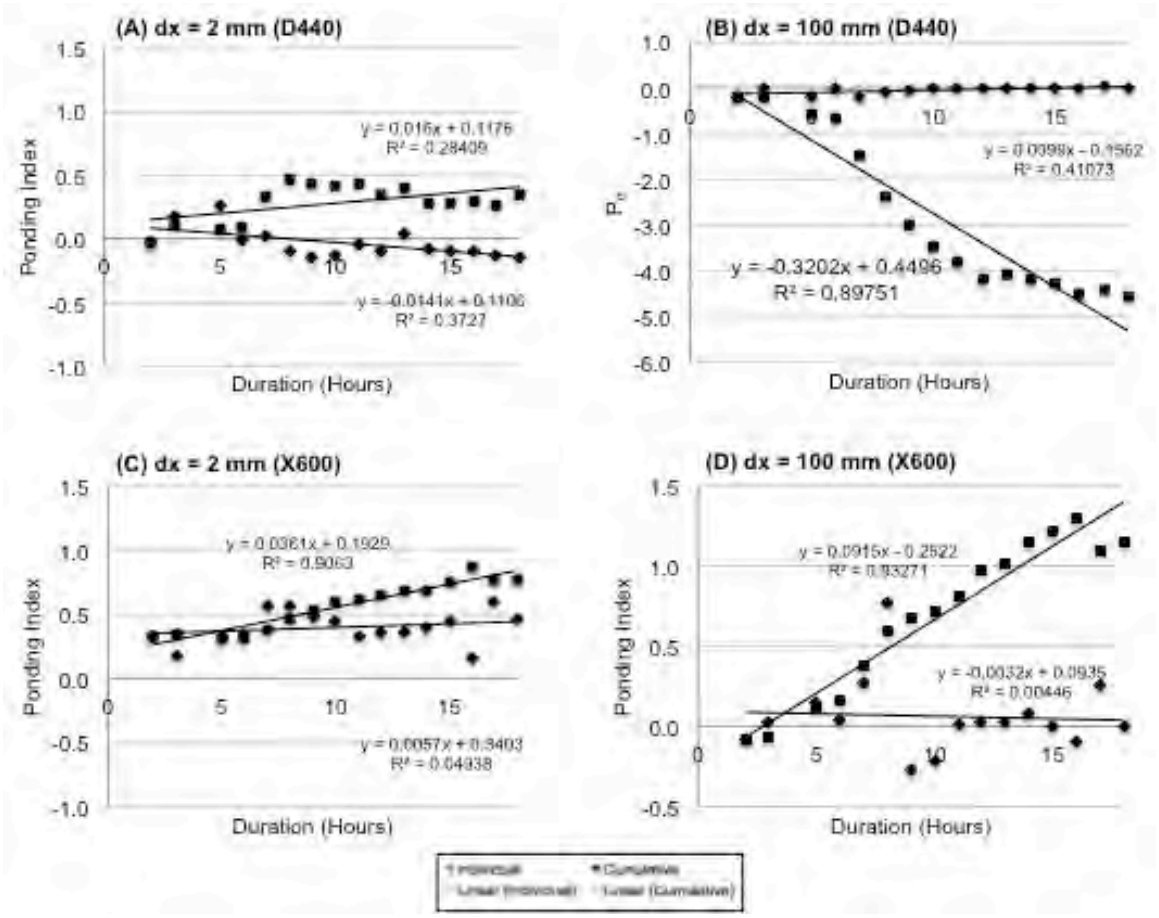


Figure 4.14: Calculated individual and cumulative ponding-index data for subbasin 1. Diamond data points depict individual deposit contributions, and square data points depict cumulative deposit contributions. Calculated ponding-index data from dip-section D440 (see Fig. 7) represented where (A) small (2 mm) and (B) large (100 mm) interval lengths applied in ponding-index calculation. Calculated ponding-index data from strike section X600 represented where (C) small (2 mm) and (D) large (100 mm) interval lengths applied. Data show that interval lengths have great influence in resulting cumulative ponding-index values, but individual $P_0$ values remain unaffected for subbasin 1.

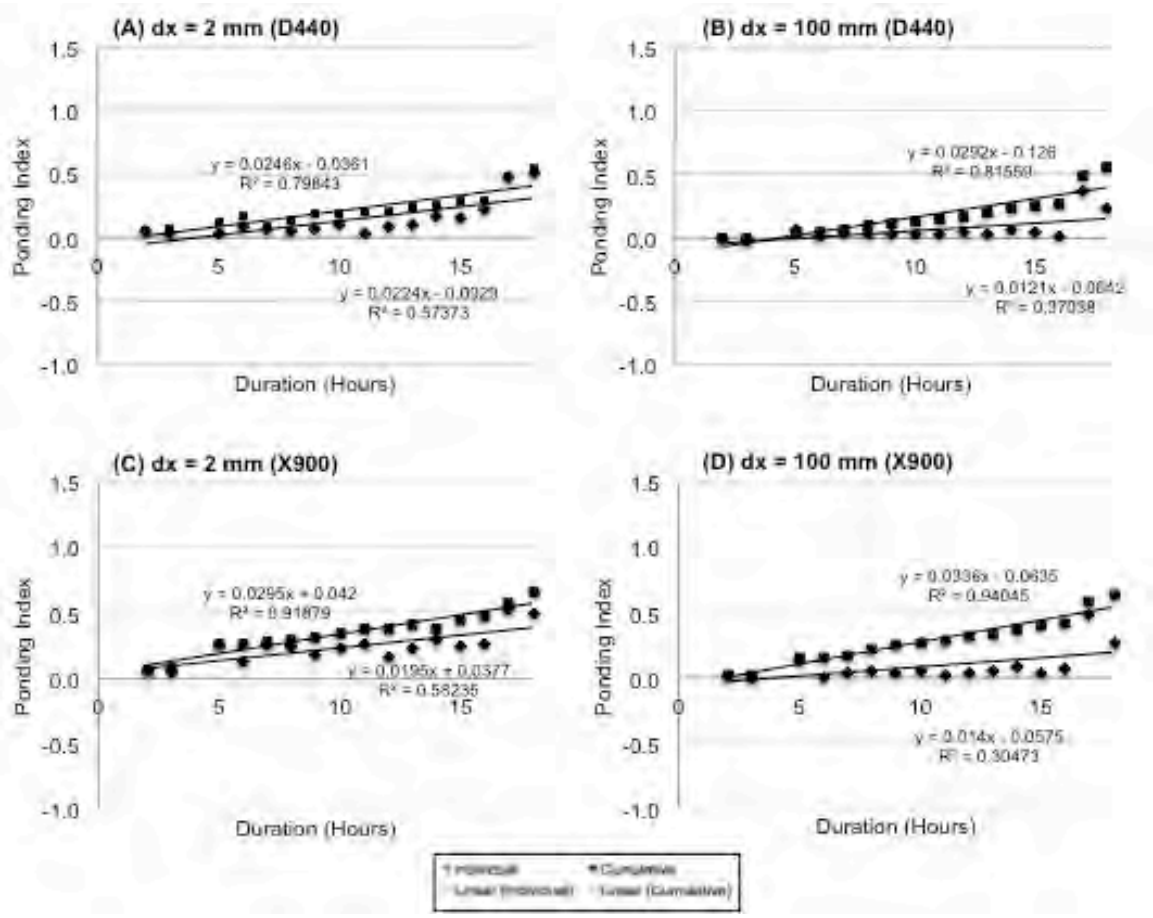


Figure 4.15: Calculated individual and cumulative ponding-index data for subbasin 2. Diamond data points depict individual deposit contributions, and square data points depict cumulative deposit contributions. Calculated ponding-index data from dip-section D440 (see Fig. 7) represented where (A) small (2 mm) and (B) large (100 mm) interval lengths are applied in ponding-index calculation. Calculated ponding-index data from strike section X900 are represented where (C) small (2 mm) and (D) large (100 mm) interval lengths are applied. Data show that both individual and cumulative $P_0$ values remain unaffected for different interval lengths in subbasin 2.

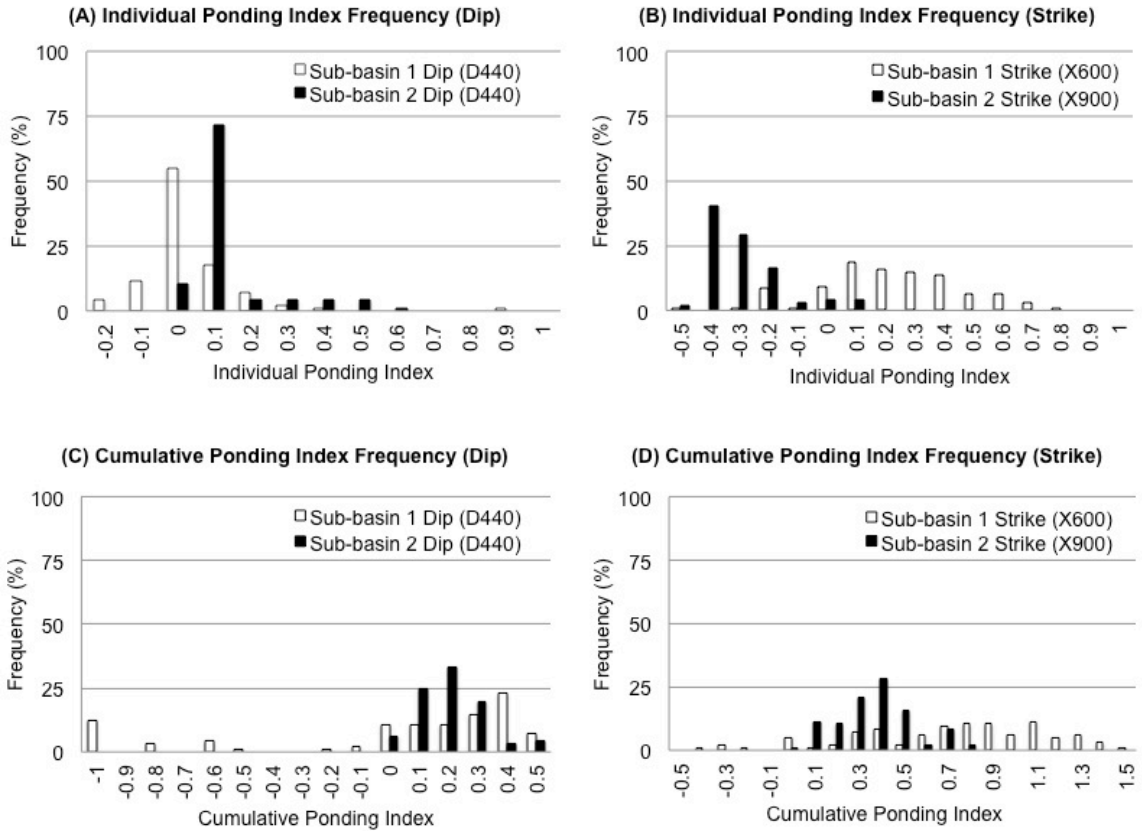


Figure 4.16: Frequency distributions of individual and cumulative ponding-index data. (A) Graph shows frequency distribution of dip-oriented individual ponding-index data for deposits in subbasins 1 and 2; (B) graph shows frequency distribution of strike-oriented individual ponding-index data for deposits in subbasins 1 and 2; (C) graph shows frequency distribution of dip-oriented cumulative ponding-index data for deposits in subbasins 1 and 2; and (D) graph shows frequency distribution of strike-oriented cumulative ponding-index data for deposits in subbasins 1 and 2. Ponding-index-frequency data for individual and cumulative deposits each plotted from 192 observations in both subbasins 1 and 2. Data calculated for interval length scales ranging from 2 to 100 mm.

## REFERENCES


Badalini, G., Kneller, B., and Winker, C.D., 2000, Architecture and processes in the late Pleistocene Brazos-Trinity turbidite system, Gulf of Mexico continental slope: Program and Abstracts - Society of Economic Paleontologists: Gulf Coast Section Research Conference, v. 20, p. 16–34.

Beaubouef, R.T., and Friedmann, S.J., 2000, High resolution seismic/sequence stratigraphic framework for the evolution of Pleistocene intra slope basins, western Gulf of Mexico; depositional models and reservoir analogs: Program and Abstracts - Society of Economic Paleontologists: Gulf Coast Section Research Conference, v. 20, p. 40–60.

Booth, J.R., Prather, B.E., and Steffens, G.S., 2002, Depositional models for ponded and healed-slope accommodation on above-grade slopes; implications for reservoir characterization: American Association of Petroleum Geologists Annual Convention, v. 11, p. 20–21.

Brunt, R.L., McCaffrey, W.D., and Kneller, B.C., 2004, Experimental modeling of the spatial distribution of grain size developed in a fill-and-spill mini-basin setting: Journal of Sedimentary Research, v. 74, p. 438–446.

Buddin, T.S., Williams, M.C., and Hall, S.H., 2002, An evolutionary 3-D model for the development of the Frontal fold belt, Atwater Valley and southern Green Canyon areas, deep-water Gulf of Mexico: American Association of Petroleum Geologists Annual Convention, v. 11, p. 25-25.

Haddad, G.A., Petersen, M., Waszczak, R.F., Young, S.W., Hufnagel, J.V., Liu, C.J., Palmer, J.R., Chlumsky, F.J., Borbas, T., Moutoux, J.J., McGee, D.T., Fitzsimmons, R.F., and Travis, P.D., 2003, Stratigraphic evolution of the Magnolia Field and surrounding area, Garden Banks blocks 783 and 784, deepwater Gulf of Mexico: American Association of Petroleum Geologists Annual Convention, v. 12, p. 69.

Hay, A.E., 1987, Turbidity currents and submarine channel formation in Rupert Inlet, British Columbia; 1, Surge observations: Journal of Geophysical Research, v. 92, p. 2875–2881.

Inman, D.L., Nordstrom, C.E., and Flick, R.E., 1976, Currents in submarine canyons; an air-sea-land interaction: Annual Review of Fluid Mechanics, v. 8, p. 275–310.

Kneller, B., and McCaffrey, W., 1999, Depositional effects of flow nonuniformity and stratification within turbidity currents approaching a bounding slope; deflection, reflection, and facies variation: Journal of Sedimentary Research, v. 69, p. 980–991.

Liu, J. Y., and W. R. Bryant, 2000, Sea floor morphology and sediment paths of the northern Gulf of Mexico deepwater, *in* A. H. Bouma, and C. G. Stone, eds., Fine-

grained turbidite systems, v. 72: Tulsa, OK, United States, American Association of Petroleum Geologists p. 13.

Lamb, M.P., Hickson, T., Marr, J.G., Sheets, B., Paola, C., and Parker, G., 2004, Surging versus continuous turbidity currents; flow dynamics and deposits in an experimental intraslope minibasin: Journal of Sedimentary Research, v. 74, p. 148–155.

Lamb, M.P., Toniolo, H., and Parker, G., 2006, Trapping of sustained turbidity currents by intraslope minibasins: Sedimentology, v. 53, p. 147–160.

Madof, A.S., and Christie-Blick, N., 2007, The role of gravity-driven sedimentation in the evolution of salt withdrawal intraslope minibasins; insights from north-central Green Canyon, Gulf of Mexico: Geological Society of America Abstracts with Programs, v. 39, p. 149–150.

Mohrig, D., and Buttles, J., 2007, Deep turbidity currents in shallow channels: Geology, v. 35, p. 155–158.

Muck, M.T., and Underwood, M.B., 1990, Upslope flow of turbidity currents —a comparison among field observations, theory, and laboratory models: Geology, v. 18, p. 54–57.

Mulder, T., and Syvitski, J.P.M., 1995, Turbidity currents generated at river mouths during exceptional discharges to the world oceans: Journal of Geology, v. 103, p. 285–299.

Paola, C., Straub, K., Mohrig, D. C., and Reinhardt, L., 2009, The 'unreasonable effectiveness' of stratigraphic and geomorphic experiments: Eos, Transactions, American Geophysical Union, v. 89, p. 1–43.

Parsons, J.D., and Garcia, M.H. 1998, Similarity of gravity current fronts: Physics of Fluids, v. 10, p. 3209–3213.

Pirmez, C., 1994, Growth of a submarine meandering channel-levee system on the Amazon Fan: Ph.D. Dissertation thesis, Columbia University, New York, 594 p.

Pirmez, C., Prather, B.E., Mallarino, G., O'Hayer, W.W., and Droxler, A.W., 2012, Chronostratigraphy of the Brazos–Trinity depositional system, western Gulf of Mexico; implications for deepwater depositional models: SEPM Special Publication, v. 99, p. 111–143.

Prather, B. E., J. R. Booth, G. S. Steffens, and P. A. Craig, 1998, Classification, lithologic calibration, and stratigraphic succession of seismic facies of intraslope basins, deep-water Gulf of Mexico: AAPG Bulletin, v. 82, p. 701-728.

Prather, B.E., 2000, Calibration and visualization of depositional process models for above-grade slopes; a case study from the Gulf of Mexico: Marine and Petroleum Geology v. 17(5) p. 619–638.

Prather, B.E., 2003, Controls on reservoir distribution, architecture and stratigraphic trapping in slope settings: Marine and Petroleum Geology, v.20 p. 529–545.

Pratson, L.F., and Ryan, W.B.F., 1994, Pliocene to Recent infilling and subsidence of intraslope basins offshore Louisiana: American Association of Petroleum Geologists, Bulletin, v. 78, p. 1483–1506.

Prior, D.B., and Bornhold, B.D., 1990, The underwater development of Holocene fan deltas: International Association of Sedimentologists, Special Publication, v. 10, p. 75–90.

Puig, P., Ogston, A.S., Mullenbach, B.L., Nittrouer, C.A., and Sternberg, R.W., 2003, Shelf-to-canyon sediment-transport processes on the Eel continental margin (Northern California): Marine Geology, v. 193, p. 129–149.

Pyles, D. R., 2008, Multiscale stratigraphic analysis of a structurally confined submarine fan; Carboniferous Ross Sandstone, Ireland: AAPG Bulletin, v. 92, p. 557-587.

Rottman, J.W., Simpson, J.E., Hunt, J.C.R., and Britter, R.E., 1985, Unsteady gravity current flows over obstacles: Some observations and analysis related to the phase II trials: Journal of Hazardous Materials, v. 11, p. 325–340.

Satterfield, W.M., and Behrens, E.W., 1990, A late Quaternary canyon channel system, Northwest Gulf of Mexico continental slope: Marine Geology, v. 92, p. 51–67.

Sequeiros, O.E., Spinewine, B., Garcia, M.H., Beaubouef, R.T., Sun, T., and Parker, G., 2009, Experiments on wedge-shaped deep sea sedimentary deposits in minibasins and/or on channel levees emplaced by turbidity currents; Part I, Documentation of the flow: Journal of Sedimentary Research, v. 79, p. 593–607.

Sinclair, H. D., and M. Tomasso, 2002, Depositional evolution of confined turbidite basins: Journal of Sedimentary Research, v. 72, p. 451-456.

Toniolo, H. A., 2002, Debris flows and turbidity current deposition in the deep sea and reservoirs: Ph.D. Dissertation, University of Minnesota, Minneapolis, Minnesota.

Toniolo, H., Lamb, M., and Parker, G., 2006, Depositional turbidity currents in diapiric minibasins on the continental slope; formulation and theory: Journal of Sedimentary Research, v. 76, p. 783–797.

Toniolo, H., Parker, G., Voller, V., and Beaubouef, R.T., 2006, Depositional turbidity currents in diapiric minibasins on the continental slope; experiments—numerical simulation and upscaling: Journal of Sedimentary Research, v. 76, p. 798–818.

Twichell, D.C., Kenyon, N.H., Parson, L.M., and McGregor, B.A., 1991, Depositional patterns of the Mississippi Fan surface; evidence from GLORIA II and high-resolution seismic profiles, *in* Frontiers in Sedimentary Geology: New York, Springer-Verlag, p. 349–363.

Violet, J., Sheets, B., Pratson, L., Paola, C., Beaubouef, R., and Parker, G., 2005, Experiment on turbidity currents and their deposits in a model 3D subsiding minibasin: Journal of Sedimentary Research, v. 75, p. 820–843.

Winker, C.D., 1996, High-resolution seismic stratigraphy of a late Pleistocene submarine fan ponded by salt-withdrawal minibasins on the Gulf of Mexico continental slope, *in* Proceedings, Offshore Technology Conference, v. 28, v. 1, p. 619–628.

# Chapter 5: Linking Effect of Turbidity Current Confinement on Flow Dynamics and Deposit Fill Characteristics in a 3-D Minibasin Setting: Experiments, Theory and Implications for Interpreting Subsurface Data


## ABSTRACT

Results are presented from the second of two series of experiments that describes an attempt to test how a turbidity current of fixed size and discharge interacts with a three-dimensional (3-D) minibasin that increases its spatial dimensions through time. I investigate how these interactions influence minibasin deposit geometry, intra-basinal sediment distribution and the extra-basinal delivery of sediment. Analysis of deposit architecture shows that deposits produced draped geometries along the primary direction of transport, while deposits tend to show compensatory stacking along strike. The thickest portions of deposits were usually more proximally located than the deepest point in the basin. The effect of current confinement was evident on the extent and magnitude of a circulatory velocity field produced in the basin during continuous flow events. Thickest parts of deposits were insensitive to changes in current velocity, primarily due to sediment advection lengths in the current. Coarse-grained accumulations however were more sensitive to current dynamics, and occurred in locations with negative trends in fall velocity. The effect of mixing demonstrated by these data had little effect on the trapping abilities of the basin for the three configurations tested, but impacted the nature of sediment deposition as the turbidity current bypassed the basin. Intra-basinal grain size distribution was not definitively correlated with velocity data, which suggests a spatial lag in the response of particle detrainment to current dynamics. Although there appeared to be no definitive link between current component velocity changes and deposit

thickness, the mechanism by which a turbidity current loses its sediment load appeared to be related to flow expansion as it entered the basin. Experimental results can be applied to field-scale minibasin deposits to better understand their fill, but key differences in deposit architecture from each scale of observation made it difficult to accurately determine the processes responsible for their deposition.

## INTRODUCTION

Intraslope salt-withdrawal basins, or minibasins, are significant bathymetric features on continental slopes influenced by underlying mobile salt substrate. These basins, economically significant due to the proliferation of hydrocarbons often contained in their strata, have been encountered from both modern and ancient sedimentary successions across the world, and include the northwestern continental slope of the Gulf of Mexico (Pratson and Ryan, 1994; Liu and Bryant, 2000; Beaubouef and Friedmann, 2000), the northwestern and western continental slopes of Africa (Tari et al., 2000), and offshore Brazil (Alves at al., 2009). It has been previously suggested that depositional turbidity currents are primarily responsible for supplying sediment that fills minibasins (e.g. Lamb et al., 2004; Toniolo et al., 2006). Within the last three decades, focused studies discuss the influence of seafloor topography and confinement on flow behavior and sediment distribution (e.g. Pickering and Hiscott, 1985; Haughton, 1994; 2000; 2001; Hodgson and Haughton, 2004; Lomas and Joseph, 2004). Confinement is a term that has been historically associated with the relationship between deep-water currents and the topography with which they interact (e.g. Lomas and Joseph, 2004; Covault and Romans, 2009).

Conceptual Gulf of Mexico-centric models of minibasin development have become the foundation for exploring and identifying strategic deep-water hydrocarbon

reserves in the fill of these basins. The abundance of subsurface lithological data and imaging available in minibasin provinces has provided the scientific community excellent constraints for building minibasin fill models that have been applied with some success. Experimental studies have also contributed to study of these phenomena and provide a platform for giving further insight into the processes responsible for filling minibasins. The processes whereby scaled turbidity currents flow into minibasins have been documented from both 2-D physical experiments (e.g. Kneller and Buckee, 2000; Toniolo, 2002; Brunt et al., 2004; Lamb at al., 2004; 2006; Toniolo et al., 2006; and Sequeiros et al., 2009) and 3-D physical experiments (e.g. Violet et al., 2005). However, in spite of the gains in understanding process, these studies do not adequately describe the relationship between the degree of 3-D basin confinement relative to the size and efficiency of currents supplying sediment to the basin, and its effect on flow processes and sediment deposition.

This paper describes an attempt to address the shortcomings of previous work through the use of physical experiments to investigate the influence of 3-D minibasin topography and confinement on turbidity current dynamics, deposit geometry, intra-basinal, and extra-basinal sediment distribution. Three static configurations of basin subsidence were established using a controlled water-bladder subsidence mechanism. The lengths, widths and depths of each successive basin configuration were increased relative to a fixed current width. A database of high-resolution bathymetry scans, turbidity-current velocity measurements, and grain size data were analyzed. Results from these experiments were compared to existing models for minibasin fill development that are primarily derived from subsurface geophysical data.

Findings from the experimental results were compared to ancient deposits recorded in a 3-D seismic volume from the Lobster area of Ewing Bank, Block 873, Gulf

of Mexico, where lithological control from well-logs was available. Although the resolution of the seismic imaging in the basin cannot be used to discern deposits from individual events, seismic data provide 3-D information about deposit character that is lacking from outcrops. The applicability of experiments for characterizing the nature of the minibasin fill and the physical processes responsible for their deposition is determined.

## EXPERIMENTAL MODELING THEORY

Dynamical scaling offers a rigorous and well-defined method for imposing experiment conditions that not only match the prototype system in appearance but also reproduce it dynamically (Paola et al., 2009). Laboratory generated turbidity currents are commonly scaled to natural turbidity currents using Froude number scaling. The model and prototype Froude numbers (Fr) are matched. Model Reynolds numbers (Re > 1000) ensure a full turbulent spectrum (Parsons and García, 1998). Further insight into modeling theory is outlined in Maharaj et al., (in review), and Chapter 4 of this dissertation.

A critical component to analyzing current velocity data was the frequency of current dynamics relative to the frequency at which the data were collected, and its influence on sediment deposition. The critical period associated with turbulence can be determined using Taylor's Hypothesis, which suggests that most of the energy in a flow is in eddies with lengths that scale with flow depth. The largest scale eddies are most effective in redistributing momentum. It can be expressed by the following equation, which described the critical period associated with flow turbulence:

$$T_{turbulence} = \frac{h}{\overline{u}} \qquad (1)$$

where $h$ is the flow height and $\bar{u}$ is the average flow velocity. A flow depth of 4 cm and average current velocity not exceeding 10 cm/s were applied as an initial condition for experiments, which suggest that the critical period should not be less than 0.4 seconds. For continuous feed experiments, measured instantaneous velocity data were averaged over 15 seconds.

## Criteria for Sedimentation from Turbidity Currents

### *Rouse Number*

Experimental studies of sediment-laden turbidity currents are also scaled to the natural system using a dimensionless Rouse number, $p$.

$$p = \frac{w_s}{\kappa u_*} \qquad (2)$$

The term in the numerator is the (downwards) sediment the sediment settling velocity $w_s$. The upwards velocity on the grain is given as a product of the von Kármán constant, $\kappa = 0.4$, and the shear velocity, $u_*$. The magnitude of the Rouse number is an indicator of the mode of transport for a sediment grain in a current and is commonly used as a proxy for sedimentation from turbidity currents. When the ratio exceeds a magnitude of 1, $w_s$ dominates and a sediment particle in suspension moves toward the bed. When the ratio is less than 1, $u_*$ dominates and a sediment particle is mixed upward into the interior of the flow.

### *Sediment Advection length*

Lamb et al., (2010) have shown that the advection length scale ($l_a$) is an important parameter in the sediment continuity equation,

$$l_a \equiv \frac{q}{r_0 w_s} \qquad (3)$$

where $q$ is the volumetric discharge of turbid flow per unit length, $r_0$ is the dimensionless ratio of near-bed to depth-averaged sediment concentration and $w_s$ is the sediment fall velocity. The advection length scale describes the average downstream distance a particle is transported before settling to the bed (Lamb et al., 2010). In a settling-dominated system (small discharge and coarse sediment), the advection length tends to zero and the volumetric discharge of suspended sediment equals the volumetric sediment transport capacity of the current (a common approximation for bedload sediment transport). The sediment flux at any specific location on the bed follows local transport capacity at the same location, which in turn is a function of local flow dynamics. On the other hand, an advection-dominated system (large discharges and fine sediment) occurs, where the advection length tends to infinity, and the volumetric discharge of suspended sediment equals the volumetric discharge of suspended sediment at the inlet. The sediment flux at any specific location therefore follows the sediment flux at the inlet and is insensitive to changes in local transport capacity associated with local accelerations and decelerations of the flow.

The importance of inlet boundary conditions to local flow dynamics is determined by comparing the length scale of the basin ($L$) to the advection length scale of the sediment ($l_a$). In the experiments, inlet discharges ranged from 2 x $10^{-4}$ to 4 x $10^{-4}$ $m^3/s$, the $D_{50}$ settling velocity was 7 x $10^{-5}$ m/s, and $r_0$ was 1.5. For current transport on a flat surface, the calculated advection length scale would have ranged from 1.9 to 3.8 meters for the experiments reported, and would be expected to decrease as a result of increased inertial effects with greater vertical basin topography. The downstream length of the basin was however <1.0 m, and suggests that $L < l_a$ and the suspended sediment would not have sufficient time to respond to the bed in the basin area due to its downstream advection. Deposit thicknesses should have been insensitive to current dynamics, which

partially is the case due to the interaction with the 3-D basin topography. Due to the 3-D depletive nature of the flow as it entered the basin, the advection length scale decreased as the current spread into and away from the basin accommodation space. As each basin configuration became larger than its previous state, there was an increase in the integrated basin length relative to the sediment advection length, which suggests that a greater total volume of sediment should be trapped.

## EXPERIMENTAL APPROACH

The experiments documented in this paper represent the second of two series of minibasin experiments performed in the University of Texas Morphodynamics Laboratory (UTML) deep basin tank (Fig. 5.1). The experimental setup is similar to that described in Maharaj et al., (in review), and Chapter 4 of this dissertation (see Chapter for description), with few modifications to model varying degrees of current confinement. Modifications to the original setup are outlined in this paper.

A 25-cm tall gravel layer was built on the platform, into which the minibasin subsidence mechanism was placed. On top of the gravel layer, a thin, flexible plastic film was installed to prevent air escape from the gravel layer into the basin fill. A 2 cm-thick layer of 300 $\mu$m and finer silica flour was placed on top to reduce the rugosity of the initial depositional surface. A guiding channel was used to confine the turbidity current and to fix their dimensions before entering the minibasin. The terminal 30 cm of the channel floor was removed to allow the currents to enter the minibasin ad the basin increased in size. As the minibasin was subsided, the confining channel walls were suspended above the basin, allowing the turbidity currents to dive (Fig. 5.2). The model minibasin was created inside of the tank by means of a controlled, water-filled bladder drainage system that was emplaced within the gravel layer and allowed to lie flat on the

sloped surface. The subsidence rate was monitored using a MassaSonic™ M-5000 acoustic sensor, which recorded water level change as it was extracted out of the plastic bladder.

In between experiments, the basin was subsided on three occasions, each representing separate morphologic configurations relative to fixed physical input turbidity current characteristics (Fig. 5.1). As the minibasin was subsided, the confining channel walls were suspended above the basin, which allowed the turbidity currents to dive at the minibasin entry point (Fig. 5.2). Initial conditions used in the experiments reported in this paper are shown in Tables 5.1 and 5.2. In all the experiments reported, sediment detrainment was insufficient to prevent sustained overspill, and a significant portion of the current surmounted the basin topography. A Keyence™ LK-G502 displacement laser was used to record initial basin topography, as well as topography at the end of each flow event. The laser was mounted to 3-axis, computer-controlled cart over the basin. Both the ADV and the laser system mapped each surface on a 2 mm x 2 mm grid, at approximately 200 $\mu$m vertical resolution. The bathymetric scanning area was 1.5 m long and 1.0 m wide.

While turbidity currents were flowing, a Nortek Vectrino 3-D Acoustic Doppler Velocimeter (ADV) mounted on an electronically controlled carriage was used to collect time-averaged near-bed turbidity current velocity component data on a 50 x 50 mm grid. The ADV was lowered into the water column to a depth of 50 mm above the bed using the automated carriage, and the base of the sampling volume was located within 2 mm above the deposit bed. The sampling volume of the ADV measured 6 x 6 x 9 mm. During later flows, a Nortek Vectrino 3-D profiling acoustic Doppler velocimeter (PADV) was used to measure complete turbidity current velocity profile component data. At each measurement location, the PADV recorded instantaneous velocity component data at a

frequency of 20Hz. The vertical measurement range PADV was 56 mm, and comprised 23 bins, each measuring 2 x 2 x 2 mm. (Fig. 5.3a).

The minibasin was subsided at a rate of 16 mm/hr to setup an initial basin condition of partial current confinement relative to basin topography, herein referred to as configuration 1 (config. 1). The initial maximum dimensions of the minibasin were 40 x 40 x 4 cm. he minibasin margins developed asymmetrically, with a relatively shallow slope near the input channel margin and a relatively steep slope at the distal basin margin. Five continuous-feed turbidity current experiments (flows 1-5) were performed in the config. 1 basin, each with an equal duration of fifteen minutes. Bathymetric maps of each post-flow deposit surface were recorded. ADV data were collected at pre-determined locations along the center dipline of the basin.

Following the fifth experiment, the bladder was subsided at a rate of 16 mm/hr to establish the second basin configuration (Config.2). The initial dimensions of the config. 2 basin were 50 x 50 x 6 cm. Nine continuous-feed turbidity current experiments were performed, three with durations of fifteen minutes (flows 6-8) and six with durations of sixty minutes each (flows 9-14). Vertical flow properties were sampled during flow 14 using a rack of eight vertically stacked siphons spaced 5 mm apart. Data from current samples were compiled to produce characteristic input vertical concentration and density profiles (Figs. 5.3b and 5.3c).

After experiment 14, the basin was subsided a third time at a rate of 9 mm/hr to assume its largest configuration (config. 3). The basin measured 60 x 60 x 8 cm. The degree of turbidity current confinement at the source was greatest relative to previous configurations. The large width and length of the basin exceeded the turbidity current width by six times. In this configuration, flows of varying durations were run. Five surge flows were run (flows 20a, 20b, 20c, 22a and 22b), each with durations of approximately

12 seconds; seven continuous flows were run (flows 15-19, 26 and 27), lasting 60 minutes each; and four long-duration, continuous flows were run (flows 21 and 23-25), lasting 120 minutes each. Bathymetric scans for flows 19, 20a and 20b were not collected due to laser errors. PADV equipment was used to measure turbidity current velocity profiles for flows 23-27.

Following configuration 3 experiments, the basin tank was drained over a 14-day interval, and the deposit was allowed to dry for a further 2 days. After the deposit was sufficiently dried, a cold coring technique was used to sample the deposit. A thin metal rod was submerged in liquid nitrogen, and placed in the deposit at specific locations for approximately 10 seconds. The mildly damp sediment froze onto the rod, and a sample was pulled from the deposit. The laser was used to estimate the deposit thickness from each configuration, which was used to estimate the bulk sampling of each core. Only samples of the config. 3 deposit were analyzed. Core samples were processed using a Horiba LA-300 Laser Particle Size Analyzer (LPSA) to determine grain size distributions within the deposit.

## BASIN AND CURRENT MORPHOLOGY

### Basin Morphology

Slope maps show the initial basin morphology for each configuration (Fig. 5.4). For configuration 1, the initial basin width was partially confined relative to the incoming current. Compared to configs. 2 and 3, the cross-sectional geometry of configuration 1 is more v-shaped, with an areally small topographic low point. For the initial setups of configs. 2 and 3, widening and deepening of the basin was complemented by localized structural collapse of the frontal and lateral margins of the minibasin (Fig. 5.4). The

collapses were associated with the over steepening of the confining margins of the minibasin as the walls exceeded the submerged angle of repose for silica flour (31°, Toniolo ad Cantelli, 2007).

**Current Morphology**

In this paper, all descriptions of fluid and sediment transport were referenced to the following orthogonal coordinate system: $X$ refers to the downstream or downslope plane; $Y$ refers to the strike plane (orthogonal to the X-plane), and $Z$ refers to the vertical plane (Fig. 5.5). Turbidity current velocity data were collected in a fixed measurement reference frame ($X$, $Y$, $Z$) for all experiments. Reference is made to the following fluid velocity components: $u$ refers to the fluid velocity component in the $X$-plane; $v$ refers to the component in the $Y$-plane; and $w$ refers to the component in the $Z$-plane. Velocity component data from each location was rotated (after Arya, 1998) to a bed-perpendicular reference frame ($X'$, $Y'$, $Z'$).

A sequence of time-lapse photos (Fig. 5.6) shows the turbidity current as it flowed through the minibasin. Spatial distribution of 3-D current profiles averaged over 15 seconds was highly variable within and around the minibasin (Fig. 5.7a). Lateral spreading and ambient fluid entrainment of the current were trapped by velocity component data from ADV and PADV equipment (Figs. 5.6 and 5.7).

A series of time-averaged $u$-component velocity profiles along the center dipline section A-A' (D380) are shown in Figure 5.7b. The current accelerated as it entered the basin (Fig. 5.7b, location II). The high-velocity core of the current near the base of the profile was well defined at this location. As the current reached the base (base) of the inlet slope, it decelerated and thickened (Fig. 5.7b, location III). When the current encountered the deepest point of the basin (Fig. 5.7b, location IV), the velocity became

more distributed in the profile. Further traversing toward the exit slope was accompanied by increased entrainment of ambient fluid. The current then thinned and exited the basin with a reduced velocity.

The instantaneous velocity contours (Fig. 5.7c) show that the strong shear instabilities developed as the current moved down the basin slope, and that instabilities are damped as the current moved out of the basin. Both ADV and PADV velocity component data were further analyzed to determine the effect of basin topography on the spatial distribution of the turbidity currents and sediment deposition patterns.

## DATA ANALYSIS

### Cross-Sectional Deposit Morphology

#### *Config. 1*

Config. 1 was established to model partial confinement of turbidity current flow into a minibasin of low relief. Figure 5.8 shows the characteristics of individual and total deposit thickness in planform and cross-sectional views. In planform view, the total deposit from the five experiments run into the basin is moderately concentric in shape, where thicker accumulations appear to be related to the irregular shape of the basin. The two thickest portions of the complete deposit (> 15 mm) are in the inlet channel leading to the basin, and on the inlet slope of the minibasin. The thickest deposit in the minibasin however did not coincide with the deepest point of the basin (Figure 5.8a). Thinning of the cumulative deposit onto the lateral and exit margins of the minibasin was common for individual and cumulative events. The spreading of the turbidity current beyond the laterally confined space of the basin margins resulted in a thin cumulative deposit

measuring between 1-5 mm. The spread angle of the deposit was approximately 45° from the primary current transport direction on either side of the basin. The point of origin associated with the spreading coincided with the thickest deposit along strike (Section B-B'), and not the inlet zone.

In dip section B-B' (D380), the basin topography is such that both the inlet and exit slope gradients are similar (~20°), but there are key differences in individual and cumulative deposit geometry on each slope. The most notable characteristic of individual deposits is their sigmoidal shape relative to basin topography (Figure 5.8b). From the turbidity current inlet area, deposits gradually thickened toward the updip basin slope to attain a maximum dip-oriented deposit thickness. The thickest portion of the deposit is maintained until the lowest point of the basin, where deposits taper gradually to thin individual deposits (< 1 mm) on the exit slope of the minibasin, which continues to drape and remains thin beyond the basin margin. Individual deposits aggrade on subsequent ones, creating a cumulative thick that is constrained to the inlet slope of the basin, and not its deepest point. Strike section C-C' (D500) is oriented perpendicular to the primary axis of flow, and was selected because of the thick deposit accumulation (Figure 5.8c). Note that this section does not coincide with the deepest point of the config. 1 basin. The section shows similar individual and cumulative deposit geometry to the centerline dip section, but the thickest portion of the deposit may be linked to an off-centered channel relative to basin symmetry, and the shallower confining slopes on the northern flank of the basin relative to its southern flank. It is postulated that since the southern flank approaches the submerged angle of repose for the cohesionless silica flour (> 30°), there is relatively little accumulation on the slope.

***Config. 2***

The broader planform and cross-sectional morphology of the config. 2 basin relative to fixed turbidity current dimensions resulted in distinctly different individual and cumulative deposit characteristics in plan-view and cross-section (Fig. 5.9). Individual deposits from flow events 6 to 9 are indiscernible in cross section, primarily due to their individual accumulations not exceeding 1 mm from the 15-minute continuous turbidity current events. The planform deposit map and dip cross-section D-D' (D380) shows that although the thickest deposits are situated in the bathymetric low point of the basin (compared to the inlet slope from the previous configuration), they are thickest at the base of the inlet slope (Fig. 5.9b). Individual deposits from later experiments (10 to 15) dip cross-section D-D' clearly show this relationship. As the basin fills, the pre-flow topography from each event becomes shallower and more u-shaped. Despite this progressive healing of basin topography, the thickest portion of the deposit in dip section also remains near the base of the inlet slope. Alternating thicks and thins on the exit slopes indicate inconsistency in fill patterns in this section related to lateral compensation of individual deposits out of the plane of the section near the exit slope. Thin accumulations on the inlet and exit slopes are also the result of steep slope angles that do not favor sediment deposition. As slope angles start to decline beyond the exit slope of the minibasin, individual deposits uniformly drape pre-existing topography, resulting in layer-cake stratigraphy.

Strike section E-E' (X520) shows compensational-style stacking of individual deposits from flows 10 to12, where the thickest portions of the deposit coincided with the topographical low for the section (Fig. 5.9c). Despite these occurrences, aggradation of the final deposit onto a bathymetric high is prominent. Tapering of individual deposits extends up the lateral flanks of the basin until slope angles become too steep for any

accumulations to occur during flows. There are relatively little deposit accumulations beyond the basin flanks due to the absence of turbidity current propagation in this zone.

***Config. 3***

Config. 3 was setup to model the greatest degree of current confinement relative to 3-D basin morphology (Fig. 5.10). The first continuous flow into the config. 3 basin was flow event 15, with a 1-hour duration. Subsequent events 16 to 19 were also of similar durations, from which bathymetry maps were recorded with the exception of the deposit surface from flow 19 because of a mapping system error. The thickness distribution of individual deposits from flow events 15-18 was similar to config. 2 deposits in both cross-sections shown. In dip section F-F' (D380), the deposits from these flows for the most part draped pre-existing topography, with their thickest accumulations being confined to the base of the inlet slope (Fig. 5.10b). However, in strike section G-G' (X500), the thickest accumulations from individual deposits favored the topographically lowest area of the section, and coincided with the cross-sectional asymmetry in basin topography (Fig. 5.10c). Compensational stacking is visible within these packages, where the loci of deposition of individual deposits shifts according to the topographically lowest point in the basin.

The mapping system error associated with flow 19 extended through surge flows 20a and 20b, the second of three successive (12-second) surge flows. Between events 19 (continuous) and 20a (surge), an anomalously thick package was emplaced, recording up to 12 mm of sediment in the thickest part of the deposit. The anomalously thick deposit occurred due to improper experimental design that led to sediment buildup and obstruction at the current outlet zone of the momentum reduction box that caused minor leakage of turbidity current material over the channel walls during flow 19. Dredging in

the channel was facilitated by an underwater vacuum pump, but the activity resulted in the reworking of sediment in the inlet channel that led to the release of a high-density, sediment-laden current into the basin. The resulting thick deposit therefore appears ponded relative to previous deposits in the basin. The cross-sectional morphology of the deposit also resembles that from flow event 16 of Series 1 experiments (Maharaj et al., in review), where a basin-scale slope collapse event occurred. The surge event of flow 20a did not significantly contribute volumetrically to the thick deposit because deposit thickness maps calculated from succeeding surge events (flows 20b, 20c, 22a and 22b) show thin deposits (< 1 mm) from each event that uniformly drape pre-flow topography. Ripple bedforms are visible in the deposit from flow 21, and occurred because of elevated primary current velocities that exceeded 10 cm/s during the experiment. Both cross-sections show that the deposits from flow events 23 and 24 for the most part draped the ripple field from flow 21. The longer-duration (2-hour) event of flow event 25 produced another anomalously thick deposit that healed the rugose bedform topography in the basin in dip and strike planes (Figs. 5.10b and c). Also responsible for this anomalously thick deposit was another instance of channel dredging due to sediment buildup at the current outlet zone of the momentum reduction box, despite efforts to not interfere with the channel-basin interface.

***Interpretation***

A strong affinity exists for individual deposits to mimic the shape of pre-existing topography, which decreases as the duration of a flow event increases. These occurrences reaffirm the tendency of turbidity currents to produce deposits that drape pre-existing topography, regardless of the degree of current confinement. Deposits from longer duration flows resulted in significantly thicker deposits that healed pre-flow rugose

topography, and the post-deposit surface no longer mimicked the shape and the smaller-scale topographic variation associated with the pre-deposit surface. The single exception occurred prior to flow event 19, where an accidental release of a high-density turbidity current resulted in an anomalously thick, ponded deposit.

Second, the primary direction of flow plays an important role on the accumulation of sediment in 3-D confined basin topography. In dip section, the thickest accumulation from individual short- and long-duration continuous flows occurs at the base of the inlet slope of the basin, regardless of configuration, whereas in the strike plane, the thickest deposit is usually encountered in the topographically lowest area. Finally, two occurrences of extra-basinal sediment deposition and possible implications are considered. First, a significant portion of sediment was deposited in the inlet channel prior to entering the minibasin, which can be observed in dip-oriented cross-sections. The volumetric implications of sediment delivery to distal locations would therefore imply that longer duration events would be necessary to overcome the sediment transport limitations associated with flow capacities of shorter-duration events. Second, the degree of confinement appeared to affect the spreading of the turbidity current past the confined space of the basin. An increase in flow confinement relative to basin width resulted in a proximal shift of the spread zone beyond the basin boundary, and will be quantified and discussed in a later section.

**Confinement and Deposit Geometry**

The analysis of deposit geometry characteristics is described using the ponding index equation (from Lamb et al., 2004). The ponding index, $P_o$, is a dimensionless number that compares the change in thickness of the deposit relative to the change in basin elevation over a given length (Chapter 4, Fig. 4.3).

$$P_o = -\frac{1}{L}\int_0^L \frac{d\theta}{d\eta} dx \qquad (4)$$

where $L$ is the integrated investigative length of the basin, $\theta$ is the thickness of the deposit, $\eta$ is the elevation of the initial (pre-flow) bed, and $dx$ is a horizontal length scale for which the thickness, $\theta$ and elevation, $\eta$ are calculated, herein referred to as the interval length. Short interval lengths emphasize small changes in topography and deposit thickness, while long interval lengths emphasize basin-scale topography and deposit thickness (Chapter 4, Fig. 4.7). For this analysis, the selected interval lengths (config. 1 – 4 mm; config. 2 – 20 mm; and config. 3 – 20 mm) were used to characterize individual and cumulative deposit geometries (Fig. 5.11).

***Config. 1***

For dip section D380 (Fig. 5.11a), the linear regression for the individual deposits shows that as the basin filled, the ponding index values are close to zero with a negative trend. However, cumulative deposit ponding index values have a positive trend, and range from approximately 0.2 and 0.3. Similar trends are observed from strike section X500 (Fig. 5.11b), but with smaller values for the cumulative deposit. Application of the ponding index suggests that individual deposits were confined to the basin margin, in this case primarily on the proximal slope, while cumulative deposit appear more ponded as the basin progressively filled.

***Config. 2***

Data from dip section D380 (Fig. 5.11c) shows that individual deposit ponding indices became more negatively as the basin filled. The three 15-minute continuous flows early in the experiment (Events 6 to 9) however showed a ponding index that is

approximately zero, compared to the results from longer duration flows later in the series of experiments. As the basin filled, the negatively trending individual ponding index magnitudes confirmed the geometries observed in cross-section, which thinned in the basin center and thicks at both the bases of the inlet and exit slopes. Cumulative ponding index data trends were however similar to config. 1 experiments, since the trend line gradient magnitudes were similar.

For strike section X500 (Fig. 5.11d), individual and cumulative ponding index data have a similar positive trend. This relationship reaffirms the previously described observation for the cross section in Figure 5.11b, where individual deposits appeared more ponded and infill topography more readily in strike section than they do along the axis of the primary current flow direction.

***Config. 3***

Individual ponding index data from dip section D380 (Fig. 5.11e) are more variable relative to previous datasets, which generally correlates with the different flow durations. For surge events, individual ponding indices are near zero, while for longer-duration events, individual ponding indices increase. The anomalously thick deposits associated with both flow events 19 and 25 have large ponding index values in both dip and strike sections=. In strike section X500 (Fig. 5.11f), individual deposits show an overall decreasing trend of ponding index magnitudes that become negative, with the exception of the two anomalously thick deposits described above that are each characterized by markedly high ponding index magnitudes. This variability is reflected in cumulative ponding index data, where two distinct cycles of draping and ponding are visible.

### *Interpretation*

The observations described above showed that linear regressions applied to individual and cumulative ponding index trends are useful to demonstrate temporal changes in the basin fill character. Individual ponding index dip-section data from all configurations show that deposits from both surge and continuous currents were more likely to drape pre-existing topography than pond within it. In most cases, the individual ponding index values had a negative trend, suggesting that the thickest portions of deposits were confined locally to one part of the basin margin. For strike sections, data suggested that a higher degree of tangential onlap of individual deposits was more likely to occur when flow durations are long relative to the basin size, while individual deposits never fully pond within the minibasin. In config. 1, shorter duration continuous events laid down deposits that did not appear ponded relative to pre-flow basin topography. Longer duration flows in config. 2 resulted in individual deposits that were more ponded based on ponding index data. Extended-duration continuous flows resulted in individual deposits with relatively higher individual ponding index magnitudes than long-duration continuous flows. Ponding index analysis did not provide quantitative information that would suggest compensational stacking of successive deposits in strike sections.

## Current Confinement, Velocity Distribution and Deposit Thickness

### *Observations*

The 3-D experiment setup provided an opportunity to investigate the effect of topography on vertical and lateral current velocity variability. Characteristic time-averaged, near-bed current data collected with the ADV from each event were combined to create current vector distribution maps that represented the time-averaged flow of

continuous turbidity currents into the basin by configuration (Figure 5.12). Velocity vector plots were superimposed on bathymetry and deposit thickness maps to illustrate the spatial relations. For each configuration, characteristic *u*- and *w*-component velocity data were compiled from the center downstream section to provide a cross-sectional perspective of the component velocity distribution.

Config. 1 near-bed velocity data were spatially limited due to the short flow durations (Fig. 5.12a). Downstream (*u*-component) velocity data show acceleration and subsequent deceleration of the current down the inlet slope prior to encountering the deepest point of the basin. The current continued to decelerate as it exited the basin. Vertical (*w*-component) velocity data show that initially, the current displays downward motion toward the bed along the inlet slope. Before the current reached the deepest point of the basin, the current moved upward, away from the bed and attained a maximum over the deepest point of the basin. The current then fell once more toward the bed upon exiting the basin. High velocities were generally confined to the updip slope of the basin, and generally decreased further downdip before the exit slope of the basin was encountered. The current was slightly diverted as it exited basin, an occurrence related to its irregular shape.

A more spatially expansive near-bed current velocity dataset collected from configs. 2 and 3 show that velocities were highest along the center dipline of the basin and decreased laterally (Fig. 5.13). Additionally, a spatially stable circulation pattern was produced from continuous turbidity current experiments in each configuration (Figs. 5.12b and 5.12c). Four main rotational cells (C1-C4) that extended beyond the basin margin made up the circulation pattern, which were oriented around the center downstream section of maximum current velocity (Figs. 5.12b and 5.12c). Of the four cells, two proximal rotational cells on either side of the basin converged toward the basin

center, and established a reversal in flow in the basin area around the dip-oriented flow along the centerline downstream section. The two distal cells rotated in a direction opposite to their upstream equivalents, and extended beyond the basin's exit slope. When flows from Configurations 2 and 3 were compared, vector magnitudes in each of the rotational cells increased spatially with an increase in the degree of confinement. An increase in the relative amount of current confinement also resulted in an increase in size of the rotational cells.

The data also shows a spatial lag between the point of maximum negative fall velocity and the thickest deposit, which are approximately 150 mm apart from each other for all configurations. Although this spatial relationship was consistently observed in cross-section, there appeared to be no direct correlation between deposit thickness and component near-bed current velocities that could have been applied predictively (Fig. 5.14). These data show that the thickest deposits generally coincided with the locations of relatively high velocities.

***Interpretation***

The current circulation pattern that was established during the continuous feed experiments demonstrated that the lateral components of flow (u- and v-components) were important for distributing sediment away from the primary axis of current transport, but may not have been important for establishing a locus of sediment deposition within a particular basin configuration. As a result, there did not appear to be a relationship between the circulation patterns and sediment deposition. Instead, sediment deposition occurred in the zone where there were strong fluctuations in the near-bed vertical velocity along the primary axis of highest near-bed horizontal velocity (Figs. 5.12 and 5.13).

Conceptual models for minibasin fill development have never provided a plausible explanation for the creation of channels that are commonly observed at the downstream ends of minibasins. The experiments suggest that flow convergence at the central exit point of the basin could contribute to focused erosion and channel development. Hypothetically, the rate at which this mechanism may be effective in producing channels may be enhanced by an increase in the intensity of current velocity magnitudes, once the appropriate flow criteria are met. Although the flow conditions tested in the reported experiments favored sediment deposition, there were no features observed that suggested channel formation.

**Confinement and Sediment Trapping**

***Observations***

Deposit thickness maps calculated from pre- and post-event bathymetry were used to calculate basin sediment trapping for each flow event. Results were compared to known input sediment flux supplied to the basin to determine trap efficiency for confined flows (after Lamb et al., 2006 and Maharaj et al., in review (Chapter 4 of this dissertation)). Three metrics of sediment volume ratios were applied to characterize the nature of sediment supply and trapping by the basin as the degree of confinement varies (Fig. 5.15). First, the ratio of cumulative sediment volume supplied to initial basin volume was considered as an initial boundary condition for comparison with other metrics. Second, the basin fill percentage is the volume of sediment trapped by the basin relative to the basin's pre-flow volume for each flow event. This metric was used to determine the relative volumes of the pre-flow basin capacity occupied by individual deposits as the basin filled (Fig. 5.15). Third, the basin trap efficiency (Lamb et al., 2006)

is a measure of the volume of sediment trapped by a basin relative to the total sediment flux to the basin. Results from Maharaj et al., (in review), and Chapter 4 of this dissertation showed that trap efficiencies from individual and cumulative events have relatively similar trends and are virtually indistinguishable, regardless of which method is applied. The individual trap efficiency metric has therefore been applied in the analysis.

Results suggest that for a fixed input condition of flow properties, sediment trap efficiency remained fairly consistent as the basin filled (Fig. 5.15). As each basin configuration filled with sediment, data trends show that the basin fill percentage increased. The increase in fill percentage for each event was however small and rarely exceeded ten percent; the main exceptions being related to documented cases of gravity collapse of the minibasin side walls during individual flow events. The basin fill percentage was generally one order higher in magnitude compared to the trap efficiency. The trap efficiency for each basin configuration in Series 2 experiments rarely exceeded 1.5%, the highest efficiencies encountered in the two least confined configurations (Series 1 and config. 1 from Series 2). The initial sediment flux to each basin configuration was usually an order in magnitude higher than the initial basin fill percentage. As experiments were completed, the cumulative sediment flux to each basin was at least four orders of magnitude greater than both the basin trap efficiency and the basin fill percentage. These can be compared to the relatively small changes in sediment trapping throughout the duration of each series of experiments. Basin fill percentage magnitudes remained similar as the degree of current confinement increased from Configurations 1 to 3.

A plot of basin fill percentage vs. trap efficiency for each basin configuration shows that there was a systematic change in trends related to the basin configurations that can be applied as a possible predictive indicator (Fig. 5.16). Results show that deposits

from unconfined flows were characterized by small basin fill percentages (<1%), and a range of trapping efficiencies. Alternatively, to achieve higher basin fill percentages, a relatively larger basin is needed to trap more of the sediment from the incoming current.

***Interpretation***

The analysis of sediment trapping suggests that although there are subtle temporal differences in trends between the basin fill percentage and the trap efficiency, their relative differences are small compared to the relative proportion of sediment delivered to the basins from continuous feed turbidity currents. Additionally, there is a general positive trend in the basin's ability to trap sediment as it fills, which is counterintuitive due to the corresponding reduction in basin topography Although horizontal turbidity current velocities are greatest along the center dipline axis of the basin, the 3-D nature of the basin exhibits a lateral component of topographical interference on turbidity current distribution within the basin that should not be discounted. The associated lateral redistribution of sediment within the basin has a profound effect on the ability for grains to accumulate in local topographic lows within the basin, and accounts for the majority of the compensational stacking patterns observed in cross section previously described.

Given the relationships presented in Figures 5.15 and 5.16, data from outcrop and subsurface minibasins may be used to generate a crude relationship of how a basin may have filled in the geological past, given the relevant spatial and temporal data needed to perform the calculations. Despite these relationships, further interpretation should be approached with caution, since a higher number of configurations are necessary to render results statistically significant. Literature also suggests that minibasins are also not exclusively filled by sediment deposited from turbidity currents, whose deposits may be

geometrically, volumetrically, and temporally different from other gravity-driven deepwater processes on an individual event-scale (e.g. Madof and Christie-Blick, 2007).

## Grain Size Distribution

### *Experiment Observations*

A continuous dataset of bulk median ($D_{50b}$) and ninetieth-percentile ($D_{90b}$) grain size data was calculated using a linear interpolation method between control data points (Fig. 5.17). The $D_{50b}$ grain size distribution map shows that the coarsest grain size fractions were generally confined to the inlet slope regions, and decreased in both downstream and lateral directions. The $D_{50b}$ grain size distribution map (Fig. 5.17a) also shows that coarsest $D_{50b}$ grain sizes (18 $\mu$m) were confined to a single zone on the inlet slope, slightly downstream of the inlet zone. Near the basin center, the average grain size decreased to approximately 12 $\mu$m, before increasing slightly to 13 $\mu$m at the base of the inlet slope. Grain sizes were lowest along the dipline transect at the exit point of the basin, and increased slightly once more downstream of the basin exit point. The relatively rapid decrease in grain size was similar on either side of the basin relative to the primary axis of current transport. Beyond the basin margins, grain size trends emulated the deposit-spreading trend previously described for config. 3 deposits. The $D_{90b}$ grain size distribution map shows that the coarsest fraction (>25 $\mu$m) deposited in the basin was also confined to the inlet slope, downstream of the inlet channel. This local region of coarse deposit however extended further downdip compared to $D_{50b}$ grain size data, and decreased abruptly at the base of slope. Coarsest grain fractions were reduced at the deepest point in the basin (~21 $\mu$m), and increased slightly (~23 $\mu$m) at the base of the exit slope, before decreasing once more further downdip. Coarse material was

encountered once more beyond the basin margins, similar to those found at the base of the basin's exit slope. Here, the grain size distribution also emulated the pattern of deposit and current spreading that occurred in the proximal basin.

Calculated grain size data were compared to deposit thickness maps, initial bathymetry and characteristic velocity profile data for continuous flows in config. 3, since they were responsible for the deposition of the bulk of the deposit volume relative to surge flows. Since most of the variation in grain size occurs in a downstream direction along the axis of highest current velocity, the relationships are examined here (Fig. 5.18). Grain sizes generally decrease in a downdip direction, with two distinct spikes in grain size at the inlet and exit slopes of the basin. The deposit dip section profile (D380) shows that there is however a divergence between the locus of sedimentation in the basin and the thickest deposit, since the thickest portion of the cumulative deposit is located downslope from the coarsest fraction of the accumulation. Current velocity component data (*u* and *w*) are considered to qualitatively determine the effect of current velocity on grain size distribution. Results show that the first spike in deposit grain size trend on the inlet slope of the basin coincides with the point where the *w* follows a negative trend and falls to zero. The downstream component, *u* is however at its peak magnitude along the profile, before commencing a trend of deceleration into the basin center. The final spike in grain size occurs at the exit point of the basin, where w continues to decrease in magnitude, despite the positive trend in *u* that suggests a resumption of current acceleration as it has exited the basin.

***Rouse Number Application***

Where current velocity measurements were recorded, the Rouse number was calculated for the input $D_{50b}$ (10.1 $\mu$m) and $D_{90b}$ (22.8 $\mu$m) grain size fractions to

determine the nature of sediment transport along the center dipline section (Fig. 5.19). The sediment settling velocity was determined using the following equations from the empirical work of Dietrich (1982):

$$D_* = \frac{RgD^3}{\upsilon^2} \tag{5}$$

$$\log W_* = -3.76715 + 1.92944(logD_*) - 0.09815(logD_*)^2 - 0.0575(logD_*)^3 + 0.00056(logD_*)^4 \tag{6}$$

$$W_s = (Rg\nu \times 10^{W_*})^{1/3} \tag{7}$$

In these equations, D is the sediment grain diameter, $\nu$ is the kinematic viscosity of salt water (1.23 x $10^{-6}$ $m^2s^{-1}$), $D_*$ is the dimensionless grain size, and $W_*$ is the dimensionless settling velocity.

The near-bed shear velocity was determined using the following equations:

$$\tau_b = \rho C_f u_{avg}^2 \tag{8}$$

$$u_* = \sqrt{\tau_b/\rho_f} \tag{9}$$

In these equations, $\tau_b$ is the boundary shear stress, $\rho_f$ is the density of the turbidity current mixture (water, salt and sediment), $u_{avg}$is the time-averaged downstream current velocity, and $u_*$ is the near-bed shear velocity.

Results show that the Rouse number rarely exceeds 0.5 along the centerline dip section of the basin for all configurations (Fig. 5.19a), while the magnitude for $D_{90b}$ fractions exceeded $D_{50b}$ fractions by approximately 5.8X (Fig. 5.19b).

***Interpretation***

A simple correlation of grain size map data and current velocity data suggest that the grain size distribution in the basin is most strongly influenced by the fall velocity, *w*, which has been shown to vary based on the cross-sectional shape of the basin. Coarsest grain size fractions occur where *w* approaches zero as the current traverses the basin.

Calculated results comparing the ratio of settling velocity to the near-bed shear velocity suggest that the $D_{90b}$ grain size fraction is more sensitive to local flow dynamics than the D50b grain size fraction, which would suggest a more rapid sedimentation of the coarsest suspended sediment material. The low degree of grain settling relative to near-bed shear velocities suggest that suspended sediment in the current would most likely remain suspended in the current due to very low Rouse numbers that rarely exceed a magnitude of 1. These results are substantiated by the low trapping efficiencies of the basin configurations that were documented in an earlier section.

Results therefore suggest that the response of coarser grain fractions to local flow dynamics is higher than the cumulative effect on deposit thickness, which may be affected by sediment advection lengths. The obstacle presented by the basin's exit slope had a minor effect on accumulation of coarse sediment, but may have played an important role in the lateral redistribution of the current and possible secondary effects on current velocity distribution. Experimental data show that the coarsest accumulations do not correlate with the deepest bathymetry in the basin relative to the basin's inlet and exit slopes. Spatial observations of velocity distributions from configs. 2 and 3 suggest that current velocity magnitudes were enhanced by the degree of current confinement relative to the basin's 3-D shape (Figs. 5.12b and 5.12c). The source of the current also played a considerable role in determining the relative distribution of sediment grains into the

basin, since grain sizes have been shown to decrease along the primary transport axis (Fig. 5.18).

**Extra-Basinal Sediment Dispersal**

The effect of confinement on the spreading of turbidity currents beyond the basins' margins is described, and the implications for sediment dispersal toward distal slope locations are discussed. Sediment deposit maps provided a record of turbidity current dispersal beyond basin margins, and are used to quantify dispersal morphology relative to basin configuration (Fig. 5.20). In addition to the deposit data gathered from the three configurations of Series 2 experiments, data from Series 1 experiments (Maharaj et al., (in review), and Chapter 4 of this dissertation) are also considered. First, a confinement width factor, $C_w$, is defined as:

$$C_w = \frac{W_c}{W_b} \qquad (10)$$

where $w_c$ is the width of the turbidity current at the upstream end of the basin, and $w_b$ is the maximum cross-stream width of the basin. Where $(C_w \geq 1)$ the current is wider than the width of the basin, and where $(0 < C_w < 1)$ the current is narrower relative to the basin's width. The Series 1 minibasin configuration was considered as an end member of relative confinement to turbidity current confinement in the dataset, where $(C_w \geq 1)$. Confinement width factor magnitudes decreased from configs. 1–3 from Series 2 experiments, with config. 3 was the most confined configuration tested.

For each minibasin configuration, there was a definable spreading point outside of the basin, herein referred to as the dispersion axis (Fig. 5.20). Due to the relatively symmetric planform geometry of each minibasin configuration, sediment dispersal was usually symmetric outside of the basin. A dispersion factor, $D_l$, is defined as:

$$D_l = \frac{L_d}{L_b} \qquad (11)$$

where $L_d$ is the dispersion length, which is the measured length between the strike axis of the basin entry point and the dispersal axis, and $L_b$is the maximum downstream length of the basin. The dispersion angle, $\theta_d$ is the angle at which turbidity currents spread relative to the primary transport direction of the turbidity current. Deposit difference maps were used to compare spreading from each basin configuration (Fig. 5.20). Average values of $C_w$, $D$, and $\theta_d$ were calculated by basin configuration, since basin width, length and current width data were virtually identical among flows in a single configuration.

***Observations***

For Series 1 experiments, the dispersal axis was usually at the downdip margin of the basin (Fig. 5.20). As the current widths became more confined in the Series 2 experiments, the sediment dispersal moved proximally, where the most proximal location tested was approximately one-sixteenth the total basin length (Fig. 5.21a). A critical threshold however exists for a confinement width factor of 0.25, where the dispersal axis began to shift proximally with a decrease in $C_w$ below its threshold magnitude (Fig. 5.21a). Where $C_w > 0.25$, the data suggests that there was virtually little effect on the shifting of the dispersal axis (Fig. 5.21a).

Average dispersal angle and confinement width factor data plotted in Figure 5.20b show how confinement of turbidity currents affects the angle at which sediments were dispersed. Results show that for the configurations tested, the individual dispersion angles ranged from 5° to ~56°. These magnitudes equate to a total turbidity current dispersal of 10° to 112° downdip of the basin, since the angles considered in Figure 5.21b

were averages of the spreading angle relative to the primary transport direction on a single side of the basin. The trend line suggests that extra-basinal deposits from unconfined flows were less dispersed than extra-basinal deposits from confined flows.

***Interpretation***

For the basin configurations tested, it was observed that an increase in turbidity current confinement relative to the basin width shifted the dispersion axis proximally, but only took effect when the dispersion length was approximately 0.25X the maximum basin length. Additionally, an increase in turbidity current confinement led to an increase in the dispersion angle of the extra-basinal deposits. When both relationships are considered together, an increase in current confinement effectively led to enhancing the dispersal area of extra-basinal deposits. Although the coverage area is enhanced, the duration of the turbidity current may however determine the relative volumes of sediment that are transported to distal locations. Because a widening and deepening of the basin relative to the current dimensions increased the exit margin width and height, it is interpreted that this would have resulted in the current decelerating further back toward the inlet, which is illustrated by cross-sectional velocity data from Figures 5.12a–c. A more proximal deceleration of the current in a wider basin may have enhanced the ability for the current to spread laterally, and when coupled with greater vertical topography, may have developed a mechanism for increased mixing within the basin, and by consequence, current spreading.

Implications also exist for the behavior of turbidity currents leaving the basin through time, which may reflect an autocyclic control related to the evolution of sediment supply on a complex slope (e.g. Beaubouef and Abreu, 2006). Key aspects of the spatial velocity distribution of turbidity currents are considered in the following section to

examine the driving mechanisms that link the degree of confinement and sediment dispersal.

## IMPLICATIONS FOR INTERPRETING FIELD-SCALE DATA

The goal of the experimental efforts was to evaluate the effect of current confinement on flow processes and resulting deposit architecture, towards improved prediction accuracy in real world minibasin systems. Observations from deposit cross-sectional and planform geomorphological analysis are applied to determine the processes that were responsible for filling the Lobster minibasin during the middle Pliocene (Figs. 5.22). Burk et al., (1999) first described the geologic evolution of the Lobster minibasin. Their reconstruction of basin evolution was performed using a dataset comprising regional 2-D seismic lines, high-resolution 3-D seismic, well-log, production history, paleontological, and core data. The interval of interest occurs in the section of the basin where lithological data is well-constrained using 3-D seismic and well-log data (Fig. 5.22). Burk et al., (1999) suggest that the earliest stage of fill was preceded by the emplacement of a massive salt canopy at the end of the Miocene. Onto the salt canopy, large basin floor fans were deposited in the early Pliocene in a moderately confined structural setting. During the middle Pliocene, basin floor fan deposition in the west side of the Lobster minibasin included the major *Buliminella 1* (*Bul. 1*) reservoirs. Basin loading resulted in the development of salt highs and increased the degree of structural confinement of the minibasin. The salt highs developed on the southeastern edge of the basin blocked sand flow into the more distally located Arnold basin. Extensive basin rim normal and tear faulting then began to develop. The final phase of middle Pliocene deposition was a channel/overbank complex on the eastern side of the *Bul. 1* reservoirs. The basin's fill history therefore provides an excellent analog for testing the effect of

increasing lateral and topographical confinement on fill morphology and architecture. In addition to cross sectional geometric analysis, a combination of attribute and frequency analyses were performed to determine the spatial and temporal variation in fill architecture and morphology.

The tuning thickness is the bed thickness at which two events become indistinguishable in time, and can be expressed by the formula $Z = \lambda/4$, where Z is the tuning thickness and $\lambda$ is the wavelength of the seismic wavelet. A dominant interval frequency of 6 Hz exists for the *Bul. 1* reservoir interval with a vertical bed resolution (tuning thickness) of approximately 11 m (36 ft). Most of the reservoir gross thicknesses are 3-20 m (10-60 ft) thick. As a result, all the reservoir intervals are at or below the tuning thickness and 'flattening' of the fill section to the uppermost horizon is considered a reasonable tool for resolving the basin's paleo-topography. In extreme cases where the paleo water depth far exceeds the seismic tuning thickness, flattening however may not be a suitable tool for resolving paleotopography (as shown in Figure 5.23).

Correct representation of the basin fill required an accurate description of the spatial and temporal variations in basin topography. Combinations of attribute extraction workflows were applied to resolve the spatial and temporal character of critical reservoir elements using the Landmark software suite. Three control horizons (A-C) were mapped from oldest to youngest respectively, with the two extreme horizons (A and C) defining the extent of gross fill interval. The fill interval incorporating the horizons was proportionally divided into ten equal slices for accurately representing the fill stratigraphy when attribute extractions were performed. The root-mean squared attribute was the main attribute applied to identify paleogeomorphic features. Spectral decomposition was also applied, from which isolated signal frequencies were extracted from the original amplitude volume onto new sub-volumes. Well log data were used to

identify the tops and bases of individual lobes, and these picks were correlated to determine the lateral extents of the lobes within the basin. Seismic amplitudes were used to guide interpretations between wells.

**Deposit Fill Sequence and Architecture**

Fill thickness was applied as an indicator for the basin's paleo-accommodation regime. Maximum basin accommodation was located in the northern (proximal) portion of the basin, interpreted from an isochore map of the interval (Fig. 5.24). Cross sections show that the fill primarily comprised a succession of alternating thick low-amplitude discontinuous and high-amplitude continuous reflectors that thinned and onlapped onto paleotopography (Figs. 5.24 and 5.25). The thickest fill of this interval was also situated in the north, which also coincided with the locations of reservoir elements (Figs. 5.24 and 5.25). The youngest section of the fill interval comprised the main reservoir elements. The internal architecture within the reservoir interval displayed high-amplitude, continuous seismic reflectors that mounded and downlapped onto pre-existing topography (Figure 5.25). Successive deposits offlapped and thinned, both laterally and distally into the basin. Offlapping of individual reflectors formed distinct lobe complexes in map view, which are imaged in the northwest, northeast, and central areas of the basin (Fig. 5.26). Relationships of reflector offlapping suggested compensatory-stacking of individual lobe complexes from west to east. Individual lobe complexes were usually associated with a disperse network of channelform features that extended further updip. Well-log correlation confirmed that the western lobes were deposited the earliest into the basin, which was succeeded by eastern channel-lobe deposits (Figs. 5.22 and 5.25). Central lobe deposits were not penetrated by wells, and were considered to be an

intermediary phase in the fill order during the reservoir fill interval. High amplitude responses in seismic coincided with presence of reservoir sandstones and hydrocarbons.

Lobe picks identified in well-log data were used to calculate individual lobe volumes contained within the basin, and the pre-fill basin volumes were also calculated using the base of the reservoir interval. The basin fill percentage calculation was then applied and compared to experimental data to determine whether there were any fill trends that can give insight into the nature of currents responsible for the deposits. Results show that individual lobe volumes range from 0.03% to 5.97%, which, when compared to individual deposit volumes from experiments, would suggest that the currents responsible for the lobe deposits may have been confined relative to the basin's lateral and vertical dimensions.

**Linking Experimental Observations to Subsurface Data**

The Lobster basin was selected as an analog for experimental deposits because of the presence of lithological control from well-log data. Concepts gleaned from experimental work were used to better understand the possible causes for deposits interpreted from attribute responses from seismic data and well-log correlation of the Lobster reservoir interval. Imaging of depositional morphologies within the basin was limited by (1) reflector extent, due to post-depositional tectonics that isolated the deposits from their correlative equivalents outside the basin; and (2) the physical extent of the seismic dataset, which terminated at the downdip flank of the basin. Interpretations of current characteristics were therefore determined using preserved evidence of deposit architecture within the basin from reflector geometries and attribute extractions. Deposits from single flow events were however difficult to resolve from conventional seismic data due to frequency response limitations, especially at increasing burial depths.

***Basin Fill Characteristics***

A post-subsidence reconstruction of the three basin configurations was performed to replicate the effect of tectonic deformation on deposit geometry, which is commonly the state of a basin observed in seismic (Fig. 5.23). The effect of pinning the youngest horizon to a datum to reconstruct paleotopography has been previously discussed, and does a poor job at replicating the true depositional paleotopography encountered by a current. In the case of comparing post-tectonic fill sequences to their pre-tectonic geometries, results show that config. 1 deposits appeared to pond in the early fill, when their post-flow morphology shows that the majority of the deposit was accumulated on the inlet slope. Similar results occur for config. 2 deposits, although some of the containing deposits uniformly draped paleotopography when they were first deposited. Unless higher-resolution data are available to properly characterize individual deposit terminations, it is difficult to determine whether the architectures observed in the current dataset are truly ponded.

***Deposit Architecture Characteristics***

Deposits from the experiments displayed similarities and differences with field deposits that they were intended to model. Without considering the implications for scale dissimilarity between event deposits from experiments and cumulative event deposits observed in the subsurface, the main characteristics in deposit similarity include: 1) for the each phase of filling, individual architectural elements (i.e. channelforms and lobeforms) are elongate along the primary direction of transport (NE-SW), (interpreted from the channelform orientations), and show compensatory stacking patterns along strike (Figs. 5.25 and 5.26); and 2) grain sizes generally decrease along the primary direction of transport, although their coarsest fractions are confined to the inlet slope and

not the deepest point of the basin. The main differences observed include 1) the intricate network and stacking patterns of architectural elements imaged from seismic attribute extractions were not present in experimental work; and 2) internal architectural element terminations in seismic displayed distinct onlap and downlap relationships to pre-existing topography, while deposits from turbidity currents drape topography (except in areas where steep slopes prevent sediment grains from accumulating). Similar observations have been made by Violet et al., (2005) who point reference the deposits of the Trinity-Brazos minibasins system.

***Interpreting Flow Processes***

The experiment reported in this chapter gives insight into the 3-D interaction between varying sizes and durations of turbidity currents and minibasin topography, which has providing a gauge for interpreting processes responsible for depositing sediment in the Lobster minibasin.

First, there are implications for interpreting flow sizes relative to the size and nature of deposits observed from experimental work. Experimental work showed that the thickness of deposits formed from pulsed turbidity currents were two orders of magnitude smaller than the thickness of the currents responsible for their deposition, while the thickness of deposits from continuous turbidity currents were one order of magnitude smaller than the current thickness. Since individual event thicknesses were not discernible using the data available, an estimate of current thickness is indefinable. Basin fill percentage data however suggest that currents entering the basin may have been confined relative to the basin's vertical and lateral extent at the time of deposition.

Second, experimental ponding index analysis showed that individual deposits from turbidity currents tend to drape pre-flow topography, while those from gravity

collapses of the minibasin sidewall are more likely to pond. The relationship is clear when comparing individual vs. cumulative events, where the cumulative deposit represents what is visible on seismic. The ponding index was however found to be a scale-dependent metric, which limits its application to data of different scales. As a result, an analysis using solely seismic-generated horizons will not truly represent the geometry of individual event deposits, since seismic data comprises low-frequency signal responses from stacked deposits at depth. Deposit thicknesses can however be better-resolved using individual reservoir lobe pick data from well-logs, which improves the vertical resolution of the analyses. Lobster well-log data suggest that the primary component of reservoirs include coarse-grained, elongate basin fans that downlap and onlap onto preexisting topography and are confined to the proximal (northern) section of the basin (Appendices C and D).

Third, the large areal extents and dispersed network of channelform and lobeform elements imaged from attribute extractions in most of the lowermost, A to B fill interval suggest that processes responsible for their formation were different from those generated in experiments. For the second reservoir fill interval, interval B to C, lithological interpretations from well-log data show net to gross (N:G) of > 40%, which suggests that turbidity currents may have also contained a significant proportion of fines (and thus larger volumes) to transport its coarser-grained load in suspension to be deposited in the minibasin (e.g. Imran and Parker, 1999; Salaheldin et al., 2000; Al Ja'Aidi at al., 2004). Considering the aforementioned relationship between current and deposit thickness, the relatively large cumulative thicknesses of deposits achieved were possible due to flow events that were frequent or of relatively long durations. Alternatively, the processes responsible for delivering sediment may be the result of turbidity currents with a bedload transport component (e.g. Sequeiros et al., 2010). Although bedload does not drive

turbidity currents, it has been suggested that they can strongly control the nature of the deposits emplaced by them (Sequeiros et al., 2010), and can produce the abrupt terminations observed from seismic data (e.g. Prather et al., 1998; Beaubouef and Friedmann, 2000). A deposit that appears on seismic amplitude attribute extractions to be point-sourced based may therefore be representing the transport pathway of the coarsest fraction along a complex slope. Such coarse fraction deposits are usually confined to the path of least resistance along the direction of transport.

Finally, experimental velocity data showed a rotational velocity field produced by sustained turbidity currents, which may be a mechanism for the establishment of channelization within the basin and at the downstream end of the basin. Channel features are commonly observed in shallow seismic and seafloor data (e.g. Winker, 1996; Beaubouef and Friedmann, 2000), but their mechanism of initiation and development is still not clear. The abundance of through-going channelform features observed from attribute extractions suggest that currents entering the basin may have been of long-duration to both establish the channelized morphologies, and facilitate the transport of coarse-grained sediment.

## CONCLUSIONS

A series of experiments were carried out to investigate the influence of 3-D minibasin topography and current confinement on turbidity current dynamics, deposit geometry, intra-basinal sediment distribution and the influence of these factors in the extra-basinal delivery of sediment. The experiments described here are different from previous attempts because of the 3-D configuration of the basin compared to previously documented experiments, which were predominantly 2-D and tested the effect of ponded flow on deposit characteristics (e.g. Toniolo et al., 2002; Lamb et al., 2004; 2006). The

experiments are also different from 3-D experiments previously reported (e.g. Violet et al., 2005) because of the varying configurations tested relative to fixed turbidity current input conditions, and a database of velocity data were recorded to support interpretations of minibasin deposit fill development. Turbidity currents tested in all experiments were able to surmount basin topography.

Analysis of the data collected results in the following conclusions:

- Turbidity currents interact differently with 3-D minibasin topography than they do with 2-D minibasins reported from previous works. Near-bed velocity component data show the establishment of a 3-D velocity field, which has implications for distributing sediment on complex 3-D bathymetric surfaces.
- Individual deposits from turbidity currents are more likely to drape minibasin topography than pond within it. An increase in the duration of an event however results in a deposit that is more wedged in character.
- The thickest portions of the deposits are usually confined to the inlet slope of the basin when the current width is equal to, or exceeds the basin width, and are transported to more distal locations on the inlet slope when the current width is less than the basin width. At no point did the thickest deposit coincide with the point of maximum accommodation in the basin, and complements the results of Violet et al., (2005) and Spinewine et al., (2009).
- The primary direction of flow plays an important role on the accumulation of sediment in 3-D confined basin topography. Deposits tend to be elongate along the primary transport direction and drape existing topography, while compensational stacking of deposits is evident along strike.
- Deposit thickness did not accurately record the changes in current fall velocity, which was considered to have a primary influence on sediment deposition.

Instead, the deposits thickened further downstream, which was influenced by the long sediment advection lengths within the current relative to the investigative basin length.

- There appears to be no definitive link between lateral components of current interaction (convergence and divergence) and deposit thickness. Most sedimentation occurs in the zone where there are strong fluctuations in the fall velocity along the primary axis of current transport. Sedimentation occurs even though high primary current velocities dominate the section relative to its lateral equivalents, and suggests that the effect of topography has a considerable effect on trapping deposits, even though sediment advection length scales are relatively high.
- For the scaled minibasin setup, the approximate event-related trap efficiency is a poor indicator of current confinement relative to basin topography, while basin fill percentage may be a better indicator. Given this scenario, data from outcrop and subsurface minibasins may be used to generate a crude relationship of how a basin may have filled in the geological past, given the relevant spatial and temporal data needed to perform the calculations.
- Grain size distribution in the basin is most strongly influenced by the vertical component of current velocity, *w*. Coarsest grain size fractions occur where the fall in *w* is greatest. The signal response of coarser grain fractions to local flow dynamics is therefore higher than the cumulative effect of deposit thickness, which appears to correlate more with advection lengths. Rouse number analysis showed that sediment are more likely to remain suspended in the current, which support the low magnitude of sediment trapping in the basin. The obstacle presented by the basin's exit slope has a minor effect on coarse accumulation of

sediment, but the positive spike in vertical velocity appears to overcome the ability for any detrainment to occur.

- An increase in turbidity current confinement relative to the basin width results in the proximal translation of the sediment dispersal axis, but only took effect when the dispersion length is less than approximately 0.25X the maximum basin length. Additionally, an increase in turbidity current confinement leads to an increase in the dispersion angle of turbidity currents. When both relationships are considered together, an increase in current confinement effectively leads to enhancing the dispersal of turbidity current material beyond the basin's margins for currents that are able to surmount 3-D confining topography.
- Results were compared to a well-constrained reservoir interval from the Lobster minibasin in the proximal Gulf of Mexico slope, and interpretations on paleo-flow processes were made. Experimental results can be applied to field-scale minibasin deposits to better understand their fill, but key differences in deposit architecture from each scale of observation made it difficult to accurately determine the processes responsible for their deposition. Higher-resolution data can alleviate the concerns of geometric scaling, and extra-basinal deposit data can improve the understanding of current extents relative to the basin.

## FIGURES

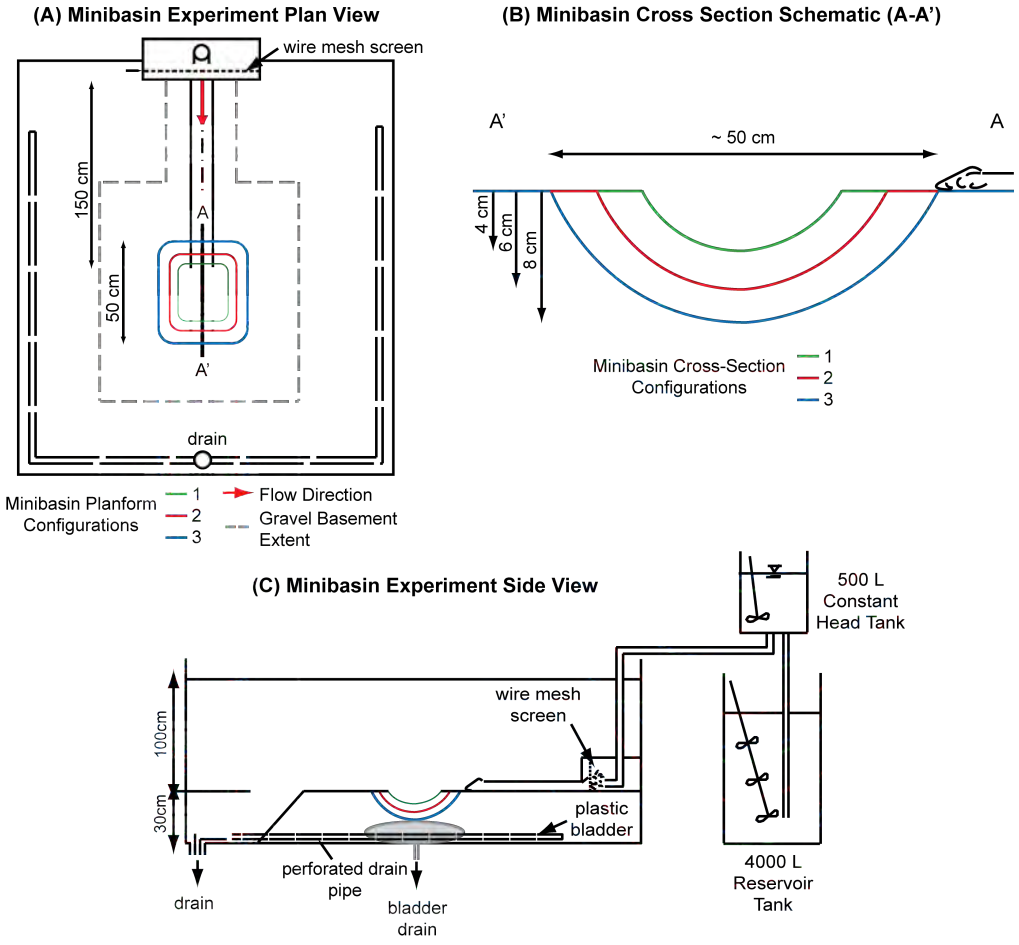


Figure 5.1: Schematic figure for Series 2 of the minibasin experiments and current generation conditions. Plan view of the basin tank (A) with the three subsided minibasin configurations 1 (smallest) to 3 (largest). The bold outline represents the extent of the false floor. Dimensions of the minibasin configurations in cross-section are shown in (B). Side View (C) shows the reservoir tank where sediment, water and salt are mixed and then pumped to the upper constant head tank. Currents were generated by releasing the mixed fluid from the head tank into the basin tank through a wire mesh screened entrance box. As the currents move over the edge of the false floor they are drained away by a system of perforated pipes in order to minimize basin tank wall reflections. The minibasin cross-sectional shape was established by controlled drainage of a water filled bladder that was buried in a gravel basement, shown in (B). The dimensions of the bladder were 40 cm (L) x 40 cm (W) x 15 cm (D). The inlet box configuration for the minibasin was oriented parallel to the long axis of the basin tank.

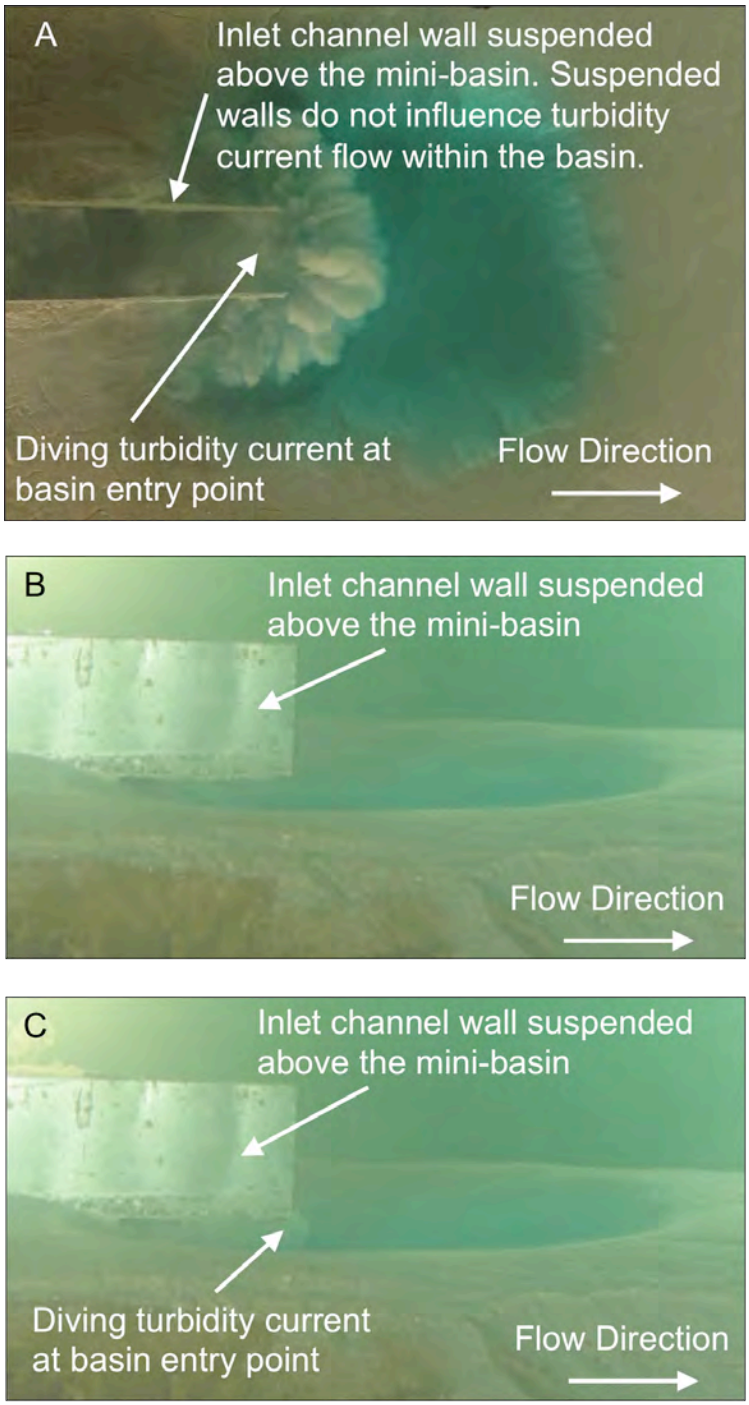


Figure 5.2: Current entry into minibasin through the confined channel wall. The figures above demonstrate the suspended confining channel that guides the turbidity current into the minibasin, and is independent of subsidence configuration in plan view (A) and side profile (B and C).

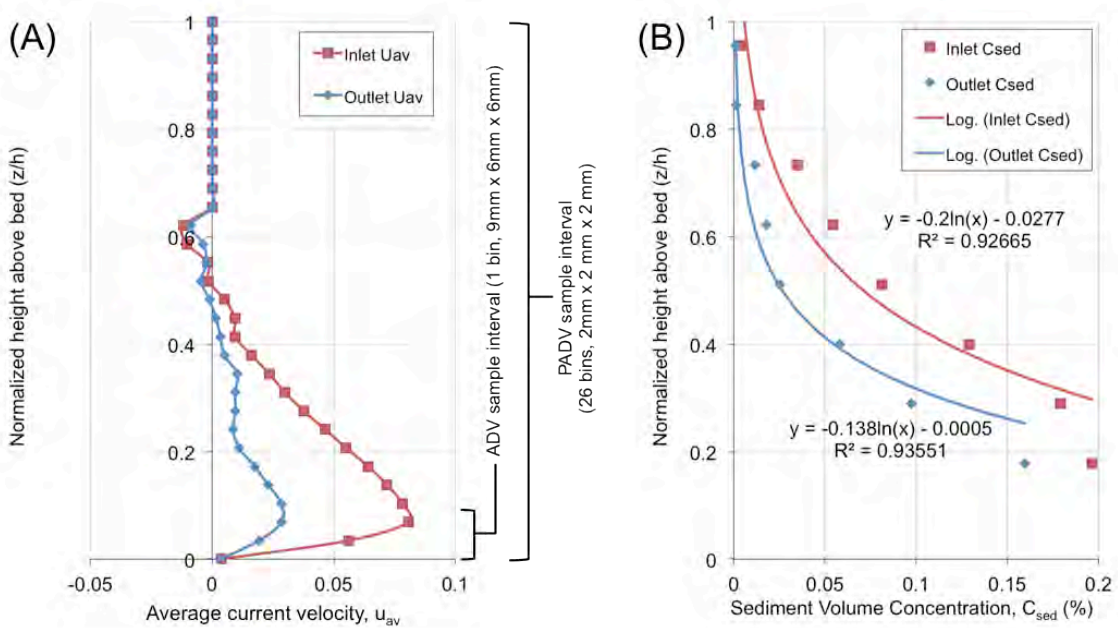


Figure 5.3: Characteristic input (red) and output (blue) velocity and sediment concentration profiles from flow 14. (A) Shows a time averaged (t=15 s) velocity profile for a turbidity current entering the minibasin collected using an Acoustic Doppler Velocimeter Profiler (PADV) and plotted with dimensionless height, z/h with h = 56mm (h=measured current depth from PADV equipment where there was no measured current velocity disturbance in the fluid column). Profile sampling dimensions and their relative locations are shown for both ADV and PADV equipment. (B) Shows typical turbidity current concentration data from an 8-component siphon rack. An exponential function is fit to the data and forward and backward extrapolated for visualization. The equation is shown on the figure.

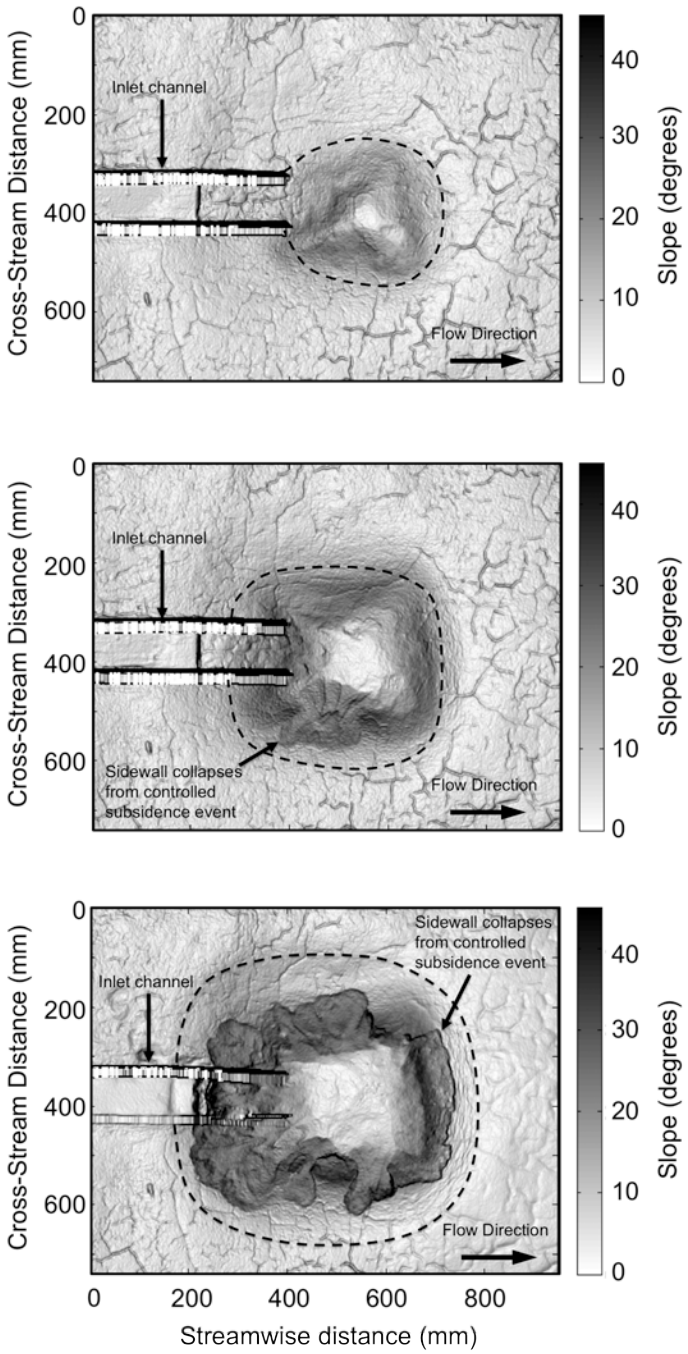


Figure 5.4: Slope maps showing initial states of three configurations of subsidence in Series 2 experiments: (A) config. 1; (B) config. 2; and (C) config. 3. Minibasin outlines for each configuration are represented by the dashed black line.

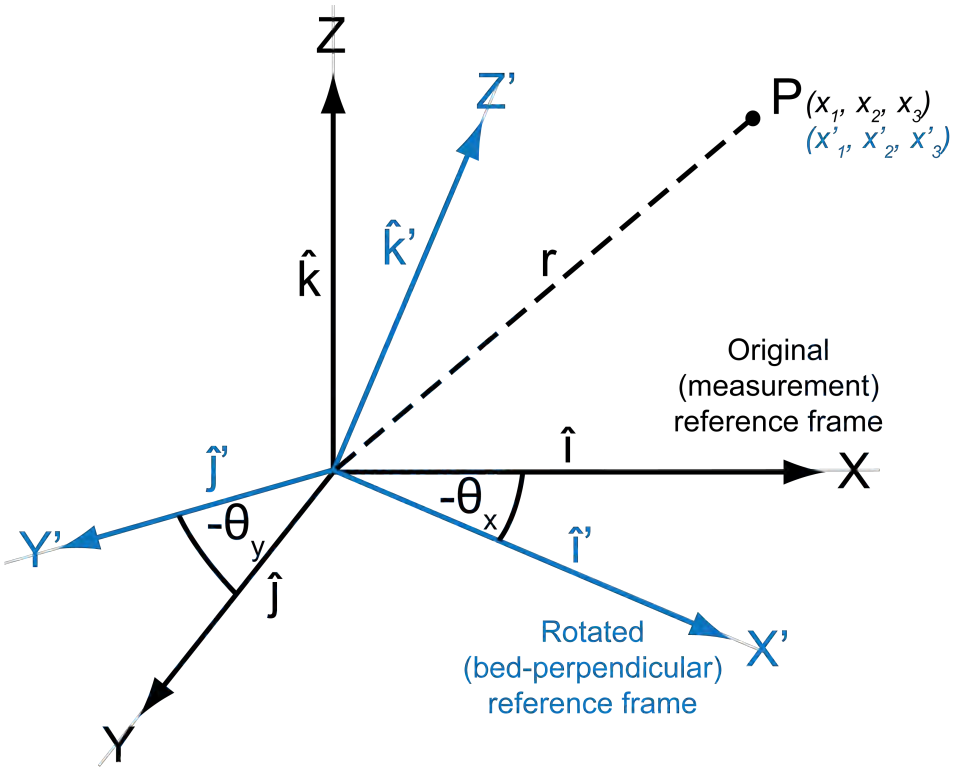


Figure 5.5: An example of 3-D coordinate rotation (modified from Arya, 1998). Coordinates of point P in two different coordinate systems rotated with respect to each other are $(x_1, x_2, x_3)$ and $(x'_1, x'_2 x'_3)$. The original (measurement) reference frame is shown in black $(X, Y, Z)$, and the rotated reference frame is shown in blue $(X', Y', Z')$.

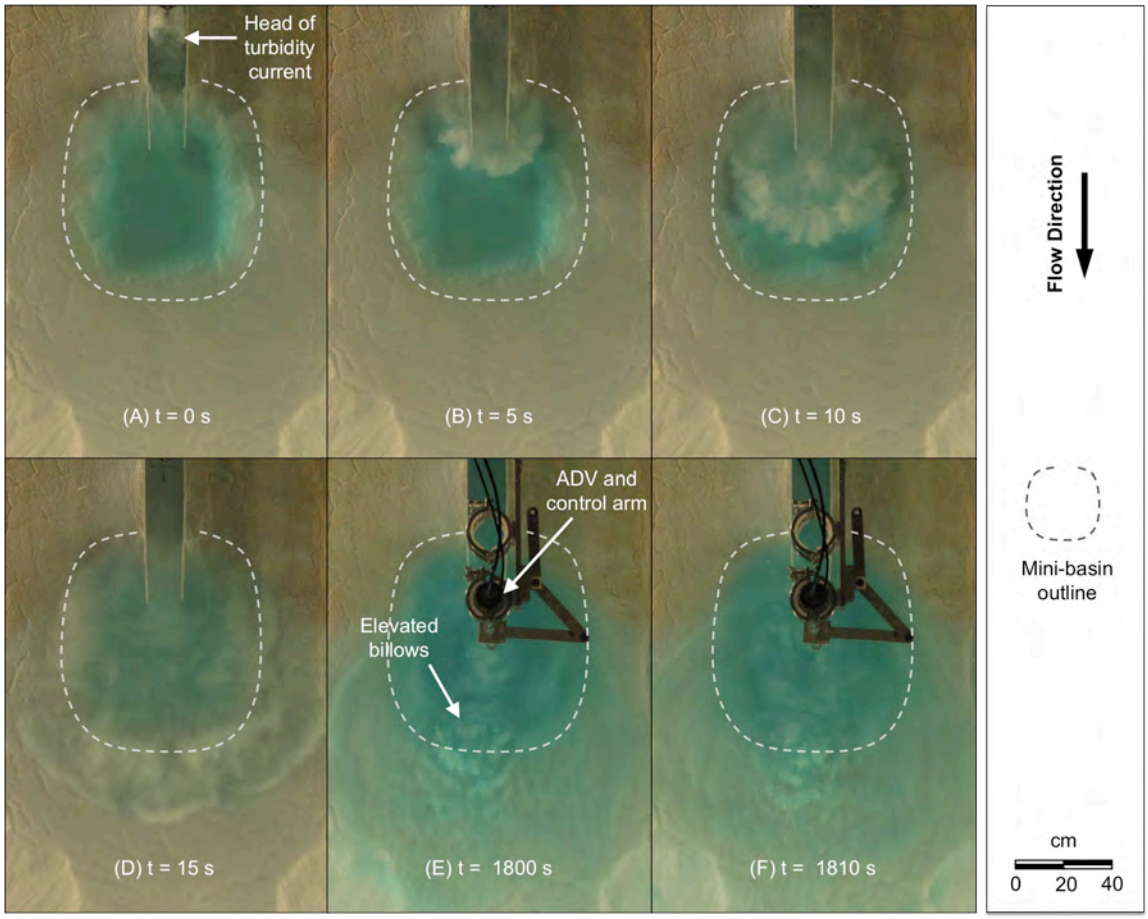


Figure 5.6: Overhead time lapse photographs showing current morphology at different stages of a continuous flow. Photographs A-D show the current as it enters the basin at the beginning of the flow (A=0s; B=5s; C=10s; D=15s) and during the flow (E=1800s; F=1810s).

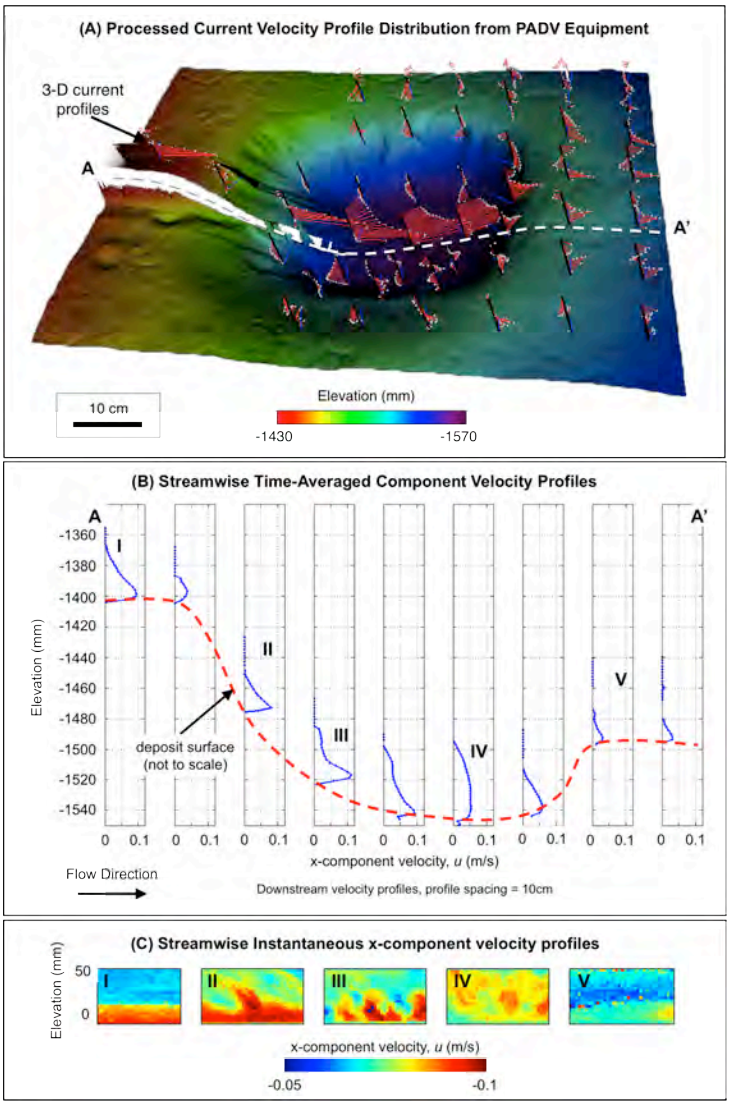


Figure 5.7: (A) 3-D rendering of time-averaged turbidity current velocity data profile data collected with PADV equipment at specific node locations; (B) The cross-section A-A' shows the velocity profile distribution at specific points along the center dipline profile of Config. 3. The character of the x-component velocity profiles (rotated to a bed-perpendicular reference frame) change from proximal to distal (e.g. the current thickness and the elevation of the high velocity core). (C) The sub-images (I-IV) above show the x-component profile time series. Mixing (stability) within the turbidity current varies from proximal to distal. The velocity data were collected using a 3-D Profiling Acoustic Doppler Velocimeter (PADV). Profiles are 5.6 cm tall and are divided into 28 bins that are 2 mm each. The base of the profile was located within 2 mm above the deposit bed.

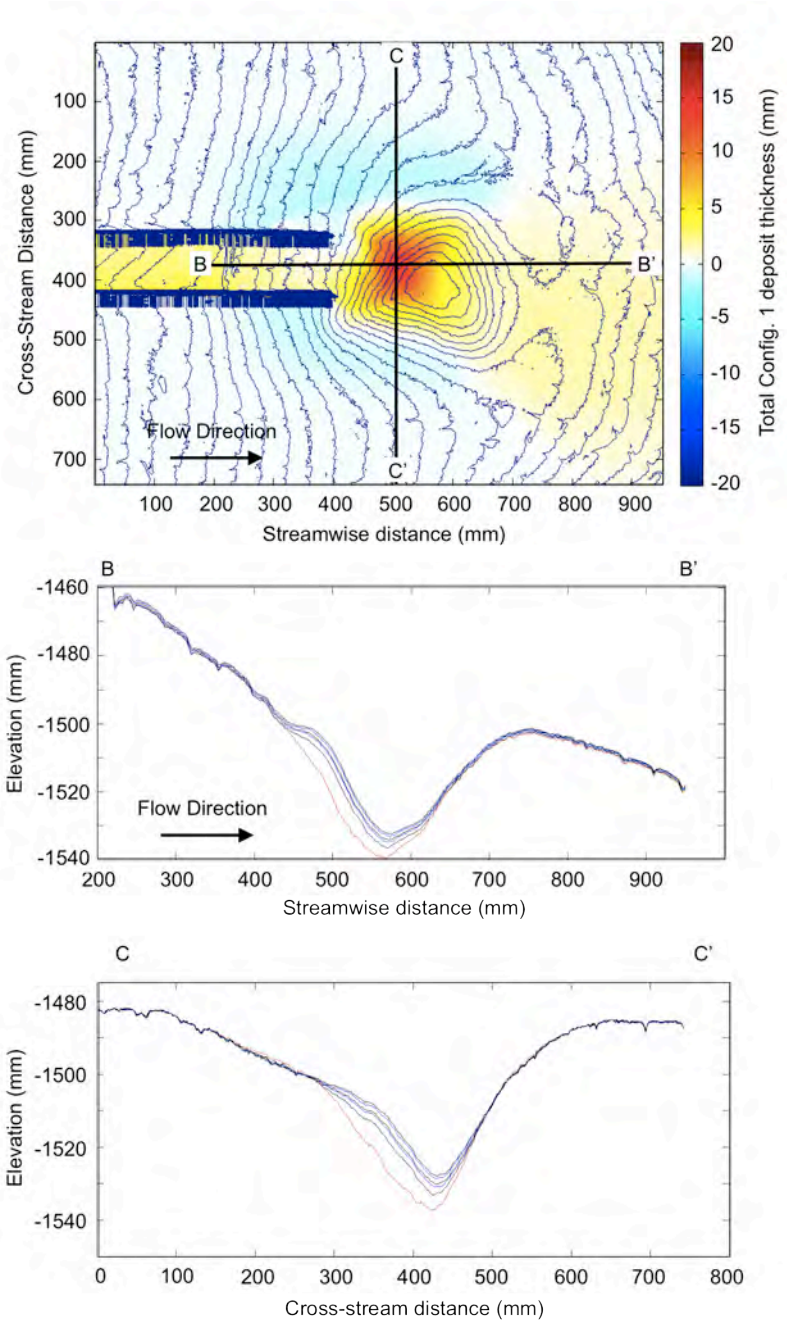


Figure 5.8: Morphology of Config. 1 basin and fill. (A) Shows a cumulative deposit thickness map from turbidity currents run into the Config. 1 basin with superimposed initial bathymetry; (B) shows the center streamwise dipline section (D380) showing the individual bed fill sequence; and (C) shows the cross-stream section through the thickest portion of the cumulative deposit (X500) showing the individual bed fill sequence.

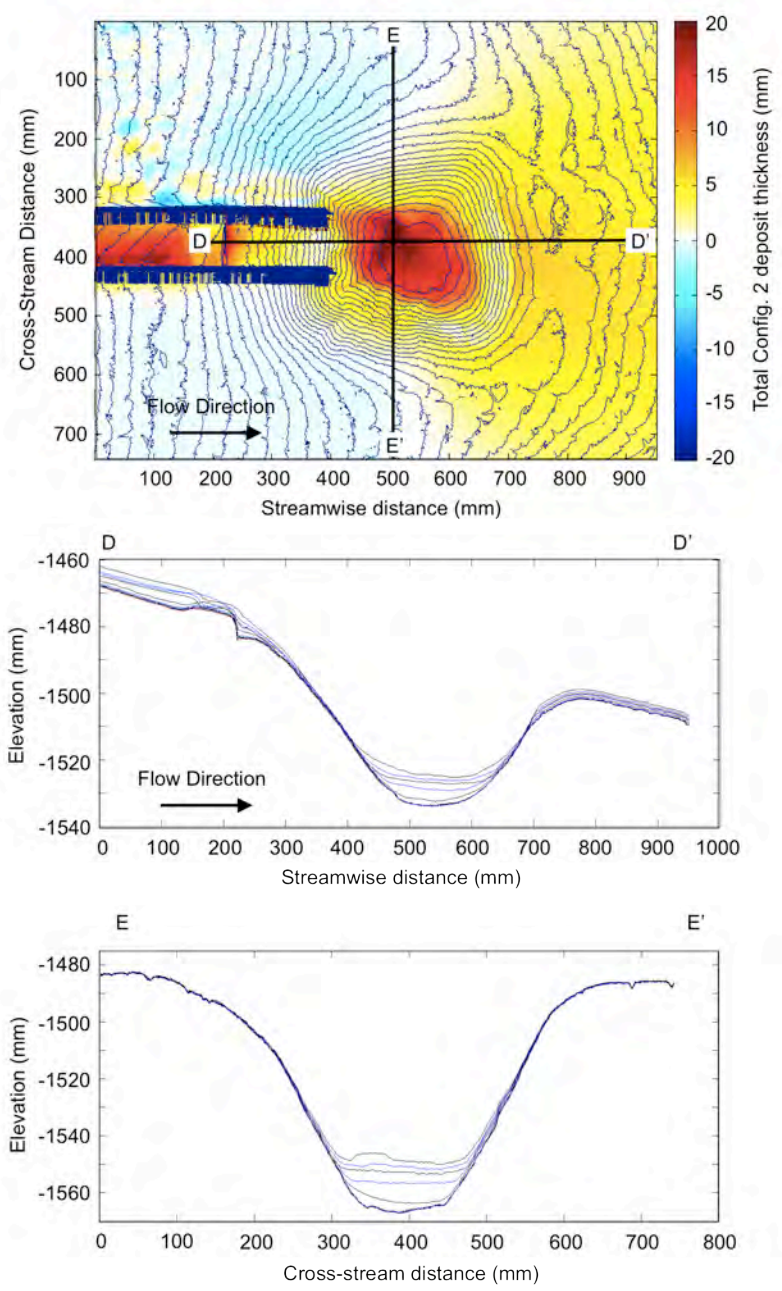


Figure 5.9: Morphology of Config. 2 basin and fill. (A) Shows a cumulative deposit thickness map from turbidity currents run into the Config. 1 basin with superimposed initial bathymetry; (B) shows the center streamwise dipline section (D380) showing the individual bed fill sequence; and (C) shows the cross-stream section through the thickest portion of the cumulative deposit (X500) showing the individual bed fill sequence.

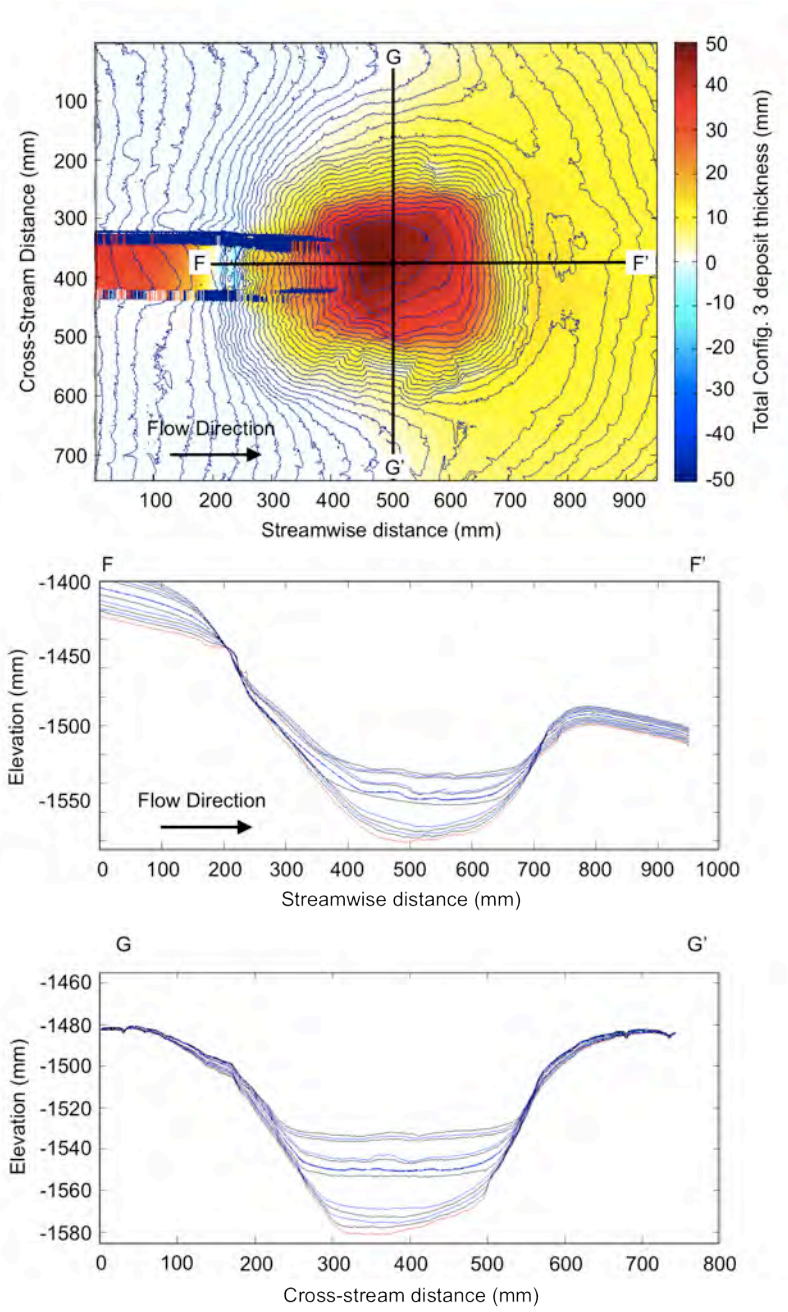


Figure 5.10: Morphology of Config. 3 basin and fill. (A) Shows a cumulative deposit thickness map from turbidity currents run into the Config. 1 basin with superimposed initial bathymetry; (B) shows the center streamwise dipline section (D380) showing the individual bed fill sequence; and (C) shows the cross-stream section through the thickest portion of the cumulative deposit (X500) showing the individual bed fill sequence.

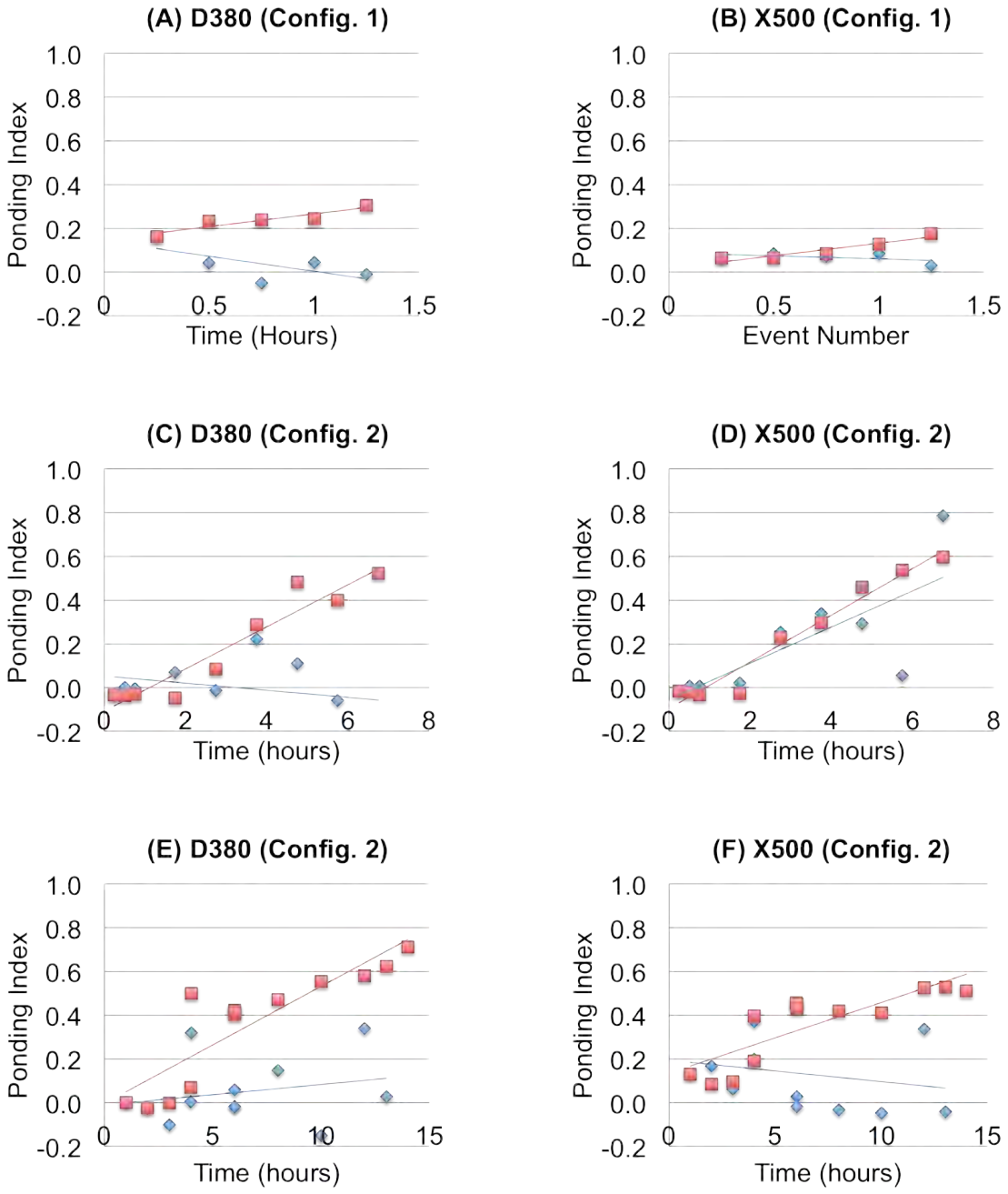


Figure 5.11: Plots of flow event number vs. ponding index data from Series 2 experiments. Calculated individual (blue) and cumulative (red) ponding index data for Series 2 deposits from center dipline section D380 and cross-stream section (X500). Data from Config. 1 deposits are shown in (A) and (B); data from Config. 1 deposits are shown in (C) and (D); and data from Config. 1 deposits are shown in (E) and (F).

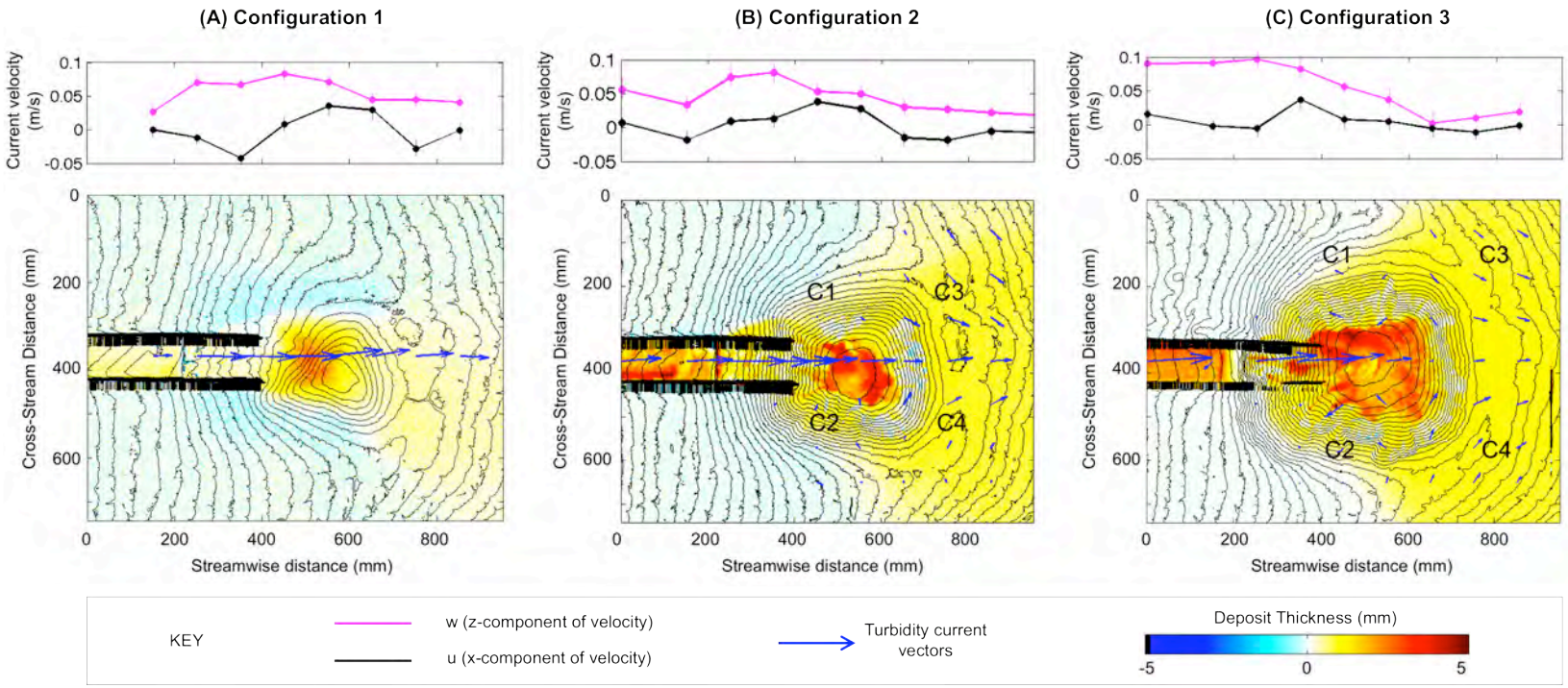


Figure 5.12: Deposit thickness maps, bathymetry and turbidity current vector velocity for Config. 1 (A), Config. 2 (B) and Config. 3 (C). For each event interval, the lower figures illustrate the relationship among the pre-event basin bathymetry, the deposit thickness, and the time-averaged vector velocity. For the upper plots, the x- (pink) and z- (black) components of flow velocity (rotated to a bed-perpendicular reference frame) are plotted from data collected along the basin center dipline section (in the middle of and parallel to confining channel long axis). Vertical bars on each data point reflect the range of measured current velocities at that location. Velocity vector rotation cells are labeled C1-C4 in (B) and (C). The velocity vector data were collected using a 3-D Acoustic Doppler Velocimeter (ADV). ADV data was collected in a 9 mm tall by 6 mm wide sampling volume with the base located within 2 mm above the deposit bed. The sampling frequency was 200 Hz.

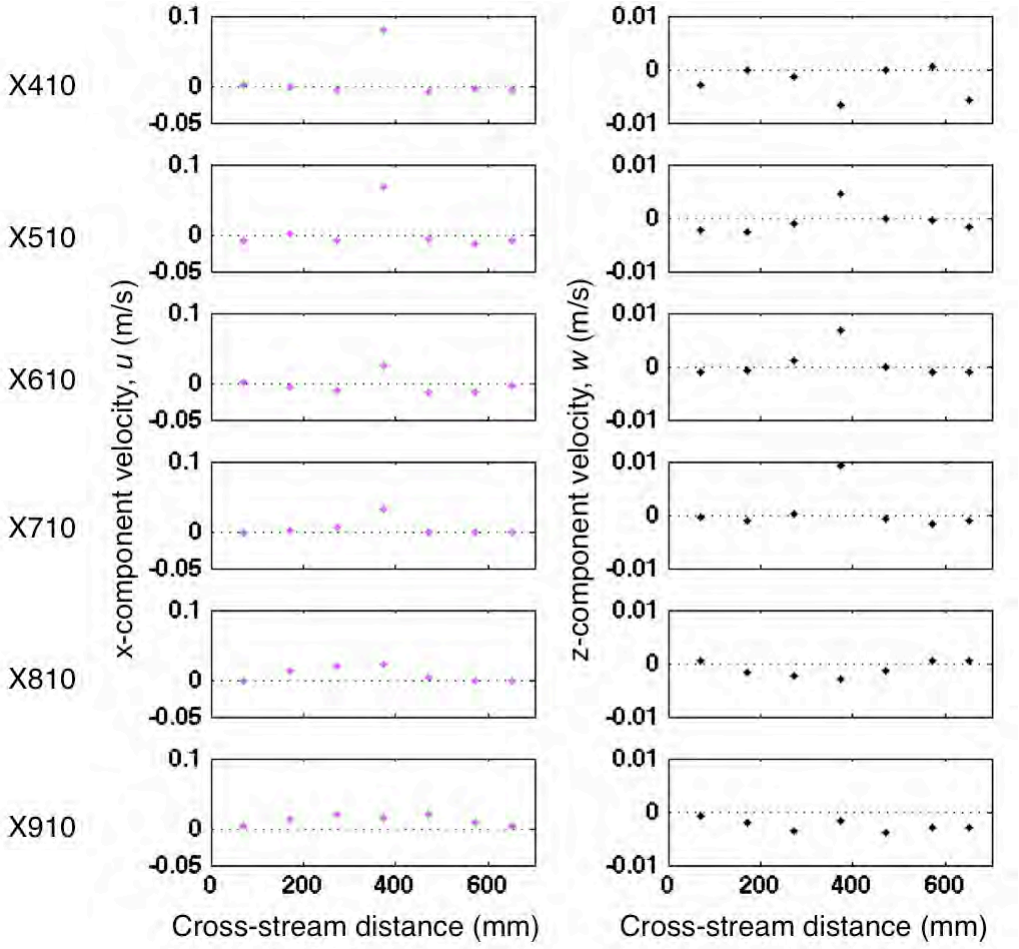


Figure 5.13: Characteristic cross-stream oriented plots of near-bed x-component current velocities (pink), and z-component current velocities (black) collected from PADV equipment, and are arranged according to distance from source from top to bottom. Refer to Figure 5.12 for cross section location. The six cross sections from which the data were plotted are from cross sections X410, X510, X610, X710, X810, and X900 (proximal to distal) from top to bottom respectively. The graphs show that the x-component center line velocities dominate the cross-sections, while z-component velocities attain negative magnitudes both nearest to and farthest away from the source. The velocity data were collected using a 3-D Profiling Acoustic Doppler Velocimeter (PADV) and sampled at a rate of 20 Hz. Profiles are 5.6 cm tall and are divided into 28 bins that are 2 mm each. The base of the profile was located within 2 mm above the deposit bed.

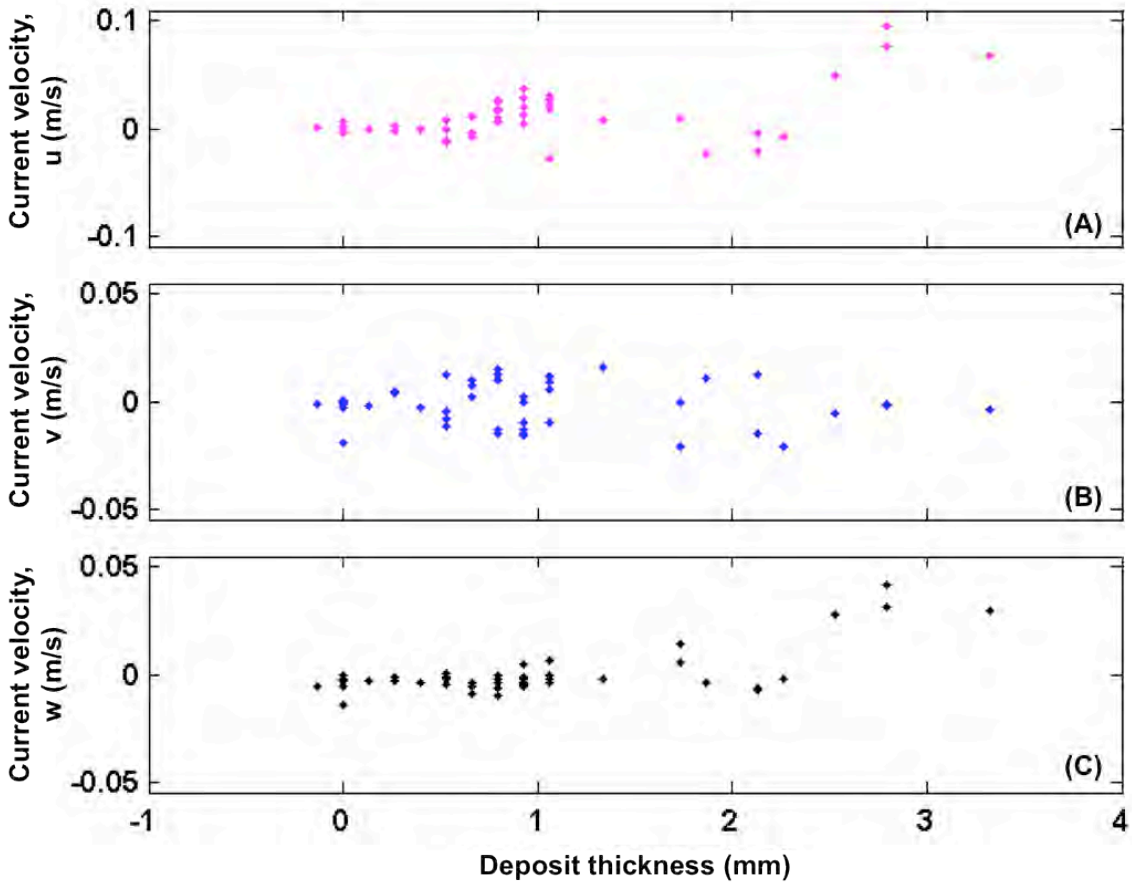


Figure 5.14: Plot of deposit thickness versus velocity component data. Component velocity data, u, v and w from flow 18 (Config. 2) are shown in (A), (B), and (C) respectively. The data suggests that there is no definitive correlation between any single component of velocity and deposit thickness, although thicker deposits usually coincide with high u- and w- component velocity magnitudes.

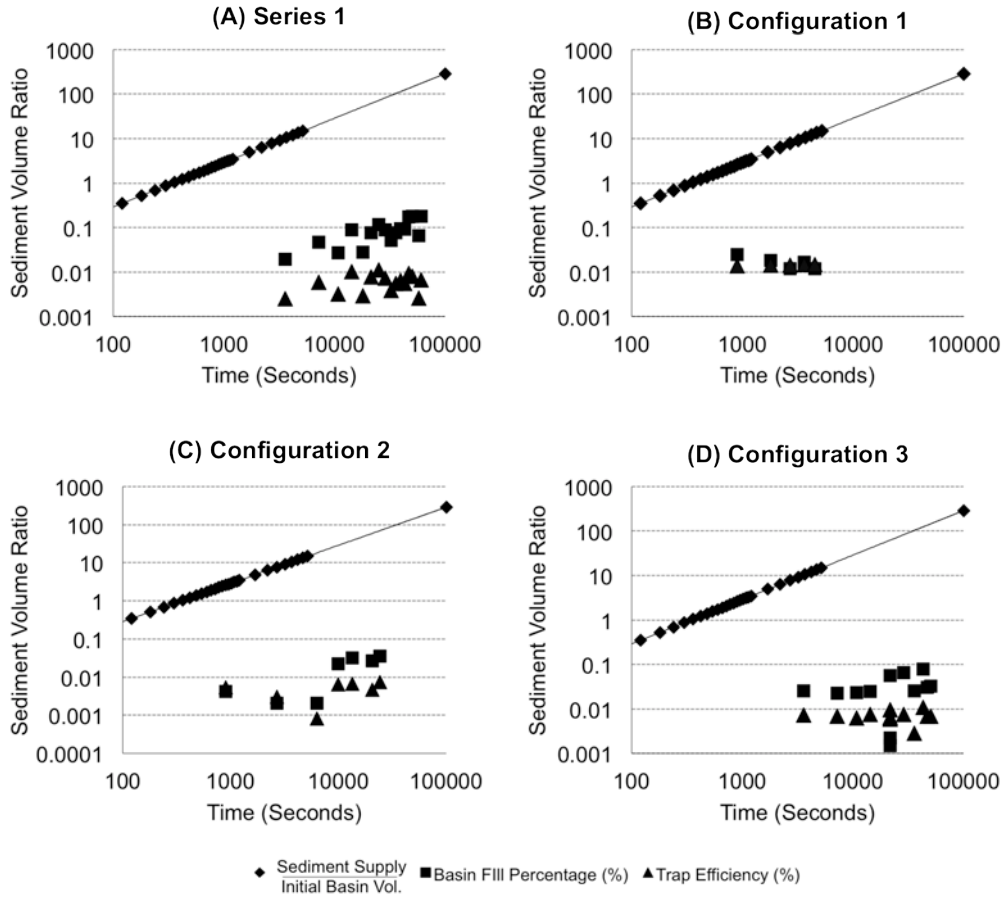


Figure 5.15: Log-log plots of time vs. three metrics of sediment volume ratios for (A) Series 1 experiments; Series 2 experiments including (B) Config. 1; (C) Config. 2; and (D) Config. 3. The three metrics include (1) the cumulative sediment flux percentage, a ratio of the cumulative sediment flux to the initial basin volume (diamond markers); (2) the basin fill percentage, a ratio of the volume of sediment captured by a basin relative to the basin's pre-flow volume (square markers); and (3) the trap efficiency (after Lamb et al., 2006), a measure of the volume of sediment captured by a basin relative to the total sediment flux to the basin (triangle markers). The ratio of cumulative sediment volume supplied to initial basin volume was considered as an initial boundary condition for comparison with other metrics. The basin fill percentage is the volume of sediment trapped by the basin relative to the basin's pre-flow volume for each flow event. The basin trap efficiency is a measure of the volume of sediment trapped by a basin relative to the total sediment flux to the basin.

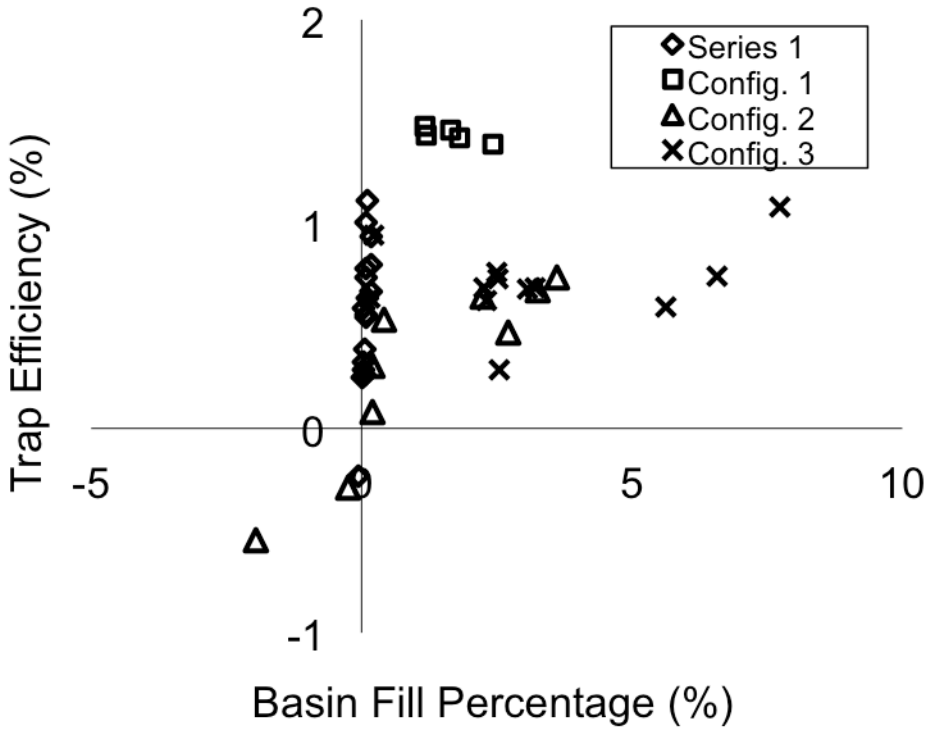


Figure 5.16: Plot of trap efficiency vs. basin fill percentage for minibasin experiments. Data are plotted from Series 1 experiments (diamond markers), Config. 1 experiments (square markers), Config. 2 experiments (triangle markers), and Config. 3 experiments (x-markers).

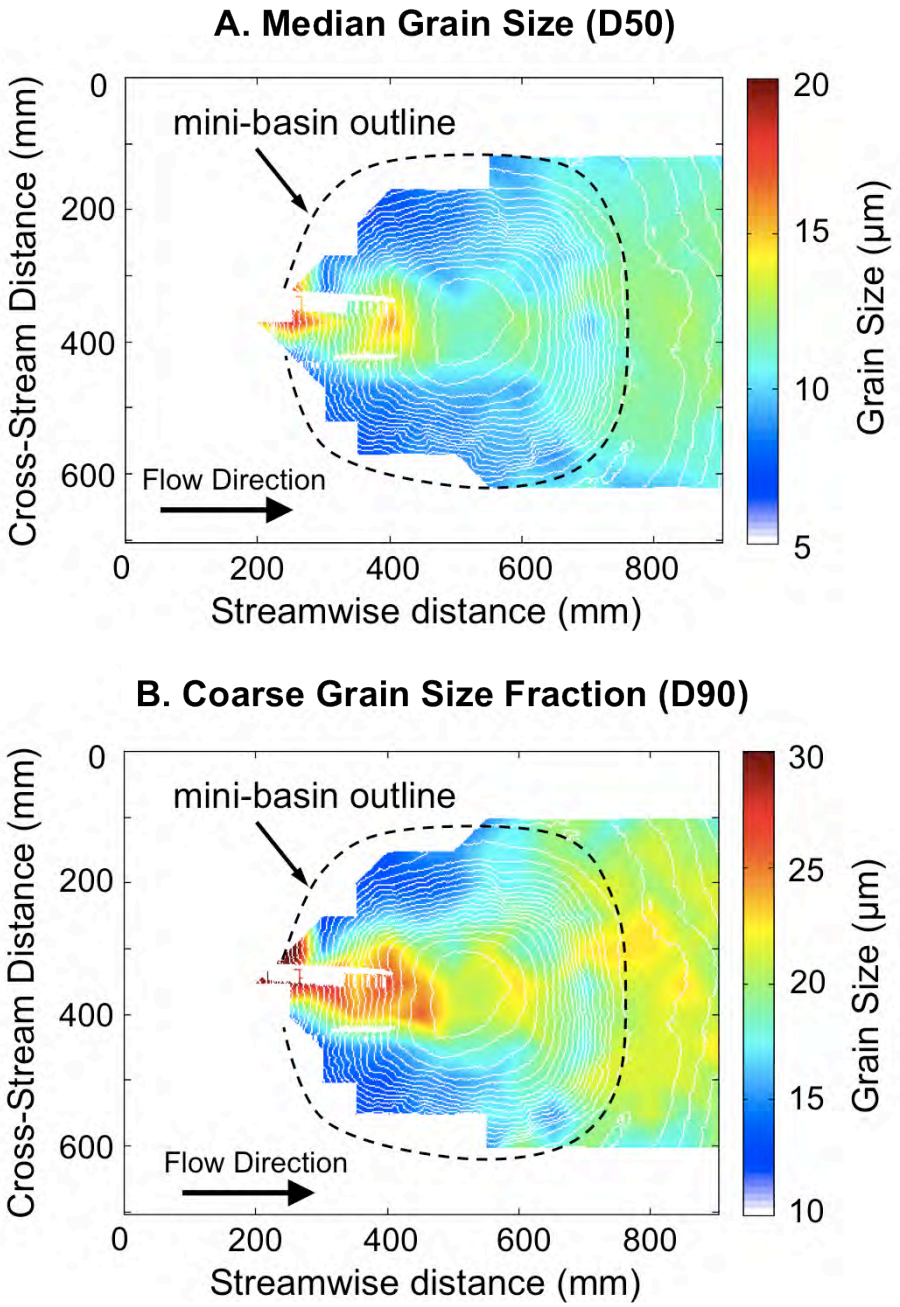


Figure 5.17: Bulk grain size distribution maps for Config. 3 deposits. A continuous dataset of (A) median (D50) and (B) coarse (D90) depth-averaged grain size data was calculated using a linear interpolation method between data points. Superimposed bathymetry (white lines) show the spatial distribution of grain size relative to basin topography. Grain size data were collected at specific node locations shown in Figure 5.4 and analyzed using LPSA equipment.

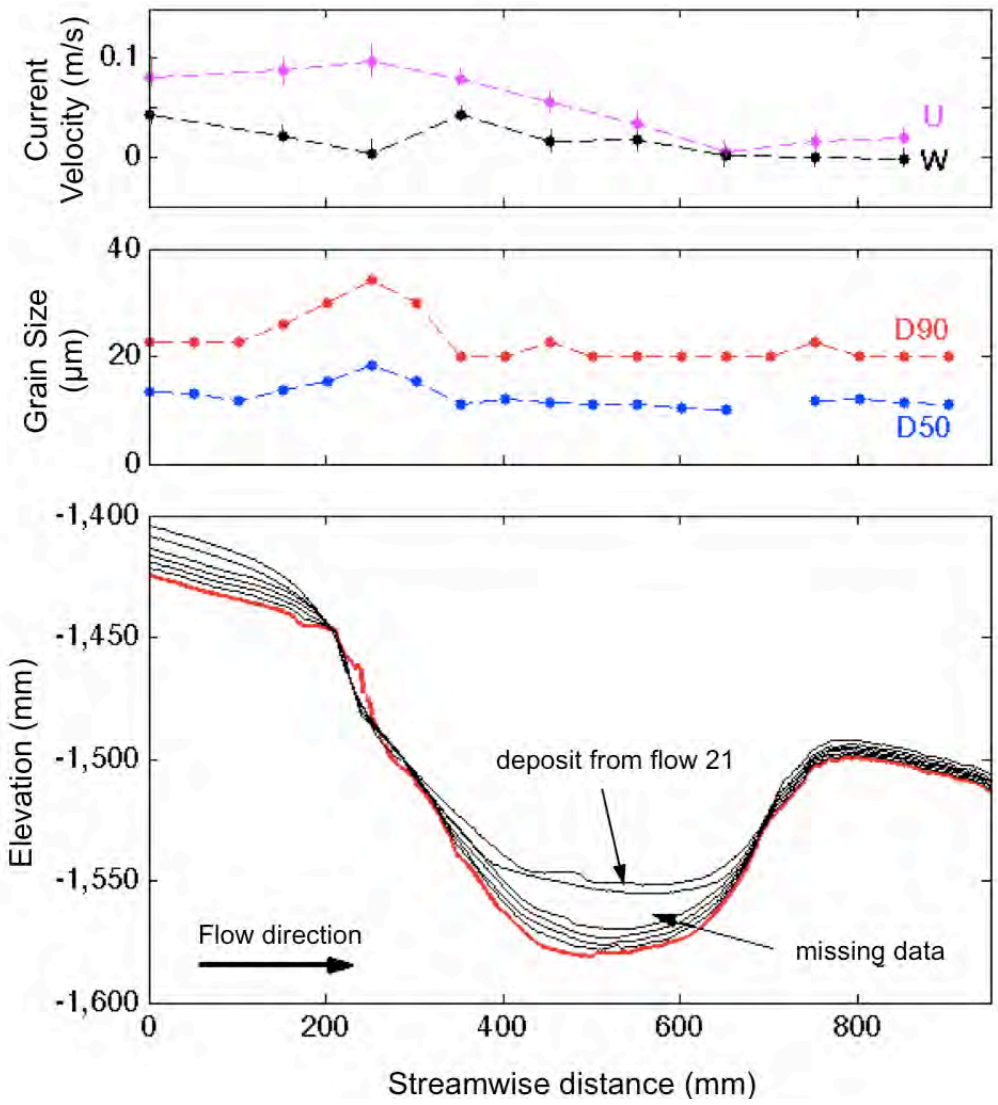


Figure 5.18: Link between component turbidity current velocity, grain size distribution, and resulting bed thickness distribution along center dipline section. For (A) the x- (pink) and z- (black) components of flow velocity (rotated to a bed-perpendicular reference frame) are plotted from data collected along the basin center dipline section (in the middle of and parallel to confining channel long axis) from flow 21. Velocity data are linked to the final deposit in the sequence shown in (C). The velocity vector data were collected using a 3-D Acoustic Doppler Velocimeter (ADV). ADV data was collected in a 9 mm tall by 6 mm wide sampling volume with the base located within 2 mm above the deposit bed. The sampling frequency was 200 Hz. For (B), D50 and D90 grain size data were calculated from cored sample grain size distributions using LPSA equipment.

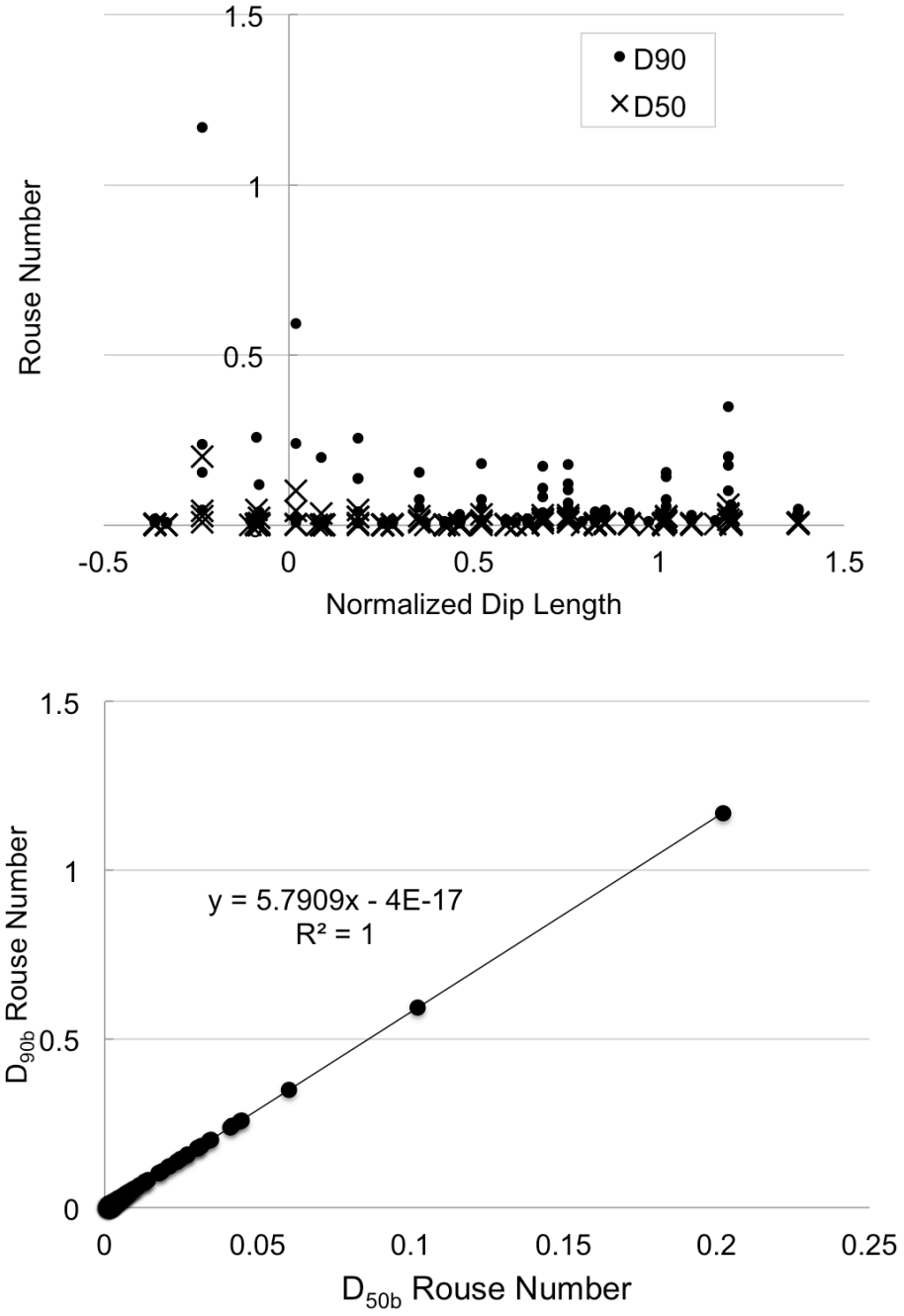


Figure 5.19: Rouse Number analysis. (A) Shows the spatial distribution of $D_{90b}$ and $D_{50b}$ Rouse numbers along the center dipline transect for all basin configurations, and (B) A plot of $D_{50b}$ vs. $D_{90b}$ Rouse numbers shows the magnitude difference between the two grain size fractions

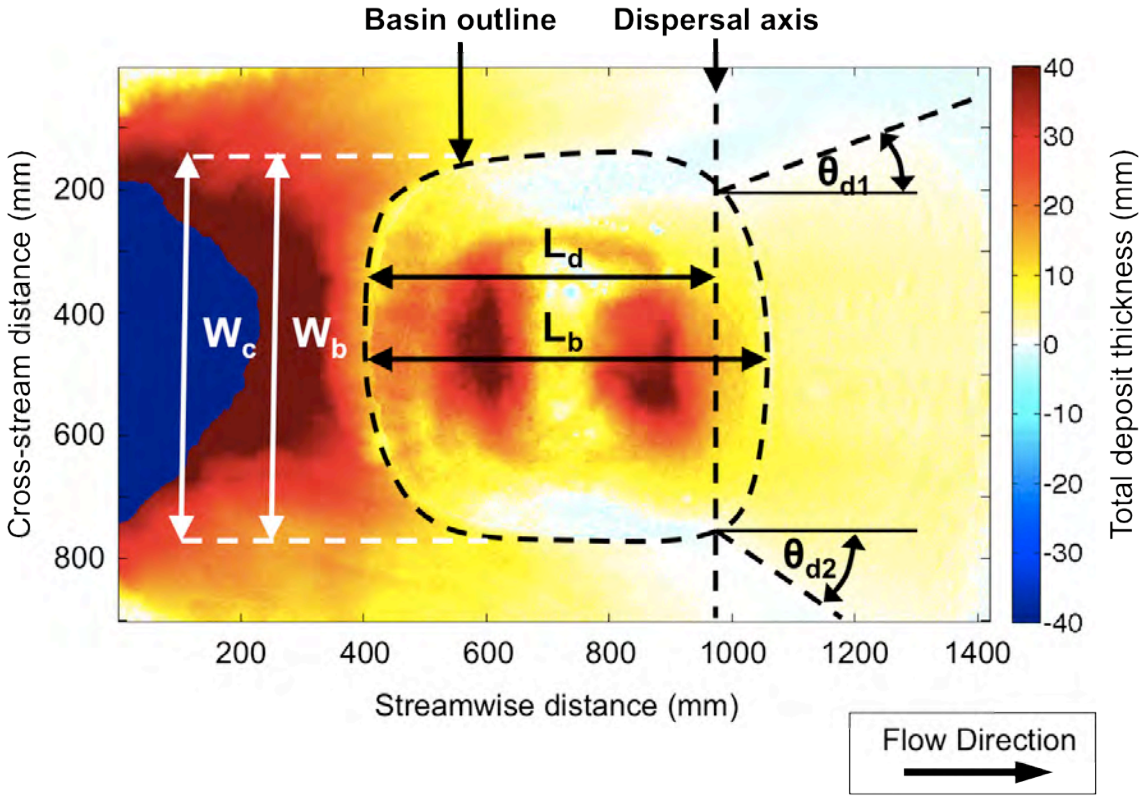


Figure 5.20: Illustration showing the concept of measuring parameters for determining the dispersion factor of a deposit using a deposit thickness map from Series 1 experiments (from Maharaj et al., in prep). $W_c$ is the width of the turbidity current width at the upstream end of the basin, and $W_b$ is the maximum cross-stream width of the basin. $L_d$ is the dispersion length, which is the measured length between the strike axis of the basin entry point and the dispersal axis, and $L_b$is the maximum streamwise length of the basin. The dispersion angle, $\theta_d$ is the angle at which turbidity currents spread relative to the primary transport direction of the turbidity current. Sediment deposit maps from individual events were used to calculate average values of $C_w$, $D$, and $\theta_d$ by basin configuration, since basin width, length and current width data were virtually identical among flows in a single configuration.

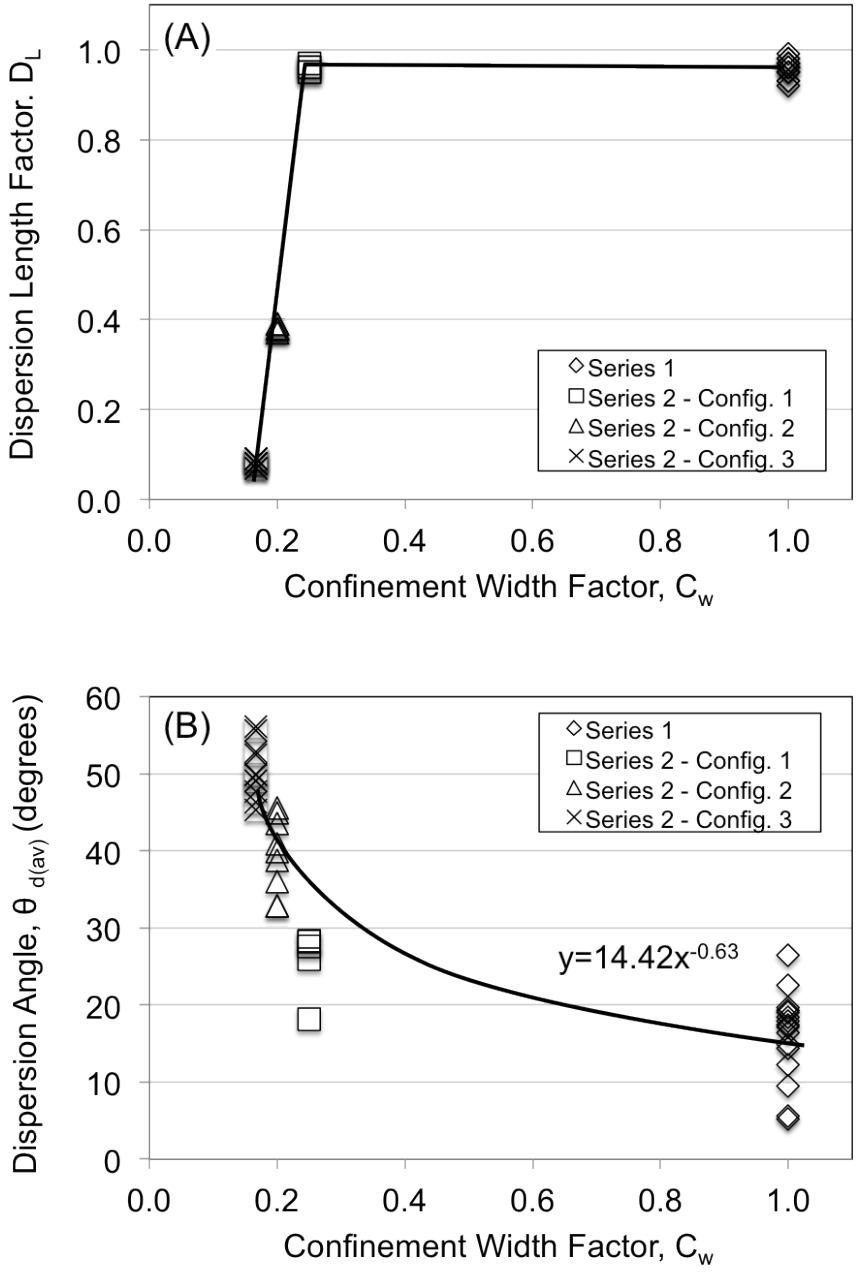


Figure 5.21: Analysis of turbidity current confinement and its effect on deposit dispersion for both Series 1 and 2 experiments. (A) Shows a plot of the confinement width factor, $C_w$, vs. the dispersion length factor $D_L$. (B) Shows a plot of the confinement width factor vs. the average dispersion angle, $\theta_{d(av)}$. See text for explanation.

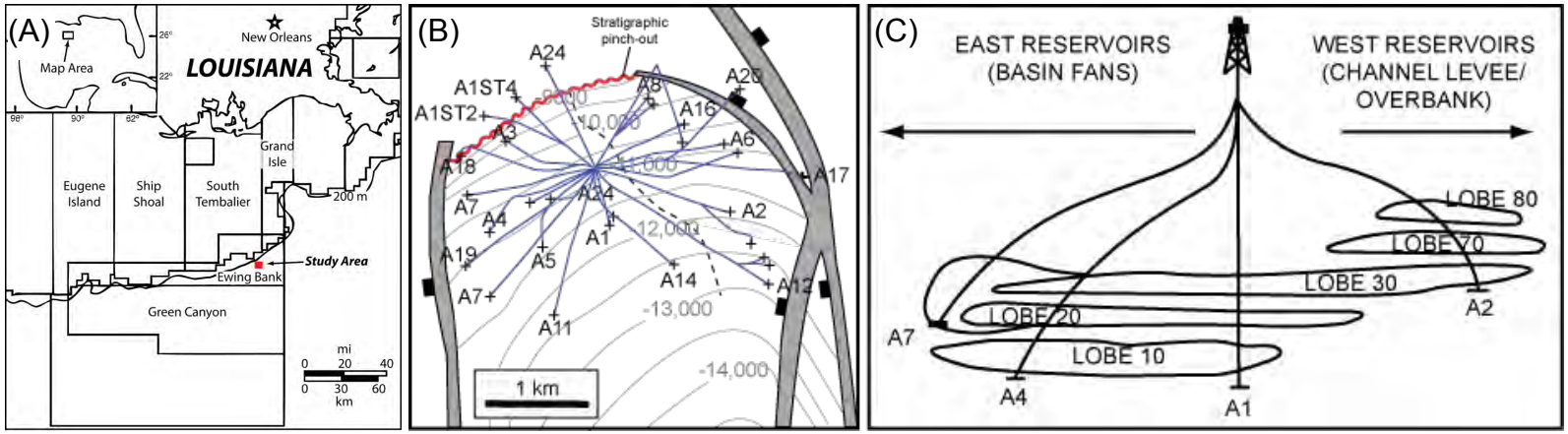


Figure 5.22: Location map and schematic illustration of the primary Lobster reservoir interval. (A) Location map of the Lobster study area relative to the Louisiana coastline. (B)Structural map of the Buliminella 1 reservoir (modified from Burk et al., 1999). Cross-hairs show reservoir well penetrations, and the dashed line shows the main reservoir compartmentalization axis that separates western basin fan sequences from eastern channel/overbank complexes. (C) Schematic cross section showing temporal and spatial distribution of individual reservoir compartments within the *Bul. 1* sequence from well data (modified from Burk et al., 1998).

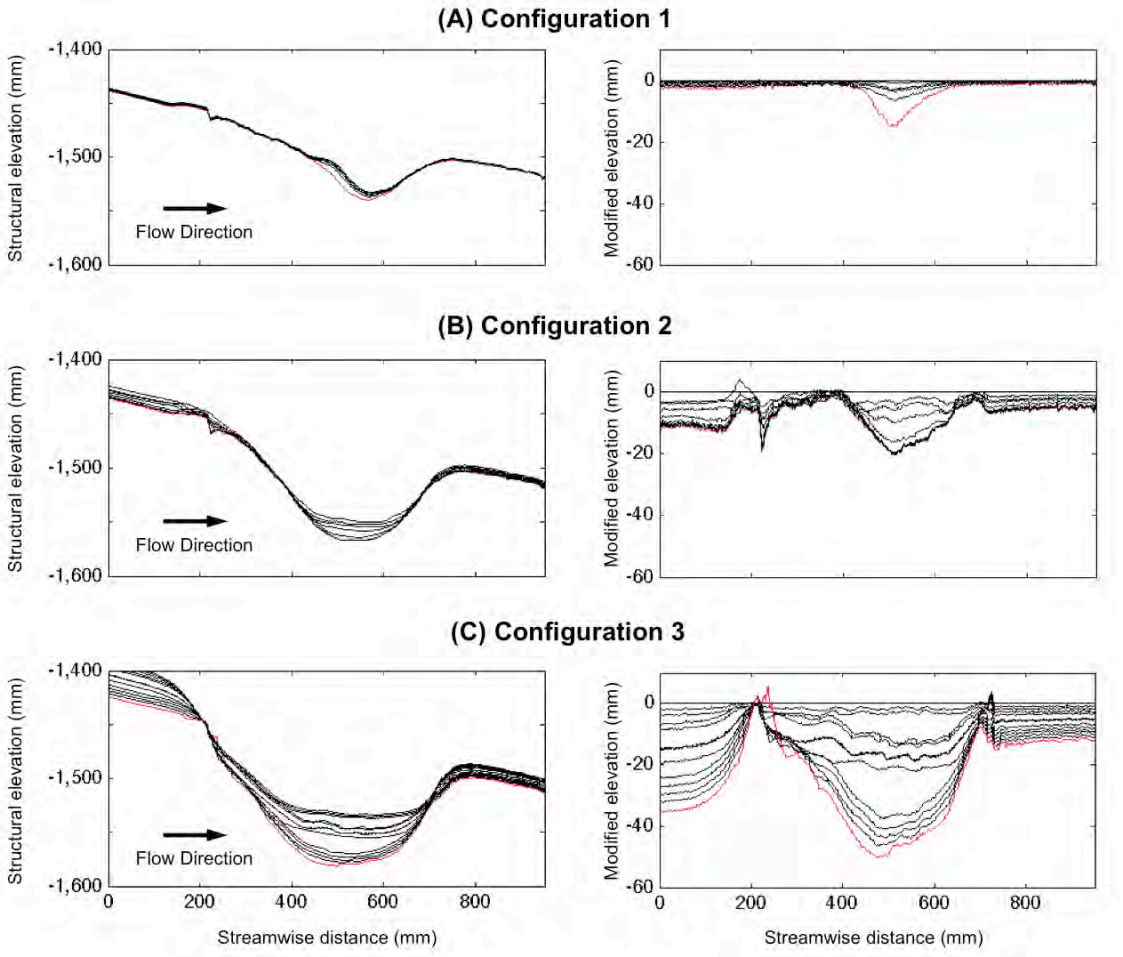


Figure 5.23: Illustration of the flattening technique and its use in resolving paleotopography from each experimental basin configuration. The figures on the left show the original depositional geometry of the basin, and the figures on the right show the corresponding fill sequences flattened on the youngest deposit surface. In cases where seismic resolution exceeds the deepest bathymetry (constrained by paleontological data), flattening cannot be used as a tool that accurately represents depositional basin topography.

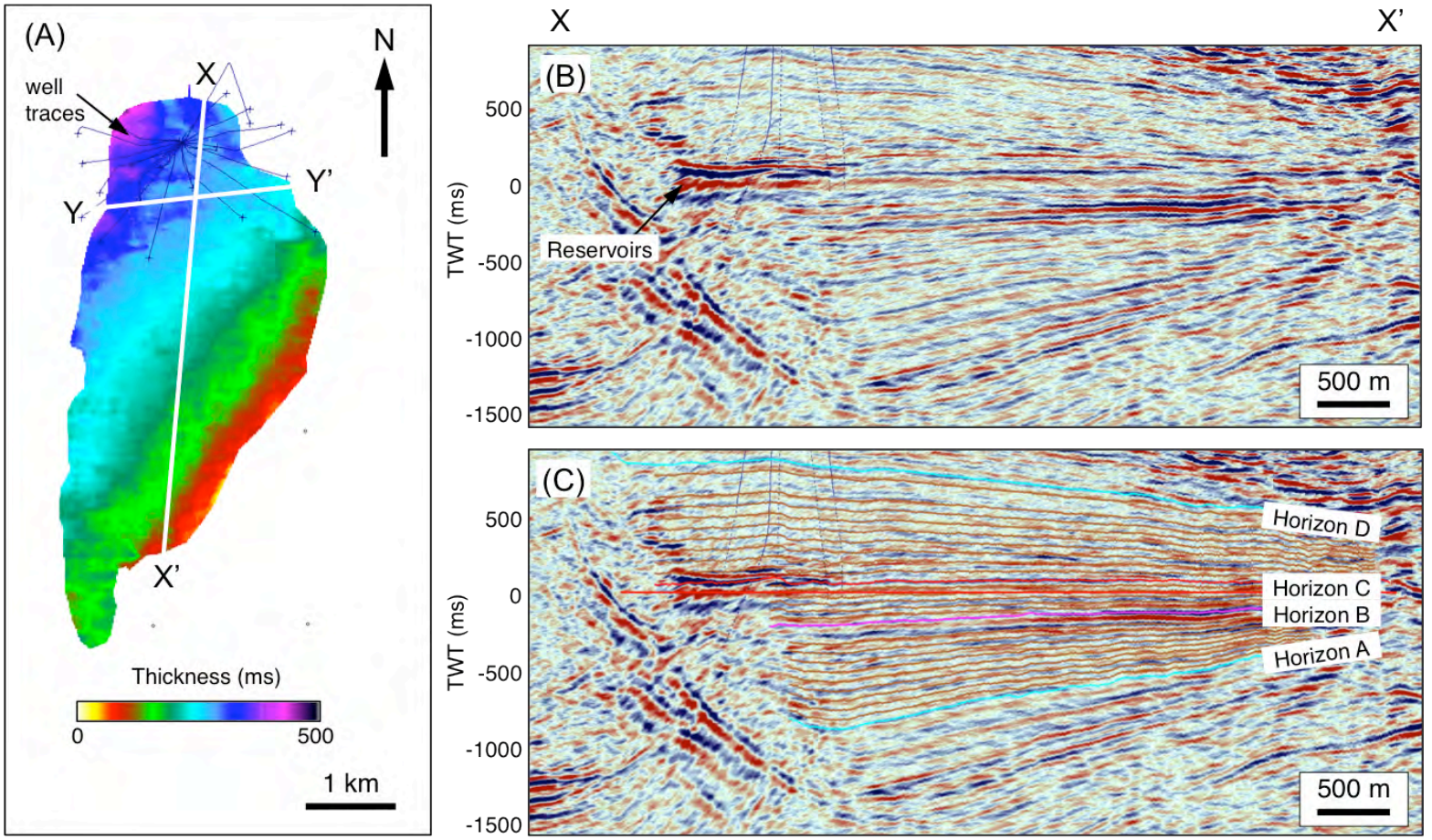


Figure 5.24: Isochore map and dip cross section of the Lobster minibasin reservoir interval, flattened on Horizon C. (A) Isochore map shows the increase in gross fill thickness toward the northwest; (B) is an uninterpreted dip line (X-X') of the fill interval investigated in this study; and (C) is an interpreted dip line of the fill interval, also flattened on Horizon C showing mapped horizons (A-D) and proportional slices (brown lines).

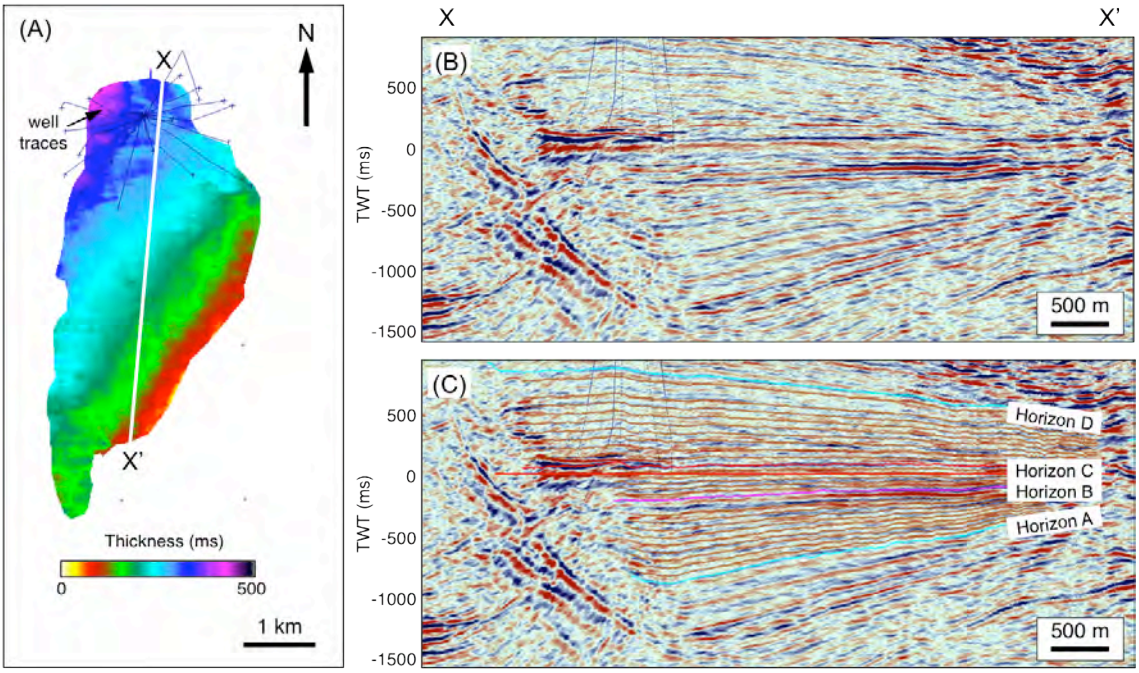


Figure 5.25: Strike cross section of the Lobster minibasin reservoir fill interval, flattened on Horizon C. (A) is an uninterpreted strike line of the fill interval investigated in this study; and (B) is an interpreted strike line of the fill interval, showing mapped horizons (A-D) and proportional slices (brown lines).

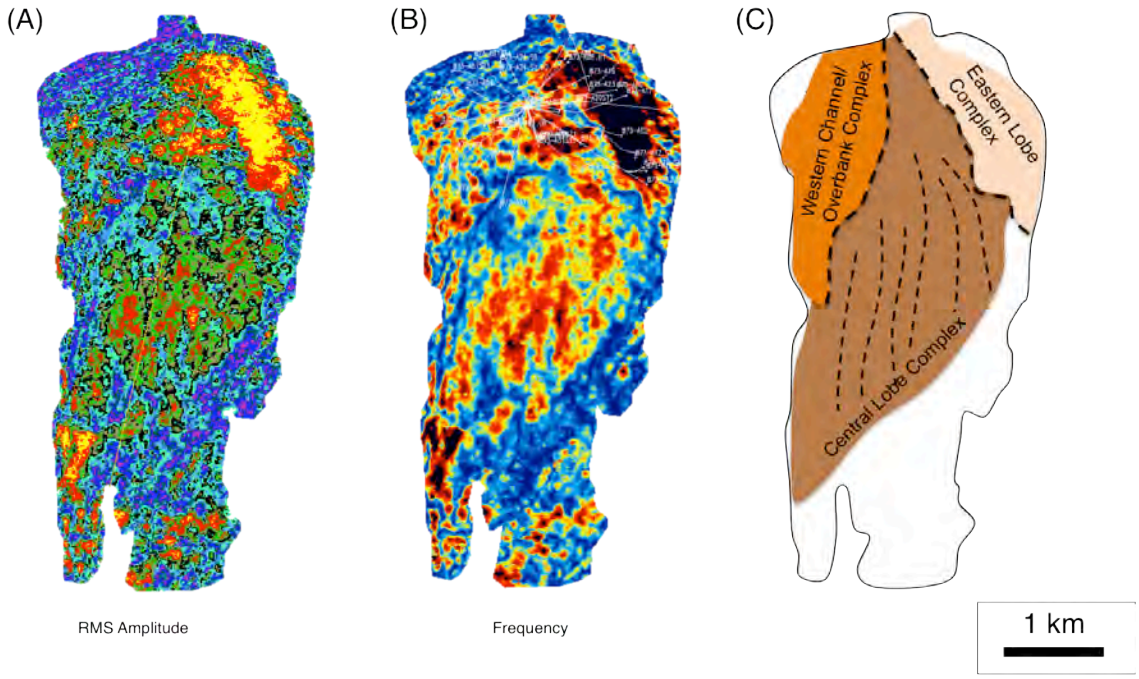


Figure 5.26: Map view of attribute extractions performed on a proportional slice within the Bul. 1 reservoir interval and interpretation of depositional morphologies. (A) Shows an RMS amplitude extraction; (B) is a 10 Hz frequency seismic volume response extraction; and (C) is a paleo-geomorphological interpretation of the deposits that comprise the main reservoir interval. Interpretations are supported by well-log and pressure data interpreted by Burk (1999).

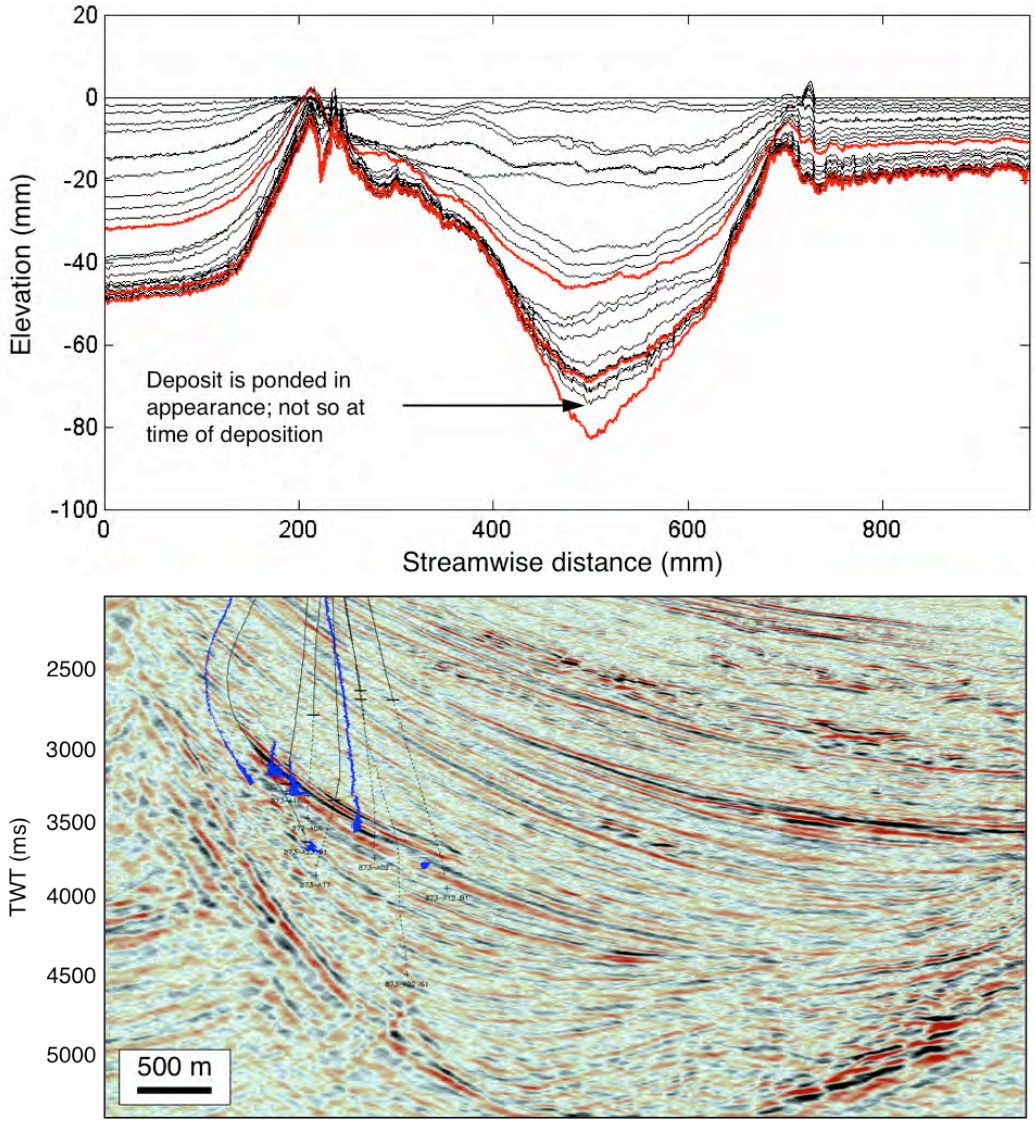


Figure 5.27: Post-tectonic (post-deformation) dip section of (A) an idealized reconstruction of deposits in the experimental basin following three episodes of subsidence; and (B) a section of the present-day Lobster minibasin. Experiment results show that for deposits that appear ponded post-subsidence may not have displayed a ponded geometry at the time of deposition (compare to Fig. 5.23). Exaggerated post-subsidence topography also masks the draping geometries of individual fill sequences from turbidity currents. Note that interpretations ignore the effects of scale differences between the two datasets, and will be more enhanced in the case of seismic data.

## REFERENCES


Al Ja'Aidi, O. S., W. D. McCaffrey, and B. C. Kneller, 2004, Factors influencing the deposit geometry of experimental turbidity currents: implications for sand-body architecture in confined basins: Geological Society, London, Special Publications, v. 222, p. 45-58.

Alves, T. M., J. Cartwright, and R. J. Davies, 2009, Faulting of salt-withdrawal basins during early halokinesis; effects on the Paleogene Rio Doce canyon system (Espirito Santo Basin, Brazil): AAPG Bulletin, v. 93, p. 617-652.

Arya, A. P., 1998, Introduction to classical mechanics: Upper Saddle River, N.J., Prentice Hall. 712 p.

Badalini, G., B. Kneller, and C. D. Winker, 2000, The late Pleistocene Trinity-Brazos turbidite system; new insights for deep turbidite reservoir interpretation: Annual Meeting Expanded Abstracts - American Association of Petroleum Geologists, v. 2000, p. 8-8.

Beaubouef, R. T., and S. J. Friedmann, 2000, High resolution seismic/sequence stratigraphic framework for the evolution of Pleistocene intra slope basins, western Gulf of Mexico; depositional models and reservoir analogs: Program and Abstracts - Society of Economic Paleontologists. Gulf Coast Section. Research Conference, v. 20, p. 40-60.

Booth, J. R., A. E. DuVernay, III, D. S. Pfeiffer, and M. J. Styzen, 2000, Sequence stratigraphic framework, depositional models, and stacking patterns of ponded and slope fan systems in the Auger Basin; central Gulf of Mexico slope: Program and Abstracts - Society of Economic Paleontologists. Gulf Coast Section. Research Conference, v. 20, p. 82-103.

Brami, T. R., C. Pirmez, C. Archie, S. Heeralal, and K. L. Holman, 2000, Late Pleistocene deep-water stratigraphy and depositional processes, offshore Trinidad and Tobago: Program and Abstracts - Society of Economic Paleontologists. Gulf Coast Section. Research Conference, v. 20, p. 104-115.

Brunt, R. L., W. D. McCaffrey, and B. C. Kneller, 2004, Experimental modeling of the spatial distribution of grain size developed in a fill-and-spill mini-basin setting: Journal of Sedimentary Research, v. 74, p. 438-446.

Burk, M. K., G. L. Brown, and D. R. Petro, 1998, Evolution of the geological model, Lobster Field (Ewing Bank 873): AAPG Discovery Series, v. 1.

Burk, M. K., G. L. Brown, and D. R. Petro, 1999, Evolution of the geological model, Lobster Field (Ewing Bank 873): AAPG Bulletin, v. 83, p. 1350-1350.

Haughton, P. D. W., 1994, Deposits of deflected and ponded turbidity currents, Sorbas Basin, Southeast Spain: Journal of Sedimentary Research, Section A: Sedimentary Petrology and Processes, v. 64, p. 233-246.

Haughton, P. D. W., 2000, Evolving turbidite systems on a deforming basin floor, Tabernas, SE Spain: Sedimentology, v. 47, p. 497-518.

Hodgson, D. M., and P. D. W. Haughton, 2004, Impact of syndepositional faulting on gravity current behaviour and deep-water stratigraphy: Tabernas-Sorbas Basin, SE Spain: Geological Society, London, Special Publications, v. 222, p. 135-158.

Imran, J., G. Parker, and C. Pirmez, 1999, A nonlinear model of flow in meandering submarine and subaerial channels: Journal of Fluid Mechanics, v. 400, p. 295-331.

Kneller, B. C., and M. J. Branney, 1995, Sustained high-density turbidity currents and the deposition of thick massive sands: Sedimentology, v. 42, p. 607-616.

Kneller, B., and C. Buckee, 2000, The structure and fluid mechanics of turbidity currents; a review of some recent studies and their geological implications: Sedimentology, v. 47, p. 62-94.

Lamb, M. P., T. Hickson, J. G. Marr, B. Sheets, C. Paola, and G. Parker, 2004, Surging versus continuous turbidity currents; flow dynamics and deposits in an experimental intraslope minibasin: Journal of Sedimentary Research, v. 74, p. 148-155.

Lamb, M. P., H. Toniolo, and G. Parker, 2006, Trapping of sustained turbidity currents by intraslope minibasins: Sedimentology, v. 53, p. 147-160.

Lamb, M. P., B. McElroy, B. Kopriva, J. Shaw, and D. Mohrig, 2010, Linking river-flood dynamics to hyperpycnal-plume deposits; experiments, theory, and geological implications: Geological Society of America Bulletin, v. 122, p. 1389-1400.

Leeder, M. R., T. E. Gray, and J. Alexander, 2005, Sediment suspension dynamics and a new criterion for the maintenance of turbulent suspensions: Sedimentology, v. 52, p. 683-691.

Liu, J. Y., and W. R. Bryant, 2000, Sea floor morphology and sediment paths of the northern Gulf of Mexico deepwater, *in* A. H. Bouma, and C. G. Stone, eds., Fine-grained turbidite systems, v. 72: Tulsa, OK, United States, American Association of Petroleum Geologists p. 13.

Lomas, S. A., and P. Joseph, 2004, Confined turbidite systems: Geological Society, London, Special Publications, v. 222, p. 1-7.

Madof, A. S., N. Christie-Blick, and M. A. Anders, 2009, Stratigraphic controls on a salt-withdrawal intraslope minibasin, north-central Green Canyon, Gulf of Mexico: Implications for misinterpreting sea level change: AAPG Bulletin, v. 93, p. 535-561.

Montoya, P., 2006, Salt tectonics and sequence-stratigraphy history of minibasins near the Sigsbee Escarpment, Gulf of Mexico, United States.

Parsons, J. D., and M. H. Garcia, 1998, Similarity of gravity current fronts: Physics of Fluids, v. 10, p. 3209-3213.

Pickering, K. T., and R. N. Hiscott, 1985, Contained (reflected) turbidity currents from the Middle Ordovician Cloridorme Formation, Quebec, Canada; an alternative to the antidune hypothesis: Sedimentology, v. 32, p. 373-394.

Prather, B. E., and A, 1998, Classification, lithologic calibration, and stratigraphic succession of seismic facies of intraslope basins, deep-water Gulf of Mexico, *in* J. R. Booth, G. S. Steffens, and P. A. Craig, eds., AAPG Bulletin, United States, American Association of Petroleum Geologists : Tulsa, OK, United States, p. 701-728.

Pratson, L. F., and W. B. F. Ryan, 1994, Pliocene to Recent infilling and subsidence of intraslope basins offshore Louisiana: AAPG Bulletin, v. 78, p. 1483-1506.

Salaheldin, T. M., J. Imran, M. H. Chaudhry, and C. Reed, 2000, Role of fine-grained sediment in turbidity current flow dynamics and resulting deposits: Marine Geology, v. 171, p. 21-38.

Sequeiros, O. E., B. Spinewine, R. T. Beaubouef, T. Sun, M. H. Garcia, and G. Parker, 2009, Bedload transport and bed resistance associated with density and turbidity currents: Sedimentology, v. 57, p. 1463-1490.

Spinewine, B., O. E. Sequeiros, M. H. Garcia, R. T. Beaubouef, T. Sun, B. Savoye, and G. Parker, 2009, Experiments on wedge-shaped deep sea sedimentary deposits in minibasins and/or on channel levees emplaced by turbidity currents; Part II, Morphodynamic evolution of the wedge and of the associated bedforms: Journal of Sedimentary Research, v. 79, p. 608-628.

Tari, G., 2000, Salt tectonics in the Atlantic margin of Morocco, *in* J. Molnar, P. Ashton, and R. Hedley, eds., Leading Edge [Tulsa, OK], United States, Society of Exploration Geophysicists : Tulsa, OK, United States, p. 1074.

Toniolo, H. A., 2002, Debris flows and turbidity current deposition in the deep sea and reservoirs, United States.

Toniolo, H., M. Lamb, and G. Parker, 2006, Depositional turbidity currents in diapiric minibasins on the continental slope; formulation and theory: Journal of Sedimentary Research, v. 76, p. 783-797.

Violet, J., B. Sheets, L. Pratson, C. Paola, R. Beaubouef, and G. Parker, 2005, Experiment on turbidity currents and their deposits in a model 3D subsiding minibasin: Journal of Sedimentary Research, v. 75, p. 820-843.

Winker, C. D., 1996, High-resolution seismic stratigraphy of a late Pleistocene submarine fan ponded by salt-withdrawal minibasins on the Gulf of Mexico continental slope: Proceedings - Offshore Technology Conference, v. 28, Vol. 1, p. 619-628.

# Chapter 6: Applying Predictive Relationships Derived from Experiments to the Middle Pliocene Lobster Minibasin Reservoir Interval

## INTRODUCTION

Physical experiments provide a platform for linking measured characteristics of deposit and flow relative to a known basin configuration. Resultant observations can assist in constraining interpretations from ancient basin fill successions. Unfortunately, such direct application of modeling results can be rife with error without careful consideration of those observations that are scale independent versus scale dependent. In this chapter, a workflow is proposed for comparing results and observations derived from morphologic measurements of several experimental basin and deposit characteristics with a real world dataset of minibasin fill from the salt basin regions of the U.S. Gulf of Mexico.

Results showed that although input current properties were fixed, dimensionless basin and deposit length ratio characteristics were similar for three very different experimental basin configurations tested. Distinguishing trends among these three outcomes were relatively indiscernible (Fig. 6.1). Frequency plots were therefore applied to constrain the spatial relationships among critical basin, deposit and flow characteristics. Spatial relationships derived from these frequency plots were used to develop interpretations of fill process in the Middle Pliocene Lobster minibasin reservoir interval. To accomplish this process, turbidite systems in the interval of interest were mapped using an integrated database of 3-D seismic, well-log and paleontological data (Chapter 2, Figs. 2.7 and 2.9). Interpretation of 45 $km^2$ (28 $mi^2$) of three-dimensional (3-D) seismic data, 21 well-logs and biostratigraphy from five wells enabled an

interpretation of the relative timing, morphology, dimensions and nature of deposit fill sequences that were then compared against experimental observations of mini-basin fill. This application of experimental results shows that such information can provide a useful predictive tool for identifying key features related to reservoir fill development, especially valuable in a basin that is deficient of subsurface data from which interpretations of lithology can be made.

## EARLY-MID PLIOCENE GEOLOGY OF THE EWING BANK AREA

The northern deep GOM is a geologically complex province consisting of Neogene-age intraslope minibasins created by sediment loading onto and evacuation of allochthonous salt (Villamil et al., 1998). The Ewing Bank area is located in the Plio-Pleistocene salt detachment province of the GOM (Diegel et al., 1995). Sedimentary fill in the Pliocene sections of northern GOM minibasins consists of bathyal turbidite systems with highly variable facies distribution (Weimer et al., 1998). These turbidite systems also form the primary turbidite reservoirs in the deepwater plays. The sea-level curve for the northern GOM (Fig. 6.2) shows major episodes of sea level fall in the Middle Pliocene (3.8–3.0 Ma), which coincide with coarse-grained deepwater turbidite deposition in the Lobster area. These reservoir deposits have been interpreted as basin floor fan turbidites and channel/ overbank complexes (Weimer et al., 1998; Burk et al., 1999).

Regional paleobathymetry in the study area from Villamil et al. (1998) and paleontological charts for the northern GOM (Witrock et al., 2003) were applied to gain a better understanding of the slope paleoenvironment and how it may have influenced sedimentation in the Lobster basin (Fig. 6.3). Interpretations were based on their study of planktonic and benthic foraminifera reports from 180 wells, calcareous nannoplankton

reports from 83 wells, and high-resolution foraminifer analyses from 60 wells. In the study area, the Early-to-Middle Pliocene topography shallowed from lower bathyal (ecozone 6; 3000-4500 ft) to middle bathyal (ecozone 5; 1500-3000 ft) paleoenvironments (See Fig. 6.3 for description). This shallowing has been attributed to diapiric rise of underlying salt and eventual evacuation to the north and south of the Lobster minibasin. For each time interval studied, there was however little variation in biozonation that suggests dramatic topographical variability within the immediate Lobster area.

Sediment accumulation plots from the five wells containing biostratigraphic data (A01.OH, A01ST02, A12ST03, A17 and A21) were used to help interpret the location of stratigraphic condensation and episodes of clastic influx in the study area using paleontological and section thickness well-log data (Fig. 6.4). On the sediment accumulation plot, the line of correlation (LOC) was derived from cross-plotting the theoretical position of microfossil extinctions in the absolute time domain vs. the stratigraphic location of extinctions (Villamil et al., 1998). The slope of the different segments of the LOC reflects the (un-decompacted) history of sediment accumulations. Line segments with steep slopes represent relatively low sedimentation rates with small thickness accumulations during long periods of time and vice versa. Well-log data shows that there were two major condensed zones in the study area, the older of which was succeeded by thick sections of fill in a relatively short duration of time (shallow slope). This thick, rapid deposition of sediment in the Middle Pliocene formed the time interval during which deposition of Lobster minibasin reservoir elements occurred (Fig. 6.4).

## MIDDLE PLIOCENE LOBSTER MINIBASIN MORPHOLOGY AND FILL

A combination of seismic and well-log mapping were performed to illustrate the nature of infilling in the Lobster basin during the Middle Pliocene. Burk et al., (1999) first described the structural and stratigraphic evolution of the Lobster area since initial salt emplacement in the late Miocene. During the Middle Pliocene (3.8 to 3.4 Ma), basin floor fan deposition into the Lobster minibasin included the major *Buliminella. 1* (*Bul. 1)* turbidite reservoirs, among other time-equivalent reservoirs identified from paleontological data (Fig. 6.5). Basin loading resulted in the development of salt highs and increased the degree of structural confinement of the minibasin (Rowan and Weimer, 1998). The salt highs, developed on the southeastern edge of the basin, blocked sand flow into the more distally located Arnold basin (Fig. 6.5) (Burk et al., 1999). Extensive basin rim normal and tear faulting then began to develop. The final phase of Middle Pliocene deposition was a channel/overbank complex on the eastern side of the *Bul. 1* reservoirs (Fig. 6.5).

### Integrated 3-D Seismic and Well-Log Mapping

The reservoir interval was bound by two mapped regional horizons. Mapping of individual architectural complex elements (e.g. lobeforms and channelforms) were performed. Seismic attribute analysis was also performed to image internal deposit architectures. Lithological interpretations of attributes were constrained by well-log data, and also improved the vertical resolution of deposit architecture not resolvable from seismic data. Gamma-ray logs from 21 wells were used to create net sand maps and therefore assess the spatial distribution of sand vs. shale in reservoir intervals when integrated with seismic attribute maps.

A northwest (landward) thickening wedge of sediment characterized the main reservoir fill interval (Fig. 6.6). This thickening may be interpreted as an indicator of relative paleo-accommodation in the basin, but experimental results from Chapters 4 and 5, as well as observations of deposit geometries from published experimental and shallow subsurface data (e.g. Violet et al., 2005; Pirmez et al., 2012) show that thickest portions of individual deposits from turbidity currents do not necessarily coincide with the zone of maximum accommodation in the basin. Instead, basin fans may have favored deposition on the inlet basin slope, but more extensive dataset of basin paleobathymetry (possibly from paleontological data) in the central and southern regions would be needed to support this interpretation.

The reservoir fill interval comprised individual continuous high-amplitude seismic reflectors, which, in cross-section displayed offlapping terminations on their northern and western edges, and downlapping terminations toward their southern and eastern edges (Fig. 6.6 b, c and d). Detailed mapping of these features resulted in the identification of eight lobate features (lobeforms) in map view (Fig. 6.7). The three earliest lobeforms of displayed high length to width (L:W) ratios, and were the most distally located in the basin (Fig. 6.7a). The oldest lobeform (S) was the largest and most distal of the three, and the two successive lobeforms (T and U) downlapped onto the older deposit. Eastward migration of lobeforms T and U also occurred, which was accompanied by a reduction in their size, as well as a decrease in their L:W ratio (Fig. 6.7b). Only one of the wells with made available to this study penetrated lobeform S. Well log data shows that lobeform S comprises a succession of vertically stacked lobe-complex intervals. These intervals, from oldest to youngest are identified as lobe-complexes 10, 20, 30 and 40 in well log section (Appendices C and D) and net sand maps (Fig. 6.9). Lobeform S displays thick, blocky gamma-ray log responses with sharp bases

and tops and net:gross (N:G) values exceeding 80 percent (Appendices C and D). These lobe-complexes are proven by well penetrations and production results to be thick, sand-rich intervals. Combinations of frequency and root mean squared (RMS) attribute extractions of the amplitude volume onto each mapped lobeform horizon display predominantly low amplitude responses with internal higher-amplitude, elongate, low-sinuosity channelform features that: (a) diverge from the proximal to distal locations (in the case of lobeform S, T and W); and (B) are through-going (in the case of lobeforms T, X, Y and Z) (Fig. 6.8). Applying the lobeform hierarchy scheme by *Prélat* et al., (2009), and the associated dimensional constraints and seismic amplitude responses, lobeforms S, T and U are interpreted as channelized distributary lobe-complexes. Based on well-log data interpreted in the more proximal, structurally shallower sections, the amplitude responses may be used to determine sand content within each lobe-complex, where high amplitudes coincide with deposits of a higher sand content, while low amplitudes coincide with deposits with a lower sand (or higher shale) content. Due to the similar L:W and proximity characteristics of these lobeforms relative to the proximal basin margin, they herein collectively referred to as lobe complex set 1 (LCS1) (Fig. 6.8).

The next three younger lobeforms identified in seismic data (V, W and X) showed a proximal shift in their location compared to lobeforms S T and U, which was also accompanied by a decrease in their size and L:W ratios (Figs. 6.7b and 6.8). Although these individual lobeforms were spatially distinguishable in seismic, well log data shows that they comprise a succession of vertically stacked lobe-complex intervals (lobe complexes 10, 20, 30 and 40) (Appendices C and D; (Fig. 6.9). Individual lobe-complexes also display blocky gamma-ray log responses with sharp bases and tops (Appendices C and D). Log-calculated N:G values ranged from 50 percent (Lobe 10 sequence) to 80 percent (Lobe 30 sequence) (Appendices C and D). High RMS

amplitudes from attribute extraction maps coincided with the sandiest, and thickest deposits, which exceeded 25 m (80 ft) thick in most instances (Figs. 6.8 and 6.9). Burk et al., (1999) interpreted this reservoir interval as an episode of basin floor fan deposition in a moderately confined structural setting. Lobe complexes V, W, and X are also characterized by similar L:W and proximity characteristics relative to the proximal basin margin, and are referred to as lobe complex set 2 (LCS2) (Fig. 6.8).

The latest episode of reservoir sedimentation is represented by lobeforms Y and Z, which showed progressive eastward shifts in sedimentation accompanied by offlapping terminations from earlier episodes of deposition (Fig. 6.6b). Lobeforms Y and Z displayed higher L:W ratios than lobe-complexes V, W and X, but remained spatially restricted to the proximal basin area. Frequency and RMS attribute extractions showed that the lobe-complexes comprised high-amplitude channelform elements that paralleled their long axis (N-S). Channelform elements identified in these lobe-complexes stack vertically and are not always discernible from seismic attribute maps (Fig. 6.8). Where individual channelforms are discernible (e.g. lobeform Y), they display low sinuosities. These lobe-complexes identified in seismic were represented by intervals 70, 80 and 90 from net sand maps (Fig. 6.9). Gamma ray logs from these intervals are dominated by high gamma, interspersed with sudden low gamma spikes interpreted to represent relatively thin sand intervals characterized by sharp bases and gradual tops representing vertically fining sequences. Although individual sand cycles are not as thick as those in lobe complexes X and Y, they still display relatively high N:G values that exceed 50 percent (Appendices C and D). Although lobe complexes Y and Z are within similar proximity to LCS2, they are categorized as a separate lobe complex set due to their higher L:W ratios and increased density of channelform elements of which they are comprised. They are therefore referred to as lobe complex set 3 (LCS3) (Fig. 6.8).

## PREDICTIVE BASIN-DEPOSIT RELATIONSHIPS

Measurements of pre-flow basin and deposit morphology from experiments were recorded along the center dip line and deepest strike line transect of each experimental basin configuration for each depositional event (Fig. 6.10). Basin morphological measurements include (a) the basin length ($A_b$); (b) the height of the basin to the inlet point ($B_b$); (c) the length from the basin entry to the deepest point of the basin ($C_b$); (d) the length of the deepest point of the basin to the basin exit ($D_b$); and (e) the height from the deepest part of the basin to the exit point ($E_b$) (Fig. 6.10). Deposit morphological characteristics include: (a) the dip length of the deposit ($A_d$), the strike width of the deposit ($B_d$); (c) the dip length from the basin entry to the thickest part of the deposit ($C_d$); (d) the dip length of the deepest point of the basin to the basin exit ($D_d$); and (e) the thickness of the thickest part of the deposit ($E_d$) (Fig. 6.10). Similar geometrical and morphological measurements were made using the Lobster 3-D seismic volume when data extent and quality allowed (see Table 6.2 for summary), and results were compared to experimental data (see Table 6.1 for summary).

The frequency plots from Figure 6.11 show the relative spatial relationships between the basin and the deposits contained within it from all experiments reported in this paper. In the following sections, spatial basin-deposit relationships are compared first from the basin entry point, and then the basin exit point for results calculated from 24 flow events (n=24), onto which, characteristic deposit length scale relationships for Lobster deposits are plotted. An interpretation of fill process for the Lobster data was then made based on observations from experimental work reported in earlier chapters.

**Relationships from Basin Entry Point**

First, the relationship between the distances to the thickest part of the deposit relative to the length of the basin from the entry point ($C_d/A_b$) is determined. Experimental results show that the thickest part of the deposit ranges between 0.3- and 0.61-times the length of the basin from the entry point, with a calculated median of 0.47 (Table 6.1). The standard deviation of the dataset is 0.09 (or 27% of the median). The frequency plot (Fig. 6.11a) shows that the distribution of data is unimodal, negatively skewed, and a magnitude length scale ratio of 0.5 is most abundant, which correlates approximately with the average calculated length ratio. Comparing data from the Lobster dataset, the thickest part of the deposit relative to the basin length shares a similar range to that of experimental data, and a magnitude length scale of 0.4 is most abundant. The locations of LCS2 and LCS3 are located within this zone, while LCS1 is more distally located.

Second, the length ratio of the thickest part of the deposit to the deepest point of the basin relative to the basin entry point ($C_d/C_b$) is determined. Experimental results show that the thickest part of the deposit ranges between 0.14- and 1.05-times the length to the deepest point of the basin from the basin entry point, with a calculated median of 0.71 (Table 6.1). The standard deviation of the dataset is 0.19 (or 27% of the median). The frequency plot (Fig. 6.11b) shows that the distribution of data is relatively broad, unimodal and negatively skewed, but the greatest abundance of data occurs for a magnitude length scale ratio of 0.8-times the length to the deepest point of the basin from the basin entry point. If the thickest deposit in the Lobster dataset were to be considered the deepest point in the basin, a comparison of results from the basin fill shows that the greatest abundance of data occurs for a magnitude length scale ratio of 1.1-times the length to the deepest point of the basin from the interpreted entry point. This result

coincides with the locations of LCS2 and LCS3, while lobe complexes from LCS1 are again more distally located.

**Relationships from Basin Exit Point**

The spatial relationship of the thickest deposit from the basin exit point as a fraction of the basin length ($D_d/A_b$) is determined. Experimental results show that the thickest part of the deposit ranges between 0.24- and 0.46-times the length of the basin from the exit point, with a calculated median of 0.37 (Table 6.1). The standard deviation of the dataset is 0.06 (or 16% of the median). The frequency plot (Fig. 6.11c) shows that the distribution of data is unimodal, negatively skewed, and a magnitude length scale ratio of 0.4 is most abundant, which also approximates to the median value. Lobster fill data shows that the thickest deposit occurred between 0.4 and 0.6-times the length of the basin from the exit point, with the most abundant occurrence at 0.6, a distance of approximately 1.6-times longer than experimental data suggest (see Appendix E for raw data). These results may therefore suggest that there are disparities in the basin shape and scale of interpretation relative to those modeled in experiments.

Second, the length ratio of the thickest part of the deposit to the deepest point of the basin relative to the basin exit point ($D_d/D_b$) is determined. Experimental data show that the thickest part of the deposit ranges between 0.6- and 1.3-times the length to the deepest point of the basin from the basin exit point, with a calculated median of 1.02 (Table 6.1). The standard deviation of the dataset is 0.17 (or 17% of the median). The frequency plot (Fig. 6.11d) shows that the distribution of data is also relatively broad, unimodal and negatively skewed, but the greatest abundance of data occurs for a magnitude length scale ratio of 1.2-times the length to the deepest point of the basin from the basin exit point. If the thickest deposit in the Lobster dataset were to be considered

the deepest point in the basin, the real world data show that the thickest part of the deposit ranges between 0.6- and 1.1-times the length to the deepest point of the basin from the exit point, with the greatest occurrence at 1.0. This high occurrence coincides with the locations of LCS2 and LCS3.

**Deposit Extent Relationships**

The spatial relationship of the characteristic deposit width to deposit length ($B_d/A_d$) is determined. Experimental results show that the deposit width ranges between 0.44- and 1.36-times the deposit length, with a calculated median of 0.81 (Table 6.1). The standard deviation of the dataset is 0.19 (or 23% of the median). The frequency plot (Fig. 6.11e) shows that the distribution of data is unimodal, slightly positively skewed, and a magnitude length scale ratio of 0.8 is most abundant, which also approximates to the median value. Lobster data also shows a similar trend, with the greatest occurrence at a magnitude length scale of 0.6. Both experimental and real world data therefore show that individual deposits are more elongate along dip than they are along strike. These deposit aspect ratios occur for all lobe complex sets (LCS1, LCS2 and LCS3).

The most likely deposit thickness for a given deposit length ($E_d/A_d$) is determined. Experimental results show that the deposit thickness ranges between 0.001- and 0.04-times the deposit length, with a calculated median of 0.01 (Table 6.1). The standard deviation of the dataset is 0.01 (or 76% of the median). The frequency plot (Fig. 6.11f) shows that the distribution of data is bimodal and broad. A similar broad distribution occurred for Lobster data results, but remained within an order of magnitude of experimental results. Results therefore suggest that the ratio of deposit thickness to its corresponding length may not be a suitable metric for establishing absolute relationships, but the data distribution ranges may provide approximate limits to their application.

## VELOCITY COMPONENT DATA AND DEPOSIT/BASIN MORPHOLOGY

Experimental data reported in Chapter 5 suggested that the near-bed fall velocity, $w$ possesses the strongest control on minibasin sedimentation compared to the horizontal components of velocity, $u$ and $v$. The influence of negative fall velocity on the thickest accumulations were additionally affected by the advection length scale, which incorporates the forward component of fall velocity and results in a delayed spatial occurrence of thick deposits. The region where the fall velocity is most negative along dip can however be used as a proxy for estimating the location for the coarsest $D50_b$ and $D90_b$ grain sizes, as shown in Chapter 5, and illustrated in Figure 6.12.

The following data presented is therefore useful for linking flow process to regions where the coarsest grain fractions are situated in a deposit of given length relative to a basin of known dimensions. Measurements of pre-flow basin and deposit morphology were performed along the center dipline section for each experimental depositional event (Fig. 6.12). Basin and deposit morphological measurements relative to the point at maximum forward velocity, $u$, include (a) the distance from the entry point to maximum $u$ ($A_u$); (b) the distance from the point at maximum $u$ to the thickest deposit ($B_u$); (c) the distance from the point at maximum $u$ to the deepest point in the basin ($C_u$); and (d) the distance from the point at maximum $u$ to the basin exit point ($D_u$) (Fig. 6.12). Basin and deposit morphological measurements relative to the point at minimum fall velocity, $w$, include (a) the distance from the entry point to minimum $w$ ($A_u$); (b) the distance from the point at minimum $w$ to the thickest deposit ($B_u$); (c) the distance from the point at minimum $w$ to the deepest point in the basin ($C_u$); and (d) the distance from the point at minimum $w$ to the basin exit point ($D_u$) (Fig. 6.12). Note the density of data collection for velocity data was coarse relative to changes in basin topography along the center dipline transect, which may introduce error associated with determining the spatial

occurrence of maximum $u$ and minimum $w$ near the current-deposit interface. Results however provide insight into the link between flow process and sedimentation in deepwater environments.

**Fall Velocity – Deposit – Basin Relationships from Entry Point**

First, the distance along the basin length at which the fall velocity is at a minimum relative to the total length of the basin ($A_w/A_b$) is determined. Experimental results show that the distance ratio ranges between 0.16- and 0.59-times the length of the basin from the entry point, with a calculated median of 0.37 (Table 6.1). The standard deviation of the dataset is 0.11 (or 29% of the median). The frequency plot (Fig. 6.13a) shows that the distribution of data is unimodal, normal, and a magnitude length scale ratio of 0.4 is most abundant, which also approximates to the median value. The data therefore favors an average value of 0.4 times the length of the basin from the entry point as a location for the most negative near-bed fall-velocity. Applying these data to the Lobster dataset would suggest that a minimum in fall velocity would occur at 0.4-times the length of the entire basin, which would coincide with the thickest deposit of LCS2 and LCS3 as previously described (Fig. 6.11a).

Second, the ratio of the distance to the point at minimum fall velocity to the distance to the point of the thickest deposit ($(A_w + B_w)/A_w$) is determined. Experimental results show that the distance to minimum fall velocity from the entry point ranges between 0.23- and 2.4-times the length to the thickest deposit from the entry point, with a calculated median of 1.26 (Table 6.1). The standard deviation of the dataset is 0.54 (or 43% of the median). The frequency plot (Fig. 6.13b) shows that the distribution of data is bimodal and broad, with the greatest occurrences at 1-1.5-times the distance from the entry point to the point of the thickest deposit. Considering this result and the occurrence

of the thickest deposit along the basin length previously described, the minimum fall velocity in the Lobster basin would occur in the vicinity of the thickest deposit for the proximal lobe complex sets (LCS2 and LCS3). No account is however given to the basin's shape (symmetry and skewedness) between the experimental and real world basin configurations.

Third, the ratio of the distance to the point at minimum fall velocity to the distance to the deepest point in the basin ($A_w/(A_w + C_w)$) is determined. Experimental results show that the distance to minimum fall velocity from the entry point ranges between 0.23- and 0.88-times the length to the deepest point in the basin from the entry point, with a calculated median of 0.62 (Table 6.1). The standard deviation of the dataset is 0.17 (or 27% of the median). The frequency plot (Fig. 6.13c) shows that the distribution of data is unimodal, negatively skewed and a magnitude length scale ratio of 0.7 is most abundant. The total Middle Pliocene reservoir thickness map of the Lobster study area (Fig. 6.6) suggested that the basin was landward-thickening; an opposite configuration to that tested in experiments. As a result, the relationship of the distance to the point at minimum fall velocity to the distance to the deepest point in the basin would be expected to occur in the lower end of the range of data suggested by experiments, and coincide with the locations of LCS2 and LCS3.

**Fall Velocity – Deposit – Basin Relationships from Exit Point**

In relating experimental data to Lobster reservoir interval data, the corresponding fall velocity–deposit–basin relationships previously described from the entry point hold in this section. First, the distance to the location where fall velocity is at a minimum relative to the entire length of the basin ($D_w/A_b$) is determined. Experimental results show that the distance ratio ranges between 0.37- and 0.84-times the length of the basin

from the entry point, with a calculated median of 0.61 (Table 6.1). The standard deviation of the dataset is 0.13 (or 21% of the median). The frequency plot (Fig. 6.13d) shows that the distribution of data is unimodal, slightly negatively skewed, and a magnitude length scale ratio of 0.7 is most abundant. The data therefore suggests a value of 0.7 times the length of the basin from the exit point as a location for the most negative near-bed fall-velocity.

Second, the ratio of the distance to the point at minimum fall velocity to the distance to the point of the thickest deposit ($(D_w - B_w)/D_w$) is determined. Experimental results show that the distance to minimum fall velocity from the exit point ranges between 0.56- and 1.46-times the length to the thickest deposit from the exit point, with a calculated median of 0.93 (Table 6.1). The standard deviation of the dataset is 0.25 (or 27% of the median). The frequency plot (Fig. 6.13e) shows that the distribution of data is bimodal and broad, with the greatest occurrences at 0.9 and 1.1-times the distance from the exit point to the point of the thickest deposit.

Third, the ratio of the distance to the point at minimum fall velocity to the distance to the deepest point in the basin ($(D_w - C_w)/D_w$) is determined. Experimental results show that the distance to minimum fall velocity from the exit point ranges between 0.37- and 0.81-times the length to the deepest point in the basin from the exit point, with a calculated median of 0.63 (Table 6.1). The standard deviation of the dataset is 0.12 (or 20% of the median). The frequency plot (Fig. 6.13f) shows that the distribution of data is unimodal, negatively skewed and a magnitude length scale ratio of 0.8 is most abundant.

## DISCUSSION

Many hydrocarbon reservoirs are in rocks originally deposited as confined turbidites in systems where the depositional pattern of turbidity currents has been strongly influenced by basin-floor topography. Predictive tools that link fill character on topographically complex slopes to depositional patterns are useful for deepwater minibasin hydrocarbon exploration and development. Several attempts have been made to systematically evaluate the nature of minibasin fill in deepwater regions, primarily from seismic and well log data in the GOM (e.g. Prather et al., 1998; Prather et al., 2000; Booth et al., 2000; Badalini et al., 1999; Badalini et al., 2000). Where lithological control was absent in these published studies, seismic facies analysis was applied to develop predictive process models that were intended to be transferable to other slope systems. Chapters 3 and 4 of this dissertation, however describe the limitations in the applicability of established models of minibasin fill development, which primarily lie in the interpretation of physical processes responsible for minibasin infilling on complex slopes. Likewise, significant work has been performed in deepwater outcrop locations toward developing models of minibasin fill (e.g. Sinclair and Tomasso, 2002; Amy et al., 2004; Pyles, 2008). Although outcrops provide a high resolution dataset of deposit composition, geometry and architectures, these datasets lack the spatial coverage of a 3-D seismic based analysis. Although the historical models have been successful in the identification of reservoir intervals in the GOM proximal slope locations in the past, exploration in increasingly distal slope locations and in increasingly terrain complex basins lead to the need for better understanding of the link between bathymetry and gravity processes.

Predictive indicators developed from experimental data were compared to a similar, but limited, dataset from the Middle Pliocene reservoir interval of the Lobster field in the northern Gulf of Mexico. Although the experimental results do not mirror the

dataset collected from the real world Lobster area, the ranges in data occurrences remain similar, while the frequencies of greatest occurrences are within one standard deviation of experimental data. For each predictive indicator applied, the greatest frequency of data from the more proximal LCS2 and LCS3 in the Lobster minibasin were within one standard deviation of the greatest frequency of data from experiments. Although the more distal and more expansive LCS1 fell within the range of predictive indicators described by experiments, it rarely coincided with incidences of greatest occurrence. Consequently, it is interpreted that LCS1 was likely deposited under a different flow regime than those from LCS2 and LCS3, or may have been deposited in a more unconfined topographic regime. Structural reconstructions of the Lobster minibasin (Burk et al., 1999) suggest that older flows may have been deposited over a much more subdued substrate prior to dramatic deepening and confining of the mini-basin. Experimental observations from Chapter 4 showed that high-density flows were more efficient in transporting sediment and were more likely to create thick deposits that are more distally located in a minibasin system. Al Ja'Aidi (2004) also showed that increases in the initial flow density, volume and proportion of fines in turbidity currents resulted in an increased amount of coarse sediment transferred to more distal locations. They attributed these factors to an increase in potential energy and maintenance of negative buoyancy in the flow for coarse-grained sediment to be transported further distally. Covault and Romans (2009) also suggest that the deposits of larger-volume flows, or those in more unconfined settings tend to be elongate like those observed in LCS1. These possible drivers (larger volume flows, increased flow density, or increased proportion of fines) will all require additional sedimentologic data to investigate fully and future well penetrations may provide such information.

The limitations in the application of the predictive metrics in this chapter follow from that outlined in Chapter 5, but three important points should be considered:

1. The experiments documented in this study focused on low density, turbidity currents. An application of the effects of topography on a broader range of sediment gravity flows will provide further insight that builds on the interpretations and analyses of deposit architecture in this work.
2. There were scale limitations in assessing the contributions of individual flows to observations of deposit architecture and geometry using subsurface data. The conclusions of Chapter 5 describe this in more detail. Despite the difference in scale between event-related bed measurements (from experiments) and stacked deposit measurements (from Lobster seismic and well-log data), the application of these relationships as a predictive tool can be useful for assessing the occurrence of reservoir intervals in frontier minibasin locations
3. In this chapter, an assessment of basin paleotopography was performed using a reservoir thickness map, which has been shown in Chapter 5 as a less than ideal indicator of basin accommodation and paleotopography. Although paleontological data was available in this study, wells were only restricted to the northern portion of the basin, and did not provide a suitable method for characterizing the Lobster basin topography in any spatially meaningful way.

## CONCLUSIONS

The assessment of predictive relationships derived from experimental data has been shown to correlate with those from lobe complex data interpreted from subsurface data in the Lobster field. Experimental results showed that favorable reservoir intervals

derived from turbidity currents are more likely to occur in the proximal area of the minibasin than distal locations. Spatial relationships derived from analysis of experimental results coincide with and accurately predict the locations of LCS2 and LCS3, while the location of LCS1 remains more distal in the basin than experimental results would suggest. As a result, it is interpreted that LCS1 was deposited by flows of different size or rheology from LCS2 and LCS3, and/or may have been deposited in a more unconfined topographic regime.

## TABLES

| | MAX | AVG | MIN | STDEV | RSD (%) |
|---|---|---|---|---|---|
| $C_d/A_b$ | 0.295 | 0.473 | 0.610 | 0.087 | 18.35 |
| $D_d/A_b$ | 0.143 | 0.710 | 1.053 | 0.193 | 27.23 |
| $C_d/C_b$ | 0.237 | 0.372 | 0.456 | 0.061 | 16.29 |
| $D_d/D_b$ | 0.683 | 1.025 | 1.289 | 0.174 | 16.95 |
| $B_d/A_d$ | 0.441 | 0.815 | 1.358 | 0.189 | 23.22 |
| $E_d/A_d$ | 0.001 | 0.014 | 0.044 | 0.010 | 76.38 |
| $A_w/A_b$ | 0.161 | 0.390 | 0.588 | 0.115 | 29.53 |
| $(A_w+B_w)/A_w$ | 0.229 | 1.260 | 2.397 | 0.538 | 42.66 |
| $A_w/(A_w+C_w)$ | 0.234 | 0.623 | 0.883 | 0.168 | 26.99 |
| $D_w/A_b$ | 0.373 | 0.606 | 0.844 | 0.128 | 21.18 |
| $(D_w-B_w)/D_w$ | 0.560 | 0.930 | 1.460 | 0.251 | 26.96 |
| $(D_w-C_w)/D_w$ | 0.372 | 0.626 | 0.811 | 0.124 | 19.75 |

Table 6.1: Statistical measures of predictive dimensionless ratios of basin morphology, deposit morphology and dimensional relationships from negative fall velocity from Series 2 experiments. These include maximum (MAX), average (AVG), minimum (MIN), standard deviation (STDEV) and relative standard deviation (RSD) values.

| | MAX | AVG | MIN | STDEV | RSD (%) |
|---|---|---|---|---|---|
| $\mathbf{C_d/A_b}$ | 0.52 | 0.41 | 0.33 | 0.08 | 20.52 |
| $\mathbf{D_d/A_b}$ | 0.61 | 0.51 | 0.36 | 0.10 | 19.62 |
| $\mathbf{C_d/C_b}$ | 1.54 | 1.20 | 0.98 | 0.25 | 20.52 |
| $\mathbf{D_d/D_b}$ | 1.02 | 0.85 | 0.61 | 0.17 | 19.55 |
| $\mathbf{B_d/A_d}$ | 1.28 | 0.75 | 0.46 | 0.30 | 39.88 |
| $\mathbf{E_d/A_d}$ | 0.03 | 0.01 | 0.01 | 0.01 | 65.58 |

Table 6.2: Statistical measures of predictive dimensionless ratios of basin and deposit morphology for Lobster minibasin lobe complexes. These include maximum (MAX), average (AVG), minimum (MIN), standard deviation (STDEV) and relative standard deviation (RSD) values.

**FIGURES**

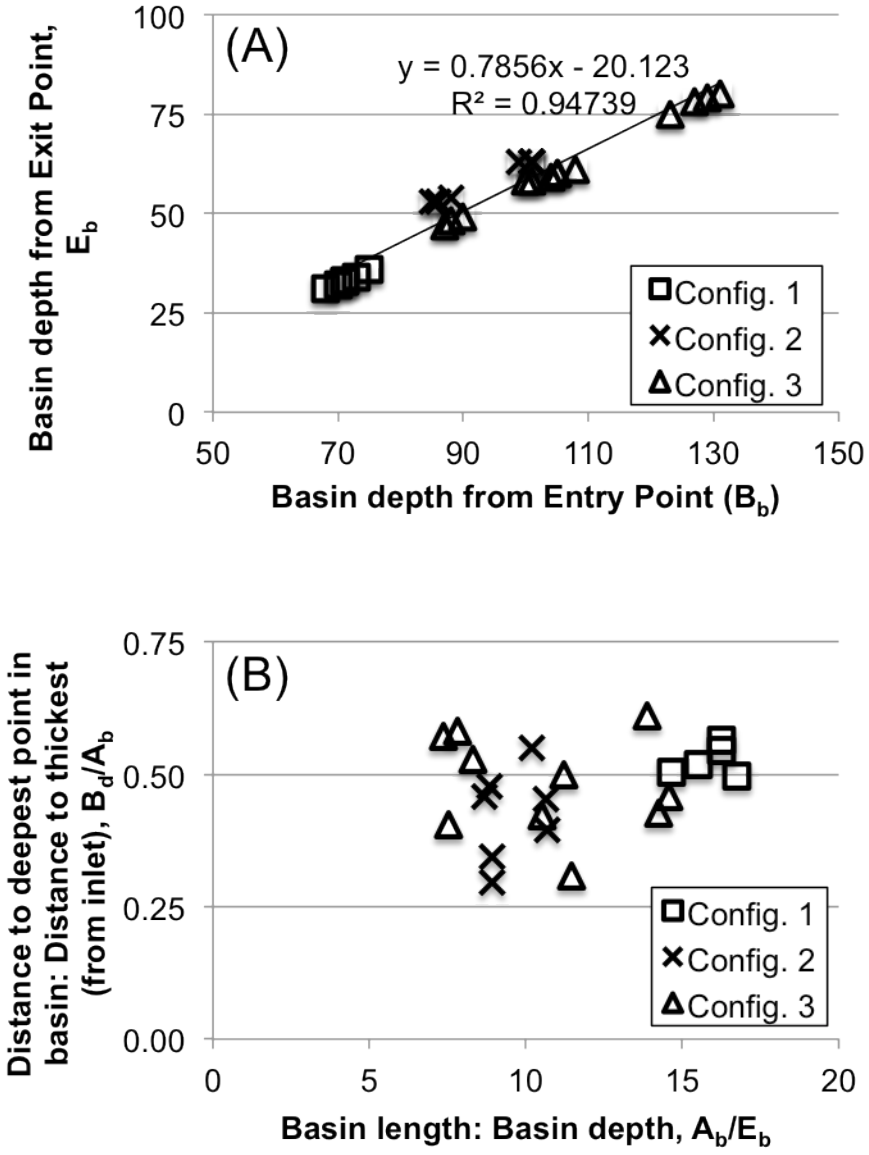


Figure 6.1: Plots of (A) basin depth from entry point vs. basin depth from exit point; and (B) basin length:depth ratio vs. distance to deepest point in basin (from inlet): distance to thickest deposit (from inlet) ratio. Similarity of basin- and deposit-dimension ratios by configuration result in indistinguishable trends among the three configurations tested. See Fig. 6.10 for description of morphology. Frequency plots from Figures 6.11 and 6.13 are therefore used in this analysis to determine predictive relationships.

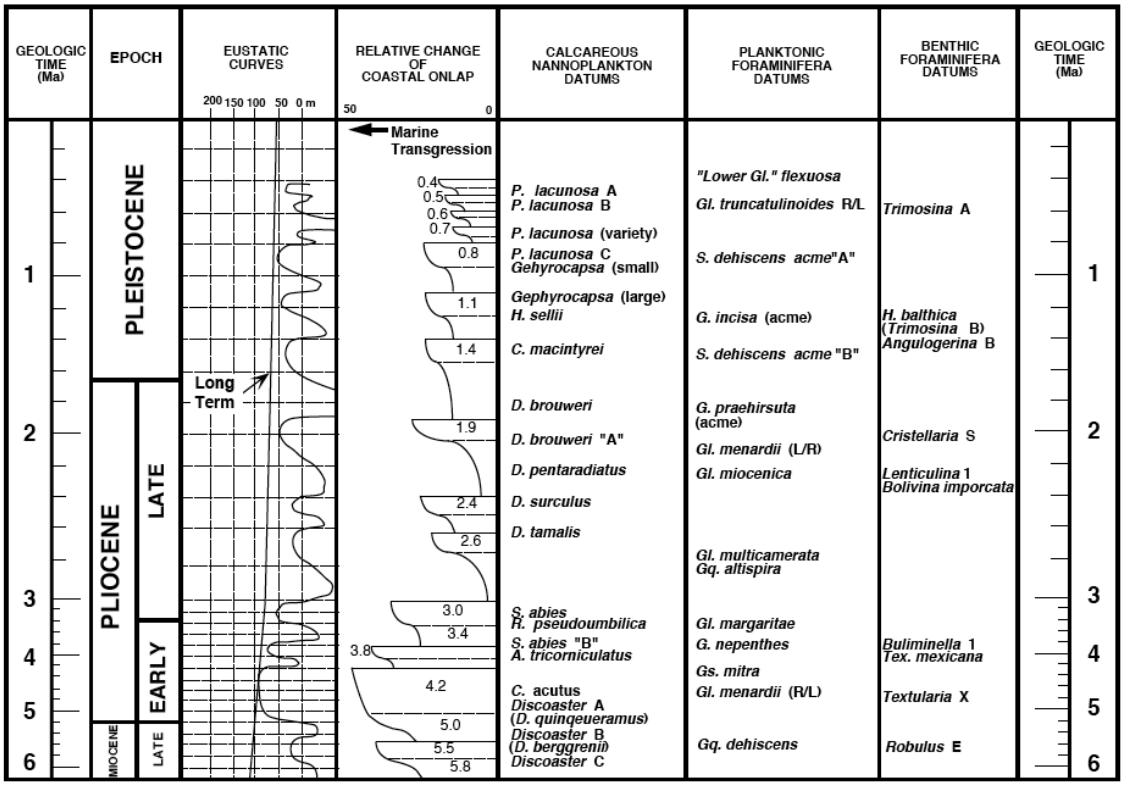


Figure 6.2: Eustasy, onlap chart and biozonation for northern GOM Neogene sediments (from Villamil et al., 1998).

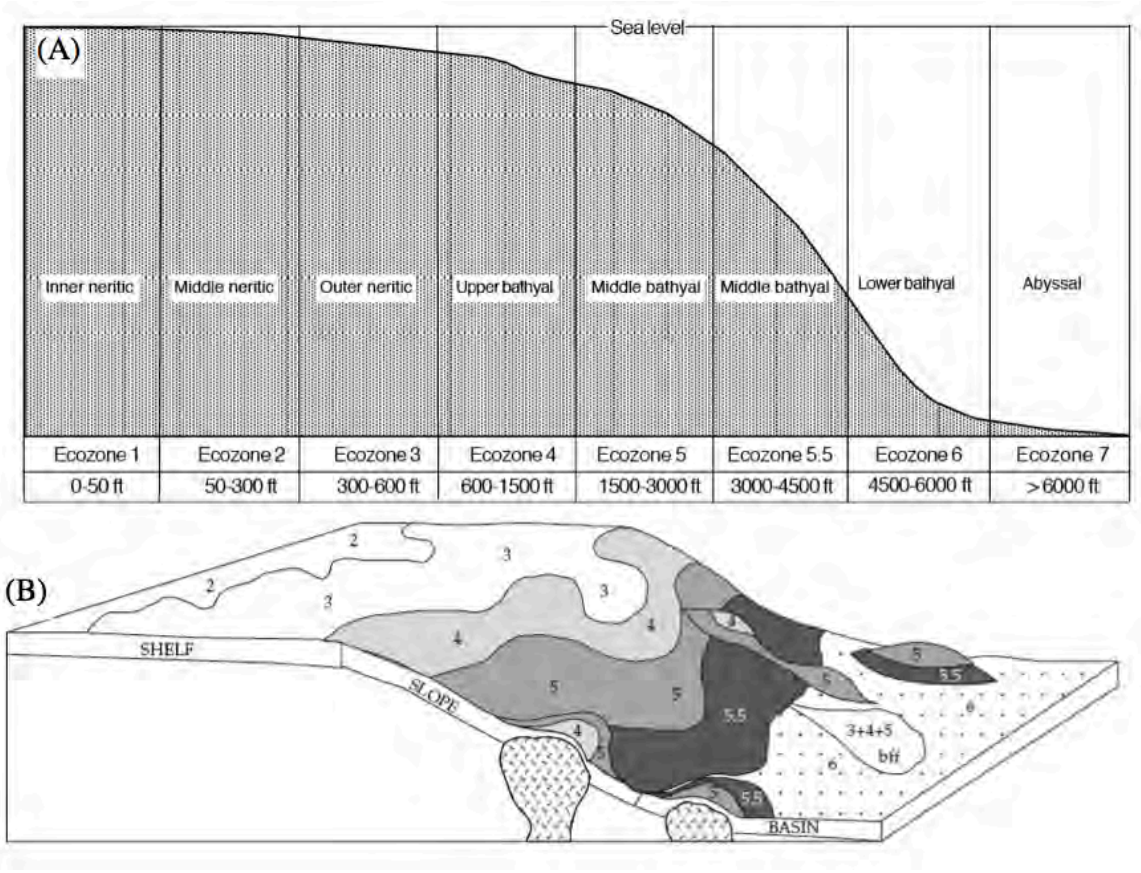


Figure 6.3: Traditional benthic biofacies model and (B) modified benthic biofacies model for the northern GOM (modified from Villamil et al., 1998).

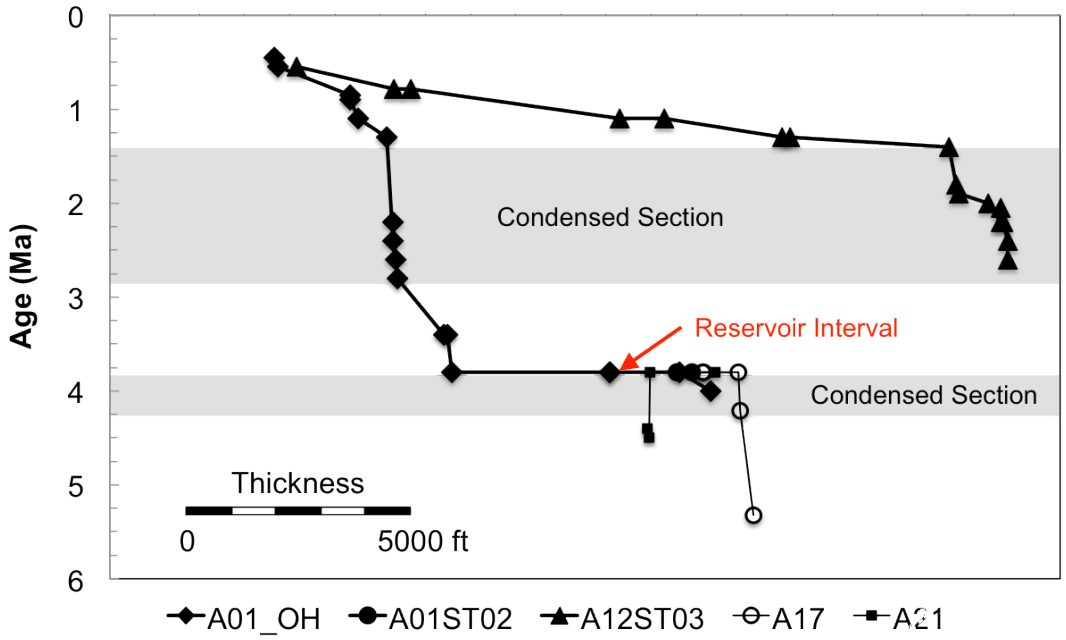


Figure 6.4: Sediment accumulation plots for Lobster wells A01_OH, A01ST02, A12ST03, A17 and A21. Vertical axis is geological time and was derived by using graphical correlation (Witrock et al., 2003). Horizontal axis represents the thickness of sediments in the well in ft. Condensation occurred between 4.2 and 3.8 Ma and 2.8 to 1.45 Ma. Note the abrupt increase in rates of sedimentation at 3.8 Ma. See Figure 6.5 for location of wells.

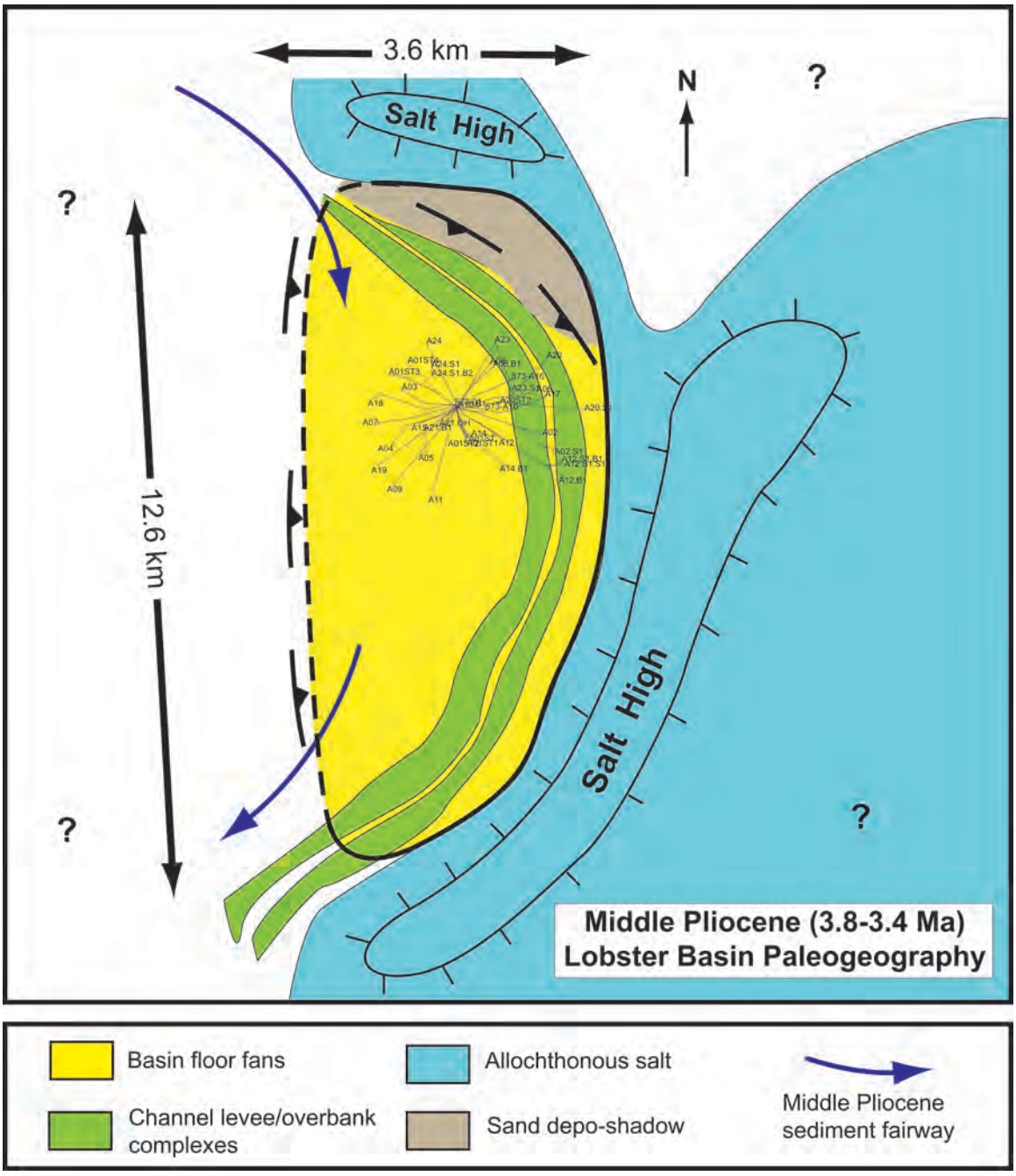


Figure 6.5: Paleogeographic map of the Lobster minibasin during the Middle Pliocene (modified from Burk et al., 1999). The polygons show the relative distribution of basin floor fans (yellow) in the early fill, channel levee/overbank complexes (green) in the later fill, exposed? allochthonous salt (blue) and the interpreted orientation of the main sediment fairway during this time. The locations of wells penetrating this interval are shown

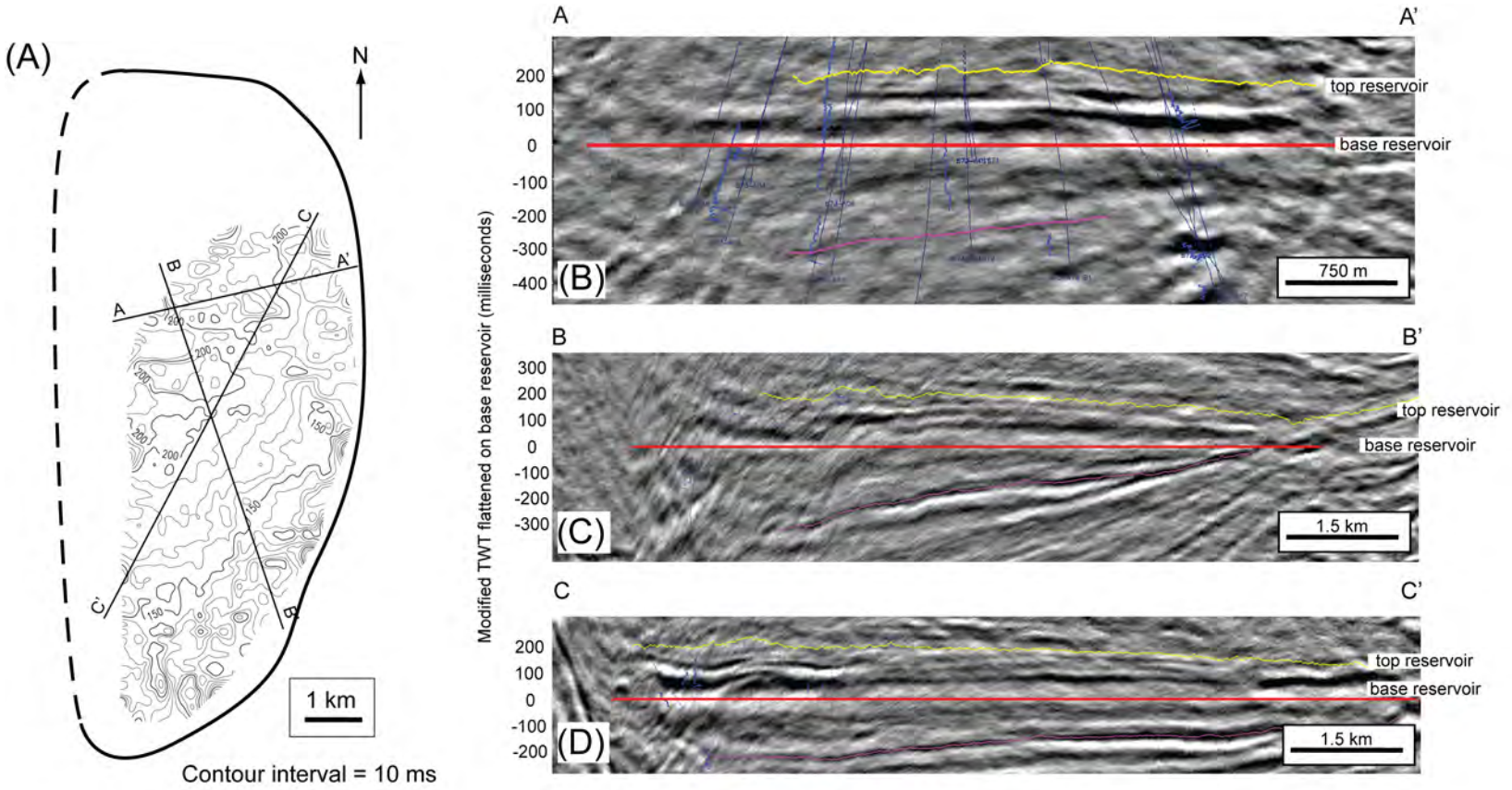


Figure 6.6: Middle Pliocene reservoir interval thickness map and cross sections. (A) reservoir thickness map was generated from regional seismic horizon mapping. Note the contour interval of 10 feet. Cross sections (B) A-A'; (C) C-C'; and (D) C-C' are shown on the map. A northwest-thickening wedge of sediment that comprises lobe-and channel-complex architectures identified in seismic and well log data characterizes the interval.

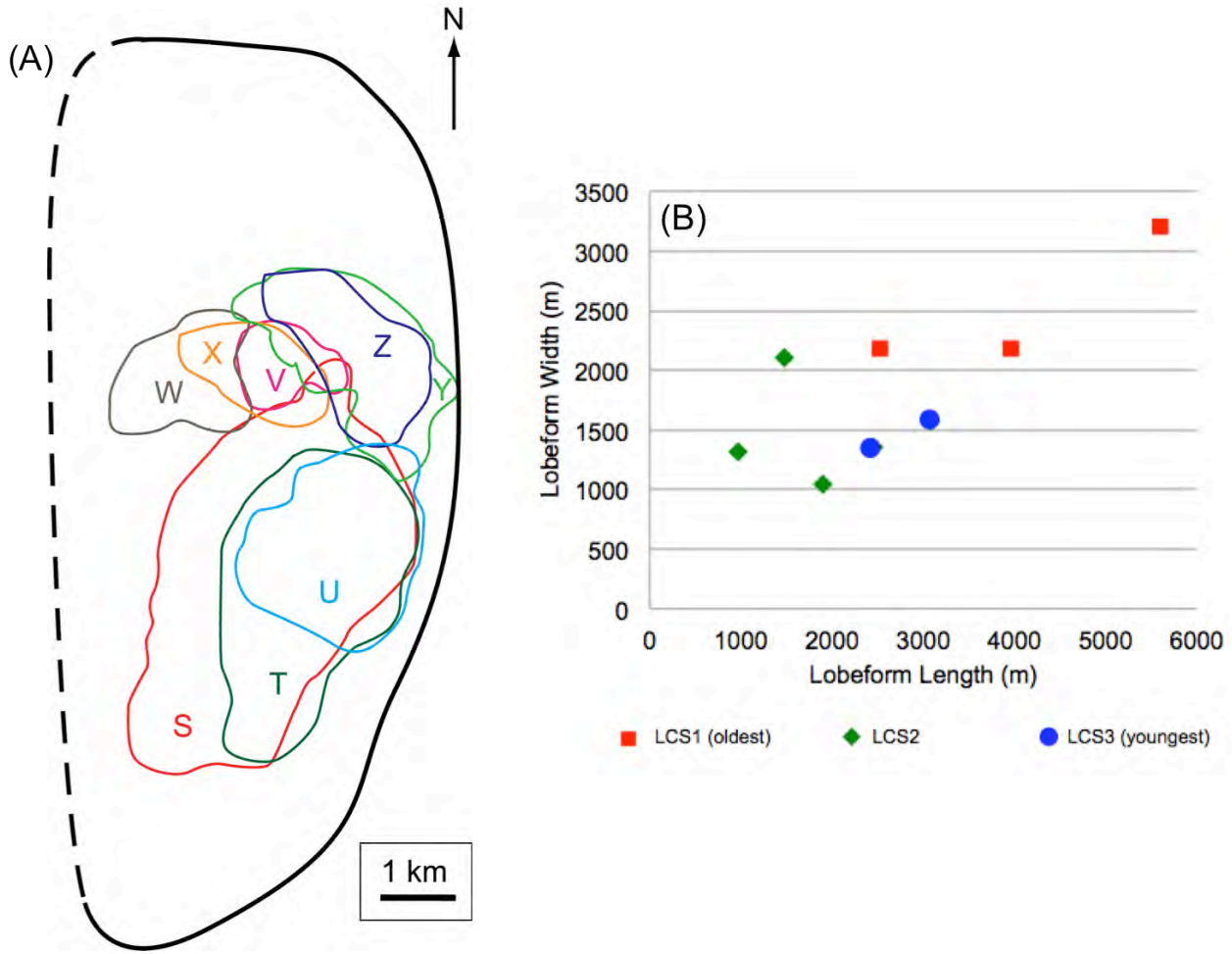


Figure 6.7: (A) Map view of mapped lobeforms identified in 3-D seismic data; and (B) graph of lobeform length vs. lobeform width. The solid black line shows the known extent of the Lobster minibasin and the dashed black line shows the interpreted western extent (after Burk et al., 1999).

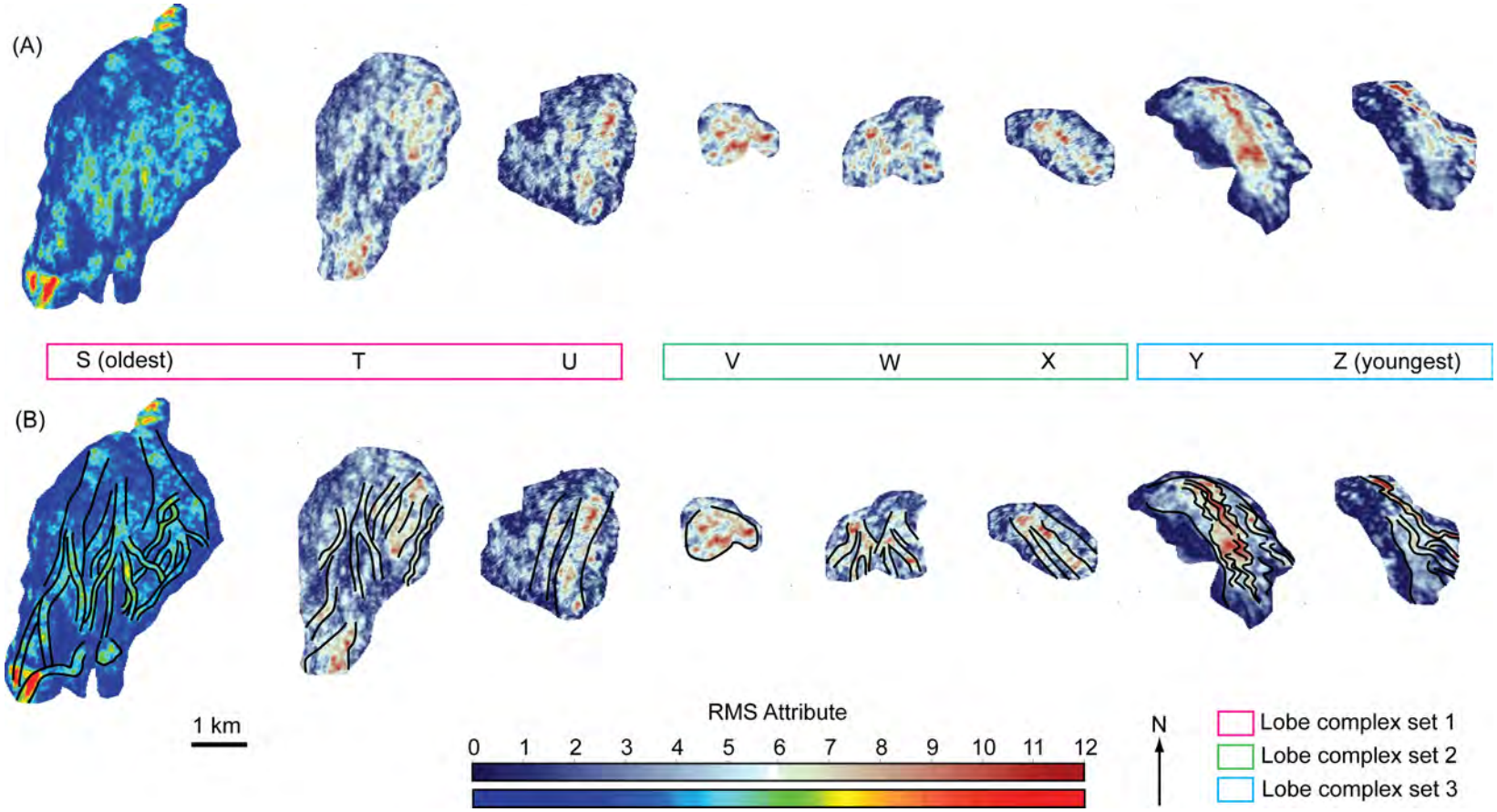


Figure 6.8: RMS attribute extraction maps superimposed on eight mapped lobeforms from 3-D seismic data. Locations of each lobeform is shown in Figure 6.7. (A) is the uninterpreted data, and (B) shows geomorphic interpretations of architectural elements including channelforms and lobes. Lobeforms are interpreted as lobe complexes, which stack into three distinct lobe complex sets: 1, 2 and 3 (LCS1, LCS2 and LCS3).

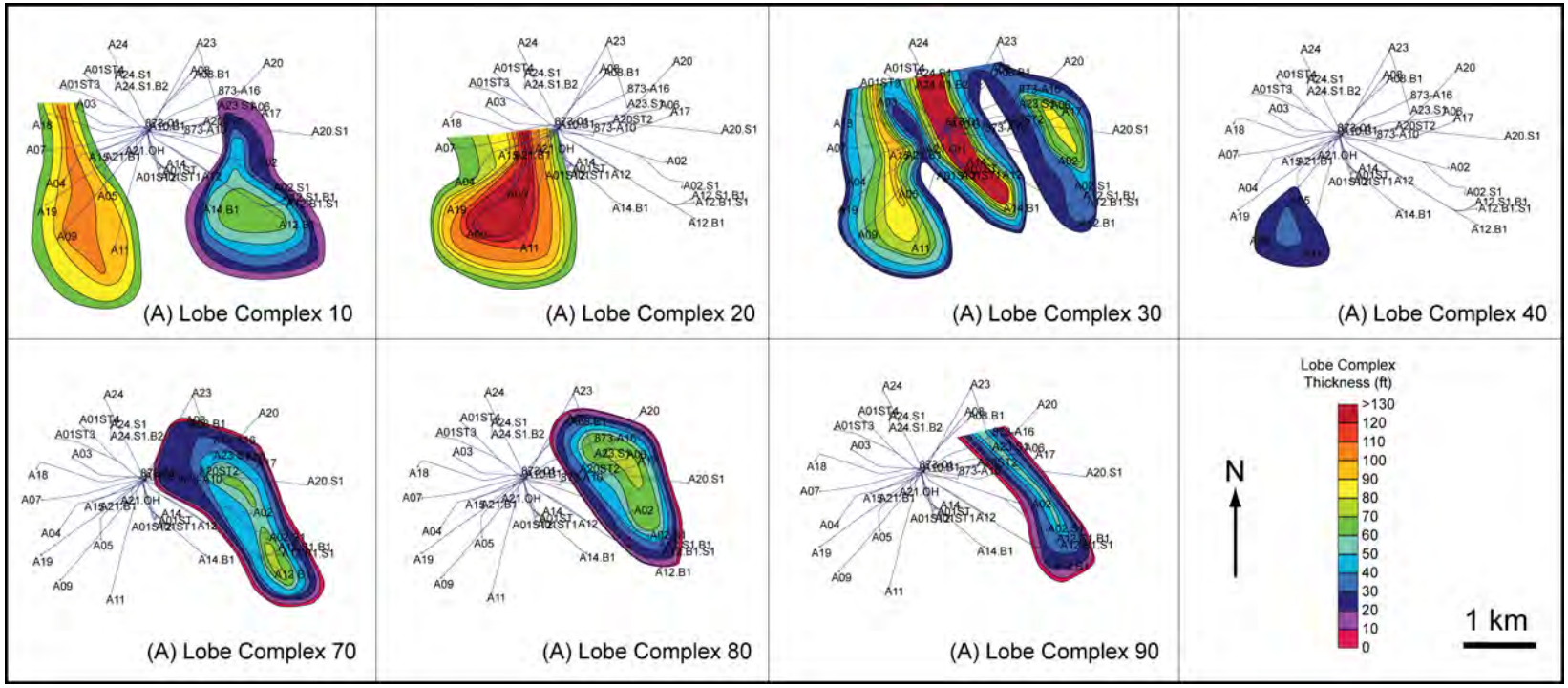


Figure 6.9: Net sand contour maps for seven lobe complex intervals in the Lobster minibasin (Lobe complexes 10, 20, 30, 40 70, 80 and 90). Maps were created from interpretations of lithology correlation from gamma-ray well logs (see appendices C and D for correlations). Contour interval spacing is 10ft.

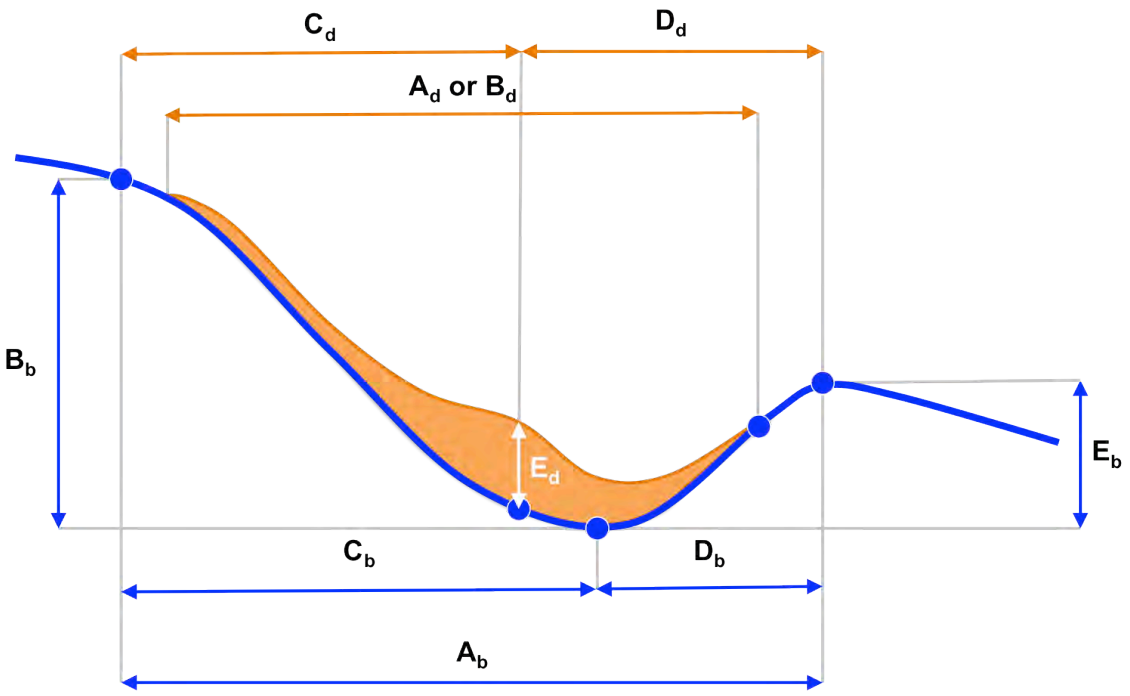


Figure 6.10: Measured basin and deposit morphometric dimensions from Series 2 experimental basins. Basin measurements include: (a) the basin length ($A_b$); (b) the height of the basin to the inlet point ($B_b$); (c) the length from the basin entry to the deepest point of the basin ($C_b$); (d) the length of the deepest point of the basin to the basin exit ($D_b$); and (e) the height of the basin to the exit point ($E_b$). Deposit morphological characteristics include: (a) The dip length of the deposit ($A_d$), the strike width of the deposit ($B_d$); (c) the dip length from the basin entry to the thickest part of the deposit ($C_d$); (d) the dip length of the deepest point of the basin to the basin exit ($D_d$); and (e) the thickness of the thickest part of the deposit ($E_d$).

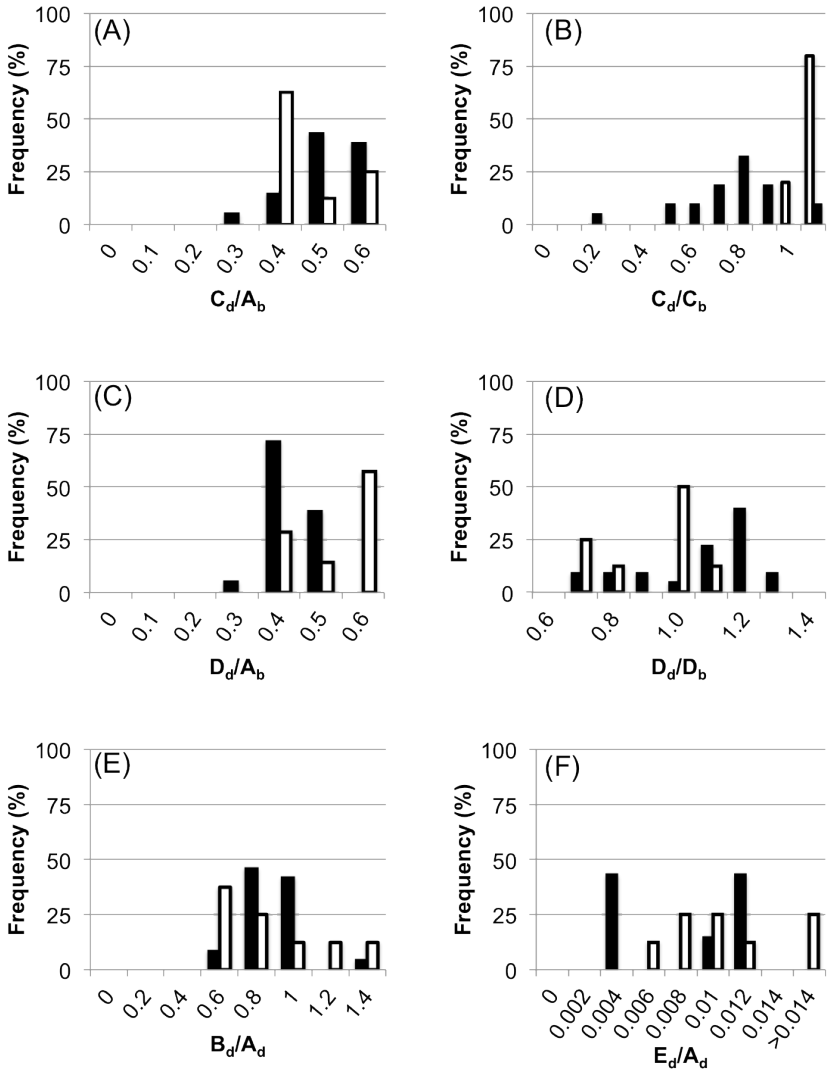


Figure 6.11: Frequency plots of dimensionless ratios of basin and deposit lengths used to establish predictive relationships (see Fig. 6.10). Solid bars show series 2 experimental data and hollow bars show Lobster reservoir interval data. (a) The distance to thickest part of the deposit relative to the length of the basin from the entry point; (b) the length ratio of the thickest part of the deposit to the deepest point of the basin relative to the basin entry point; (c) the thickest deposit from the basin exit point as a fraction of the basin length; (d) the length ratio of the thickest part of the deposit to the deepest point of the basin relative to the basin exit point; (e) the characteristic deposit width to deposit length; and (f) the most likely deposit thickness for a given deposit length.

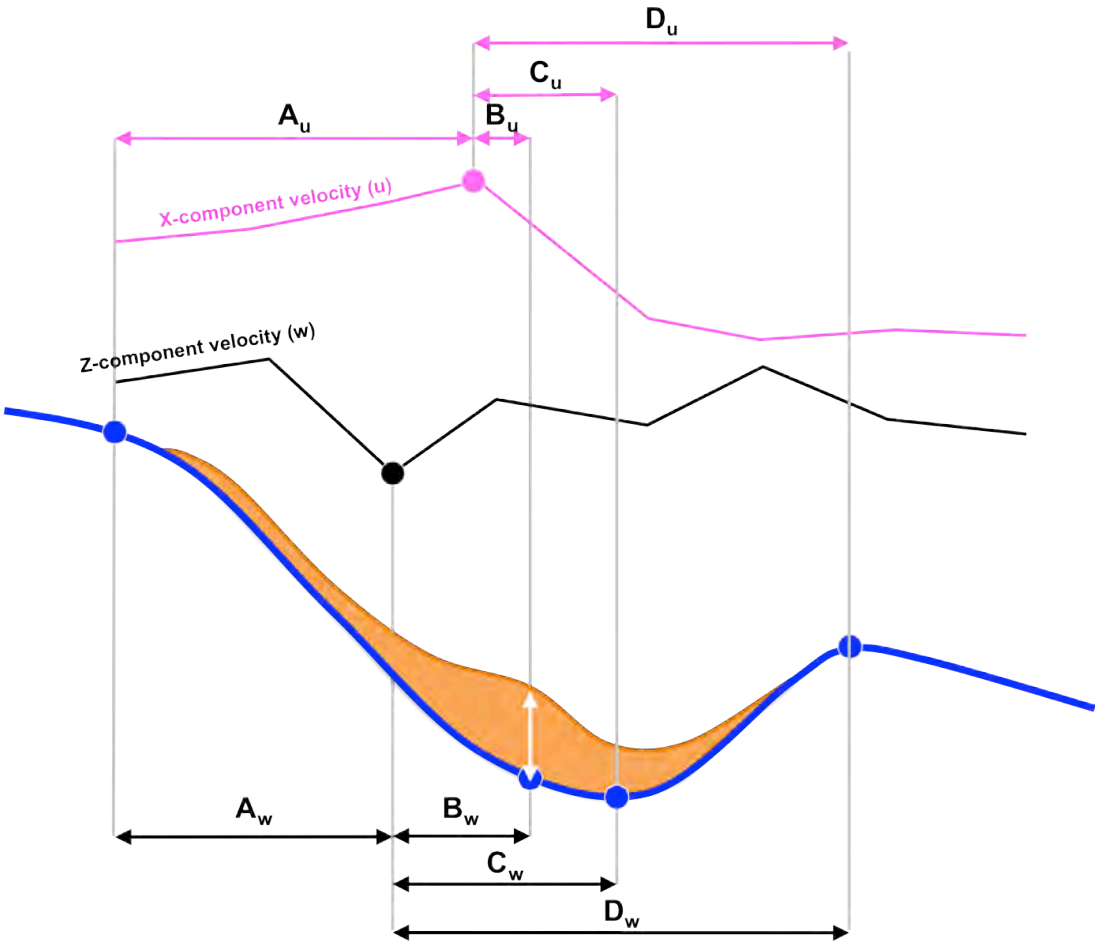


Figure 6.12: Spatial relationships between changes in near-bed velocity component data measured relative to the basin length. Basin and deposit morphological measurements relative to the point at maximum forward velocity, $u$, include (a) the distance from the entry point to maximum $u$ ($A_u$); (b) the distance from the point at maximum $u$ to the thickest deposit ($B_u$); (c) the distance from the point at maximum $u$ to the deepest point in the basin ($C_u$); and (d) the distance from the point at maximum $u$ to the basin exit point ($D_u$) Basin and deposit morphological measurements relative to the point at minimum fall velocity, $w$, include (a) the distance from the entry point to minimum $w$ ($A_u$); (b) the distance from the point at minimum $w$ to the thickest deposit ($B_u$); (c) the distance from the point at minimum $w$ to the deepest point in the basin ($C_u$); and (d) the distance from the point at minimum $w$ to the basin exit point ($D_u$).

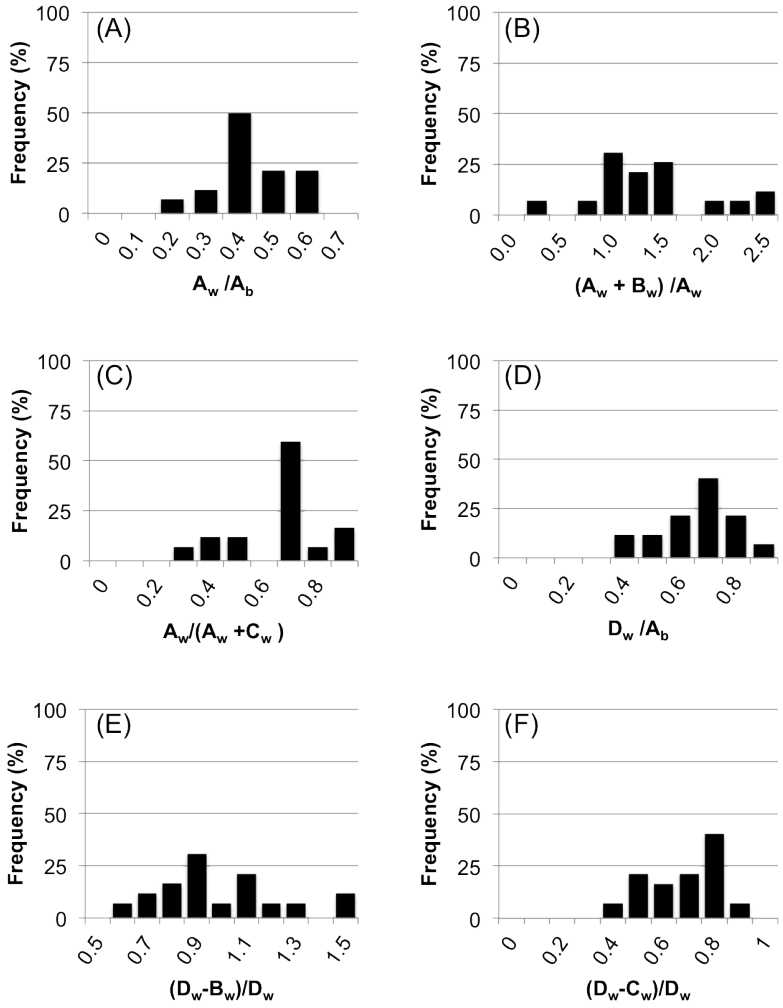


Figure 6.13: Frequency plots of dimensionless ratios of basin and deposit lengths relative to lengths where changes in near-bed fall velocity occurs (see. Fig. 6.12) derived from series 2 experiments: (a) the distance along the basin length at which the fall velocity is at a minimum relative to the total length of the basin; (b) the ratio of the distance to the point at minimum fall velocity to the distance to the point of the thickest deposit; (c) the ratio of the distance to the point at minimum fall velocity to the distance to the deepest point in the basin (d) the distance to the location where fall velocity is at a minimum relative to the entire length of the basin; (e) the ratio of the distance to the point at minimum fall velocity to the distance to the point of the thickest deposit; and (f) the ratio of the distance to the point at minimum fall velocity to the distance to the deepest point in the basin.

## REFERENCES


Al Ja'Aidi, O. S., W. D. McCaffrey, and B. C. Kneller, 2004, Factors influencing the deposit geometry of experimental turbidity currents: implications for sand-body architecture in confined basins: Geological Society, London, Special Publications, v. 222, p. 45-58.

Amy, L. A., W. D. McCaffrey, and B. C. Kneller, 2004, The influence of a lateral basin-slope on the depositional patterns of natural and experimental turbidity currents: Geological Society Special Publications, v. 221, p. 311-330.

Badalini, G., B. Kneller, and C. D. Winker, 1999, Late Pleistocene Trinity-Brazos turbidite system; depositional processes and architectures in a ponded mini-basin system, Gulf of Mexico continental slope: AAPG Bulletin, v. 83, p. 1297-1298.

Badalini, G., B. Kneller, and C. D. Winker, 2000, Architecture and processes in the late Pleistocene Brazos-Trinity turbidite system, Gulf of Mexico continental slope: Program and Abstracts - Society of Economic Paleontologists. Gulf Coast Section. Research Conference, v. 20, p. 16-34.

Booth, J. R., A. E. DuVernay, III, D. S. Pfeiffer, and M. J. Styzen, 2000, Sequence stratigraphic framework, depositional models, and stacking patterns of ponded and slope fan systems in the Auger Basin; central Gulf of Mexico slope: Program and Abstracts - Society of Economic Paleontologists. Gulf Coast Section. Research Conference, v. 20, p. 82-103.

Burk, M. K., G. L. Brown, and D. R. Petro, 1999, Evolution of the geological model, Lobster Field (Ewing Bank 873): AAPG Bulletin, v. 83, p. 1350-1350.

Covault, J. A., 2009, Growth patterns of deep-sea fans revisited; turbidite-system morphology in confined basins, examples from the California Borderland, *in* B. W. Romans, ed., Marine Geology, Netherlands, Elsevier : Amsterdam, Netherlands, p. 51-66.

Diegel, F. A., J. F. Karlo, D. C. Schuster, R. C. Shoup, and P. R. Tauvers, 1995, Cenozoic structural evolution and tectono-stratigraphic framework of the northern Gulf Coast continental margin: AAPG Memoir, v. 65, p. 109-151.

Pirmez, C., B. E. Prather, G. Mallarino, W. W. O'Hayer, and A. W. Droxler, 2012, Chronostratigraphy of the Brazos–Trinity Depositional System, Western Gulf of Mexico: Implications For Deepwater Depositional Models: SEPM Special Publication, v. 99, p. 111-143.

Prather, B. E., 1998, Classification, lithologic calibration, and stratigraphic succession of seismic facies of intraslope basins, deep-water Gulf of Mexico; errata, *in* J. R. Booth, G. S. Steffens, and P. A. Craig, eds., AAPG Bulletin, United States,

American Association of Petroleum Geologists : Tulsa, OK, United States, p. 707R-707R.

Prather, B. E., 2000, Calibration and visualization of depositional process models for above-grade slopes; a case study from the Gulf of Mexico, Marine and Petroleum Geology, United Kingdom, Elsevier : Oxford, United Kingdom, p. 619-638.

Pr*é*lat, A., D. M. Hodgson, and S. S. Flint, 2009, Evolution, architecture and hierarchy of distributary deep-water deposits: a high-resolution outcrop investigation from the Permian Karoo Basin, South Africa: Sedimentology, v. 56, p. 2132-2154.

Pyles, D. R., 2008, Multiscale stratigraphic analysis of a structurally confined submarine fan; Carboniferous Ross Sandstone, Ireland: AAPG Bulletin, v. 92, p. 557-587.

Rowan, M. G., and P. Weimer, 1998, Salt-sediment interaction, northern Green Canyon and Ewing Bank (offshore Louisiana), northern Gulf of Mexico: AAPG Bulletin, v. 82, p. 1055-1082.

Sinclair, H. D., and M. Tomasso, 2002, Depositional evolution of confined turbidite basins: Journal of Sedimentary Research, v. 72, p. 451-456.

Villamil, T., C. Arango, P. Weimer, A. Waterman, M. G. Rowan, P. Varnai, A. J. Pulham, and J. R. Crews, 1998, Biostratigraphic techniques for analyzing benthic biofacies, stratigraphic condensation, and key surface identification, Pliocene and Pleistocene sediments, northern Green Canyon and Ewing Bank (offshore Louisiana), northern Gulf of Mexico: AAPG Bulletin, v. 82, p. 961-985.

Violet, J., B. Sheets, L. Pratson, C. Paola, R. Beaubouef, and G. Parker, 2005, Experiment on turbidity currents and their deposits in a model 3D subsiding minibasin: Journal of Sedimentary Research, v. 75, p. 820-843.

Weimer, P., P. Varnai, F. M. Budhijanto, Z. M. Acosta, R. E. Martinez, A. F. Navarro, M. G. Rowan, B. C. McBride, T. Villamil, C. Arango, J. R. Crews, and A. J. Pulham, 1998, Sequence stratigraphy of Pliocene and Pleistocene turbidite systems, northern Green Canyon and Ewing Bank (offshore Louisiana), northern Gulf of Mexico: AAPG Bulletin, v. 82, p. 918-960.

Witrock, R. B., L. D. Nixon, P. J. Post, and K. M. Ross, 2003, Biostratigraphic Chart of the Gulf of Mexico Offshore Region, Jurassic to Quaternary, New Orleans, Louisiana, U.S. Department of the Interior, Bureau of Ocean Energy Management.

# Chapter 7: Paleo-geomorphologic Bathymetry in Isolated Minibasin Development as an Indication of Tectonic State


## ABSTRACT

Recent publications (Hudec, 2006; Hudec et al., 2008) have renewed discussion of minibasin formation processes and resultant deposits in basins overlying mobile substrate margins (including salt, shale, and crustal subsidence) around the world. Minibasin provinces produce enormous volumes of hydrocarbons, besides forming supramobile substrate topography that controls how sediment volumes are transferred from shelf edges to ultimate sinks in the deep ocean. Increasing exploration and production in ever-deepening regions of the world's oceans warrant a revisit to many of these concepts of accommodation development, sediment generation, sediment movement, and ultimate geometry and distribution of resulting deposits.

The objective of this study is to utilize an extensive 3D seismic data volume from the Safi Haute Mer (SHM) permit area, offshore Morocco to examine the Cretaceous through Tertiary fill of an isolated minibasin, and to investigate the effect of paleo-geomorphologic bathymetry as an indication of tectonic state within the margin. Our hypothesis is that minibasins change their fill architecture and composition in response to changes in slope, bathymetry, bottom topography, sediment sources, and structural stability. Therefore, in basins undergoing deformation, such as along tectonically active margins, under conditions of rafting or in shelf-distal locations, systematic changes in these variables should be reflected in geometry and morphology of the fill making up basin strata. Seismic attribute analysis is used to investigate the change in character of the fill through time, and the influence of regional structural features developed during the

evolution of the Moroccan continental slope is combined with our observations to develop a model for the minibasin's evolution.

A methodology is proposed to reconstruct the tectonic evolution of the minibasin by implementing observations from geomorphological and structural analysis using 3D seismic data. Results from this distal slope minibasin show that the evolutionary history can be described in four phases of structural development, the latter three of which are linked to four distinct phases of sedimentary fill. Observations noted from each stage of the analytical process are compared and contrasted to existing models of minibasin development to evaluate their validity and application in a distal, sediment-starved setting such as the lower slope of the Morocco continental margin.

## INTRODUCTION

New and more sophisticated imaging technologies have increased the interest in exploration of ultra-deep water minibasin hydrocarbon provinces, both supra- and sub-salt. However, the exploration and development of such offshore regions still remains quite costly. Important decisions pertaining to well and facilities design in these settings are often made with analogous subsurface data obtained from proximal, shallower water minibasin developments. Accurate characterization of ultra-deep water reservoirs, and subsequent resource volumes and distributions are critical to successful business ventures in these expensive and dangerous basin regions. With this being a primary driver, there is a need to revisit many of concepts of accommodation development, sediment generation, sediment movement, and ultimate geometry and distribution of resulting deposits that are prevalent in distal minibasin settings compared to proximal minibasin settings. Such

characterization is critical for making decisions regarding the sustainability preceding the implementation of such large-scale projects.

Salt basins are some of the most complex basin types because of the mobilization of underlying salt substrate and the effect that syn-tectonic and post-tectonic deformation have on the overlying sedimentary strata. However, the sedimentary fill in these minibasins is a function of the balance of sedimentation and accommodation. Therefore, it stands to reason that the phases of local and regional structural-induced accommodation development (i.e., salt inflation and deflations, compression, extension, etc.) should be accompanied by a unique expression in the geomorphic framework of the basin fills. Through improved understanding of the fill histories within minibasins, we can improve our knowledge of how these basins form and the processes that influence their fill, as well as improve our estimates of the timing and the volumes of sediment which make their way to the deep ocean seafloor.

The offshore Moroccan salt basins of the northwest African margin (Figure 1) are an excellent locality to test this hypothesis of the linkage between unique geomorphologic character of fill and basin accommodation history. This margin contains strata that record the tectonics and sedimentation of the regions since the Triassic, including the record of the initial rifting and development of the Atlantic Ocean. The present-day margin is structurally complex and contains diverse and extensive salt structures.

This study is focused on combining techniques in seismic geomorphological analysis and structural analysis to reconstruct the evolutionary history of a minibasin located within the SHM 3D seismic dataset in the Essaouira segment of the Moroccan

continental margin (Figures 1 and 2). The basins of onshore western Morocco have proven to be prolific hydrocarbon provinces. The Essaouira Basin is particularly productive and is the most important oil-producing basin in Morocco (Broughton and Trepaniér, 1993; Morabet et al., 1998). In the onshore portion of the basin, seven fields have been discovered, with six producing from Jurassic and one from Triassic reservoirs (Davison, 2005). Lithologic data available for this study is relatively limited. To date, only 28 wells have been drilled offshore of Morocco; all of which are restricted to the shelf. The nearest direct subsurface stratigraphic records are from Deep Sea Drilling Project (DSDP), Leg 50 boreholes drilled in 1976 in water depths ranging from 2794 to 4191 m (9167 to 13750 ft) (Lancelot and Winterer, 1980a) (Figure 1). The onshore portions of the western Moroccan basins have been extensively studied (e.g. Hafid et al., 2000). Exploratory wells and outcrops of Mesozoic strata are abundant (Lancelot and Winterer, 1980b). Wells drilled onshore and on the shelf provide insight into macro-scale regional subsurface stratigraphy, but higher-resolution deepwater stratigraphy remains largely unknown because of the lack of available information within these frontier deepwater regions. Previous studies are solely based on interpretations using 2D seismic lines. The paucity of data limits the detail to which the evolution of the salt margin can be reconstructed. The 3D survey used in this research allows us to study the three-dimensional architecture of the sedimentary fill and the morphologies that characterize the fill episodes. These documented phases can be then linked to a tectonic history of basin evolution.

## MODELS OF MINIBASIN DEVELOPMENT

Although several global examples of minibasin provinces exist, models of minibasin development are dominated by Gulf of Mexico examples, principally the Booth et al. (2000) model, also known as The "Fill and Spill" Model. This model suggests a process dominated by sediment-driven-subsidence accommodation tied to eustatic sea-level changes along the margin. In this model, developed principally through work in the Auger and Macaroni basins in the Gulf of Mexico, Booth et al., (2000) defined five phases of minibasin development. These include (a) healing phase in intra-slope sinks; (b) ponded phase sheets in distal sinks; (c) bypass of channel and overbanks; (d) gorge system development and bypass to more distal sinks; and e) normal faulting in proximal slope with footwall fills. Similarly, Sinclair and Tomasso (2002) attempted to define a simplistic model for confined turbidite basins by incorporating outcrop data from upper slope Tertiary Alpine basins with subsurface data from the Gulf of Mexico. They concluded that the progressive infill of confined turbidite basins can be characterized by four phases: (a) flow ponding, where incoming flows are totally trapped; (b) flow stripping, where the finer, more dilute portion of the flow is able to escape over the confining topography; (c) flow bypass, either by flows traversing over the filled basin or by switching of feeder channels away from the basin; and (d) Blanketing, of the basin and surrounding topography due to base-level rise. Wood (2006) suggested that such a process might vary dramatically in the more distal minibasin systems of the Gulf of Mexico, where basins are farther removed from the influences of eustatically-driven shelf edge sediment supply changes (Figure 3). Similar things can be said for the minibasins along the western Moroccan slope, where the influence of large terrigenous sediment

supplies is suspect. Evidence from the Tertiary section of the SHM dataset shows that sediment supply in the sediment-starved Moroccan continental margin may be attributed reworking due to bottom currents. In addition, gravity–driven subsidence models propose successive basinward migration of subsidence and accommodation. More complex accommodation scenarios in more distal settings generate more complex accommodation and sedimentation histories, and require new models (sensu Montoya, 2007).

## GEOLOGY OF THE WESTERN MOROCCO CONTINENTAL MARGIN

### Regional Geology

The geology of the continental margin is relatively similar along the northwest African Atlantic margin, with syn-rift continental clastics, carbonates and evaporates overlain by Cretaceous and Tertiary clastics (Hafid et al., 2000) (Figure 4). Major tectonic events influencing the development and evolution of the margin include the Devonian to Westphalian-age Hercynian orogeny, the rifting of the central Atlantic and the late Cretaceous and-Miocene Alpine orogeny.

In the study area, basement rock is made up of metamorphosed, foliated Paleozoic rocks that were sutured onto the African craton during the Hercynian orogeny (Heyman, 1989). Wells from onshore Morocco basins show that the western continental basement is composed of Precambrian schists, limestones and dolomites (Le Roy and Piqué, 2001). At the end of Hercynian orogeny, the Paleozoic basement rocks were uplifted and eroded. The onset of rifting in the Triassic was contemporaneous with adjacent onshore rifts (Lancelot and Winterer, 1980b; Hinz et al., 1982; Heyman, 1989; Davison, 2005). Crustal thinning and clastic red-bed deposition was associated with rifting, which was facilitated

by normal listric faults striking north-northeast to south-southwest (Heyman, 1989; Medina, 1995). Movement along the normal listric faults created a series of half-grabens in which substantial thickness of syn-rift continental clastics were deposited (Heyman, 1989; Davison, 2005).

A major magmatic event created a magmatic province known as the Central Atlantic Magmatic Province (CAMP), which occurred in a 1 My period with dykes, lavas and plutons occurred along the whole Central Atlantic margin at 200 Ma (Hames et al., 2003). The magmatism occurred approximately 25 My after rifting began and may have been the result of a plume channeled along a thinned lithosphere (Davison, 2005). Evaporites occur within and above the basalts, suggesting no uplift associated with the magmatism (Davison, 2005).

Continued extension allowed seas to flood the structural lows created by the half-grabens, probably from the north (proto-Atlantic) and east (Tethys) (Heyman, 1989). A restricted marine environment was created, and evaporite deposition began. Evaporite distribution was controlled by infilling structural lows created between pre-Mesozoic basement highs (Tari et al., 2000). Precipitation of evaporites along the margin continued into the Early Jurassic. Davison (2005) estimates the original salt thickness to have exceeded 1.5 km in the region of offshore Morocco, and the rate of salt deposition to have averaged about 1 mm/yr. Further extension and subsidence led to an open communication with the Tethys Sea to the east and finally to the development of open marine conditions.

During the Bathonian, ocean opening began and proceeded from south to north (Heyman, 1989). The spreading of the Atlantic Ocean during the Jurassic allowed the

initiation and development of a carbonate system along the newly formed margin. Continued carbonate deposition led to deformation and diapiric rise of the underlying evaporites (Figure 4). Jurassic carbonate reef deposition continued until the early Cretaceous, when a global sea level fall ended carbonate deposition offshore (von Rad and Sarti, 1986). Prograding deltas deposited a thick sedimentary wedge of clastics across the Jurassic platform (Heyman, 1989) and loaded the underlying carbonates and evaporites. The rapid sedimentary loading caused growth faulting and further deformation of the underlying evaporites (Mehdi, 2004). By the Late Cretaceous, clastic influx had decreased, and deep-water muds and marls were deposited offshore (Heyman, 1989). Upper Cretaceous strata are condensed at DSDP Sites 415 and 416 (Vincent et al., 1980). A major hiatus depleted all record of the Cretaceous-Tertiary boundary and was followed by several periods of erosion or non-deposition during the Cenozoic (Vincent et al., 1980; Lancelot and Winterer, 1980a; Hinz et al., 1982).

The Alpine orogeny began during the Late Cretaceous (Lancelot and Winterer, 1980b; Ellouz et al., 2003; Züheke et al., 2004) and continued into the Late Tertiary. During the Alpine orogeny, inversion and right-lateral shear occurred along the Mesozoic rifts and produced the Atlas Mountains (Morabet et al., 1998; Beauchamp, 1999). Rafting, triggered in the mid-Cretaceous, resulted in extensional features below the shelf that grade into compressional features near the lower continental slope. Consequently, an Upper Cretaceous rejuvenation of salt diapirism in the lower continental slope areas is observed. The onset of Alpine uplift of the region is thought to be the cause of large-scale gravity sliding during the Late Cretaceous (Price, 1980). DSDP Hole 415 penetrated a 450 m (1476 ft) Upper Cretaceous allochthonous unit (Price, 1980). The apex of the

allochthon coincides with the strike continuation of the Atlas tectonic trend and the areal extent of the deposits is estimated to be at least 10,000 $km^2$.

The present-day structural configuration of the Moroccan margin is illustrated in Figure 5. Both seaward and landward dipping normal listric faults are prominent in the region and form half-grabens bounded by east-west striking transfer faults. The South Atlas Fault Zone is to the south and the Gibraltar Fracture Zone is to the north. Hafid et al. (2006) show many strike-slip, reverse faults in the Tafelney Plateau area of the Essaouira Basin. A study by Le Roy and Piqué (2001) of profiles derived from seismic along the margin confirms the structural framework of the margin (Figure 6).

**Physiographic Setting**

The offshore basins of Morocco's Atlantic margin represent the westernmost exploration frontier area in North Africa (Tari et al., 2000). Morocco contains the largest offshore exploration area in North Africa, covering an area over 300,000 $km^2$ (115, 831 $mi^2$) on both the continental margin and deepwater provinces. The study area is located in the northern offshore portion of the Essaouira Basin, also referred to as the Safi sub-basin (Tari et al., 2003a). The physiographic setting of the study area puts it the base of the Moroccan continental rise, near the western termination of the Atlas fold-belt (Figure 7). The width of the Moroccan continental shelf ranges between 40 to 60 km (25 to 37 mi), and the shelf break usually occurs at water depths of 110 to 150 m (361 to 492 ft) (Seibold, 1982). The complex geological history of the margin has been responsible for several large-scale events, all of which include the mobilization of Jurassic salt, regional-scale mass-wasting deposits and reworking of strata. The resulting morphology makes the Moroccan continental margin topographically complex and influences the sedimentary

processes that occur in the study area. The continental slope exhibits a range in gradient between 1-6 degrees, and transitions into the continental rise at water depths of 1500 to 4000 m (4921 to 13123 ft) (Seibold, 1982).

Prominent bathymetric features near the study area include the Essaouira Canyon immediately north of the survey, the Tafelney Plateau to the southeast, and the Agadir Canyon to the south (Figure 7). The Essaouira Canyon empties onto the Seine Abyssal Plain and is one of the many canyons dissecting the continental slope. Because of its proximity to the study area, the Essaouira Canyon has likely transported sediments eroded from the survey area. The Tafelney Plateau is interpreted as a high-relief accommodation zone inherited from the rifting stage of the central Atlantic basin (Tari et al., 2002). The topographic high has a tectonic history involving Mesozoic extension, Late Cretaceous inversion and Late Tertiary doming (Hedley and Warburton, 1999). The Agadir canyon extends from the shelf break to the upper rise to a water depth of at least 3200 m and separates the Tafelney Plateau from the North Tarfaya margin to the south (Seibold, 1982).

**Previous Work**

Few publications specific to the study area exist with the exception of those done in recent years using data available through recent industry activity. Publications by Tari et al. (2000, 2001, 2003a, 2003b) use the 3D survey acquired in 2000 to compare styles of salt tectonics of Morocco with those of other basins along West Africa and the Gulf of Mexico.

Weisenburger (2007) provides an excellent overview of the existing work done within the study area, and documents the author's own sub-regional-scale analysis of the

morphology of the lower continental slope. He primarily focuses on determining the emplacement history of allochthonous salt structures and examines regional-scale temporal changes in the interaction of structure and sedimentation. Structural restorations and isopach maps of Jurassic through Tertiary strata prove to be key elements in demonstrating the evolution of the margin.

## DATA AND METHODS

The 3D seismic dataset used for this study is the result of re-processing two overlapping surveys in the offshore Safi Haute Mer (SHM) block, offshore Morocco. It is industry-collected and processed data. One survey covering 3025 $km^2$ (1168 $mi^2$) was acquired in 2001 in the SHM and Ras Tafelney permit areas. The northern 400 $km^2$ (154 $mi^2$) of that survey was reprocessed and merged with a second, more recently acquired 3D survey shot in 2005 that covers 719 $km^2$ (278 $mi^2$). The 3D seismic survey used in this study covers an area of 1064 $km^2$ (411 $mi^2$) in the lower continental slope between 31.99682° N and 31.41798° N and between 11.30082° W and 10.54431° W (Figure 2). The extent of the survey ranges in water depths of 1200 m (3937 ft) in the southeast to 2800 m (9186 ft) in the northwest.

Exploration drilling in the Essaouria Basin has been limited to on-shelf shallow water and to the active onshore program in the eastern part of the basin. Therefore, no deterministic well control exists for defining the age of the section of interest or relationships between seismic data and lithology (Dunlap et al., 2010). Access to data from Deep Sea Drilling Project (DSDP) boreholes from leg 50 drilled in 1976, however, provide insight into the overall stratigraphy within the abyssal plains near the study area (Figures 1 and 4). DSDP Borehole 416 in a water depth of 4191 m (13750 ft) (Lancelot

and Winterer, 1980a) is located approximately 100 km north-northwest of the study area. The maximum depth achieved at site 416 is 1624 m (5328 ft) sub-bottom and the oldest strata encountered were Upper Jurassic (Kimmeridgian–Tithonian) distal turbidites. The stratigraphy encountered at this drill site comprised deep-water turbidite sands, gravels and siltstones, and pelagic muds, marls and chalk. DSDP Borehole 415 in a water depth of 2794 m (9167 ft) (Lancelot and Winterer, 1980a) is located approximately 85 km (53 mi) southwest of the study area. The maximum depth achieved at site 415 is 1080 m (3543 ft) sub-bottom, and the oldest strata encountered are Albian in age. These wells both show that sandy turbidites were moving through the more eastward slope minibasins during the Tertiary.

We mapped 16 key surfaces within the isolated minibasin fill using the 3D seismic data volume. Although horizon ages were not determined, their relative positions in the stratigraphy of the minibasin fill is used to compare the geometric relationships within and among the fill intervals that each horizon defined. Additional proportional slices were generated between each of the 16 key surfaces, and usually conform to the vertical resolution of seismic data (~20ms). The subsequent investigation into the fill and structural evolution of the minibasin is three-fold. Firstly, geometry of the large-scale seismic packages is defined base on criteria that include seismic reflection relationships along the base and top of each package, as well as overall geometry, seismic wavelet reflectivity and continuity. The geometry of these packages can be used to infer the paleo-water depth of the basin center relative to the basin margins. Horizons bounding these major packages are mapped and used to flatten fill packages and to guide proportional slicing of the fill for seismic attributes analysis.

Secondly, isochore maps and reflection amplitude maps, including root-mean-squared (RMS) amplitude extractions are used in analysis of the geomorphologic elements that characterize these stratigraphic intervals. Isochore maps are created to investigate the changes in spatial fill thickness, which is an indicator of shifting depocenters and localized accommodation development throughout the life of the minibasin. Localized accommodation development can be then linked to geomorphologic elements within the fill package. Proportional horizon slices, guided by package bounding surfaces are created within fill packages and geomorphic features are sketch mapped (for more discussion, see Wood, 2007). The size and orientations of geomorphologic features relative to size and geometry of receiving basin are also noted.

Thirdly, a traditional model of salt movement and structural history of the surrounding sediments is constructed and the geomorphologic observations made in sequential fill packages are interpreted within the context of a traditional model of salt history (i.e., Weisenburger, 2007). These observations are ultimately used in tandem to reconstruct the minibasin's evolution, a reconstruction made all the stronger for the integration of geomorphology of the fill with the classic structural history.

## SEISMIC GEOMORPHOLOGY

### Seafloor Geomorphology

A variety of allochthonous salt structures can be seen in the SHM seismic data, with a large number occurring near the edge of the salt basin. Figure 1 shows the distribution of these salt structures in map view. The seafloor over the study basin shows a startling degree of rugosity with the presence of minibasins, raised basin rims, and

linear canyons with hanging valleys slumping sediments to the north, as well as mass transport processes active in more western portions (Dunlap et al., 2010) (Fig. 7.8a,b). The seafloor map shows the fill within the study minibasin to host extensional cracks, evidence of presently active subsidence. Based on the abundant truncation seismic reflection geometries within the Tertiary section preserved in the SHM dataset, it is evident that reworking of the slope material was dominant due to the structural reconfiguration of the margin relative to the poorly established sediment delivery system from a terrigenous source. Slope instability and shallow allochthonous salt movement are thought to be the result of crustal-scale tectonic activity since the Late Cretaceous (Price, 1980).

**Structural Morphology of the SHM Minibasin**

A large circular feature on the seafloor in the proximal portion of the survey is the surface expression of a salt withdrawal minibasin that is the focus of this study (Fig. 7.8b). The bathymetric feature has a lowered rim and a lowered center with linear features cutting the surface. Other depressions on the seafloor also have shapes characteristic of shallow salt withdrawal suggesting that salt continues to move up to the present day.

The study minibasin preserves the thickest Tertiary strata (3km) within the larger slope imaged by seismic (Fig. 7.8c). The minibasin is sub-circular in map view and measures eight kilometers in diameter. The lack of well data within the study area makes it difficult to determine the age of the oldest strata preserved in the minibasin. In our investigation, the similarity of geomorphic features in the oldest package suggests that these strata may be Albian in age, although Weisenburger (2007) believed that the

minibasin primarily comprises Tertiary strata. Assuming uniform salt withdrawal and deposition rates, three kilometers of sedimentary fill since the Albian would require 30 m/My of sedimentation and salt withdrawal. This rate of sedimentation would be relatively high.

Observations from our analysis of the minibasin fill suggest that as the basin's topography is progressively infilled, paleo-bathymetric highs along the eastern, western and southern flanks of the minibasin became less of a barrier to through-going sediments. There also appears to be a consistent input for sediments along the northern flank of the minibasin that persists throughout the minibasin's evolution.

Vincent et al. (1980) reports a major depositional hiatus at both DSDP Sites 415 and 416 at the Cretaceous-Tertiary boundary lasting approximately 40 My. It is assumed that the hiatus lasted throughout most of the Cretaceous since Lower Paleocene sediments were found at both sites. At Site-416 another unconformity representing approximately 1 My was found at the Pliocene-Pleistocene boundary, whereas at Site-415 the Pliocene-Pleistocene sequence is apparently continuous. Using the data in Price (1980), Tertiary sedimentation at Site-416 averaged 10.5 m/My (34 ft/My), and 17 m/My (56 ft/My) at Site-415. It can therefore be established that the deposition rate within the subsiding minibasin was two to three-times faster than areas unaffected by salt withdrawal.

Structural features bounding the basin are also illustrated in Figure 8c. Salt welds are associated with these bounding structural features, and become an important factor for determining the causal mechanisms through which the minibasin evolved. Normal faults bound the southeast portion of the basin and appear to be associated with extensional strain associated with the evacuation of salt during the evolutionary life of the

minibasin's development. In the northwest, overturned Albian beds bound the basin. The overturned beds appear to be semi-rigid and do not display any internal deformation that may be associated with compression. Most of the minibasin fill onlaps onto these overturned beds. To the east, a thrusted anticline is associated with compression and uplift of the minibasin margin.

## Character of the Minibasin Fill

### *Fill Geometries*

Observations and mapping of the minibasin fill shows the presence of four types of fill geometries, a) ponded; b) draped; c) wedged and d) complex fill (Fig. 7.9). Ponded fill patterns display terminal onlap of seismic reflectors with relatively higher taper rates. Unlike the high-amplitude ponded seismic facies defined by Prather et al., (1998) from Gulf-of-Mexico data, the amplitude character of this facies is not always high amplitude. Draped fill geometries tend to "drape" underlying fills and surrounding uplifted walls. These fills are relatively consistent in their thickness when compared to the aforementioned ponded or the later discussed wedge fills. These geometries are usually associated with steady state sedimentation in minibasins with either low bathymetric relief or little syn-depositional change in bathymetry. Wedged fill geometries display thinning onlap and relatively low reflection taper rates. Unlike ponded fills whose reflections end abruptly at the basin's margins, reflections associated with wedged fill phases thin gently onto the margin of the basin, suggesting steady state subsidence accommodation during deposition. Lastly, complex fill patterns are a heterogeneous, multi-phased fill that comprises multiple episodes of cut and fill. On rare occasions they

may also be related to gravity-driven events triggered by a relatively rapid change in slope associated with boundary instability. They are usually localized within other fill packages, unless events cover the extent in which accommodation is available. Each of these fill types stack in systematic and repetitive sequences designed to fill negative bathymetry produced by a variety of tectonic mechanism; i.e., thrusting, wall inflation, gravity subsidence. Each fill geometry type is believed to show a characteristic suite of morphologic elements, whose occurrence are controlled by variables intrinsic to the condition of the minibasin at the moment of that fill geometry development. For example, ponded fill patterns are usually associated with steep inter-basin bathymetry. Geomorphologically they contain unleveed channel incisions and fans appear to be restricted to the boundaries of the minibasin. External forcing elements may include surrounding salt massif uplift and high-energy sediment flows from wall regions.

***Fill Packages and Cycles***

Sixteen regionally conformable horizons (mb_1 to mb_16) mapped within the minibasin fill mega-sequence bound fifteen fill sequences associated with cyclic infilling of the minibasin from the Middle Cretaceous to Recent (Fig. 7.10). Using this framework, we can infer that at least 15 depositional episodes shape the basin fill. Within the minibasin province, eight cross sections (A to G) are analyzed to demonstrate the seismic character of fill packages, accommodation trends and nature of stratigraphic terminations within the minibasin (Fig. 7.11a). For purposes of keeping this paper concise, we have graphically reproduced one that demonstrates the majority of geometric elements that are consistent throughout the study area (Fig. 7.11b).

Based on a systematic review of the fill geometries within the minibasin, it appears that cycles stack most typically in the order of ponded followed upward by wedged followed upward by draped geometric packages. Ponded-fill geometries usually form the basal phase of a sequence with some exceptions and draped phases form the termination phase of a cycle. Wedged-fill geometries exist in cycles where active subsidence is concurrent with sediment deposition. Draped-fill geometries mark a sequence of events that involve the initiation of salt massif uplift and/or shutting-off of sediment supply. Complex fill geometries are usually localized and are a rather inconsistent part of these cycles of fill. Regardless of where sediment is being supplied from at the larger basin's shelf edge, the mechanisms creating accommodation (thrusting, compressional uplift, isostatic subsidence, etc.) in a distal setting such as this, appears to be the primary control on the fill geometries within the minibasin.

Within the fill sequence, eight truncation events were identified following a review of the reflection terminations. This has led us to believe that eight major truncation events are established within the basin fill mega-sequence, most of which appear to be related to changes in minibasin topography and slope (Fig. 7.11b). Unlike some deep-water basins where major amplitude changes across these truncation surfaces herald the onset of high-amplitude reflectors (interpreted coarser-grained sediment), in this minibasin, little change in amplitude character is seen across these erosional boundaries. This continuity of amplitude character across erosional boundaries suggest little driver of sea level or sediment supply changes influencing these cycles. Draped-fill geometries usually succeed the eroded strata and reflectors tend to be low-amplitude and continuous in character; however, there is a single exception to this observation. An

erosional event post mb_7 is striking in that the succeeding three fill intervals are characterized by high-amplitude fill that pond and onlap onto the underlying erosional surface (Fig. 7.11b). With the exception of the previously described high-amplitude interval, horizons mapped within the minibasin fill sequence coincide with the end of drape episodes.

The individual geometric fills of the minibasin can be grouped into four separate large-scale fill packages based on the character and geometry of seismic reflectors. Package 1 is unique in that it comprises the lower fill (mb_1 to mb_3), which, unlike the subsequent packages, contains relatively high-amplitude reflectors that onlap the present day minibasin center, and not the minibasin fringes. Package 2 (mb_3 to mb_7) contains sequences that display ponded-wedge-draped fill sequences, each generally displaying continuous, moderate- to low-amplitude reflectors. Package 3, (mb_7 to mb_10), comprises a series of ponded and complex geometric fill phases. Seismic reflectors in this interval are heterogeneous and display high reflector intensities. The high impedance contrast among reflectors is unique to this particular interval, and may have implications for interpreting the fill lithologies within these intervals relative to other large-scale packages. The geometries of these reflectors pond onto the minibasin flanks and draping are largely absent. The fourth large-scale package, Package 4, comprises the upper fill (mb_10 to mb_16), and displays relatively continuous, moderate- to low-amplitude reflections with occasional isolated, chaotic, variable-amplitude-reflector packages within the lower portion of the package.

### *Accommodation Distribution*

The thickness of sediment packages in the minibasin under study is a function of sediment supply and accommodation available at the time of deposition. In a deepwater setting, accommodation can be generated by a variety of mechanisms, including subsidence and uplift, and intrinsic processes of compensated deposition and compaction (localized sediment loading). However, the thickest intervals of the fill within the SHM minibasin tend to correspond to areas where accommodation was created through salt evacuation. Likewise, areas preserving thin sediments tend to correspond to the location of paleo-highs associated with salt-inflation or compressionally induced uplifts.

The locus of sedimentation is usually associated with the point of maximum accommodation (deepest point on a reflector when the horizon above is flattened) in strike section, assuming sediment sources into the study area are consistently from the north and northeast. Similarly, seismic reflectors tend to be of higher amplitude reflectivity at these points relative to their equivalent intervals on the minibasin flanks. Isochore maps provide a birds-eye perspective on the distribution of sediments and point of maximum accommodation within each stage of basin fill (Fig. 7.12). These maps show distinct changes in basin fill morphology occurring post-mb_3 and again post-mb_7. These events sub-divide the entire fill sequence into four phases of fill development. The existence of these four phases suggests a complex relationship among slope, bathymetry, sediment sources, and structural stability through time. Each phase is treated as four independent "fill packages" in the subsequent seismic attribute analysis and discussion sections of this paper (Fig. 7.13). Trends established by observing the spatial and

temporal changes in accommodation in cross-section and plan view are combined with seismic attribute analysis, to develop an integrated model of minibasin evolution.

**Seismic Attribute Analysis**

Proportional (stratigraphic) slices guided by basal and upper surfaces bounding individual geometric packages allow us to extract geomorphologic data from intervals of interest (Fig. 7.10b). RMS amplitude extractions within a window of twenty milliseconds above and below each slice enable us to image the amplitude patterns associated with that specific time-interval of the minibasin fill and map the temporal changes in depositional morphology that characterize the minibasin's fill. The morphologic character of these fill phases can be linked to previously described accommodation trends to interpret controls on the geomorphologic nature of the fill. The geomorphic character of the fill is discussed here within the framework of the four phases of minibasin fill described in the preceding discussion of Fill Packages and Cycles. Within each major package of basin fill, changes in geomorphic features are described.

***Morphology of Package 1 (mb_1 to mb_3)***

An RMS extraction on a stratigraphic slice within Interval 1 (between horizons mb_1 and mb_2) (Fig. 7.14) shows a thin preserved interval of moderate to high-amplitude fill concentrated on the northern and southern fringes of the present-day minibasin that appears to be locally sourced. The fill propagates perpendicular to regional dip. Strong positive RMS amplitude anomalies in the southern limits of the minibasin coincide with areas of high accommodation from our previous analysis of this interval (Figs 12 and 13). Poor data frequency content at depth limits seismic imaging of the

internal structure of these deeper geomorphic elements. Accommodation trends shown previously in Figure 13 indicate that these deposits coincide with the points of maximum accommodation during the early stages of minibasin development. The initial fill of the minibasin contains the relatively low-amplitude, ponded fill that indicates active subsidence during this period of minibasin development.

***Morphology of Package 2 (mb_3 to mb_7)***

The point of maximum accommodation changes to the central portion of the minibasin post-mb_3 and remains in this configuration for the rest of the life of the minibasin (Fig. 7.13). This event defines the initiation of the second interval fill within this Package and corresponds to a major structurally influenced event in the development of the minibasin. RMS amplitude extractions within these intervals show significantly different amplitude architecture than the previous sub-interval, in that elongate, low-amplitude anomalies are preserved (Fig. 7.15). These anomalies appear strike-oriented, and are regularly spaced among each other. They trend perpendicular to regional dip, but are strike-oriented relative to the local dip that existed in the minibasin. We interpret this change in character to be associated with reworking by ocean-bottom currents, creating morphologies resembling sediment waves. A comparison of similar morphologies observed in deeper sections of the SHM dataset is later discussed.

***Morphology of Package 3 (mb_7 to mb_10)***

In the third major package of fill development, a significant increase in reflector amplitude intensity is characteristic of the three sub-packages succeeding the post-mb_7 unconformity. Ponded fill geometries dominate this period of development; however,

isolated areas of geometrically complex fill do occur, usually associated with changes in bottom topography as accommodation space is filled. RMS amplitude extractions performed on proportional slices also reveal a significant change in the geomorphic character of deposits (Fig. 7.16). Large-scale, through-going channelforms are the dominant morphology recognizable in the three, high-amplitude fill sub-packages. The RMS amplitude response of the channelform features is higher than the surrounding sediment, and channelform boundaries are clearly discernible. In all cases, there appears to be uniformity in flow direction, from north to south. In cross-section, these features display heterogeneous, high-amplitude geometries with multiple episodes of reflector truncation. Individual channelform widths increase from the north to south, and range between 200-500 m. Channelform orientations are perpendicular to regional dip and bypass the minibasin center continuing to locations southward, beyond the minibasin walls. These features are interpreted as deepwater channels, which act as localized sediment delivery systems into areas of relatively higher accommodation within and adjacent to the study area. The existence of such through-going deepwater channels suggests some degree of linkage in the delivery of sediment among the surrounding areas (from the north to south) relative to intervals comprising primarily draped- and wedged-fill geometries.

An RMS extraction on a proportional slice within mb_9-to-mb_10 interval (Fig. 7.17) also shows large-scale, through-going channelforms present in the minibasin during this time, but the channelforms do not appear to be as isolated as the interval previously described. Their amplitude responses are not as high as the previously described interval, and their boundaries are not as clearly discernible. A relative decrease in sinuosity of the

channelform features is also observed, and the density of channelforms increases. Like the previously described interval, channelforms do, however seem to bypass the minibasin depocenter. Individual channelform widths within the mb_9-to-mb_10 interval remain constant from north to south and the cannibalizing nature of the channelform features within this interval makes it difficult to measure the true width of individual channelforms. The maximum channelform width measured on this attribute slice is 600 m (1969 ft). This change in character is interpreted as the fill transitioning into a more highly amalgamated "sheet-like" unit from the previous system. We interpret this interval to represent an increase in deepwater channel development associated with an increase in the regional gradient. The increased efficiency of sediment delivery toward the south beyond the minibasin locality suggests increased linkage and a larger sedimentary delivery system in the lower slope. As accommodation is progressively filled, we observe the reestablishment of primarily draped geometries and a decrease in amplitude character within the basin's fill. It is possible that the change in seismic facies is caused by a change in depositional process and the type of sediment delivered to the basin, but the lack of well data inhibits the ability to develop the interpretation.

***Morphology of Package 4 (mb_10 to mb_16)***

The fourth and final major package of fill development within the minibasin is characterized by a relatively rapid change in fill pattern and depositional character following the mb_9-to-mb_10 interval. Cross-sectional seismic patterns in Package 3 are usually draping. These draped fill geometries display low-amplitude with relatively semi-continuous to continuous seismic reflectors continuity. There does appear to be some variability of intensities depending on the morphology of the seismic features. However,

unlike the second package of fill development, these features tend to be more localized and ephemeral. RMS amplitude extractions from proportional slices within the mb10-to-mb11 interval show few discernable amplitude-based morphologies and virtually no channel-form features. Amplitude extractions from the mb_11-to-mb_12 interval (Fig. 7.18) do show a linear channelform with amplitude anomalies associated with its boundaries. Maps also show a chaotic, localized anomaly near the northern margin of the minibasin.

## SEISMIC GEOMORPHOLOGIC EXPRESSION OF SALT TECTONICS

The record of salt movement is not recorded in the salt, but in the sediment deposition surrounding the salt and deformation around the salt structures (Seni and Jackson, 1984; Jackson et al., 1991). Therefore, any study of salt structures and their related generative features requires an analysis of the surrounding strata. Strata surrounding the minibasin record paleo-topography, structural disturbances and salt inflation or withdrawal, so it is necessary to understand and interpret the dynamic interaction between stratigraphy and structure within the study area to reconstruct the evolution of this distal minibasin. A bounding principle is established in that thicknesses of sediment packages will be relatively constant in areas unaffected by salt movement, but can vary greatly in areas affected by salt withdrawal or inflation. For example, sediment packages tend to be thicker in areas of salt withdrawal because of the syn-depositional creation of accommodation and thinner in areas that were affected by salt inflation or uplift during sedimentation.

Previous work by Weisenburger (2007) linked the development of the minibasin under investigation in this study to regional salt sheet movements. He proposed that the

minibasin developed following a phase of compression, where isostatic subsidence and salt withdrawal created accommodation space in the form of a salt withdrawal basin. In his model, the evacuated salt was pushed north of the present-day location of the minibasin, following which the inflating sheet caused seafloor instability and the deposition of high-amplitude, chaotic deposits in the later stages of fill development. His structural restoration analysis produced this simplistic model for the evolution of the minibasin, but did not incorporate observations from geomorphic features within the fill of the minibasin. In this section, we intend to refine this model of minibasin development by incorporating the structural interpretation of Weisenburger (2007) with our own seismic geomorphologic analysis. Our attempt to better understand the evolutionary processes that contributed to the fill architecture of the minibasin is put in a framework that links our observations to the record of salt movement by analyzing trends in stratigraphy and structure surrounding the minibasin.

**Phase 1**

The first phase of structural development within the study area (Fig. 7.19a) involves the formation of half-grabens during the Early Mesozoic. Grabens and half-graben structures are known to have existed in the study area because they are regionally mappable in the distal portions of the Safi seismic survey where salt is absent (Fig. 7.20). The majority of the basement faults that can be imaged are listric normal faults striking north-northeast, forming a series of half-grabens. Below the area affected by allochthonous salt, basement faulting cannot be seismically imaged. It is inferred, however to have a faulting pattern similar to that which is observed outside the limits of the mobile salt. The subsequent deposition of evaporites was prevalent within these

restricted half-graben provinces, and continued into the Early Jurassic. Carbonate and clastic deposition mobilized the salt, and within the study area was responsible for the initial development of a salt stock.

**Phase 2**

In the second phase of structural development (Fig. 7.19b), our observations within the early fill of the minibasin locality shows a thin basin center with divergent seismic reflectors that thicken in the north and south in cross-section through the core of Interval 1 (Fig. 7.21). Strata surrounding the minibasin show a similar trend in accommodation that may be associated with phenomena associated with the rise of the salt stock. To the west of the minibasin we observe a thick sediment package, regionally defined as Jurassic-Aptian deposits that thin toward the west. On the east side of the minibasin, an opposing relationship exists, as the thinnest Jurassic-Aptian deposits are adjacent to the minibasin that thickens to the east. We interpret that these trends in accommodation suggest a rising salt stock near the seafloor that acted as a topographic high, where higher subsidence rates occurred toward the west of the stock and lower subsidence rates occurred in the east. RMS amplitude anomalies from Interval 1 confirm this relationship as described from seismic attribute analysis. In this early stage of development, salt supply that fed the stock was high and differential subsidence around the growing stock resulted in the basinward migration of the mother salt.

**Phase 3**

Our interpretation for the third phase of structural development is complemented by our observations from seismic attribute analysis from Package 2. This phase of

structural development represents the first stage of basin infilling, and the associated change in accommodation regime in this phase can be attributed to extension and subsequent diapir collapse within the study area (Fig. 7.19c). This extension may be attributed to several factors and cannot be fully constrained by the data available in this study. Beyond the minibasin locality, normal faulting is observed within Middle Cretaceous strata, where thickening also exists near the fault boundaries (Fig. 7.22). Within the minibasin locality, we also observe normal faults within corresponding deposits that extend up-section in the northeastern and eastern flanks. Similarly, Dunlap and Wood (2010) and Weisenburger (2007) have suggested the existence of a paleo-volcano west of the minibasin. A strong amplitude seismic reflector anomaly that extends beyond the western flanks of the paleo-volcano near the minibasin may be associated with this extension in the form of an igneous dike. This interpretation is speculative and contains no supporting lithological evidence for its existence. The overturning of Albian beds in the western portions of the minibasin may be associated with the collapse of the diapir when accommodation created in the minibasin depocenter progressively loaded onto the western minibasin flanks.

Within the corresponding fill, deposits appear to be driven by regional-scale events and are also unaffected by the flanks of the minibasin. The presence of draping geometries and absence of baselap indicates that the event existed beyond the boundaries defined by the young minibasin. A seismic geomorphologic study by Dunlap and Wood (2010) of downdip Albian deposits unaffected by salt deposition shows similar morphologies within a restricted interval that have been described as sediment waves (Fig. 7.23). Although their morphologies are much larger in cross-section (wavelengths

up to 2 km), they do appear to be affected by paleo-bathymetry and the existence of salt barriers. Since the morphologies are restricted to the Albian in the areas relatively unaffected by salt, we propose that the initial minibasin fill is of similar age. This interpretation is however limited to observations based on morphological similarities, and cannot be confirmed without the existence of paleontological and other dating information.

**Phase 4**

The fourth phase of structural development is defined geomorphologically by the onset of extensive channelization that may be associated with a regional increase in slope, which affected sediment type, distribution and entry into the minibasin (Fig. 7.19d). This phase coincides with the fill of Package 3. The change in seismic character of the fill following Interval 7 can be attributed to a regional-scale erosional event associated with a change in slope topography. The onlapping of Intervals 7, 8 and 9 onto the erosional surface can be associated with a rejuvenation of sediment supply that may be linked to external forcing into the minibasin system as previously described (Figs. 7.15 and 7.16). Supporting this argument is the absence of mounding reflectors in cross-section, which suggests an absence of levees on the channelform boundaries and a relatively high depositional slope. When attribute extractions for this interval are compared to the corresponding isopach map, the resulting through-going unleveed channelforms appear to be unaffected by topography associated with the boundary of the minibasin. Their geometries also do not appear to terminate within the minibasin depocenter.

Structural features supporting this phase of development include a thrusted anticline outboard the eastern flanks of the minibasin that deforms Albian strata (Fig.

7.23). A thin (300 ms) interval of high-amplitude folds accompanies this thrusted anticline, and the timing of shortening coincides with Cretaceous-to-Miocene aged Alpine orogeny. The structural effects of this uplift are dampened in the study area relative to onshore deformation, but the fill displays a marked change in seismic and geomorphic character as previously described.

In a later stage of Phase 4, the low-amplitude, wedged deposits of Interval 10 record more passive deposition, and the cessation of channelization and sediment supply. The cross-sectional geometries within this interval indicate conditions of structural stabilization and healed slope topography within this segment of the continental margin. The deposits observed within attribute slices from Interval 11 can be attributed to a gravitational reactivation of sediment on the northern flanks of the minibasin that resulted from continued, but waning effects of Atlas compression (Fig. 7.19). The complex geometries observed in cross section are characteristic of these types of deposits.

## DISCUSSION

### Timing of the Initiation of Minibasin Development

The seismic geomorphologic analysis of the lower slope of the SHM study area by Dunlap and Wood (2010) demonstrates active bottom-water currents in the late Albian. Subtle effects of similar geomorphologic forms are observed in the oldest fill of the minibasin, suggesting active Atlantic bottom-water currents during this time. This in turn suggests a Mid-Cretaceous age to the initial fill and development of the minibasin.

**Models of Minibasin Development and the SHM Minibasin**

We have recognized that models of minibasin development are dominated by Gulf of Mexico examples, which usually suggest processes dominated by sediment-driven-subsidence accommodation but often tied strongly to eustasy. Our analysis of the SHM minibasin fill suggests that this Gulf of Mexico-centric model of filling localized accommodation and spilling into adjacent areas of higher accommodation once the proximal locality has been filled is not necessarily applicable in the Moroccan continental margin based on two main factors. These factors are (a) differing mode of sediment delivery than that seen in the Gulf of Mexico; (b) overriding influence of salt tectonics relative to sea level change.

The sediment influx in the Gulf of Mexico was controlled by eight principal extra-basinal fluvial axes that provided the bulk of the sediment infill in the basin (Galloway et al., 2000). By comparison, extensive fluvial drainage systems were for the most part, absent in the Moroccan margin. Upper-most Cretaceous to Tertiary sedimentation in the Moroccan continental margin was responding to diminished influence of distant Atlantic seafloor spreading and the emergence of compressive Atlasic tectonics. (Broughton and Trepaniér, 1993). This transition resulted in a shift from quiescent shelf sedimentation with accumulation of thick shale and limestone strata to widespread erosion with preservation of coarser conglomeratic siliciclastics in structural lows. The relatively minor influence of extensive drainage systems in the lower slope of the Moroccan continental shelf is reflected in the seismic geomorphology of the entire SHM dataset, beyond the extent of the minibasin under investigation (see Dunlap et al., 2010).

The SHM dataset records stratigraphy that was deposited during a series of events controlled primarily by the structural evolution of the Atlantic margin during its initial development (extensional features associated with rifting), and slope instability attributed to mobilized salt substrate since the Late Jurassic and Alpine orogeny in the Tertiary. The influence of sediment reworking by ocean bottom currents in the Atlantic margin from the Cretaceous to Recent are secondary, and is further discussed by Weaver et al., (2000) and Dunlap and Wood (2010). Passive sediment fallout in the water column is also recorded in the stratigraphy as draped geometries in cross-section, and also comprises a significant portion of the SHM deepwater stratigraphy.

Our observations and analysis brings very little evidence to suggest a strong sea-level influence on resultant deposits that filled the minibasin. As a result, we can expect that the nature in which the salt withdrawal basin under investigation filled is inherently different from Gulf of Mexico examples, and cannot be explained by existing models of minibasin development. Montoya (2007) investigated lower slope salt withdrawal minibasins in the Gulf of Mexico and recognized the increased role of salt-induced accommodation in the evolution and development of distal minibasins. Like our study, she recognized that minibasin sedimentation was strongly cyclical, with periods of low sedimentation associated with drapes above each interpreted erosional surface, which she interpreted as sequence boundaries. We refrain from using such terminology in this study as a source-to-sink linkage cannot be established with the existing data, and the increased role of salt withdrawal in the creation of accommodation and its influence of bathymetry negates a sequence stratigraphic interpretation of stratigraphic surfaces that comprise the minibasin fill. When we compare established geometries associated with minibasin

evolution in the literature, our observations suggest that in a sediment-starved margin such as the Moroccan margin, the existence of channelforms do not appear to correlate temporally nor spatially within each cycle observed. They are however influenced by increased topography and slope associated with Atlas orogeny.

## CONCLUSIONS

Within the study area in the lower slope of the Moroccan continental margin, our combined seismic geomorphologic and structural analysis has enabled us to determine that the evolution of the SHM isolated, distal minibasin comprises four major phases of structural development and four phases of fill development. Salt was deposited during the Triassic to Late Jurassic, following which thick carbonate and clastic successions were deposited. The initiation of the growth of a salt stock in the study area was associated with the mobilization of salt. The growth and development of a passive diapir in Jurassic to Early Cretaceous defined the second stage of structural development. Low-to-moderate amplitude fill in high accommodation zones occurred around an actively rising diapir in response to sediment loading. Thirdly, extension in the Lower to Middle Cretaceous created salt-withdrawal accommodation as salt supply was starved and welds were created as sediment infilled. When compared to previously proposed models, the age of initial infilling of the minibasin is supported by low-amplitude wedged fill with depositional morphologies resembling Albian sediment waves in the distal portions of the study area. Finally, compression in the Early Tertiary attributed to Atlas orogeny resulted in a change in the accommodation configuration of the minibasin. High-amplitude wedged fill baselapped onto minibasin margins and extensive unleveed channelforms prevailed. An increase in the size and scale of channel morphologies up-section in

Intervals 9 and 10 suggested an increased slope associated with onshore mountain building and an increased linkage of lower slope depocenters. Later on in the minibasin history, point-sourced, smaller-scale leveed channelized systems accompanied by mass transport events suggest unstable minibasin margins. Instability is still visible on modern seafloor, and suggests that salt is still mobile and the minibasin is presently actively subsiding.

## FIGURES

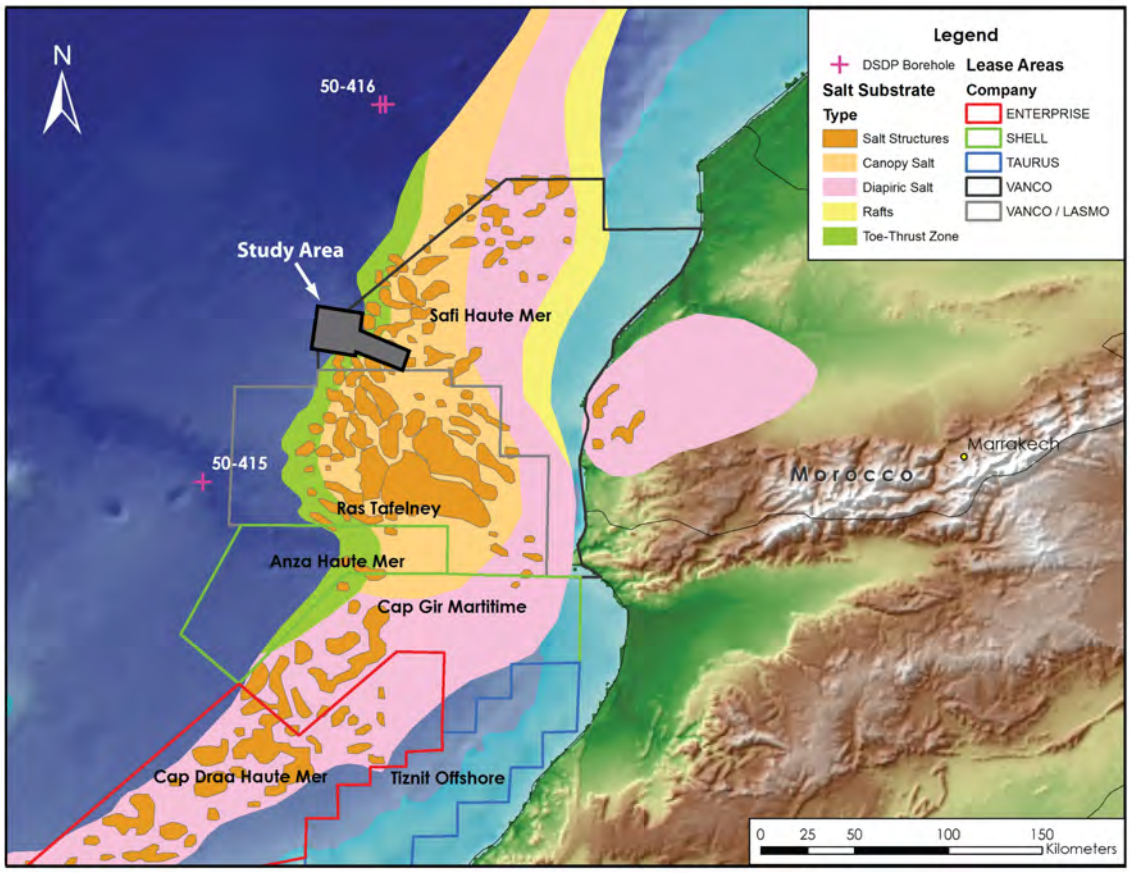


Figure 7.1: Shaded relief profile of the Moroccan continental margin showing the extent of the study area (grey filled polygon) relative to the Moroccan coastline. Variability in structural controls is mainly due to the types of salt substrate present. Offshore permit areas are outlined by polygons.

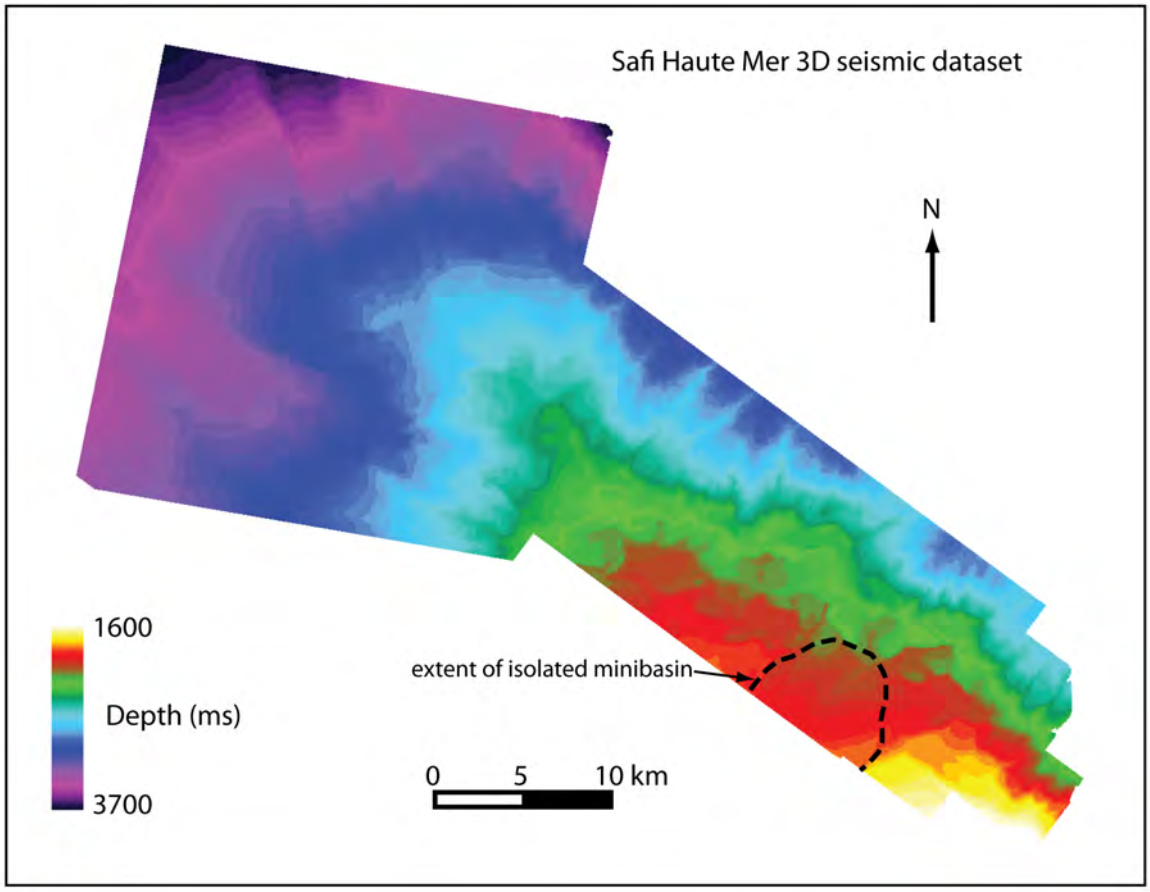


Figure 7.2: Live trace seismic outline of the Safi Haute Mer 3-D dataset with a superimposed structure map of the present-day seafloor. The dashed line represents the outline of the isolated minibasin within the dataset.

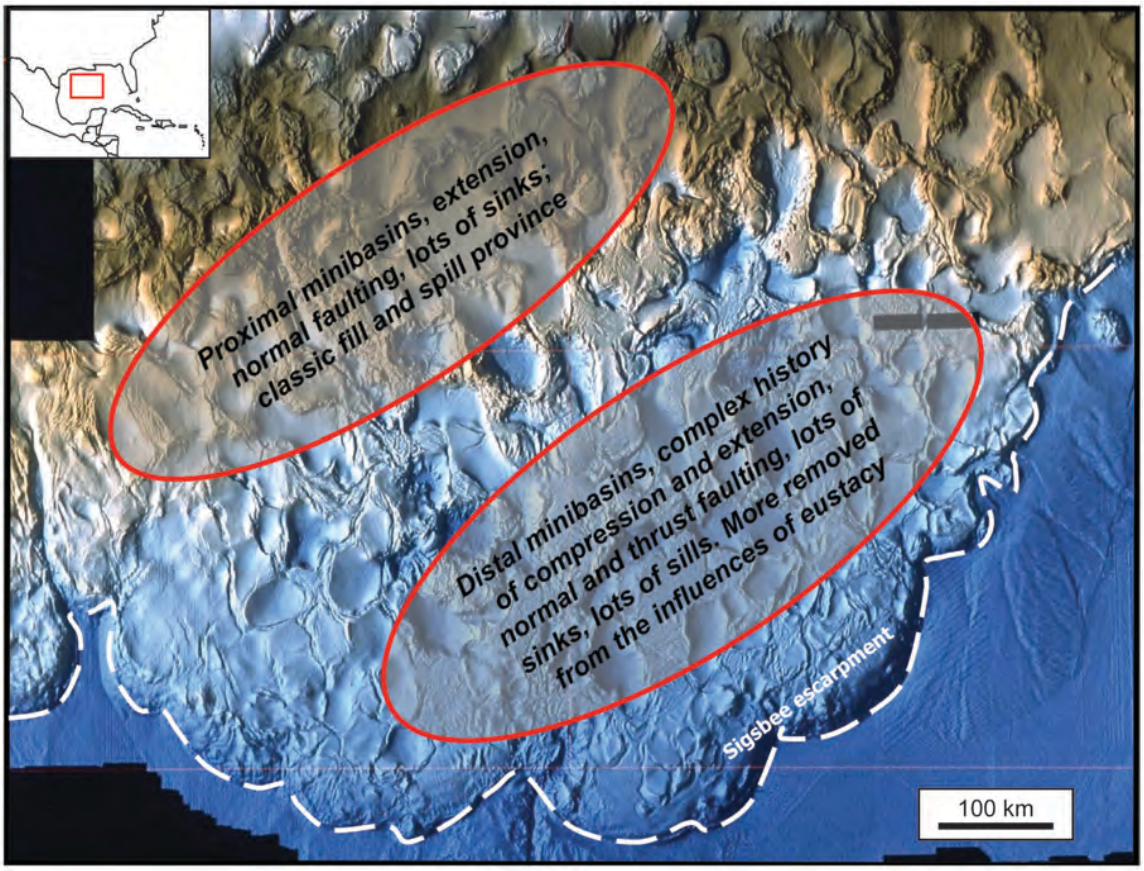


Figure 7.3: Shaded relief map of the present-day seafloor of the Gulf of Mexico basin. Minibasins exist in the area influenced by mobile salt substrate, and can be described as proximal and distal relative to the coastline. The extent of the basin affected by underlying salt substrate terminates at the Sigsbee Escarpment (white dashed line) in the south of the basin.

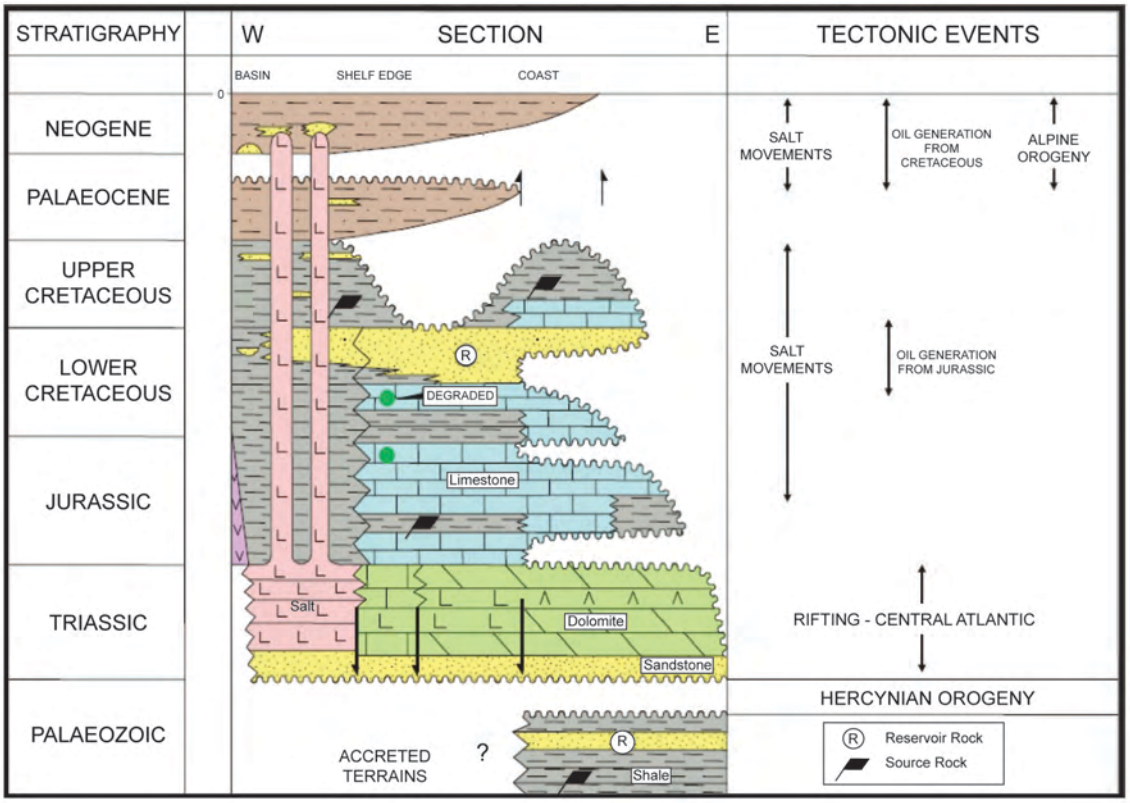


Figure 7.4: Chronostratigraphic chart for the Atlantic Margin of Morocco (modified from Davison (2005)).

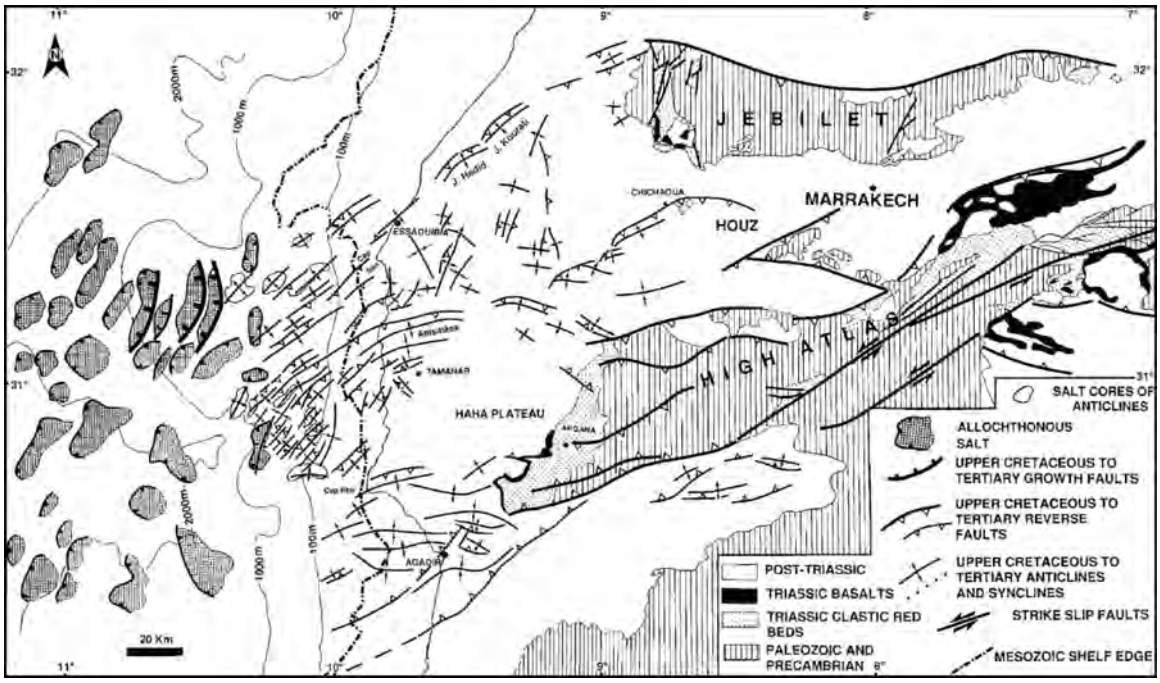


Figure 7.5: Present-day structural configuration of the Moroccan margin, excluding the influence of mobile salt substrate (modified from Hafid et al., (2006)).

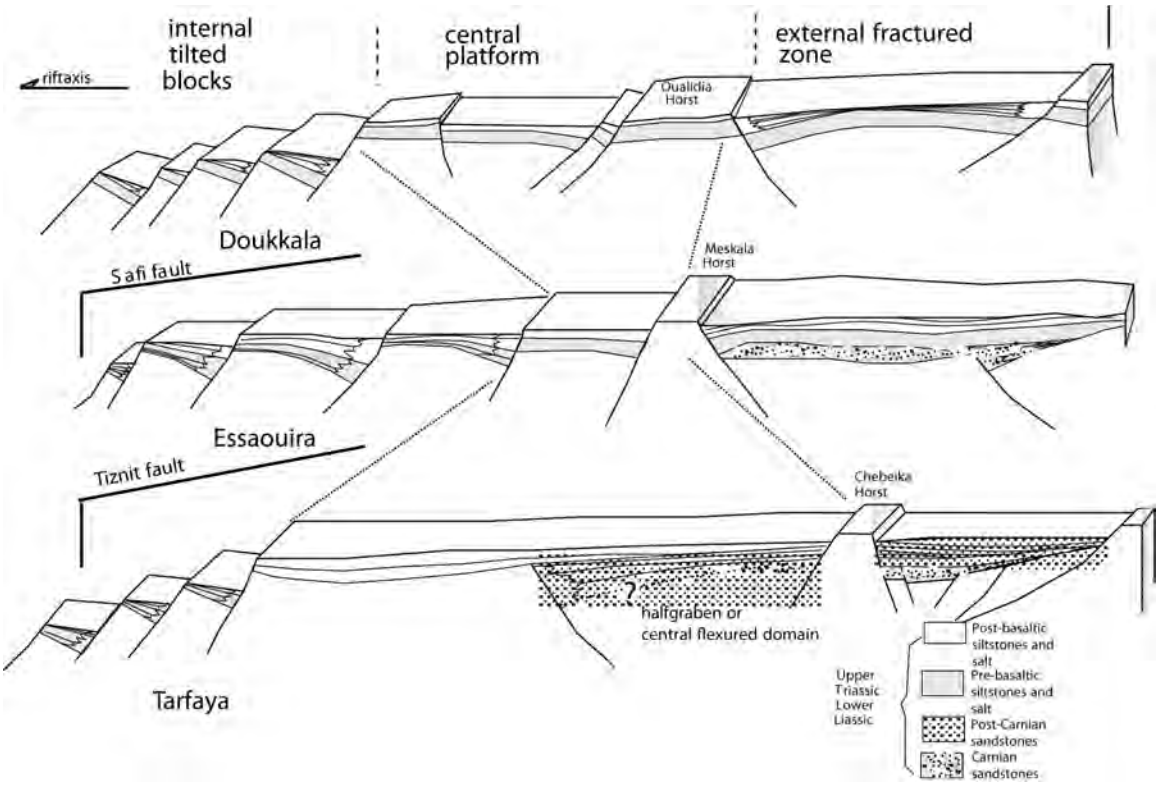


Figure 7.6: Summary diagrams showing the basement geometry and synrift infilling in the various segments of the Atlantic Moroccan margin (modified from Le Roy and Pique (2001)).

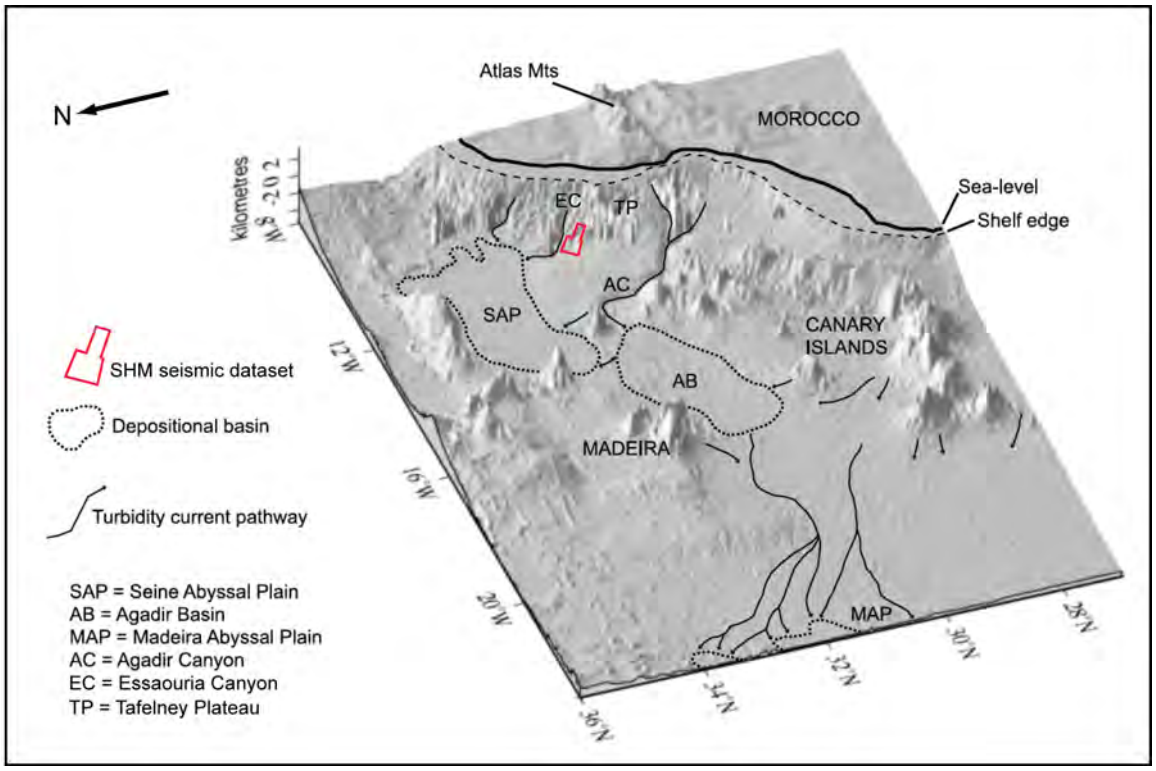


Figure 7.7: 3D structural map of the Moroccan continental margin showing major bathymetric features (modified from Wynn et al., (2002)). View is toward the southeast and the study area is outlined in red.

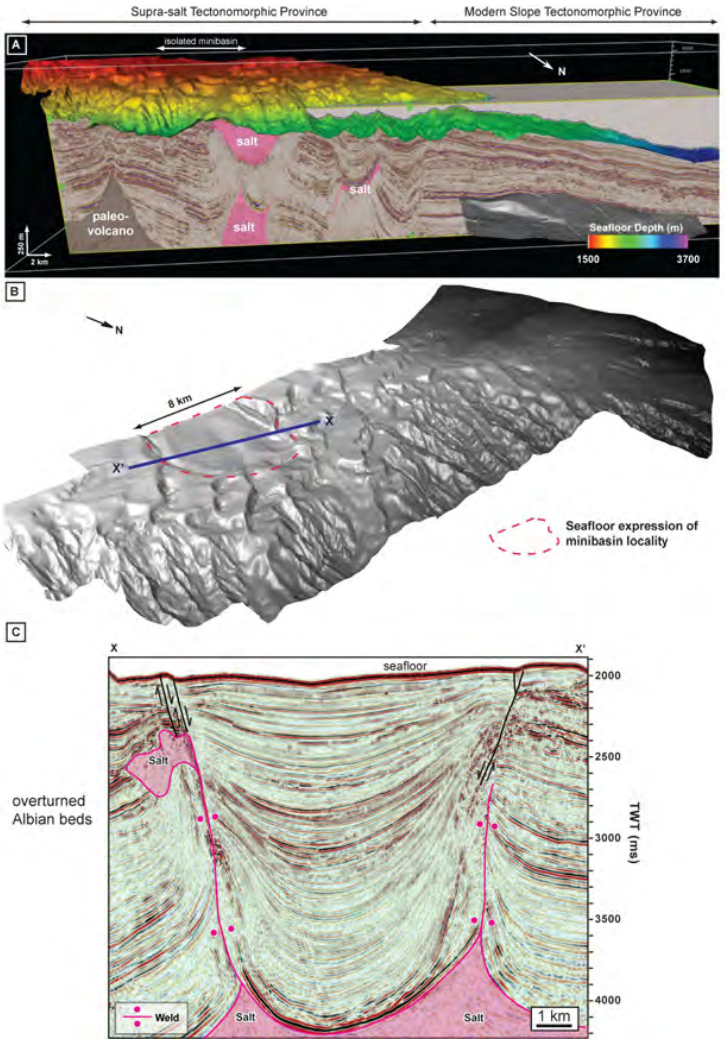


Figure 7.8: (a) Seismic dip section of the study area with superimposed structure map of the seafloor. The seismic section illustrates the Triassic to Recent stratigraphy preserved in the study area. Irregularly deformed features shaded in pink is interpreted as mobile salt substrate, and the conical feature shaded in brown within the proximal portion of the dataset is interpreted as a paleovolcano; (b) a structure map, shown in three dimensions, completed on the Moroccan seafloor illustrates the relationship between the isolated minibasin under investigation (outlined in red) and the rest of the 3D seismic volume; and (c) an arbitrary seismic cross section (X-X') shows the 3 kilometers of stratigraphy preserved within the subsiding minibasin. Interpreted underlying present-day salt structures are outlined and shaded pink.

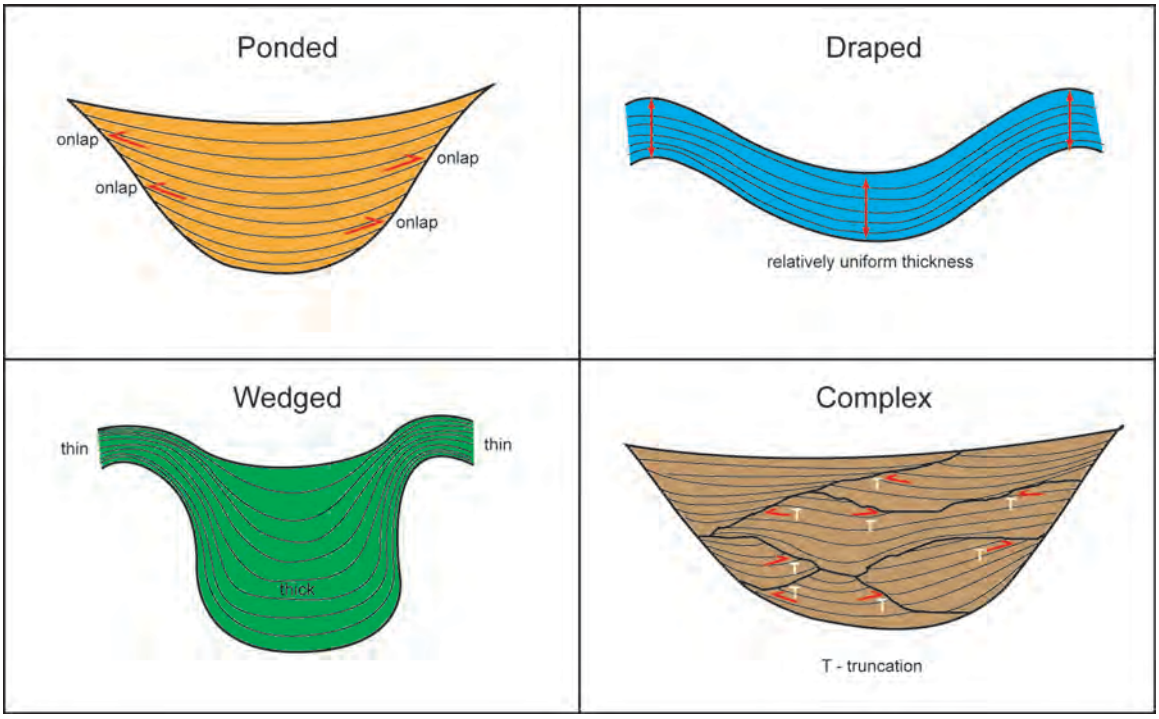


Figure 7.9: Four types of fill geometries recorded within minibasins. (a) Ponded fill patterns display terminal onlap of seismic reflectors with relatively higher taper rates; (b) draped fill geometries tend to blanket underlying fills and surrounding walls and do not taper; (c) wedged fill geometries display thinning onlap and relatively low reflections taper rates; and (d) complex fill patterns are a heterogeneous, multi-phased fill that comprises multiple episodes of cut and fill.

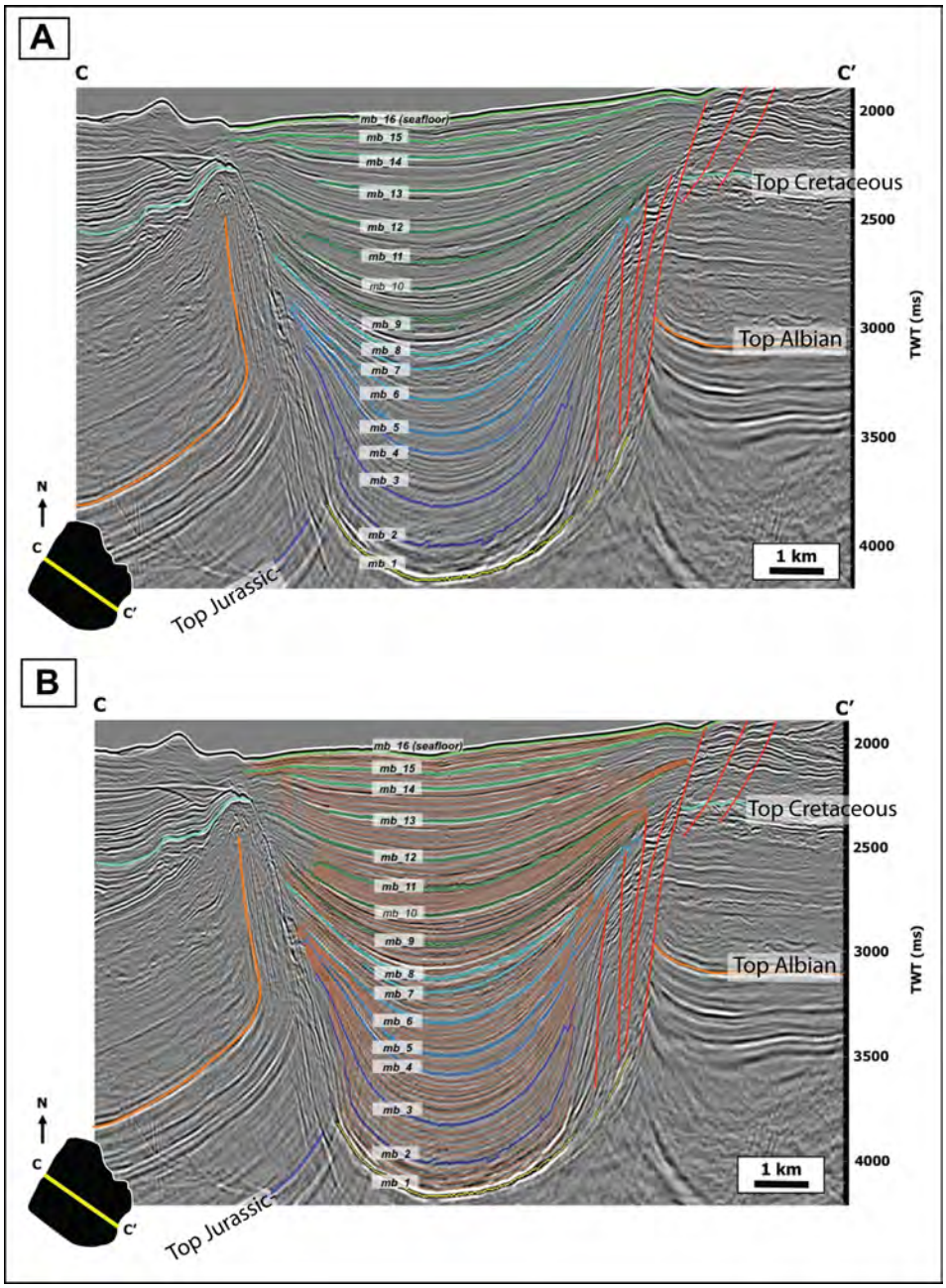


Figure 7.10: (a) Uninterpreted and (b) interpreted cross section C-C' within the isolated minibasin. Sixteen regionally conformable horizons (mb_1 to mb_16) are interpreted within the minibasin fill mega-sequence, which bound fifteen fill sequences associated with cyclic infilling of the minibasin from the Middle Cretaceous to Recent.

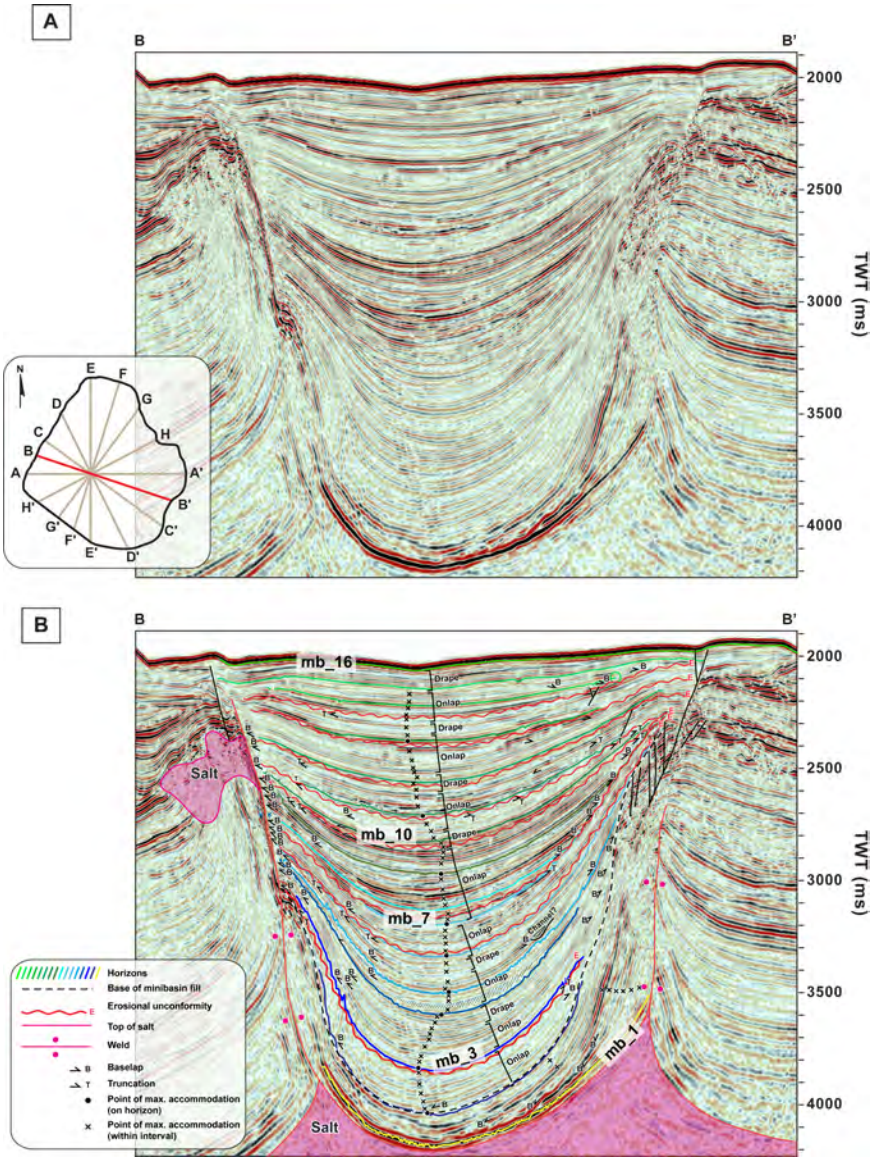


Figure 7.11: Seismic cross section B-B' is used to demonstrate the seismic character of fill packages, accommodation trends and nature of stratigraphic terminations within the minibasin (a) is uninterpreted and (b) is interpreted to show major horizons within the fill, major erosional unconformities, the base of the fill (dashed black line), geometric terminations (truncation, baselap,) and points of maximum accommodation within the fill. Direct observation, seismic mapping and derived isochore maps enhance the accuracy of these interpretations.

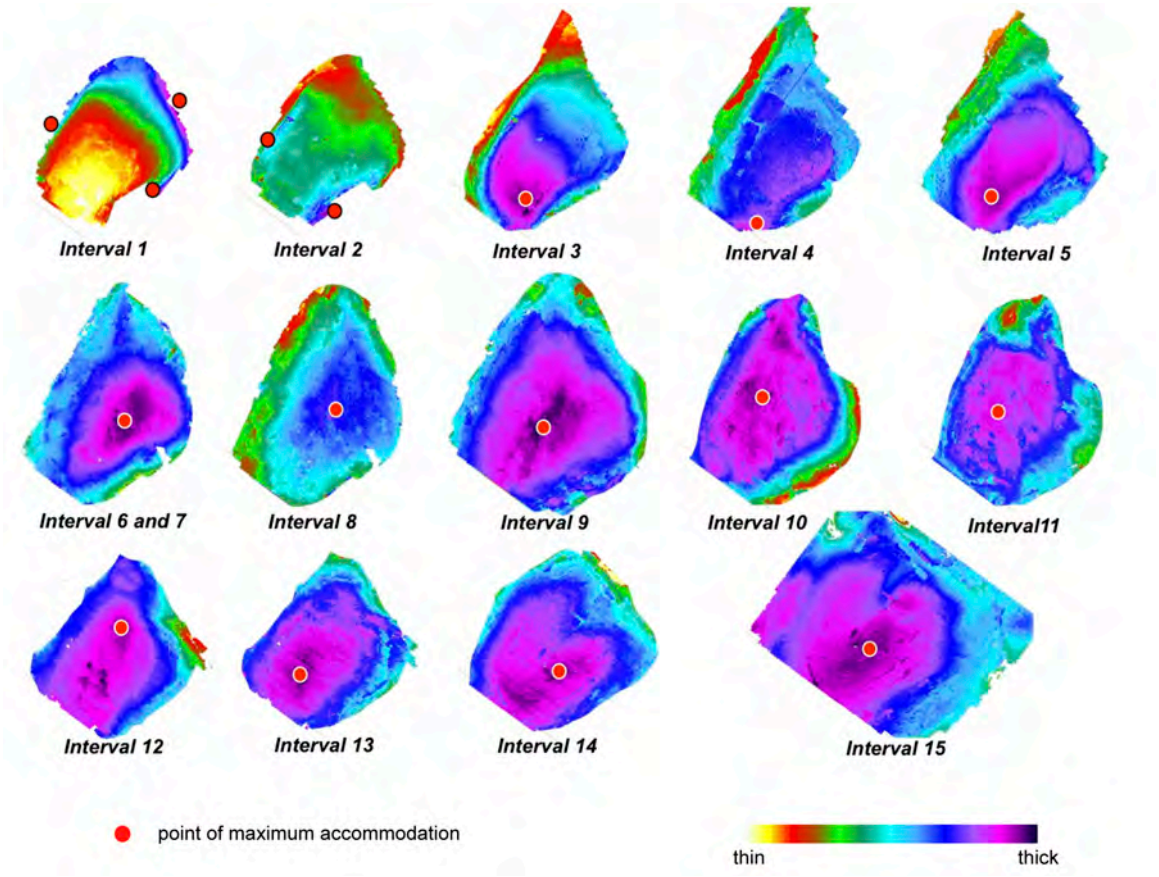


Figure 7.12: Isochore maps provide a birds-eye perspective on the distribution of sediments and point of maximum accommodation within each stage of basin fill. Each map represents a stratigraphic interval bounded by two conformable horizons within the minibasin (from oldest to youngest). Thicker areas (high accommodation) are purple and thinner areas (low accommodation) are yellow. The point of maximum accommodation for each interval is interpreted as the point where thickest strata are preserved.

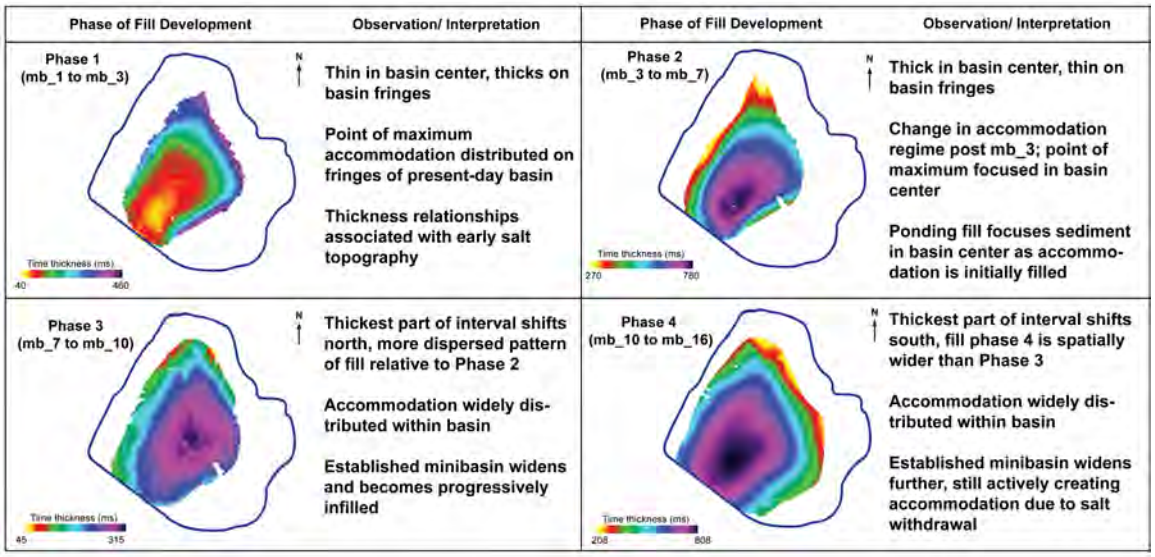


Figure 7.13: Individual geometric fills of the minibasin are grouped into four separate large-scale fill packages based on the character and geometry of seismic reflectors. Package 1 (mb_1 to mb_3) contains relatively high amplitude reflectors that onlap the present day minibasin center. Package 2 (mb_3 to mb_7) contains sequences that display ponded-wedge-draped fill sequences. Package 3, (mb_7 to mb_10), comprises a series of ponded and complex geometric fill phases.

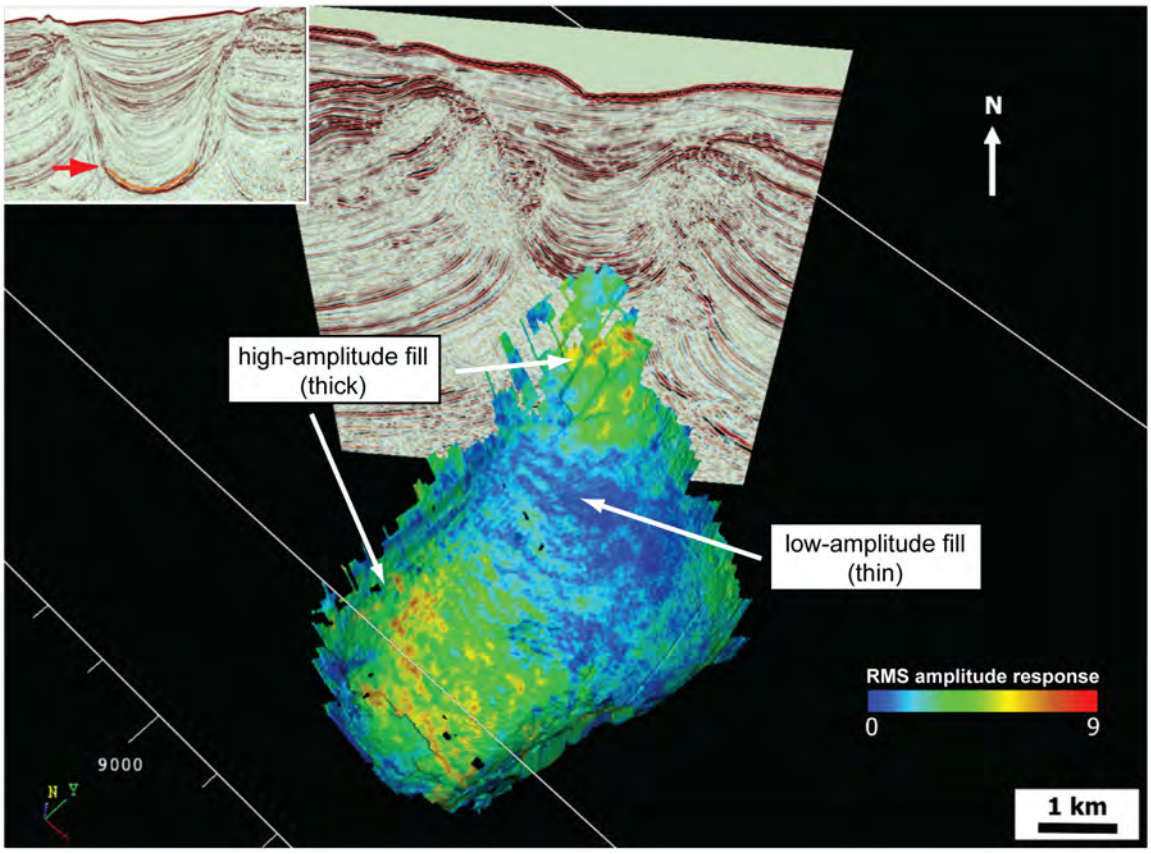


Figure 7.14: A root-mean-squared (RMS) extraction (+-10ms) draped on a stratigraphic horizon slice within Package 1 is shown in 3D. Higher-amplitude responses of the fill (warmer colors) in isolated northern and southern regions of the minibasin are interpreted to represent depocenters, where accommodation is well developed. Poor data frequency content at depth limits seismic imaging of the internal structure of these deeper geomorphic elements.

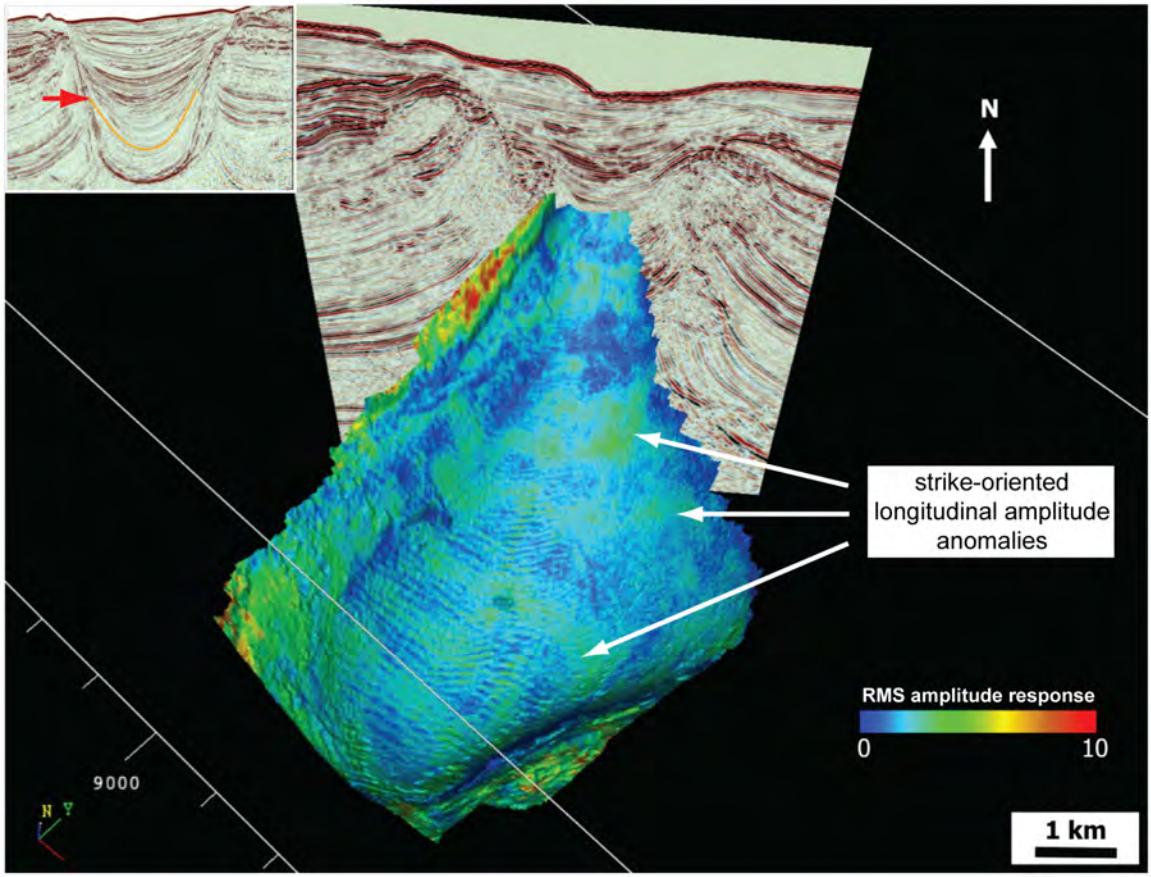


Figure 7.15: A root-mean-squared (RMS) extraction (+-10ms) draped on a stratigraphic horizon slice within Package 2 is shown in 3D. The elongate RMS anomalies preserved are equidistant, display a low-amplitude character and trend perpendicular to regional dip. We suggest that this change in character to be associated with a high influence of reworking due to ocean currents, creating morphologies resembling sediment waves as observed in Dunlap and Wood (2010).

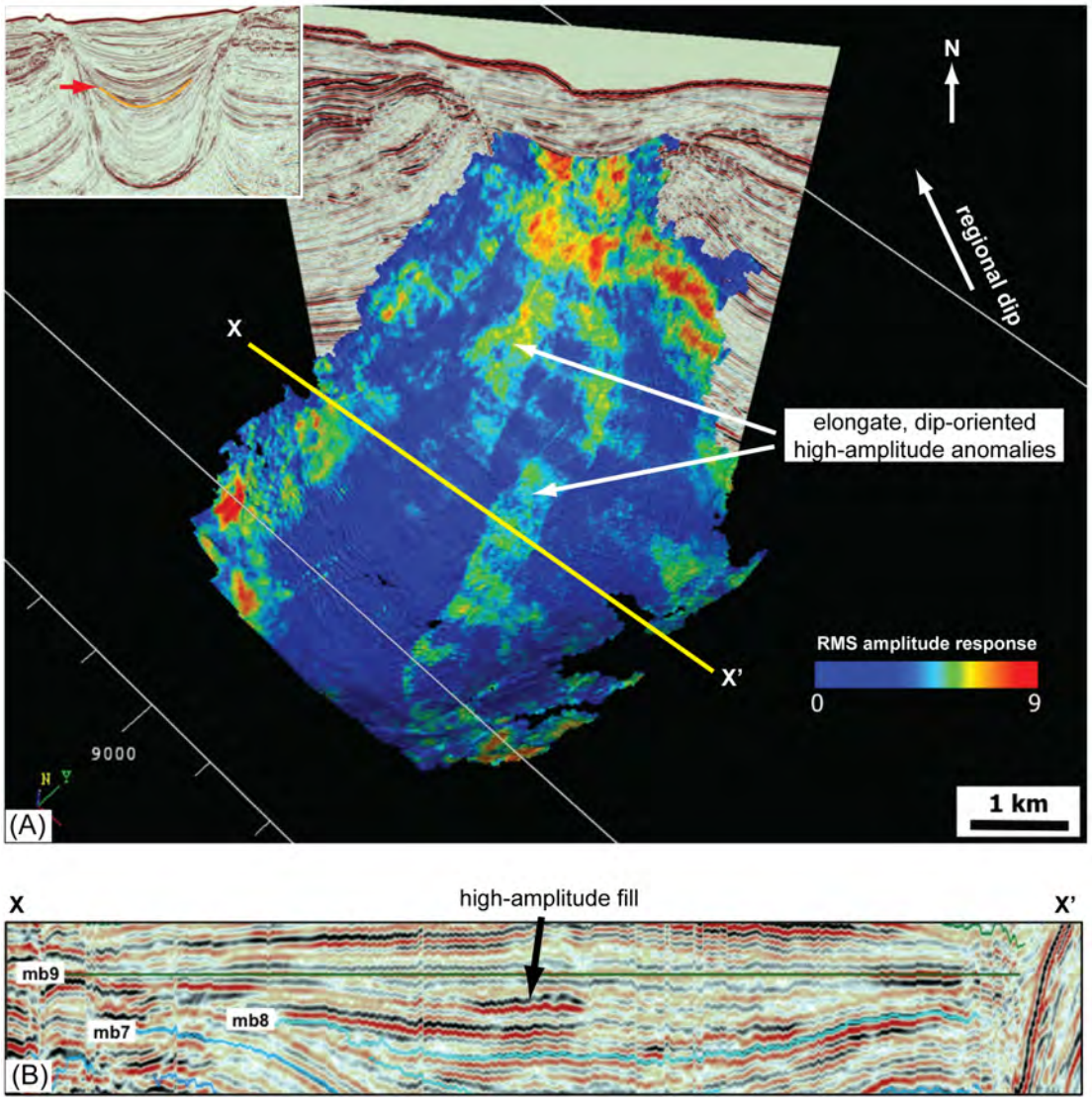


Figure 7.16: (A) A root-mean-squared (RMS) extraction (+-10ms) draped on a stratigraphic horizon slice from the mb_7 to mb_8 interval within Package 3 is shown in 3D. The high-amplitude, large-scale, through-going anomalies are interpreted to represent channelforms and are oriented north-south. They are the dominant morphology recognizable in the three, high amplitude fill sub-packages that comprise Package 3. The RMS amplitude response of the channelform features is higher than its surrounding environment, and channelform boundaries are clearly discernible; and (B) Seismic cross-section X-X' illustrating the high amplitude channel fill observed in the RMS extraction map.

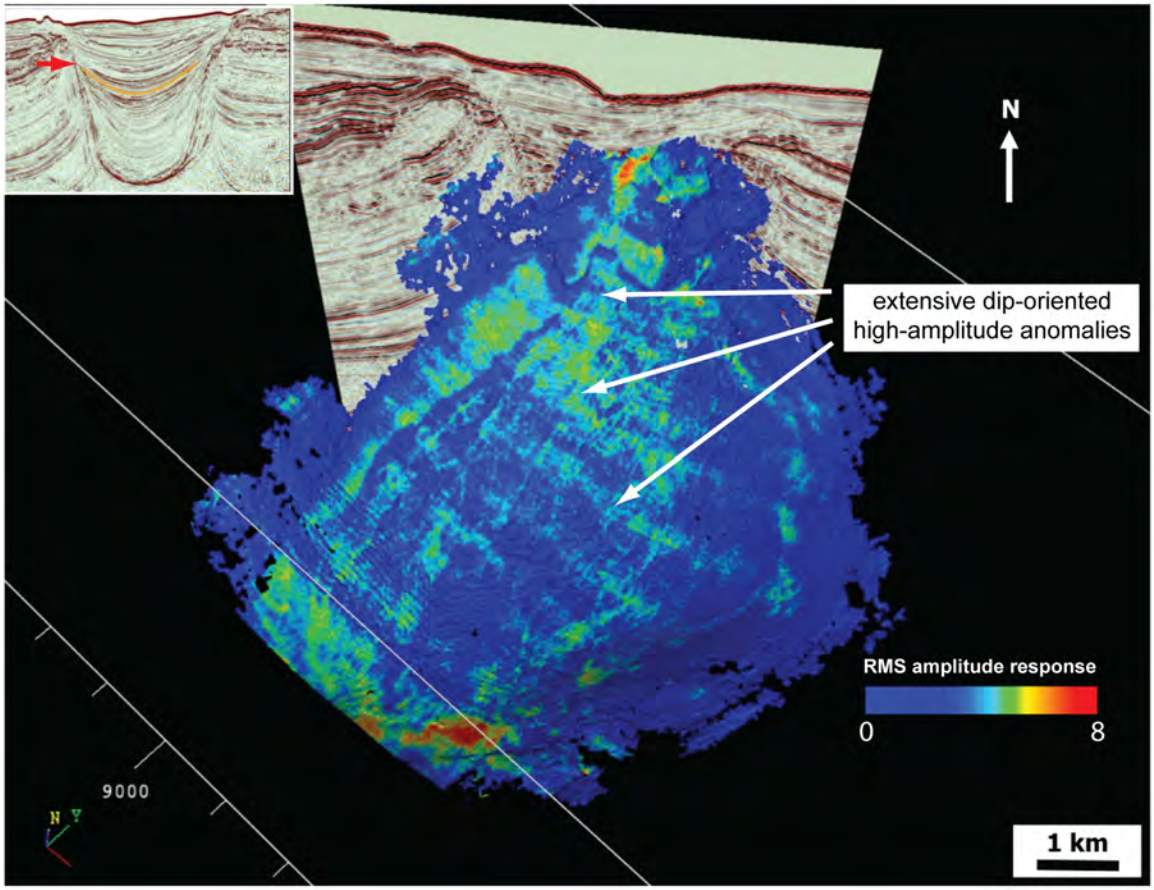


Figure 7.17: A root-mean-squared (RMS) extraction (+-10ms) draped on a stratigraphic horizon slice from the mb_9-to-mb_10 interval within Package 3 is shown in 3D. Elongate morphologies observed are abundant and less confined to a particular area. The anomalies are also less pronounced than those described in Fig. 16, and a relative decrease in sinuosity of the channelform features is also observed. Channelform orientations remain predominantly north-south.

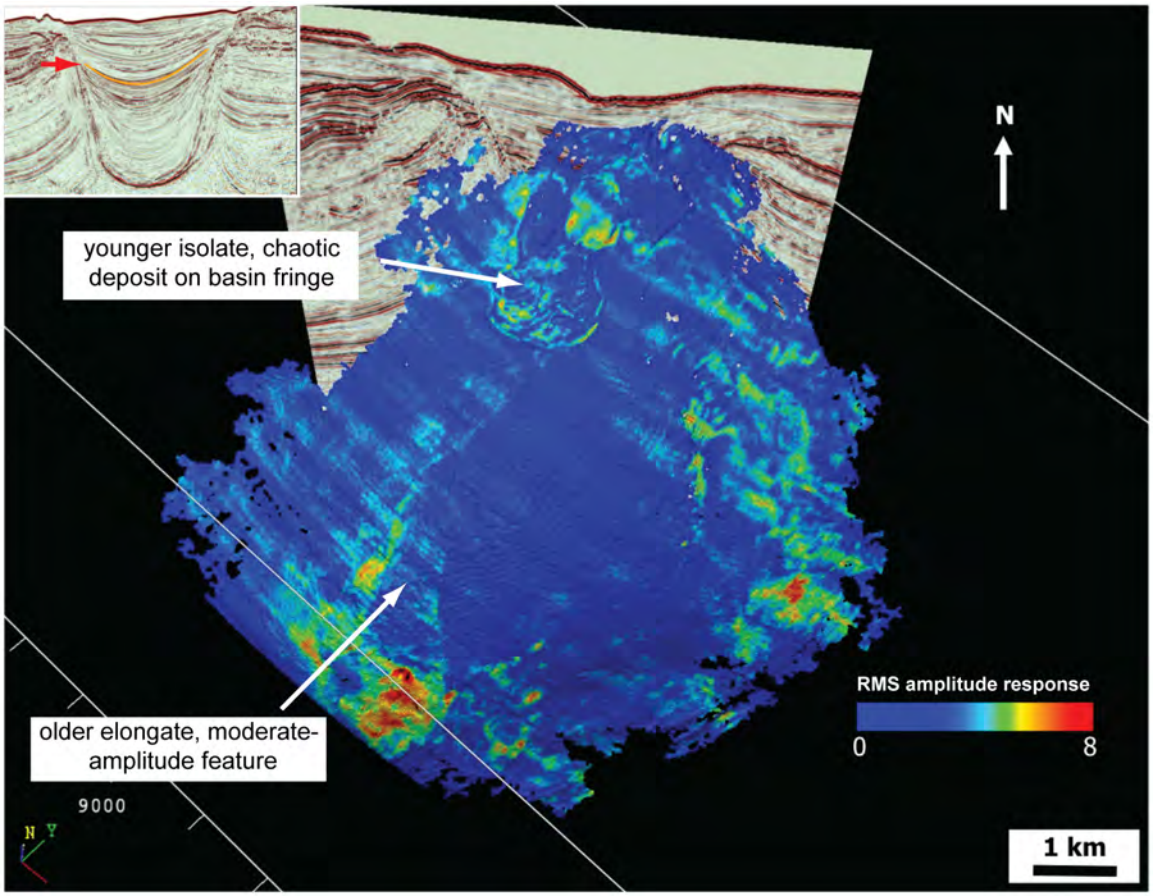


Figure 7.18: A root-mean-squared (RMS) extraction (+-10ms) draped on a stratigraphic horizon slice from the mb_11-to-mb_12 interval within Package 4 is shown in 3D. A marked decrease in high-amplitude anomalies is observed relative to older, deeper intervals. In this extraction map, a linear channelform with amplitude anomalies associated with its boundaries and a chaotic, localized anomaly near the northern margin of the minibasin are observed. These are interpreted to represent the end of a channelization phase and instability on the minibasin flanks due to uplift, ultimately leading to sediment slumping.

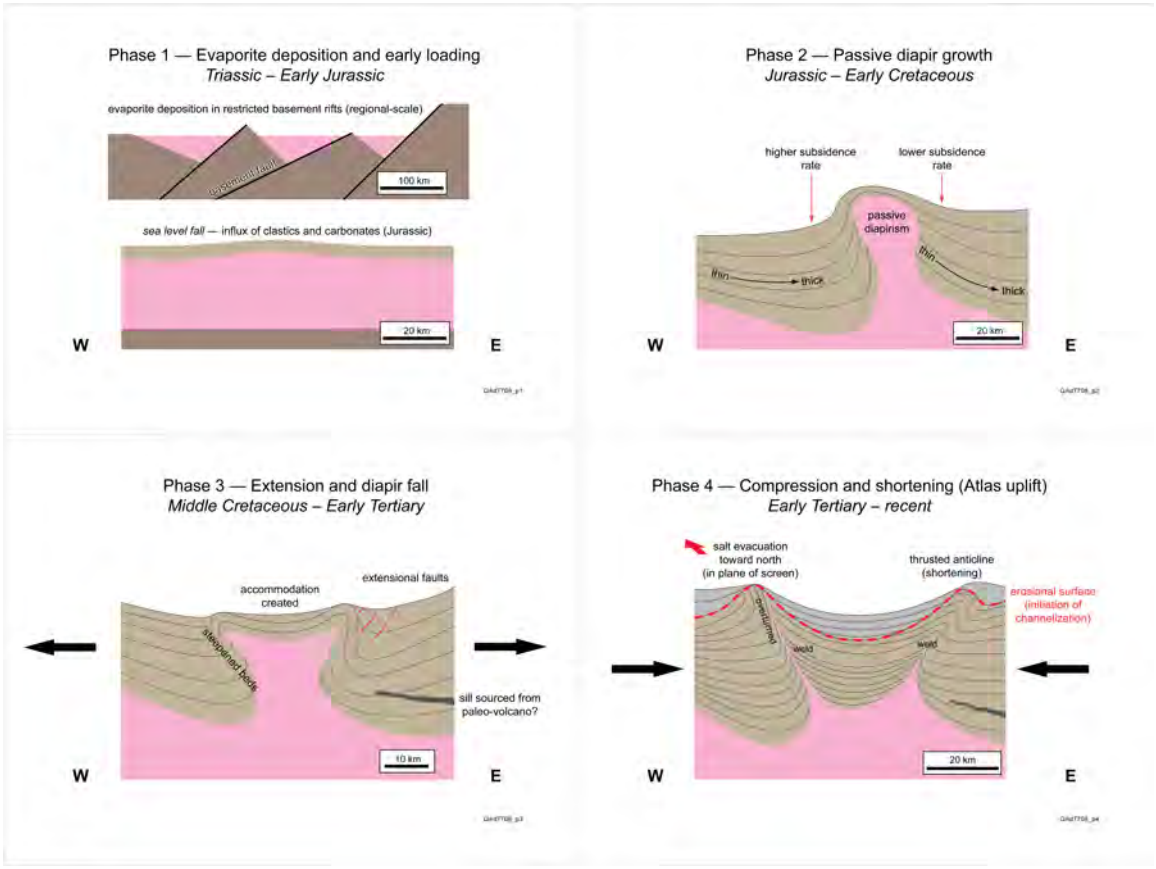


Figure 7.19: Four phases of structural development of the SHM minibasin as it relates to the seismic geomorphologic expression of salt tectonics.

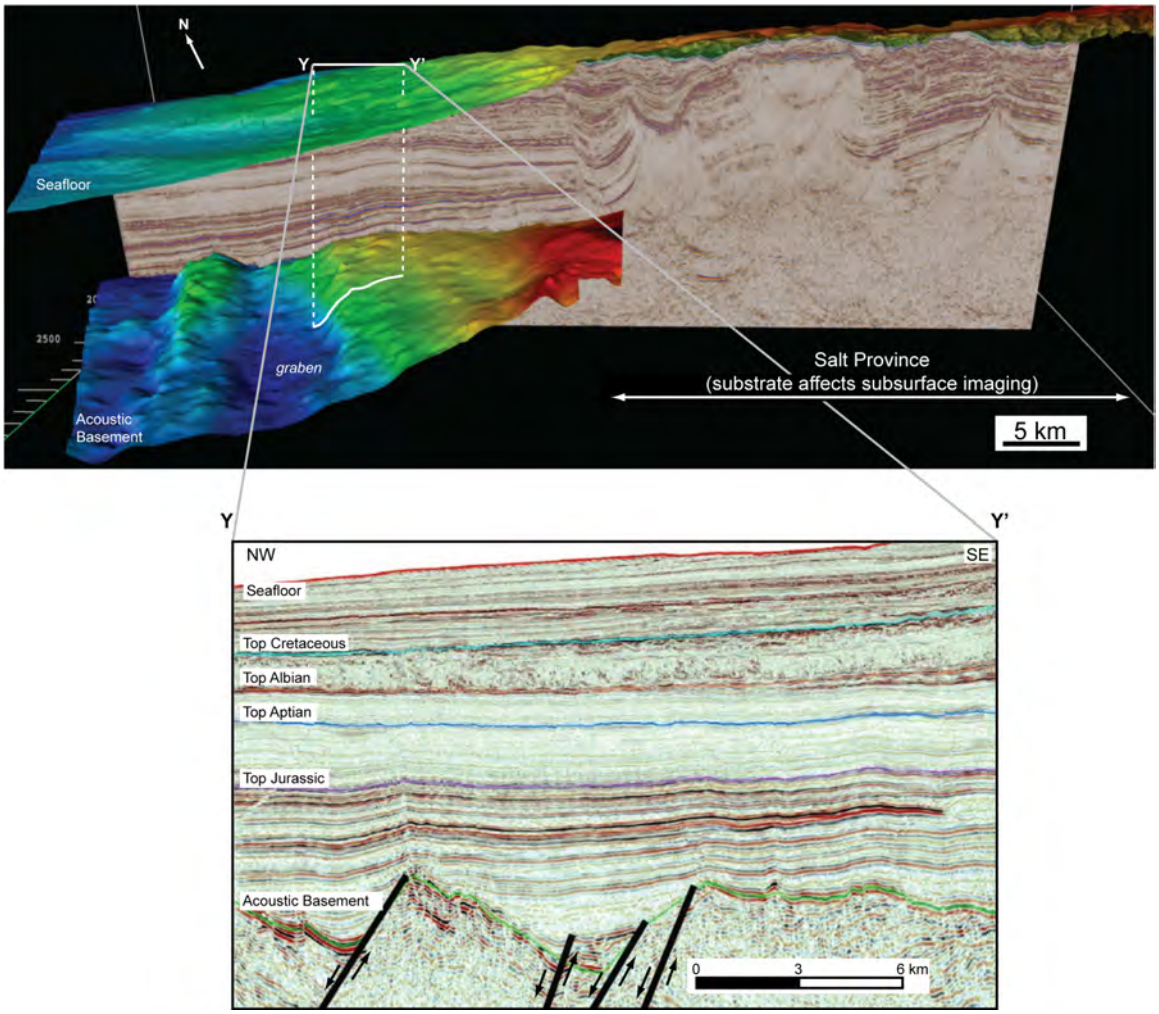


Figure 7.20: Dip-section of SHM seismic survey with seafloor and acoustic basement overlays in three dimensions. Dip-section Y-Y shows the detailed basement structure and preserved stratigraphy in the distal portion of the survey where allochthonous salt does not affect imaging. Early Mesozoic half-grabens record the initial opening of the Atlantic Ocean and the subsequent deposition of evaporites was prevalent within these restricted half-graben provinces, continuing into the Early Jurassic.

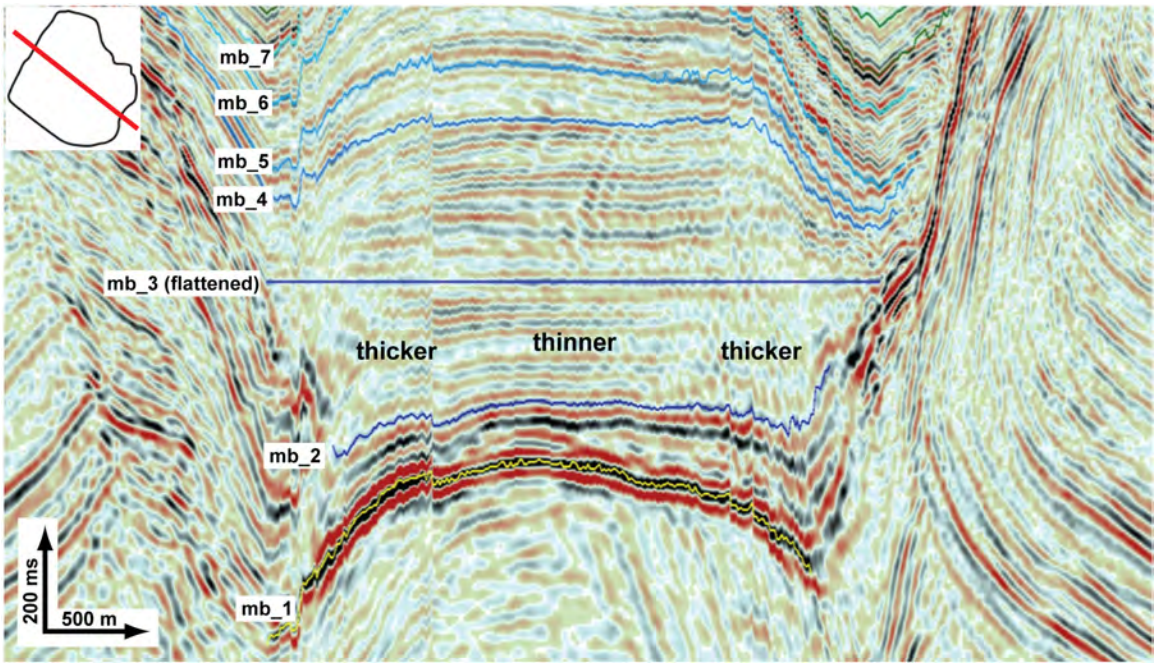


Figure 7.21: Arbitrary cross-section within the early minibasin fill flattened on horizon mb_3 shows a thin basin center with divergent seismic reflectors that thicken in the north and south in cross-section through the core of Interval 1. This fill sequence records the second phase of structural development within the study locality.

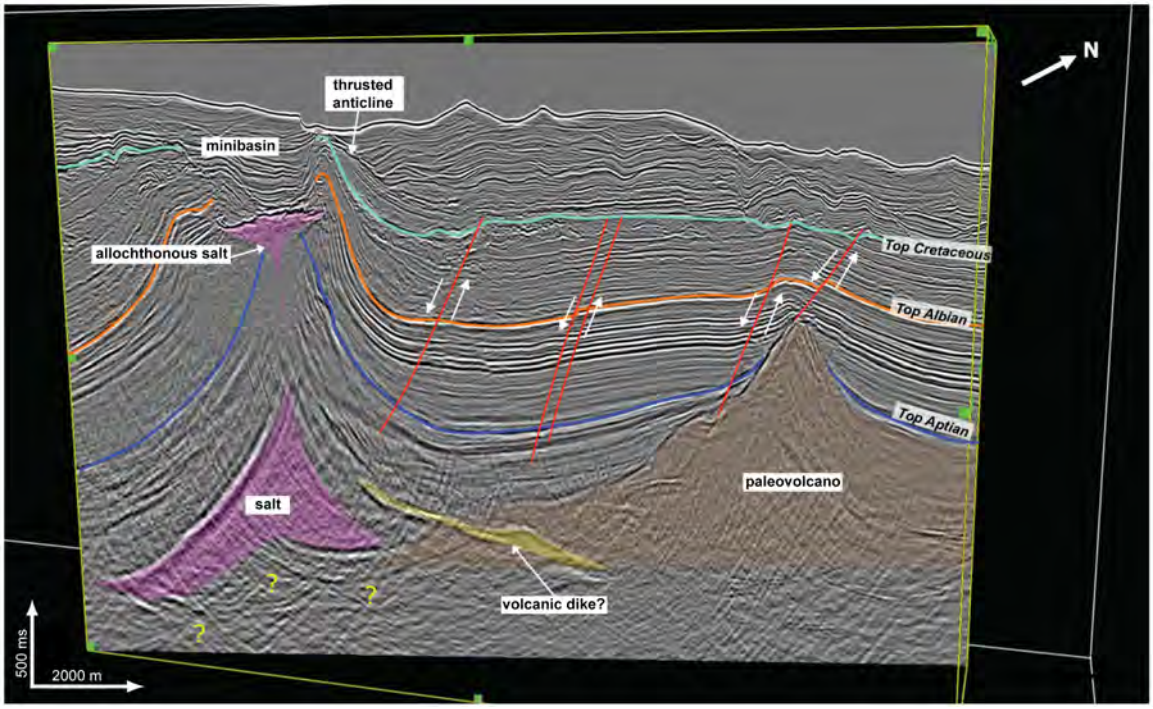


Figure 7.22: Arbitrary dipline from SHM survey shows major structural features outboard of the eastern flanks of the mini-basin to illustrate Phase 3 of structural development within the study locality. Extension in the Mid-Cretaceous is evident based on the relationships between normal faulting observed within Middle Cretaceous strata, stratal thickening near the fault boundaries and a strong amplitude seismic reflector anomaly that extends beyond the western flanks of the paleo-volcano near the mini-basin which is interpreted as an igneous dike associated with the extension.

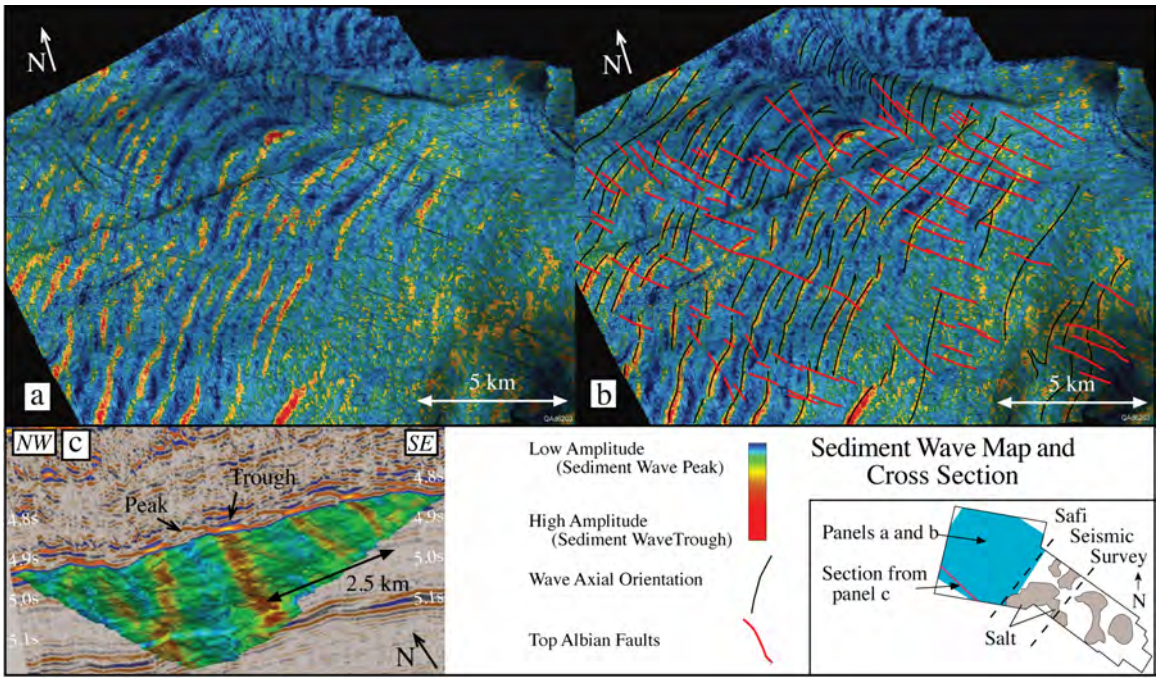


Figure 7.23: (a) Uninterpreted and (b) interpreted north-facing 3-D images of the top Albian structure surface with a maximum peak amplitude (20–40 ms above the top Albian) drape, illustrating the lateral continuity of the SHM Cenomanian sediment wavefield. Waves show little sinuosity or bifurcation. (c) Northeast-facing view of the top Albian/seismic cross section showing resolvability of the top of sediment waves (from Dunlap et al., 2010).

## REFERENCES


Beauchamp, W., Allmendinger, R.W., Baranzagi, M., Demnati, A., El Aliji, M., Dahmani, M., 1999, Inversion tectonics and the evolution of the High Atlas Mountains, Morocco, based on a geological/geophysical transect: Tectonics v. 18, p. 163–184.

Booth, J. R., 2000, Sequence stratigraphic framework, depositional models, and stacking patterns of ponded and slope fan systems in the Auger Basin; central Gulf of Mexico slope. Program and Abstracts - Society of Economic Paleontologists. Gulf Coast Section. Research Conference. A. E. DuVernay, III, D. S. Pfeiffer and M. J. Styzen. United States, Society for Sedimentary Geology, Gulf Coast Section : [Dallas, TX], United States. 20: 103-82.

Broughton, P., Trepaniér, A., 1993, Hydrocarbon generation in the Essaouira Basin of Western Morocco: AAPG Bulletin, v. 77, p. 999–1015.

Davison, I., 2005, Central Atlantic margin basins of North West Africa: Geology and hydrocarbon potential (Morocco to Guinea): Journal of African Earth Sciences, v. 43, p. 254-274.

Dunlap, D. B., Wood L.J., Weisenburger, C., and Jabour, H., 2010, Seismic geomorphology of offshore Morocco's east margin, Safi Haute Mer area: AAPG Bulletin, United States, American Association of Petroleum Geologists: Tulsa, OK, United States, p. 28.

Ellouz, N., Patriat, M., Gauier, J.-P., Bouatmani, R., Sabounji, S., 2003, From rifting to Alpine inversion: Mesozoic and Cenozoic subsidence history of some Moroccan Basins: Sedimentary Geology v. 156, p. 185–212.

Galloway, W. E., Ganey-Curry, P.E., Li, X. and Buffler, R., 2000, Cenozoic depositional history of the Gulf of Mexico basin: AAPG Bulletin, United States, American Association of Petroleum Geologists : Tulsa, OK, United States, p. 1743-1774.

Hafid, M., Ait Salem, A., & Bally, A.W., 2000, The western termination of the Jebilet-High Atlas system (Offshore Essaouira Basin, Morocco): Marine and Petroleum Geology, v. 17, p. 431-443.

Hafid, M., Zizi, M., Ait Salem, A. and Bally, A.W., 2006, Structural styles of the western onshore and offshore termination of the High Atlas, Morocco: Comptes Rendus Geoscience v. 338, p. 50-64.

Hames, W.E., McHone, J.G., Renne, P.R. and Ruppel, C., 2003, The Central Atlantic Magmatic Province: Geophysical Monograph Series; American Geophysical Union: Washington, DC, p. 267.

Hedley, R. and Warburton, J., 1999, The structural evolution of the Tafelney Plateau, offshore Morocco: AAPG Bulletin, United States, American Association of Petroleum Geologists : Tulsa, OK, United States, p. 1316-1316.

Heyman, M.A., 1989, Tectonic and depositional history of the Moroccan Continental Margin: in Tankard, A., Balkwill, H., (Eds), Extensional Tectonics and Stratigraphy of the North Atlantic Margin: AAPG Memoir 46, p. 323–340.

Hinz, K., Dostmann, H. and Fritsch, J., 1982, The continental margin of Morocco: seismic sequences, structural elements and geological development: in Von Raad, U. (Ed.), Geology of the North West African Continental Margin, Springer-Verlag, Berlin, p. 34-60.

Hudec, M. R., (2006). Advance of allochthonous salt sheets in passive margins and orogens. AAPG Bulletin. M. P. A. Jackson. United States, American Association of Petroleum Geologists : Tulsa, OK, United States. 90: 1564-1535.

Hudec, M.R., M.P.A. Jackson, and D. D. Schultz-Ela, in press, The paradox of minibasin subsidence into salt: Clues to the evolution of crustal basins: GSA Bulletin.

Jackson, M. P. A., B. C. Vendeville, and D. D. Schultz-Ela, 1994, Salt-related structures in the Gulf of Mexico: A field guide for geophysicists: The Leading Edge, v. 13, p. 837-842.

Lancelot, Y. and Winterer, E. L., 1980, Introduction and summary of results, Deep Sea Drilling Project Leg 50: in Lancelot, Y. and Winterer, E. L. (Eds.) Initial Reports of the DSDP, US Government Printing Office, Washington, 50, p. 801-821. 91

Lancelot, Y. and Winterer, E. L., 1980, Evolution of the Moroccan oceanic basin and adjacent continental margin: a synthesis: in Lancelot, Y. and Winterer, E. L. (Eds.) Initial Reports of the DSDP, US Government Printing Office, Washington, 50, p. 801-821.

Le Roy, P., Piqué, A., 2001, Triassic–Liassic Western Moroccan synrift basins in relation to the Central Atlantic opening: Marine Geology v. 172, p. 359–381.

Medina, F., 1995, Syn- and post-rift evolution of the El Jadida-Agadir basin (Morocco): constraints for the rifting models of the central Atlantic: Canadian Journal of Earth Sciences, v. 32, p.1273-1291.

Mehdi, K., Griboulard, R., and Bobier, C., 2004, Role of halokinesis in the Essaouira Basin evolution (SW Morocco): Comptes Rendus Geoscience v. 336, p. 587-595.

Montoya, P., 2007, Active salt tectonics and its effect on the internal architecture and connectivity between minibasins near the Sigsbee Escarpment, Gulf of Mexico, in M. R. Hudec, ed., Abstracts: Annual Meeting - American Association of Petroleum Geologists, United States, American Association of Petroleum

Geologists and Society for Sedimentary Geology : Tulsa, OK, United States, p. 96-96.

Morabet, A.M., Bouchta, R., Jabour, H., 1998, An overview of the petroleum systems of Morocco: in Macgregor, D.S., Moody, R.T.J., Clark-Lowes, D.D. (Eds.), Petroleum Geology of North Africa, v. 132, Geological Society of London Special Publication, p. 283–296.

Price, I., 1980, Gravity tectonics on a passive margin: Deep Sea Drilling Project Site 415 in relation to regional seismic data: in Lancelot, Y. and Winterer, E. L. (Eds.) Initial Reports of the DSDP, US Government Printing Office, Washington, 50, p. 759-771.

Seibold, E. 1982, The northwest African continental margin—An introduction: in Von Rad, U., Hinz, K., Sarnthein, M., Seibold, E. (Eds.), Geology of the Northwest African Continental Margin, Springer Verlag, Berlin, p. 215–269. 92

Seni, S. J., 1983, Evolution of salt structures, East Texas diapir province; Part 1, Sedimentary record of halokinesis, in M. P. A. Jackson, ed., AAPG Bulletin, United States, American Association of Petroleum Geologists : Tulsa, OK, United States, p. 1219-1244.

Sinclair, H. D., 2002, Depositional evolution of confined turbidite basins, in M. Tomasso, ed., Journal of Sedimentary Research, United States, Society of Economic Paleontologists and Mineralogists : Tulsa, OK, United States, p. 451-456.

Tari, G., Molnar, J., Ashton, P., Hedley, R., 2000, Salt tectonics in the Atlantic margin of Morocco: The Leading Edge v. 15, p. 1074–1078.

Tari, G. C., Ashton, P. R., et al., 2001, Examples of deepwater salt tectonics from West Africa: are they analogs of the deepwater salt-cored foldbelts of the Gulf of Mexico?: Gulf Coast Section of the Society of Economic Paleontologists and Mineralogists Transactions, v.21, p. 251-269.

Tari, G. C., P. R. Ashton, J. S. Molnar, P. Thompson, 2002, Expression of the Atlas inversion tectonics in deep-water offshore Morocco; implications for hydrocarbon exploration: in AAPG Annual Meeting Expanded Abstracts, v. 2002, p.174.

Tari, G., P. Ashton, J. Molnar, M. Sorgenfrei, P. Thompson, and D. Valasek, 2003, Comparison between the salt basins of Morocco and Madagascar (abs.): AAPG Annual Meeting Program, v. 12, p. A167.

Tari, G., J. Molnar, and P. Ashton, 2003, Examples of salt tectonics from west Africa: A comparative approach: in T. J. Arthur, D. S. MacGregor, and N. R. Cameron, eds., Petroleum geology of Africa: New themes and developing technologies: Geological Society (London) Special Publication 207, p. 85–104.

Vincent, E., Cepek, P., Sliter, W. V., Westberg, M. J., and Gartner, S., 1980, Biostratigraphy and depositional history of the Moroccan basin, eastern North Atlantic, Deep Sea Drilling Project Leg 50 : in Lancelot, Y. and Winterer, E. L. (Eds.) Initial Reports of the DSDP, US Government Printing Office, Washington, 50, p. 775-799.

Von Rad, U., and Sarti, M., 1986, Early Cretaceous events in the evolution of the eastern and western North Atlantic continental margins: Geologische Rundschau v. 75, p. 139–158.

Weaver, P. P. E., 2000, Continental margin sedimentation, with special reference to the North-east Atlantic margin, in R. B. Wynn, N. H. Kenyon, and J. Evans, eds., Sedimentology, International, International Association of Sedimentologists, International, p. 239-256.

Weisenburger, C.M., 2007, Salt Tectonics, Sedimentation, and Basin Development in Safi Haute Mer, offshore Morocco, University of Texas at Austin, Austin, TX, 106 p.

Wood, L. J., 2006, Source-to-sink sediment movements in structurally complex setting: the role of gateway basins (abs.): American Association of Petroleum Geologists Annual Convention, v. 15, p. 115.

Wood, L. J., 2007, Quantitative seismic geomorphology of Pliocene and Miocene fluvial systems in the northern Gulf of Mexico, U.S.A, Journal of Sedimentary Research, United States, Society for Sedimentary Geology : Tulsa, OK, United States, p. 713-730.

Wynn, R. B., Masson, D. G., Stow, D. A. V., Weaver, P. P. E., 2000, The Northwest African slope apron: a modern analogue for deep-water systems with complex seafloor topography: Marine and Petroleum Geology, v. 17, p. 253-265.

Zühlke, R., Bouaouda, M-S., Ouajhain, B., Bechstädt, T., and Leinfelder, R., 2004, Quantitative Meso-/Cenozoic developmet of the eastern Central Atlantic continental shelf, western High Atlas, Morocco: Marine and Petroleum Geology, v. 21, p. 225-276.

# Chapter 8: Conclusions

## SUMMARY

The chapters of this dissertation have described important scientific advancements toward the understanding of how turbidity currents interact with three-dimensional (3-D) topography, and the characteristics of the deposits that result from this interaction. In minibasin provinces, Gulf of Mexico-centric models have become the foundation of exploring for and identifying strategic deep-water hydrocarbon reserves. In a systematic identification of positive aspects, negative paradigms and possible pitfalls of current knowledge, this dissertation sought to test four hypotheses:

5. The *fill and spill* model (Booth et al., 2000) is inadequate for explaining sediment delivery to minibasins on complex slopes.
6. Confinement of minibasin deposits is not exclusively related to ponded accommodation and confined turbidity current conditions.
7. Differences in minibasin configuration and input turbidity current conditions will result in significant differences in the character of deposit geometry, architecture and grain size distribution.
8. The paleo-topographic state of a minibasin can be reconstructed based on resultant fill character and geometry.

My attempt to meet these research goals was met by applying a detailed qualitative and quantitative analysis of minibasin fill in three phases of research. These phases include (1) physically modeling flow behavior under conditions of varying topographic relief; (2) examining deep water fills in the Lobster salt basin of the proximal Gulf of Mexico shelf; and (3) examining deep water fills in the Safi Haute Mer (SHM)

minibasin from the distal shelf of offshore Morocco. The conclusions listed below are evidence of having accomplished these goals, and advances our knowledge of the consequences of turbidity current interaction with 3-D minibasin topography. This improved understanding of minibasin fill is applicable to industry for increasing confidence in subsurface interpretations and reducing risk while exploring deepwater regions.

**Physical Experiments**

Analysis of minibasin fill processes from turbidity currents has shown that:

1. Turbidity currents interact differently with 3-D minibasin topography than they do with 2-D minibasins reported from previous works. Near-bed velocity component data show the establishment of a 3-D velocity field, which has implications for distributing sediment on complex 3-D bathymetric surfaces.
2. The primary direction of flow plays an important role on the accumulation of sediment in 3-D confined basin topography. Deposits tend to be elongate along the primary transport direction and drape existing topography, while compensational stacking of deposits is evident along strike. Such strike component stacking is lacking in 2D studies and has important implications for sand distribution within these systems.
3. An increase in current confinement effectively leads to enhancing the dispersal of turbidity current material beyond the basin's margins for currents that are able to surmount 3-D confining topography. This result is due to a) increased current confinement leading to an increase in the

dispersion angle of the turbidity current; and b) increased current confinement resulting in the proximal translation of the sediment dispersal axis when the dispersion length is less than approximately ¼ the maximum basin length.

4. Coeval filling of two spatially successive basins is possible, especially under conditions of high current-efficiency and/or low basin-trapping rates.
5. Flow stripping is a more likely process by which sediments are moving across minibasin topography but is insufficient for describing fill evolution within a 3-D minibasin environment because flows can deflect around internal basin obstacles and slopes that affect the resulting deposit geometry.

Analysis of deposit geometries produced from modeled turbidity currents shows:

1. Ponding index calculations (Lamb et al., 2004) suggest that individual deposits from turbidity currents are more draped than ponded within minibasin topography. An increase in the duration of an event however will result in a deposit that is more wedged in shape.
2. Ponded deposits can occur as a result of two processes: (a) episodic, high-concentration gravity failure events; and (b) cumulative stacking of small-scale thickness changes of individual-event deposits in a minibasin fill.
3. Therefore, event-scale ponding of deposits may not necessarily reflect the dynamics of low-density turbidity currents, as depicted in published

literature models of minibasin fill, but instead may be the result of higher-concentration sediment-gravity flows.

Observations and analysis of minibasin deposit fill characteristics showed that:

1. The thickest portions of the deposits are usually confined to the inlet slope of the basin when the current width is equal to, or exceeds the basin width, and sediments are transported to more distal locations on the inlet slope when the current width is less than the basin width. At no point did the thickest deposit coincide with the contemporaneous point of maximum accommodation in the basin.
2. The geometry of individual deposits can change dramatically in a stratigraphic section taken though a basin fill, depending on the orientation of the stratigraphic section.
3. The coarsest grain sizes in a minibasin fill were encountered on the slope proximal to the sediment input, and did not coincide with either the thickest part of the deposit, nor the deepest part of the basin.
4. Reconstructions of basin topography employ methods of using deposit thickness to discern the local accommodation regime in the basin. Experimental results showed that individual deposits do not accumulate in the deepest point in the basin. Cumulatively, these deposits stack to eventually fill local basin accommodation. The distinction between processes responsible for the geometry of individual deposits and those for the cumulative (stacked) deposit should therefore be made prior to interpreting such scales of resolution.

In an attempt to resolve the relationship between turbidity current dynamics and deposit characteristics, analysis of results showed that:

1. The fall velocity of material was considered to have a primary influence on coarse-grained sediment deposition, however deposit thickness did not correlate to the fall velocity of the turbidity current. Deposits thickened further downstream than the point of maximum flow fall velocity. A positive relationship exists between the long sediment advection lengths within the current relative to the investigative basin length.
2. There appeared to be no definitive link between horizontal components of current interaction (flow convergence and divergence) and deposit thickness. Most sedimentation occurs in the zone where there are strong fluctuations in the fall velocity along the primary axis of current transport.
3. Sedimentation occurs even though high primary current velocities dominate the section relative to its lateral equivalents, and suggests that topography has a considerable effect on trapping deposits, even though sediment advection length scales are relatively high.
4. Grain size distribution in the basin is most strongly influenced by the vertical component of current velocity, $w$. Coarsest grain size fractions occur where the fall in $w$ is greatest. Low Rouse number values showed that sediments are more likely to remain suspended in the current than be deposited in the basin, which support the low magnitude of sediment trapping in the basin.

5. The obstacle presented by the basin's exit slope has a minor effect on coarse accumulation of sediment. However, the positive spike in vertical velocity associated with the obstacle appears to overcome the ability for any sediment detrainment to occur on the proximal side of these obstacles.

**Lobster Minibasin Study**

1. The assessment of predictive relationships derived from experimental data has been shown to correlate with those from lobe complex data interpreted from subsurface data in the Lobster field. Experimental results showed that favorable reservoir intervals derived from turbidity currents are more likely to occur in the proximal area of the minibasin than distal locations. Relationships from experiments coincide with the locations of LCS2 and LCS3, while the location of LCS1 remains more distal in the basin than experimental results would suggest. As a result, it is interpreted that LCS1 was deposited by flows of different size or rheology from LCS2 and LCS3, and/or may have been deposited in a more unconfined topographic regime.

**Safi Haute Mer (SHM) Minibasin Study**

The SHM minibasin study offered the opportunity to examine the fill history of a low-sediment supply, distal, rapidly subsiding minibasin. A combined seismic geomorphologic and structural analysis showed that the evolution of the SHM minibasin comprised four major phases of structural development and four phases of fill development.

1. During Phase 1, salt was deposited during the Triassic to Late Jurassic, which was followed by deposition of thick carbonate and clastic successions.
2. During Phase 2, the initiation of the growth of a salt stock in the study area was associated with the mobilization of salt. The growth and development of a passive diapir in Jurassic to Early Cretaceous time defined the second stage of structural development. Low-to-moderate seismic amplitude material filled in high accommodation zones occurring around an actively diaper, rising in response to sediment loading.
3. During Phase 3, extension in the Lower to Middle Cretaceous created salt-withdrawal accommodation as salt supply was starved and welds were created as the basin was infilled with sediment. The age of initial infilling of the mini-basin is supported by low-seismic amplitude sediment wedged fill with seismic geomorphologies interpreted as Albian-age marine sediment waves imaged in the distal portions of the study area.
4. During Phase 4, compression in the Early Tertiary attributed to the Atlas orogeny resulted in a change in the accommodation configuration of the mini-basin. High-seismic amplitude, wedged fill baselapped onto the mini-basin margins and extensive unleveed channelforms prevailed. An increase in the size and scale of channel morphologies up-section in Intervals 9 and 10 suggested an increased depositional slope, likely associated with onshore mountain building and an increased linkage of lower slope depocenters. Later on in the mini-basin history, point-sourced,

smaller-scale leveed channelized systems accompanied by mass transport events suggest unstable mini-basin margins.

5. Instability is still visible on modern seafloor, and suggests that salt is still mobile and the SHM mini-basin is presently subsiding.

**LIMITATIONS AND RECOMMENDATIONS REGARDING THIS WORK**

The conclusions of this study emphasize the importance of this dissertation to the understanding of how complex slope topography influences turbidity currents and the distribution of their resulting deposits. Nonetheless, there are limitations to this study that should be noted. Acknowledgement of the limitations in this research will form a template for building future work:

1. A spectrum of sediment gravity flows, flow durations and flow scales exist in deepwater settings. The experiments documented in this study focused on low-density turbidity currents. An application of the effects of topography on a broader range of sediment gravity flows will provide further insight that builds on the interpretations and analyses of deposit architecture in this work.
2. The experiments documented herein were scaled to three main parameters: $Fr$, $Re$, and the ratio of particle fall velocity to shear velocity, ($p = w_s/\kappa u_*$). Although these dimensionless variables were sufficiently scaled to natural systems (e.g Parsons and Garcia, 1988), the Reynolds number is still small relative to those found in natural systems. This is a limitation that I do not have a recommendation for at this time.

3. There is a need for experiments that employ different degrees of minibasin slopes. Initial condition slopes of the minibasin topography designed in experiments were large to overcome the effects of high internal frictional forces in the turbidity current at low velocities. This design may have influenced the outcome of deposit geometries contrary to natural systems.
4. Although current velocity data provided significant insights into the nature of turbidity current interaction with basin topography, improvement in the spatial density of data collection is needed to better characterize the distribution of local variations in current velocity and its relationship to sediment deposition.
5. The small scale of the experiment and resultant small scale of individual bed thicknesses made it difficult to accurately sample for vertical resolution of grain size changes. A larger experimental set up will allow one to build and thus sample thicker beds and improve the grain size analysis.
6. The spatial frequency at which you measure the thickness of an interval to calculate its ponding index will have an effect on the outcome of the calculation. The outcome of ponding index calculation will vary depending on the scale of architecture upon which calculations are made; for example in a bedset versus a bed. Therefore, calculations of ponding indices are dependent upon scale of observation and therefore influenced by the vertical and spatial resolution of a dataset. Care should be taken to

obtain as high a resolution dataset as possible when using deposit geometry as an indicator of flow process.

7. Experimental modeling was not able to replicate the intricate network and stacking patterns of architectural elements interpreted from seismic attribute extractions and well-logs. Experiments should be viewed as representations of large-scale processes that occur in nature and can provide profound insight into behavior in multiple areas of a system occurring simultaneously. They allow the effects of influencing variables to be observed in isolation and provide an opportunity to revisit the resulting deposits.
8. Deep mapping of seismic data was subject to limitations in vertical resolution of the data. As a result, the discerning of individual morphological features within stacked imaged systems and its application to experimental data is improved by higher resolution well-log data. Higher vertical resolution well data may not provide insight into event-scale processes as would whole core data, they do provide a starting point for analyzing how deposit geometry and architecture changed through time. Higher resolution seismic data will provide the best bridge between event scale stratigraphic processes and subsurface strata.
9. Seismic and well-log datasets were spatially limited and did not cover the full extents of both minibasins in this study. Effort should be made to obtain data over the entire minibasin extent when applying experimental observations because many of the relationships documented in

experimental work are premised upon understanding the entire extent of the basin.

# Appendices

## Appendix A: An Atlas of Results from Two Cases of Mini-basin Subsidence and Fill


### Summary

This atlas is a product of a joint-industry collaboration between the Subsurface Technology team at ConocoPhillips and a research team at the Morphodynamics Lab at the University of Texas at Austin to investigate submarine flow behavior under conditions of varying three-dimensional (3-D) topographic relief. The research presented comprises a significant portion of Vishal Maharaj's Ph.D. work at the Jackson School of Geosciences and is under the mentorship of Dr. Jim Buttles and Prof. David Mohrig.

Two series of experiments were executed, the data and results of which are comprehensively presented in this atlas. In the first experiment, a series of scaled unconfined turbidity current flows is run into a deep 3-D basin to investigate the character of the deposits as the basin fills. In the second series, an incremental subsidence and fill approach is implemented to investigate the effect of varying degrees of 3-D confining topography and fixed scaled turbidity current.

An extensive dataset was collected to characterize the dynamics of the turbidity currents, in addition to various data that characterizes the resulting deposits. In the analysis of mini-basin fill, stratigraphic geometries on various scales are used to calculate a 1-D Ponding index. The principle of mass conservation is applied to experimental turbidity currents to investigate the sediment trapping in mini-basins. Principles and relationships presented in this research can be used to enhance interpretations of subsurface deepwater stratigraphy and reservoir characterization as it applies to mini-basin provinces.

# TABLE OF CONTENTS (Continued)

# TABLE OF CONTENTS (Continued)

# TABLE OF CONTENTS

# 1.1 Experiment Conditions – Geometric and Fluid Parameters

**1. Sediment-Fluid Mixture Properties (Initial Conditions)**

| | | |
|---|---|---|
| Water temperature | 23 | °C |
| Ambient fluid density, $r_w$ | 0.998 | kg/L , g/cm$^3$ |
| Density of solution $r_{salt+H2O}$ | 1.006 | kg/L , g/cm$^3$ |
| Specific gravity of solution, $SG_{salt+H2O}$ | 1.007 | |
| Density of solution $r_{salt+H2O}$ | 1.005 | kg/L , g/cm$^3$ |
| Density of sediment, $r_s$ | 2.65 | kg/L , g/cm$^3$ |
| Volume concentration, $C_{s+salt+H2O}$ | 2.3 | % |
| Density of solution and sediment mixture, $r_{s+salt+H2O}$ | 1.048 | kg/L , g/cm$^3$ |
| Excess density | 5.1 | % |
| | | |
| Number of flows – Series 1 | 18 | flows |
| Average flow duration | 60 | minutes |
| Number of flows – Series 2 | 27 | flows |
| Flow duration (1-8) | 15 | minutes |
| Flow duration (8-19, 21, 23, 24, 27) | 60 | minutes |
| Flow duration (20a, 20b, 20c, 22a, 22b) | 15 | seconds |
| Flow duration (25-26) | 120 | minutes |

**2. Input Turbidity Current Dynamics**

| | | |
|---|---|---|
| Input current velocity range | 4.75-10.00 | cm/s |
| Discharge | 200-500 | cm$^3$/s |
| Reynolds Number, Re | 3000-5000 | |
| Froude Number, Fr | 0.5-0.8 | |
| Current width (Series 1) | Unconfined (Approximately equal to basin width) | |
| Current width (Series 2) | 10 | cm |
| Current thickness | 2.0-4.0 | cm |

**3. Mini-basin Container Properties**

| | Series 1 | Series 2 (Config. 1) | Series 2 (Config. 2) | Series 2 (Config. 3) |
|---|---|---|---|---|
| Length (centerline), cm | 52 | 53 | 56 | 59 |
| Width (centerline), cm | 45 | 55 | 57 | 65 |
| Maximum Depth (centerline), mm | 12 | 35 | 60 | 80 |
| Inlet Slope, $s_{i(av)}$ (initial condition), degrees | 20 | 15 | 25 | 25 |
| Outlet Slope, $s_{o(av)}$ (initial condition), degrees | 25 | 20 | 25 | 25 |

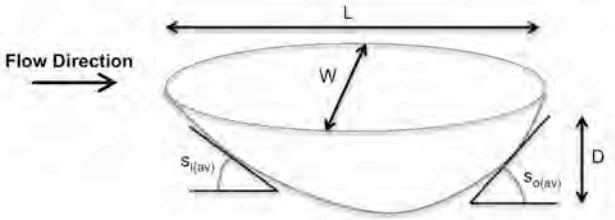


**Initial and boundary conditions for mini-basin Series 1 and 2 experiments.** Table 1 shows density properties of materials used for creating turbidity current (solution and sediment) mixture, followed by the number of flows and their durations for each series of mini-basin experiments. Table 2 lists the turbidity current fluid dynamics properties that characterize flows for Series 1 and 2. Table 3 summarizes initial basin configurations following controlled subsidence prior to turbidity current flow events. Series 2 comprises three basin configurations, and is annotated as Configurations 1, 2 and 3. The accompanying 3-D schematic figure below table 3 illustrates the dimensions relative to the basin geometry. The averaged inlet and outlet slopes are annotated as $s_{i(av)}$ and $s_{o(av)}$ respectively.

# 1.2 Experiment Conditions – Measured Silica Flour Grain Size Data (Input Condition)

| Grain Size ($x10^{-6}$ m) | Frequency | Fraction Contribution | Adjusted Concentration |
|---|---|---|---|
| 1.32 | 0.223 | 2.23E-03 | 5.80E-05 |
| 1.51 | 0.484 | 4.84E-03 | 1.26E-04 |
| 1.73 | 0.880 | 8.80E-03 | 2.29E-04 |
| 1.98 | 1.336 | 1.34E-02 | 3.47E-04 |
| 2.27 | 1.832 | 1.83E-02 | 4.76E-04 |
| 2.60 | 2.182 | 2.18E-02 | 5.67E-04 |
| 2.98 | 2.537 | 2.54E-02 | 6.60E-04 |
| 3.41 | 2.833 | 2.83E-02 | 7.37E-04 |
| 3.91 | 3.212 | 3.21E-02 | 8.35E-04 |
| 4.47 | 3.661 | 3.66E-02 | 9.52E-04 |
| 5.12 | 4.202 | 4.20E-02 | 1.09E-03 |
| 5.87 | 4.816 | 4.82E-02 | 1.25E-03 |
| 6.72 | 5.463 | 5.46E-02 | 1.42E-03 |
| 7.70 | 6.085 | 6.09E-02 | 1.58E-03 |
| 8.82 | 6.669 | 6.67E-02 | 1.73E-03 |
| 10.10 | 7.161 | 7.16E-02 | 1.86E-03 |
| 11.57 | 7.606 | 7.61E-02 | 1.98E-03 |
| 13.25 | 7.345 | 7.35E-02 | 1.91E-03 |
| 15.17 | 6.935 | 6.94E-02 | 1.80E-03 |
| 17.38 | 6.200 | 6.20E-02 | 1.61E-03 |
| 19.90 | 5.078 | 5.08E-02 | 1.32E-03 |
| 22.80 | 4.218 | 4.22E-02 | 1.10E-03 |
| 26.11 | 3.091 | 3.09E-02 | 8.04E-04 |
| 29.91 | 2.193 | 2.19E-02 | 5.70E-04 |
| 34.26 | 1.481 | 1.48E-02 | 3.85E-04 |
| 39.23 | 0.954 | 9.54E-03 | 2.48E-04 |
| 44.94 | 0.598 | 5.98E-03 | 1.55E-04 |
| 51.47 | 0.367 | 3.67E-03 | 9.54E-05 |
| 58.95 | 0.223 | 2.23E-03 | 5.80E-05 |
| 67.52 | 0.134 | 1.34E-03 | 3.48E-05 |

| Statistic | Grain Size |
|---|---|
| Median | 9.44 μm |
| Mean ($D_{50}$) | 11.43 μm |
| Variance | 71.55 $\mu m^2$ |
| S.D. | 8.46 μm |
| Mode | 10.82 μm |
| $D_{10}$ | 2.98 μm |
| $D_{90}$ | 22.80 μm |

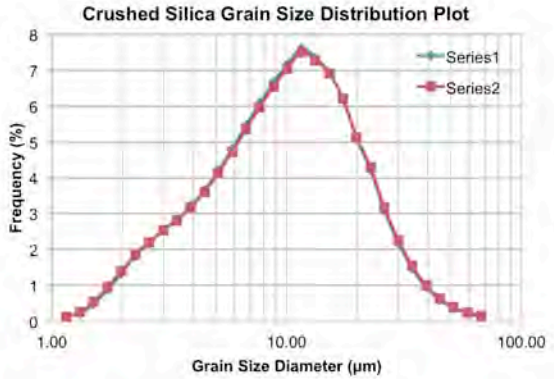


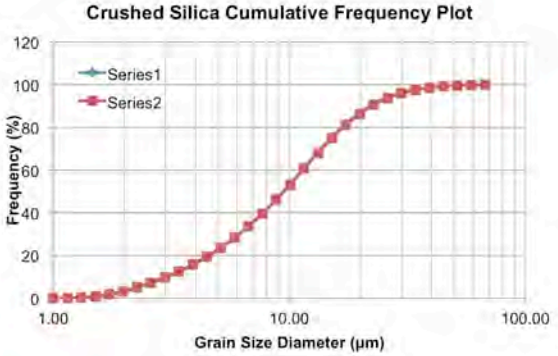


**Typical input grain size distribution data for silica flour used in turbidity current solution and sediment mixture**. Grain size data were collected from cold core samples located in the confining channel of Series 2 experiments. The table at the extreme left shows the detailed distribution of silica flour grain sizes, and range from 1.32 to 67.52 micrometers. The center table summarizes the grain size distribution by grain diameter. The median, mean, standard deviation (S.D), mode, tenth (D10) and ninetieth (D90) percentiles are recorded. The data is graphically illustrated in the frequency distribution plot in the extreme top right, and the cumulative frequency plot in the extreme bottom right of the panel.

## 1.3 Experiment Conditions – Characteristic Input Turbidity Current Velocity, Density and Sediment Concentration Profiles

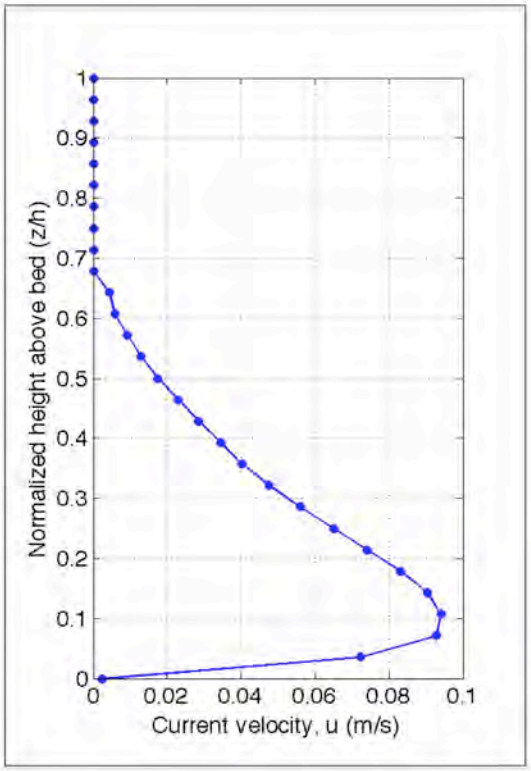


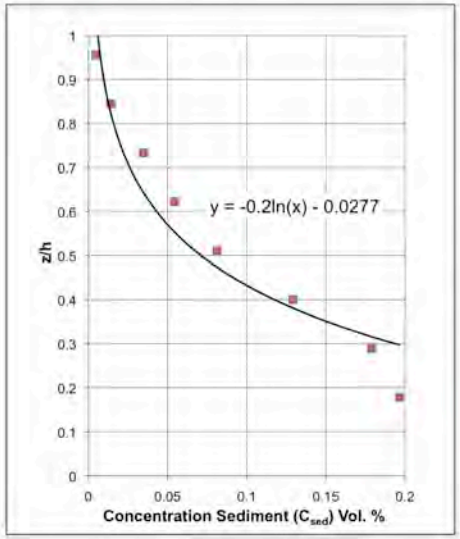


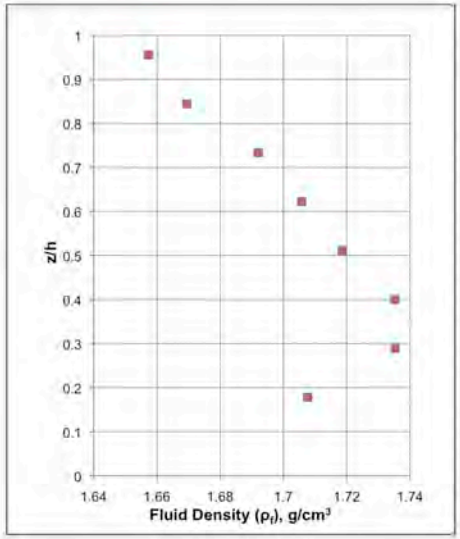


**Characteristic input velocity, and estimated current density and sediment concentration profiles for Series 2 experiment (t=14).** (A) shows a time averaged (t=15 s) velocity profile for a turbidity current entering the mini-basin collected using an Acoustic Doppler Velocimeter Profiler (PADV) and plotted with dimensionless height, z/h with h = 56mm (h=measured current thickness). (B) shows typical turbidity current concentration data from an 8-component siphon rack. An exponential function is fit to the data and forward and backward extrapolated for visualization. The equation is shown on the figure. (C) shows calculated vertical density profile from $\rho_f = \rho_{salt}(1+RC_{sed})$ using C determined in figure (B).

## 1.4 Experiment Conditions – UT Morphodynamics Laboratory Mini-basin Setup

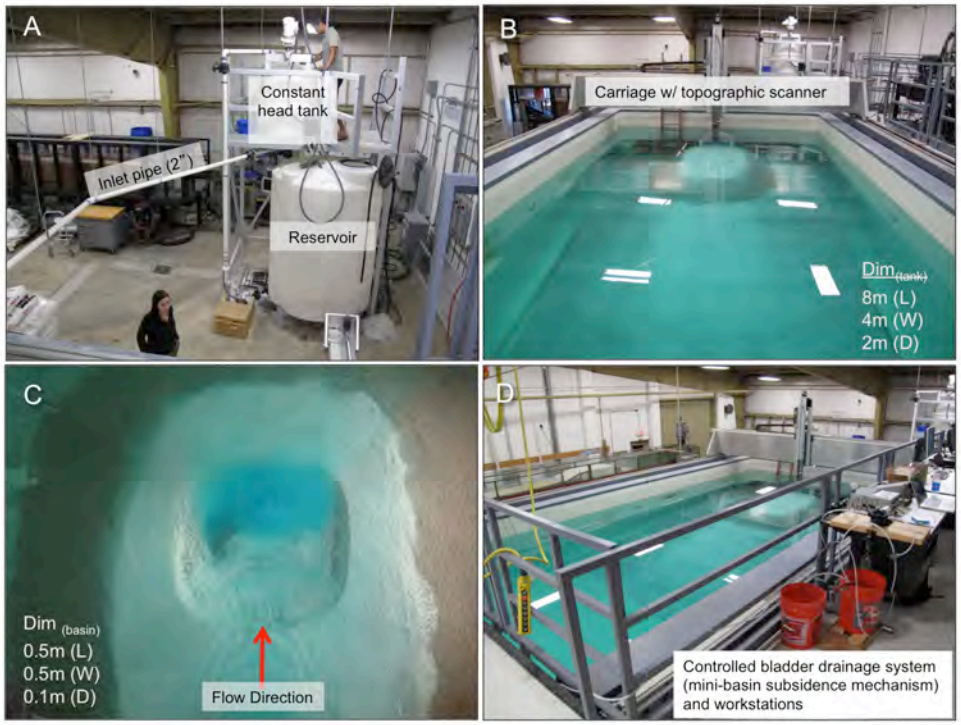


**Mini-basin experiment setup in the UT Morphodynamics Laboratory.**

Figure A shows the reservoir mixing tank where salt, sediment and water are combined to form the turbidity current slurry. The slurry is pumped to the constant head tank, and released through the inlet pipe to the experimental tank shown in Figure B. Attached to the motorized carriage is a laser topographic scanner, onto which other measuring equipment can be placed for measuring turbidity current properties (e.g. Acoustic Doppler Velocimeter (ADV), siphons and sonar equipment). Figure C shows a plan view of a fully subsided mini-basin from Series 1 experiments, and D shows the controlled bladder drainage system used to subside the experimental mini-basin.

# 2.1 Experiment Scaling – Turbidity Current Scaling Principles

## Governing Dimensionless Parameters

$$Fr = \frac{U}{\sqrt{\left(\rho_f / \rho_a - 1\right) gH}} \qquad \mathrm{Re} = \frac{UH}{\nu_f} \qquad p = \frac{w_s}{u_*}$$

Re > 1000, ensuring turbulent flow conditions on the laboratory scale (Parsons and Garcia,1998)

## Approximate Dynamic Similarity

$$(Fr)_M = (Fr)_P$$

Adapted from Mohrig and Buttles (2008)

**Laboratory scale turbidity currents (model, M) are commonly scaled to natural turbidity currents (prototype, P) using Froude number scaling.**
In the case of turbidity current scaling, the model and prototype Froude numbers (Fr) are matched. Model Reynolds numbers Re >1000 ensure a full turbulent spectrum (Parsons and García, *Phys. Fluids*, 1998). $U$ is the depth-averaged current velocity, $\rho_f$ is the average density of the turbidity current fluid, $\rho_a$ is the density of the ambient fluid (freshwater), $H$ is the depth averaged height of the current, $\nu_f$ is to the kinematic viscosity of the mixture, and g is gravity.

The dimensionless Rouse Number, p, is also used, where $w_s$ is grain settling velocity (D50 for example) and $u^*$ is the current shear velocity.

# 2.2 Experiment Scaling – Geometric Scaling: Present-day Gulf of Mexico Mini-basins

| Basin | Length (km) | Width (km) | Perimeter (km) | Area (km) | Volume (km3) | Relief (m) | Strata Geometry |
|---|---|---|---|---|---|---|---|
| Stewart | 17.6 | 9.3 | 21.8 | 31.3 | 176.2 | 60 | bowl |
| Harrison | 12.5 | 4.3 | 34.8 | 41.8 | 60.3 | 35 | bowl |
| Longvinn | 16.7 | 6.3 | 54.0 | 93.9 | 142.7 | 227 | box |
| Tiger | 21.6 | 8.3 | 55.0 | 120.2 | 297.1 | 184 | barrier |
| Lapper | 4.0 | 1.8 | 9.9 | 5.5 | 5.6 | 75 | |
| Timbalier | 7.2 | 3.8 | 21.4 | 24.5 | 39.0 | 160 | box |
| Tamu | 17.2 | 9.8 | 50.4 | 125.0 | 188.6 | 166 | barrier |
| Hancock | 17.5 | 9.3 | 51.8 | 131.3 | 209.8 | 346 | barrier |
| Ship | 13.9 | 6.8 | 44.8 | 113.4 | 189.6 | 156 | barrier |
| West Tamu | 8.3 | 4.3 | 24.2 | 27.9 | 39.2 | 78 | barrier |
| Cat | 7.6 | 5.3 | 20.8 | 30.7 | 45.2 | 101 | bowl |
| Pigmy | 28.7 | 9.8 | 86.3 | 236.1 | 452.7 | 521 | box |
| Cameron | 6.0 | 3.3 | 14.5 | 12.3 | 20.0 | 53 | barrier |
| Tiber | 15.3 | 5.3 | 42.6 | 60.8 | 106.5 | 270 | box |
| Saint Tammany | 17.8 | 8.3 | 55.5 | 109.9 | 210.6 | 305 | barrier |
| Researcher | 9.1 | 8.3 | 28.5 | 61.2 | 105.7 | 174 | bowl |
| Vermillion | 13.6 | 5.3 | 35.6 | 51.9 | 86.8 | 200 | bowl |
| Green | 12.9 | 6.8 | 36.4 | 65.8 | 112.7 | 57 | bowl |
| West Pigmy | 5.0 | 3.3 | 16.0 | 14.1 | 25.6 | 106 | box |
| Orleans | 11.3 | 7.3 | 32.0 | 64.3 | 127.2 | 150 | barrier |
| North Terrebonne | 16.3 | 5.3 | 44.6 | 56.2 | 119.5 | 247 | box |
| Orca | 26.6 | 12.8 | 83.2 | 311.8 | 684.1 | 466 | box |
| Pilsbury | 10.3 | 7.3 | 30.8 | 61.6 | 117.2 | 169 | bowl |
| Saint Mary | 25.7 | 8.3 | 75.4 | 156.3 | 289.1 | 184 | bowl |
| Jefferson | 14.9 | 7.3 | 44.3 | 80.4 | 165.8 | 228 | box |
| Terrebonne | 33.3 | 11.3 | 114.4 | 295.0 | 626.1 | 281 | box |
| Aggasiz | 23.7 | 8.3 | 86.9 | 146.3 | 299.5 | 301 | box |
| Mitchell | 19.2 | 9.8 | 53.2 | 148.8 | 289.3 | 216 | bowl |
| Saint Bernard | 8.8 | 4.8 | 20.5 | 25.2 | 53.0 | 93 | barrier |
| LaBalarche | 6.1 | 6.3 | 23.0 | 38.2 | 70.9 | 51 | |
| Choctaw | 25.5 | 12.8 | 88.6 | 242.7 | 550.5 | 443 | box |
| Mollison | 7.8 | 5.8 | 21.6 | 33.3 | 68.1 | 75 | |
| Natchez | 11.2 | 9.3 | 35.1 | 84.8 | 169.1 | 227 | |
| Hydrographer | 13.8 | 7.3 | 38.9 | 85.4 | 192.1 | 212 | bowl |
| Plaquemines | 9.6 | 6.3 | 26.4 | 45.0 | 93.2 | 75 | bowl |
| West Chitimacha | 24.1 | 13.3 | 92.8 | 251.9 | 584.8 | 442 | box |
| East Chitimacha | 23.7 | 13.3 | 88.2 | 214.5 | 495.5 | 282 | bowl |
| Atakapa | 21.6 | 9.8 | 74.9 | 175.6 | 404.4 | 399 | box |
| Arellano | 9.7 | 2.3 | 22.4 | 18.6 | 40.2 | 77 | |
| Doomes | 16.4 | 8.3 | 47.7 | 118.9 | 267.5 | 242 | barrier |
| Karankawa | 15.9 | 6.8 | 43.9 | 84.8 | 193.5 | 324 | barrier |
| Desoto | 7.9 | 5.3 | 21.6 | 29.6 | 64.0 | 66 | bowl |
| Castillo | 8.9 | 5.3 | 24.1 | 38.5 | 84.1 | 106 | |
| Estevanico | 14.2 | 9.3 | 40.2 | 101.1 | 231.4 | 126 | bowl |
| Iberia | 9.0 | 2.3 | 21.9 | 14.6 | 34.9 | 200 | box |
| Vera | 22.9 | 12.8 | 72.3 | 241.7 | 594.2 | 412 | bowl |
| **Minimum** | 4.0 | 1.8 | 9.9 | 5.5 | 5.6 | 51 | |
| **Maximum** | 33.3 | 13.3 | 114.4 | 311.8 | 684.1 | 521 | |
| **Average** | 15.0 | 7.4 | 43.7 | 96.1 | 202.8 | 204 | |
| **Standard Deviation** | 7.1 | 3.0 | 23.6 | 80.4 | 181.2 | 123.6 | |

**Geometric Scaling**

$(L)_{Model} = \lambda(L)_{Prototype}$

$\lambda_h = 1/10{,}000$

(10cm/1km)

**Gulf of Mexico mini-basin dimensions and scaled mini-basins from experiments.** The table to the left comprises simple geometry data for present-day Gulf of Mexico mini-basins (n=46) compiled by Pratson and Ryan (1994). The data include individual mini-basin length, width, perimeter, area, relief and geometry. The average, maximum, minimum and standard deviations are also represented in the lowermost section of the table. This data is used to establish dimensional relationships that illustrate trends as shown in the three plots on the right of this panel. Using a geometric scale of 1:10,000 the spatial characteristics of the experimental mini-basin can be compared.

Plot A shows the distribution of Gulf of Mexico mini-basin length vs. width ($R^2 = 0.648$); plot B shows the distribution of area vs. volume ($R^2 = 0.966$); and plot C shows the distribution of length vs. relief ($R^2 = 0.613$). Superimposed on these plots is the scaled mini-basin data represented by the yellow star for the Series 1 experimental basin and Configuration 3 of the Series 2 experiment.

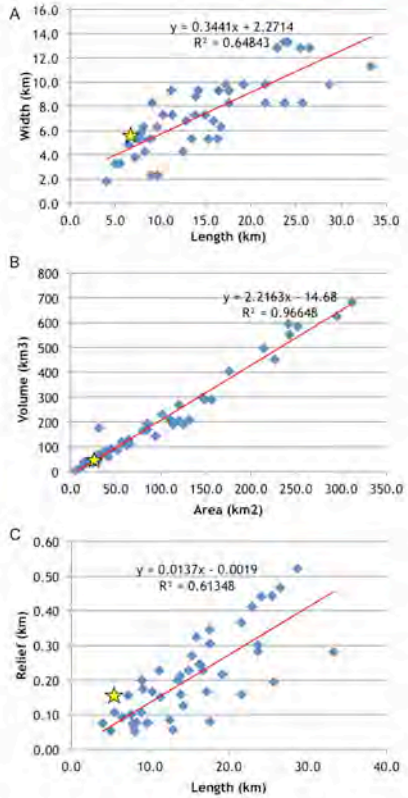


Data Source: Pratson, L.F., and Ryan, W.B.F., 1994, Pliocene to Recent infilling and subsidence of intraslope basins offshore Louisiana: American Association of Petroleum Geologists, Bulletin, v. 78, p. 1483–1506.

## 3.1 Series 1 – Experiment Condition: Mini-basin Schematic and Current Generation

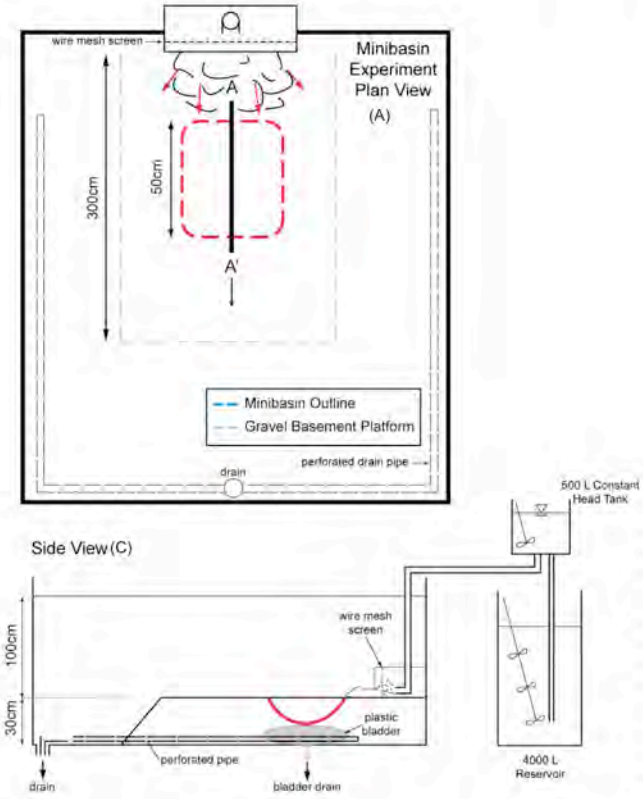


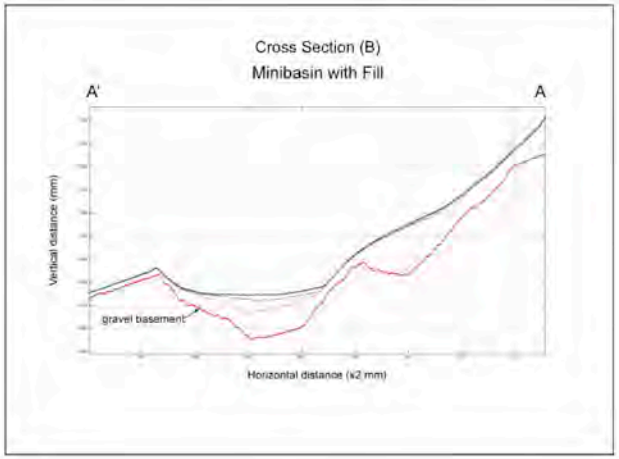


**Schematic figure for Series 1 of the mini-basin experiments and current generation conditions.** Plan view of the basin tank (A) with the completely subsided mini-basin configuration. The bold outline represents the extent of the false floor, and the dashed red outline represents the extent of the mini-basin. Dimensions of the mini-basin cross-section is shown in (B). Side View (C) shows the reservoir tank where sediment, water and salt are mixed and then pumped to the upper constant head tank. Currents are generated by releasing the mixed fluid from the head tank into the basin tank/ mini-basin through a wire mesh screened entrance box. As the currents move over the edge of the false floor they are drained away by a system of perforated pipes in order to minimize basin tank wall reflections. The mini-basin cross-sectional shape was established by controlled drainage of a water filled bladder that was buried in a gravel basement, shown in (B). The dimensions of the bladder were 40 cm (L) x 40 cm (W) x 15 cm (D). The inlet box configuration for the mini-basin was oriented parallel to the long axis of the basin tank.

## 3.2 Series 1 – Bathymetry and Slope Maps

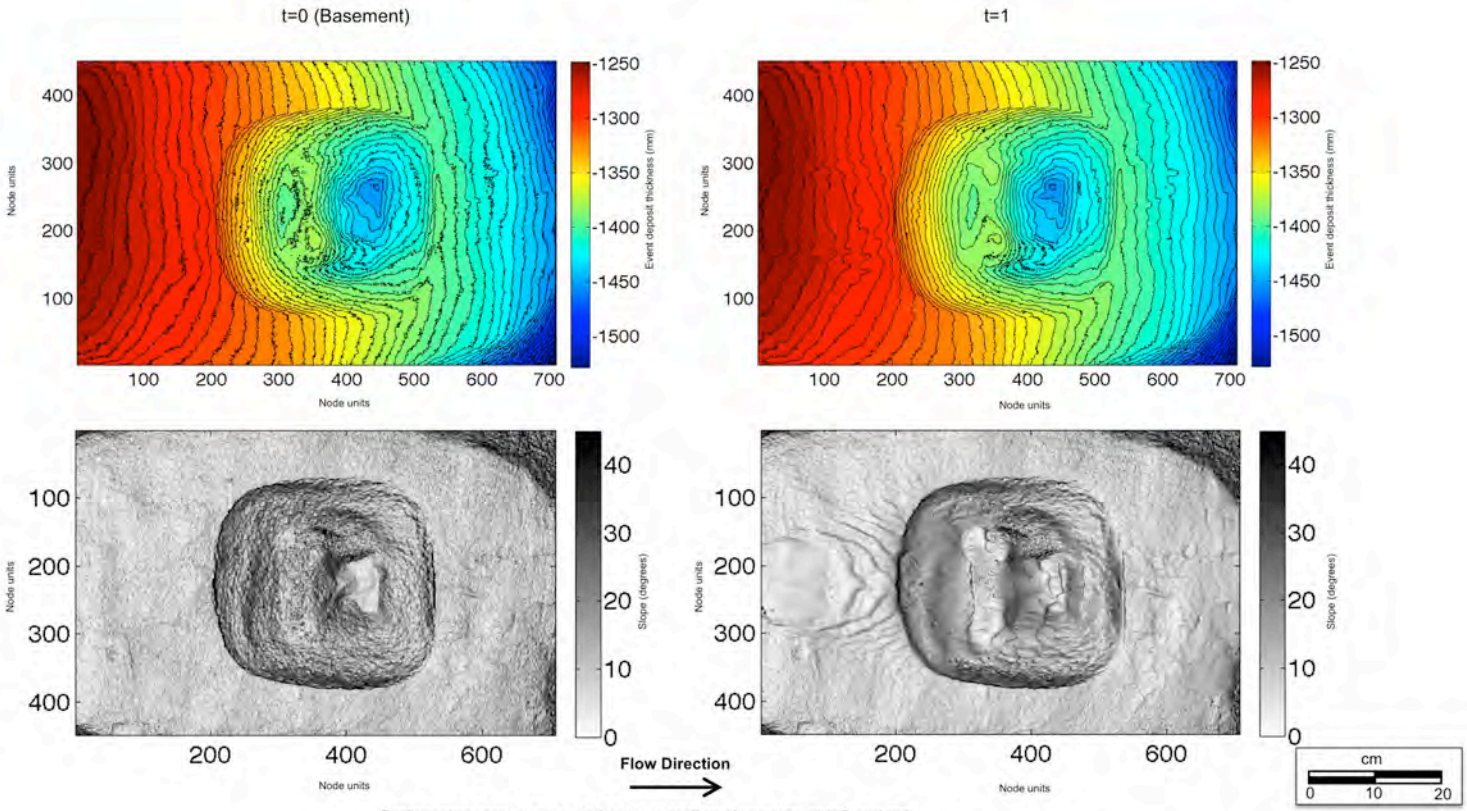


**Bathymetry contour map and corresponding slope map at t=0 and t=1.**
The surface at t=0 represents the initial basin configuration at maximum basin subsidence, and the surface at t=1 represents the depositional surface following flow event 1.

Note: 1 node unit = 2 millimeters

## 3.2 Series 1 – Bathymetry and Slope Maps

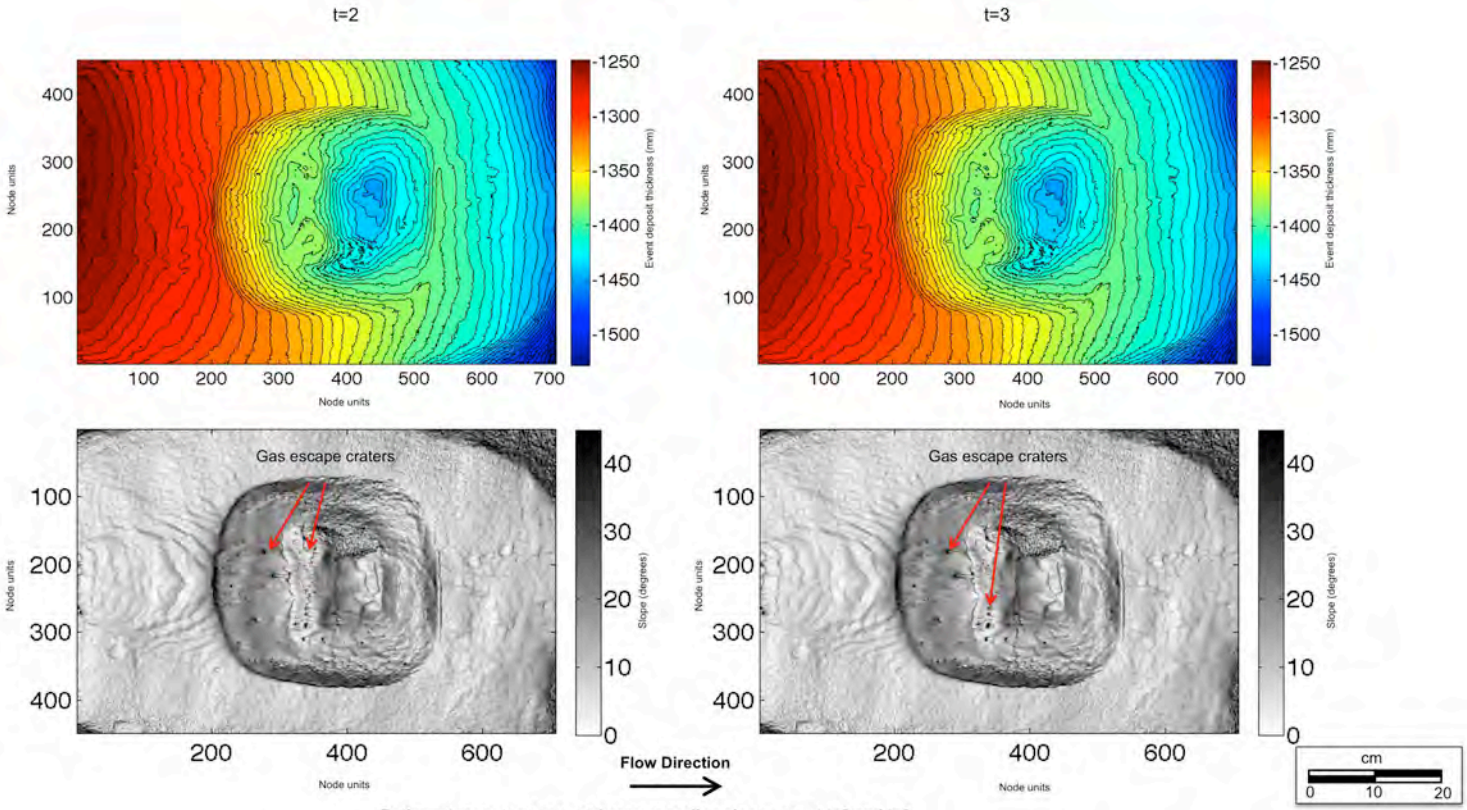


**Bathymetry contour map and corresponding slope map at t=2 and t=3.**
Gas escape craters are due to air release from gravel basement.

Note: 1 node unit = 2 millimeters

## 3.2 Series 1 – Bathymetry and Slope Maps

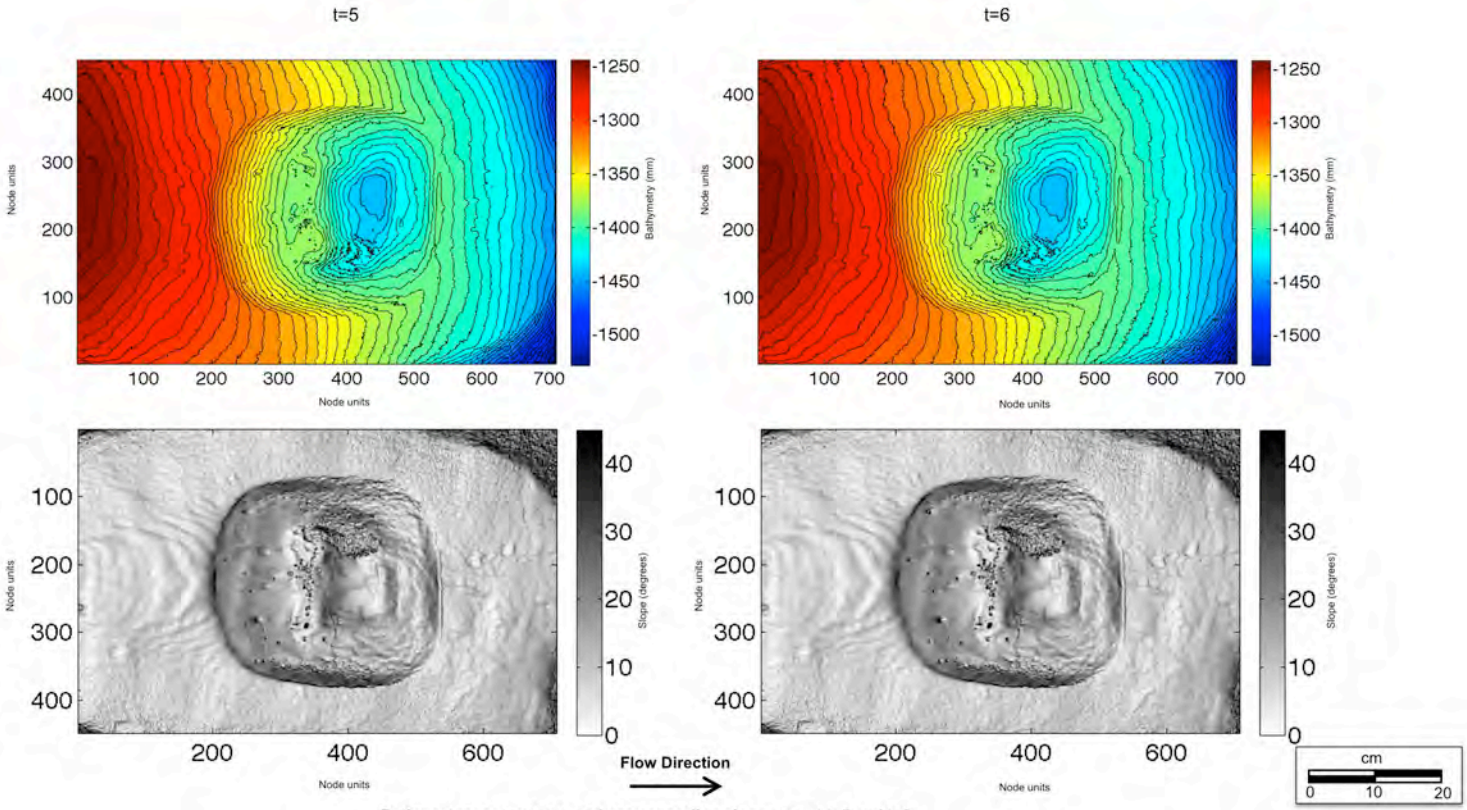


**Bathymetry contour map and corresponding slope map at t=5 and t=6.**
Note: map at t=4 is not included.

Note: 1 node unit = 2 millimeters

## 3.2 Series 1 – Bathymetry and Slope Maps

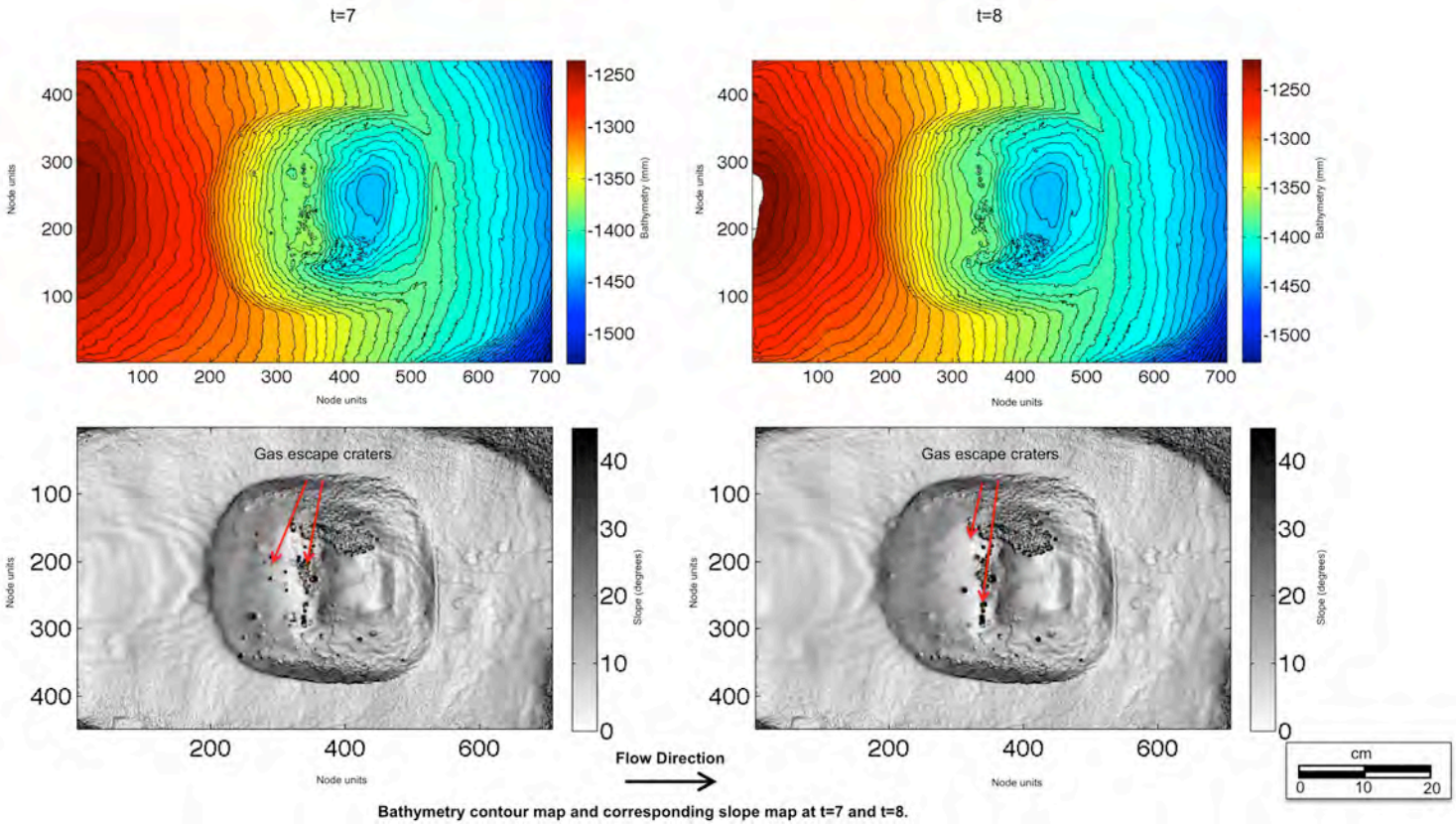


**Bathymetry contour map and corresponding slope map at t=7 and t=8.**

Note: 1 node unit = 2 millimeters

## 3.2 Series 1 – Bathymetry and Slope Maps

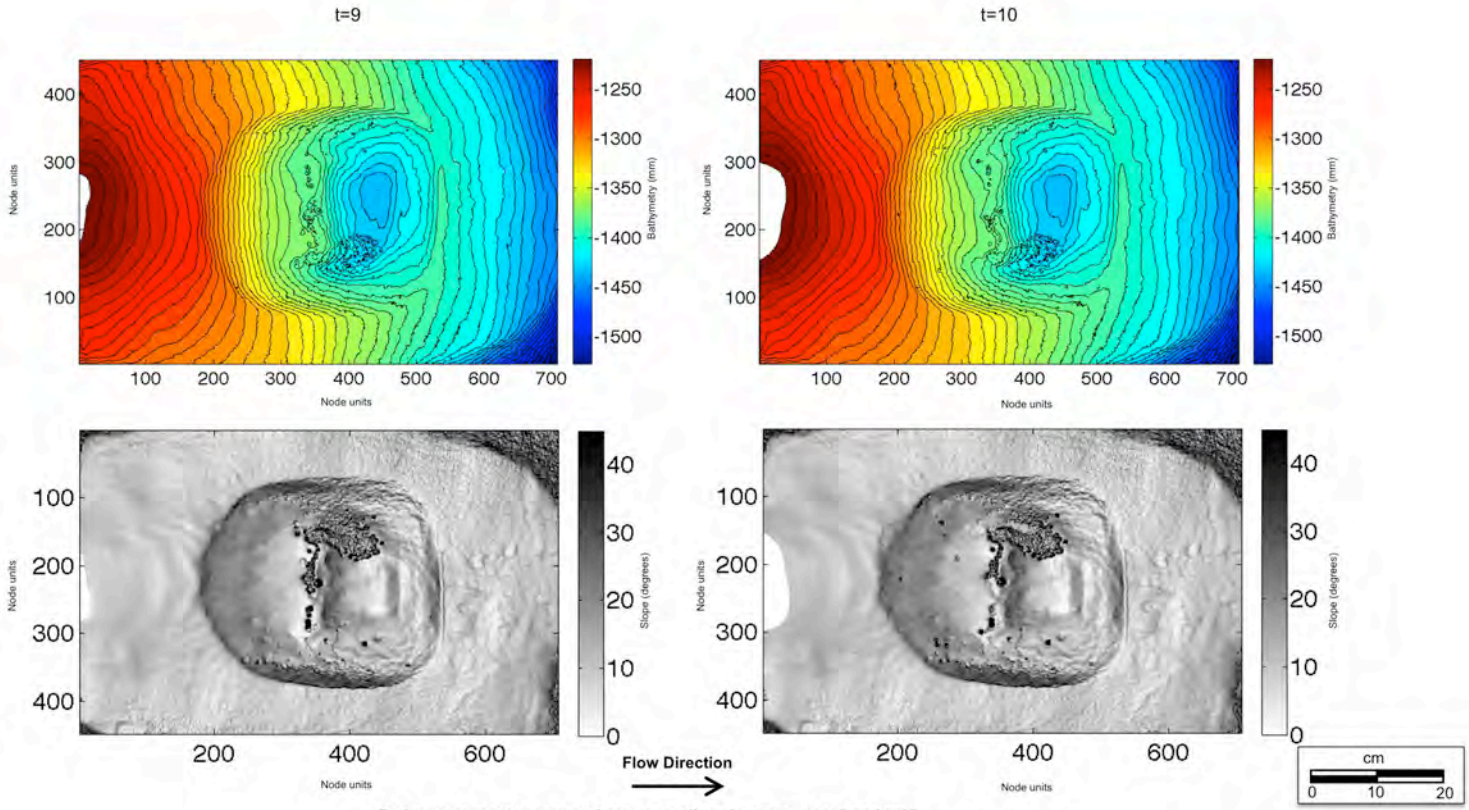


**Bathymetry contour map and corresponding slope map at t=9 and t=10.**
White area near the input (source) is due to a loss of map data.

Note: 1 node unit = 2 millimeters

## 3.2 Series 1 – Bathymetry and Slope Maps

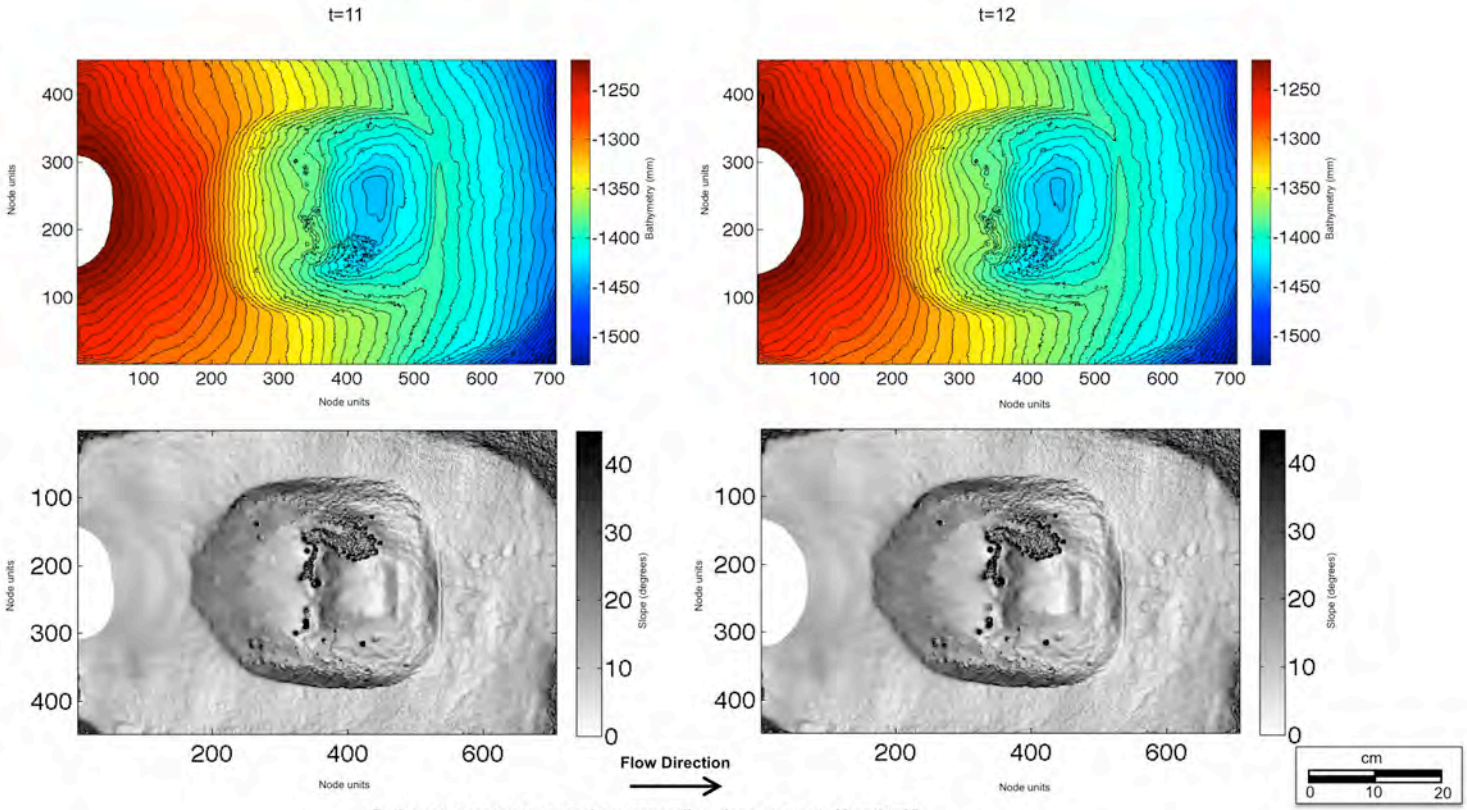


**Bathymetry contour map and corresponding slope map at t=11 and t=12.**
White area near the input (source) is due to a loss of map data.

Note: 1 node unit = 2 millimeters

## 3.2 Series 1 – Bathymetry and Slope Maps

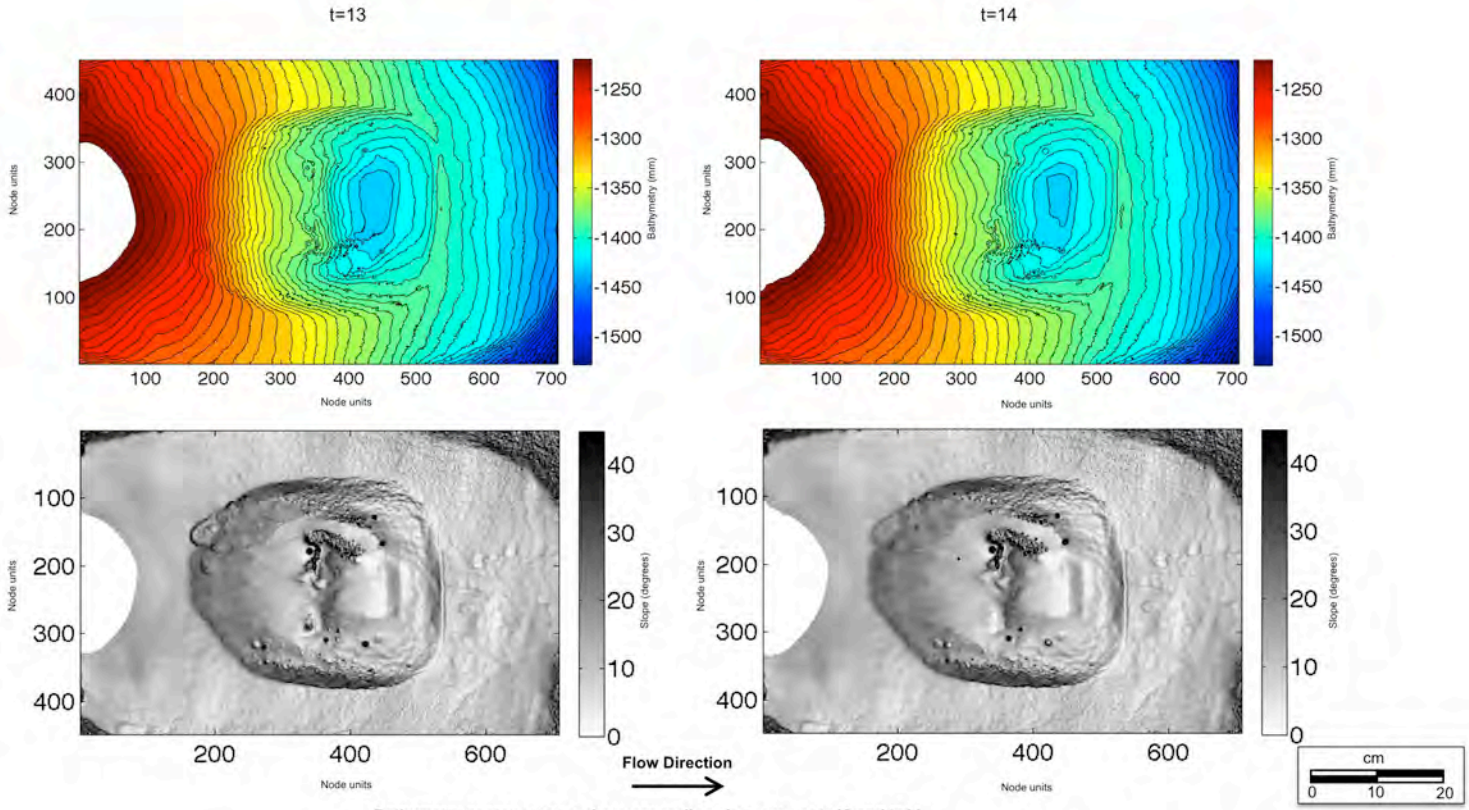


**Bathymetry contour map and corresponding slope map at t=13 and t=14.**
White area near the input (source) is due to a loss of map data.

Note: 1 node unit = 2 millimeters

## 3.2 Series 1 – Bathymetry and Slope Maps

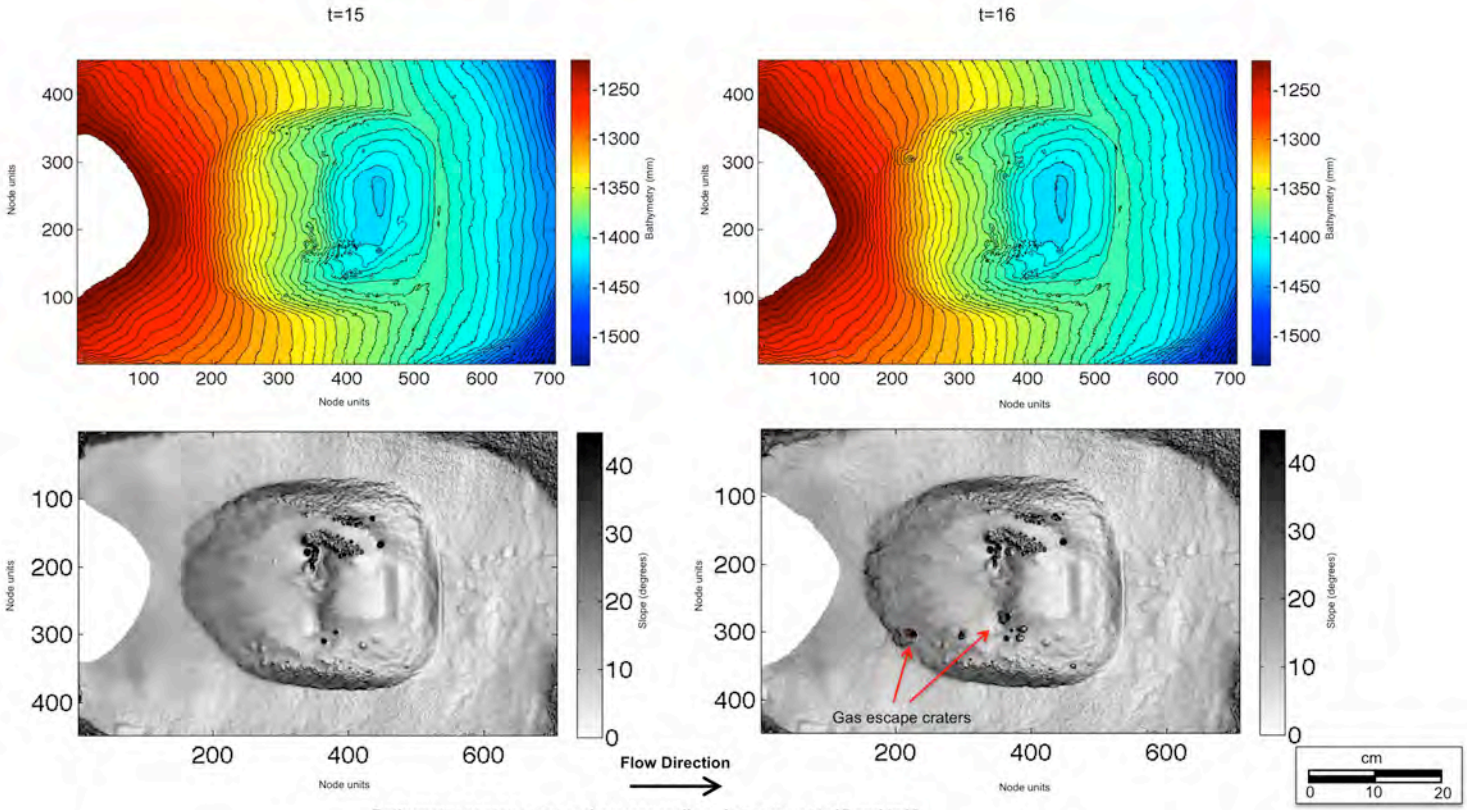


**Bathymetry contour map and corresponding slope map at t=15 and t=16.**
White area near the input (source) is due to a loss of map data.

Note: 1 node unit = 2 millimeters

## 3.2 Series 1 – Bathymetry and Slope Maps

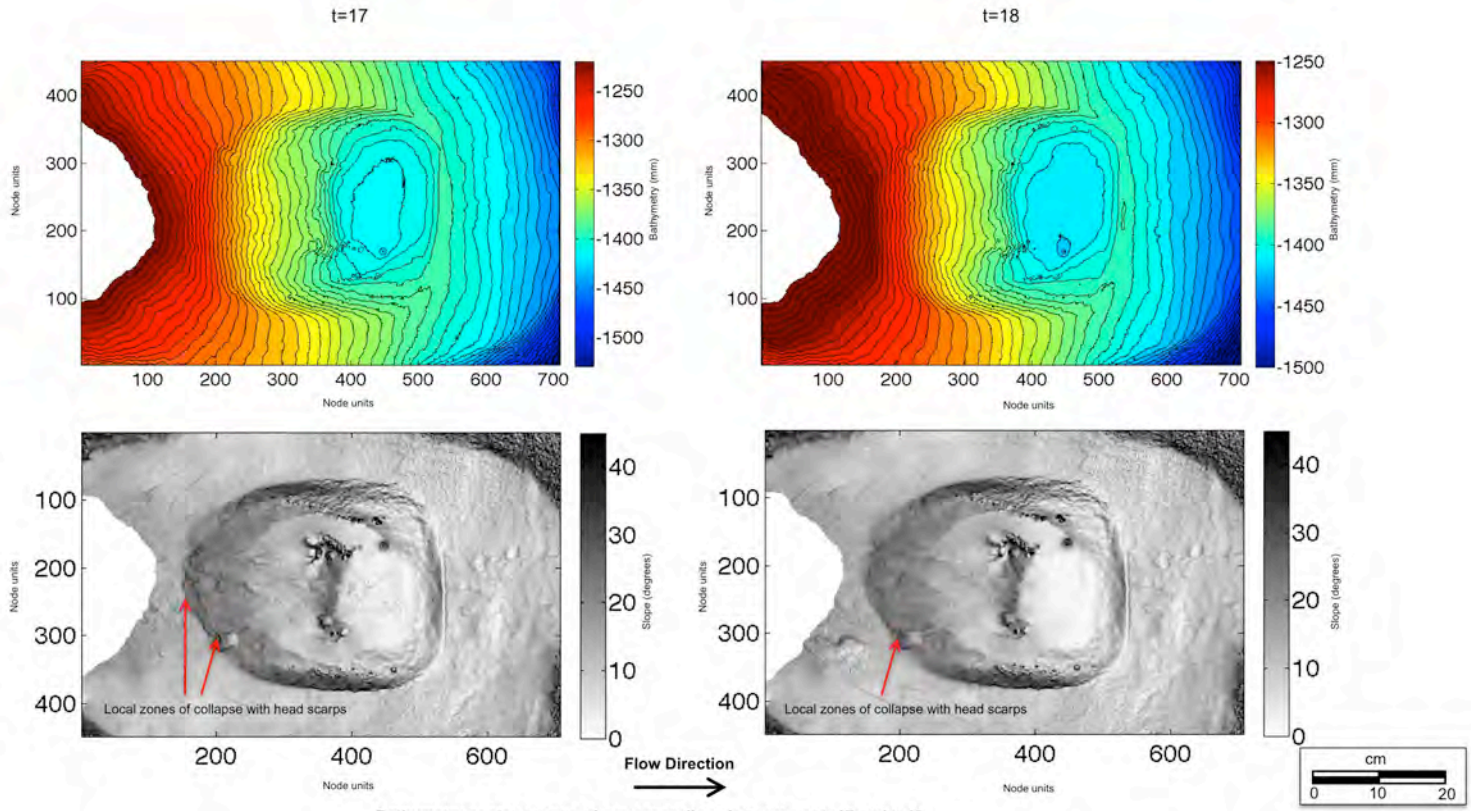


**Bathymetry contour map and corresponding slope map at t=17 and t=18.**
Deposit instability on basin slope margins during flows resulted in local zones of collapse with distinct head scarps.
White area near the input (source) is due to a loss of map data.

Note: 1 node unit = 2 millimeters

## 3.3 Series 1 – Deposit Thickness Maps

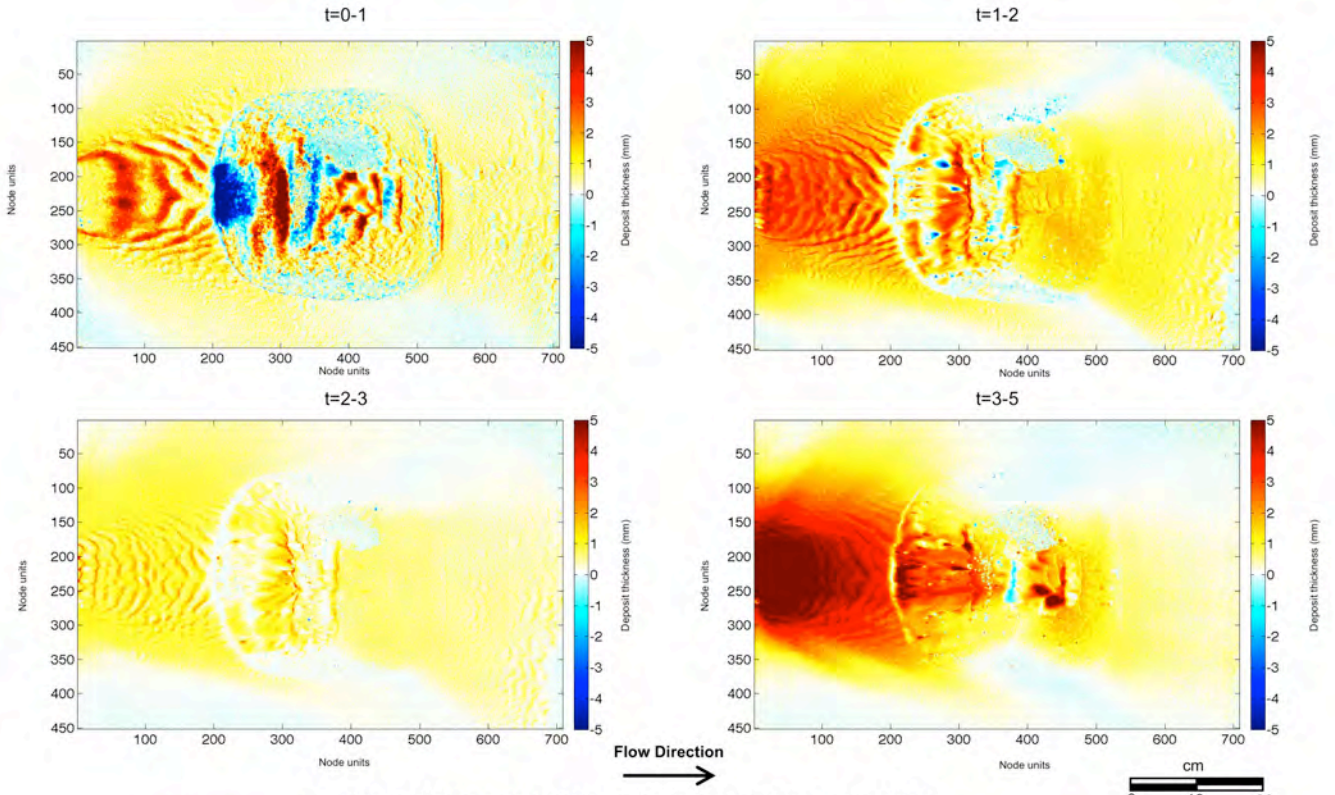


**Deposit thickness maps for flows 1-5. The surface from flow 4 is not included.**

Deposit thickness is calculated by subtracting the pre-event bathymetry from the post-event bathymetry. The colorbar ranges from negative to positive such that red regions represent addition of sediment, white represents no sediment deposition, and blue represents subtraction of sediment.

Note: 1 node unit = 2 millimeters

## 3.3 Series 1 – Deposit Thickness Maps

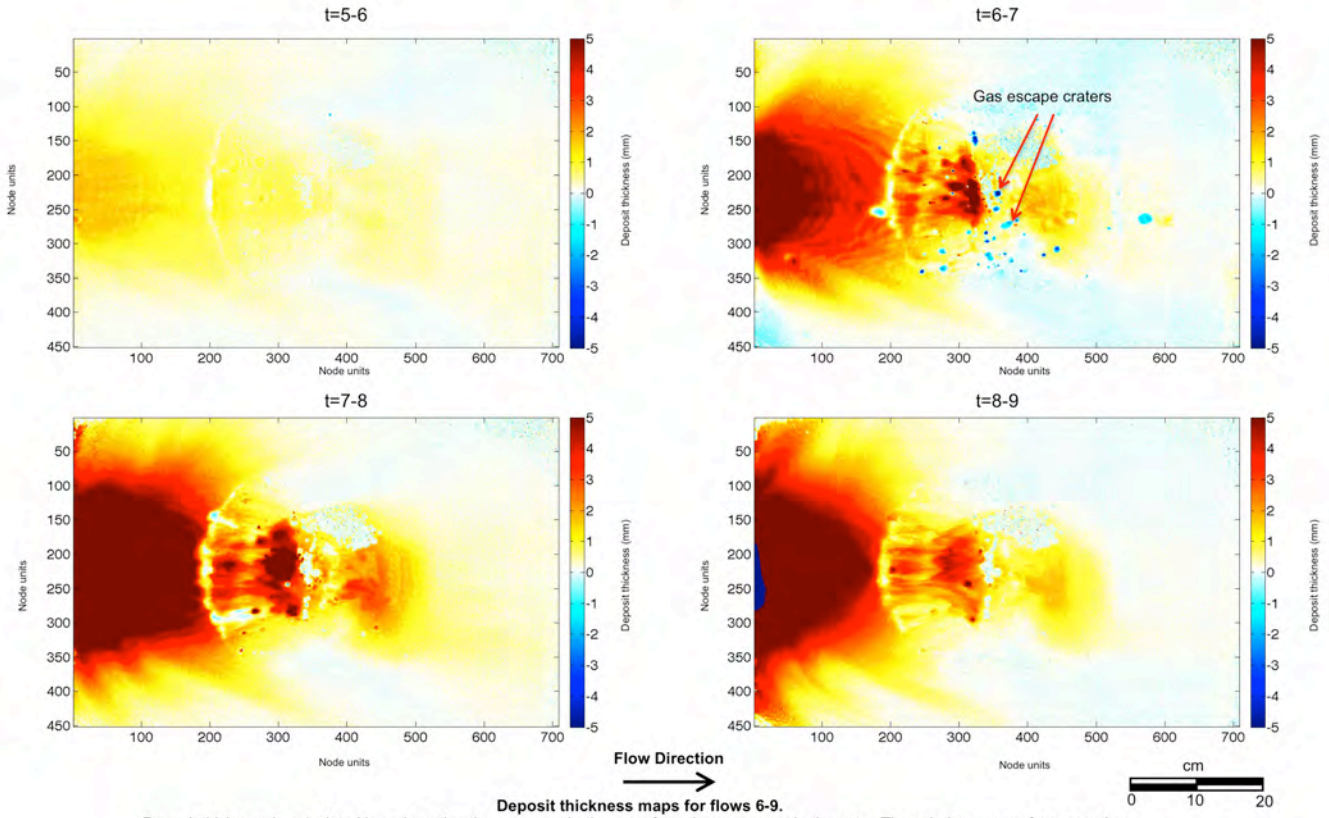


**Deposit thickness maps for flows 6-9.**

Deposit thickness is calculated by subtracting the pre-event bathymetry from the post-event bathymetry. The colorbar ranges from negative to positive such that red regions represent addition of sediment, white represents no sediment deposition, and blue represents subtraction of sediment. Note: the dark blue area near the entry point for the flow 9 deposit (t=8-9) represents null data due to laser range limitations.

Note: 1 node unit = 2 millimeters

## 3.3 Series 1 – Deposit Thickness Maps

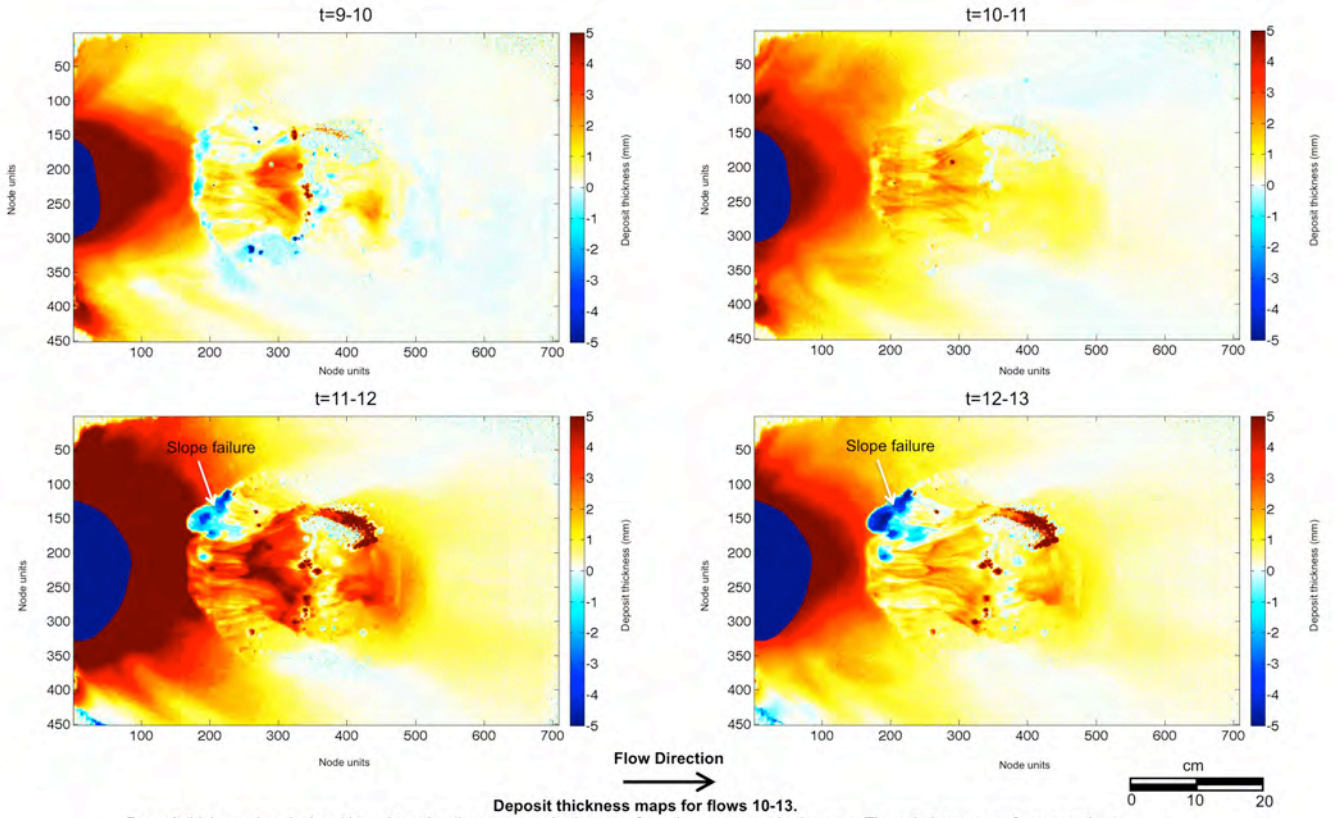


**Deposit thickness maps for flows 10-13.**

Deposit thickness is calculated by subtracting the pre-event bathymetry from the post-event bathymetry. The colorbar ranges from negative to positive such that red regions represent addition of sediment, white represents no sediment deposition, and blue represents subtraction of sediment. Note: the dark blue area near the entry point represents null data due to laser range limitations.

Note: 1 node unit = 2 millimeters

## 3.3 Series 1 – Deposit Thickness Maps

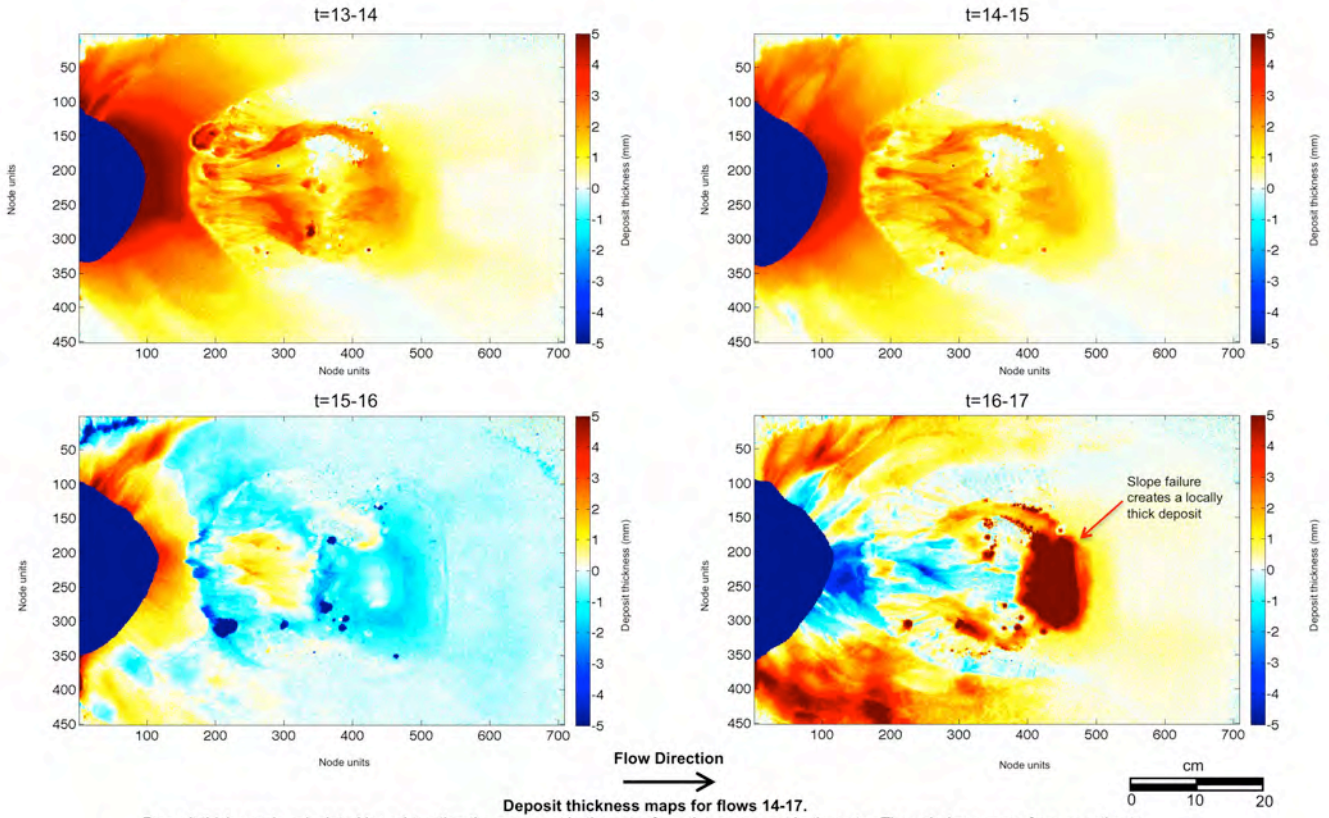


**Deposit thickness maps for flows 14-17.**

Deposit thickness is calculated by subtracting the pre-event bathymetry from the post-event bathymetry. The colorbar ranges from negative to positive such that red regions represent addition of sediment, white represents no sediment deposition, and blue represents subtraction of sediment. Note: the dark blue area near the entry point represents null data due to laser range limitations.

Note: 1 node unit = 2 millimeters

## 3.3 Series 1 – Deposit Thickness Maps

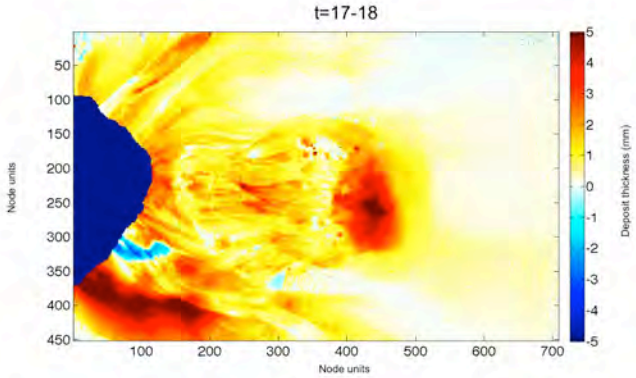


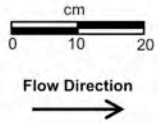


**Deposit thickness maps for flow 18.**

Deposit thickness is calculated by subtracting the pre-event bathymetry from the post-event bathymetry. The colorbar ranges from negative to positive such that red regions represent addition of sediment, white represents no sediment deposition, and blue represents subtraction of sediment. Note: the dark blue area near the entry point for the flow 18 deposit (t=17-18) represents represents null data due to laser range limitations.

Note: 1 node unit = 2 millimeters

## 3.4.1 Series 1 – Dip Cross Sections (y=160)

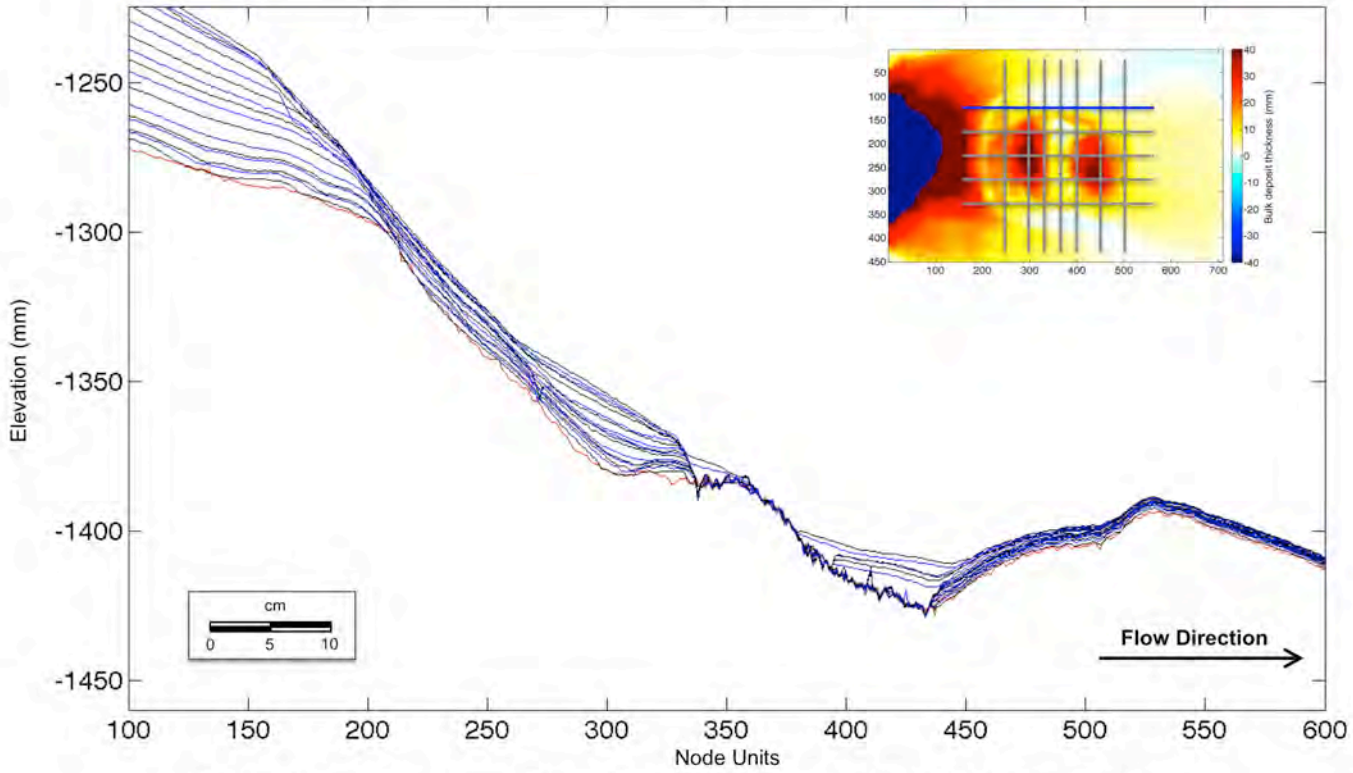


**Mini-basin (dip-oriented) cross-sections of initial surface (red) and bathymetry surfaces resulting from 18 turbidity current events.** The cross section location is also displayed in plan view, and is superimposed on a deposit thickness map of the final surface minus the initial basin surface. Note axes units: x-axis is displayed in node units, and y-axis is displayed in millimeters.

Note: 1 node unit = 2 millimeters

## 3.4.1 Series 1 – Dip Cross Sections (y=180)

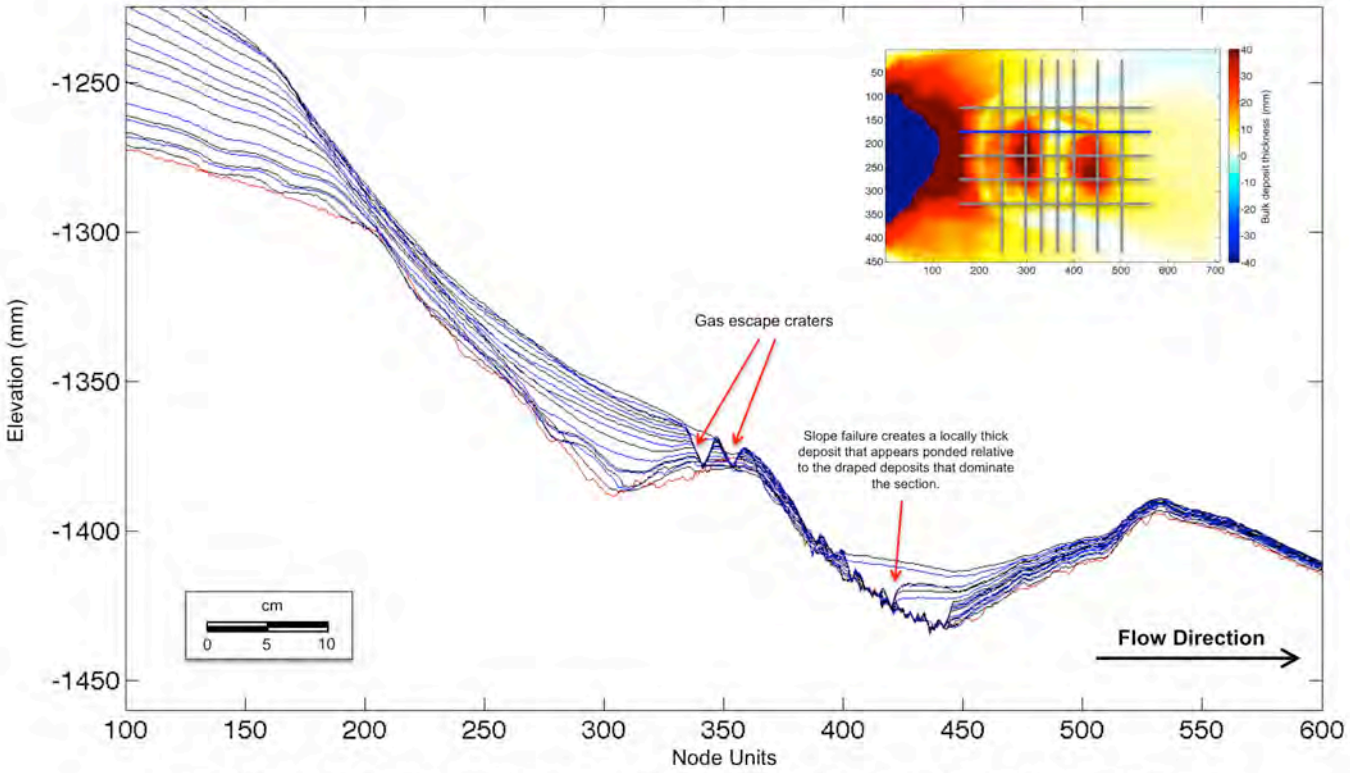


**Mini-basin (dip-oriented) cross-sections of initial surface (red) and bathymetry surfaces resulting from 18 turbidity current events.** The cross section location is also displayed in plan view, and is superimposed on a deposit thickness map of the final surface minus the initial basin surface. Note axes units: x-axis is displayed in node units, and y-axis is displayed in millimeters. For the locally thick deposit, refer to planform deposit thickness map t=16-17 in Section 3.3, Series 1 – Deposit Thickness Maps.

Note: 1 node unit = 2 millimeters

## 3.4.1 Series 1 – Dip Cross Sections (y=220)

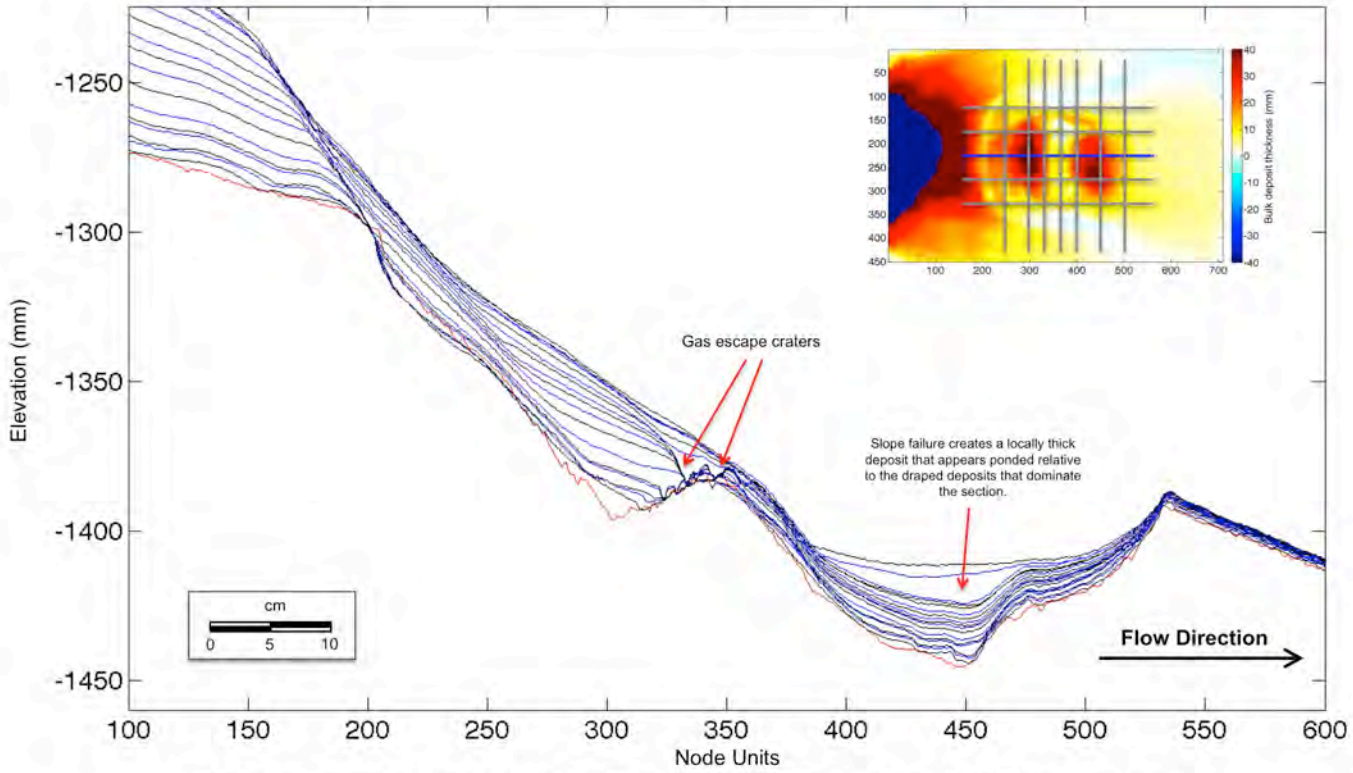


**Mini-basin (dip-oriented) cross-sections of initial surface (red) and bathymetry surfaces resulting from 18 turbidity current events.** The cross section location is also displayed in plan view, and is superimposed on a deposit thickness map of the final surface minus the initial basin surface. Note axes units: x-axis is displayed in node units, and y-axis is displayed in millimeters. For the locally thick deposit, refer to planform deposit thickness map t=16-17 in Section 3.3, Series 1 – Deposit Thickness Maps.

Note: 1 node unit = 2 millimeters

## 3.4.1 Series 1 – Dip Cross Sections (y=260)

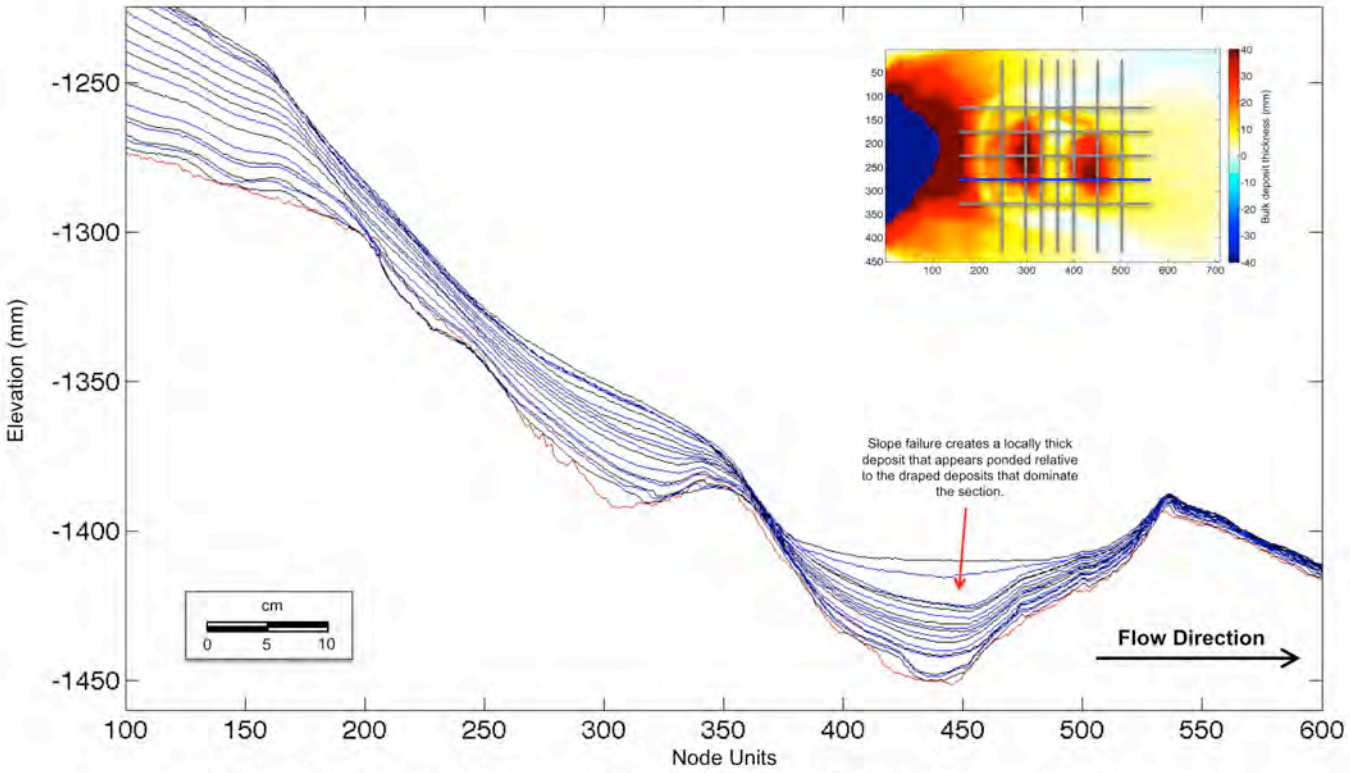


**Mini-basin (dip-oriented) cross-sections of initial surface (red) and bathymetry surfaces resulting from 18 turbidity current events.** The cross section location is also displayed in plan view, and is superimposed on a deposit thickness map of the final surface minus the initial basin surface. Note axes units: x-axis is displayed in node units, and y-axis is displayed in millimeters. Refer to planform deposit thickness map t=16-17 in Section 3.3, Series 1 – Deposit Thickness Maps.

Note: 1 node unit = 2 millimeters

## 3.4.1 Series 1 – Dip Cross Sections (y=280)

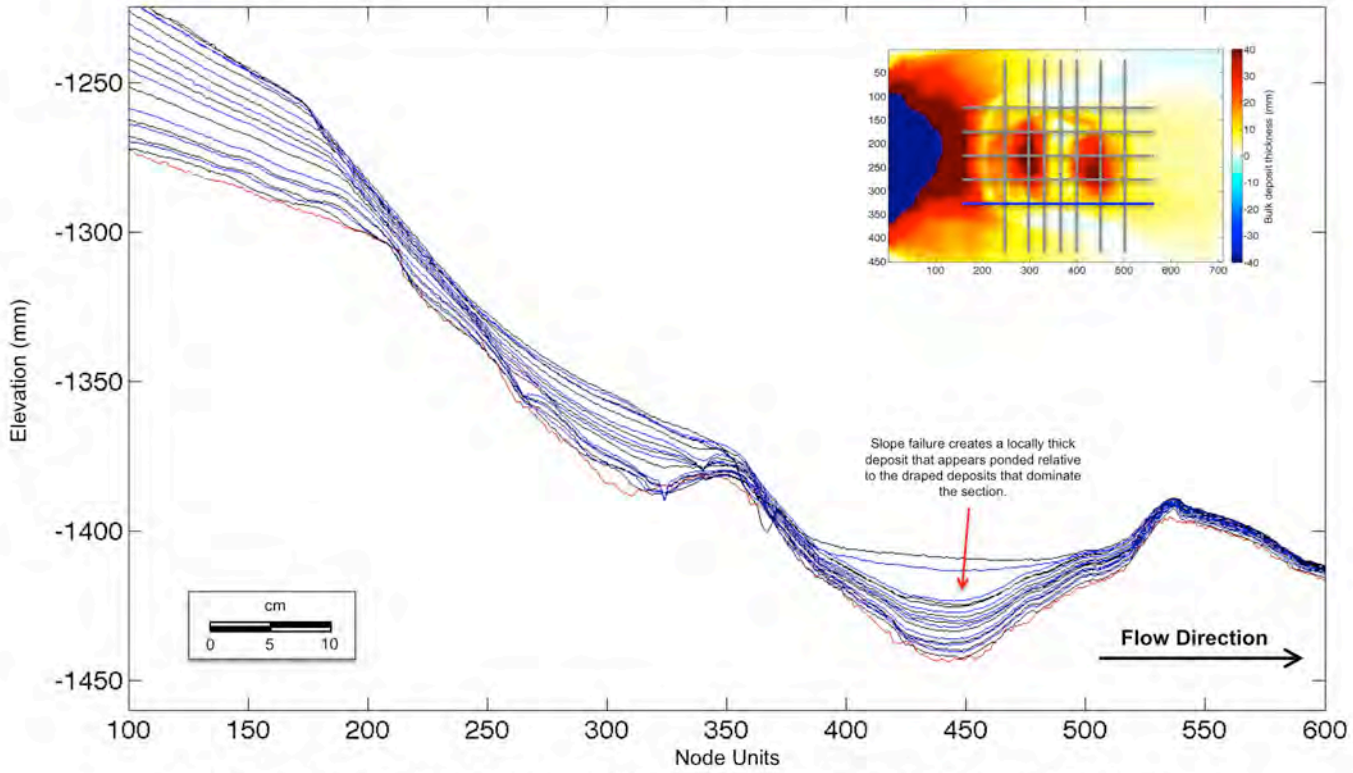


**Mini-basin (dip-oriented) cross-sections of initial surface (red) and bathymetry surfaces resulting from 18 turbidity current events.** The cross section location is also displayed in plan view, and is superimposed on a deposit thickness map of the final surface minus the initial basin surface. Note axes units: x-axis is displayed in node units, and y-axis is displayed in millimeters. Refer to planform deposit thickness map t=16-17 in Section 3.3, Series 1 – Deposit Thickness Maps.

Note: 1 node unit = 2 millimeters

## 3.4.2 Series 1 – Strike Cross Section (x=300)

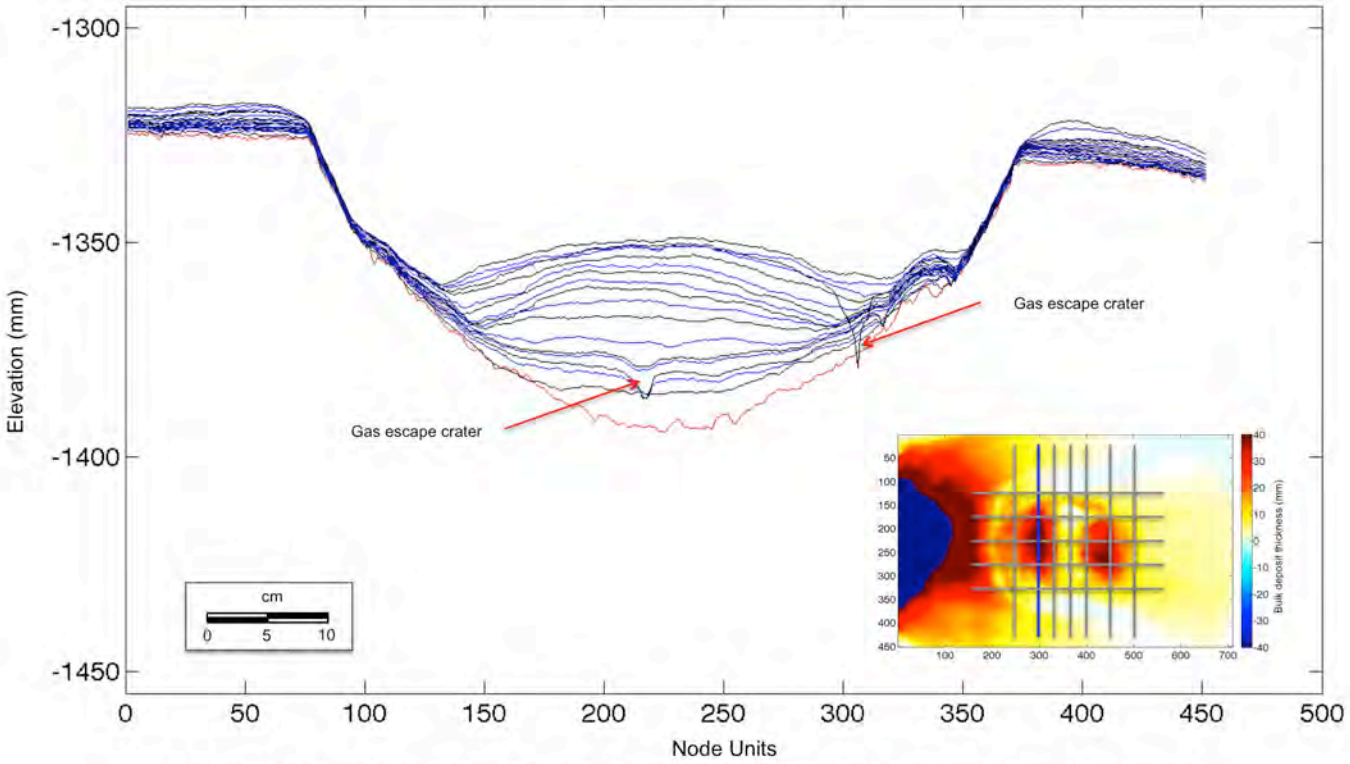


**Mini-basin (strike-oriented) cross-sections of initial surface (red) and bathymetry surfaces resulting from 18 turbidity current events.** The cross section location is also displayed in plan view, and is superimposed on a deposit thickness map of the final surface minus the initial basin surface. The panel is oriented as if you were looking downstream. Note axes units: x-axis is displayed in node units, and y-axis is displayed in millimeters.

Note: 1 node unit = 2 millimeters

## 3.4.2 Series 1 – Strike Cross Sections (x=240)

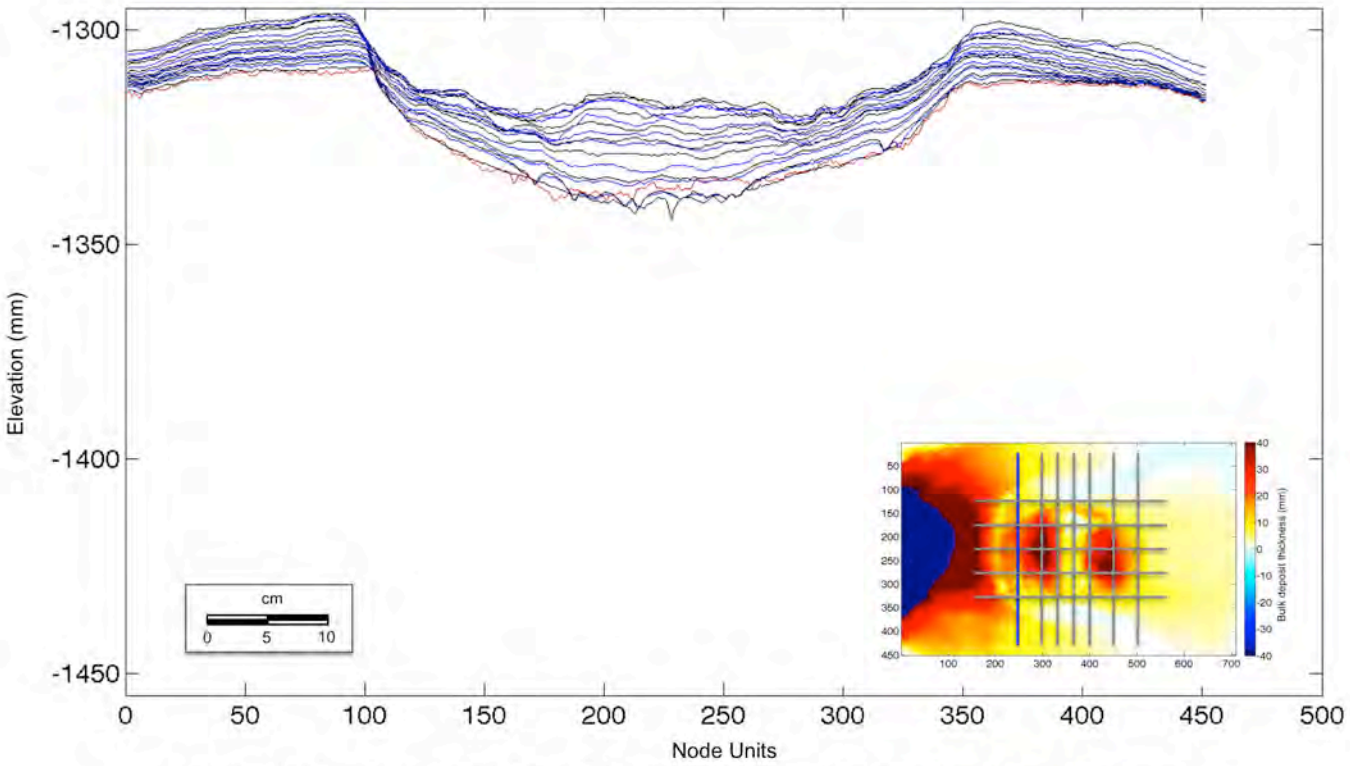


**Mini-basin (strike-oriented) cross-sections of initial surface (red) and bathymetry surfaces resulting from 18 turbidity current events.** The cross section location is also displayed in plan view, and is superimposed on a deposit thickness map of the final surface minus the initial basin surface. The panel is oriented as if you were looking downstream. Note axes units: x-axis is displayed in node units, and y-axis is displayed in millimeters.

Note: 1 node unit = 2 millimeters

## 3.4.2 Series 1 – Strike Cross Sectio (x=340)

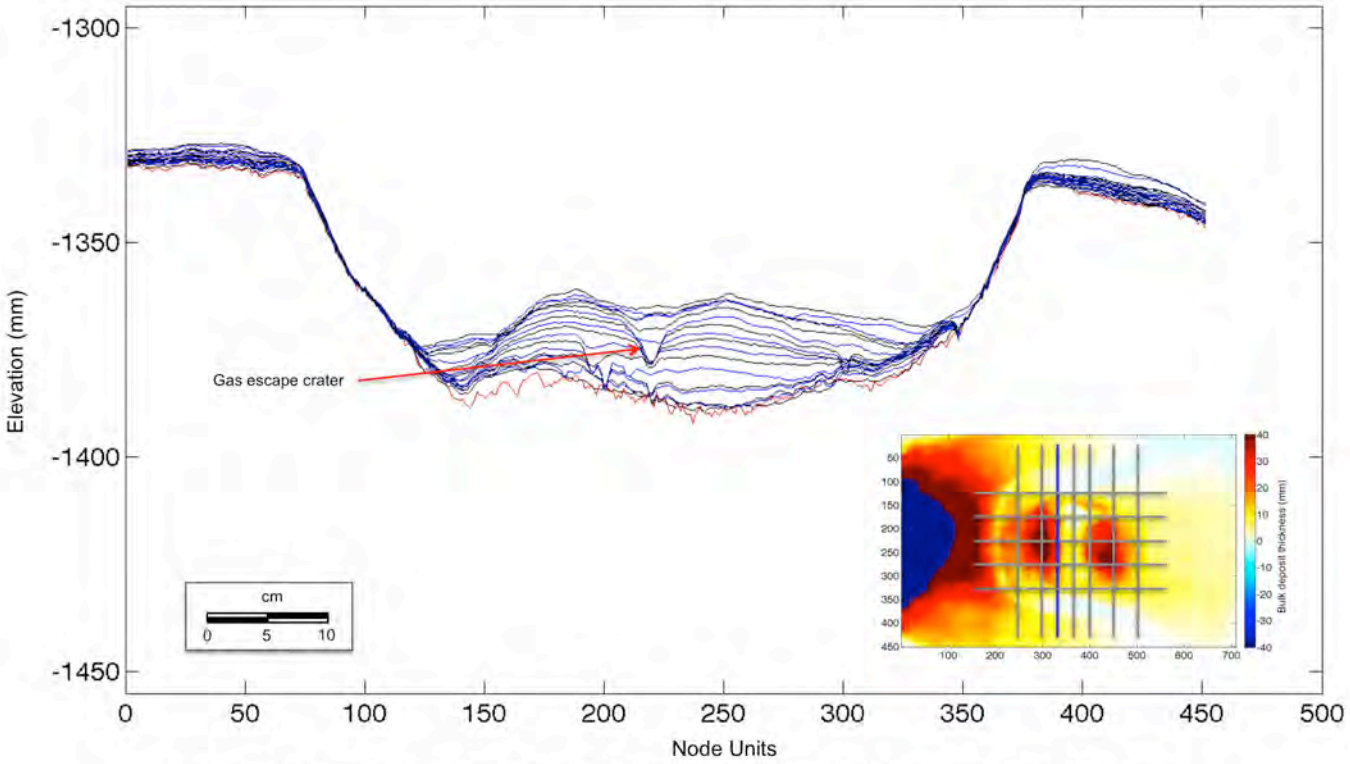


**Mini-basin (strike-oriented) cross-sections of initial surface (red) and bathymetry surfaces resulting from 18 turbidity current events.** The cross section location is also displayed in plan view, and is superimposed on a deposit thickness map of the final surface minus the initial basin surface. The panel is oriented as if you were looking downstream. Note axes units: x-axis is displayed in node units, and y-axis is displayed in millimeters.

Note: 1 node unit = 2 millimeters

## 3.4.2 Series 1 – Strike Cross Sections (x=360)

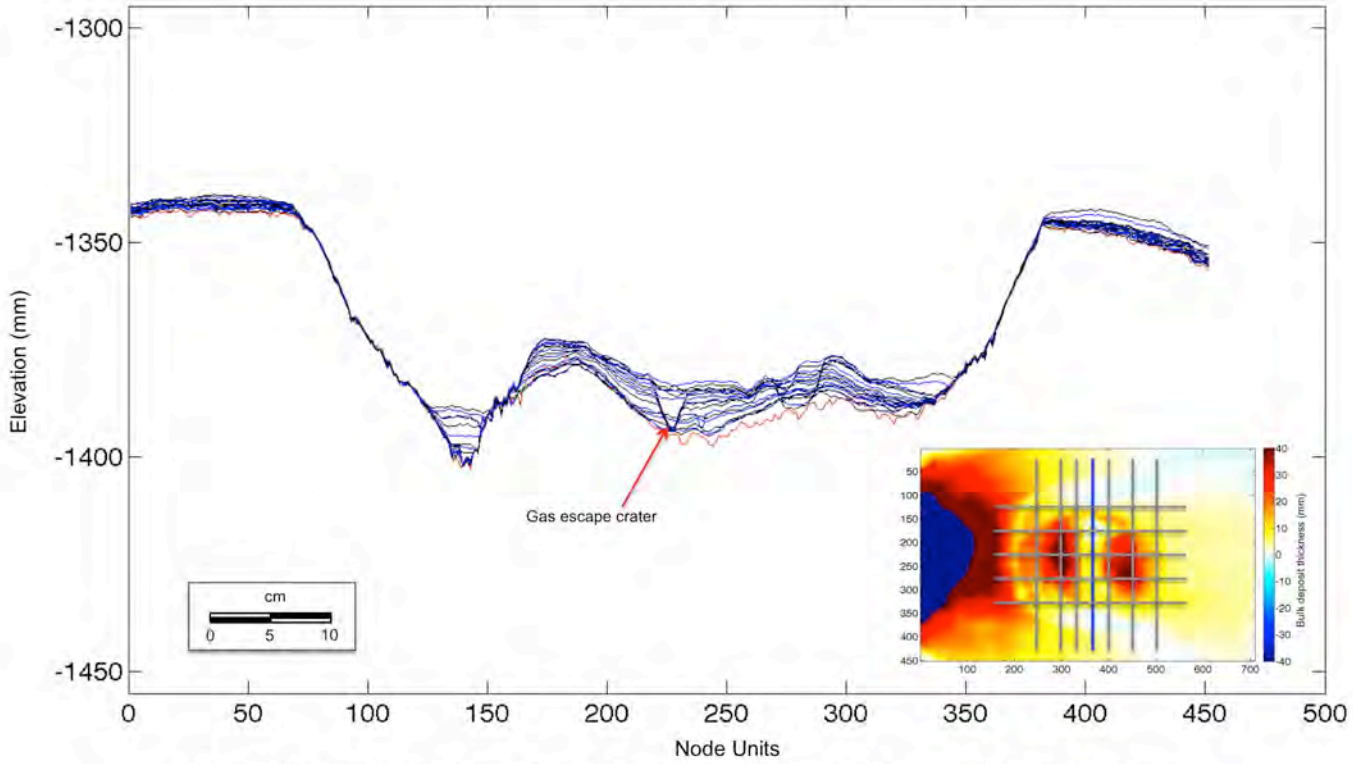


**Mini-basin (strike-oriented) cross-sections of initial surface (red) and bathymetry surfaces resulting from 18 turbidity current events.** The cross section location is also displayed in plan view, and is superimposed on a deposit thickness map of the final surface minus the initial basin surface. The panel is oriented as if you were looking downstream. Note axes units: x-axis is displayed in node units, and y-axis is displayed in millimeters.

Note: 1 node unit = 2 millimeters

## 3.4.2 Series 1 – Strike Cross Section (x=400)

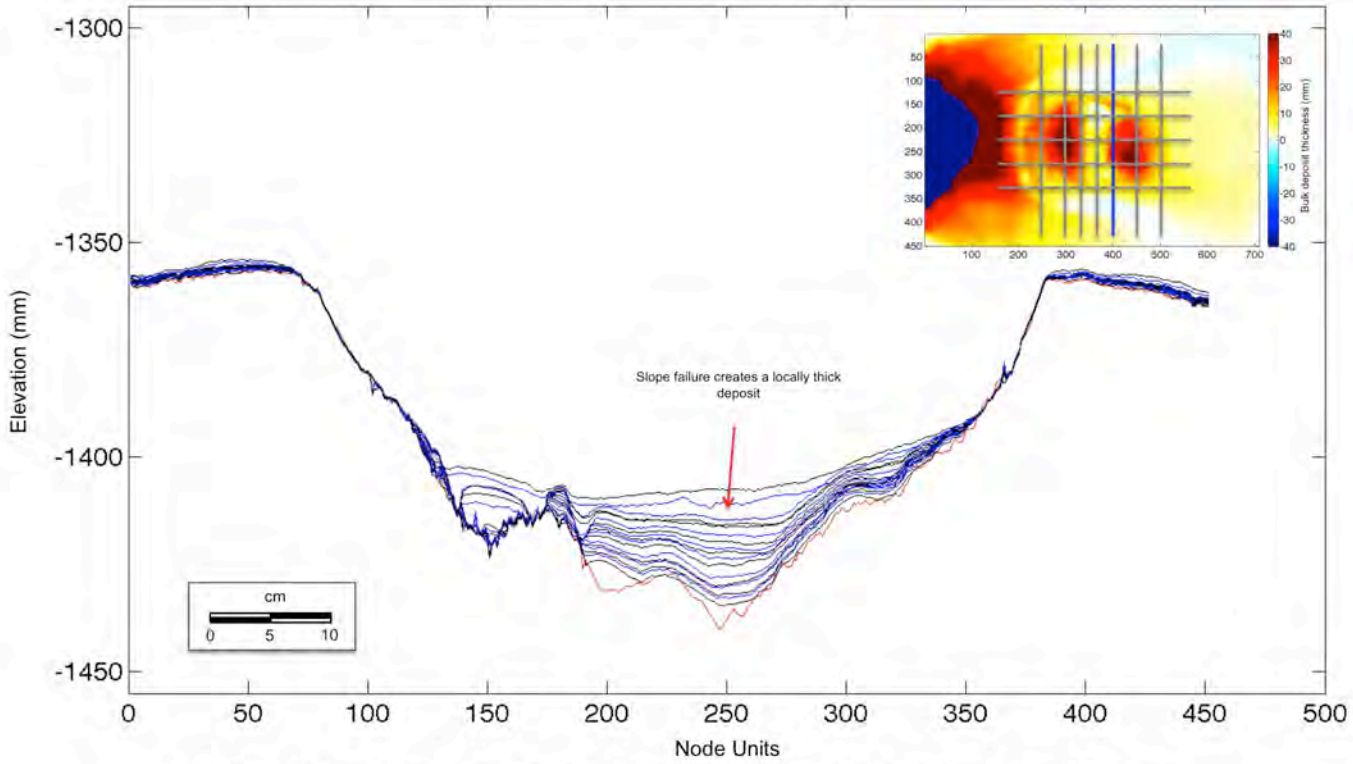


**Mini-basin (strike-oriented) cross-sections of initial surface (red) and bathymetry surfaces resulting from 18 turbidity current events.** The cross section location is also displayed in plan view, and is superimposed on a deposit thickness map of the final surface minus the initial basin surface. The panel is oriented as if you were looking downstream. Note axes units: x-axis is displayed in node units, and y-axis is displayed in millimeters. For the locally thick deposit, refer to planform deposit thickness map t=16-17 in Section 3.3, Series 1 – Deposit Thickness Maps.

Note: 1 node unit = 2 millimeters

## 3.4.2 Series 1 – Strike Cross Section (x=450)

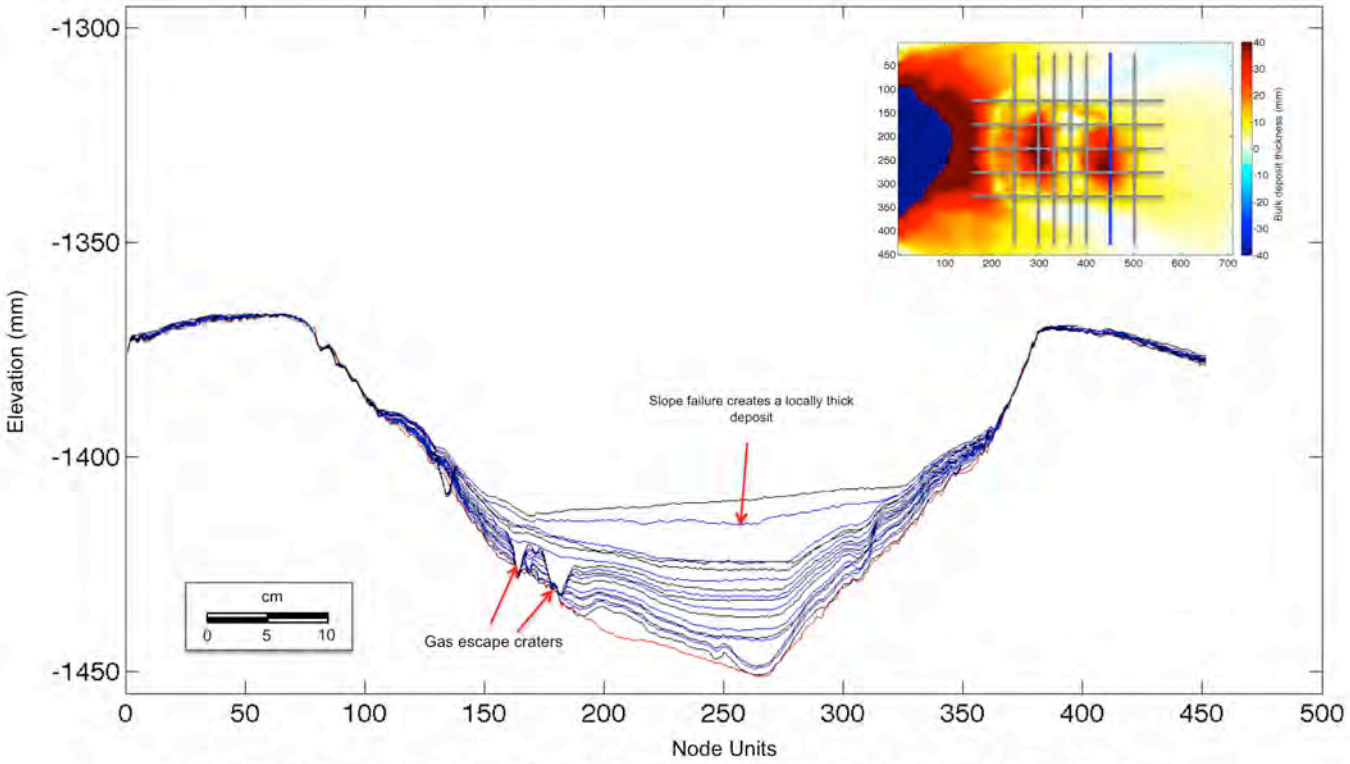


**Mini-basin (strike-oriented) cross-sections of initial surface (red) and bathymetry surfaces resulting from 18 turbidity current events.** The cross section location is also displayed in plan view, and is superimposed on a deposit thickness map of the final surface minus the initial basin surface. The panel is oriented as if you were looking downstream. Note axes units: x-axis is displayed in node units, and y-axis is displayed in millimeters. For the locally thick deposit, refer to planform deposit thickness map t=16-17 in Section 3.3, Series 1 – Deposit Thickness Maps.

Note: 1 node unit = 2 millimeters

## 3.4.2 Series 1 – Strike Cross Section (x=500)

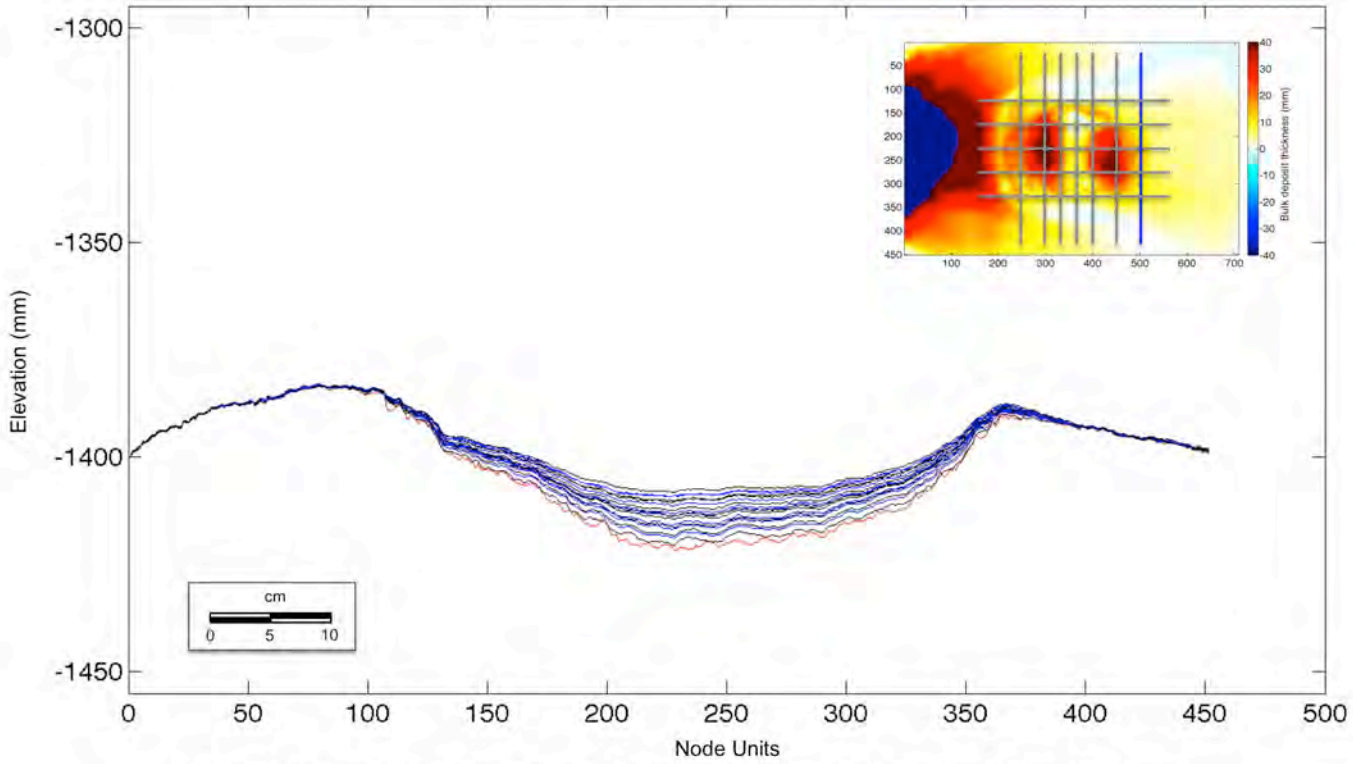


**Mini-basin (strike-oriented) cross-sections of initial surface (red) and bathymetry surfaces resulting from 18 turbidity current events.** The cross section location is also displayed in plan view, and is superimposed on a deposit thickness map of the final surface minus the initial basin surface. The panel is oriented as if you were looking downstream. Note axes units: x-axis is displayed in node units, and y-axis is displayed in millimeters.

Note: 1 node unit = 2 millimeters

# 3.5 Series 1 – Ponding Index Theory

**2-D Ponding Index, $P_0$**
**(Equation 1)**

$$P_o = -\frac{1}{L}\int_0^L \frac{d\theta}{d\eta}dx$$

x = downdip, x-contribution
L = streamwise length of basin
θ = thickness of deposit
η = elevation of initial (pre-flow) bed

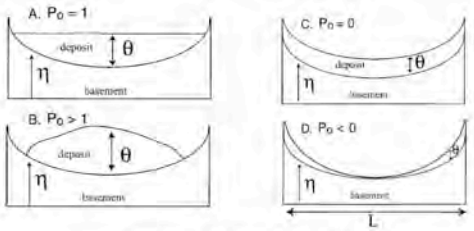


Figures modified from Lamb et al. (2004)

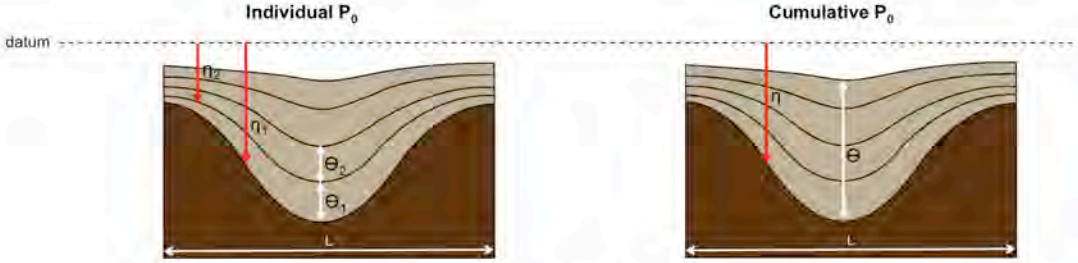


**A dimensionless 2-D Ponding Index number (Po) is used to describe the experimental deposits.**
The index is a number that compares the change in thickness of the deposit relative to the change in basin elevation over a given length (L). A deposit ponding index equal to one represents a completely ponded deposit (A, upper right figure), a deposit ponding index greater than one represents a mounded deposit (B, upper right figure), and a deposit ponding index equal to zero represents a draped deposit (C, upper right figure). A deposit with accentuated highs, meaning that the flow deposits preferentially on the slopes rather than the center of the basin, would have a negative deposit ponding index (D, upper right figure). The individual Ponding Index characterizes the geometry of a single bed relative to a prior basin deposit surface (lower left figure). The cumulative Ponding Index characterizes the geometry of a number of beds relative to the initial basin surface (lower right figure).

# 3.6 Series 1 – Ponding Index Application Summary

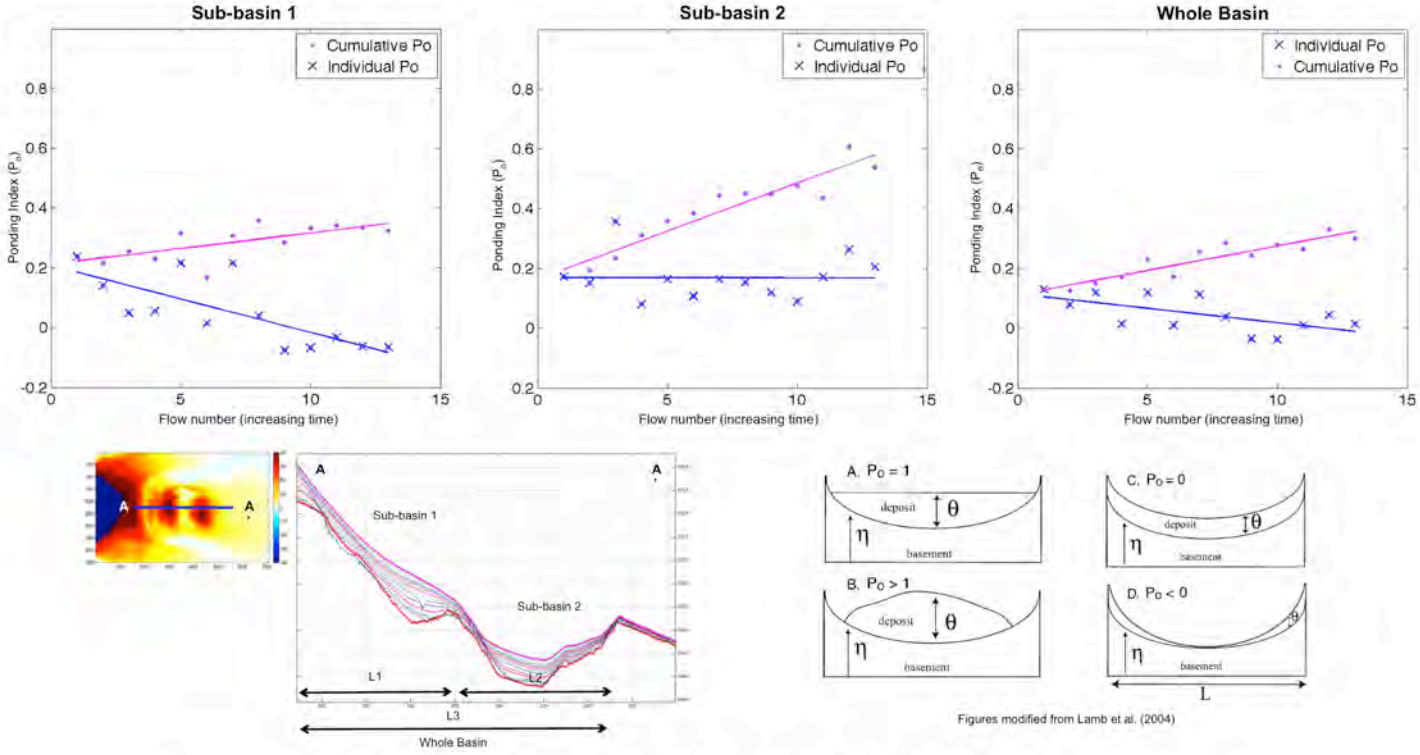


Figures modified from Lamb et al. (2004)

**Ponding Index application for deposits from 15 turbidity current events along cross-section line A-A'.**
Ponding Index is plotted as a function of flow number. In Series 1, the Ponding Index is applied to sub-basin 1, sub-basin 2 and the entire basin (lower left figure). Individual $P_o$ (blue) values trend toward a draping geometry with time (C in lower right figure). Cumulative $P_o$ (pink) values trend toward a ponded geometry with time (A in lower right figures). Whole basin Ponding Indices trend similarly.

# 3.7 Series 1 – Ponding Index Analysis (Strike-Oriented)

Proximal

Distal

Sub-Basin 1

x240

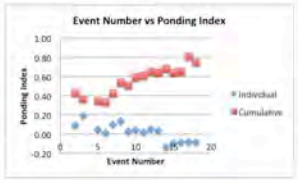


x300

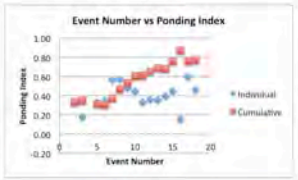


x340

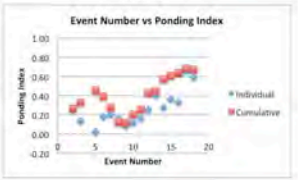


Proximal

Distal

Sub-basin 2

x360


x400

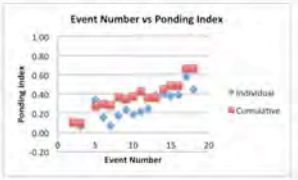


x450


x500


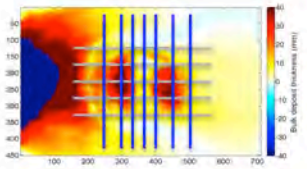

# 3.7 Series 1 – Ponding Index Analysis (Dip-Oriented)

## 4.1 Series 2 – Experiment Condition: Mini-basin Schematic and Current Generation

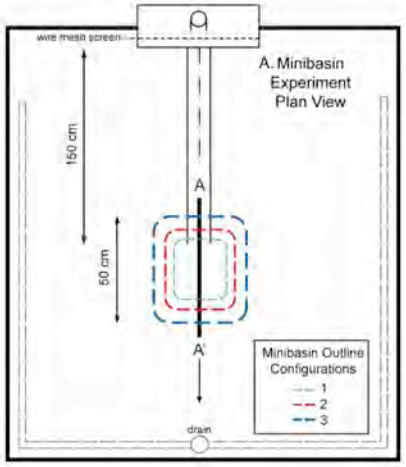


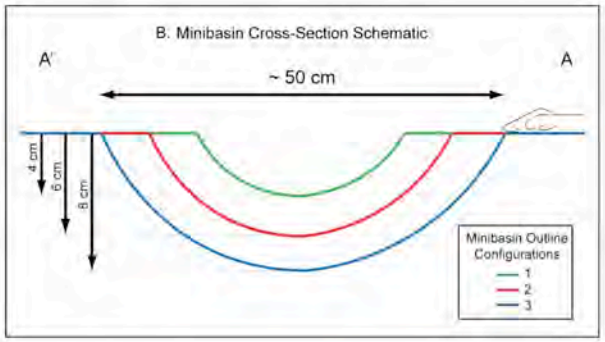


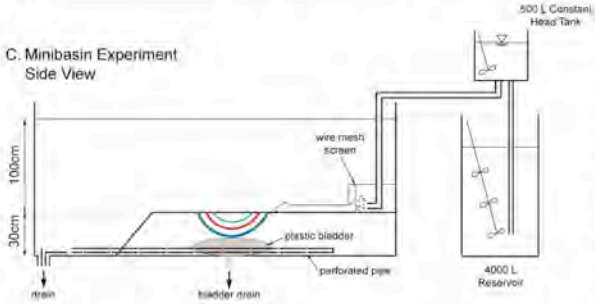


**Schematic figure for Series 2 of the mini-basin experiments and current generation conditions.** Plan view (A) of the basin tank with the extents of the three mini-basin subsidence configurations. The bold black outline represents the extent of the false floor, and the dashed green, red and blue outlines represent the extent of the mini-basin at the three subsidence configurations from initial to final. Ideal dimensions of the mini-basin cross-section (A-A' ) is shown in (B). Side View (C) shows the reservoir tank where sediment, water and salt are mixed and then pumped to the upper constant head tank. Currents are generated by releasing the mixed fluid from the head tank into the basin tank/ mini-basin through a wire mesh screened entrance box. As the currents move over the edge of the false floor they are drained away by a system of perforated pipes in order to minimize basin tank wall reflections. The mini-basin cross-sectional shapes were established by three separate controlled drainages of a water filled bladder that was buried in a gravel basement, shown in (B). The dimensions of the bladder were 40 cm (L) x 40 cm (W) x 15 cm (D). The inlet box configuration for the mini-basin was oriented parallel to the long axis of the basin tank. Turbidity currents flow down a confining channel of 150 cm (L) x 10 cm (W) x 8 cm (D) that extends from the inlet box to the entrance of the mini-basin (Figure A).

## 4.2 Series 2 – Confining Channel Configuration at Mini-basin Entry Point

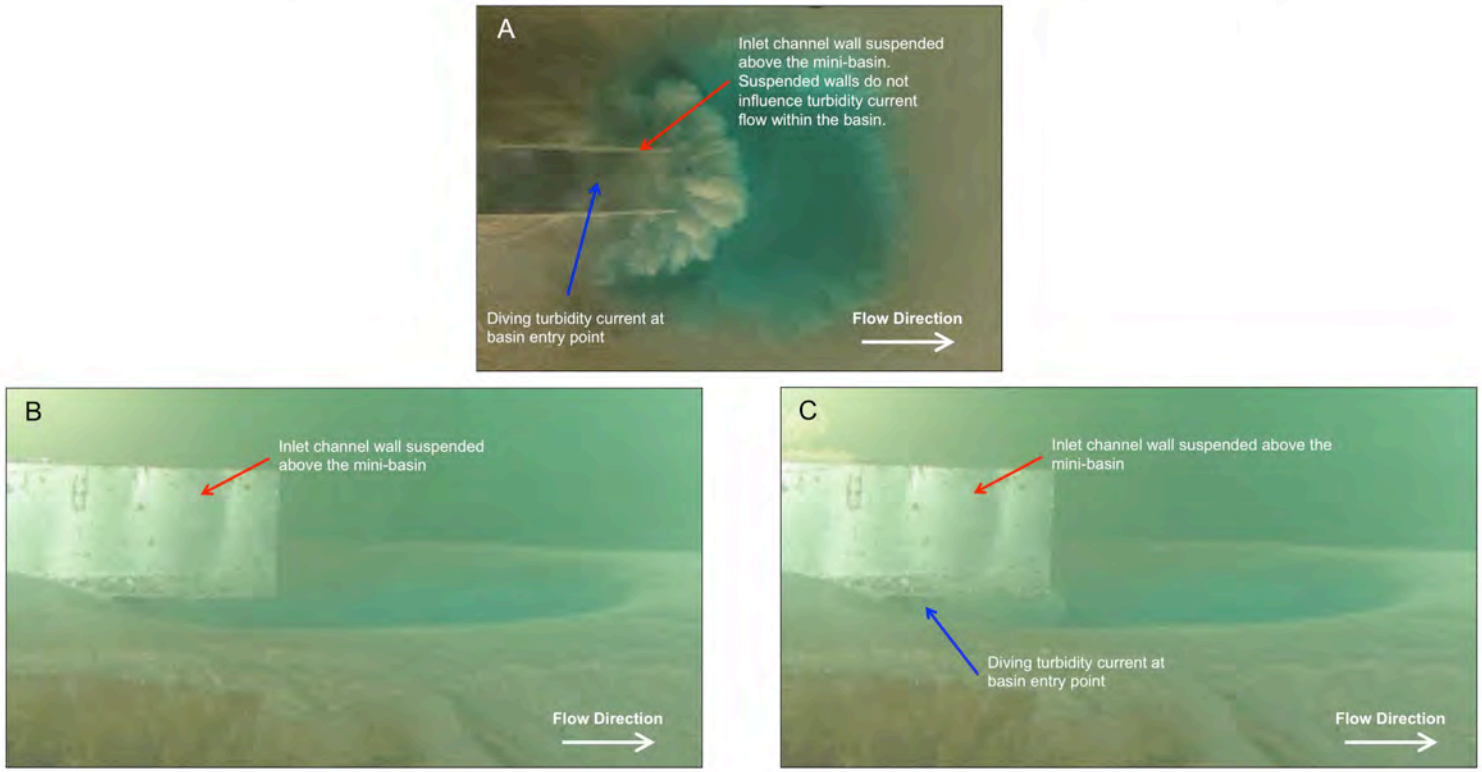


**Plan and side-view of mini-basin experiment setup for Configuration 2.**
The plan view in Figure A shows the confining inlet channel that guides the turbidity current into the basin. The terminal 30 cm of the channel floor is removed as an initial condition. As the mini-basin is subsided, the confining channel walls are suspended above the basin, which allows the turbidity currents to dive at the mini-basin entry point. Suspended channel walls do not influence turbidity current flow within the basin. This concept is illustrated in Figures B and C.

## 4.3.1 Series 2 – Bathymetry and Slope Maps (Configuration 1)

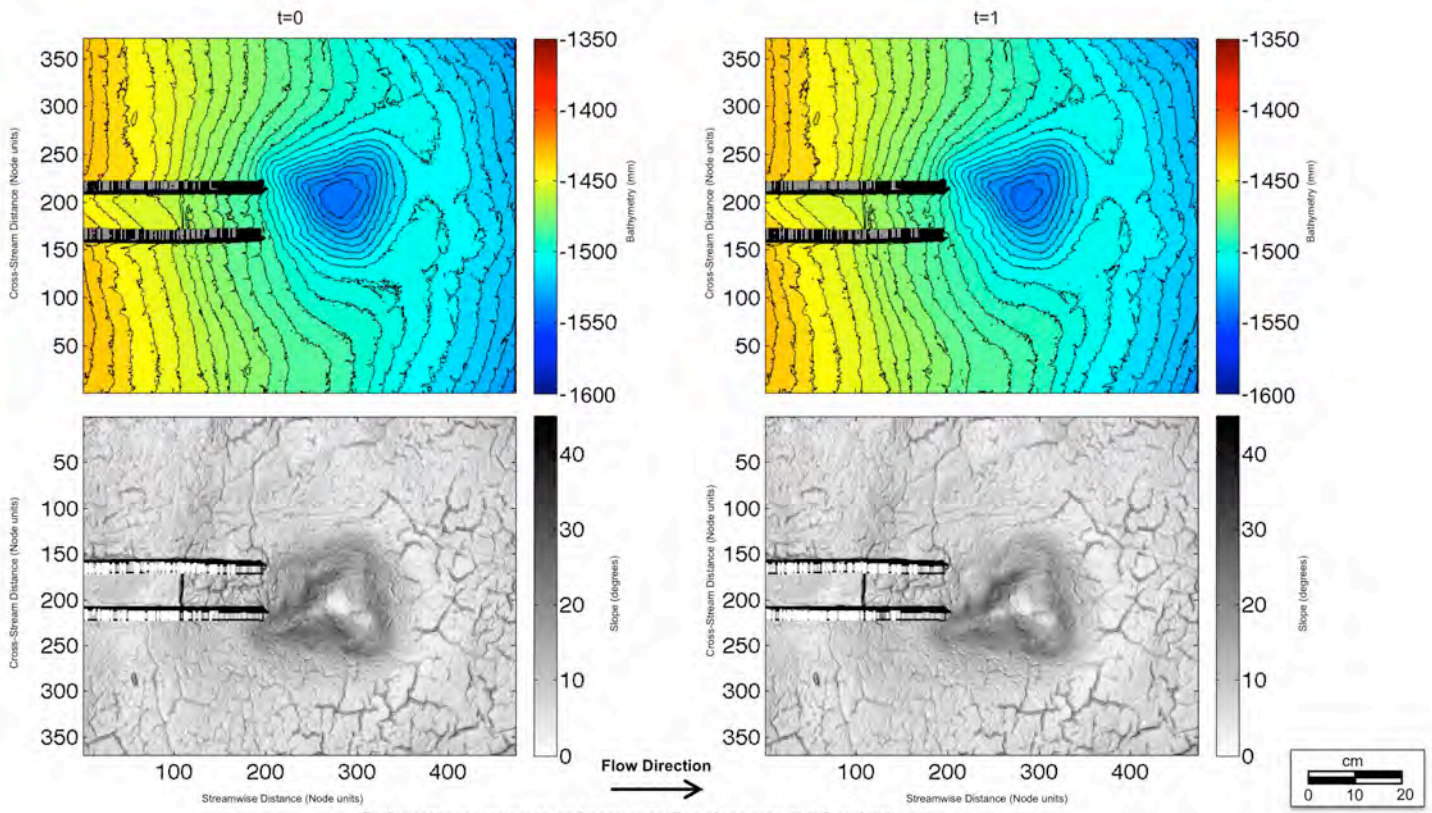


**Bathymetry contour map and corresponding slope map at t=0 and t=1.**
The surface at t=0 represents the initial topography for configuration 1, and the surface at t=1 represents the depositional surface following flow event 1. The confining channel is seen as two parallel lines entering from the left.

Note: 1 node unit = 2 millimeters

## 4.3.1 Series 2 – Bathymetry and Slope Maps (Configuration 1)

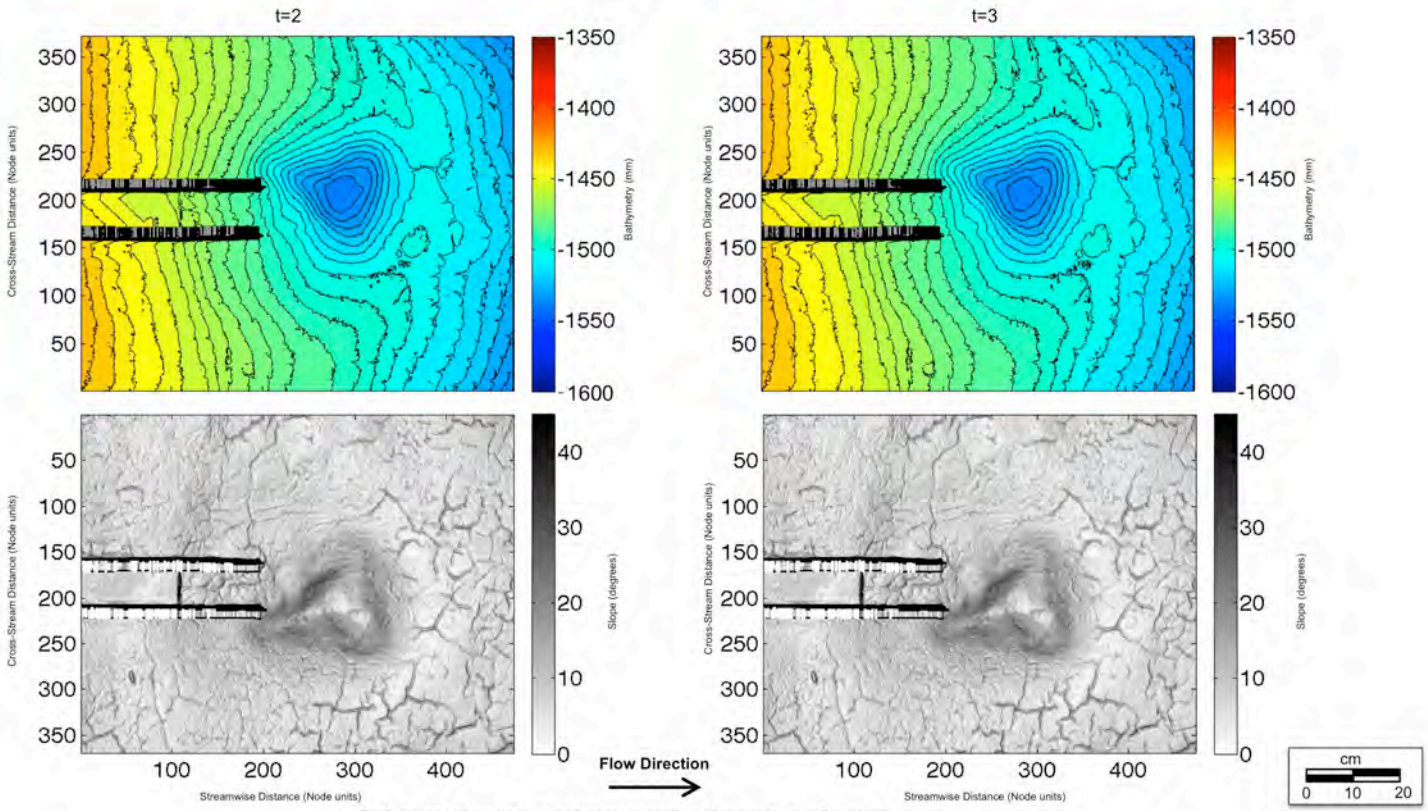


**Bathymetry contour map and corresponding slope map at t=2 and t=3.**
The confining channel is seen as two parallel lines entering from the left.

Note: 1 node unit = 2 millimeters

## 4.3.1 Series 2 – Bathymetry and Slope Maps (Configuration 1)

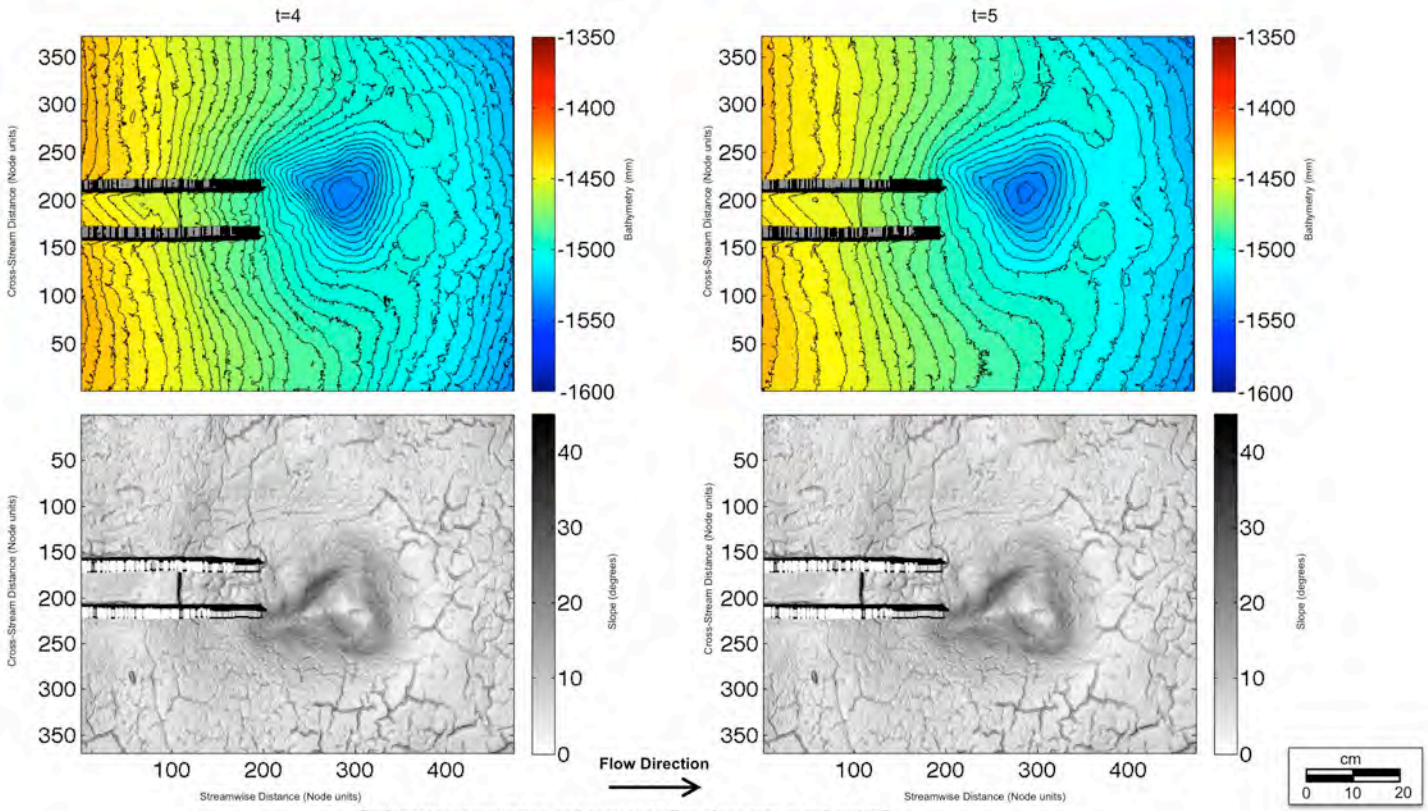


**Bathymetry contour map and corresponding slope map at t=4 and t=5.**
The confining channel is seen as two parallel lines entering from the left.

Note: 1 node unit = 2 millimeters

## 4.3.2 Series 2 – Event Deposit Thickness Maps (Configuration 1)

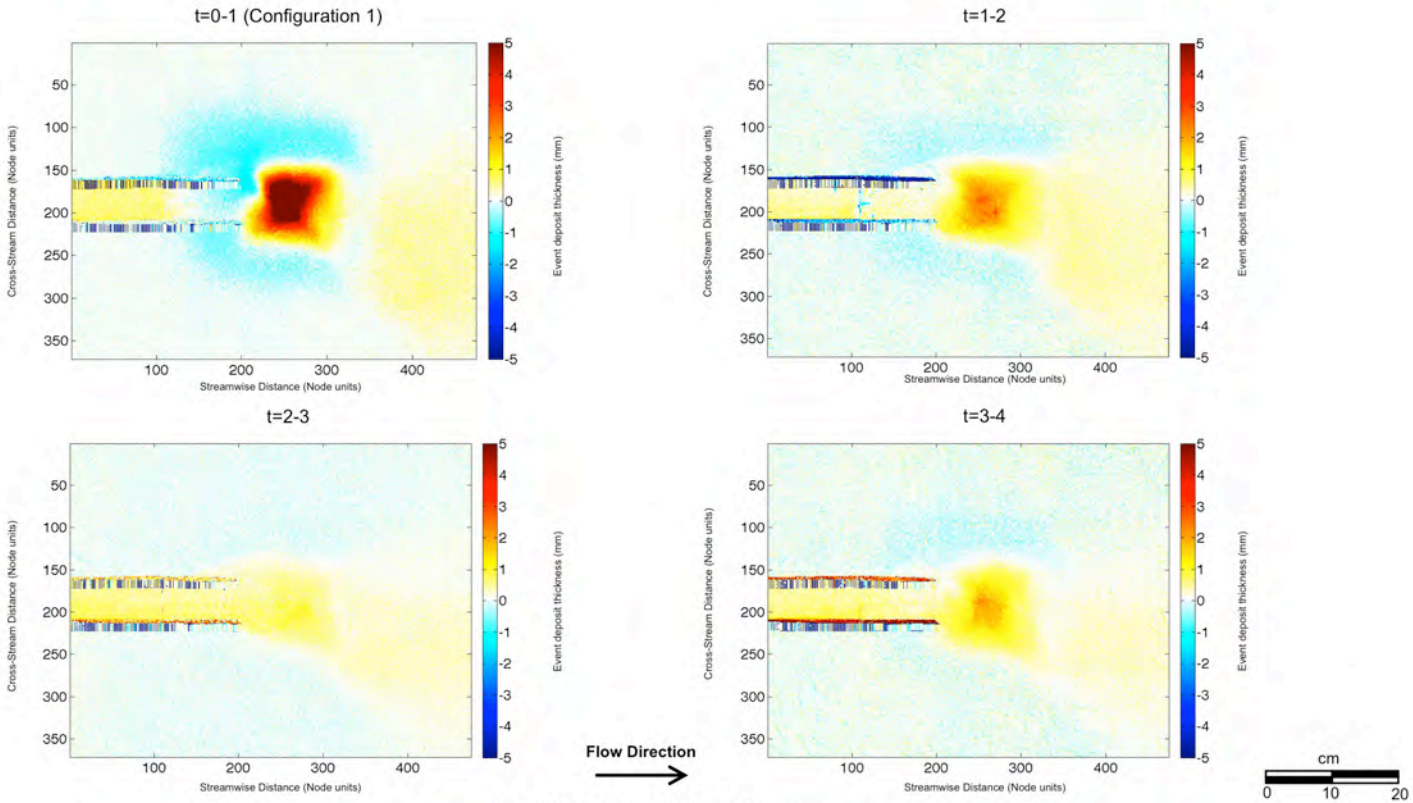


**Deposit thickness maps for flows 1-4.**

The map of interval t=0-1 is the deposit from the first turbidity current run in Configuration 1. See datasheet for details. Deposit thickness is calculated by subtracting the pre-event bathymetry from the post-event bathymetry. The colorbar ranges from negative to positive such that red regions represent addition of sediment, white represents no sediment deposition, and blue represents subtraction of sediment. The confining channel is seen as two parallel lines entering from the left.

Note: 1 node unit = 2 millimeters

## 4.3.2 Series 2 – Event Deposit Thickness Maps (Configuration 1)

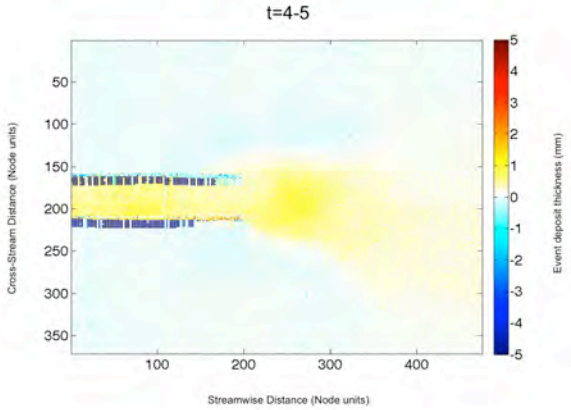


**Flow Direction**

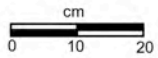


**Deposit thickness maps for flow 5.**

Deposit thickness is calculated by subtracting the pre-event bathymetry from the post-event bathymetry. The colorbar ranges from negative to positive such that red regions represent addition of sediment, white represents no sediment deposition, and blue represents subtraction of sediment. The confining channel is seen as two parallel lines entering from the left.

Note: 1 node unit = 2 millimeters

## 4.3.3 Series 2 – Dip Cross Sections (Configuration 1, y=160)

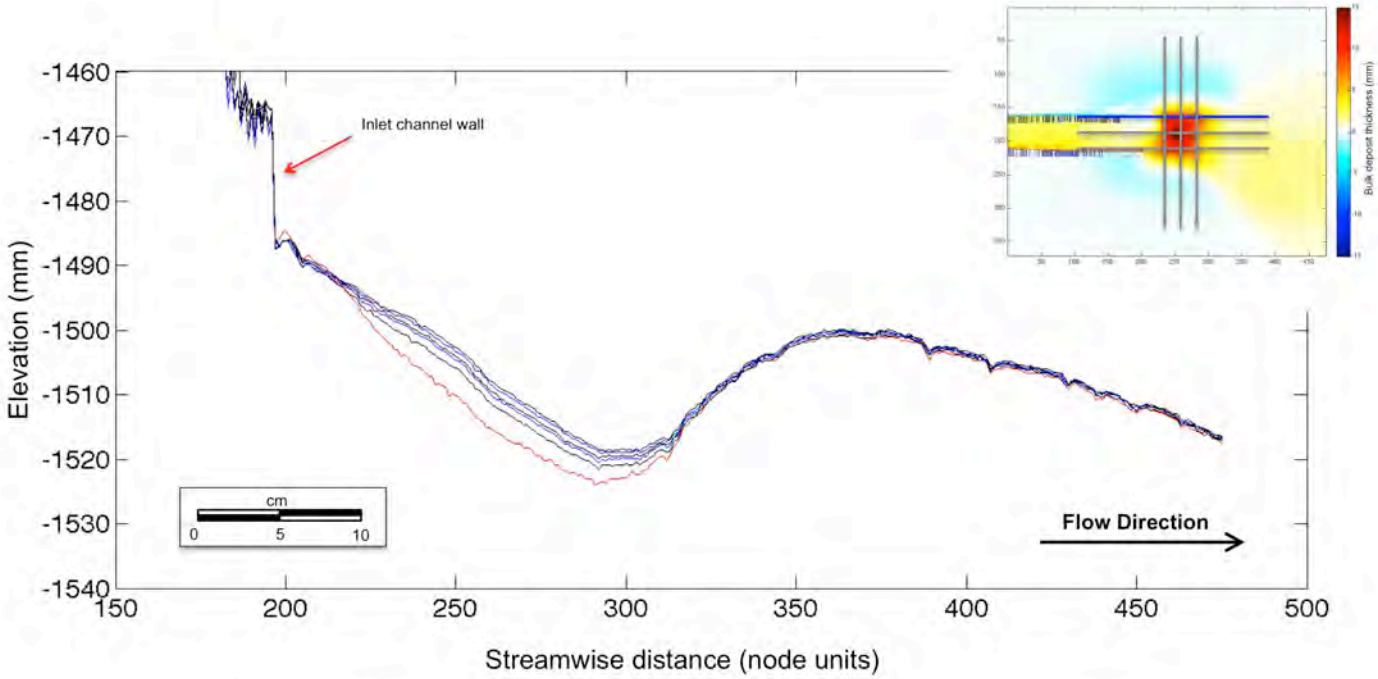


**Dip-oriented cross-sections for Configuration 1 showing initial surface (red) and bathymetry surfaces resulting from five turbidity current events (t=1 to t=5).** The cross section location is also displayed in plan view, and is superimposed on a deposit thickness map of the final surface minus the initial basin surface. Note axes units: x-axis is displayed in node units, and y-axis is displayed in millimeters.

Note: 1 node unit = 2 millimeters

## 4.3.3 Series 2 – Dip Cross Sections (Configuration 1, y=190)

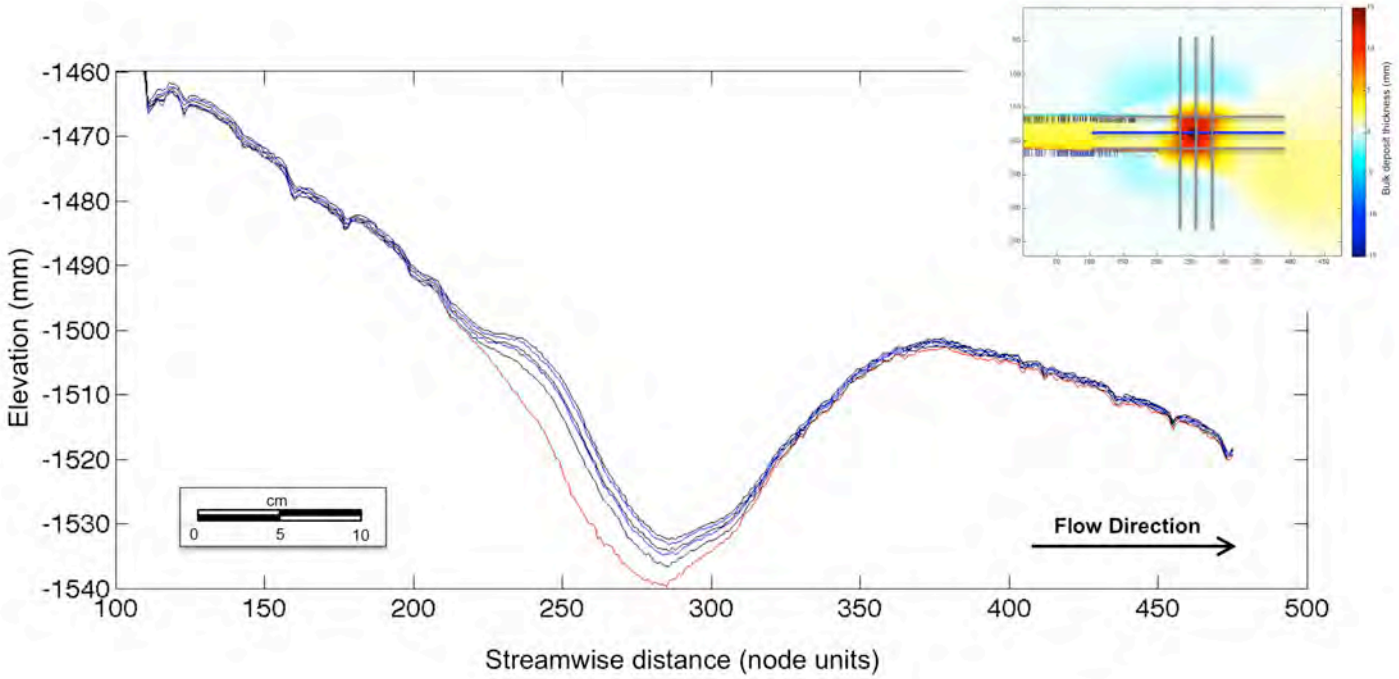


**Dip-oriented cross-sections for Configuration 1 showing initial surface (red) and bathymetry surfaces resulting from five turbidity current events (t=1 to t=5).** The cross section location is also displayed in plan view, and is superimposed on a deposit thickness map of the final surface minus the initial basin surface. Note axes units: x-axis is displayed in node units, and y-axis is displayed in millimeters.

Note: 1 node unit = 2 millimeters

## 4.3.3 Series 2 – Dip Cross Sections (Configuration 1, y=210)

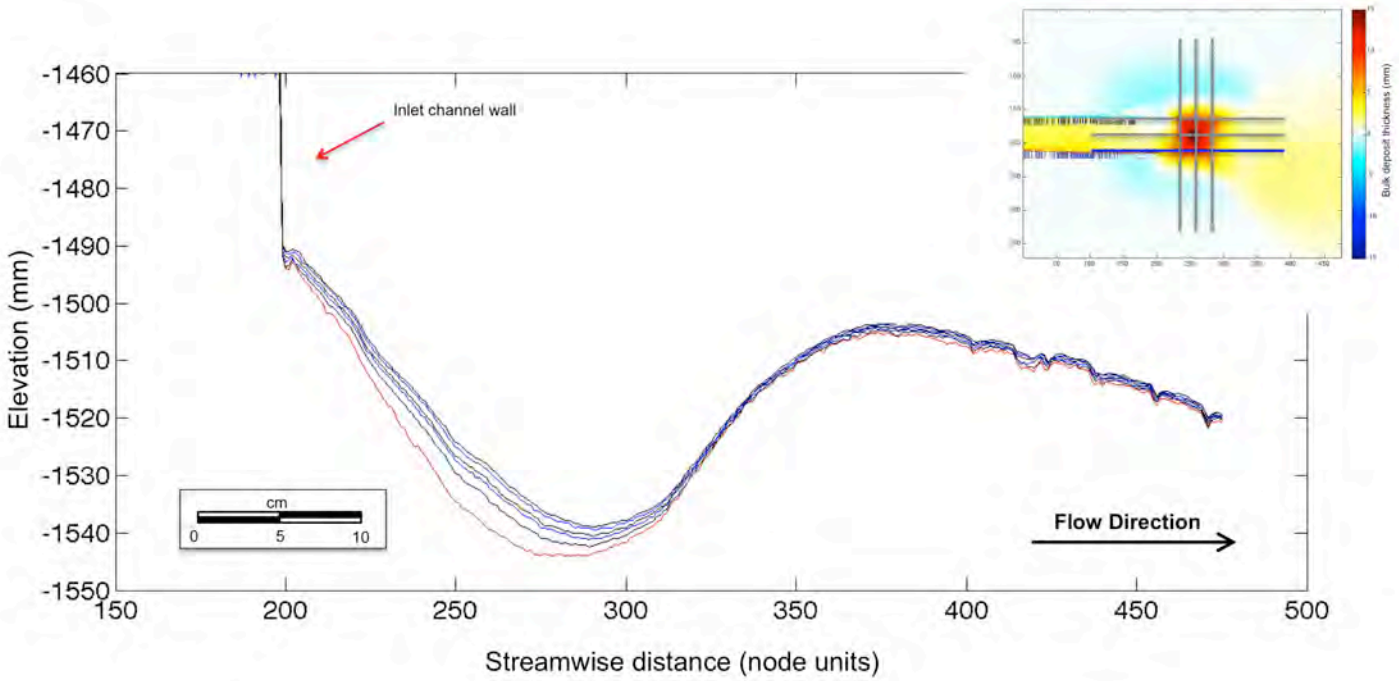


**Dip-oriented cross-sections for Configuration 1 showing initial surface (red) and bathymetry surfaces resulting from five turbidity current events (t=1 to t=5).** The cross section location is also displayed in plan view, and is superimposed on a deposit thickness map of the final surface minus the initial basin surface. Note axes units: x-axis is displayed in node units, and y-axis is displayed in millimeters.

Note: 1 node unit = 2 millimeters

## 4.3.4 Series 2 – Strike Cross Sections (Configuration 1, x=230)

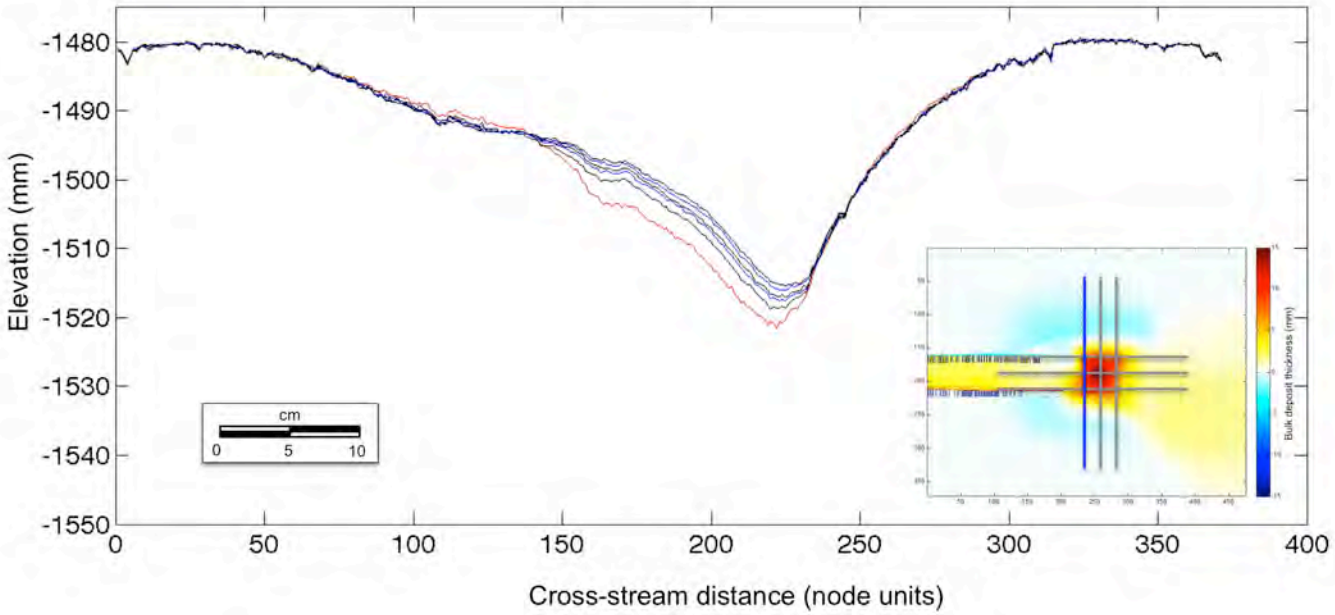


**Strike-oriented cross-sections for Configuration 1 showing initial surface (red) and bathymetry surfaces resulting from five turbidity current events (t=1 to t=5).** The cross section location is also displayed in plan view, and is superimposed on a deposit thickness map of the final surface minus the initial basin surface. The panel is oriented as if you were looking downstream. Note axes units: x-axis is displayed in node units. and y-axis is displayed in millimeters.

Note: 1 node unit = 2 millimeters

## 4.3.4 Series 2 – Strike Cross Sections (Configuration 1, x=250)

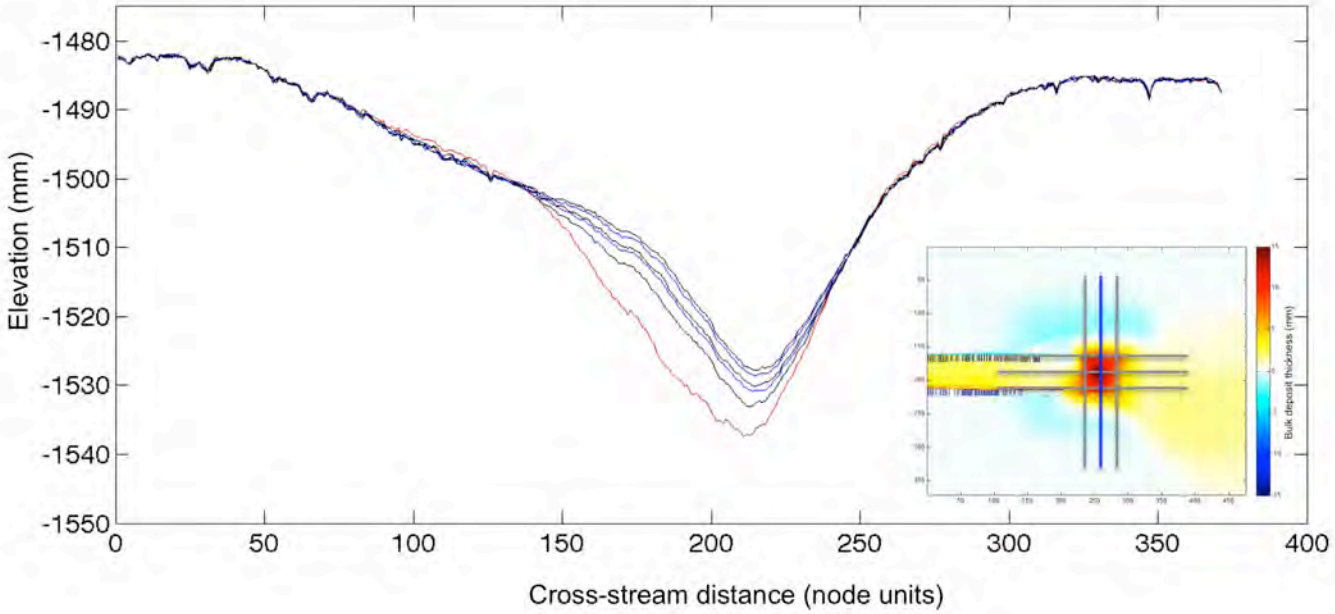


**Strike-oriented cross-sections for Configuration 1 showing initial surface (red) and bathymetry surfaces resulting from five turbidity current events (t=1 to t=5).** The cross section location is also displayed in plan view, and is superimposed on a deposit thickness map of the final surface minus the initial basin surface. The panel is oriented as if you were looking downstream. Note axes units: x-axis is displayed in node units. and y-axis is displayed in millimeters.

Note: 1 node unit = 2 millimeters

## 4.3.4 Series 2 – Strike Cross Sections (Configuration 1, x=280)

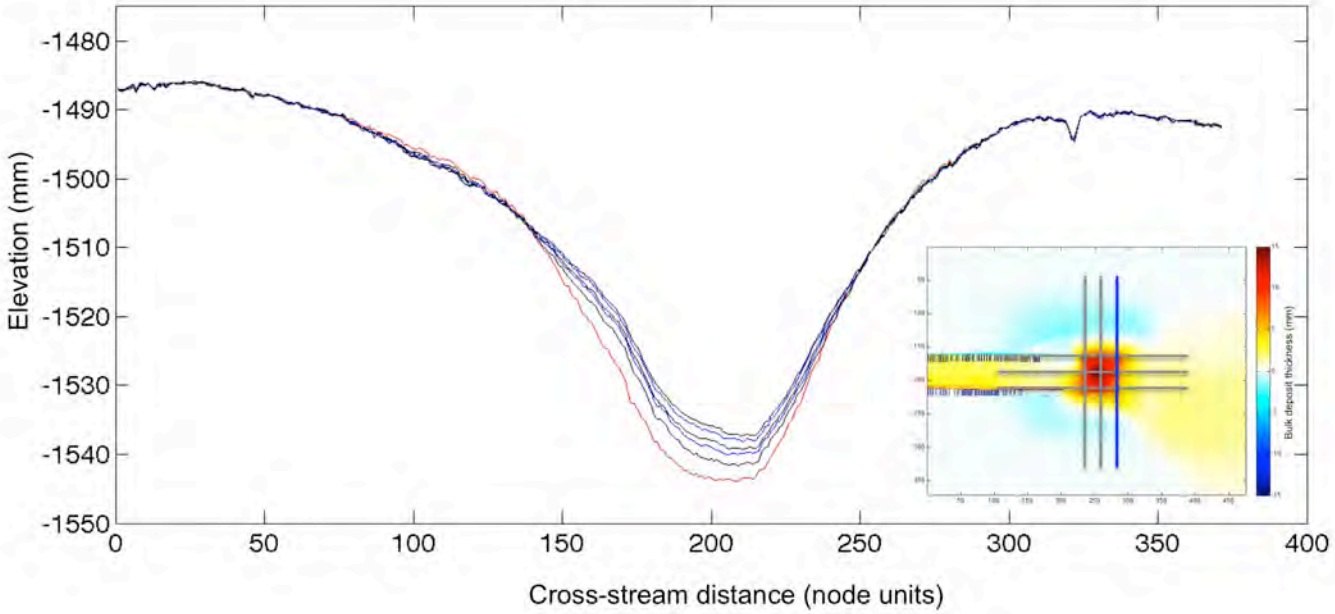


**Strike-oriented cross-sections for Configuration 1 showing initial surface (red) and bathymetry surfaces resulting from five turbidity current events (t=1 to t=5).** The cross section location is also displayed in plan view, and is superimposed on a deposit thickness map of the final surface minus the initial basin surface. The panel is oriented as if you were looking downstream. Note axes units: x-axis is displayed in node units. and y-axis is displayed in millimeters.

Note: 1 node unit = 2 millimeters

## 4.4.1 Series 2 – Bathymetry and Slope Maps (Configuration 2)

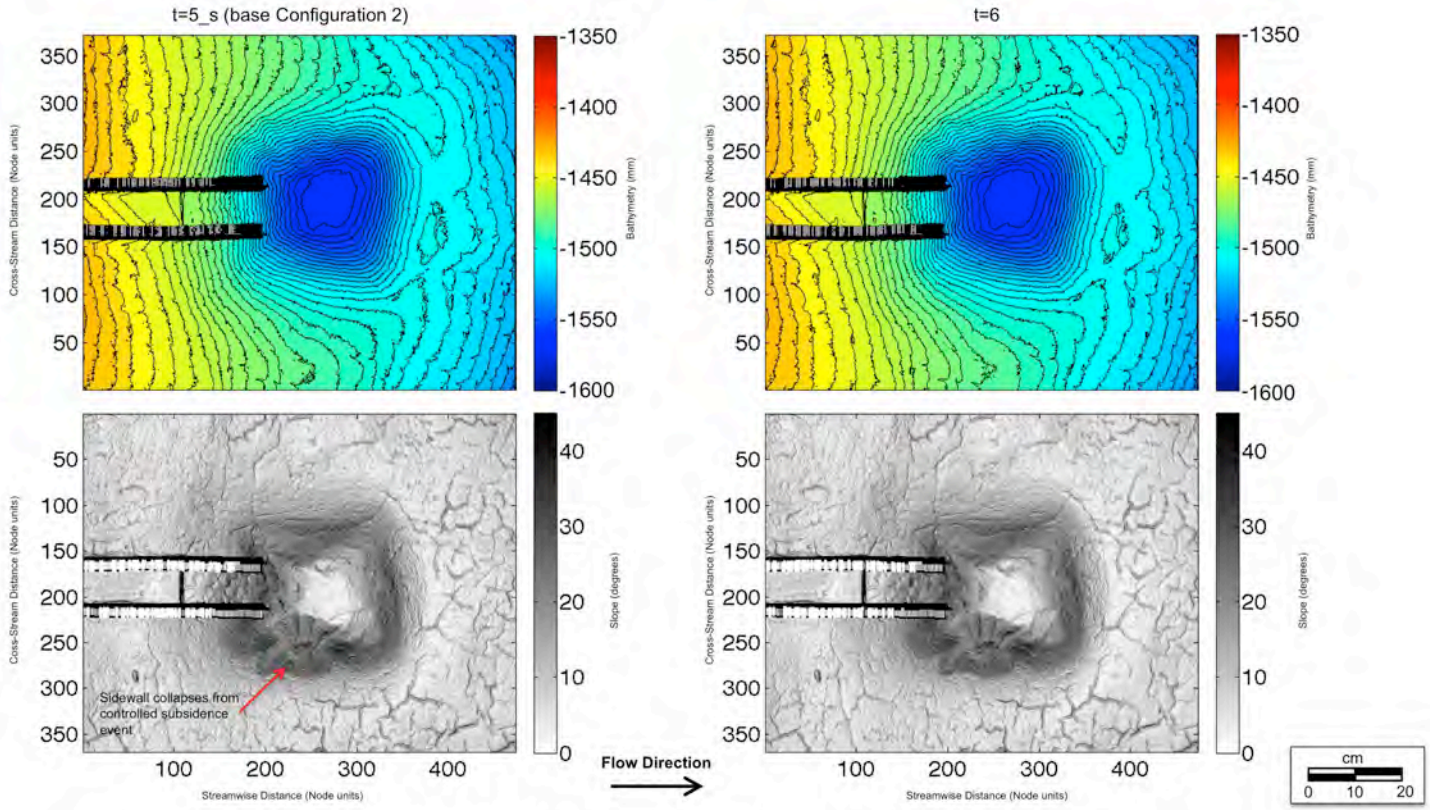


**Bathymetry contour map and corresponding slope map at t=5_s and t=6.**
The surface t=5_s represents the subsided surface of the final deposit from Configuration 1, and is the initial surface for Configuration 2.
The confining channel is seen as two parallel lines entering from the left.

Note: 1 node unit = 2 millimeters

## 4.4.1 Series 2 – Bathymetry and Slope Maps (Configuration 2)

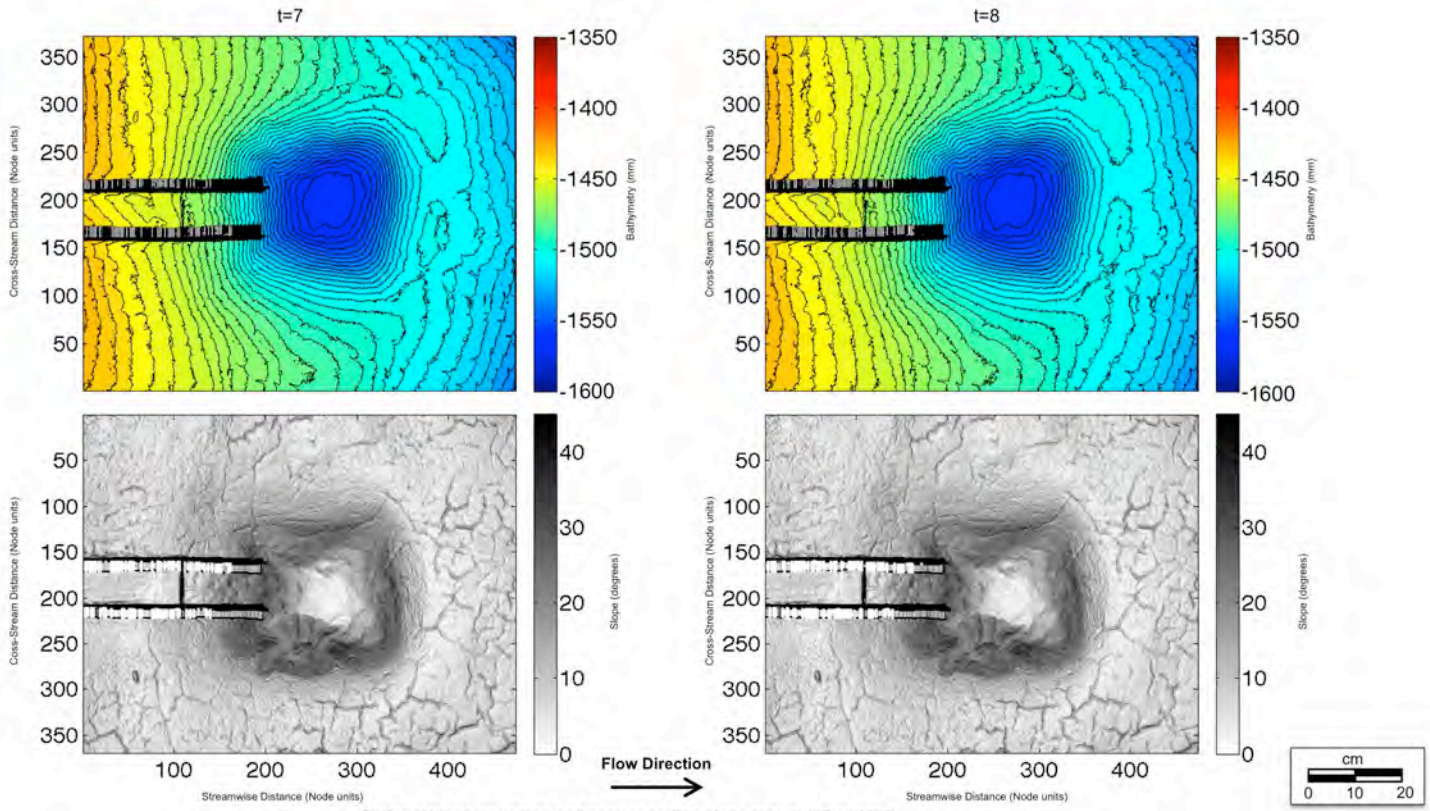


**Bathymetry contour map and corresponding slope map at t=7 and t=8.**
The confining channel is seen as two parallel lines entering from the left.

Note: 1 node unit = 2 millimeters

## 4.4.1 Series 2 – Bathymetry and Slope Maps (Configuration 2)

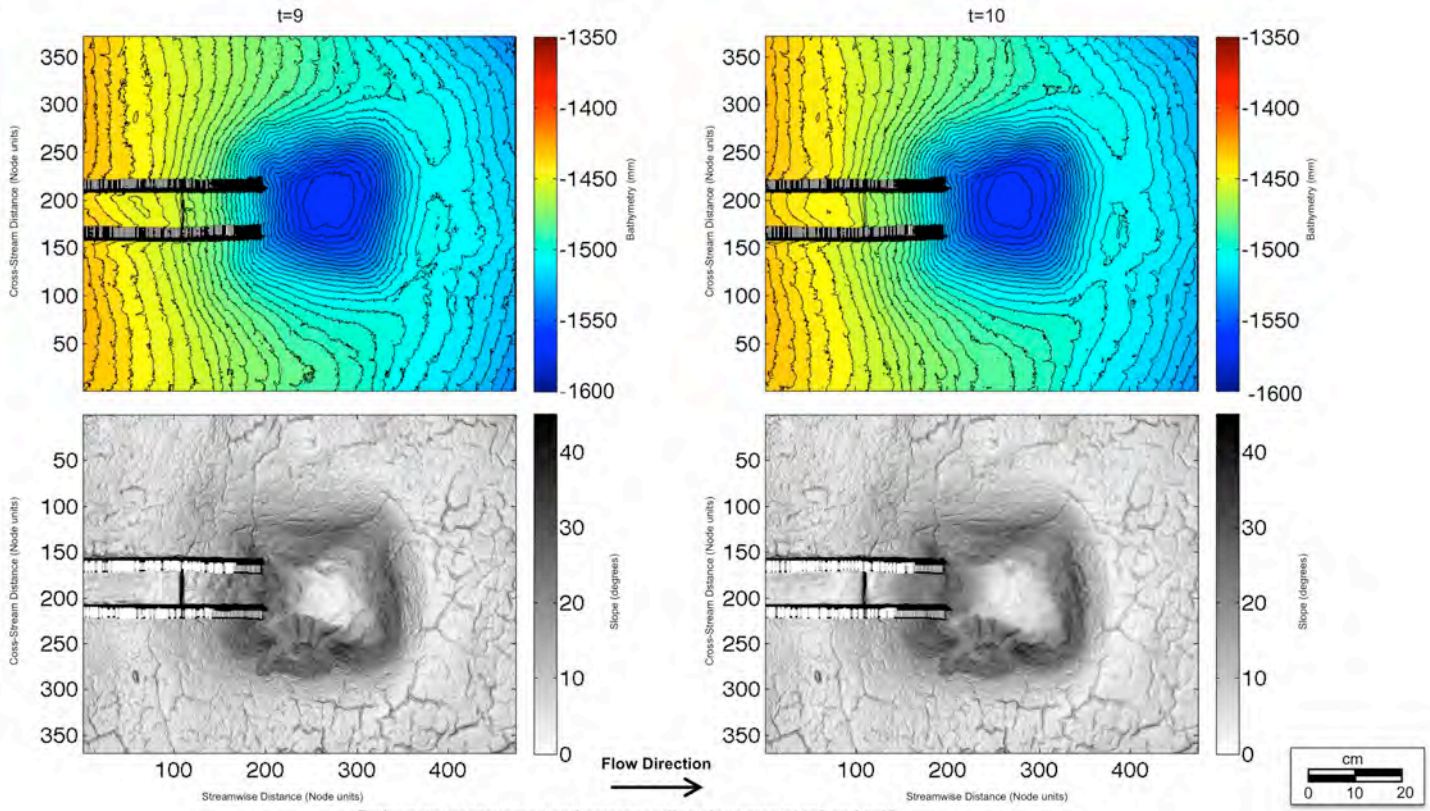


**Bathymetry contour map and corresponding slope map at t=9 and t=10.**
The confining channel is seen as two parallel lines entering from the left.

Note: 1 node unit = 2 millimeters

## 4.4.1 Series 2 – Bathymetry and Slope Maps (Configuration 2)

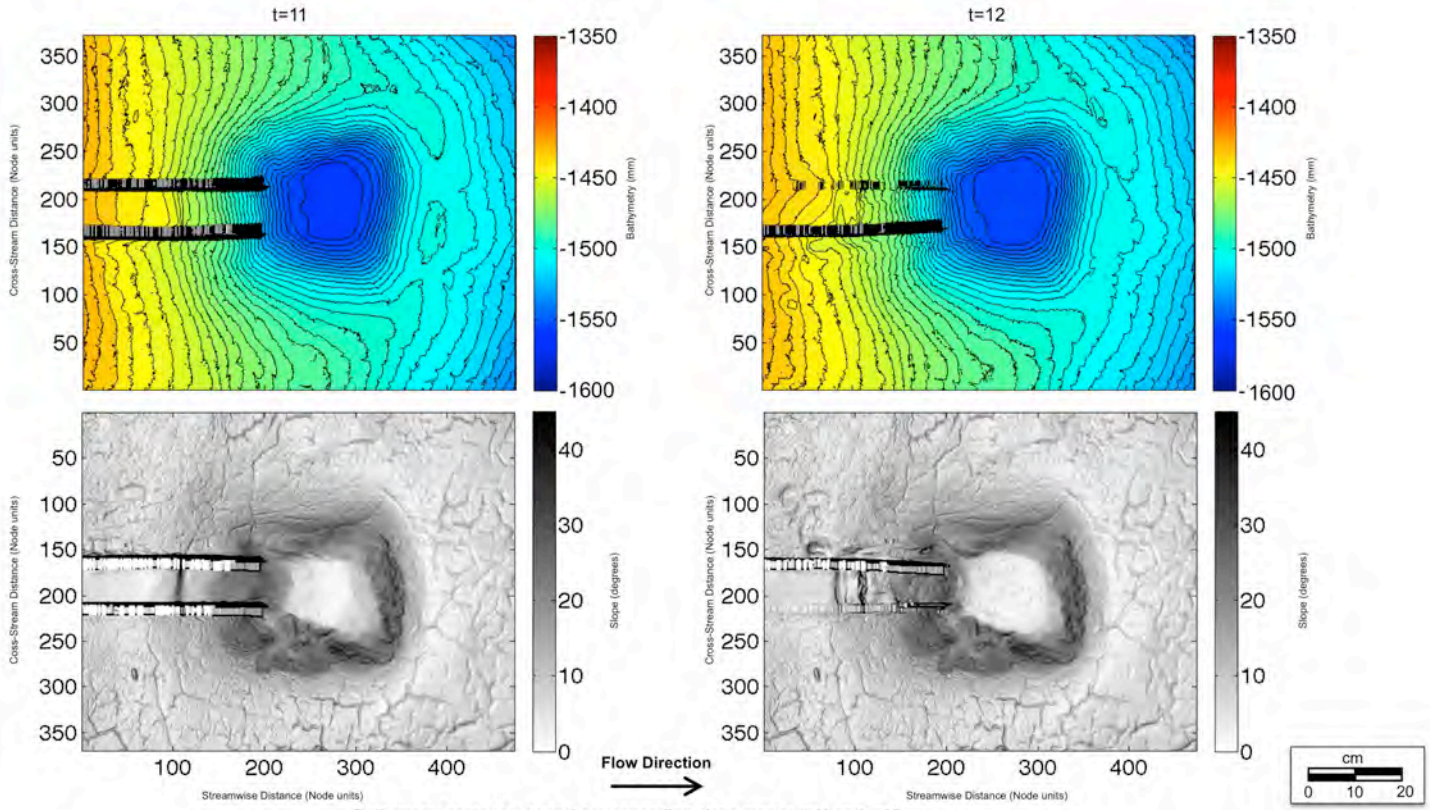


**Bathymetry contour map and corresponding slope map at t=11 and t=12.**
The confining channel is seen as two parallel lines entering from the left.

Note: 1 node unit = 2 millimeters

## 4.4.1 Series 2 – Bathymetry and Slope Maps (Configuration 2)

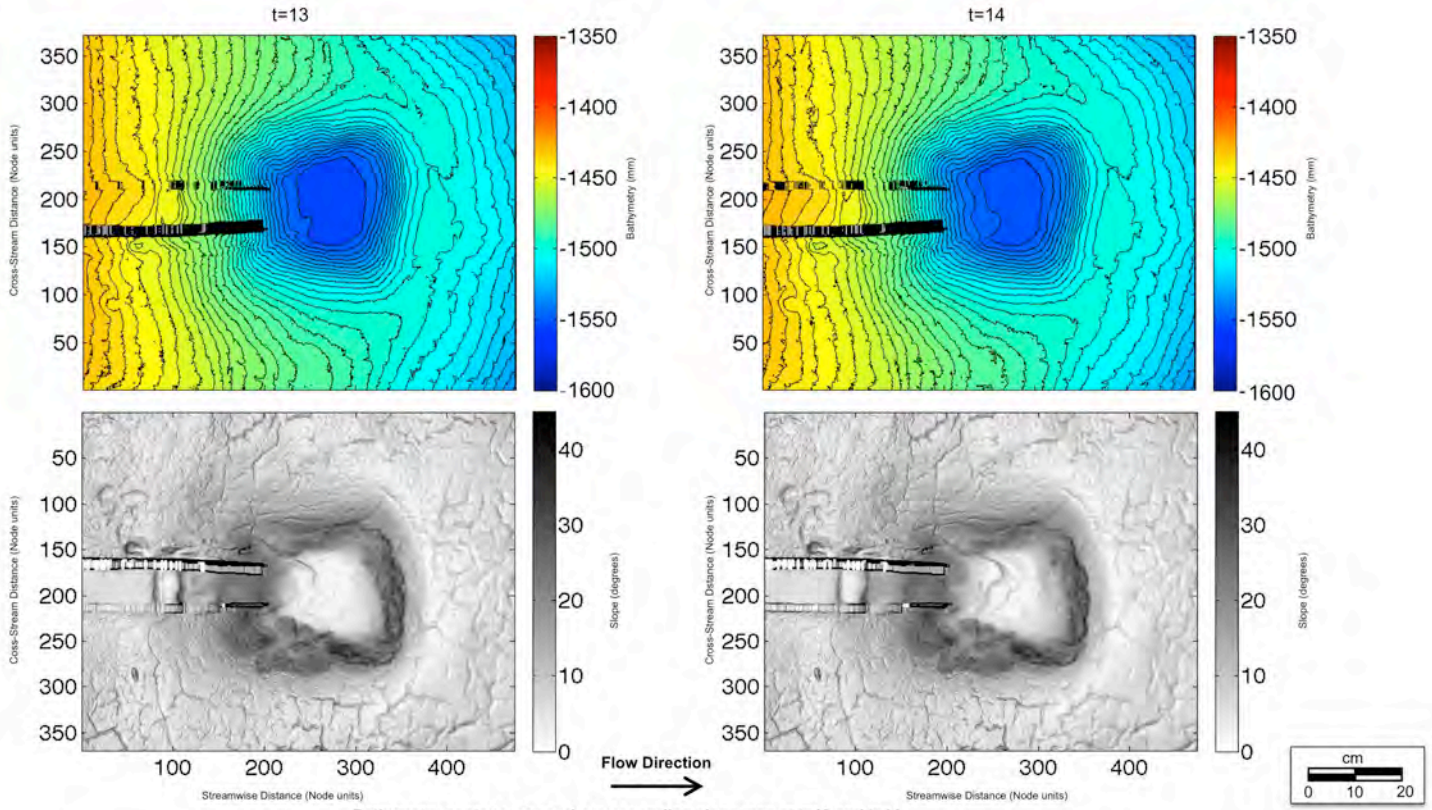


**Bathymetry contour map and corresponding slope map at t=13 and t=14.**
The confining channel is seen as two parallel lines entering from the left.

Note: 1 node unit = 2 millimeters

## 4.4.2 Series 2 – Event Deposit Thickness Maps (Configuration 2)

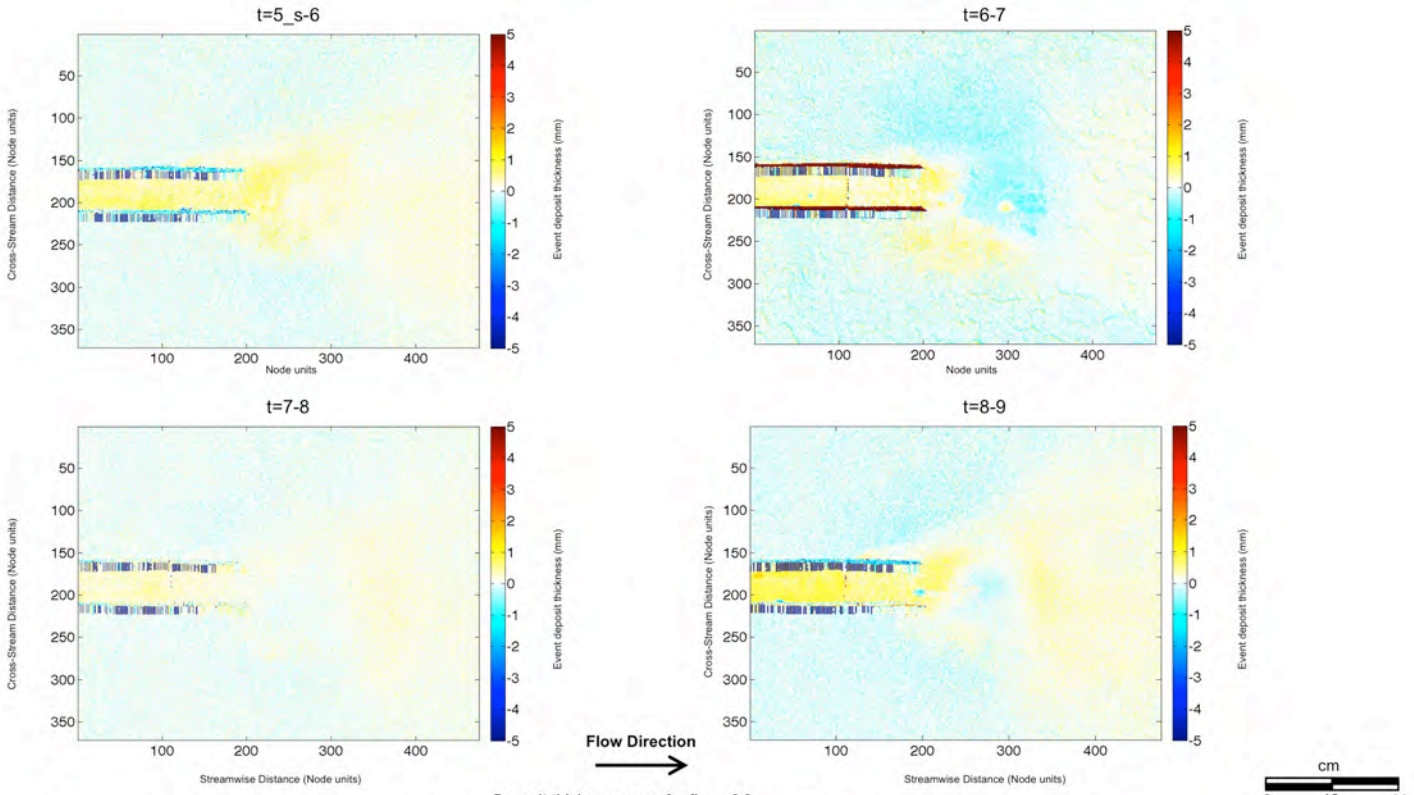


**Deposit thickness maps for flows 6-9.**

The map of interval t=5_s-6 is the deposit from the first turbidity current run in Configuration 2. See datasheet on slide 6 for details. Deposit thickness is calculated by subtracting the pre-event bathymetry from the post-event bathymetry. The colorbar ranges from negative to positive such that red regions represent addition of sediment, white represents no sediment deposition, and blue represents subtraction of sediment. The confining channel is seen as two parallel lines entering from the left.

Note: 1 node unit = 2 millimeters

## 4.4.2 Series 2 – Event Deposit Thickness Maps (Configuration 2)

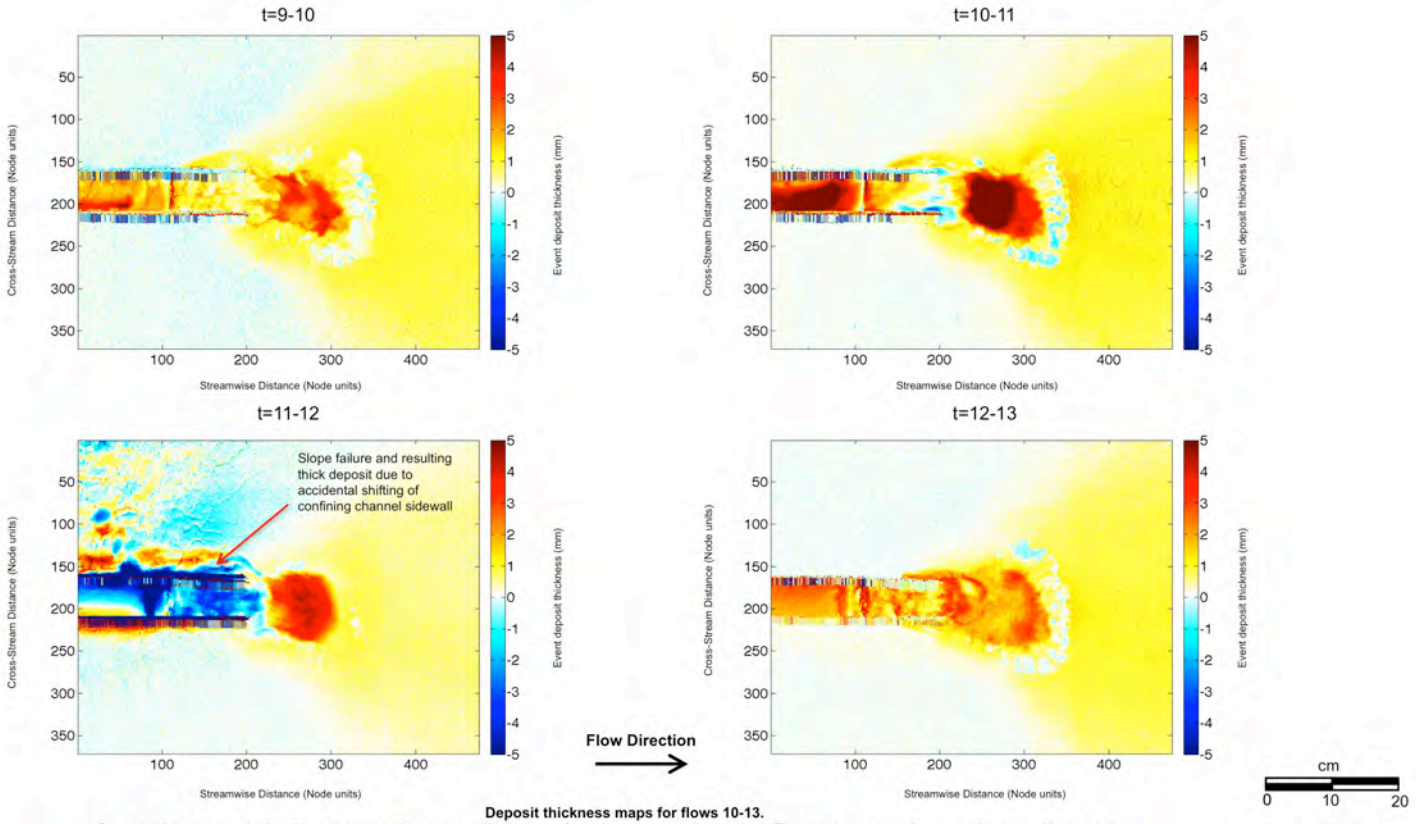


**Deposit thickness maps for flows 10-13.**

Deposit thickness is calculated by subtracting the pre-event bathymetry from the post-event bathymetry. The colorbar ranges from negative to positive such that red regions represent addition of sediment, white represents no sediment deposition, and blue represents subtraction of sediment. The confining channel is seen as two parallel lines entering from the left.

Note: 1 node unit = 2 millimeters

## 4.4.2 Series 2 – Event Deposit Thickness Maps (Configuration 2)

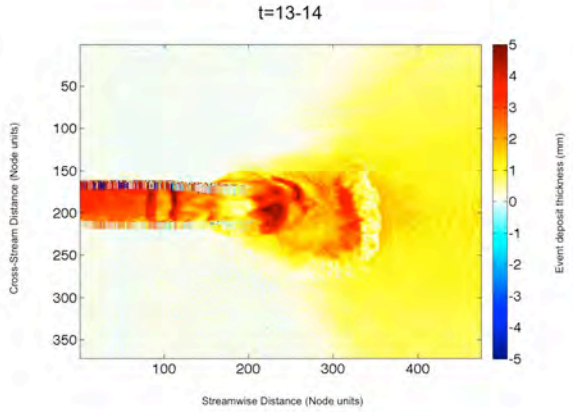


**Flow Direction**

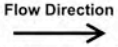

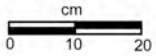


**Deposit thickness maps for flow 14.**

Deposit thickness is calculated by subtracting the pre-event bathymetry from the post-event bathymetry. The colorbar ranges from negative to positive such that red regions represent addition of sediment, white represents no sediment deposition, and blue represents subtraction of sediment. The confining channel is seen as two parallel lines entering from the left.

Note: 1 node unit = 2 millimeters

## 4.4.3 Series 2 – Dip Cross Sections (Configuration 2, y=150)

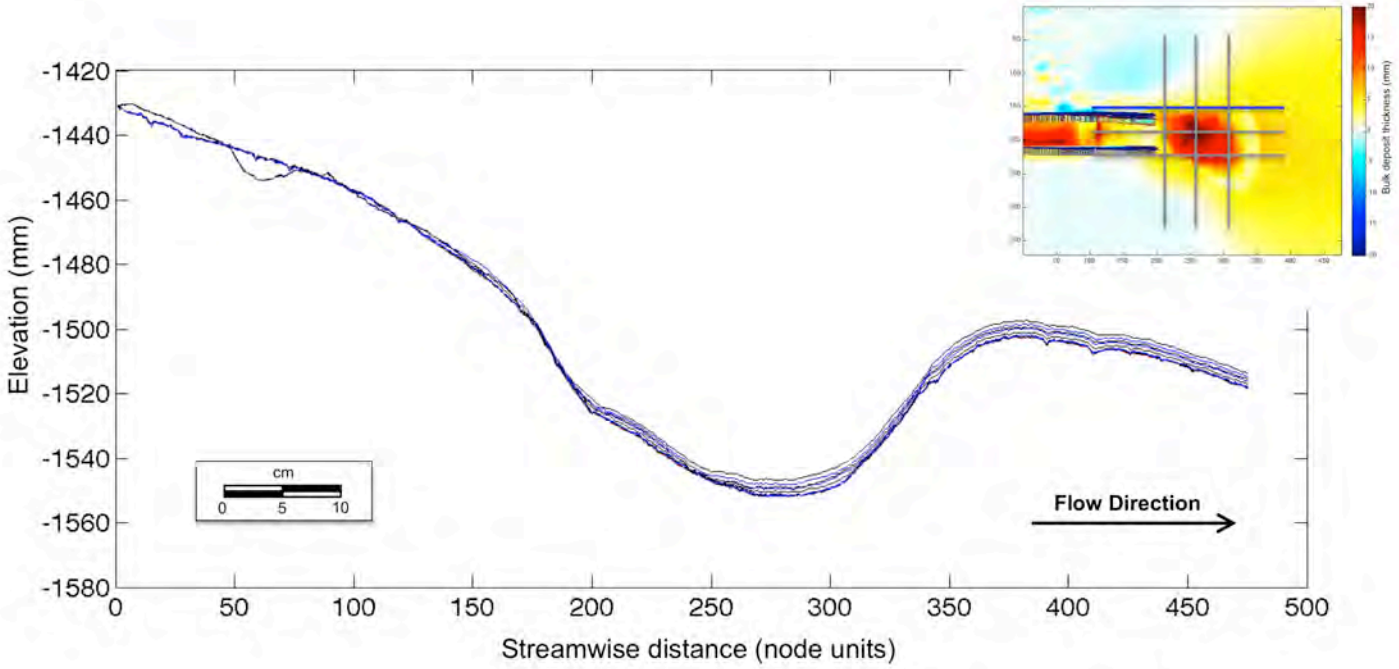


**Dip-oriented cross-sections for Configuration 2 showing initial surface (red) and bathymetry surfaces resulting from nine turbidity current events (t=6 to t=14).** The cross section location is also displayed in plan view, and is superimposed on a deposit thickness map of the final surface minus the initial basin surface. Note axes units: x-axis is displayed in node units, and y-axis is displayed in millimeters.

Note: 1 node unit = 2 millimeters

## 4.4.3 Series 2 – Dip Cross Sections (Configuration 2, y=190)

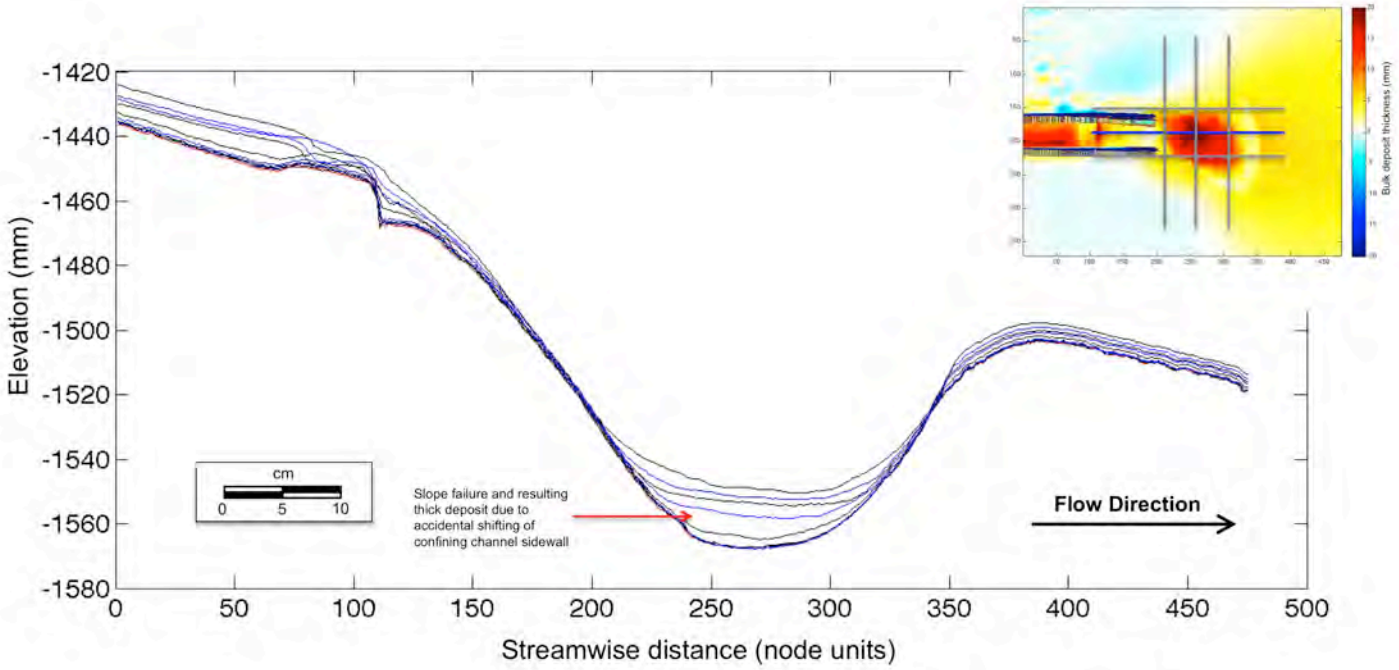


**Dip-oriented cross-sections for Configuration 2 showing initial surface (red) and bathymetry surfaces resulting from nine turbidity current events (t=6 to t=14).** The cross section location is also displayed in plan view, and is superimposed on a deposit thickness map of the final surface minus the initial basin surface. Note axes units: x-axis is displayed in node units, and y-axis is displayed in millimeters.

Note: 1 node unit = 2 millimeters

## 4.4.4 Series 2 – Strike Cross Sections (Configuration 2, x=210)

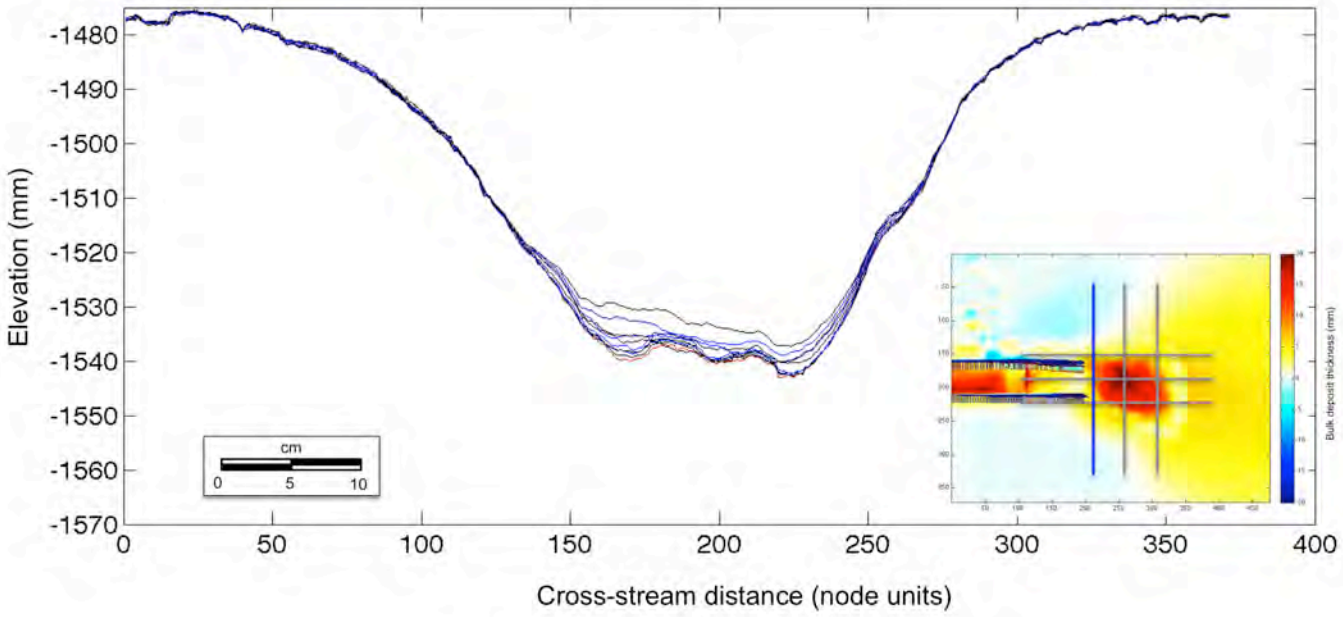


**Strike-oriented cross-sections for Configuration 1 showing initial surface (red) and bathymetry surfaces resulting from nine turbidity current events (t=6 to t=14).** The cross section location is also displayed in plan view, and is superimposed on a deposit thickness map of the final surface minus the initial basin surface. The panel is oriented as if you were looking downstream. Note axes units: x-axis is displayed in node units. and y-axis is displayed in millimeters.

Note: 1 node unit = 2 millimeters

## 4.4.3 Series 2 – Dip Cross Sections (Configuration 2, y=230)

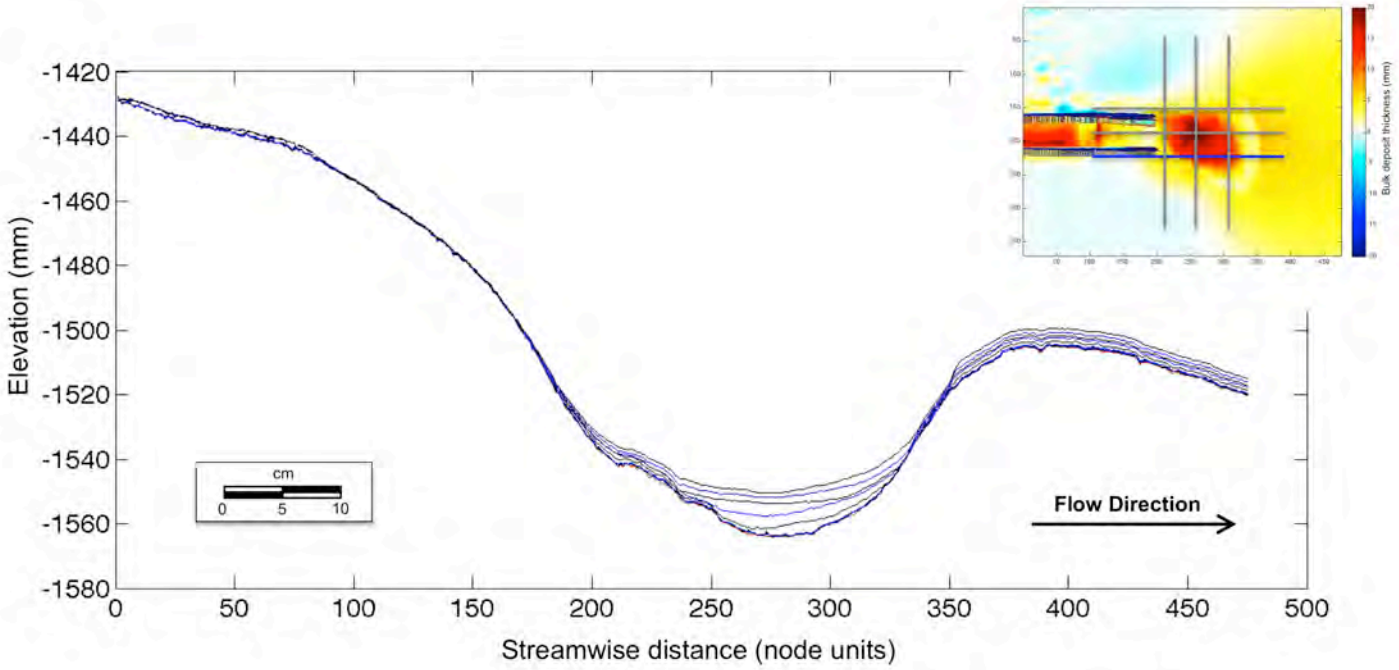


**Dip-oriented cross-sections for Configuration 2 showing initial surface (red) and bathymetry surfaces resulting from nine turbidity current events (t=6 to t=14).** The cross section location is also displayed in plan view, and is superimposed on a deposit thickness map of the final surface minus the initial basin surface. Note axes units: x-axis is displayed in node units, and y-axis is displayed in millimeters.

Note: 1 node unit = 2 millimeters

## 4.4.4 Series 2 – Strike Cross Sections (Configuration 2, x=255)

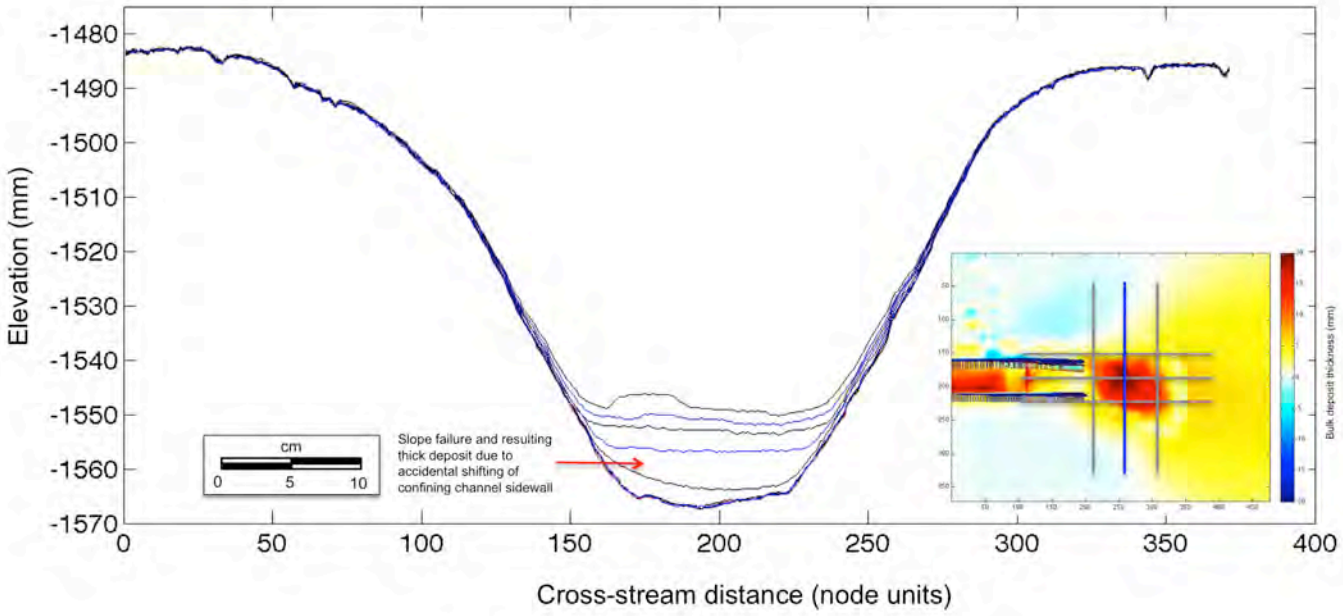


**Strike-oriented cross-sections for Configuration 1 showing initial surface (red) and bathymetry surfaces resulting from nine turbidity current events (t=6 to t=14).** The cross section location is also displayed in plan view, and is superimposed on a deposit thickness map of the final surface minus the initial basin surface. The panel is oriented as if you were looking downstream. Note axes units: x-axis is displayed in node units. and y-axis is displayed in millimeters.

Note: 1 node unit = 2 millimeters

## 4.4.4 Series 2 – Strike Cross Sections (Configuration 2, x=310)

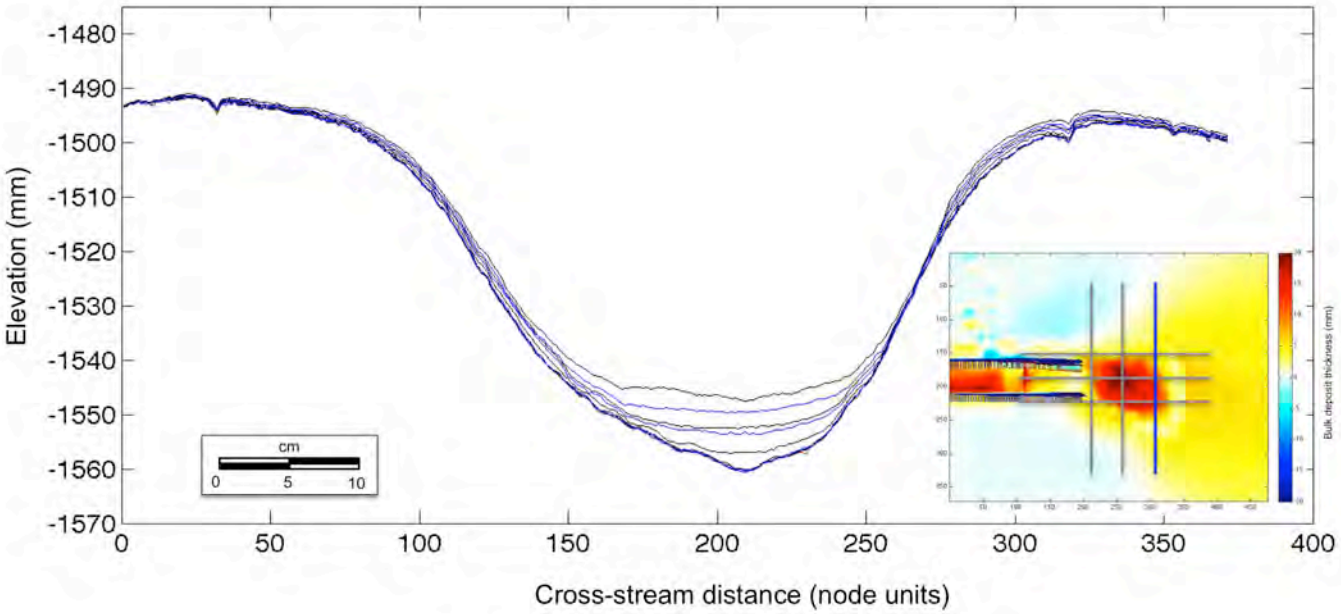


**Strike-oriented cross-sections for Configuration 1 showing initial surface (red) and bathymetry surfaces resulting from nine turbidity current events (t=6 to t=14).** The cross section location is also displayed in plan view, and is superimposed on a deposit thickness map of the final surface minus the initial basin surface. The panel is oriented as if you were looking downstream. Note axes units: x-axis is displayed in node units. and y-axis is displayed in millimeters.

Note: 1 node unit = 2 millimeters

## 4.5.1 Series 2 – Bathymetry and Slope Maps (Configuration 3)

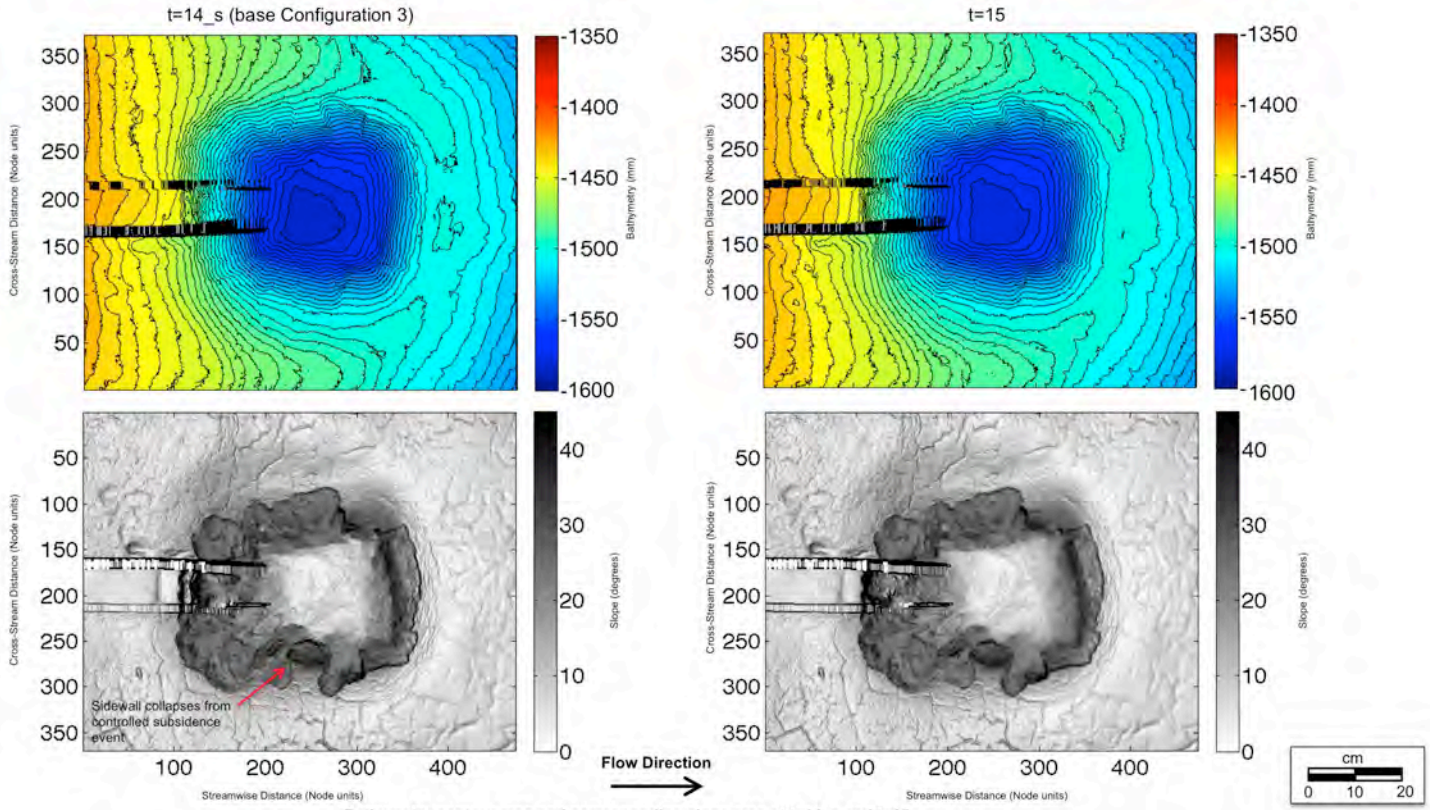


**Bathymetry contour map and corresponding slope map at t=14_s and t=15.**
The surface t=14_s represents the subsided surface of the final deposit from Configuration 2, and is the initial surface for Configuration 3.
The confining channel is seen as two parallel lines entering from the left.

Note: 1 node unit = 2 millimeters

## 4.5.1 Series 2 – Bathymetry and Slope Maps (Configuration 3)

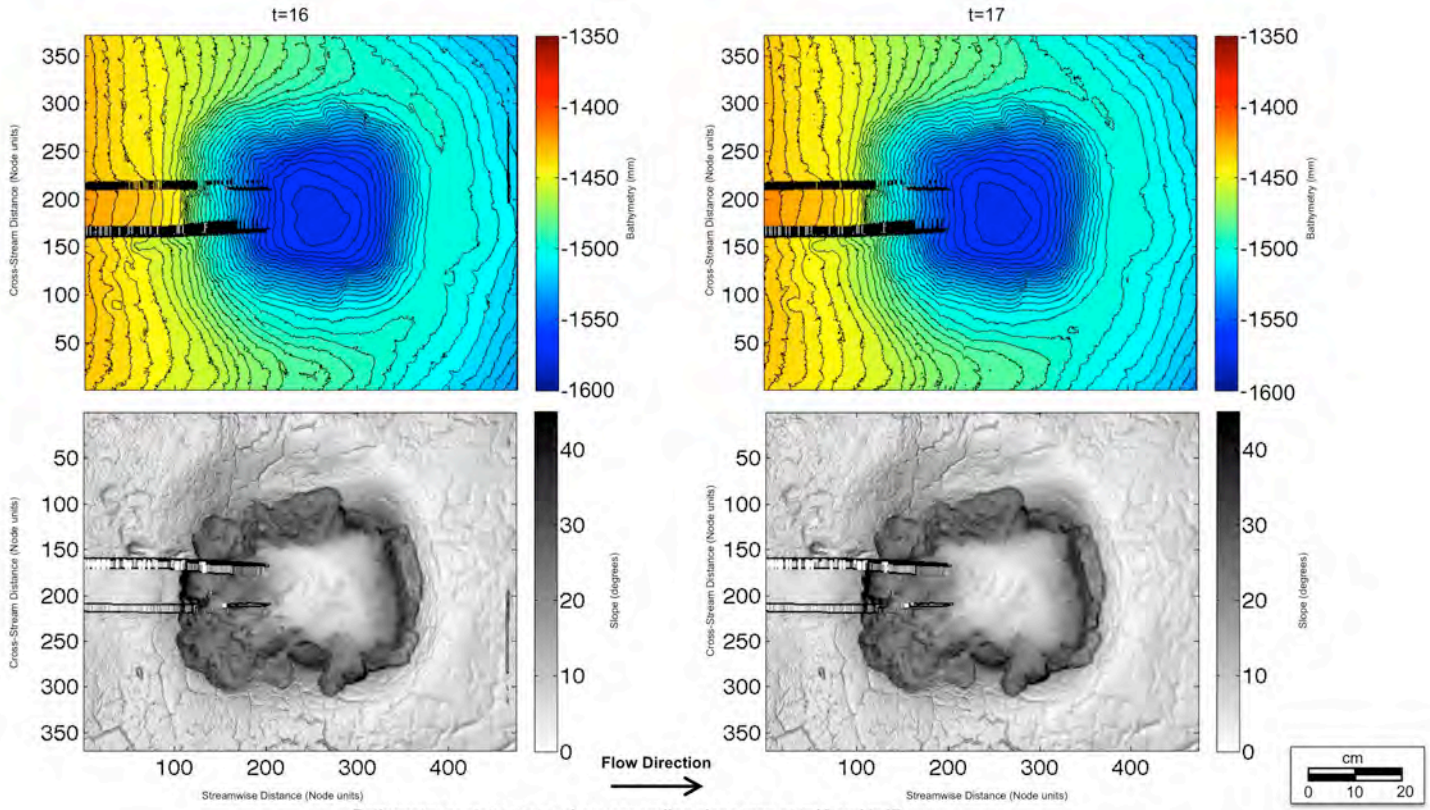


**Bathymetry contour map and corresponding slope map at t=16 and t=17.**
The confining channel is seen as two parallel lines entering from the left.

Note: 1 node unit = 2 millimeters

## 4.5.1 Series 2 – Bathymetry and Slope Maps (Configuration 3)

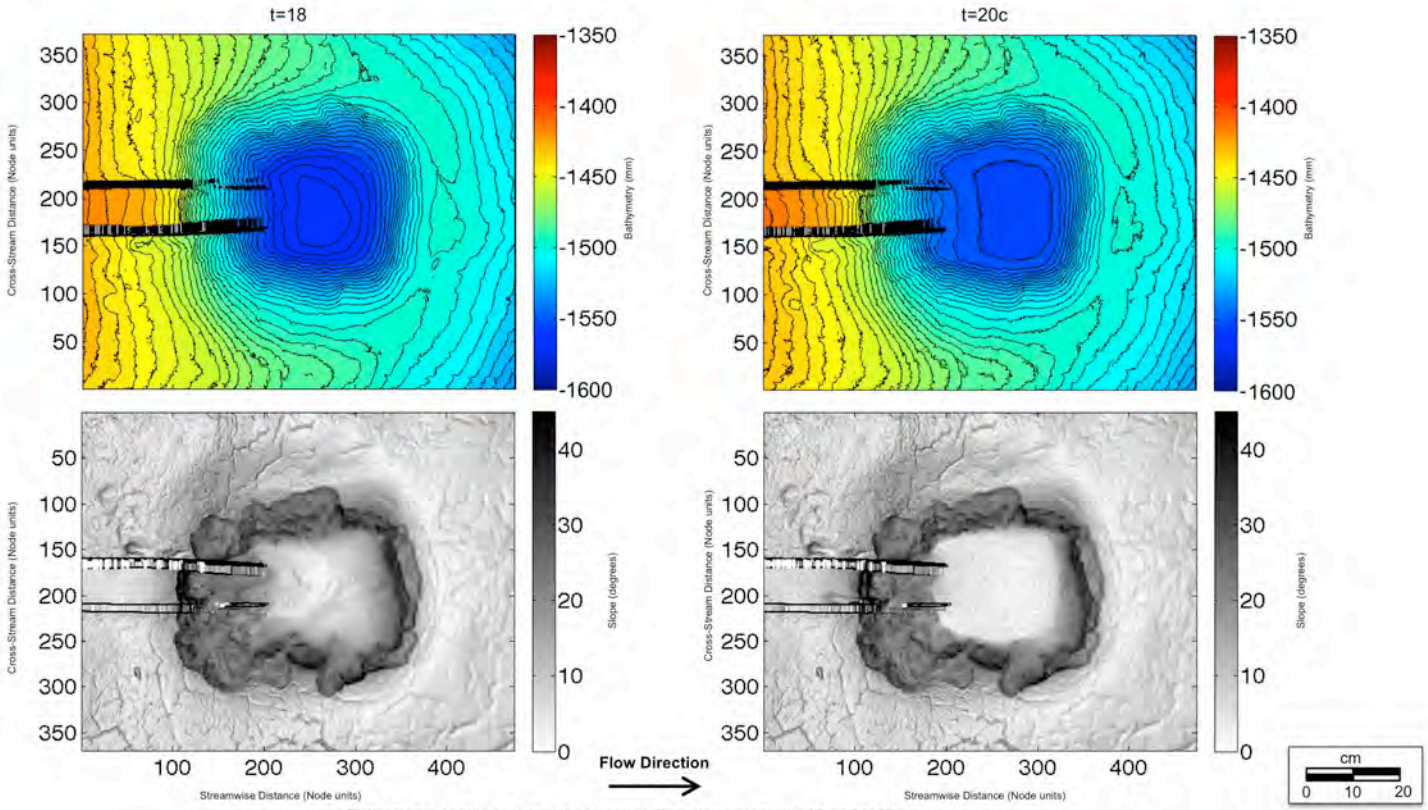


**Bathymetry contour map and corresponding slope map at t=18 and t=20c.**
The confining channel is seen as two parallel lines entering from the left.

Note: 1 node unit = 2 millimeters

## 4.5.1 Series 2 – Bathymetry and Slope Maps (Configuration 3)

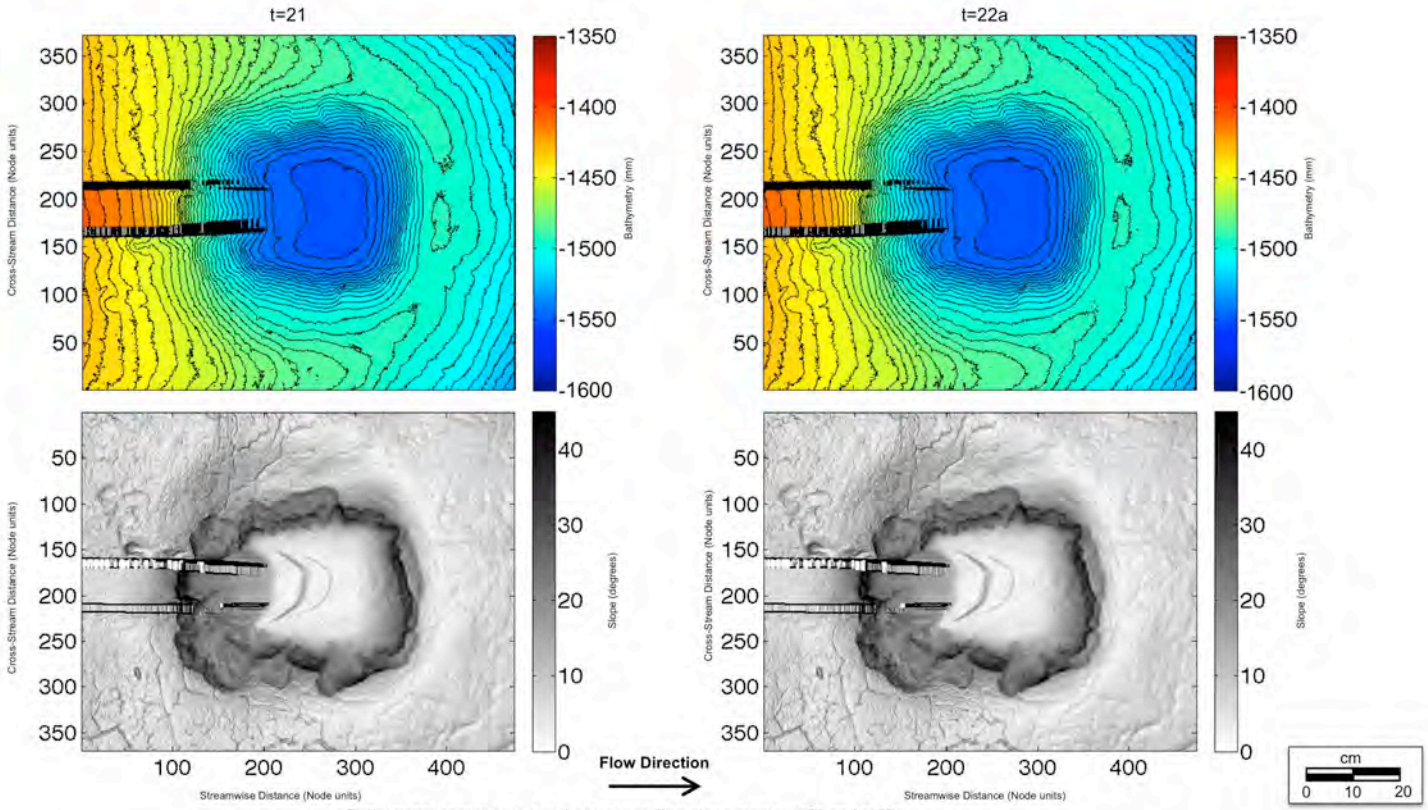


**Bathymetry contour map and corresponding slope map at t=21 and t=22a.**
The confining channel is seen as two parallel lines entering from the left.

Note: 1 node unit = 2 millimeters

## 4.5.1 Series 2 – Bathymetry and Slope Maps (Configuration 3)

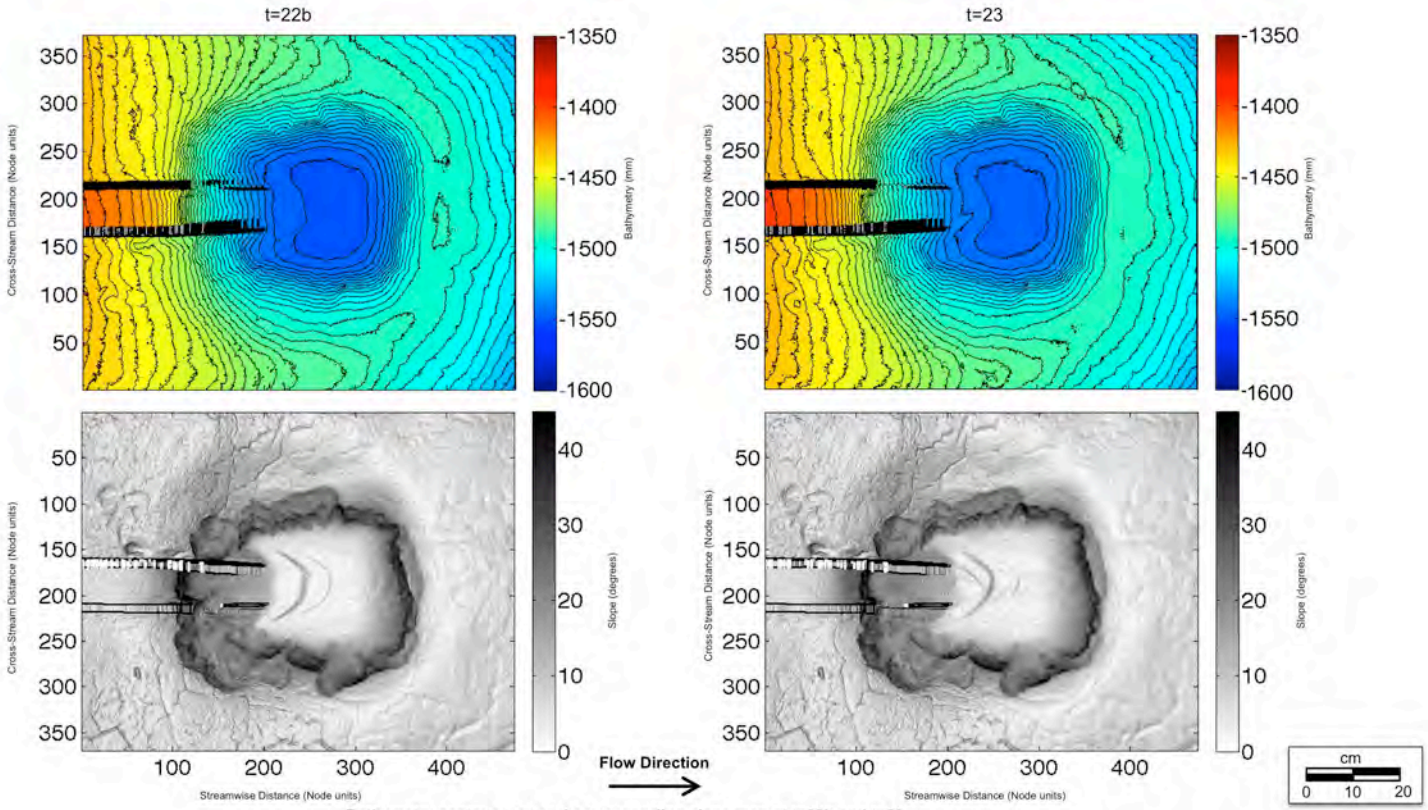


**Bathymetry contour map and corresponding slope map at t=22b and t=23.**
The confining channel is seen as two parallel lines entering from the left.

Note: 1 node unit = 2 millimeters

## 4.5.1 Series 2 – Bathymetry and Slope Maps (Configuration 3)

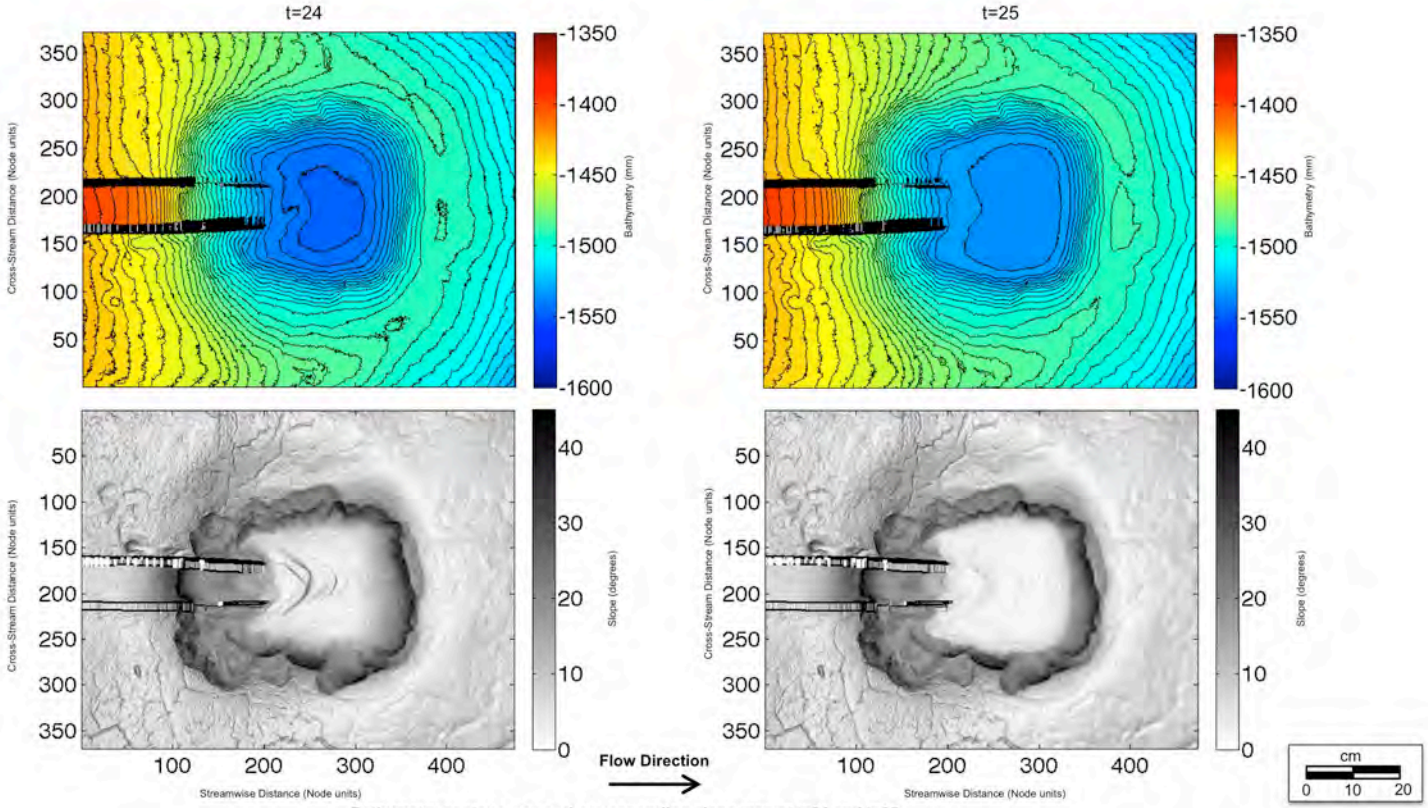


**Bathymetry contour map and corresponding slope map at t=24 and t=25.**
The confining channel is seen as two parallel lines entering from the left.

Note: 1 node unit = 2 millimeters

## 4.5.1 Series 2 – Bathymetry and Slope Maps (Configuration 3)

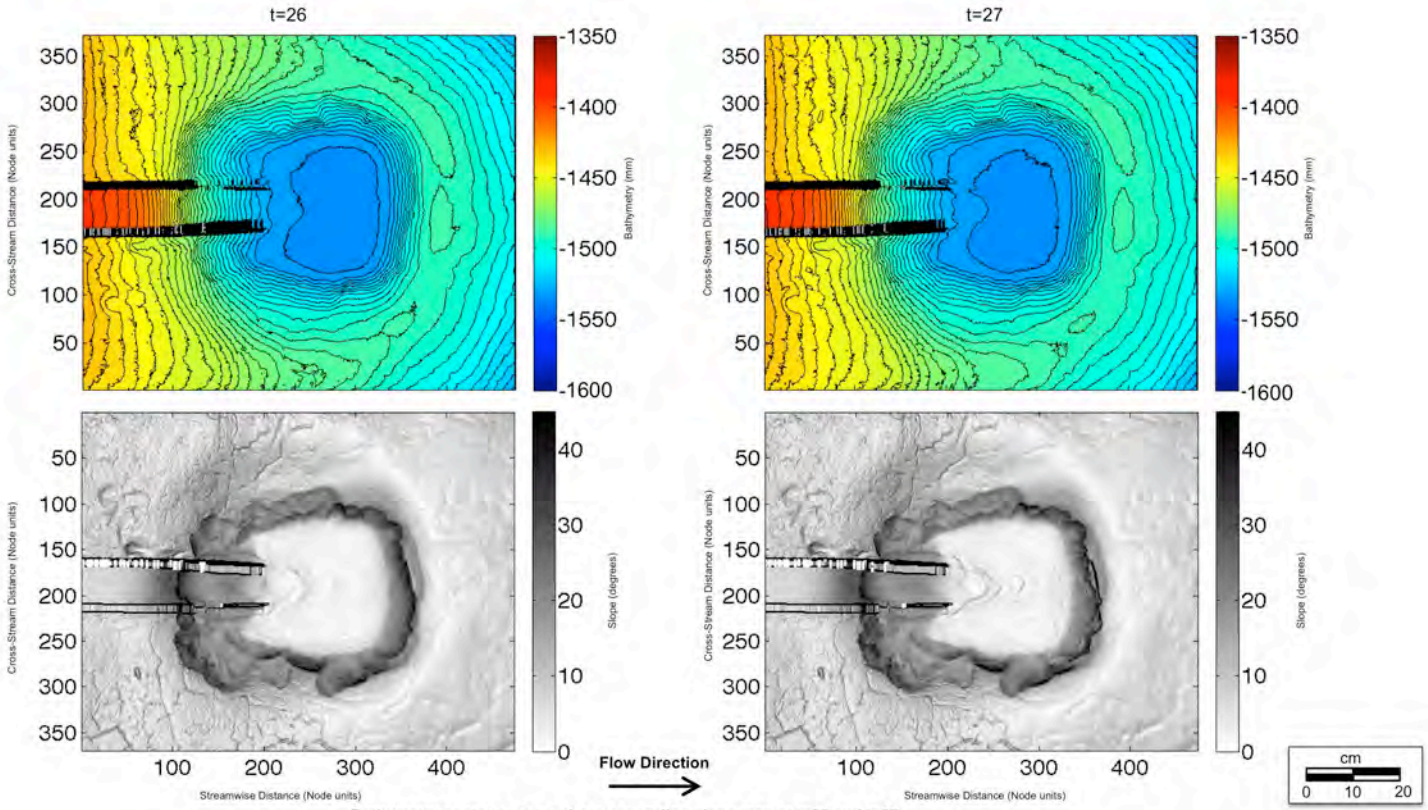


**Bathymetry contour map and corresponding slope map at t=26 and t=27.**
The confining channel is seen as two parallel lines entering from the left.

Note: 1 node unit = 2 millimeters

## 4.5.2 Series 2 – Event Deposit Thickness Maps (Configuration 3)

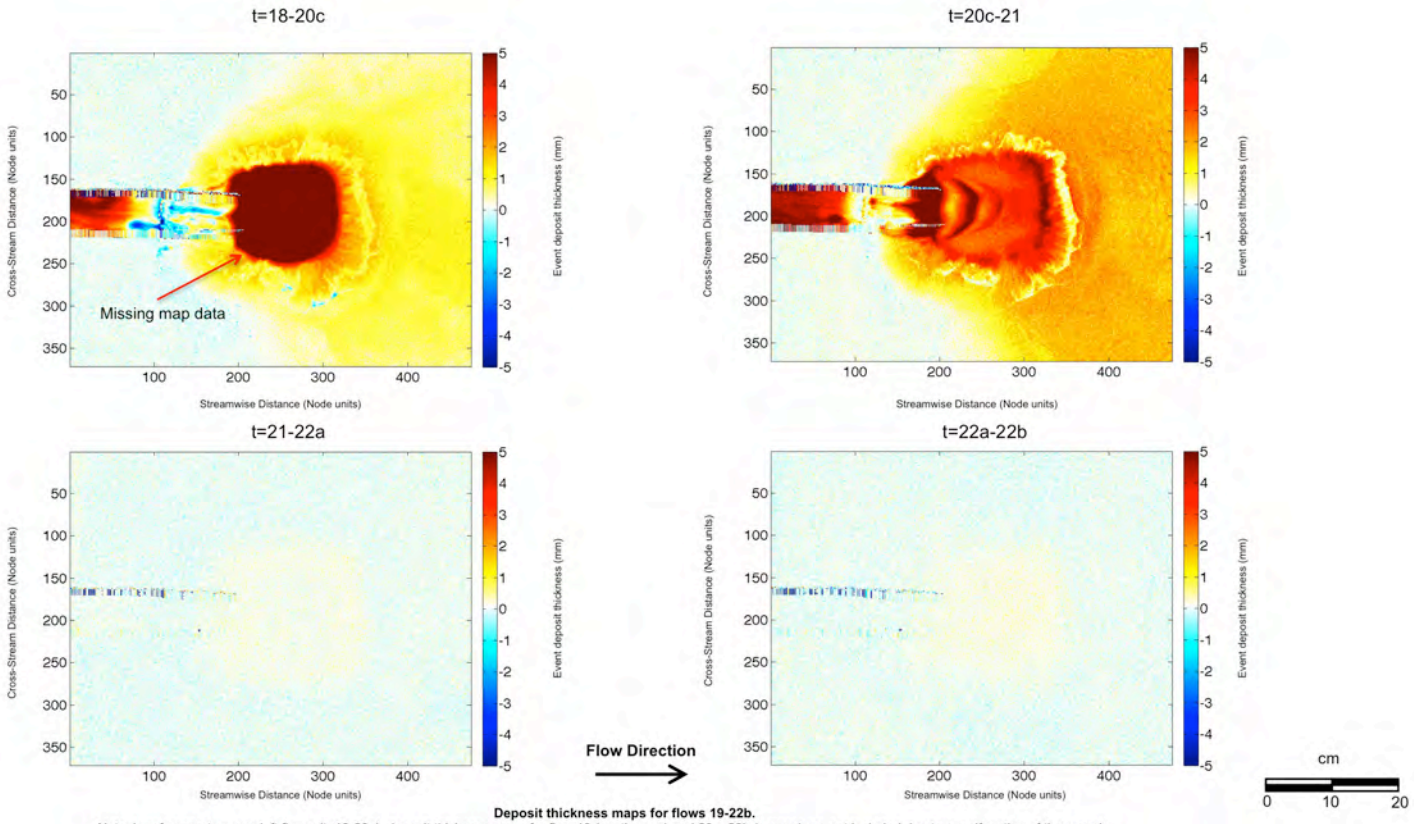


**Deposit thickness maps for flows 19-22b.**

Note: in reference to upper left figure (t=18-20c), deposit thickness maps for flow 19 (continuous) and 20a, 20b (surges) are not included due to a malfunction of the mapping system. An unusually thick deposit was produced during these flows. We speculate that this thick deposit is the result of successive surge flows (20a-20c) interacting with a residual dense fluid layer formed during flow 19. Also note the lack of sediment deposition in the basin from surge events 22a and 22b. The confining channel is seen as two parallel lines entering from the left.

Note: 1 node unit = 2 millimeters

## 4.5.2 Series 2 – Event Deposit Thickness Maps (Configuration 3)

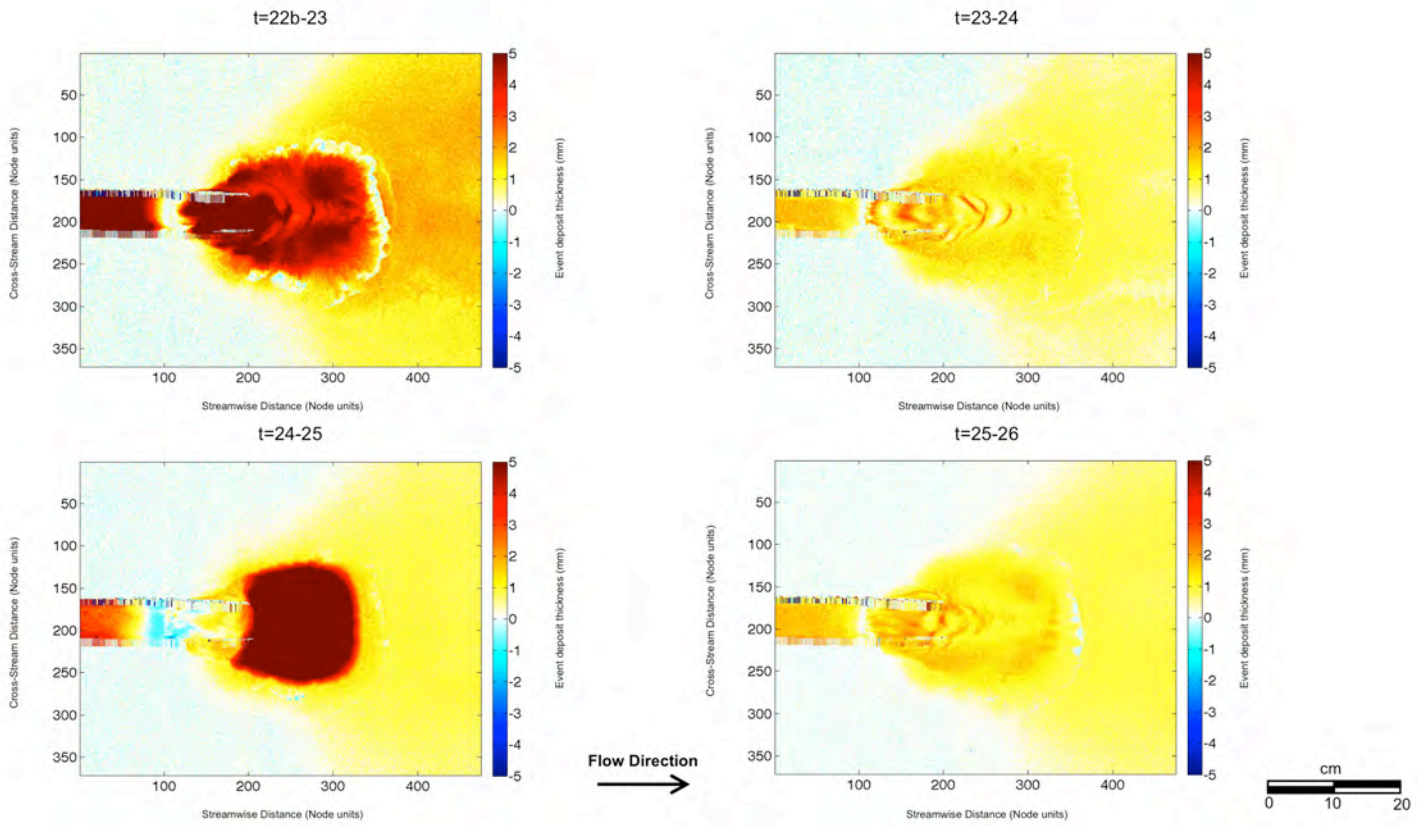


**Deposit thickness maps for flows 23-26.**
The confining channel is seen as two parallel lines entering from the left.

Note: 1 node unit = 2 millimeters

## 4.5.2 Series 2 – Event Deposit Thickness Maps (Configuration 3)

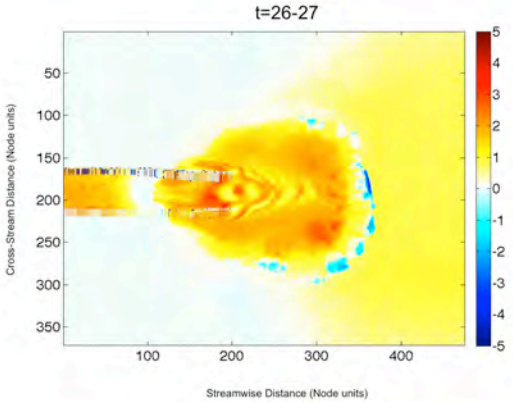


Flow Direction

cm
0 10 20

**Deposit thickness maps for flow 27.**
The confining channel is seen as two parallel lines entering from the left.

Note: 1 node unit = 2 millimeters

## 4.5.3 Series 2 – Dip Cross Sections (Configuration 3, y=130)

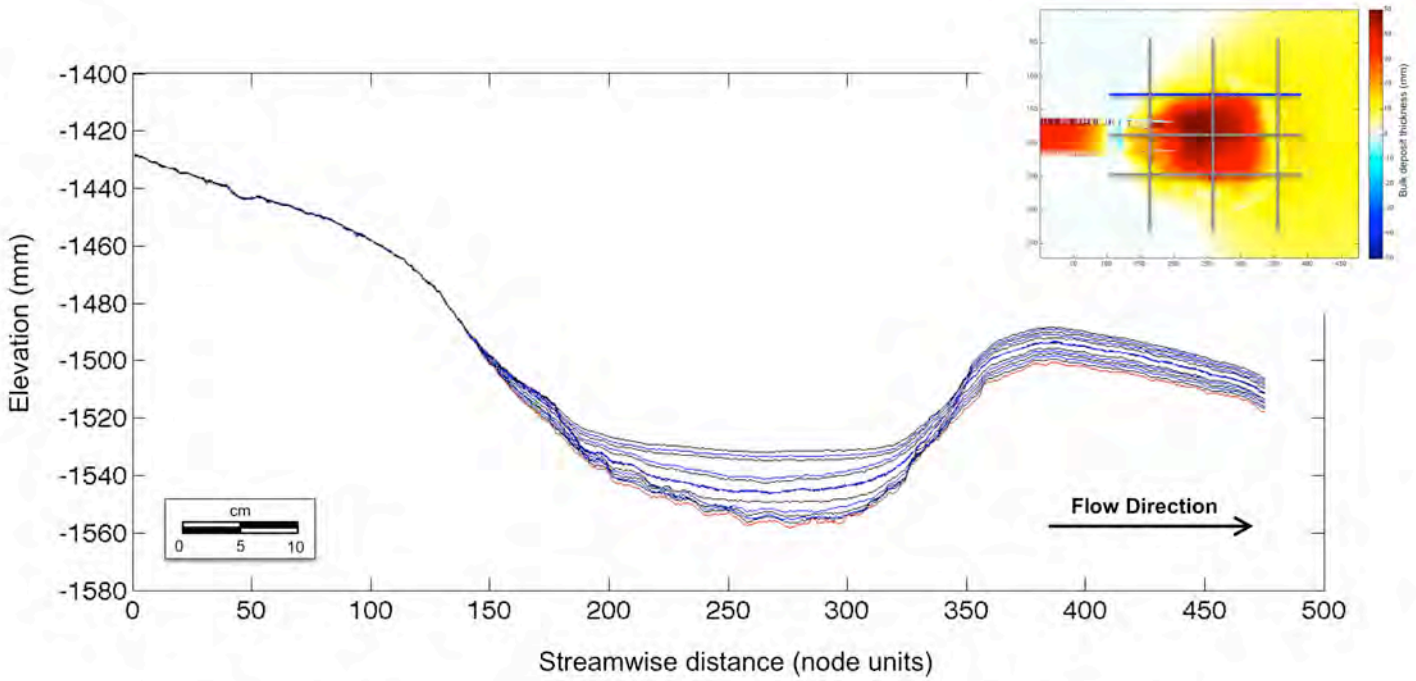


**Dip-oriented cross-sections for Configuration 3 showing initial surface (red) and bathymetry surfaces resulting from sixteen turbidity current events (t=15 to t=27).** The cross section location is also displayed in plan view, and is superimposed on a deposit thickness map of the final surface minus the initial basin surface. Note axes units: x-axis is displayed in node units, and y-axis is displayed in millimeters.

Note: 1 node unit = 2 millimeters

## 4.5.3 Series 2 – Dip Cross Sections (Configuration 3, y=190)

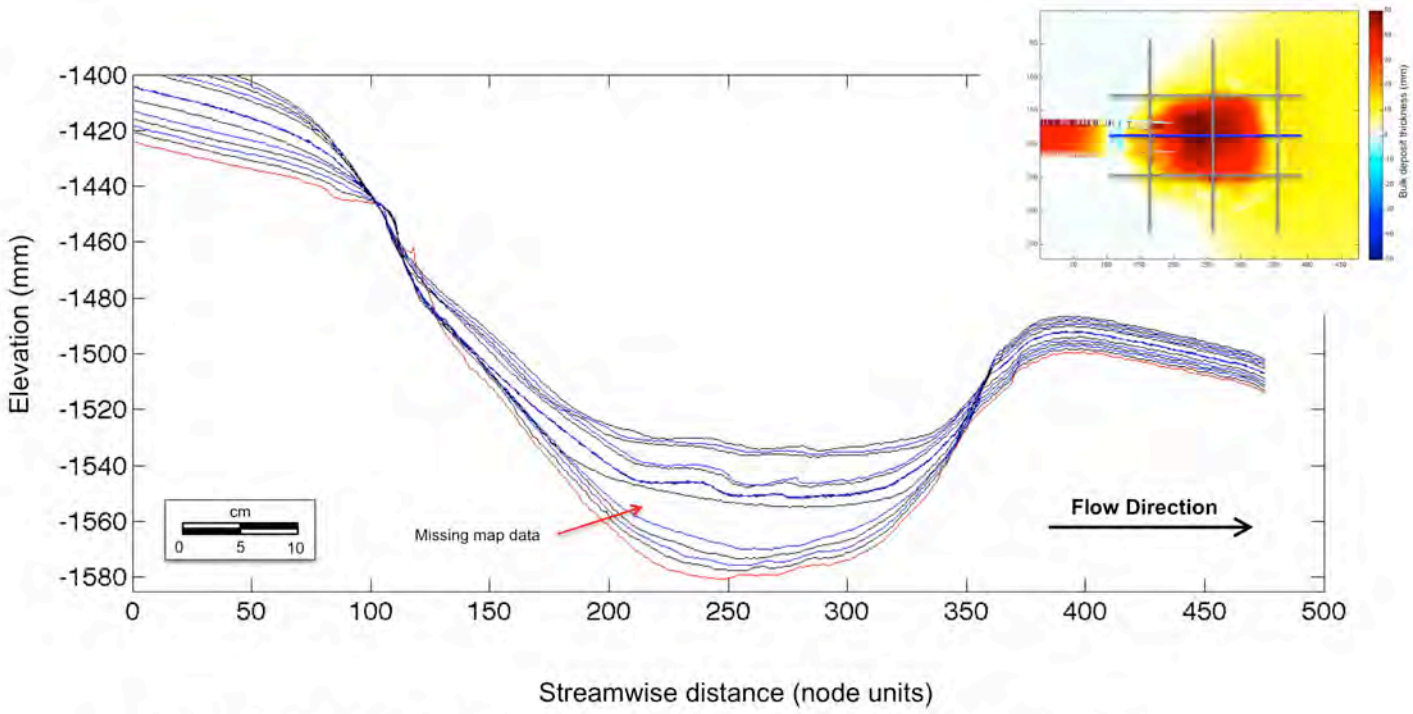


**Dip-oriented cross-sections for Configuration 3 showing initial surface (red) and bathymetry surfaces resulting from sixteen turbidity current events (t=15 to t=27).** The cross section location is also displayed in plan view, and is superimposed on a deposit thickness map of the final surface minus the initial basin surface. Note: maps for flow 19 (continuous) and 20a, 20b (surges) are not included due to a malfunction of the mapping system. An unusually thick deposit was produced during these flows. We speculate that this thick deposit is the result of successive surge flows (20a-20c) interacting with a residual dense fluid layer formed during flow 19. Also note the ponded character of this deposit relative to the draped deposits that dominate the section. X-axis is displayed in node units, and y-axis is displayed in millimeters.

Note: 1 node unit = 2 millimeters

## 4.5.3 Series 2 – Strike Cross Sections (Configuration 3, x=150)

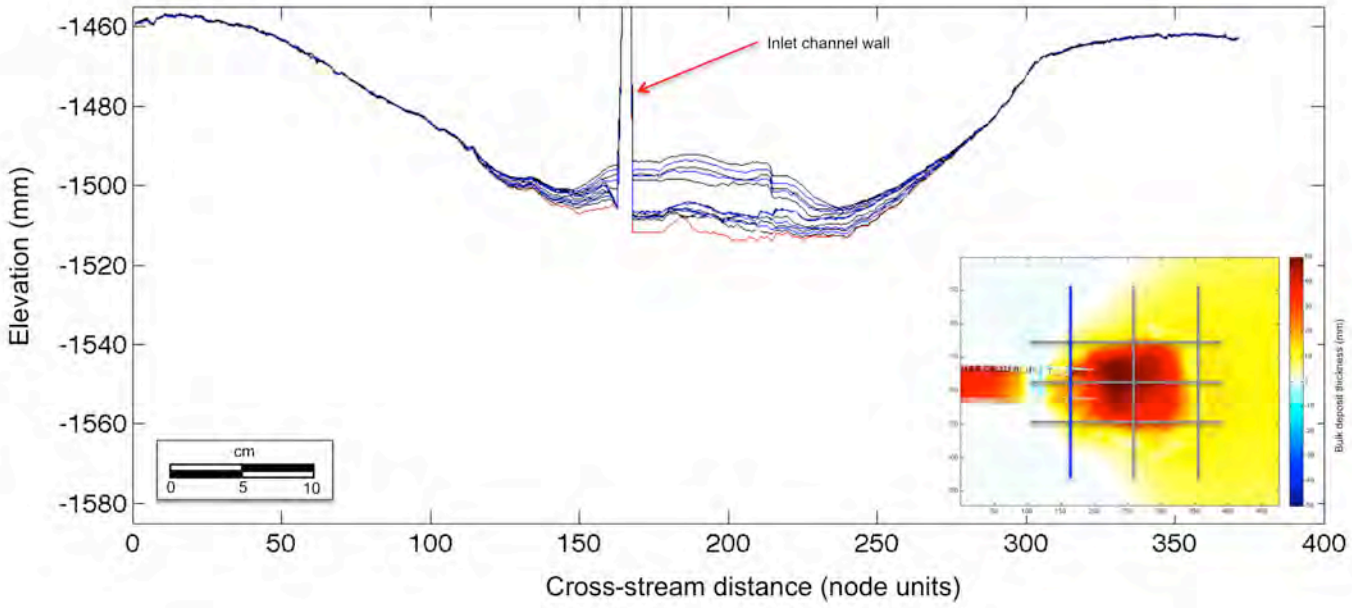


**Strike-oriented cross-sections for Configuration 3 showing initial surface (red) and bathymetry surfaces resulting from sixteen turbidity current events (t=15 to t=27).** The cross section location is also displayed in plan view, and is superimposed on a deposit thickness map of the final surface minus the initial basin surface. The panel is oriented as if you were looking downstream. Note axes units: x-axis is displayed in node units, and y-axis is displayed in millimeters.

Note: 1 node unit = 2 millimeters

## 4.5.3 Series 2 – Dip Cross Sections (Configuration 3, y=250)

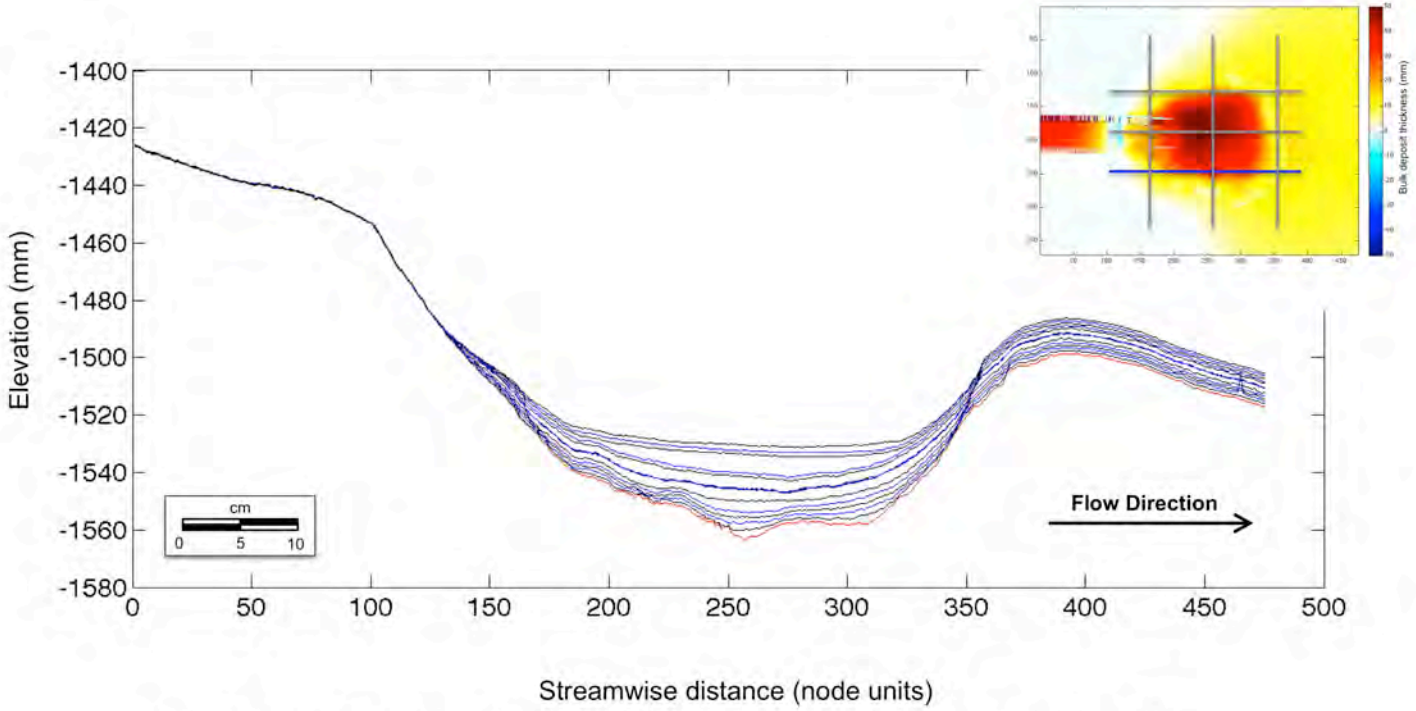


**Dip-oriented cross-sections for Configuration 3 showing initial surface (red) and bathymetry surfaces resulting from sixteen turbidity current events (t=15 to t=27).** The cross section location is also displayed in plan view, and is superimposed on a deposit thickness map of the final surface minus the initial basin surface. Note axes units: x-axis is displayed in node units, and y-axis is displayed in millimeters.

Note: 1 node unit = 2 millimeters

## 4.5.3 Series 2 – Strike Cross Sections (Configuration 3, x=150)

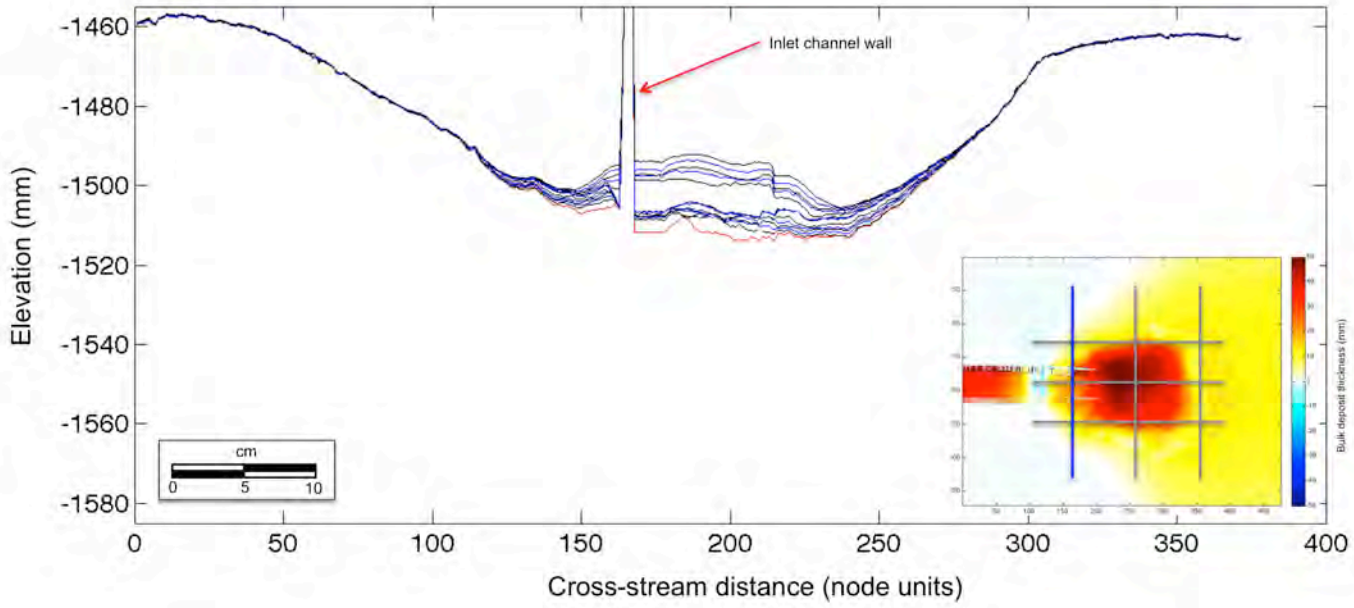


**Strike-oriented cross-sections for Configuration 3 showing initial surface (red) and bathymetry surfaces resulting from sixteen turbidity current events (t=15 to t=27).** The cross section location is also displayed in plan view, and is superimposed on a deposit thickness map of the final surface minus the initial basin surface. The panel is oriented as if you were looking downstream. Note axes units: x-axis is displayed in node units, and y-axis is displayed in millimeters.

Note: 1 node unit = 2 millimeters

## Series 2 – Strike Cross Sections (Configuration 3, x=250)

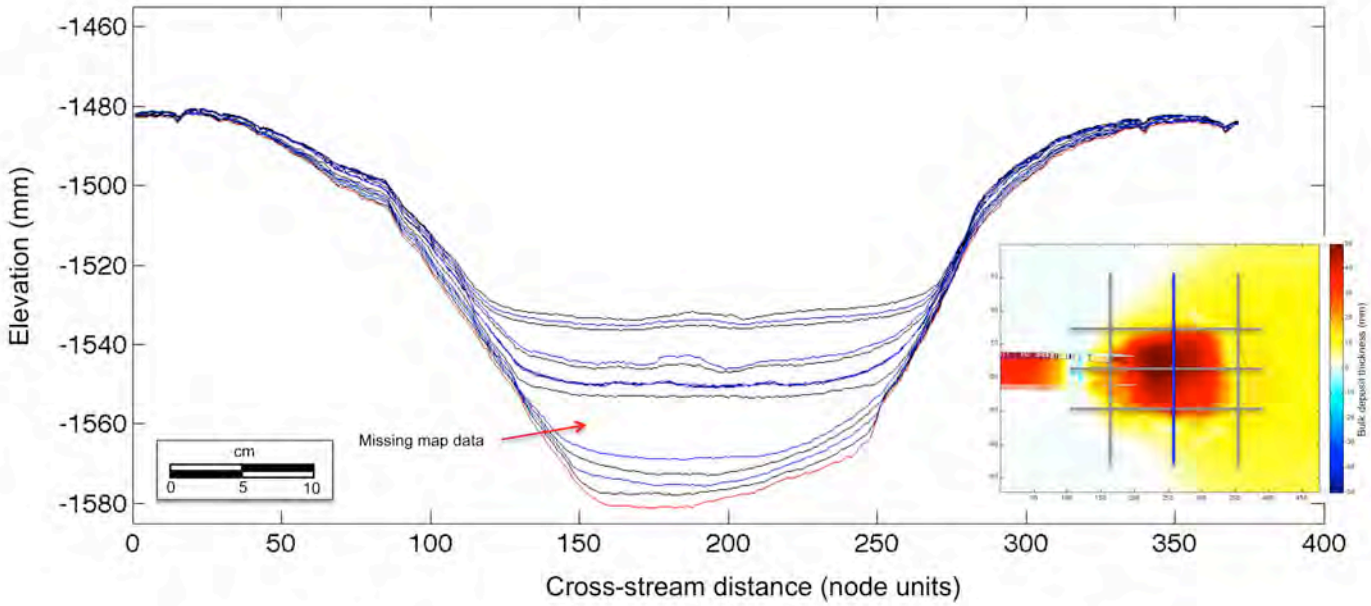


**Strike-oriented cross-sections for Configuration 3 showing initial surface (red) and bathymetry surfaces resulting from sixteen turbidity current events (t=15 to t=27).** The cross section location is also displayed in plan view, and is superimposed on a deposit thickness map of the final surface minus the initial basin surface. Note: maps for flow 19 (continuous) and 20a, 20b (surges) are not included due to a malfunction of the mapping system. An unusually thick deposit was produced during these flows. We speculate that this thick deposit is the result of successive surge flows (20a-20c) interacting with a residual dense fluid layer formed during flow 19. Also note the ponded character of this deposit relative to the draped deposits that dominate the section. X-axis is displayed in node units, and y-axis is displayed in millimeters.

Note: 1 node unit = 2 millimeters

## 4.5.3 Series 2 – Strike Cross Sections (Configuration 3, x=350)

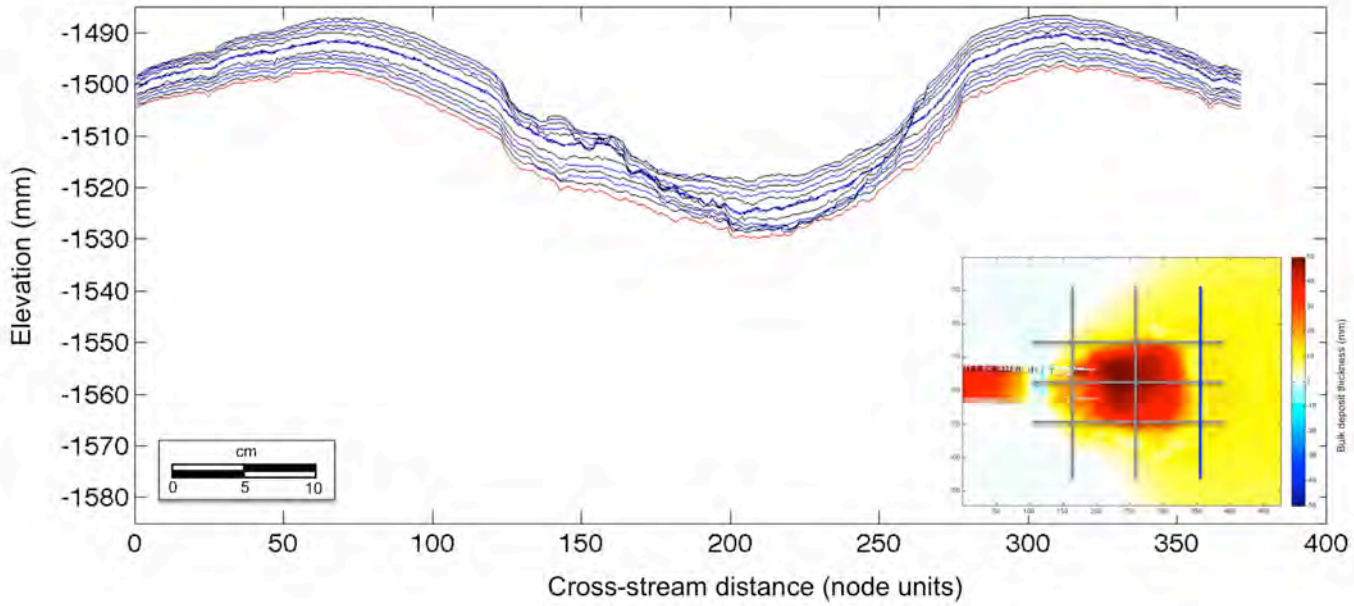


**Strike-oriented cross-sections for Configuration 3 showing initial surface (red) and bathymetry surfaces resulting from sixteen turbidity current events (t=15 to t=27).** The cross section location is also displayed in plan view, and is superimposed on a deposit thickness map of the final surface minus the initial basin surface. The panel is oriented as if you were looking downstream. Note axes units: x-axis is displayed in node units, and y-axis is displayed in millimeters.

Note: 1 node unit = 2 millimeters

# 4.6 Series 2 – End Experiment Fill Reconstruction (y=190)

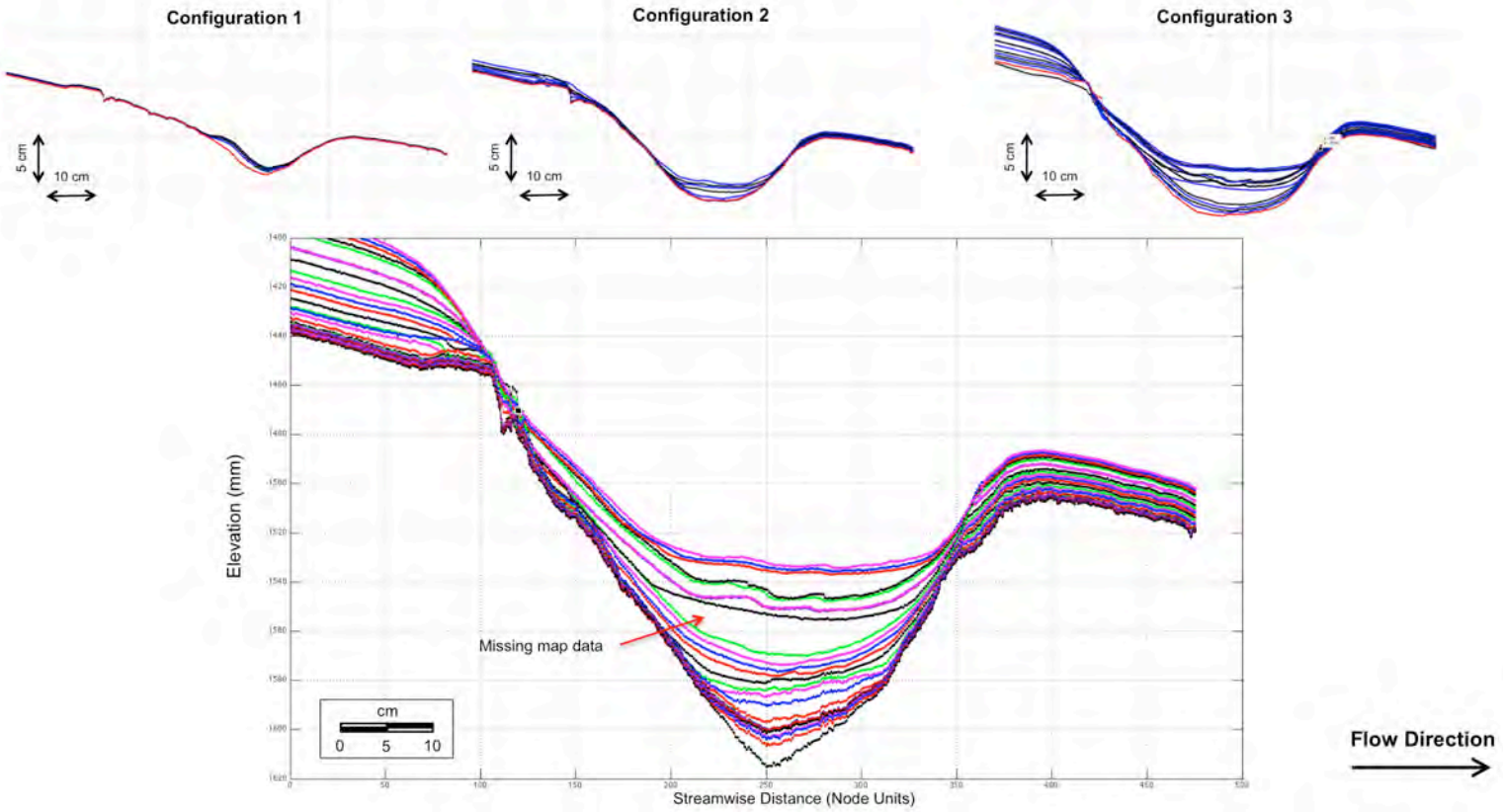


**Complete center-line dip section reconstruction (lower figure) of mini-basin deposits incorporating individual packages from Configurations 1, 2 and 3 (upper figures).** The reconstruction was performed by using the final surface (t=27) as the reference surface onto which each individual deposit was appended, and assumes no sidewall failures during controlled subsidence events.

Note: 1 node unit = 2 millimeters

## 4.7 Series 2 – Typical Continuous Turbidity Current Flow Sequence (t=0 seconds)


**Typical continuous turbidity current flow sequence (overhead view) into the mini-basin.**
The dashed white line shows the mini-basin outline.

## 4.7 Series 2 – Typical Continuous Turbidity Current Flow Sequence (t=10 seconds)

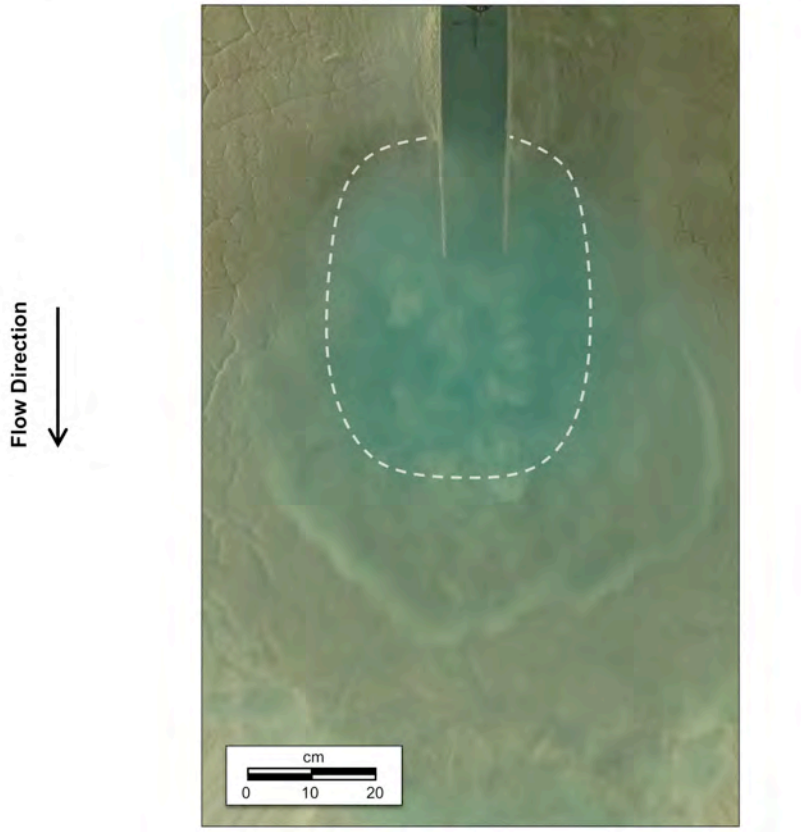


**Typical continuous turbidity current flow sequence (overhead view) into the mini-basin.**
The dashed white line shows the mini-basin outline.

## 4.7 Series 2 – Typical Continuous Turbidity Current Flow Sequence (t=20 seconds)


**Typical continuous turbidity current flow sequence (overhead view) into the mini-basin.**
The dashed white line shows the mini-basin outline.

## 4.7 Series 2 – Typical Continuous Turbidity Current Flow Sequence (t=30 seconds)

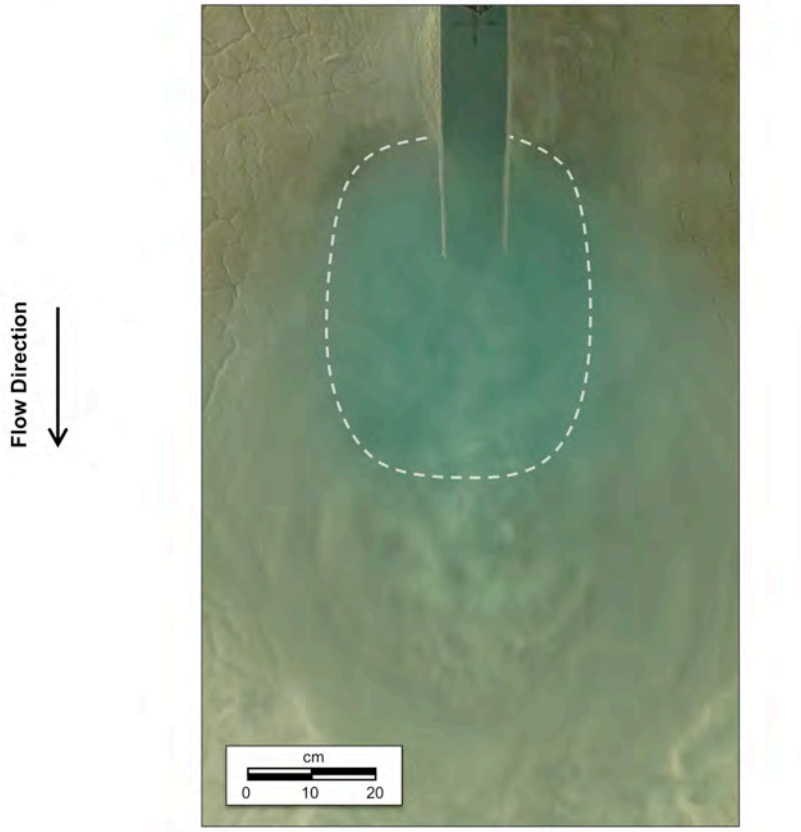


**Typical continuous turbidity current flow sequence (overhead view) into the mini-basin.**
The dashed white line shows the mini-basin outline.

## 4.7 Series 2 – Typical Continuous Turbidity Current Flow Sequence (t=40 seconds)

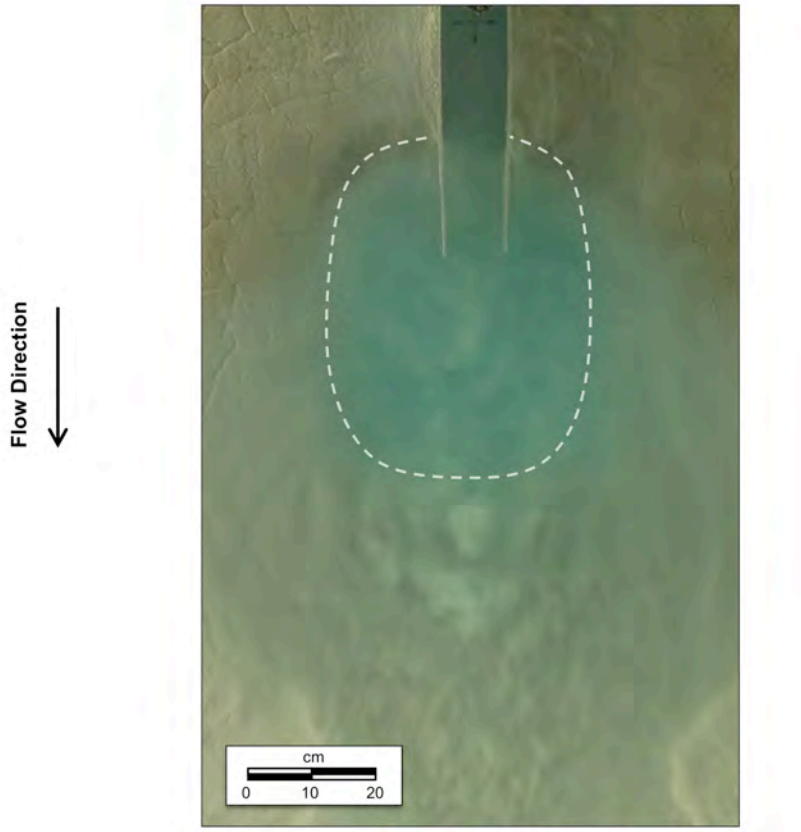


**Typical continuous turbidity current flow sequence (overhead view) into the mini-basin.**
The dashed white line shows the mini-basin outline.

## 4.7 Series 2 – Typical Continuous Turbidity Current Flow Sequence (t=50 seconds)

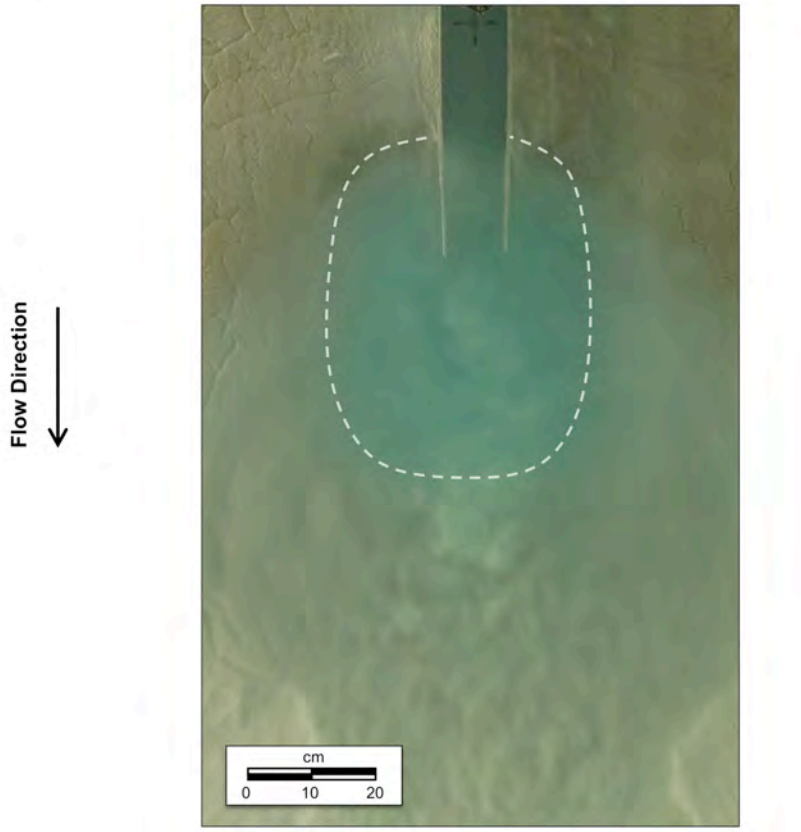


**Typical continuous turbidity current flow sequence (overhead view) into the mini-basin.**
The dashed white line shows the mini-basin outline.

## 4.7 Series 2 – Typical Continuous Turbidity Current Flow Sequence (t=60 seconds)

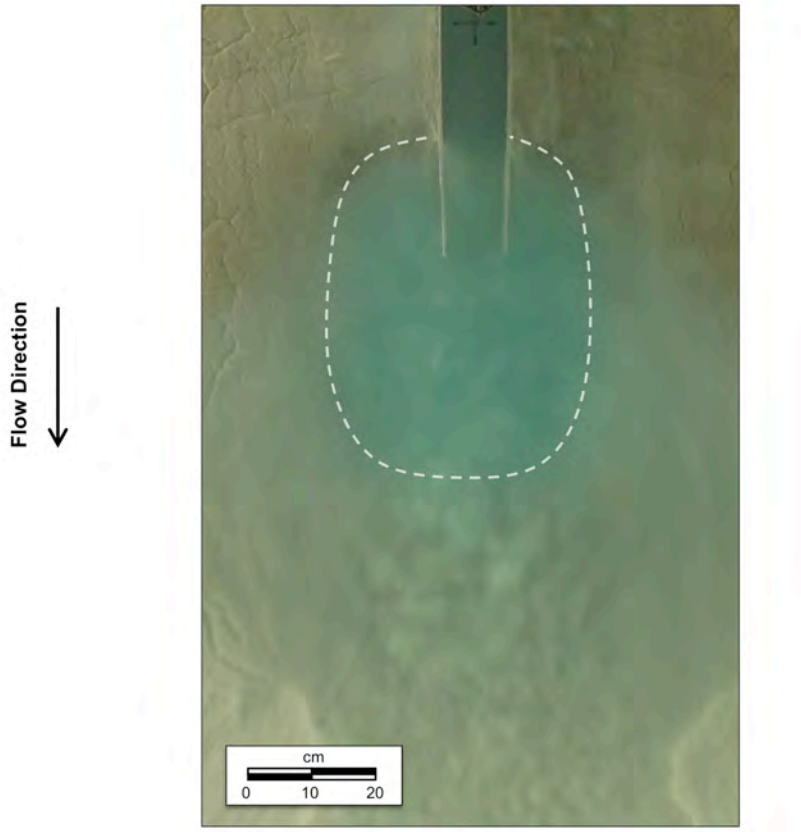


**Typical continuous turbidity current flow sequence (overhead view) into the mini-basin.**
The dashed white line shows the mini-basin outline.

## 4.8 Series 2 – Sediment Trapped in Basin by Configuration

| Configuration | Current Velocity (cm/s) | Discharge ($cm^3/s$) | Duration (s) | Trapped Sediment in Basin ($cm^3$) | Sediment trapped on Platform ($cm^3$) | Sediment Bypassed ($cm^3$) | Rate of trapping ($cm^3/s$) |
|---|---|---|---|---|---|---|---|
| 1 | 4.450 | 178.01 | 948 | 45 | 81 | 4339 | 0.047 |
| 2 | 6.588 | 263.53 | 3600 | 177 | 393 | 27852 | 0.049 |
| 3 | 8.632 | 345.28 | 4246 | 301 | 512 | 38874 | 0.071 |

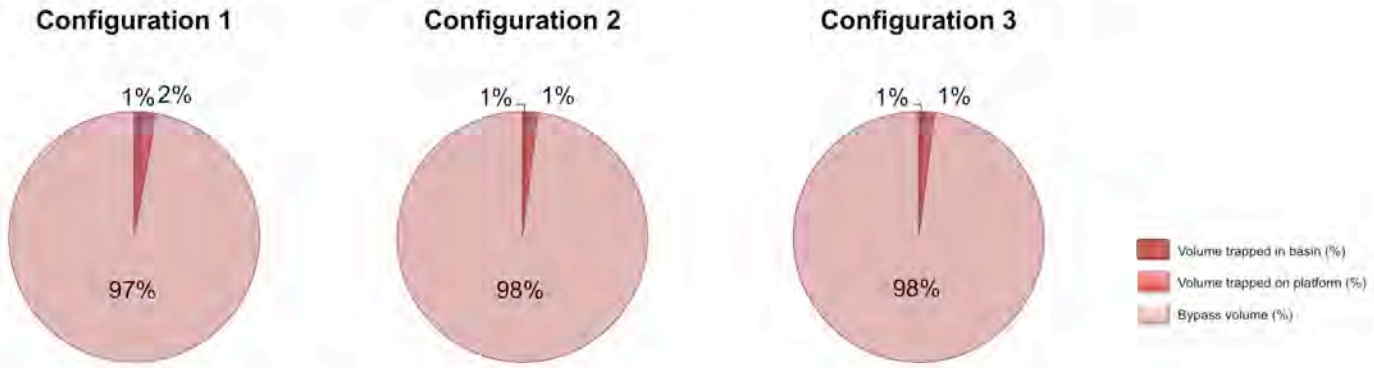


**Summary of sediment trapped in basin by configuration.**
The table above shows the average current flow conditions for each configuration, and the total volume of sediments that are captured by the mini-basin. The pie charts summarize partitioning of sediment deposition in the system by configuration. The rate of trapping is the trapped sediment in the basin divided by the total flow time for each configuration.

## 4.8 Series 2 – Sediment Trapped in Basin by Configuration

| Configuration | Current Velocity (cm/s) | Discharge ($cm^3/s$) | Duration (s) | Trapped Sediment in Basin ($cm^3$) | Sediment trapped on Platform ($cm^3$) | Sediment Bypassed ($cm^3$) | Rate of trapping ($cm^3/s$) |
|---|---|---|---|---|---|---|---|
| 1 | 4.450 | 178.01 | 948 | 45 | 81 | 4339 | 0.047 |
| 2 | 6.588 | 263.53 | 3600 | 177 | 393 | 27852 | 0.049 |
| 3 | 8.632 | 345.28 | 4246 | 301 | 512 | 38874 | 0.071 |

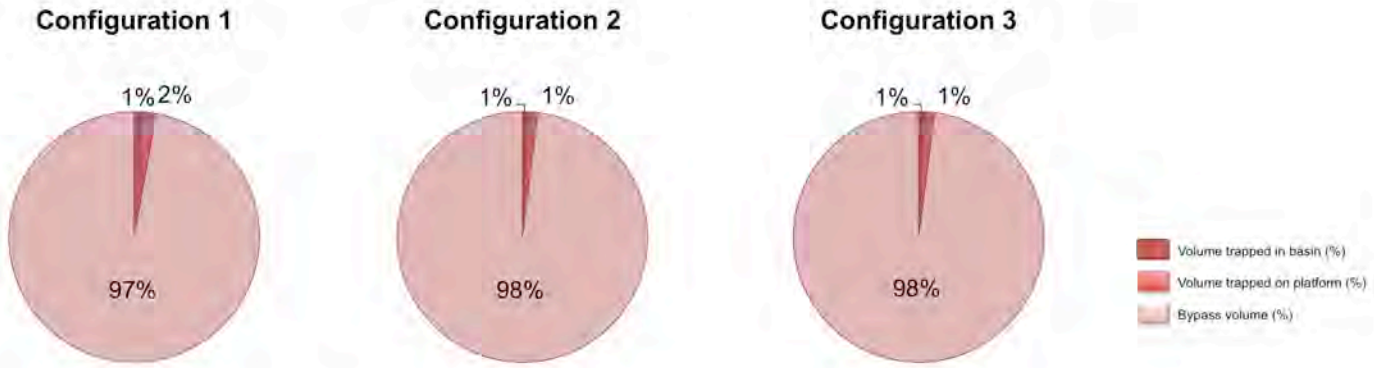


**Summary of sediment trapped in basin by configuration.**
The table above shows the average current flow conditions for each configuration, and the total volume of sediments that are captured by the mini-basin. The pie charts summarize partitioning of sediment deposition in the system by configuration. The rate of trapping is the trapped sediment in the basin divided by the total flow time for each configuration.

## 4.9.1 Series 2 – Deposit Cross Section and Dipline Velocity ($x_{avg}$) Distributions (Configuration 1)

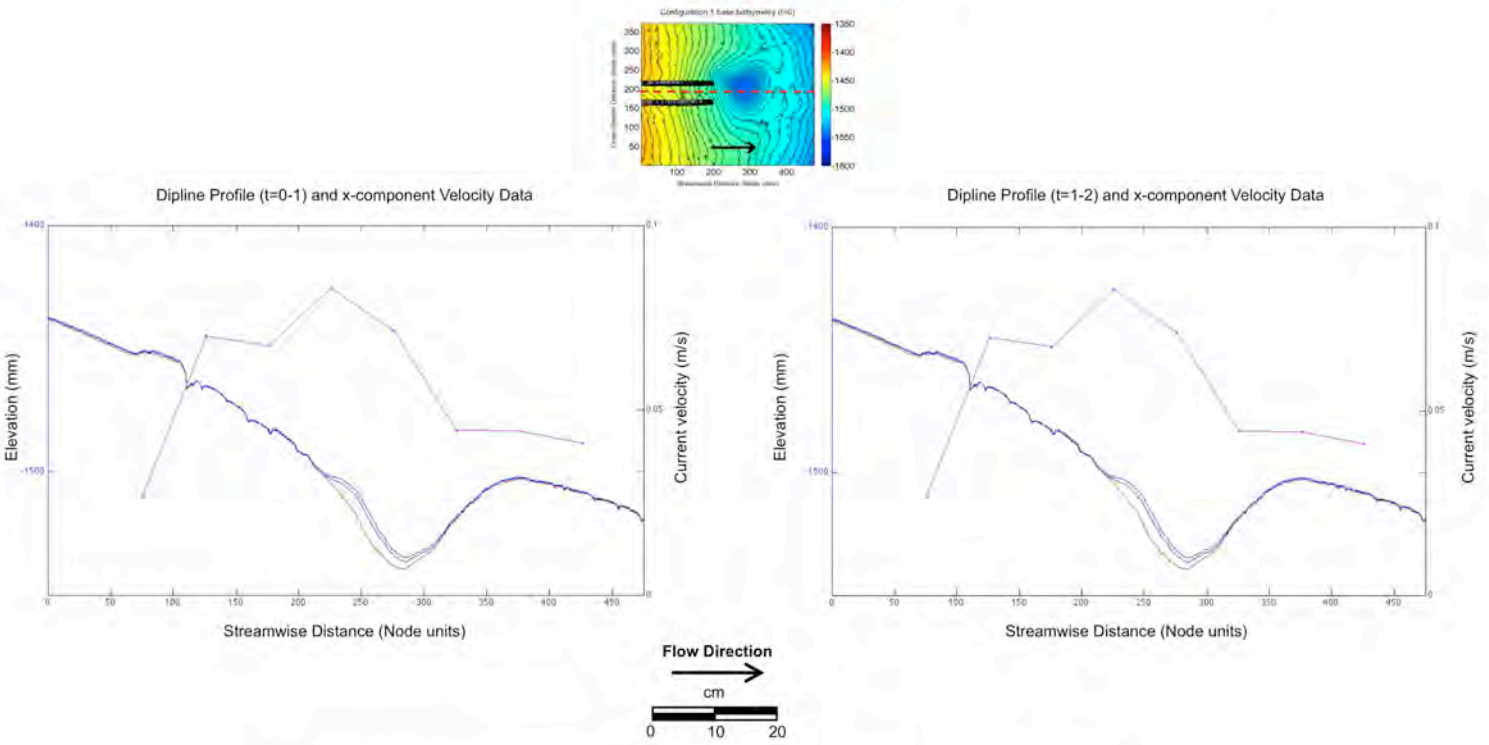


**Time-averaged near-bed x-component turbidity current velocity data and deposit geometry along the center dipline profile.**
Each plot above shows successive deposits from Configuration 1 along the center dipline section, the position of which is illustrated by the dashed red line on the t=0 bathymetry inset map above. Superimposed on the lower plots are the time averaged x-component current velocity, *u*, collected at equal spacing along the transect. Velocity component data are rotated to a bed-perpendicular reference frame (2-D calculation in the x-z plane). Each velocity data point is averaged over a 15 second interval and was collected in a 9 mm tall by 6 mm wide sampling volume with the base located within 2 mm above the deposit bed.

Note: 1 node unit = 2 millimeters

## 4.9.1 Series 2 – Deposit Cross Section and Dipline Velocity ($x_{avg}$) Distributions (Configuration 1)

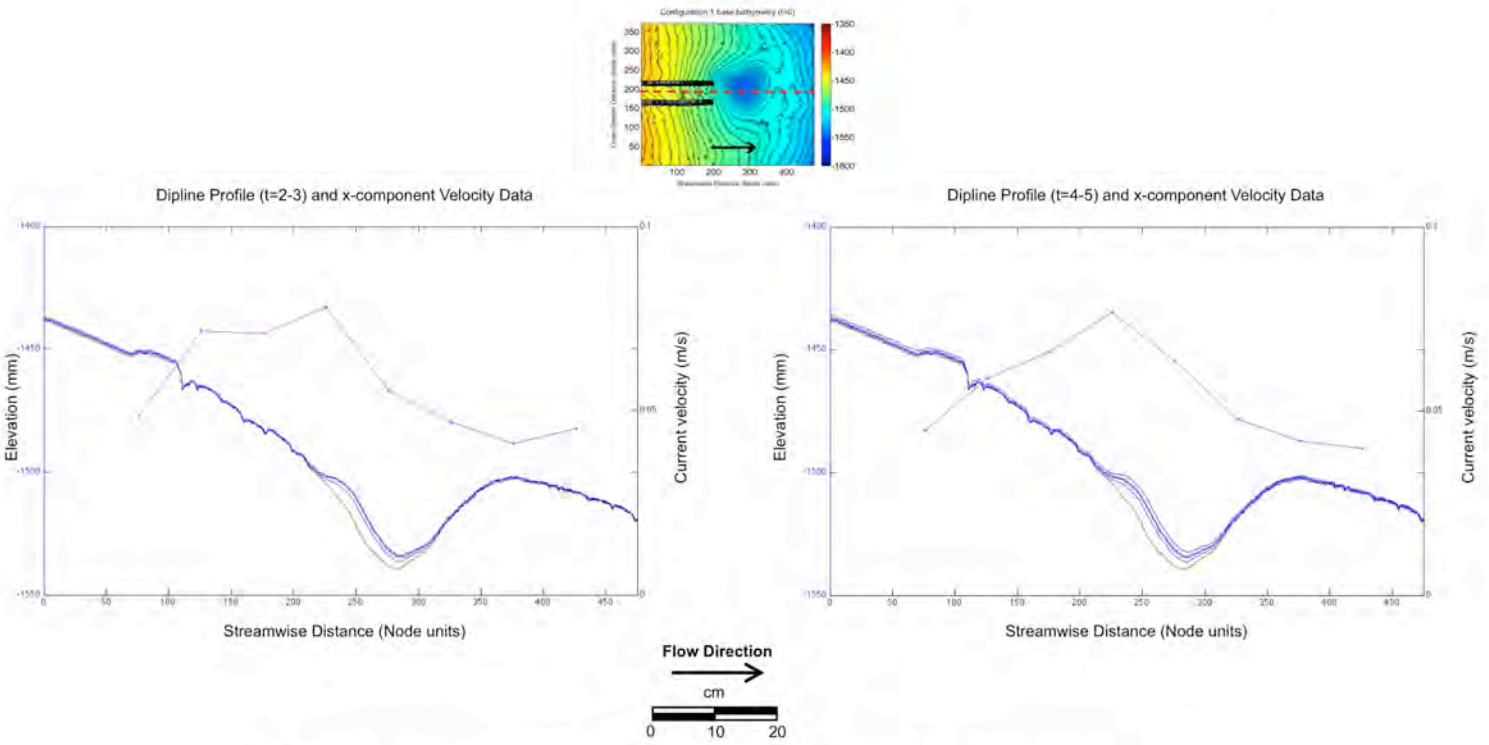


**Time-averaged near-bed x-component turbidity current velocity data and deposit geometry along the center dipline profile.**
Each plot above shows successive deposits from Configuration 1 along the center dipline section, the position of which is illustrated by the dashed red line on the t=0 bathymetry inset map above. Superimposed on the lower plots are the time averaged x-component current velocity, *u*, collected at equal spacing along the transect. Velocity component data are rotated to a bed-perpendicular reference frame (2-D calculation in the x-z plane). Each velocity data point is averaged over a 15 second interval and was collected in a 9 mm tall by 6 mm wide sampling volume with the base located within 2 mm above the deposit bed.

Note: 1 node unit = 2 millimeters

## 4.9.2 Series 2 – Deposit Cross Section and Dipline Velocity ($x_{avg}$) Distributions (Configuration 2)

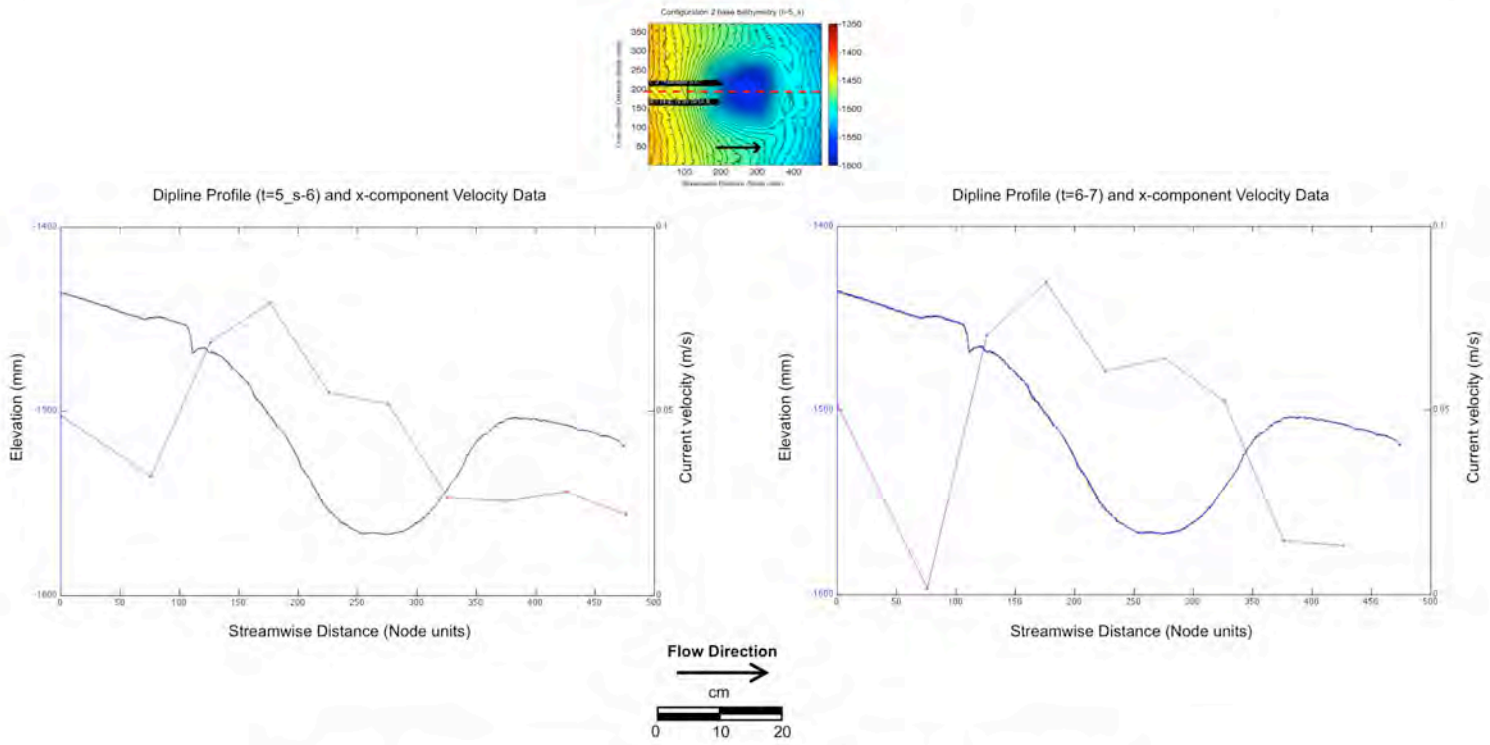


**Time-averaged near-bed x-component turbidity current velocity data and deposit geometry along the center dipline profile.**
Each plot above shows successive deposits from Configuration 2 along the center dipline section, the position of which is illustrated by the dashed red line on the t=0 bathymetry inset map above. Superimposed on the lower plots are the time averaged x-component current velocity, *u*, collected at equal spacing along the transect. Velocity component data are rotated to a bed-perpendicular reference frame (2-D calculation in the x-z plane). Each velocity data point is averaged over a 15 second interval and was collected in a 9 mm tall by 6 mm wide sampling volume with the base located within 2 mm above the deposit bed.

Note: 1 node unit = 2 millimeters

## 4.9.2 Series 2 – Deposit Cross Section and Dipline Velocity ($x_{avg}$) Distributions (Configuration 2)

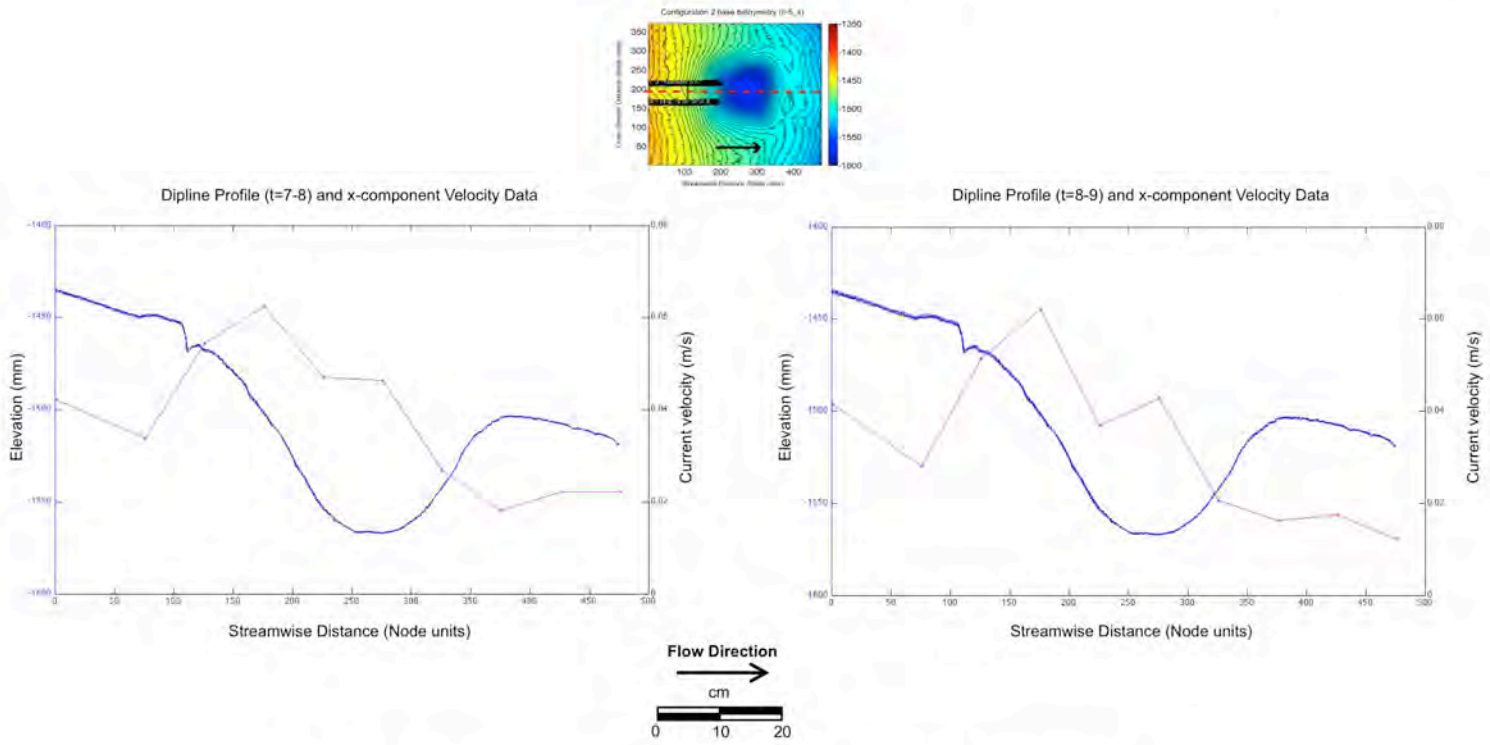


**Time-averaged near-bed x-component turbidity current velocity data and deposit geometry along the center dipline profile.**
Each plot above shows successive deposits from Configuration 2 along the center dipline section, the position of which is illustrated by the dashed red line on the t=0 bathymetry inset map above. Superimposed on the lower plots are the time averaged x-component current velocity, *u*, collected at equal spacing along the transect. Velocity component data are rotated to a bed-perpendicular reference frame (2-D calculation in the x-z plane). Each velocity data point is averaged over a 15 second interval and was collected in a 9 mm tall by 6 mm wide sampling volume with the base located within 2 mm above the deposit bed.

Note: 1 node unit = 2 millimeters

## 4.9.2 Series 2 – Deposit Cross Section and Dipline Velocity ($x_{avg}$) Distributions (Configuration 2)

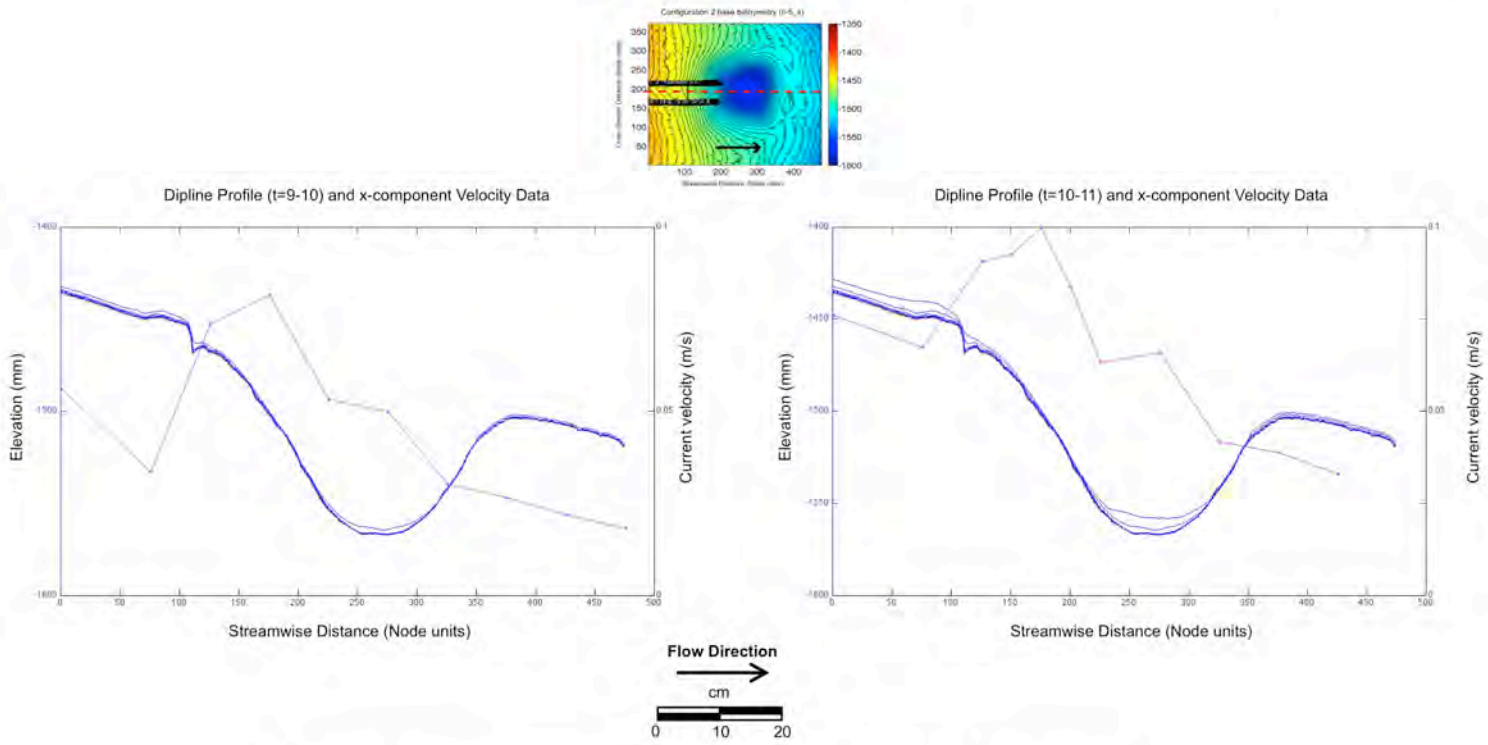


**Time-averaged near-bed x-component turbidity current velocity data and deposit geometry along the center dipline profile.**
Each plot above shows successive deposits from Configuration 2 along the center dipline section, the position of which is illustrated by the dashed red line on the t=0 bathymetry inset map above. Superimposed on the lower plots are the time averaged x-component current velocity, *u*, collected at equal spacing along the transect. Velocity component data are rotated to a bed-perpendicular reference frame (2-D calculation in the x-z plane). Each velocity data point is averaged over a 15 second interval and was collected in a 9 mm tall by 6 mm wide sampling volume with the base located within 2 mm above the deposit bed.

Note: 1 node unit = 2 millimeters

## 4.9.2 Series 2 – Deposit Cross Section and Dipline Velocity ($x_{avg}$) Distributions (Configuration 2)

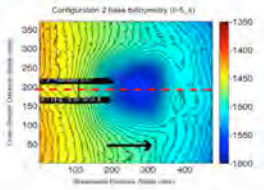

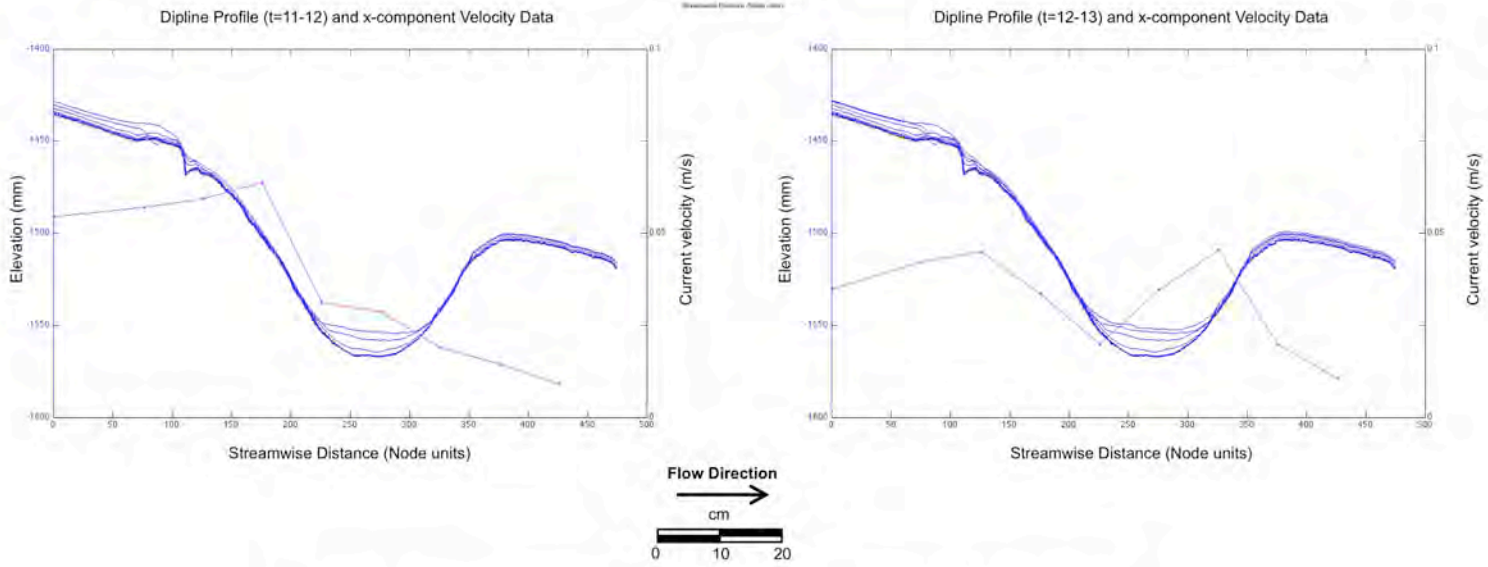


**Time-averaged near-bed x-component turbidity current velocity data and deposit geometry along the center dipline profile.**
Each plot above shows successive deposits from Configuration 2 along the center dipline section, the position of which is illustrated by the dashed red line on the t=0 bathymetry inset map above. Superimposed on the lower plots are the time averaged x-component current velocity, *u*, collected at equal spacing along the transect. Velocity component data are rotated to a bed-perpendicular reference frame (2-D calculation in the x-z plane). Each velocity data point is averaged over a 15 second interval and was collected in a 9 mm tall by 6 mm wide sampling volume with the base located within 2 mm above the deposit bed.

Note: 1 node unit = 2 millimeters

## 4.9.3 Series 2 – Deposit Cross Section and Dipline Velocity ($x_{avg}$) Distributions (Configuration 3)

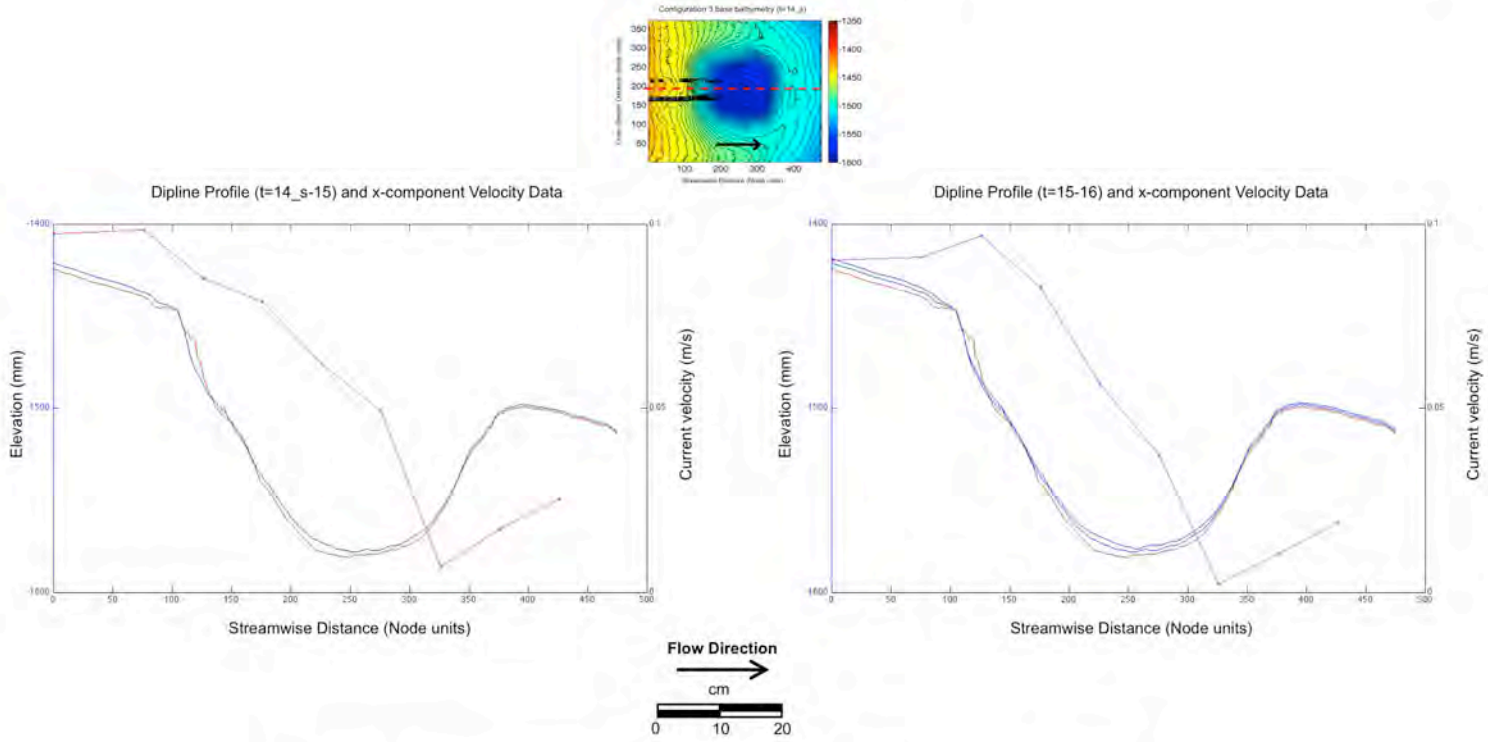


**Time-averaged near-bed x-component turbidity current velocity data and deposit geometry along the center dipline profile.**
Each plot above shows successive deposits from Configuration 3 along the center dipline section, the position of which is illustrated by the dashed red line on the t=0 bathymetry inset map above. Superimposed on the lower plots are the time averaged x-component current velocity, *u*, collected at equal spacing along the transect. Velocity component data are rotated to a bed-perpendicular reference frame (2-D calculation in the x-z plane). Each velocity data point is averaged over a 15 second interval and was collected in a 9 mm tall by 6 mm wide sampling volume with the base located within 2 mm above the deposit bed.

Note: 1 node unit = 2 millimeters

## 4.9.3 Series 2 – Deposit Cross Section and Dipline Velocity ($x_{avg}$) Distributions (Configuration 3)

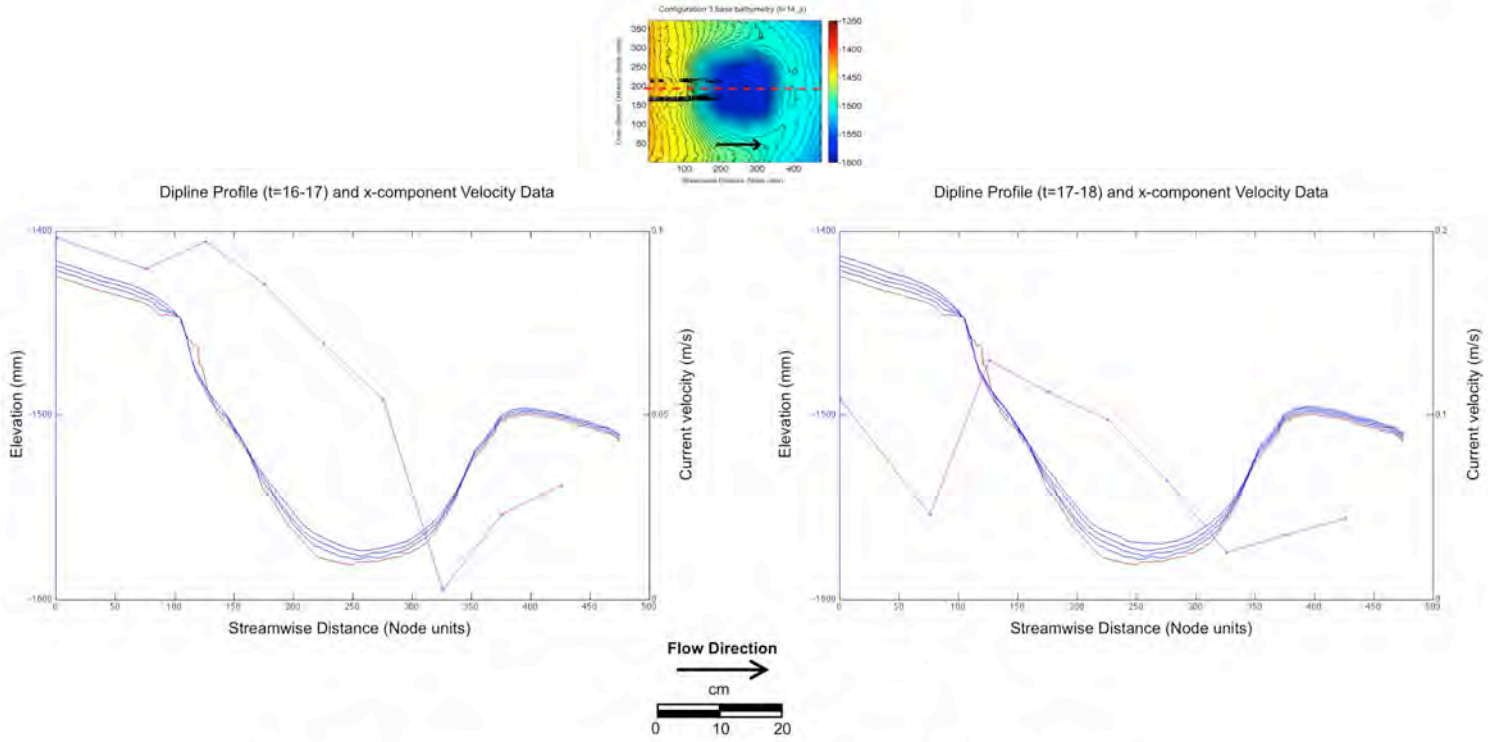


**Time-averaged near-bed x-component turbidity current velocity data and deposit geometry along the center dipline profile.**
Each plot above shows successive deposits from Configuration 3 along the center dipline section, the position of which is illustrated by the dashed red line on the t=0 bathymetry inset map above. Superimposed on the lower plots are the time averaged x-component current velocity, *u*, collected at equal spacing along the transect. Velocity component data are rotated to a bed-perpendicular reference frame (2-D calculation in the x-z plane). Each velocity data point is averaged over a 15 second interval and was collected in a 9 mm tall by 6 mm wide sampling volume with the base located within 2 mm above the deposit bed.

Note: 1 node unit = 2 millimeters

## 4.9.3 Series 2 – Deposit Cross Section and Dipline Velocity ($x_{avg}$) Distributions (Configuration 3)

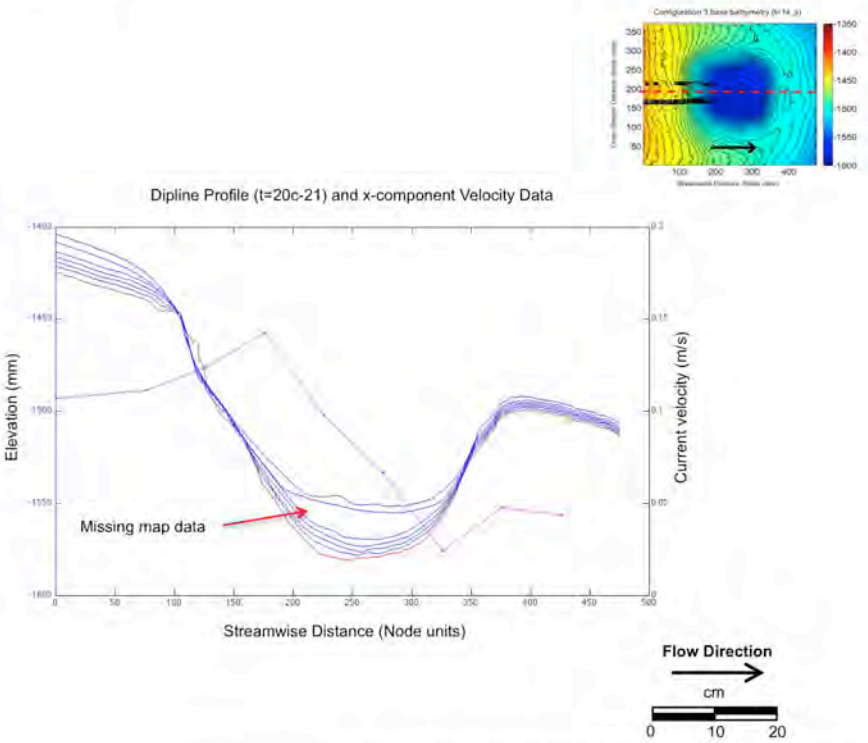


**Time-averaged near-bed x-component turbidity current velocity data and deposit geometry along the center dipline profile.**
Each plot above shows successive deposits from Configuration 3 along the center dipline section, the position of which is illustrated by the dashed red line on the t=0 bathymetry inset map above. Superimposed on the lower plots are the time averaged x-component current velocity, *u*, collected at equal spacing along the transect. Velocity component data are rotated to a bed-perpendicular reference frame (2-D calculation in the x-z plane). Each velocity data point is averaged over a 15 second interval and was collected in a 9 mm tall by 6 mm wide sampling volume with the base located within 2 mm above the deposit bed. Note: maps for flow 19 (continuous) and 20a, 20b (surges) are not included due to a malfunction of the mapping system. An unusually thick deposit was produced during these flows. We speculate that this thick deposit is the result of successive surge flows (20a-20c) interacting with a residual dense fluid layer formed during flow 19. Also note the ponded character of this deposit relative to the draped deposits that dominate the section. X-axis is displayed in node units, and y-axis is displayed in millimeters.

Note: 1 node unit = 2 millimeters

## 4.9.4 Series 2 – Deposit Thickness Maps and Time-Averaged Velocity Distributions (Configuration 1)

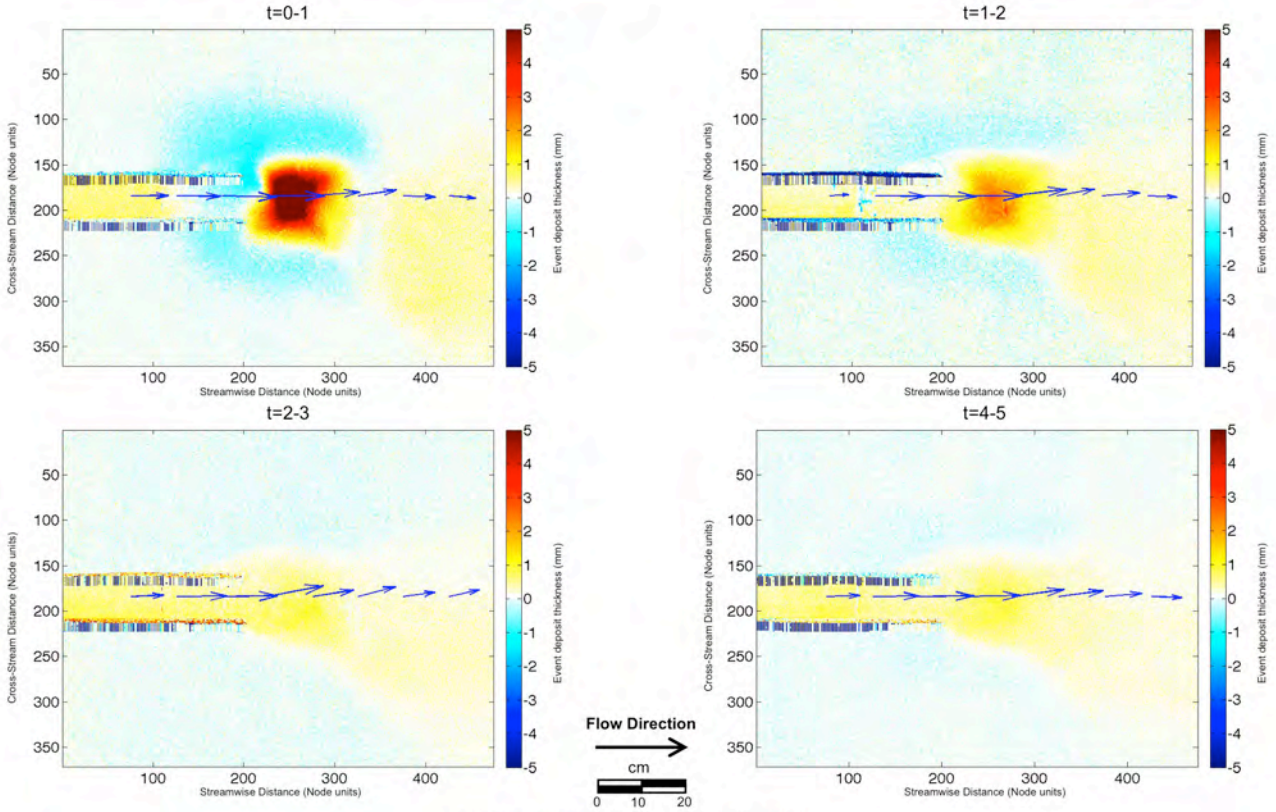


**Deposit thickness maps and turbidity current vector velocity.**
Time-averaged (over 15 seconds) flow velocity vectors superimposed on deposit thickness. The velocity vector data were collected at 10 cm intervals using a 3-D Acoustic Doppler Velocimeter (ADV). ADV data was collected in a 9 mm tall by 6 mm wide sampling volume with the base located within 2 mm above the deposit bed. The sampling frequency was 200 Hz.

Note: 1 node unit = 2 millimeters

## 4.9.5 Series 2 – Deposit Thickness Maps and Time-Averaged Velocity Distributions (Configuration 2)

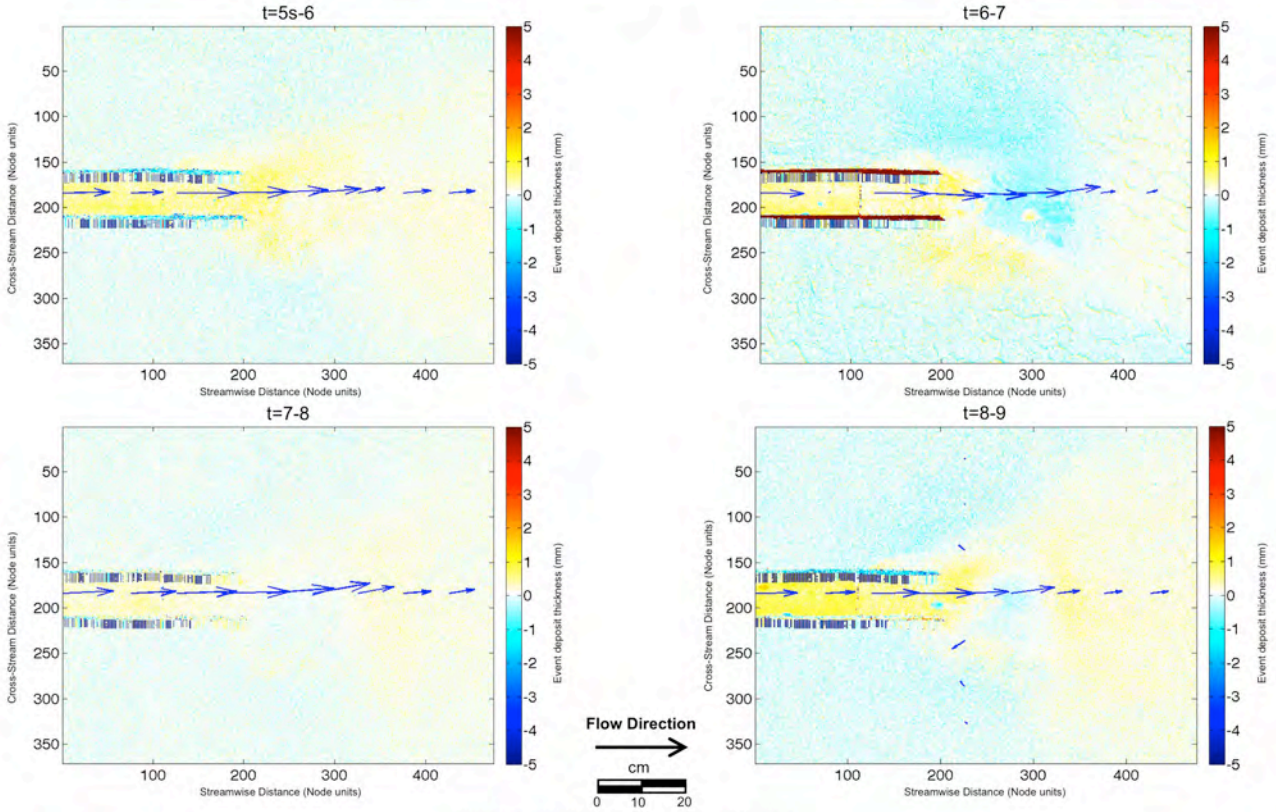


**Deposit thickness maps and turbidity current vector velocity.**
Time-averaged (over 15 seconds) flow velocity vectors superimposed on deposit thickness. The velocity vector data were collected at 10 cm intervals using a 3-D Acoustic Doppler Velocimeter (ADV). ADV data was collected in a 9 mm tall by 6 mm wide sampling volume with the base located within 2 mm above the deposit bed. The sampling frequency was 200 Hz.

Note: 1 node unit = 2 millimeters

## 4.9.5 Series 2 – Deposit Thickness Maps and Time-Averaged Velocity Distributions (Configuration 2)

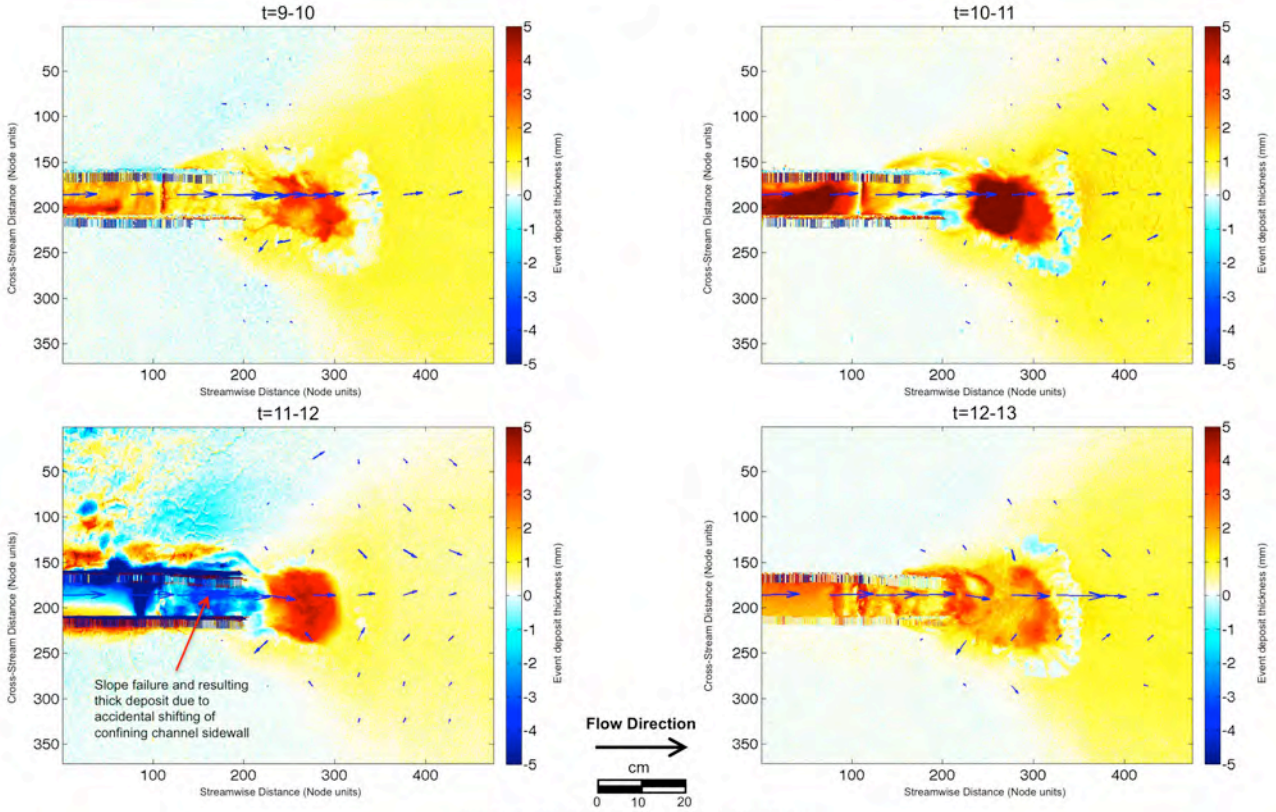


**Deposit thickness maps and turbidity current vector velocity.**
Time-averaged (over 15 seconds) flow velocity vectors superimposed on deposit thickness. The velocity vector data were collected at 10 cm intervals using a 3-D Acoustic Doppler Velocimeter (ADV). ADV data was collected in a 9 mm tall by 6 mm wide sampling volume with the base located within 2 mm above the deposit bed. The sampling frequency was 200 Hz.

Note: 1 node unit = 2 millimeters

## 4.9.6 Series 2 – Deposit Thickness Maps and Time-Averaged Velocity Distributions (Configuration 3)

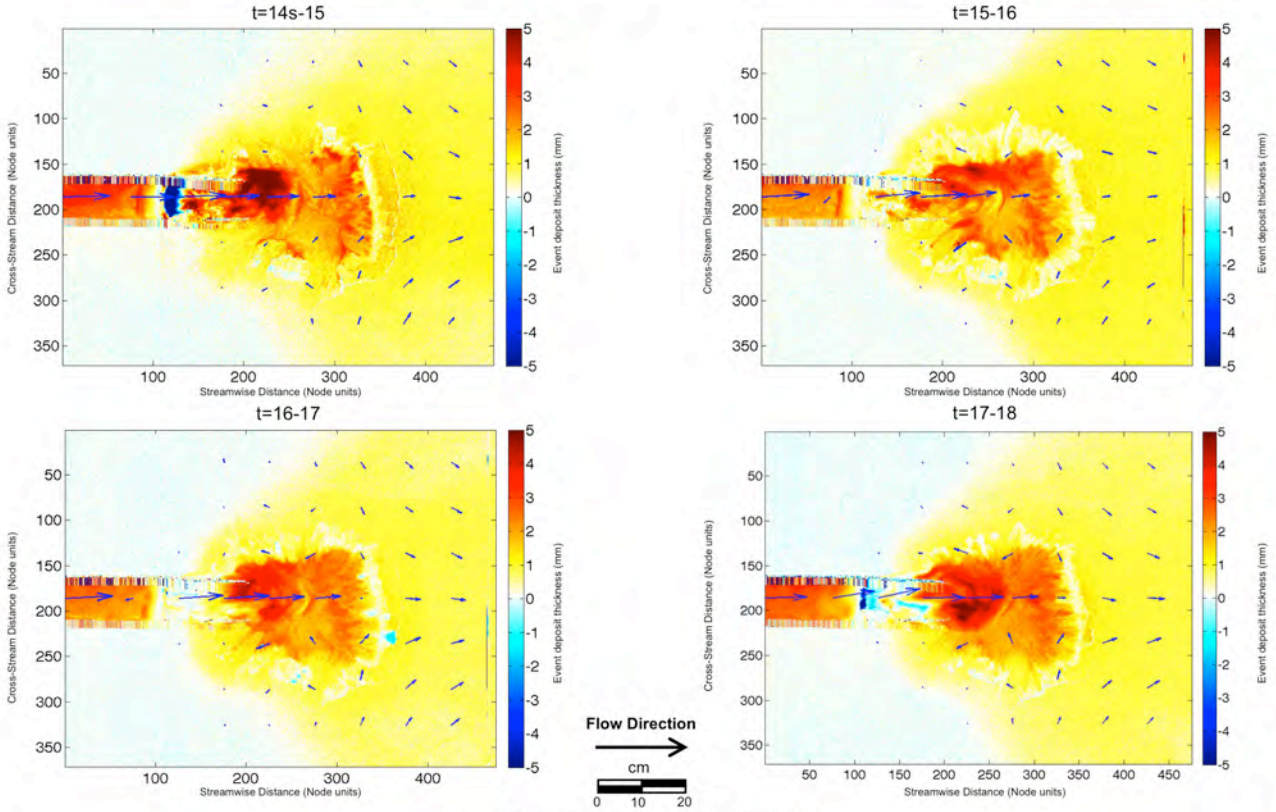


**Deposit thickness maps and turbidity current vector velocity.**
Time-averaged (over 15 seconds) flow velocity vectors superimposed on deposit thickness. The velocity vector data were collected at 10 cm intervals using a 3-D Acoustic Doppler Velocimeter (ADV). ADV data was collected in a 9 mm tall by 6 mm wide sampling volume with the base located within 2 mm above the deposit bed. The sampling frequency was 200 Hz.

Note: 1 node unit = 2 millimeters

## 4.9.7 Series 2 – Deposit Thickness, Velocity and Bathymetry Relationships (Configuration 1)

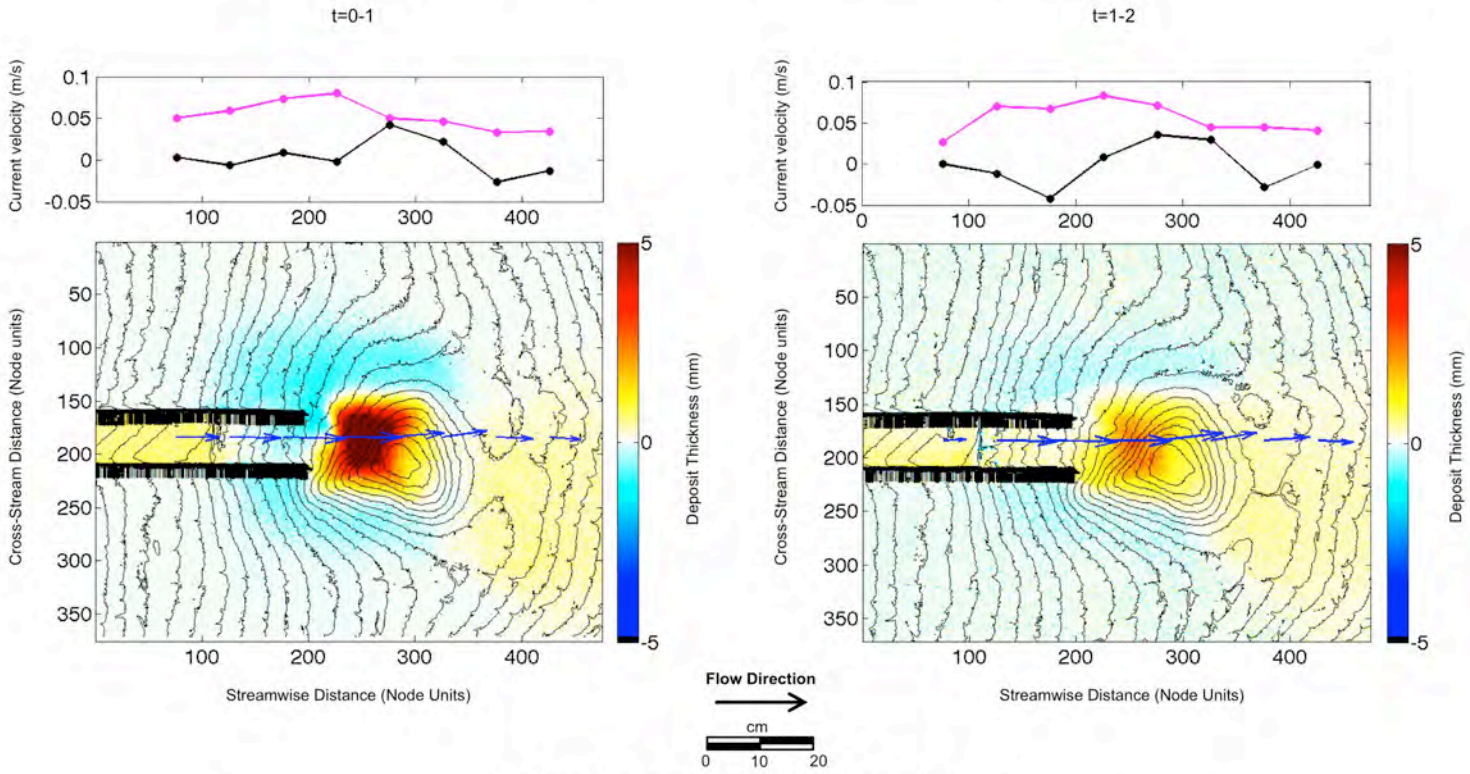


**Deposit thickness maps, bathymetry and turbidity current vector velocity.**

For each event interval, the lower figures illustrate the relationship among the pre-event basin bathymetry, the deposit thickness, and the time-averaged vector velocity. For the upper plots, the x- (pink) and z- (black) components of flow velocity (rotated to a bed-perpendicular reference frame) are plotted from data collected along the basin center dipline section (in the middle of and parallel to confining channel long axis). The velocity vector data were collected using a 3-D Acoustic Doppler Velocimeter (ADV). ADV data was collected in a 9 mm tall by 6 mm wide sampling volume with the base located within 2 mm above the deposit bed. The sampling frequency was 200 Hz.

Note: 1 node unit = 2 millimeters

## 4.9.7 Series 2 – Deposit Thickness, Velocity and Bathymetry Relationships (Configuration 1)

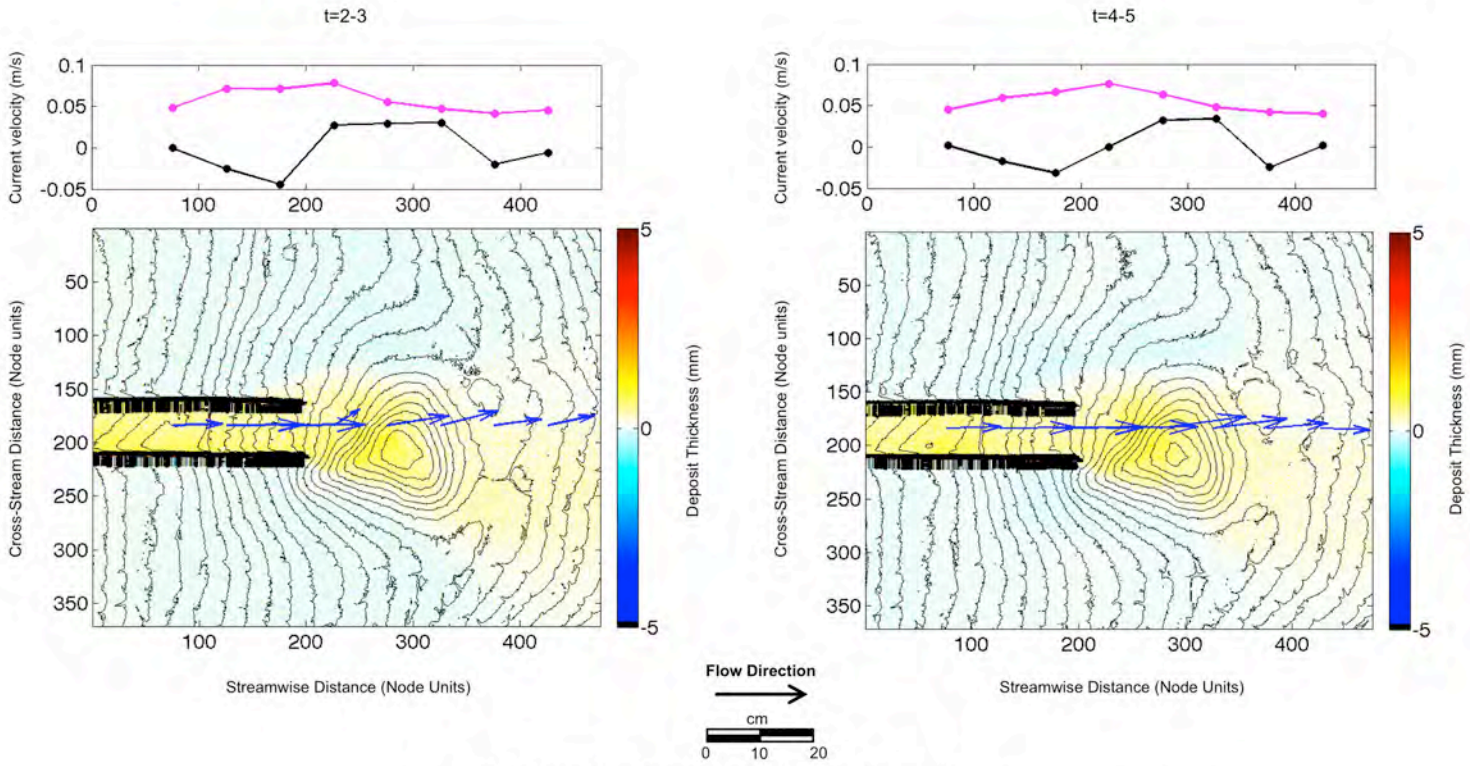


**Deposit thickness maps, bathymetry and turbidity current vector velocity.**

For each event interval, the lower figures illustrate the relationship among the pre-event basin bathymetry, the deposit thickness, and the time-averaged vector velocity. For the upper plots, the x- (pink) and z- (black) components of flow velocity (rotated to a bed-perpendicular reference frame) are plotted from data collected along the basin center dipline section (in the middle of and parallel to confining channel long axis). The velocity vector data were collected using a 3-D Acoustic Doppler Velocimeter (ADV). ADV data was collected in a 9 mm tall by 6 mm wide sampling volume with the base located within 2 mm above the deposit bed. The sampling frequency was 200 Hz.

Note: 1 node unit = 2 millimeters

## 4.9.8 Series 2 – Deposit Thickness, Velocity and Bathymetry Relationships (Configuration 2)

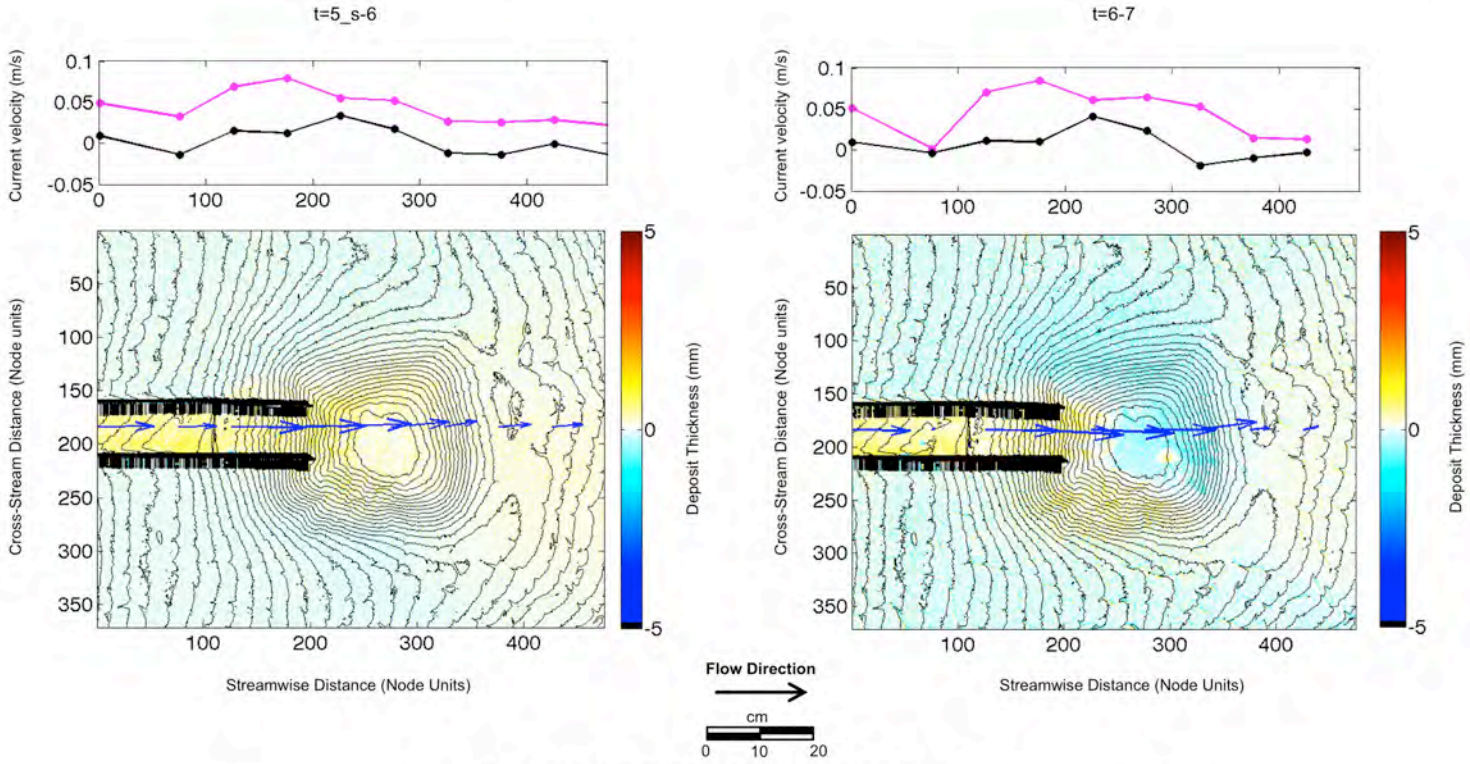


**Deposit thickness maps, bathymetry and turbidity current vector velocity.**

For each event interval, the lower figures illustrate the relationship among the pre-event basin bathymetry, the deposit thickness, and the time-averaged vector velocity. For the upper plots, the x- (pink) and z- (black) components of flow velocity (rotated to a bed-perpendicular reference frame) are plotted from data collected along the basin center dipline section (in the middle of and parallel to confining channel long axis). The velocity vector data were collected using a 3-D Acoustic Doppler Velocimeter (ADV). ADV data was collected in a 9 mm tall by 6 mm wide sampling volume with the base located within 2 mm above the deposit bed. The sampling frequency was 200 Hz.

Note: 1 node unit = 2 millimeters

## 4.9.8 Series 2 – Deposit Thickness, Velocity and Bathymetry Relationships (Configuration 2)

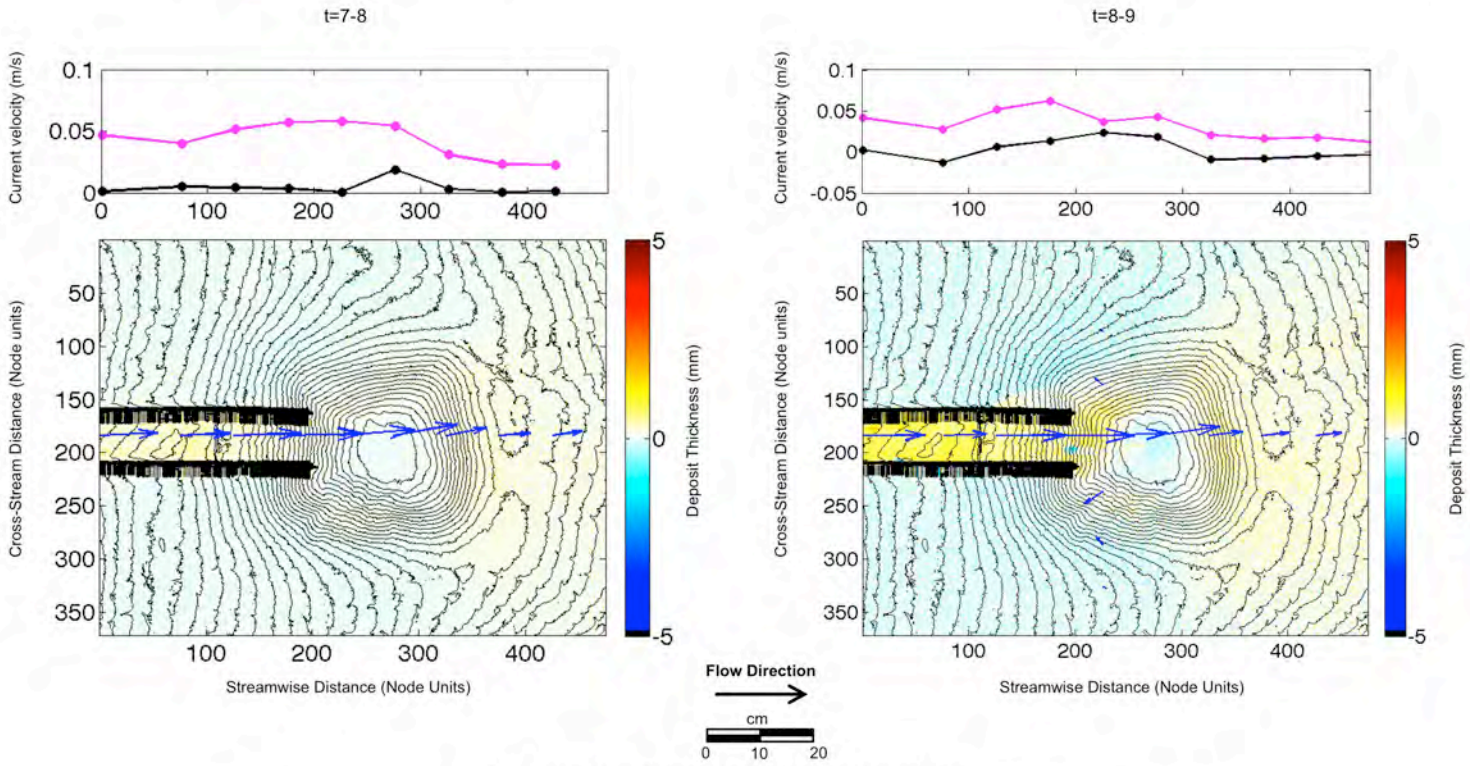


**Deposit thickness maps, bathymetry and turbidity current vector velocity.**

For each event interval, the lower figures illustrate the relationship among the pre-event basin bathymetry, the deposit thickness, and the time-averaged vector velocity. For the upper plots, the x- (pink) and z- (black) components of flow velocity (rotated to a bed-perpendicular reference frame) are plotted from data collected along the basin center dipline section (in the middle of and parallel to confining channel long axis). The velocity vector data were collected using a 3-D Acoustic Doppler Velocimeter (ADV). ADV data was collected in a 9 mm tall by 6 mm wide sampling volume with the base located within 2 mm above the deposit bed. The sampling frequency was 200 Hz.

Note: 1 node unit = 2 millimeters

## 4.9.8 Series 2 – Deposit Thickness, Velocity and Bathymetry Relationships (Configuration 2)

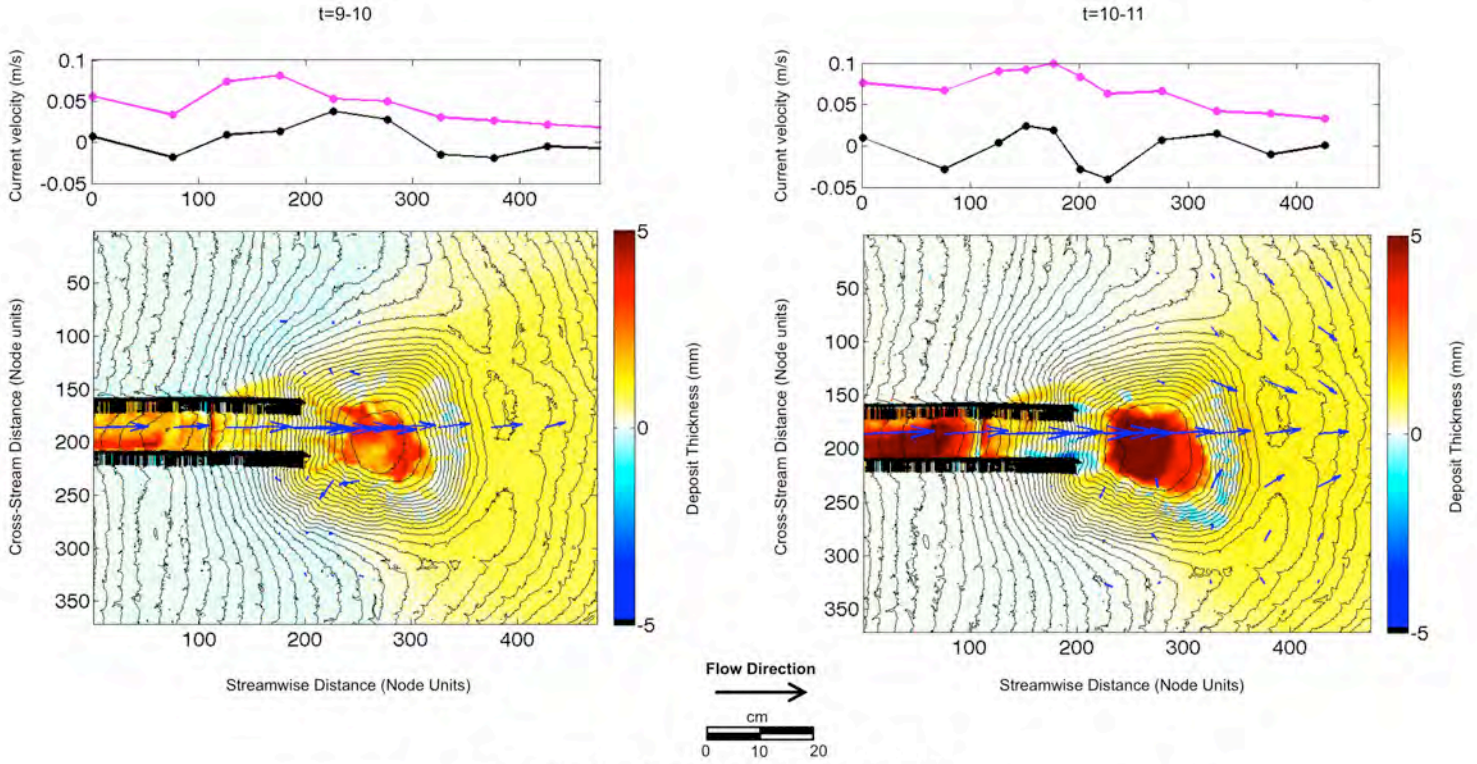


**Deposit thickness maps, bathymetry and turbidity current vector velocity.**

For each event interval, the lower figures illustrate the relationship among the pre-event basin bathymetry, the deposit thickness, and the time-averaged vector velocity. For the upper plots, the x- (pink) and z- (black) components of flow velocity (rotated to a bed-perpendicular reference frame) are plotted from data collected along the basin center dipline section (in the middle of and parallel to confining channel long axis). The velocity vector data were collected using a 3-D Acoustic Doppler Velocimeter (ADV). ADV data was collected in a 9 mm tall by 6 mm wide sampling volume with the base located within 2 mm above the deposit bed. The sampling frequency was 200 Hz.

Note: 1 node unit = 2 millimeters

## 4.9.8 Series 2 – Deposit Thickness, Velocity and Bathymetry Relationships (Configuration 2)

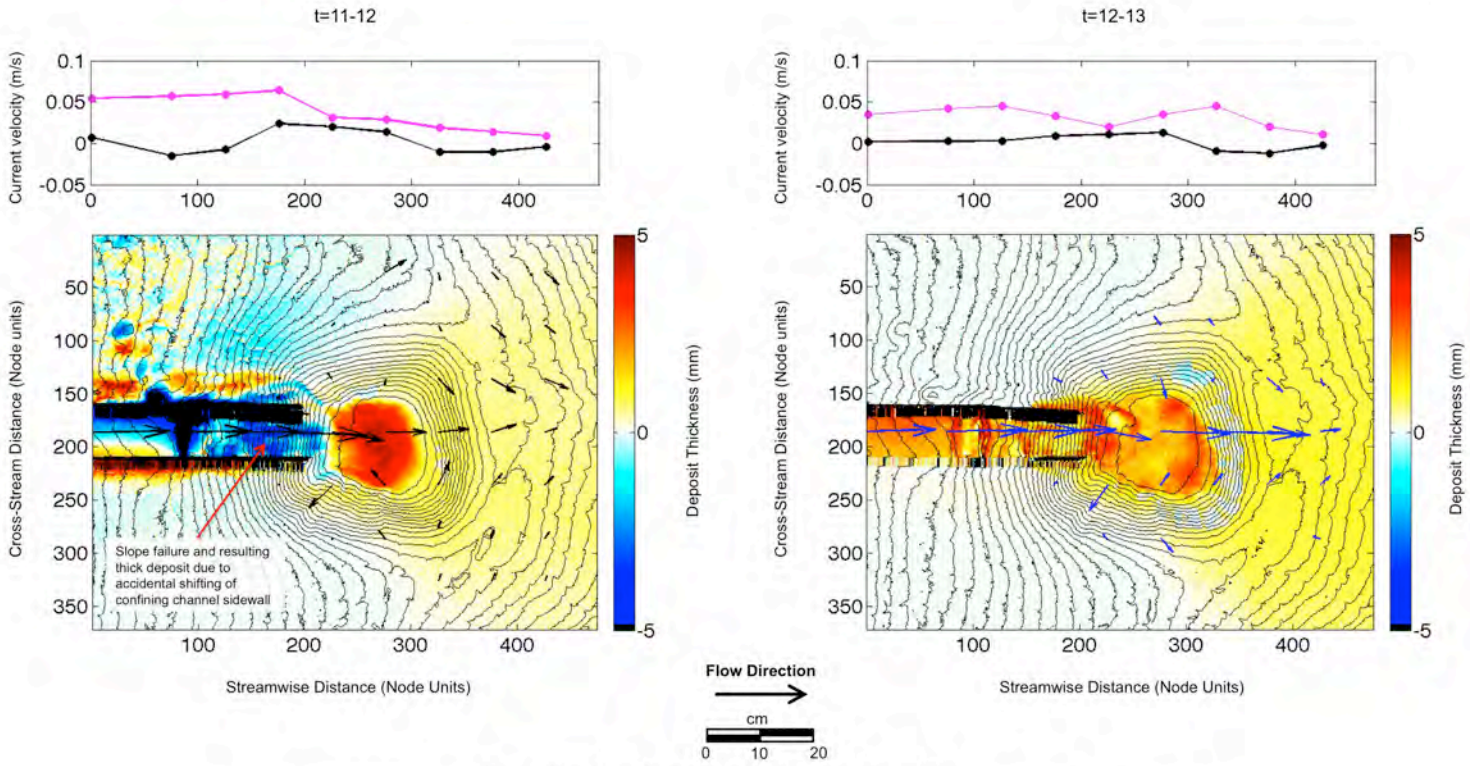


**Deposit thickness maps, bathymetry and turbidity current vector velocity.**

For each event interval, the lower figures illustrate the relationship among the pre-event basin bathymetry, the deposit thickness, and the time-averaged vector velocity. For the upper plots, the x- (pink) and z- (black) components of flow velocity (rotated to a bed-perpendicular reference frame) are plotted from data collected along the basin center dipline section (in the middle of and parallel to confining channel long axis). The velocity vector data were collected using a 3-D Acoustic Doppler Velocimeter (ADV). ADV data was collected in a 9 mm tall by 6 mm wide sampling volume with the base located within 2 mm above the deposit bed. The sampling frequency was 200 Hz.

Note: 1 node unit = 2 millimeters

## 4.9.9 Series 2 – Deposit Thickness, Velocity and Bathymetry Relationships (Configuration 3)

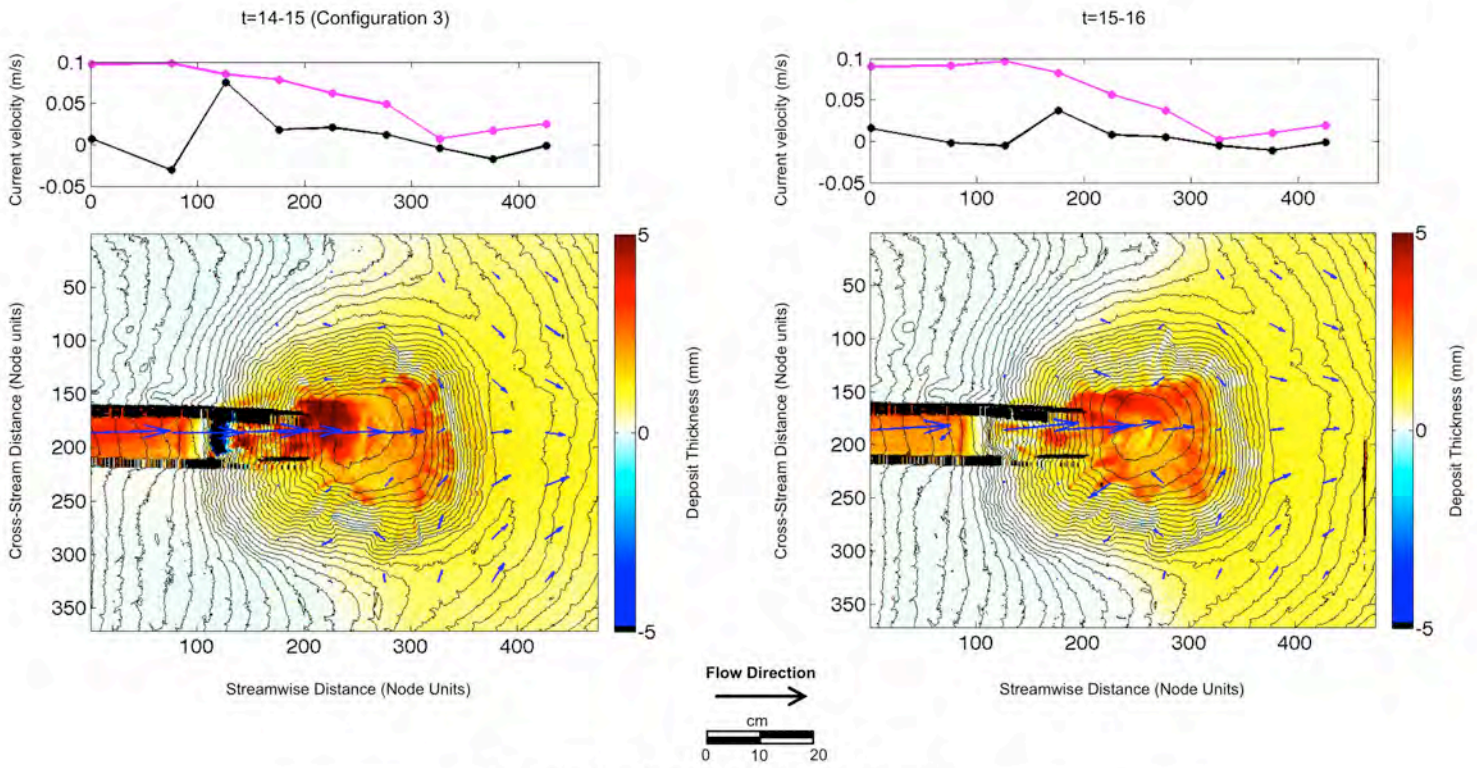


**Deposit thickness maps, bathymetry and turbidity current vector velocity.**
For each event interval, the lower figures illustrate the relationship among the pre-event basin bathymetry, the deposit thickness, and the time-averaged vector velocity. For the upper plots, the x- (pink) and z- (black) components of flow velocity (rotated to a bed-perpendicular reference frame) are plotted from data collected along the basin center dipline section (in the middle of and parallel to confining channel long axis). The velocity vector data were collected using a 3-D Acoustic Doppler Velocimeter (ADV). ADV data was collected in a 9 mm tall by 6 mm wide sampling volume with the base located within 2 mm above the deposit bed. The sampling frequency was 200 Hz.

Note: 1 node unit = 2 millimeters

## 4.9.9 Series 2 – Deposit Thickness, Velocity and Bathymetry Relationships (Configuration 3)

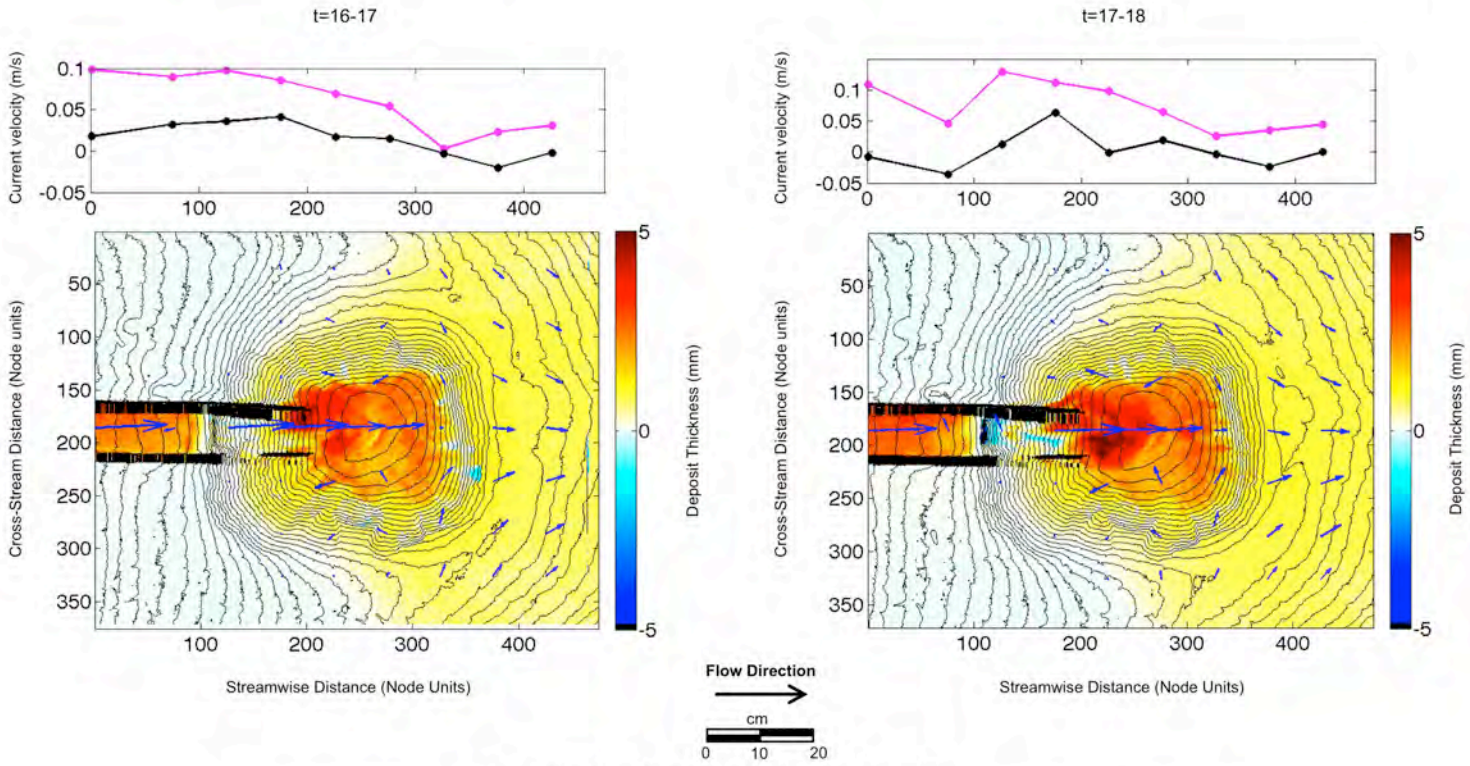


**Deposit thickness maps, bathymetry and turbidity current vector velocity.**

For each event interval, the lower figures illustrate the relationship among the pre-event basin bathymetry, the deposit thickness, and the time-averaged vector velocity. For the upper plots, the x- (pink) and z- (black) components of flow velocity (rotated to a bed-perpendicular reference frame) are plotted from data collected along the basin center dipline section (in the middle of and parallel to confining channel long axis). The velocity vector data were collected using a 3-D Acoustic Doppler Velocimeter (ADV). ADV data was collected in a 9 mm tall by 6 mm wide sampling volume with the base located within 2 mm above the deposit bed. The sampling frequency was 200 Hz.

Note: 1 node unit = 2 millimeters

## 4.9.9 Series 2 – Deposit Thickness, Velocity and Bathymetry Relationships (Configuration 3)

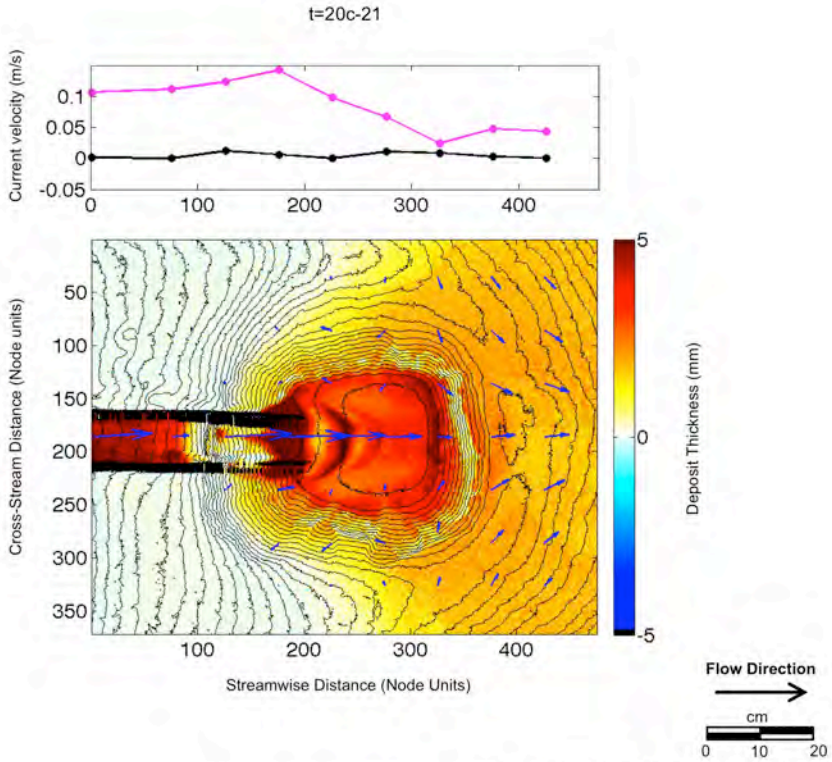


**Deposit thickness maps, bathymetry and turbidity current vector velocity.**
For each event interval, the lower figures illustrate the relationship among the pre-event basin bathymetry, the deposit thickness, and the time-averaged vector velocity. For the upper plots, the x- (pink) and z- (black) components of flow velocity (rotated to a bed-perpendicular reference frame) are plotted from data collected along the basin center dipline section (in the middle of and parallel to confining channel long axis). The velocity vector data were collected using a 3-D Acoustic Doppler Velocimeter (ADV). ADV data was collected in a 9 mm tall by 6 mm wide sampling volume with the base located within 2 mm above the deposit bed. The sampling frequency was 200 Hz.

Note: 1 node unit = 2 millimeters

## 4.9.10 Series 2 – Characteristic Streamwise Velocity Profile and Basin Topography (Configuration 3)

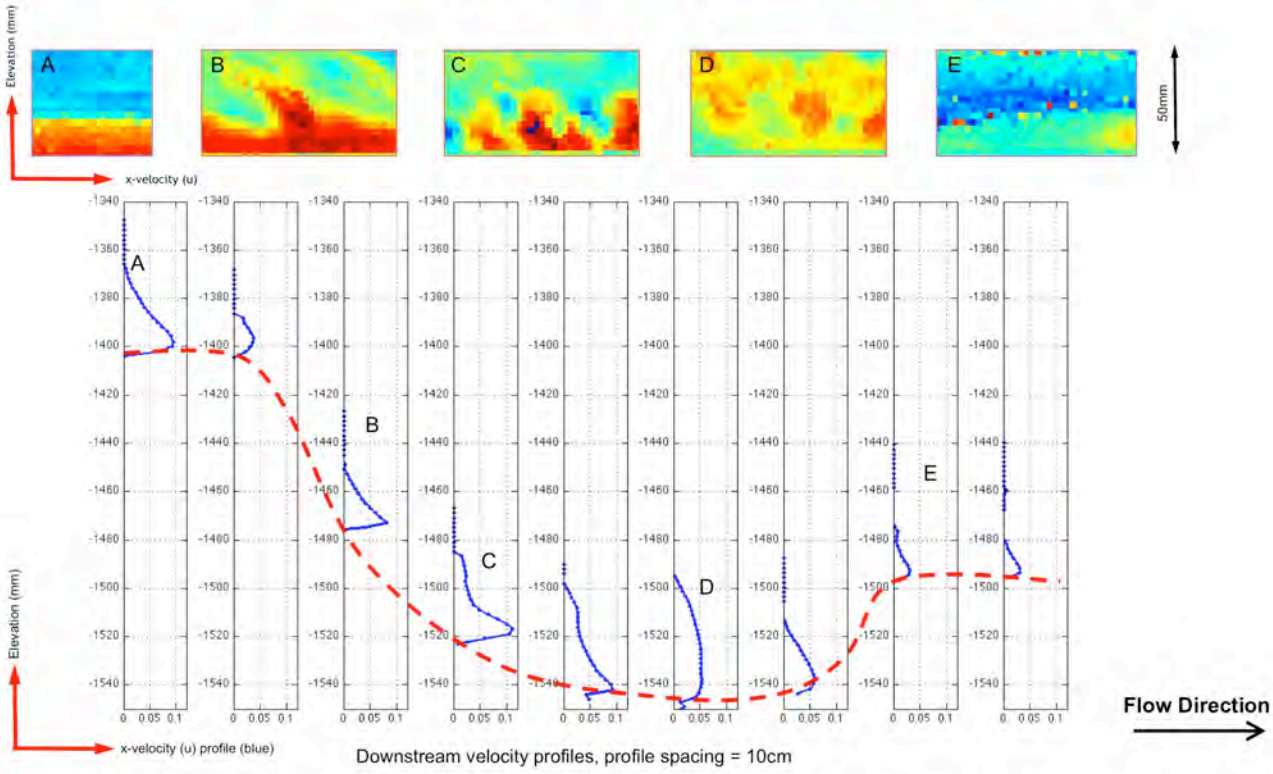


**The cross-section above shows the velocity profile distribution at specific points along the center dipline profile of Configuration 3.**
The character of the x-component velocity profiles (rotated to a bed-perpendicular reference frame) change from proximal to distal (e.g. the current thickness and the elevation of the high velocity core). The sub-images (A-E) above show the x-component profile time series. Mixing (stability) within the turbidity current varies from proximal to distal. The velocity data were collected using a 3-D Profiling Acoustic Doppler Velocimeter (PADV). Profiles are 5.6 cm tall and are divided into 28 bins that are 2 mm each. The base of the profile was located within 2 mm above the deposit bed.

## 4.9.11 Series 2 – Typical Turbidity Current Streamwise Velocity Profile (Configuration 3)

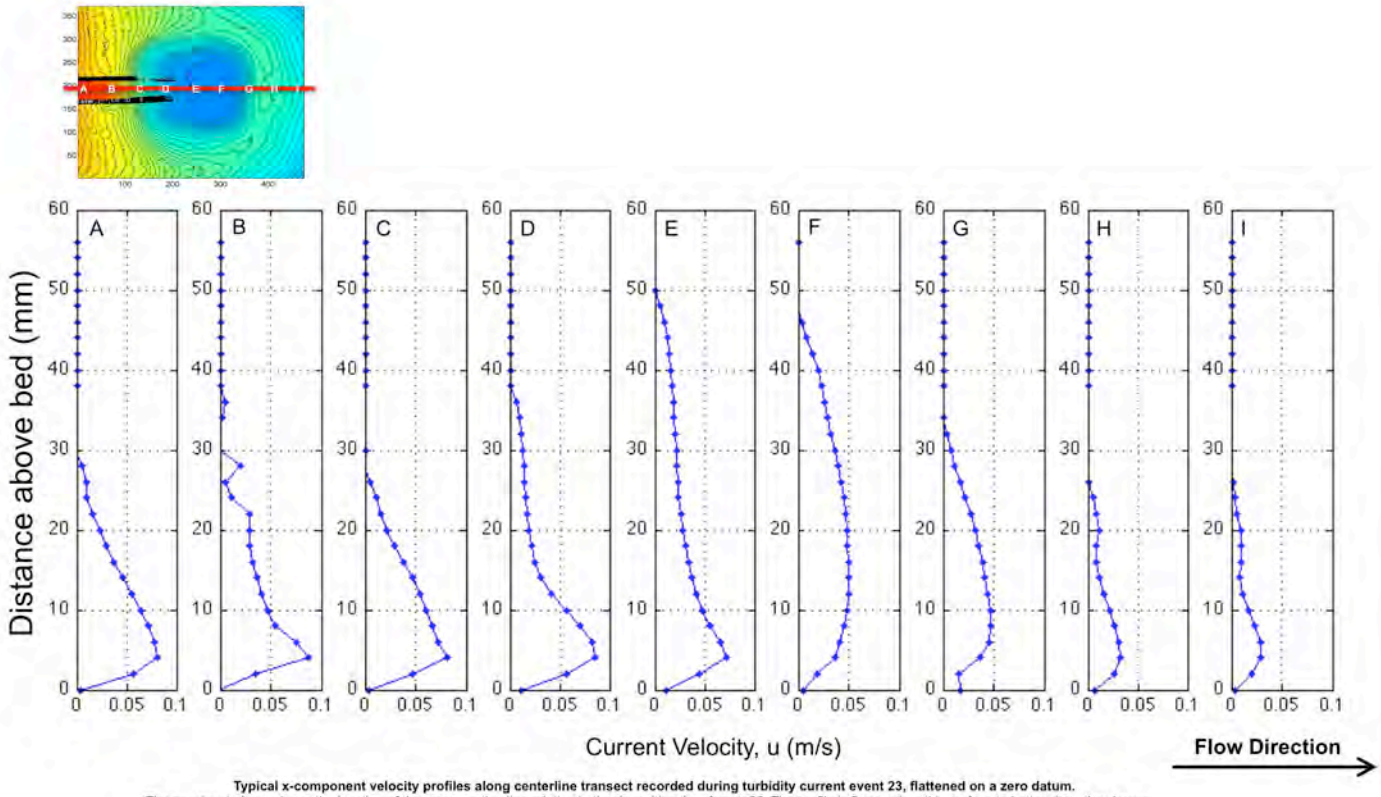


**Typical x-component velocity profiles along centerline transect recorded during turbidity current event 23, flattened on a zero datum.**
The map inset above shows the location of the cross-section line relative to the depositional surface t=22. The profile is flattened on this surface to better show the change in current properties along the center line transect. Each profile sub-image (A-I) is referenced to the inset map (upper left figure) . The character of the x-component velocity profiles (rotated to a bed-perpendicular reference frame) change from proximal to distal (e.g. the current thickness and the elevation of the high velocity core). The velocity data were collected using a 3-D Profiling Acoustic Doppler Velocimeter (PADV). Profiles are 5.6 cm tall and are divided into 28 bins that are 2 mm each. The base of the profile was located within 2 mm above the deposit bed.

# 4.10 Series 2 – Final Deposit Mosaics and Cross Sections


**Axial dipline section of complete basin deposit (A-A').**
Deposit sections show the preserved stratigraphy within the basin and the internal architecture/ geometries. Note: An unusually thick deposit was produced during flow 19 (continuous) and 20a, 20b (surges). We speculate that this thick deposit is the result of successive surge flows (20a-20c) interacting with a residual dense fluid layer formed during flow 19. Also note the ponded character and lack of structure of this deposit relative to the draped deposits that dominate the section.

# 4.10 Series 2 – Final Deposit Mosaics and Cross Sections


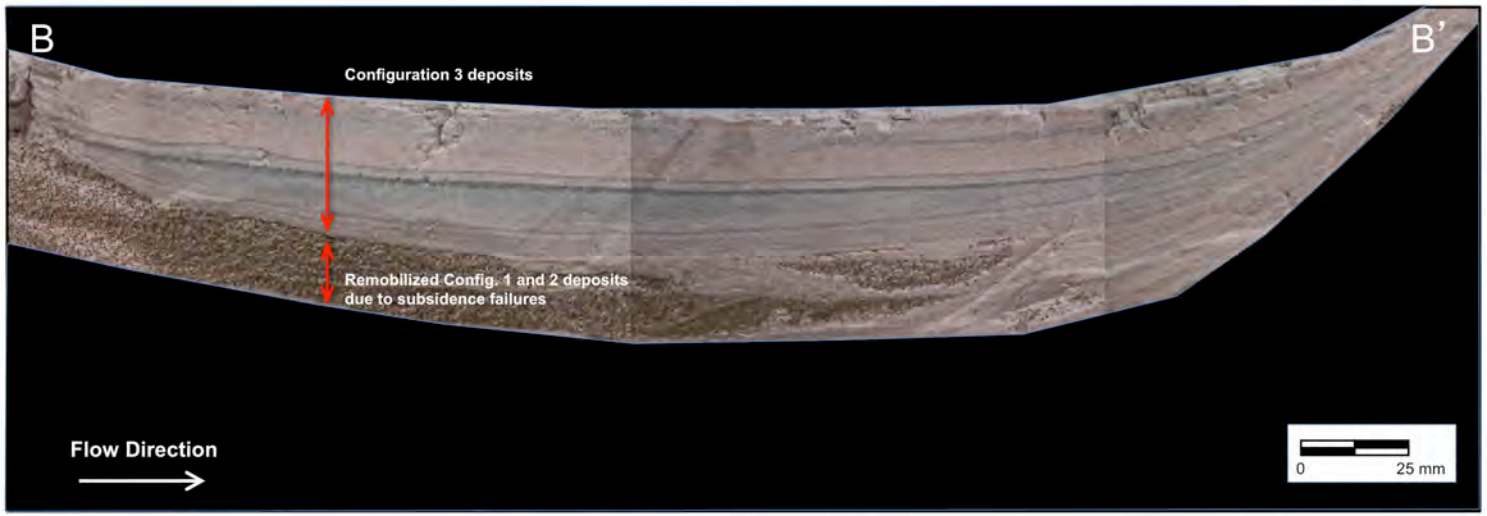


**Dipline section of complete basin deposit (B-B').**
Deposit sections show the preserved stratigraphy within the basin and the internal architecture/ geometries. Note: An unusually thick deposit was produced during flow 19 (continuous) and 20a, 20b (surges). We speculate that this thick deposit is the result of successive surge flows (20a-20c) interacting with a residual dense fluid layer formed during flow 19. Also note the ponded character and lack of structure of this deposit relative to the draped deposits that dominate the section.

# 4.10 Series 2 – Final Deposit Mosaics and Cross Sections

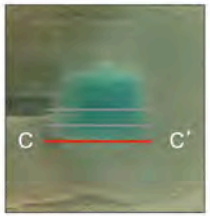



**Dipline section of complete basin deposit (C-C').**
Deposit sections show the preserved stratigraphy within the basin and the internal architecture/ geometries. Note: An unusually thick deposit was produced during flow 19 (continuous) and 20a, 20b (surges). We speculate that this thick deposit is the result of successive surge flows (20a-20c) interacting with a residual dense fluid layer formed during flow 19. Also note the ponded character and lack of structure of this deposit relative to the draped deposits that dominate the section.

# 4.11 Series 2 – Cold Core Sample Locations of Mini-Basin Deposit

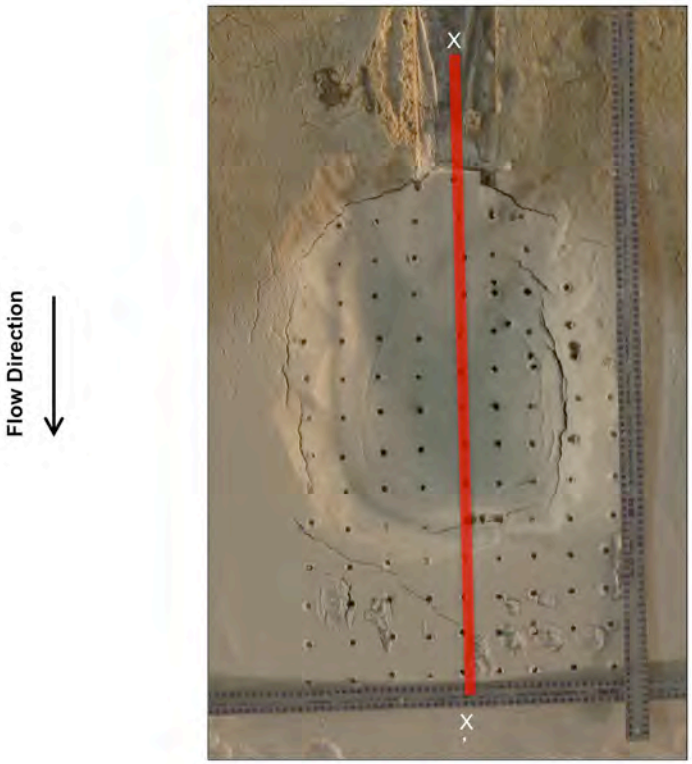


**Cold-core sample locations in plan view.**

The overhead photography shows the plan view of the final mini-basin deposit which was sampled in a 5 cm x 5 cm grid using the cold core technique. Following the experiment, the tank was drained over a two-week period and the deposit was allowed to dry for an additional week. A thin metal rod was submerged in liquid nitrogen, and used to sample the deposit. Each core sample was cut into thirds. Samples were then processed using a Laser Particle Size Analyzer (LPSA) to determine grain size distributions within the deposit. Refer to transect X-X' in Section 4.12.2 Series 2 – Bulk Grain Size Distribution, Center Dip Section and Current Velocity (Configuration 3).

## 4.12.1 Series 2 – Bulk Deposit Grain Size Maps (Configuration 3)

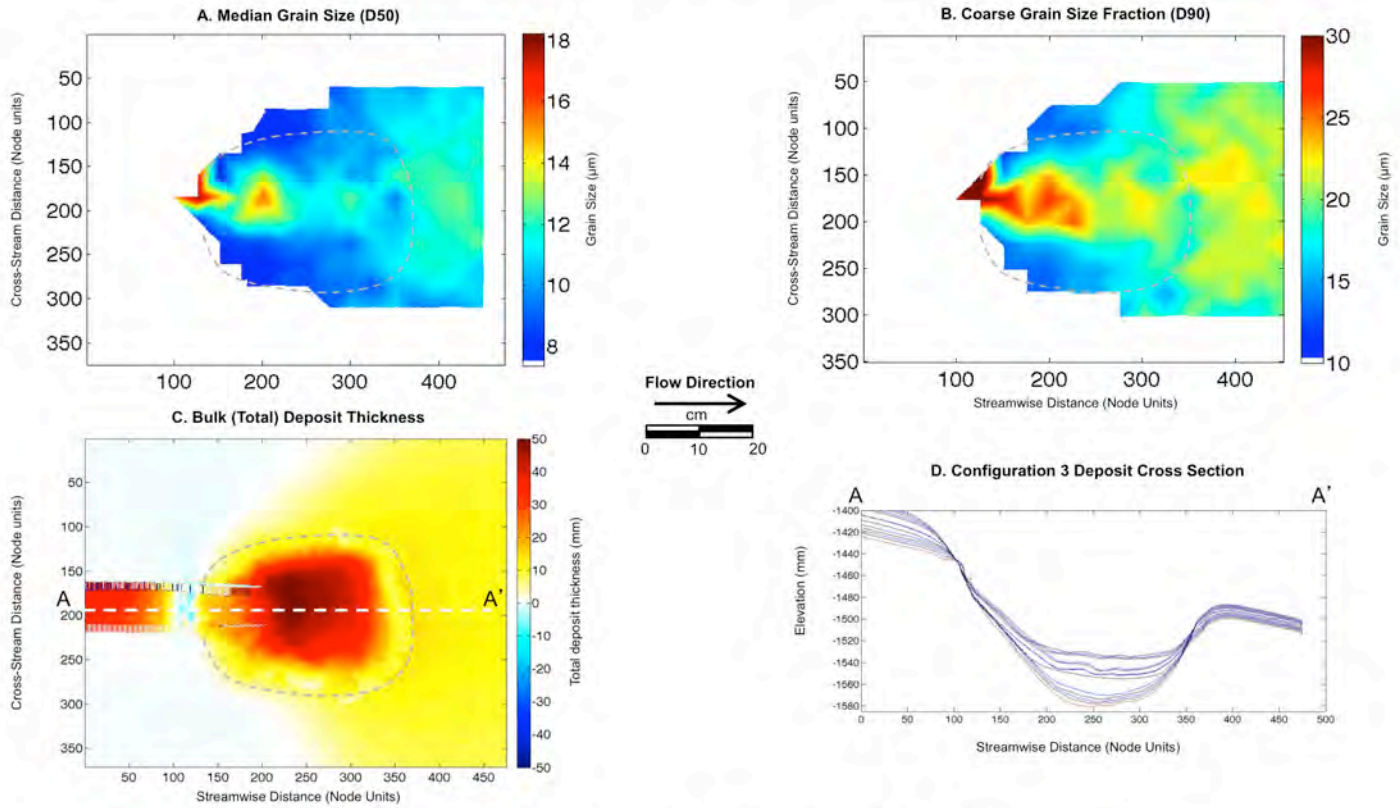


**Bulk deposit grain size maps for deposits from turbidity current events in Configuration 3.**

Figure A shows a map view of interpolated median grain size data collected from 137 core locations (refer to Section 4.11, Series 2 – Cold Core Sample Locations of Mini-Basin Deposit) for the Configuration 3 deposit. Figure B shows a map view of interpolated D90 grain size data for the Configuration 3 deposit. For reference purposes, a plan view of the bulk (total) deposit thickness is shown in Figure C and a cross section (A-A') of the Configuration 3 deposit is shown in Figure D.

Note: 1 node unit = 2 millimeters

## 4.12.2 Series 2 – Bulk Grain Size Distribution, Center Dip Section and Current Velocity (Configuration 3)

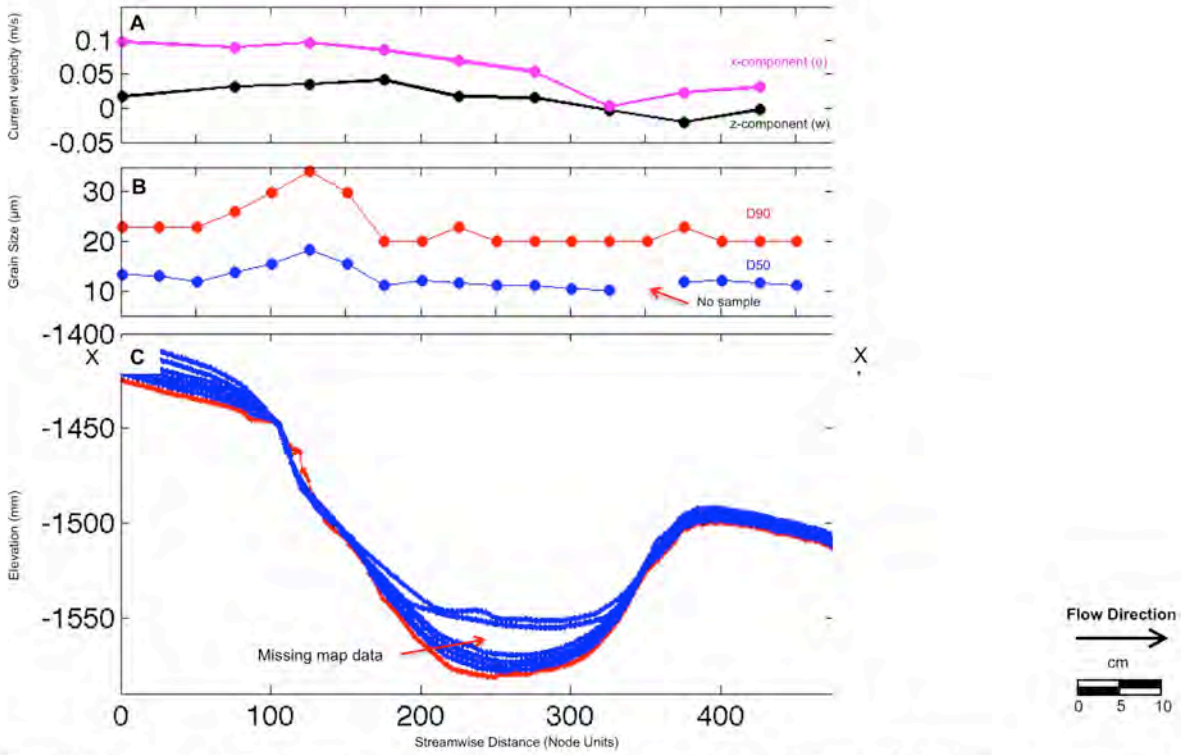


**Center dip deposit section, grain size and x- (pink) and z- (black) velocity components (rotated to a bed-perpendicular reference frame) from Configuration 3.** In Figure B, the D50 and D90 grain size data are plotted along the dip line. Figure C shows the centerline cross section for events 15-27. Refer to overhead photo in Section 4.11 Series 2 – Cold Core Sample Locations of Mini-Basin Deposit.

Note: 1 node unit = 2 millimeters

## APPENDIX B: EXPERIMENTAL RESULTS AND ANALYSIS TABLES

Series 1 – Sub-basin 1 Sediment Volume Data

| | Basin and Sediment Volume Data | | | | | | |
|---|---|---|---|---|---|---|---|
| Event ID | Initial vol. (cm3) | Final volume (cm3) | Trapped sed. vol. (cm3) | Initial vol./ final vol. | Final vol./ initial vol. | Trapped sed. vol./ initial vol. | Initial vol./ trapped sed. vol. |
| 1 | 3250 | 3187 | 63 | 1.02 | 0.98 | 0.02 | 51.22 |
| 2 | 3187 | 3036 | 151 | 1.05 | 0.95 | 0.05 | 21.08 |
| 3 | 3036 | 2953 | 83 | 1.03 | 0.97 | 0.03 | 36.74 |
| 5 | 2953 | 2694 | 259 | 1.10 | 0.91 | 0.09 | 11.41 |
| 6 | 2694 | 2620 | 74 | 1.03 | 0.97 | 0.03 | 36.32 |
| 7 | 2620 | 2419 | 201 | 1.08 | 0.92 | 0.08 | 13.04 |
| 8 | 2419 | 2133 | 286 | 1.13 | 0.88 | 0.12 | 8.47 |
| 9 | 2133 | 1944 | 189 | 1.10 | 0.91 | 0.09 | 11.27 |
| 10 | 1944 | 1846 | 99 | 1.05 | 0.95 | 0.05 | 19.74 |
| 11 | 1846 | 1706 | 140 | 1.08 | 0.92 | 0.08 | 13.20 |
| 12 | 1706 | 1543 | 163 | 1.11 | 0.90 | 0.10 | 10.47 |
| 13 | 1543 | 1401 | 142 | 1.10 | 0.91 | 0.09 | 10.86 |
| 14 | 1401 | 1161 | 240 | 1.21 | 0.83 | 0.17 | 5.84 |
| 15 | 1161 | 956 | 205 | 1.21 | 0.82 | 0.18 | 5.65 |
| 16 | 956 | 1016 | -61 | 0.94 | 1.06 | -0.06 | -15.78 |
| 17 | 1016 | 949 | 67 | 1.07 | 0.93 | 0.07 | 15.18 |
| 18 | 949 | 778 | 171 | 1.22 | 0.82 | 0.18 | 5.54 |

Series 1 – Sub-basin 2 Sediment Volume Data

| | Basin and Sediment Volume Data | | | | | | |
|---|---|---|---|---|---|---|---|
| Event ID | Initial vol. (cm3) | Final volume (cm3) | Trapped sed. vol. (cm3) | Initial vol./ final vol. | Final vol./ initial vol. | Trapped sed. vol./ initial vol. | Initial vol./ trapped sed. vol. |
| 1 | 4344 | 4239 | 104 | 1.02 | 0.98 | 0.02 | 41.58 |
| 2 | 4239 | 4085 | 154 | 1.04 | 0.96 | 0.04 | 27.55 |
| 3 | 4085 | 4015 | 70 | 1.02 | 0.98 | 0.02 | 58.07 |
| 5 | 4015 | 3872 | 143 | 1.04 | 0.96 | 0.04 | 28.16 |
| 6 | 3872 | 3825 | 47 | 1.01 | 0.99 | 0.01 | 82.20 |
| 7 | 3825 | 3759 | 66 | 1.02 | 0.98 | 0.02 | 57.90 |
| 8 | 3759 | 3599 | 160 | 1.04 | 0.96 | 0.04 | 23.48 |
| 9 | 3599 | 3513 | 86 | 1.02 | 0.98 | 0.02 | 41.83 |
| 10 | 3513 | 3471 | 42 | 1.01 | 0.99 | 0.01 | 83.14 |
| 11 | 3471 | 3398 | 73 | 1.02 | 0.98 | 0.02 | 47.65 |
| 12 | 3398 | 3308 | 90 | 1.03 | 0.97 | 0.03 | 37.67 |
| 13 | 3308 | 3147 | 161 | 1.05 | 0.95 | 0.05 | 20.52 |
| 14 | 3147 | 2965 | 181 | 1.06 | 0.94 | 0.06 | 17.36 |
| 15 | 2965 | 2816 | 150 | 1.05 | 0.95 | 0.05 | 19.79 |
| 16 | 2816 | 2957 | -141 | 0.95 | 1.05 | -0.05 | -19.93 |
| 17 | 2957 | 2558 | 399 | 1.16 | 0.87 | 0.13 | 7.41 |
| 18 | 2558 | 2323 | 235 | 1.10 | 0.91 | 0.09 | 10.87 |

Whole Basin Sediment Volume Data

| | Basin and Sediment Volume Data | | | | | | |
|---|---|---|---|---|---|---|---|
| Event ID | Initial vol. (cm3) | Final volume (cm3) | Trapped sed. vol. (cm3) | Initial vol./ final vol. | Final vol./ initial vol. | Trapped sed. vol./ initial vol. | Initial vol./ trapped sed. vol. |
| 1 | 14181 | 14014 | 167 | 1.01 | 0.99 | 0.01 | 84.78 |
| 2 | 14014 | 13709 | 305 | 1.02 | 0.98 | 0.02 | 45.96 |
| 3 | 13709 | 13556 | 153 | 1.01 | 0.99 | 0.01 | 89.71 |
| 5 | 13556 | 13156 | 401 | 1.03 | 0.97 | 0.03 | 33.83 |
| 6 | 13156 | 13035 | 121 | 1.01 | 0.99 | 0.01 | 108.68 |
| 7 | 13035 | 12768 | 267 | 1.02 | 0.98 | 0.02 | 48.85 |
| 8 | 12768 | 12323 | 445 | 1.04 | 0.97 | 0.03 | 28.69 |
| 9 | 12323 | 12048 | 275 | 1.02 | 0.98 | 0.02 | 44.83 |
| 10 | 12048 | 11907 | 141 | 1.01 | 0.99 | 0.01 | 85.64 |
| 11 | 11907 | 11695 | 212 | 1.02 | 0.98 | 0.02 | 56.11 |
| 12 | 11695 | 11442 | 253 | 1.02 | 0.98 | 0.02 | 46.28 |
| 13 | 11442 | 11140 | 303 | 1.03 | 0.97 | 0.03 | 37.79 |
| 14 | 11140 | 10719 | 420 | 1.04 | 0.96 | 0.04 | 26.51 |
| 15 | 10719 | 10365 | 355 | 1.03 | 0.97 | 0.03 | 30.23 |
| 16 | 10365 | 10565 | -201 | 0.98 | 1.02 | -0.02 | -51.66 |
| 17 | 10565 | 10100 | 465 | 1.05 | 0.96 | 0.04 | 22.71 |
| 18 | 10100 | 9694 | 406 | 1.04 | 0.96 | 0.04 | 24.88 |
| | 9694 | | | | | | |

Series 1 - Sediment Partitioning Between Two Sub-basins

| Event ID | Event sediment supply (cm3) | Cumulative sediment supply (cm3) | Initial vol. (cm3) | Final vol. (cm3) | Trapped sed. vol. (cm3) | Cumulative trapped sed. vol. (cm3) | % Captured in SB1 | % Captured in SB2 | Event capture efficiency (%) | Cumulative capture efficiency (%) |
|---|---|---|---|---|---|---|---|---|---|---|
| 1 | 16847 | 16847 | 14181 | 14014 | 167 | 167 | 38 | 62 | 0.99 | 0.99 |
| 2 | 16847 | 33694 | 14014 | 13709 | 305 | 472 | 50 | 50 | 1.87 | 1.40 |
| 3 | 16847 | 50541 | 13709 | 13556 | 153 | 625 | 54 | 46 | 0.92 | 1.24 |
| 5 | 16847 | 67388 | 13556 | 13156 | 401 | 1026 | 65 | 36 | 2.49 | 1.52 |
| 6 | 16847 | 84235 | 13156 | 13035 | 121 | 1147 | 61 | 39 | 0.73 | 1.36 |
| 7 | 16847 | 101082 | 13035 | 12768 | 267 | 1414 | 75 | 25 | 1.66 | 1.40 |
| 8 | 16847 | 117929 | 12768 | 12323 | 445 | 1859 | 64 | 36 | 2.88 | 1.58 |
| 9 | 16847 | 134776 | 12323 | 12048 | 275 | 2133 | 69 | 31 | 1.73 | 1.58 |
| 10 | 16847 | 151623 | 12048 | 11907 | 141 | 2274 | 70 | 30 | 0.86 | 1.50 |
| 11 | 16847 | 168470 | 11907 | 11695 | 212 | 2486 | 66 | 34 | 1.30 | 1.48 |
| 12 | 16847 | 185317 | 11695 | 11442 | 253 | 2739 | 64 | 36 | 1.58 | 1.48 |
| 13 | 16847 | 202164 | 11442 | 11140 | 303 | 3042 | 47 | 53 | 1.84 | 1.50 |
| 14 | 16847 | 219011 | 11140 | 10719 | 420 | 3462 | 57 | 43 | 2.55 | 1.58 |
| 15 | 16847 | 235858 | 10719 | 10365 | 355 | 3817 | 58 | 42 | 2.14 | 1.62 |
| 16 | 16847 | 252705 | 10365 | 10565 | -201 | 3616 | 30 | 70 | -1.19 | 1.43 |
| 17 | 16847 | 269552 | 10565 | 10100 | 465 | 4081 | 14 | 86 | 2.77 | 1.51 |
| 18 | 16847 | 286399 | 10100 | 9694 | 406 | 4487 | 42 | 58 | 2.44 | 1.57 |

Series 1 Ponding Index Data [ L = Sub-basin 1 (dx=2) ]

| Pi data (dip-oriented) | | | | | | | | | | Proximal | | Pi data (strike-oriented) | | | | | | | | | | Distal |
|---|---|---|---|---|---|---|---|---|---|---|---|---|---|---|---|---|---|---|---|---|---|---|
| d160 | | d180 | | d220 | | d260 | | d280 | | x240 | | x300 | | x340 | | x360 | | x400 | | x450 | | x500 |
| I | C | I | C | I | C | I | C | I | C | I | C | I | C | I | C | I | C | I | C | I | C | I | C |
| 0.09 | 0.09 | -0.16 | -0.16 | -0.03 | -0.03 | 0.06 | 0.06 | 0.06 | 0.06 | 0.43 | 0.43 | 0.33 | 0.33 | 0.26 | 0.26 | | | | | | | |
| 0.19 | 0.08 | -0.04 | -0.10 | 0.18 | 0.11 | -0.04 | -0.03 | -0.04 | -0.03 | 0.05 | 0.36 | 0.18 | 0.35 | 0.14 | 0.33 | | | | | | | |
| 0.05 | 0.10 | 0.15 | 0.01 | 0.26 | 0.07 | -0.01 | 0.17 | -0.01 | 0.17 | 0.39 | 0.35 | 0.33 | 0.31 | 0.03 | 0.46 | | | | | | | |
| 0.02 | 0.07 | 0.02 | 0.02 | -0.02 | 0.09 | 0.06 | 0.11 | 0.06 | 0.11 | 0.32 | 0.33 | 0.35 | 0.31 | 0.18 | 0.39 | | | | | | | |
| 0.10 | 0.10 | 0.10 | 0.12 | 0.02 | 0.32 | 0.08 | 0.14 | 0.08 | 0.14 | 0.49 | 0.43 | 0.57 | 0.37 | 0.20 | 0.28 | | | | | | | |
| 0.14 | 0.15 | -0.03 | 0.19 | -0.10 | 0.47 | -0.01 | 0.18 | -0.01 | 0.18 | 0.41 | 0.54 | 0.57 | 0.47 | 0.16 | 0.12 | | | | | | | |
| 0.03 | 0.19 | -0.06 | 0.23 | -0.14 | 0.44 | -0.01 | 0.25 | -0.01 | 0.25 | 0.50 | 0.51 | 0.49 | 0.53 | 0.09 | 0.12 | | | | | | | |
| 0.05 | 0.10 | -0.01 | 0.26 | -0.12 | 0.41 | -0.01 | 0.22 | -0.01 | 0.22 | 0.56 | 0.59 | 0.45 | 0.60 | 0.12 | 0.21 | | | | | | | |
| 0.02 | 0.13 | -0.03 | 0.26 | -0.04 | 0.44 | -0.06 | 0.26 | -0.06 | 0.26 | 0.50 | 0.61 | 0.33 | 0.61 | 0.16 | 0.26 | | | | | | | |
| 0.05 | 0.19 | -0.10 | 0.26 | -0.10 | 0.35 | -0.03 | 0.27 | -0.03 | 0.27 | 0.44 | 0.65 | 0.36 | 0.65 | 0.25 | 0.43 | | | | | | | |
| 0.04 | 0.25 | -0.08 | 0.28 | 0.03 | 0.39 | -0.06 | 0.25 | -0.06 | 0.25 | 0.30 | 0.64 | 0.36 | 0.69 | 0.41 | 0.45 | | | | | | | |
| -0.13 | 0.29 | -0.05 | 0.28 | -0.08 | 0.28 | -0.09 | 0.27 | -0.09 | 0.27 | 0.59 | 0.68 | 0.40 | 0.68 | 0.28 | 0.57 | | | | | | | |
| -0.09 | 0.33 | -0.08 | 0.34 | -0.09 | 0.29 | -0.05 | 0.24 | -0.05 | 0.24 | 0.52 | 0.64 | 0.45 | 0.76 | 0.37 | 0.61 | | | | | | | |
| -0.08 | 0.36 | -0.07 | 0.31 | -0.09 | 0.29 | -0.12 | 0.23 | -0.12 | 0.23 | 0.68 | 0.65 | 0.16 | 0.87 | 0.33 | 0.64 | | | | | | | |
| -0.08 | 0.41 | 0.01 | 0.32 | -0.12 | 0.27 | -0.11 | 0.27 | -0.11 | 0.27 | 0.47 | 0.81 | 0.60 | 0.76 | 0.66 | 0.68 | | | | | | | |
| -0.08 | 0.40 | -0.04 | 0.37 | -0.15 | 0.34 | -0.11 | 0.22 | -0.11 | 0.22 | 0.44 | 0.75 | 0.46 | 0.77 | 0.59 | 0.67 | | | | | | | |

Pi = Ponding Index I = Individual C = Cumulative

Series 1 Ponding Index Data [ L = Sub-basin 1 (dx=4) ]

| Pi data (dip-oriented) | | | | | | | | | | Proximal | | Pi data (strike-oriented) | | | | | | | | | Distal |
|---|---|---|---|---|---|---|---|---|---|---|---|---|---|---|---|---|---|---|---|---|---|
| d160 | | d180 | | d220 | | d260 | | d280 | | x240 | | x300 | | x340 | | x360 | | x400 | | x450 | | x500 | |
| I | C | I | C | I | C | I | C | I | C | I | C | I | C | I | C | I | C | I | C | I | C | I | C |
| -0.11 | -0.11 | -0.22 | -0.22 | 0.25 | 0.25 | 0.01 | 0.01 | 0.16 | 0.16 | 0.21 | 0.21 | 0.30 | 0.30 | 0.37 | 0.37 | | | | | | | | |
| 0.16 | 0.09 | -0.02 | -0.08 | 0.11 | 0.23 | -0.01 | -0.02 | -0.05 | 0.14 | -0.08 | 0.16 | 0.12 | 0.39 | 0.08 | 0.52 | | | | | | | | |
| -0.02 | 0.08 | 0.09 | 0.06 | 0.07 | 0.07 | 0.01 | -0.04 | -0.03 | 0.15 | 0.30 | 0.28 | 0.24 | 0.28 | 0.08 | 0.69 | | | | | | | | |
| 0.04 | 0.03 | -0.03 | 0.05 | 0.02 | 0.00 | 0.03 | -0.06 | -0.01 | 0.11 | 0.23 | 0.28 | 0.16 | 0.24 | -0.01 | 0.77 | | | | | | | | |
| 0.12 | 0.08 | 0.02 | 0.19 | 0.04 | 0.04 | 0.07 | -0.07 | 0.04 | 0.03 | 0.33 | 0.28 | 0.44 | 0.40 | 0.02 | 0.97 | | | | | | | | |
| 0.09 | 0.23 | -0.03 | 0.24 | -0.17 | 0.18 | -0.07 | -0.03 | 0.19 | 0.23 | 0.21 | 0.43 | 0.53 | 0.57 | 0.06 | 0.82 | | | | | | | | |
| -0.01 | 0.24 | -0.04 | 0.32 | -0.11 | 0.29 | 0.06 | 0.04 | 0.04 | 0.33 | 0.44 | 0.48 | 0.40 | 0.58 | 0.04 | 0.80 | | | | | | | | |
| 0.02 | 0.10 | -0.01 | 0.33 | -0.04 | 0.24 | -0.05 | 0.11 | -0.07 | 0.41 | 0.40 | 0.53 | 0.31 | 0.69 | 0.10 | 0.58 | | | | | | | | |
| -0.01 | 0.19 | -0.04 | 0.32 | -0.06 | 0.17 | -0.07 | 0.09 | -0.11 | 0.44 | 0.15 | 0.61 | 0.19 | 0.71 | 0.06 | 0.59 | | | | | | | | |
| 0.05 | 0.21 | -0.02 | 0.35 | -0.05 | 0.14 | -0.07 | 0.15 | -0.06 | 0.46 | 0.22 | 0.59 | 0.23 | 0.78 | 0.03 | 0.52 | | | | | | | | |
| -0.06 | 0.22 | 0.01 | 0.38 | 0.18 | 0.37 | -0.06 | 0.14 | -0.01 | 0.18 | 0.18 | 0.64 | 0.22 | 0.84 | 0.11 | 0.27 | | | | | | | | |
| -0.17 | 0.31 | -0.05 | 0.37 | -0.12 | 0.37 | -0.04 | 0.13 | 0.03 | 0.49 | 0.49 | 0.71 | 0.27 | 0.80 | 0.18 | 0.62 | | | | | | | | |
| -0.03 | 0.30 | -0.02 | 0.37 | -0.04 | 0.34 | -0.04 | 0.13 | 0.04 | 0.49 | 0.49 | 0.76 | 0.15 | 0.82 | 0.25 | 0.70 | | | | | | | | |
| -0.03 | 0.41 | -0.03 | 0.38 | -0.04 | 0.32 | -0.05 | 0.16 | -0.23 | 0.36 | 0.36 | 0.78 | -0.20 | 0.86 | 0.21 | 0.76 | | | | | | | | |
| -0.11 | 0.49 | -0.03 | 0.37 | -0.03 | 0.34 | -0.05 | 0.18 | -0.08 | 0.58 | 0.25 | 0.80 | 0.36 | 0.78 | 0.58 | 0.80 | | | | | | | | |
| -0.03 | 0.59 | -0.05 | 0.44 | -0.04 | 0.33 | -0.05 | 0.17 | -0.06 | 0.60 | 0.15 | 0.79 | 0.42 | 0.79 | 0.23 | 0.75 | | | | | | | | |

Pi = Ponding Index I = Individual C = Cumulative

Series 1 Ponding Index Data [ L = Sub-basin 1 (dx=10) ]

| Pi data (dip-oriented) | | | | | | | | | | Proximal | | Pi data (strike-oriented) | | | | | | | | | Distal |
|---|---|---|---|---|---|---|---|---|---|---|---|---|---|---|---|---|---|---|---|---|---|
| d160 | | d180 | | d220 | | d260 | | d280 | | x240 | | x300 | | x340 | | x360 | | x400 | | x450 | | x500 | |
| I | C | I | C | I | C | I | C | I | C | I | C | I | C | I | C | I | C | I | C | I | C | I | C |
| 0.14 | 0.14 | -0.27 | -0.27 | 0.17 | 0.17 | -0.05 | -0.05 | 0.01 | 0.01 | 0.10 | 0.10 | 0.27 | 0.27 | -0.24 | -0.24 | | | | | | | | |
| -0.02 | 0.13 | -0.15 | -0.26 | 0.18 | 0.22 | -0.09 | 0.13 | 0.00 | -0.04 | -0.16 | 0.09 | 0.01 | 0.33 | 0.01 | -0.24 | | | | | | | | |
| 0.05 | 0.19 | 0.05 | 0.06 | -0.05 | 0.24 | -0.01 | 0.15 | -0.04 | 0.00 | 0.31 | 0.20 | 0.17 | 0.22 | -0.01 | -0.26 | | | | | | | | |
| 0.00 | 0.17 | 0.00 | 0.04 | 0.03 | 0.24 | 0.00 | 0.17 | 0.03 | -0.01 | 0.13 | 0.21 | 0.08 | 0.28 | -0.05 | -0.27 | | | | | | | | |
| 0.06 | 0.18 | -0.07 | 0.23 | 0.10 | 0.29 | 0.11 | 0.22 | 0.05 | 0.06 | 0.34 | 0.30 | 0.64 | 0.53 | 0.39 | 0.26 | | | | | | | | |
| 0.11 | 0.35 | 0.00 | 0.32 | -0.22 | 0.39 | -0.01 | 0.19 | 0.19 | 0.16 | 0.32 | 0.35 | 0.53 | 0.72 | -0.09 | 0.30 | | | | | | | | |
| -0.02 | 0.33 | -0.05 | 0.36 | -0.09 | 0.43 | 0.05 | 0.21 | -0.02 | 0.21 | 0.37 | 0.46 | 0.27 | 0.81 | -0.07 | 0.28 | | | | | | | | |
| 0.05 | 0.23 | 0.01 | 0.38 | -0.07 | 0.40 | -0.18 | 0.25 | -0.04 | 0.30 | 0.05 | 0.55 | -0.04 | 0.93 | 0.13 | 0.40 | | | | | | | | |
| 0.02 | 0.27 | -0.02 | 0.43 | -0.09 | 0.35 | -0.03 | 0.25 | -0.05 | 0.26 | 0.11 | 0.54 | 0.09 | 0.85 | -0.11 | 0.39 | | | | | | | | |
| 0.11 | 0.40 | -0.02 | 0.41 | -0.10 | 0.30 | -0.04 | 0.30 | -0.04 | 0.28 | 0.30 | 0.54 | 0.08 | 0.94 | 0.09 | 0.28 | | | | | | | | |
| -0.01 | 0.47 | 0.02 | 0.46 | 0.15 | 0.36 | -0.03 | 0.32 | 0.00 | 0.30 | 0.02 | 0.54 | 0.12 | 1.01 | 0.21 | 0.35 | | | | | | | | |
| -0.11 | 0.58 | -0.04 | 0.44 | -0.11 | 0.36 | -0.03 | 0.34 | 0.07 | 0.40 | 0.37 | 0.72 | 0.23 | 1.03 | 0.10 | 0.65 | | | | | | | | |
| -0.02 | 0.66 | -0.01 | 0.45 | -0.02 | 0.36 | -0.02 | 0.39 | -0.02 | 0.43 | 0.29 | 0.74 | 0.08 | 1.03 | 0.12 | 0.72 | | | | | | | | |
| -0.02 | 0.72 | -0.03 | 0.45 | -0.02 | 0.38 | -0.03 | 0.47 | -0.17 | 0.48 | 0.11 | 0.78 | -0.23 | 1.08 | 0.14 | 0.76 | | | | | | | | |
| -0.03 | 0.91 | 0.00 | 0.46 | -0.01 | 0.38 | -0.01 | 0.46 | -0.04 | 0.41 | 0.04 | 0.72 | 0.25 | 0.85 | 0.48 | 0.86 | | | | | | | | |
| -0.01 | 1.05 | -0.02 | 0.51 | -0.02 | 0.45 | -0.03 | 0.48 | -0.03 | 0.40 | 0.17 | 0.73 | 0.13 | 0.94 | 0.19 | 0.81 | | | | | | | | |

Pi = Ponding Index I = Individual C = Cumulative

Series 1 Ponding Index Data [ L = Sub-basin 1 (dx=20) ]

| Pi data (dip-oriented) | | | | | | | | | | Proximal | | Pi data (strike-oriented) | | | | | | | | | Distal |
|---|---|---|---|---|---|---|---|---|---|---|---|---|---|---|---|---|---|---|---|---|---|
| d160 | | d180 | | d220 | | d260 | | d280 | | x240 | | x300 | | x340 | | x360 | | x400 | | x450 | | x500 | |
| I | C | I | C | I | C | I | C | I | C | I | C | I | C | I | C | I | C | I | C | I | C | I | C |
| 0.04 | 0.04 | -0.25 | -0.25 | 0.04 | 0.04 | 0.01 | 0.01 | -0.03 | -0.03 | 0.04 | 0.04 | -0.39 | -0.39 | 0.19 | 0.19 | | | | | | | | |
| -0.03 | 0.01 | 0.02 | -0.28 | 0.05 | 0.09 | -0.06 | 0.07 | -0.03 | -0.09 | 0.06 | -0.01 | -0.05 | -0.44 | 0.07 | 0.23 | | | | | | | | |
| 0.05 | 0.03 | 0.04 | -0.03 | 0.06 | 0.13 | -0.02 | 0.12 | 0.02 | -0.04 | 0.53 | 0.14 | 0.19 | -0.04 | 0.08 | 0.39 | | | | | | | | |
| 0.00 | 0.00 | -0.01 | -0.03 | -0.02 | 0.18 | 0.01 | 0.14 | 0.02 | -0.06 | 0.09 | 0.18 | 0.08 | -0.03 | 0.06 | 0.43 | | | | | | | | |
| 0.13 | 0.11 | 0.17 | 0.09 | 0.10 | 0.31 | 0.09 | 0.27 | -0.01 | -0.06 | 0.33 | 0.25 | 0.67 | 0.56 | 0.14 | 0.37 | | | | | | | | |
| 0.01 | 0.43 | 0.00 | 0.18 | -0.11 | 0.39 | -0.05 | 0.27 | 0.12 | 0.17 | 0.29 | 0.36 | 0.59 | 0.62 | -0.14 | 0.31 | | | | | | | | |
| -0.03 | 0.44 | 0.06 | 0.24 | -0.16 | 0.40 | 0.02 | 0.31 | -0.17 | 0.29 | 0.48 | 0.41 | 0.13 | 0.87 | -0.04 | 0.31 | | | | | | | | |
| 0.02 | 0.27 | 0.14 | 0.28 | 0.03 | 0.39 | -0.27 | 0.38 | -0.08 | 0.33 | 0.30 | 0.49 | -0.22 | 1.01 | -0.02 | 0.16 | | | | | | | | |
| -0.05 | 0.32 | -0.02 | 0.26 | 0.04 | 0.35 | -0.02 | 0.39 | -0.05 | 0.32 | 0.15 | 0.50 | -0.09 | 0.96 | 0.05 | 0.15 | | | | | | | | |
| -0.14 | 0.60 | -0.03 | 0.29 | -0.08 | 0.27 | -0.03 | 0.41 | -0.15 | 0.34 | 0.02 | 0.52 | 0.10 | 1.04 | -0.02 | 0.23 | | | | | | | | |
| 0.01 | 0.62 | 0.02 | 0.30 | 0.11 | 0.03 | -0.02 | 0.41 | -0.02 | 0.43 | -0.08 | 0.51 | 0.29 | 1.11 | 0.20 | 0.31 | | | | | | | | |
| -0.09 | 1.04 | -0.03 | 0.27 | -0.03 | -0.05 | -0.02 | 0.43 | 0.05 | 0.50 | 0.23 | 0.58 | 0.27 | 1.05 | 0.09 | 0.33 | | | | | | | | |
| -0.02 | 1.26 | -0.02 | 0.27 | -0.01 | -0.04 | -0.02 | 0.46 | -0.10 | 0.44 | 0.23 | 0.71 | 0.10 | 1.06 | 0.10 | 0.43 | | | | | | | | |
| -0.01 | 1.29 | -0.03 | 0.31 | -0.02 | -0.07 | -0.02 | 0.57 | -0.16 | 0.43 | -0.11 | 0.81 | 0.39 | 1.14 | 0.15 | 0.46 | | | | | | | | |
| 0.00 | 1.57 | 0.00 | 0.39 | 0.00 | -0.05 | 0.00 | 0.56 | -0.03 | 0.34 | 0.06 | 0.73 | 0.18 | 0.82 | 0.37 | 0.88 | | | | | | | | |
| 0.00 | 1.70 | -0.01 | 0.39 | -0.02 | 0.00 | -0.03 | 0.61 | -0.01 | 0.33 | 0.12 | 0.75 | -0.11 | 0.94 | 0.06 | 0.94 | | | | | | | | |

Pi = Ponding Index I = Individual C = Cumulative

Series 1 Ponding Index Data [ L = Sub-basin 1 (dx=50) ]

| Pi data (dip-oriented) | | | | | | | | | | Proximal | | Pi data (strike-oriented) | | | | | | | | | Distal |
|---|---|---|---|---|---|---|---|---|---|---|---|---|---|---|---|---|---|---|---|---|---|
| d160 | | d180 | | d220 | | d260 | | d280 | | x240 | | x300 | | x340 | | x360 | | x400 | | x450 | | x500 | |
| I | C | I | C | I | C | I | C | I | C | I | C | I | C | I | C | I | C | I | C | I | C | I | C |
| -0.03 | -0.03 | 0.02 | 0.02 | 0.06 | 0.06 | -0.07 | -0.07 | 0.02 | 0.02 | 0.01 | 0.01 | -0.30 | -0.30 | 0.22 | 0.22 | | | | | | | | |
| 0.05 | -0.01 | 0.05 | 0.02 | 0.05 | 0.11 | -0.02 | -0.11 | 0.05 | 0.04 | 0.01 | 0.00 | 0.05 | -0.33 | -0.05 | 0.25 | | | | | | | | |
| -0.16 | 0.01 | 0.05 | 0.09 | -0.01 | 0.13 | 0.10 | -0.15 | -0.02 | 0.05 | 0.20 | 0.14 | 0.14 | -0.03 | 0.04 | 0.37 | | | | | | | | |
| -0.01 | 0.00 | 0.00 | 0.09 | -0.05 | 0.15 | 0.01 | -0.15 | 0.01 | 0.03 | 0.00 | 0.15 | 0.05 | 0.01 | 0.01 | 0.41 | | | | | | | | |
| -0.08 | 0.06 | 0.22 | 0.22 | 0.35 | -0.03 | 0.11 | -0.16 | -0.02 | 0.02 | 0.41 | 0.32 | 0.36 | 0.22 | -0.16 | 0.60 | | | | | | | | |
| -0.09 | 0.16 | -0.11 | 0.34 | -0.27 | 0.02 | -0.31 | -0.21 | 0.14 | 0.19 | 0.29 | 0.40 | 0.58 | 0.70 | 0.00 | 0.74 | | | | | | | | |
| -0.03 | 0.13 | -0.27 | 0.42 | -0.05 | -0.03 | -0.05 | -0.25 | 0.03 | 0.25 | 0.04 | 0.55 | -0.59 | 1.00 | -0.06 | 0.85 | | | | | | | | |
| 0.00 | 0.05 | -0.07 | 0.51 | -0.03 | -0.06 | -0.07 | -0.30 | -0.10 | 0.33 | 0.07 | 0.60 | -0.22 | 1.19 | 0.16 | 0.90 | | | | | | | | |
| -0.02 | 0.06 | -0.03 | 0.53 | -0.01 | -0.09 | -0.02 | -0.32 | -0.02 | 0.34 | 0.17 | 0.61 | -0.10 | 1.26 | -0.04 | 0.99 | | | | | | | | |
| -0.03 | 0.19 | -0.04 | 0.58 | -0.01 | -0.10 | -0.02 | -0.35 | -0.02 | 0.37 | 0.15 | 0.70 | 0.08 | 1.35 | 0.00 | 1.06 | | | | | | | | |
| 0.00 | 0.23 | 0.01 | 0.63 | 0.89 | -0.52 | -0.01 | -0.38 | -0.02 | 0.39 | -0.33 | 0.74 | 0.17 | 1.34 | 0.12 | 0.75 | | | | | | | | |
| -0.05 | 0.34 | -0.04 | 0.65 | -0.02 | -0.62 | -0.02 | -0.44 | -0.04 | 0.37 | 0.07 | 0.77 | 0.26 | 1.29 | 0.38 | 0.34 | | | | | | | | |
| -0.02 | 0.41 | -0.03 | 0.70 | -0.01 | -0.69 | -0.01 | -0.45 | -0.02 | 0.38 | 0.12 | 0.88 | 0.06 | 1.32 | -0.01 | 0.32 | | | | | | | | |
| 0.00 | 0.43 | -0.02 | 0.70 | -0.02 | -0.83 | -0.02 | -0.46 | -0.13 | 0.47 | -0.28 | 1.00 | -0.25 | 1.45 | 0.08 | 0.22 | | | | | | | | |
| 0.02 | 0.64 | 0.03 | 0.72 | 0.01 | -0.80 | 0.00 | -0.51 | 0.00 | 0.47 | 0.16 | 0.97 | 0.31 | 1.25 | 0.38 | 0.35 | | | | | | | | |
| 0.00 | 0.72 | 0.00 | 0.72 | -0.01 | -0.85 | -0.02 | -0.56 | 0.00 | 0.53 | -0.09 | 1.02 | -0.03 | 1.20 | -0.11 | 0.44 | | | | | | | | |

Pi = Ponding Index I = Individual C = Cumulative

Series 1 Ponding Index Data [ L = Sub-basin 1 (dx=100) ]

| Pi data (dip-oriented) | | | | | | | | | | Proximal | | Pi data (strike-oriented) | | | | | | | | | Distal |
|---|---|---|---|---|---|---|---|---|---|---|---|---|---|---|---|---|---|---|---|---|---|
| d160 | | d180 | | d220 | | d260 | | d280 | | x240 | | x300 | | x340 | | x360 | | x400 | | x450 | | x500 | |
| I | C | I | C | I | C | I | C | I | C | I | C | I | C | I | C | I | C | I | C | I | C | I | C |
| -0.10 | -0.10 | 0.39 | 0.39 | -0.20 | -0.20 | -0.10 | -0.10 | -0.12 | -0.12 | 0.04 | 0.04 | -0.09 | -0.09 | -0.09 | -0.09 | | | | | | | | |
| -0.03 | -0.14 | 0.10 | 0.46 | 0.00 | -0.20 | -0.02 | -0.13 | -0.01 | -0.14 | 0.03 | 0.08 | 0.03 | -0.07 | 0.04 | -0.08 | | | | | | | | |
| -0.04 | -0.19 | -0.04 | 0.54 | -0.22 | -0.60 | -0.06 | -0.23 | -0.05 | -0.21 | 0.04 | 0.12 | 0.15 | 0.12 | 0.00 | 0.01 | | | | | | | | |
| -0.01 | -0.20 | 0.05 | 0.57 | -0.02 | -0.66 | -0.01 | -0.24 | -0.01 | -0.23 | 0.02 | 0.15 | 0.04 | 0.15 | -0.04 | 0.04 | | | | | | | | |
| -0.03 | -0.26 | 0.36 | 0.74 | -0.18 | -1.49 | -0.05 | -0.35 | -0.03 | -0.28 | 0.05 | 0.17 | 0.27 | 0.38 | 0.05 | 0.19 | | | | | | | | |
| -0.06 | -0.38 | -0.22 | 1.01 | -0.10 | -2.39 | -0.05 | -0.49 | -0.08 | -0.44 | 0.06 | 0.23 | 0.77 | 0.60 | -0.07 | 0.17 | | | | | | | | |
| -0.03 | -0.46 | -0.08 | 1.25 | -0.05 | -3.01 | -0.02 | -0.57 | -0.02 | -0.53 | 0.03 | 0.26 | -0.27 | 0.67 | -0.14 | 0.14 | | | | | | | | |
| -0.01 | -0.46 | -0.03 | 1.41 | -0.02 | -3.48 | -0.03 | -0.71 | -0.02 | -0.61 | 0.03 | 0.25 | -0.21 | 0.71 | 0.05 | 0.37 | | | | | | | | |
| -0.02 | -0.52 | -0.03 | 1.50 | -0.02 | -3.79 | -0.01 | -0.73 | -0.01 | -0.67 | 0.04 | 0.29 | 0.01 | 0.81 | 0.01 | 0.46 | | | | | | | | |
| -0.03 | -0.63 | -0.04 | 1.61 | -0.02 | -4.17 | -0.01 | -0.81 | -0.02 | -0.74 | 0.02 | 0.33 | 0.02 | 0.97 | 0.09 | 0.71 | | | | | | | | |
| 0.00 | -0.66 | 0.01 | 1.76 | -0.02 | -4.06 | 0.00 | -0.89 | 0.00 | -0.80 | 0.05 | 0.36 | 0.03 | 1.01 | -0.02 | 0.93 | | | | | | | | |
| -0.05 | -0.82 | -0.04 | 1.84 | -0.01 | -4.19 | -0.01 | -0.98 | -0.02 | -0.95 | 0.03 | 0.41 | 0.08 | 1.14 | 0.12 | 1.10 | | | | | | | | |
| -0.02 | -0.92 | -0.03 | 1.97 | -0.01 | -4.26 | -0.01 | -1.03 | -0.01 | -1.05 | 0.04 | 0.47 | 0.00 | 1.22 | -0.11 | 1.19 | | | | | | | | |
| 0.01 | -0.89 | -0.06 | 2.25 | -0.02 | -4.50 | -0.01 | -1.14 | -0.07 | -1.57 | -0.04 | 0.41 | -0.09 | 1.29 | 0.06 | 1.09 | | | | | | | | |
| 0.01 | -0.90 | 0.02 | 2.32 | 0.02 | -4.40 | 0.02 | -1.16 | 0.00 | -1.59 | 0.06 | 0.48 | 0.25 | 1.09 | 0.29 | 0.83 | | | | | | | | |
| -0.01 | -0.92 | 0.00 | 2.43 | -0.01 | -4.55 | -0.01 | -1.22 | 0.00 | -1.57 | 0.07 | 0.52 | 0.00 | 1.15 | -0.09 | 0.84 | | | | | | | | |

Pi = Ponding Index I = Individual C = Cumulative

Series 1 Ponding Index Data [ L = Sub-basin 2 (dx=2) ]

| Pi data (dip-oriented) | | | | | | | | | | Proximal | | Pi data (strike-oriented) | | | | | | | | | Distal |
|---|---|---|---|---|---|---|---|---|---|---|---|---|---|---|---|---|---|---|---|---|---|
| d160 | | d180 | | d220 | | d260 | | d280 | | x240 | | x300 | | x340 | | x360 | | x400 | | x450 | | x500 | |
| I | C | I | C | I | C | I | C | I | C | I | C | I | C | I | C | I | C | I | C | I | C | I | C |
| 0.22 | 0.22 | -0.19 | -0.19 | 0.04 | 0.04 | 0.05 | 0.05 | -0.01 | -0.01 | | | | | | | 0.07 | 0.07 | 0.11 | 0.11 | 0.07 | 0.07 | 0.20 | 0.20 |
| 0.19 | 0.19 | 0.04 | -0.39 | 0.03 | 0.07 | 0.07 | 0.03 | 0.04 | 0.03 | | | | | | | 0.25 | 0.13 | 0.07 | 0.10 | 0.05 | 0.08 | 0.23 | 0.23 |
| 0.10 | 0.28 | -0.12 | -0.30 | 0.03 | 0.13 | 0.13 | 0.18 | 0.10 | 0.11 | | | | | | | 0.21 | 0.18 | 0.35 | 0.28 | 0.26 | 0.26 | 0.34 | 0.27 |
| 0.13 | 0.40 | -0.01 | -0.27 | 0.09 | 0.17 | 0.08 | 0.21 | 0.08 | 0.11 | | | | | | | 0.29 | 0.26 | 0.16 | 0.30 | 0.13 | 0.25 | 0.32 | 0.27 |
| 0.06 | 0.39 | 0.09 | -0.23 | 0.07 | 0.08 | 0.01 | 0.18 | 0.12 | 0.10 | | | | | | | 0.18 | 0.17 | 0.07 | 0.28 | 0.26 | 0.28 | 0.37 | 0.24 |
| 0.09 | 0.50 | 0.10 | -0.09 | 0.05 | 0.13 | 0.04 | 0.27 | 0.12 | 0.13 | | | | | | | 0.31 | 0.23 | 0.18 | 0.37 | 0.24 | 0.30 | 0.35 | 0.35 |
| 0.09 | 0.52 | 0.13 | -0.05 | 0.06 | 0.18 | -0.03 | 0.27 | 0.12 | 0.18 | | | | | | | 0.29 | 0.20 | 0.24 | 0.35 | 0.17 | 0.32 | 0.39 | 0.37 |
| 0.24 | 0.64 | -0.01 | -0.06 | 0.10 | 0.19 | 0.08 | 0.31 | 0.05 | 0.23 | | | | | | | 0.24 | 0.27 | 0.19 | 0.38 | 0.22 | 0.34 | 0.37 | 0.45 |
| 0.23 | 0.58 | 0.12 | -0.14 | 0.04 | 0.20 | 0.10 | 0.33 | 0.10 | 0.22 | | | | | | | 0.19 | 0.18 | 0.22 | 0.43 | 0.27 | 0.37 | 0.33 | 0.35 |
| 0.09 | 0.64 | 0.14 | -0.15 | 0.09 | 0.21 | 0.13 | 0.33 | 0.04 | 0.19 | | | | | | | 0.26 | 0.19 | 0.25 | 0.37 | 0.16 | 0.37 | 0.39 | 0.36 |
| 0.33 | 0.57 | 0.14 | 0.12 | 0.10 | 0.24 | 0.11 | 0.35 | 0.10 | 0.22 | | | | | | | 0.38 | 0.37 | 0.39 | 0.37 | 0.22 | 0.40 | 0.43 | 0.40 |
| 0.16 | 0.62 | 0.21 | 0.02 | 0.16 | 0.25 | 0.11 | 0.40 | 0.17 | 0.27 | | | | | | | 0.35 | 0.48 | 0.40 | 0.45 | 0.30 | 0.37 | 0.40 | 0.40 |
| 0.24 | 0.67 | 0.14 | 0.06 | 0.15 | 0.29 | 0.14 | 0.41 | 0.08 | 0.31 | | | | | | | 0.31 | 0.53 | 0.38 | 0.49 | 0.24 | 0.45 | 0.54 | 0.41 |
| 0.24 | 0.71 | 0.18 | -0.03 | 0.22 | 0.29 | 0.12 | 0.45 | 0.14 | 0.28 | | | | | | | 0.20 | 0.39 | 0.39 | 0.49 | 0.25 | 0.48 | 0.46 | 0.46 |
| 0.36 | 0.62 | 0.37 | 0.41 | 0.48 | 0.48 | 0.50 | 0.62 | 0.52 | 0.56 | | | | | | | 0.52 | 0.59 | 0.59 | 0.67 | 0.53 | 0.58 | 0.54 | 0.39 |
| 0.24 | 0.68 | 0.35 | 0.39 | 0.51 | 0.55 | 0.53 | 0.63 | 0.42 | 0.60 | | | | | | | 0.32 | 0.56 | 0.45 | 0.67 | 0.48 | 0.65 | 0.39 | 0.43 |

Pi = Ponding Index I = Individual C = Cumulative

Series 1 Ponding Index Data [ L = Sub-basin 2 (dx=4) ]

| Pi data (dip-oriented) | | | | | | | | | | Proximal | | Pi data (strike-oriented) | | | | | | | | | Distal |
|---|---|---|---|---|---|---|---|---|---|---|---|---|---|---|---|---|---|---|---|---|---|
| d160 | | d180 | | d220 | | d260 | | d280 | | x240 | | x300 | | x340 | | x360 | | x400 | | x450 | | x500 | |
| I | C | I | C | I | C | I | C | I | C | I | C | I | C | I | C | I | C | I | C | I | C | I | C |
| 0.12 | 0.12 | 0.06 | 0.06 | 0.01 | 0.01 | 0.01 | 0.01 | 0.04 | 0.04 | | | | | | | 0.03 | 0.03 | 0.09 | 0.09 | 0.07 | 0.07 | 0.11 | 0.11 |
| -0.01 | 0.28 | 0.11 | 0.03 | 0.01 | -0.02 | 0.00 | 0.00 | -0.01 | 0.01 | | | | | | | 0.07 | 0.04 | 0.08 | 0.13 | 0.01 | 0.07 | 0.08 | 0.13 |
| 0.00 | 0.21 | 0.01 | 0.16 | 0.04 | 0.00 | 0.12 | 0.16 | 0.09 | 0.06 | | | | | | | 0.17 | 0.00 | 0.26 | 0.16 | 0.25 | 0.20 | 0.23 | 0.22 |
| 0.01 | 0.44 | 0.10 | 0.15 | 0.05 | 0.02 | 0.00 | 0.16 | 0.02 | 0.08 | | | | | | | -0.01 | -0.01 | 0.04 | 0.16 | 0.10 | 0.22 | 0.18 | 0.21 |
| 0.01 | 0.31 | -0.05 | 0.18 | 0.00 | 0.02 | -0.01 | 0.19 | 0.09 | 0.08 | | | | | | | 0.07 | 0.08 | 0.11 | 0.22 | 0.15 | 0.21 | 0.16 | 0.19 |
| -0.22 | 0.35 | -0.02 | 0.22 | 0.05 | 0.05 | 0.07 | 0.24 | 0.09 | 0.15 | | | | | | | 0.15 | 0.12 | 0.13 | 0.30 | 0.10 | 0.26 | 0.21 | 0.30 |
| 0.05 | 0.37 | 0.15 | 0.18 | 0.05 | 0.06 | 0.01 | 0.28 | 0.05 | 0.15 | | | | | | | 0.10 | 0.09 | 0.04 | 0.29 | 0.09 | 0.30 | 0.24 | 0.31 |
| 0.08 | 0.30 | 0.05 | 0.14 | 0.08 | 0.07 | 0.09 | 0.35 | 0.08 | 0.18 | | | | | | | 0.12 | 0.17 | 0.22 | 0.33 | 0.13 | 0.32 | 0.16 | 0.31 |
| 0.12 | -0.01 | 0.10 | 0.06 | 0.03 | 0.11 | 0.01 | 0.35 | 0.04 | 0.21 | | | | | | | 0.15 | 0.12 | 0.16 | 0.35 | 0.17 | 0.32 | 0.18 | 0.31 |
| -0.01 | 0.41 | 0.22 | -0.01 | 0.03 | 0.13 | 0.09 | 0.39 | 0.05 | 0.20 | | | | | | | 0.17 | 0.19 | 0.17 | 0.38 | 0.13 | 0.34 | 0.18 | 0.32 |
| 0.28 | 0.47 | 0.22 | 0.37 | 0.04 | 0.18 | 0.07 | 0.42 | 0.03 | 0.25 | | | | | | | 0.26 | 0.16 | 0.23 | 0.38 | 0.20 | 0.37 | 0.19 | 0.32 |
| -0.05 | 0.52 | 0.15 | 0.37 | 0.06 | 0.18 | 0.06 | 0.46 | 0.09 | 0.25 | | | | | | | 0.25 | 0.21 | 0.27 | 0.44 | 0.27 | 0.44 | 0.24 | 0.33 |
| 0.05 | 0.47 | 0.03 | 0.40 | 0.06 | 0.25 | 0.01 | 0.45 | 0.06 | 0.30 | | | | | | | 0.20 | 0.22 | 0.17 | 0.50 | 0.18 | 0.45 | 0.24 | 0.44 |
| 0.01 | 0.47 | 0.08 | 0.39 | -0.09 | 0.16 | 0.05 | 0.45 | 0.04 | 0.29 | | | | | | | 0.00 | 0.26 | 0.18 | 0.50 | 0.20 | 0.46 | 0.23 | 0.33 |
| 0.15 | 0.72 | 0.36 | 0.40 | 0.45 | 0.45 | 0.45 | 0.64 | 0.42 | 0.59 | | | | | | | 0.35 | 0.38 | 0.49 | 0.73 | 0.60 | 0.62 | 0.32 | 0.40 |
| -0.02 | 0.67 | 0.07 | 0.44 | 0.36 | 0.52 | 0.44 | 0.72 | 0.35 | 0.64 | | | | | | | 0.13 | 0.39 | 0.32 | 0.73 | 0.42 | 0.68 | 0.21 | 0.45 |

Pi = Ponding Index  I = Individual  C = Cumulative

Series 1 Ponding Index Data [ L = Sub-basin 2 (dx=10) ]

| Pi data (dip-oriented) | | | | | | | | | | Proximal | | | | | | Pi data (strike-oriented) | | | | | | | Distal |
|---|---|---|---|---|---|---|---|---|---|---|---|---|---|---|---|---|---|---|---|---|---|---|---|
| d160 | | d180 | | d220 | | d260 | | d280 | | x240 | | x300 | | x340 | | x360 | | x400 | | x450 | | x500 | |
| I | C | I | C | I | C | I | C | I | C | I | C | I | C | I | C | I | C | I | C | I | C | I | C |
| -0.02 | -0.02 | -0.09 | -0.09 | 0.01 | 0.01 | -0.01 | -0.01 | 0.02 | 0.02 | | | | | | | 0.14 | 0.14 | 0.07 | 0.07 | -0.01 | -0.01 | 0.05 | 0.05 |
| -0.02 | -0.07 | -0.01 | -0.11 | 0.01 | 0.01 | -0.01 | -0.03 | -0.01 | 0.01 | | | | | | | 0.02 | 0.05 | 0.00 | 0.09 | 0.02 | 0.00 | 0.05 | 0.03 |
| -0.16 | -0.07 | 0.04 | -0.04 | 0.11 | 0.06 | 0.07 | 0.06 | 0.04 | 0.09 | | | | | | | 0.07 | 0.12 | -0.03 | 0.09 | 0.11 | 0.16 | 0.09 | 0.07 |
| 0.00 | -0.11 | 0.01 | -0.03 | 0.02 | 0.07 | -0.03 | 0.06 | 0.01 | 0.09 | | | | | | | 0.01 | 0.09 | 0.00 | 0.10 | 0.03 | 0.16 | 0.06 | 0.11 |
| 0.03 | -0.11 | 0.07 | 0.01 | 0.02 | 0.07 | 0.03 | 0.09 | 0.04 | 0.10 | | | | | | | 0.03 | 0.00 | 0.08 | 0.16 | 0.10 | 0.19 | 0.04 | 0.09 |
| 0.12 | -0.17 | -0.03 | 0.06 | 0.04 | 0.13 | 0.05 | 0.11 | 0.04 | 0.14 | | | | | | | 0.07 | 0.01 | 0.16 | 0.25 | 0.13 | 0.23 | 0.10 | 0.14 |
| -0.01 | -0.17 | 0.01 | 0.03 | 0.03 | 0.14 | 0.01 | 0.16 | 0.01 | 0.14 | | | | | | | 0.04 | 0.00 | 0.03 | 0.28 | 0.12 | 0.27 | 0.07 | 0.18 |
| 0.06 | -0.16 | 0.03 | 0.02 | 0.07 | 0.16 | 0.11 | 0.21 | 0.04 | 0.15 | | | | | | | 0.03 | 0.00 | 0.17 | 0.35 | 0.12 | 0.29 | 0.03 | 0.18 |
| 0.03 | -0.18 | 0.00 | 0.05 | 0.01 | 0.15 | 0.01 | 0.25 | 0.03 | 0.16 | | | | | | | 0.06 | -0.03 | 0.01 | 0.36 | 0.07 | 0.31 | 0.07 | 0.16 |
| 0.06 | -0.20 | -0.05 | 0.04 | 0.02 | 0.21 | 0.05 | 0.28 | 0.01 | 0.19 | | | | | | | 0.01 | -0.01 | 0.07 | 0.38 | 0.14 | 0.33 | 0.05 | 0.19 |
| 0.03 | 0.04 | 0.21 | 0.19 | 0.04 | 0.25 | 0.03 | 0.31 | 0.03 | 0.21 | | | | | | | 0.17 | 0.06 | 0.22 | 0.50 | 0.12 | 0.35 | 0.08 | 0.22 |
| 0.06 | 0.12 | 0.07 | 0.28 | 0.05 | 0.32 | 0.04 | 0.34 | 0.06 | 0.25 | | | | | | | 0.21 | 0.06 | 0.11 | 0.66 | 0.23 | 0.43 | 0.10 | 0.25 |
| 0.03 | 0.18 | 0.03 | 0.37 | 0.02 | 0.34 | 0.02 | 0.33 | 0.04 | 0.27 | | | | | | | 0.02 | 0.12 | 0.11 | 0.75 | 0.17 | 0.45 | 0.09 | 0.25 |
| -0.03 | 0.19 | -0.02 | 0.36 | 0.00 | 0.34 | -0.03 | 0.38 | 0.03 | 0.25 | | | | | | | 0.32 | 0.31 | 0.17 | 0.74 | 0.10 | 0.46 | 0.02 | 0.21 |
| 0.34 | 0.28 | 0.41 | 0.37 | 0.47 | 0.50 | 0.44 | 0.56 | 0.43 | 0.54 | | | | | | | 0.30 | 0.40 | 0.40 | 0.75 | 0.56 | 0.62 | 0.18 | 0.23 |
| -0.01 | 0.35 | 0.03 | 0.39 | 0.32 | 0.60 | 0.45 | 0.70 | 0.28 | 0.61 | | | | | | | 0.15 | 0.44 | 0.27 | 0.77 | 0.36 | 0.68 | 0.08 | 0.27 |

Pi = Ponding Index I = Individual C = Cumulative

Series 1 Ponding Index Data [ L = Sub-basin 2 (dx=20) ]

| Pi data (dip-oriented) | | | | | | | | | | Proximal | | Pi data (strike-oriented) | | | | | | | | | Distal |
|---|---|---|---|---|---|---|---|---|---|---|---|---|---|---|---|---|---|---|---|---|---|
| d160 | | d180 | | d220 | | d260 | | d280 | | x240 | | x300 | | x340 | | x360 | | x400 | | x450 | | x500 | |
| I | C | I | C | I | C | I | C | I | C | I | C | I | C | I | C | I | C | I | C | I | C | I | C |
| -0.04 | -0.04 | 0.00 | 0.00 | 0.01 | 0.01 | 0.00 | 0.00 | 0.04 | 0.04 | | | | | | | 0.12 | 0.12 | 0.10 | 0.10 | 0.06 | 0.06 | 0.03 | 0.03 |
| 0.07 | -0.02 | 0.00 | -0.02 | 0.01 | 0.03 | 0.01 | 0.01 | 0.00 | 0.03 | | | | | | | 0.07 | 0.08 | 0.04 | 0.14 | 0.05 | 0.08 | -0.01 | 0.03 |
| -0.01 | -0.05 | -0.18 | -0.07 | 0.01 | 0.12 | 0.16 | 0.08 | 0.05 | 0.10 | | | | | | | 0.13 | 0.10 | 0.08 | 0.22 | 0.21 | 0.24 | 0.07 | 0.11 |
| -0.03 | -0.06 | -0.02 | -0.08 | 0.01 | 0.10 | 0.00 | 0.09 | 0.01 | 0.11 | | | | | | | 0.03 | 0.12 | 0.05 | 0.27 | 0.00 | 0.26 | 0.03 | 0.11 |
| 0.01 | -0.02 | -0.02 | -0.10 | 0.00 | 0.13 | 0.03 | 0.13 | 0.02 | 0.11 | | | | | | | 0.03 | 0.00 | 0.04 | 0.35 | 0.06 | 0.29 | 0.05 | 0.12 |
| -0.03 | -0.03 | -0.02 | -0.16 | 0.03 | 0.15 | 0.07 | 0.16 | 0.06 | 0.17 | | | | | | | -0.01 | -0.31 | 0.03 | 0.46 | 0.06 | 0.36 | 0.04 | 0.16 |
| -0.01 | -0.02 | 0.00 | -0.19 | 0.03 | 0.17 | 0.04 | 0.18 | 0.03 | 0.17 | | | | | | | 0.00 | -0.43 | 0.03 | 0.50 | 0.08 | 0.35 | 0.07 | 0.20 |
| -0.02 | -0.05 | -0.05 | -0.20 | 0.02 | 0.15 | 0.10 | 0.24 | 0.10 | 0.18 | | | | | | | 0.02 | -0.45 | 0.24 | 0.59 | 0.10 | 0.37 | 0.00 | 0.18 |
| 0.05 | -0.15 | -0.01 | -0.23 | 0.01 | 0.18 | -0.01 | 0.25 | 0.00 | 0.18 | | | | | | | 0.02 | -0.59 | 0.06 | 0.62 | 0.08 | 0.37 | 0.03 | 0.18 |
| 0.04 | -0.02 | -0.01 | -0.27 | 0.02 | 0.22 | 0.03 | 0.28 | 0.03 | 0.21 | | | | | | | 0.03 | -0.67 | 0.03 | 0.58 | 0.11 | 0.38 | 0.05 | 0.21 |
| 0.25 | 0.08 | 0.24 | 0.19 | -0.01 | 0.23 | 0.07 | 0.32 | 0.02 | 0.24 | | | | | | | 0.03 | -0.05 | 0.22 | 0.68 | 0.17 | 0.39 | 0.07 | 0.25 |
| -0.02 | 0.12 | 0.09 | 0.25 | 0.05 | 0.26 | 0.04 | 0.35 | 0.01 | 0.27 | | | | | | | 0.11 | 0.07 | 0.14 | 0.81 | 0.12 | 0.44 | 0.07 | 0.26 |
| 0.09 | 0.18 | 0.01 | 0.30 | 0.03 | 0.29 | 0.03 | 0.37 | 0.05 | 0.31 | | | | | | | 0.13 | 0.12 | 0.10 | 0.88 | 0.11 | 0.48 | 0.08 | 0.25 |
| -0.05 | 0.14 | -0.15 | 0.37 | 0.00 | 0.26 | 0.01 | 0.40 | 0.05 | 0.29 | | | | | | | 0.08 | -0.01 | 0.12 | 0.81 | 0.13 | 0.49 | -0.02 | 0.23 |
| 0.22 | 0.26 | 0.25 | 0.39 | 0.45 | 0.58 | 0.50 | 0.58 | 0.55 | 0.57 | | | | | | | 0.29 | 0.24 | 0.41 | 0.76 | 0.56 | 0.62 | 0.14 | 0.24 |
| 0.01 | 0.28 | 0.01 | 0.44 | 0.27 | 0.58 | 0.45 | 0.72 | 0.41 | 0.64 | | | | | | | 0.09 | 0.32 | 0.29 | 0.75 | 0.38 | 0.76 | 0.06 | 0.26 |

Pi = Ponding Index I = Individual C = Cumulative

Series 1 Ponding Index Data [ L = Sub-basin 2 (dx=50) ]

| Pi data (dip-oriented) | | | | | | | | | | Proximal | | Pi data (strike-oriented) | | | | | | | | | Distal |
|---|---|---|---|---|---|---|---|---|---|---|---|---|---|---|---|---|---|---|---|---|---|
| d160 | | d180 | | d220 | | d260 | | d280 | | x240 | | x300 | | x340 | | x360 | | x400 | | x450 | | x500 | |
| I | C | I | C | I | C | I | C | I | C | I | C | I | C | I | C | I | C | I | C | I | C | I | C |
| 0.01 | 0.01 | -0.04 | -0.04 | 0.00 | 0.00 | 0.01 | 0.01 | 0.02 | 0.02 | | | | | | | 0.07 | 0.07 | 0.03 | 0.03 | 0.02 | 0.02 | 0.00 | 0.00 |
| 0.02 | 0.01 | 0.01 | -0.06 | 0.00 | 0.00 | 0.00 | 0.01 | 0.00 | 0.02 | | | | | | | 0.03 | 0.15 | 0.02 | 0.05 | 0.01 | 0.03 | 0.01 | -0.01 |
| 0.00 | 0.03 | -0.04 | -0.07 | 0.01 | 0.03 | 0.14 | 0.14 | 0.03 | 0.05 | | | | | | | 0.05 | 0.19 | 0.03 | 0.06 | 0.12 | 0.14 | 0.00 | 0.01 |
| 0.01 | 0.04 | 0.00 | -0.07 | -0.01 | 0.03 | 0.01 | 0.15 | 0.02 | 0.05 | | | | | | | 0.03 | 0.20 | 0.02 | 0.07 | 0.03 | 0.15 | 0.01 | -0.01 |
| 0.02 | 0.05 | -0.01 | -0.08 | 0.03 | 0.06 | 0.01 | 0.17 | 0.02 | 0.09 | | | | | | | -0.10 | 0.18 | 0.09 | 0.11 | 0.04 | 0.17 | 0.05 | 0.03 |
| 0.06 | 0.05 | 0.02 | -0.09 | 0.04 | 0.09 | 0.05 | 0.21 | 0.04 | 0.13 | | | | | | | -0.03 | 0.17 | 0.10 | 0.19 | 0.07 | 0.22 | 0.04 | 0.08 |
| -0.03 | 0.05 | -0.01 | -0.09 | 0.03 | 0.11 | 0.05 | 0.23 | 0.03 | 0.16 | | | | | | | -0.02 | 0.18 | 0.07 | 0.23 | 0.05 | 0.24 | 0.03 | 0.10 |
| -0.01 | 0.04 | 0.02 | -0.09 | 0.01 | 0.13 | 0.02 | 0.28 | 0.05 | 0.20 | | | | | | | -0.05 | 0.15 | 0.04 | 0.26 | 0.10 | 0.29 | -0.06 | 0.11 |
| 0.00 | 0.05 | -0.02 | -0.09 | 0.03 | 0.14 | 0.01 | 0.29 | 0.02 | 0.21 | | | | | | | 0.01 | 0.14 | 0.07 | 0.28 | 0.04 | 0.30 | 0.03 | 0.13 |
| -0.03 | 0.08 | 0.01 | -0.12 | 0.05 | 0.17 | 0.03 | 0.31 | 0.02 | 0.23 | | | | | | | 0.00 | 0.15 | 0.06 | 0.33 | 0.04 | 0.32 | 0.05 | 0.16 |
| 0.13 | 0.17 | 0.31 | 0.17 | 0.02 | 0.20 | 0.01 | 0.35 | 0.03 | 0.25 | | | | | | | 0.05 | 0.26 | 0.27 | 0.47 | 0.12 | 0.37 | 0.05 | 0.18 |
| 0.10 | 0.22 | 0.16 | 0.23 | 0.07 | 0.24 | 0.04 | 0.38 | 0.05 | 0.27 | | | | | | | 0.11 | 0.32 | 0.07 | 0.54 | 0.07 | 0.40 | 0.07 | 0.23 |
| 0.08 | 0.27 | 0.06 | 0.28 | 0.03 | 0.26 | 0.04 | 0.40 | 0.06 | 0.31 | | | | | | | 0.08 | 0.33 | 0.09 | 0.60 | 0.00 | 0.42 | 0.06 | 0.27 |
| 0.01 | 0.26 | 0.22 | 0.34 | 0.04 | 0.23 | 0.01 | 0.41 | 0.00 | 0.34 | | | | | | | -0.01 | 0.47 | 0.05 | 0.60 | 0.12 | 0.44 | -0.04 | 0.24 |
| 0.09 | 0.34 | 0.49 | 0.43 | 0.34 | 0.60 | 0.43 | 0.62 | 0.41 | 0.60 | | | | | | | 0.16 | 0.39 | 0.51 | 0.63 | 0.34 | 0.60 | 0.08 | 0.28 |
| -0.01 | 0.37 | 0.07 | 0.47 | 0.29 | 0.63 | 0.44 | 0.71 | 0.34 | 0.67 | | | | | | | 0.06 | 0.34 | 0.03 | 0.72 | 0.43 | 0.73 | 0.06 | 0.31 |

Pi = Ponding Index I = Individual C = Cumulative

Series 1 Ponding Index Data [ L = Sub-basin 2 (dx=100) ]

| Pi data (dip-oriented) | | | | | | | | | | Proximal | | Pi data (strike-oriented) | | | | | | | | | Distal |
|---|---|---|---|---|---|---|---|---|---|---|---|---|---|---|---|---|---|---|---|---|---|
| d160 | | d180 | | d220 | | d260 | | d280 | | x240 | | x300 | | x340 | | x360 | | x400 | | x450 | | x500 | |
| I | C | I | C | I | C | I | C | I | C | I | C | I | C | I | C | I | C | I | C | I | C | I | C |
| 0.00 | 0.00 | 0.00 | 0.00 | 0.00 | 0.00 | 0.01 | 0.01 | 0.01 | 0.01 | | | | | | | -0.03 | -0.03 | 0.03 | 0.03 | 0.02 | 0.02 | 0.04 | 0.04 |
| -0.01 | 0.01 | 0.00 | -0.01 | -0.03 | 0.00 | 0.01 | 0.02 | -0.01 | 0.00 | | | | | | | 0.00 | -0.06 | 0.01 | 0.04 | 0.00 | 0.02 | 0.03 | 0.08 |
| 0.00 | 0.01 | 0.04 | -0.02 | 0.06 | 0.04 | 0.10 | 0.13 | 0.02 | 0.04 | | | | | | | 0.07 | -0.06 | 0.04 | 0.09 | 0.13 | 0.15 | 0.04 | 0.12 |
| -0.04 | 0.01 | -0.06 | -0.01 | 0.00 | 0.05 | 0.02 | 0.14 | 0.01 | 0.05 | | | | | | | 0.00 | -0.02 | 0.02 | 0.10 | 0.01 | 0.15 | 0.02 | 0.15 |
| 0.02 | 0.04 | 0.01 | -0.01 | 0.05 | 0.07 | -0.03 | 0.21 | 0.04 | 0.05 | | | | | | | -0.08 | -0.09 | 0.06 | 0.14 | 0.03 | 0.17 | 0.05 | 0.17 |
| 0.01 | 0.06 | -0.03 | -0.01 | 0.04 | 0.10 | 0.05 | 0.25 | 0.06 | 0.12 | | | | | | | -0.01 | -0.05 | 0.22 | 0.21 | 0.06 | 0.22 | 0.06 | 0.23 |
| 0.01 | 0.07 | -0.02 | 0.01 | 0.02 | 0.12 | 0.04 | 0.29 | 0.06 | 0.16 | | | | | | | 0.01 | -0.03 | 0.06 | 0.25 | 0.04 | 0.25 | 0.03 | 0.26 |
| 0.02 | 0.07 | 0.00 | 0.01 | 0.03 | 0.13 | 0.02 | 0.34 | 0.04 | 0.19 | | | | | | | 0.01 | -0.18 | 0.05 | 0.27 | 0.05 | 0.27 | 0.03 | 0.25 |
| -0.01 | 0.09 | 0.00 | 0.00 | 0.03 | 0.15 | 0.02 | 0.35 | 0.01 | 0.20 | | | | | | | 0.00 | -0.15 | 0.03 | 0.29 | 0.02 | 0.29 | 0.04 | 0.29 |
| 0.01 | 0.10 | 0.04 | 0.02 | 0.04 | 0.17 | 0.03 | 0.37 | 0.03 | 0.24 | | | | | | | -0.03 | -0.13 | 0.11 | 0.33 | 0.04 | 0.31 | 0.02 | 0.33 |
| 0.18 | 0.19 | 0.03 | 0.13 | 0.02 | 0.19 | 0.07 | 0.44 | 0.02 | 0.27 | | | | | | | 0.05 | -0.03 | 0.28 | 0.32 | 0.06 | 0.33 | 0.05 | 0.36 |
| 0.08 | 0.21 | 0.04 | 0.18 | 0.06 | 0.23 | 0.02 | 0.48 | 0.06 | 0.31 | | | | | | | 0.04 | -0.01 | 0.14 | 0.35 | 0.08 | 0.37 | 0.03 | 0.41 |
| 0.04 | 0.25 | 0.04 | 0.23 | 0.04 | 0.26 | 0.04 | 0.52 | 0.03 | 0.37 | | | | | | | 0.12 | 0.07 | 0.12 | 0.38 | 0.04 | 0.39 | 0.04 | 0.47 |
| -0.02 | 0.22 | 0.02 | 0.25 | 0.02 | 0.26 | 0.02 | 0.52 | 0.02 | 0.37 | | | | | | | 0.31 | 0.26 | -0.11 | 0.35 | 0.07 | 0.41 | -0.04 | 0.41 |
| 0.01 | 0.22 | 0.25 | 0.37 | 0.36 | 0.49 | 0.40 | 0.69 | 0.36 | 0.65 | | | | | | | -0.04 | 0.37 | 0.32 | 0.43 | 0.49 | 0.58 | 0.06 | 0.48 |
| 0.06 | 0.23 | 0.08 | 0.41 | 0.24 | 0.56 | 0.49 | 0.77 | 0.33 | 0.74 | | | | | | | 0.06 | 0.36 | 0.03 | 0.48 | 0.27 | 0.64 | 0.07 | 0.52 |

Pi = Ponding Index I = Individual C = Cumulative

Series 1 Ponding Index Data [ L = Whole Basin (dx=2) ]

| Pi data (dip-oriented) | | | | | | | | | | Proximal | | Pi data (strike-oriented) | | | | | | | | | Distal |
|---|---|---|---|---|---|---|---|---|---|---|---|---|---|---|---|---|---|---|---|---|---|
| d160 | | d180 | | d220 | | d260 | | d280 | | x240 | | x300 | | x340 | | x360 | | x400 | | x450 | | x500 | |
| I | C | I | C | I | C | I | C | I | C | I | C | I | C | I | C | I | C | I | C | I | C | I | C |
| 0.20 | 0.20 | -0.09 | -0.09 | 0.00 | 0.00 | 0.05 | 0.05 | -0.05 | -0.05 | 0.43 | 0.43 | 0.33 | 0.33 | 0.26 | 0.26 | 0.07 | 0.07 | 0.11 | 0.11 | 0.07 | 0.07 | 0.20 | 0.20 |
| 0.17 | 0.20 | 0.03 | -0.24 | 0.10 | 0.09 | 0.01 | 0.00 | 0.01 | -0.04 | 0.05 | 0.36 | 0.18 | 0.35 | 0.14 | 0.33 | 0.25 | 0.13 | 0.07 | 0.10 | 0.05 | 0.08 | 0.23 | 0.23 |
| 0.04 | 0.27 | -0.01 | -0.15 | 0.13 | 0.09 | 0.06 | 0.18 | 0.08 | -0.02 | 0.39 | 0.35 | 0.33 | 0.31 | 0.03 | 0.46 | 0.21 | 0.18 | 0.35 | 0.28 | 0.26 | 0.26 | 0.34 | 0.27 |
| 0.07 | 0.32 | 0.02 | -0.12 | 0.04 | 0.12 | 0.07 | 0.16 | 0.05 | -0.04 | 0.32 | 0.33 | 0.35 | 0.31 | 0.18 | 0.39 | 0.29 | 0.26 | 0.16 | 0.30 | 0.13 | 0.25 | 0.32 | 0.27 |
| 0.07 | 0.35 | 0.11 | 0.00 | 0.04 | 0.17 | 0.04 | 0.16 | 0.05 | -0.09 | 0.49 | 0.43 | 0.57 | 0.37 | 0.20 | 0.28 | 0.18 | 0.17 | 0.07 | 0.28 | 0.26 | 0.28 | 0.37 | 0.24 |
| 0.05 | 0.45 | 0.06 | 0.09 | -0.02 | 0.27 | 0.02 | 0.23 | 0.14 | 0.12 | 0.41 | 0.54 | 0.57 | 0.47 | 0.16 | 0.12 | 0.31 | 0.23 | 0.18 | 0.37 | 0.24 | 0.30 | 0.35 | 0.35 |
| 0.04 | 0.49 | 0.04 | 0.16 | -0.03 | 0.29 | -0.02 | 0.26 | 0.12 | 0.15 | 0.50 | 0.51 | 0.49 | 0.53 | 0.09 | 0.12 | 0.29 | 0.20 | 0.24 | 0.35 | 0.17 | 0.32 | 0.39 | 0.37 |
| 0.14 | 0.50 | 0.01 | 0.22 | 0.00 | 0.28 | 0.03 | 0.27 | 0.03 | 0.20 | 0.56 | 0.59 | 0.45 | 0.60 | 0.12 | 0.21 | 0.24 | 0.27 | 0.19 | 0.38 | 0.22 | 0.34 | 0.37 | 0.45 |
| 0.13 | 0.48 | 0.06 | 0.19 | 0.01 | 0.30 | 0.02 | 0.30 | 0.05 | 0.22 | 0.50 | 0.61 | 0.33 | 0.61 | 0.16 | 0.26 | 0.19 | 0.18 | 0.22 | 0.43 | 0.27 | 0.37 | 0.33 | 0.35 |
| 0.08 | 0.56 | 0.02 | 0.18 | -0.01 | 0.26 | 0.05 | 0.30 | 0.01 | 0.19 | 0.44 | 0.65 | 0.36 | 0.65 | 0.25 | 0.43 | 0.26 | 0.19 | 0.25 | 0.37 | 0.16 | 0.37 | 0.39 | 0.36 |
| 0.17 | 0.53 | 0.03 | 0.33 | 0.07 | 0.30 | 0.03 | 0.30 | 0.02 | 0.27 | 0.30 | 0.64 | 0.36 | 0.69 | 0.41 | 0.45 | 0.38 | 0.37 | 0.39 | 0.37 | 0.22 | 0.40 | 0.43 | 0.40 |
| 0.03 | 0.57 | 0.12 | 0.31 | 0.04 | 0.26 | 0.01 | 0.34 | 0.08 | 0.29 | 0.59 | 0.68 | 0.40 | 0.68 | 0.28 | 0.57 | 0.35 | 0.48 | 0.40 | 0.45 | 0.30 | 0.37 | 0.40 | 0.40 |
| 0.08 | 0.60 | 0.01 | 0.33 | 0.03 | 0.28 | 0.05 | 0.32 | 0.03 | 0.29 | 0.52 | 0.64 | 0.45 | 0.76 | 0.37 | 0.61 | 0.31 | 0.53 | 0.38 | 0.49 | 0.24 | 0.45 | 0.54 | 0.41 |
| 0.09 | 0.58 | 0.05 | 0.25 | 0.07 | 0.29 | 0.00 | 0.34 | -0.03 | 0.28 | 0.68 | 0.65 | 0.16 | 0.87 | 0.33 | 0.64 | 0.20 | 0.39 | 0.39 | 0.49 | 0.25 | 0.48 | 0.46 | 0.46 |
| 0.22 | 0.53 | 0.20 | 0.54 | 0.20 | 0.37 | 0.20 | 0.45 | 0.21 | 0.37 | 0.47 | 0.81 | 0.60 | 0.76 | 0.66 | 0.68 | 0.52 | 0.59 | 0.59 | 0.67 | 0.53 | 0.58 | 0.54 | 0.39 |
| 0.08 | 0.57 | 0.18 | 0.43 | 0.19 | 0.43 | 0.21 | 0.43 | 0.20 | 0.40 | 0.44 | 0.75 | 0.46 | 0.77 | 0.59 | 0.67 | 0.32 | 0.56 | 0.45 | 0.67 | 0.48 | 0.65 | 0.39 | 0.43 |

Pi = Ponding Index I = Individual C = Cumulative

Series 1 Ponding Index Data [ L = Whole Basin (dx=4) ]

| Pi data (dip-oriented) | | | | | | | | | | Proximal | | Pi data (strike-oriented) | | | | | | | | | | Distal | |
|---|---|---|---|---|---|---|---|---|---|---|---|---|---|---|---|---|---|---|---|---|---|---|---|
| d160 | | d180 | | d220 | | d260 | | d280 | | x240 | | x300 | | x340 | | x360 | | x400 | | x450 | | x500 | |
| I | C | I | C | I | C | I | C | I | C | I | C | I | C | I | C | I | C | I | C | I | C | I | C |
| -0.04 | -0.04 | 0.01 | 0.01 | 0.12 | 0.12 | 0.01 | 0.01 | 0.09 | 0.09 | 0.21 | 0.21 | 0.30 | 0.30 | 0.37 | 0.37 | 0.03 | 0.03 | 0.09 | 0.09 | 0.07 | 0.07 | 0.11 | 0.11 |
| 0.07 | 0.12 | 0.08 | -0.01 | 0.06 | 0.09 | 0.00 | -0.01 | -0.03 | 0.06 | -0.08 | 0.16 | 0.12 | 0.39 | 0.08 | 0.52 | 0.07 | 0.04 | 0.08 | 0.13 | 0.01 | 0.07 | 0.08 | 0.13 |
| 0.02 | 0.06 | 0.06 | 0.08 | 0.05 | 0.03 | 0.07 | 0.06 | 0.03 | 0.10 | 0.30 | 0.28 | 0.24 | 0.28 | 0.08 | 0.69 | 0.17 | 0.00 | 0.26 | 0.16 | 0.25 | 0.20 | 0.23 | 0.22 |
| 0.01 | 0.15 | 0.07 | 0.08 | 0.04 | 0.00 | 0.02 | 0.05 | 0.01 | 0.08 | 0.23 | 0.28 | 0.16 | 0.24 | -0.01 | 0.77 | -0.01 | -0.01 | 0.04 | 0.16 | 0.10 | 0.22 | 0.18 | 0.21 |
| 0.04 | 0.08 | -0.02 | 0.11 | 0.01 | 0.01 | 0.03 | 0.06 | 0.06 | 0.05 | 0.33 | 0.28 | 0.44 | 0.40 | 0.02 | 0.97 | 0.07 | 0.08 | 0.11 | 0.22 | 0.15 | 0.21 | 0.16 | 0.19 |
| -0.12 | 0.12 | -0.04 | 0.14 | -0.05 | 0.10 | 0.00 | 0.11 | 0.13 | 0.17 | 0.21 | 0.43 | 0.53 | 0.57 | 0.06 | 0.82 | 0.15 | 0.12 | 0.13 | 0.30 | 0.10 | 0.26 | 0.21 | 0.30 |
| 0.01 | 0.11 | 0.02 | 0.20 | -0.02 | 0.16 | 0.03 | 0.16 | 0.04 | 0.22 | 0.44 | 0.48 | 0.40 | 0.58 | 0.04 | 0.80 | 0.10 | 0.09 | 0.04 | 0.29 | 0.09 | 0.30 | 0.24 | 0.31 |
| 0.05 | -0.01 | 0.03 | 0.25 | 0.03 | 0.14 | 0.02 | 0.23 | 0.02 | 0.28 | 0.40 | 0.53 | 0.31 | 0.69 | 0.10 | 0.58 | 0.12 | 0.17 | 0.22 | 0.33 | 0.13 | 0.32 | 0.16 | 0.31 |
| 0.06 | -0.12 | 0.04 | 0.24 | -0.01 | 0.13 | -0.02 | 0.22 | -0.02 | 0.31 | 0.15 | 0.61 | 0.19 | 0.71 | 0.06 | 0.59 | 0.15 | 0.12 | 0.16 | 0.35 | 0.17 | 0.32 | 0.18 | 0.31 |
| 0.03 | 0.10 | 0.06 | 0.16 | 0.00 | 0.13 | 0.01 | 0.27 | -0.01 | 0.30 | 0.22 | 0.59 | 0.23 | 0.78 | 0.03 | 0.52 | 0.17 | 0.19 | 0.17 | 0.38 | 0.13 | 0.34 | 0.18 | 0.32 |
| 0.12 | 0.13 | 0.09 | 0.44 | 0.10 | 0.26 | 0.01 | 0.28 | 0.01 | 0.40 | 0.18 | 0.64 | 0.22 | 0.84 | 0.11 | 0.27 | 0.26 | 0.16 | 0.23 | 0.38 | 0.20 | 0.37 | 0.19 | 0.32 |
| -0.09 | 0.19 | 0.05 | 0.45 | -0.05 | 0.26 | 0.01 | 0.30 | 0.05 | 0.38 | 0.49 | 0.71 | 0.27 | 0.80 | 0.18 | 0.62 | 0.25 | 0.21 | 0.27 | 0.44 | 0.27 | 0.44 | 0.24 | 0.33 |
| 0.00 | 0.17 | -0.02 | 0.47 | 0.01 | 0.29 | -0.01 | 0.30 | 0.04 | 0.39 | 0.49 | 0.76 | 0.15 | 0.82 | 0.25 | 0.70 | 0.20 | 0.22 | 0.17 | 0.50 | 0.18 | 0.45 | 0.24 | 0.44 |
| 0.00 | 0.20 | 0.02 | 0.43 | -0.07 | 0.23 | 0.00 | 0.31 | -0.11 | 0.38 | 0.36 | 0.78 | -0.20 | 0.86 | 0.21 | 0.76 | 0.00 | 0.26 | 0.18 | 0.50 | 0.20 | 0.46 | 0.23 | 0.33 |
| 0.10 | 0.61 | 0.21 | 0.67 | 0.22 | 0.39 | 0.20 | 0.42 | 0.19 | 0.49 | 0.25 | 0.80 | 0.36 | 0.78 | 0.58 | 0.80 | 0.35 | 0.38 | 0.49 | 0.73 | 0.60 | 0.62 | 0.32 | 0.40 |
| -0.06 | 0.64 | 0.05 | 0.61 | 0.16 | 0.42 | 0.20 | 0.45 | 0.16 | 0.53 | 0.15 | 0.79 | 0.42 | 0.79 | 0.23 | 0.75 | 0.13 | 0.39 | 0.32 | 0.73 | 0.42 | 0.68 | 0.21 | 0.45 |

Pi = Ponding Index I = Individual C = Cumulative

Series 1 Ponding Index Data [ L = Whole basin (dx=10) ]

| Pi data (dip-oriented) | | | | | | | | | | Proximal | | Pi data (strike-oriented) | | | | | | | | | | Distal | |
|---|---|---|---|---|---|---|---|---|---|---|---|---|---|---|---|---|---|---|---|---|---|---|---|
| d160 | | d180 | | d220 | | d260 | | d280 | | x240 | | x300 | | x340 | | x360 | | x400 | | x450 | | x500 | |
| I | C | I | C | I | C | I | C | I | C | I | C | I | C | I | C | I | C | I | C | I | C | I | C |
| 0.03 | 0.03 | -0.01 | -0.01 | 0.08 | 0.08 | -0.03 | -0.03 | 0.01 | 0.01 | 0.10 | 0.10 | 0.27 | 0.27 | -0.24 | -0.24 | 0.14 | 0.14 | 0.07 | 0.07 | -0.01 | -0.01 | 0.05 | 0.05 |
| -0.01 | 0.01 | -0.11 | 0.01 | 0.09 | 0.10 | -0.05 | 0.04 | 0.00 | -0.01 | -0.16 | 0.09 | 0.01 | 0.33 | 0.01 | -0.24 | 0.02 | 0.05 | 0.00 | 0.09 | 0.02 | 0.00 | 0.05 | 0.03 |
| -0.09 | 0.02 | 0.04 | 0.13 | 0.03 | 0.14 | 0.03 | 0.10 | 0.00 | 0.04 | 0.31 | 0.20 | 0.17 | 0.22 | -0.01 | -0.26 | 0.07 | 0.12 | -0.03 | 0.09 | 0.11 | 0.16 | 0.09 | 0.07 |
| -0.01 | 0.01 | 0.00 | 0.12 | 0.02 | 0.14 | -0.01 | 0.11 | 0.02 | 0.04 | 0.13 | 0.21 | 0.08 | 0.28 | -0.05 | -0.27 | 0.01 | 0.09 | 0.00 | 0.10 | 0.03 | 0.16 | 0.06 | 0.11 |
| 0.05 | 0.00 | 0.00 | 0.18 | 0.05 | 0.15 | 0.07 | 0.15 | 0.04 | 0.07 | 0.34 | 0.30 | 0.64 | 0.53 | 0.39 | 0.26 | 0.03 | 0.00 | 0.08 | 0.16 | 0.10 | 0.19 | 0.04 | 0.09 |
| 0.08 | 0.01 | -0.13 | 0.25 | -0.08 | 0.24 | 0.02 | 0.15 | 0.10 | 0.14 | 0.32 | 0.35 | 0.53 | 0.72 | -0.09 | 0.30 | 0.07 | 0.01 | 0.16 | 0.25 | 0.13 | 0.23 | 0.10 | 0.14 |
| -0.04 | -0.01 | 0.03 | 0.26 | -0.02 | 0.26 | 0.03 | 0.18 | 0.00 | 0.16 | 0.37 | 0.46 | 0.27 | 0.81 | -0.07 | 0.28 | 0.04 | 0.00 | 0.03 | 0.28 | 0.12 | 0.27 | 0.07 | 0.18 |
| 0.05 | -0.04 | 0.05 | 0.30 | 0.01 | 0.26 | -0.04 | 0.23 | 0.01 | 0.21 | 0.05 | 0.55 | -0.04 | 0.93 | 0.13 | 0.40 | 0.03 | 0.00 | 0.17 | 0.35 | 0.12 | 0.29 | 0.03 | 0.18 |
| 0.03 | -0.03 | -0.01 | 0.33 | -0.03 | 0.24 | -0.01 | 0.25 | 0.00 | 0.20 | 0.11 | 0.54 | 0.09 | 0.85 | -0.11 | 0.39 | 0.06 | -0.03 | 0.01 | 0.36 | 0.07 | 0.31 | 0.07 | 0.16 |
| 0.07 | 0.02 | -0.06 | 0.25 | -0.03 | 0.24 | 0.01 | 0.29 | -0.02 | 0.22 | 0.30 | 0.54 | 0.08 | 0.94 | 0.09 | 0.28 | 0.01 | -0.01 | 0.07 | 0.38 | 0.14 | 0.33 | 0.05 | 0.19 |
| 0.00 | 0.16 | 0.10 | 0.36 | 0.09 | 0.29 | 0.00 | 0.31 | 0.02 | 0.24 | 0.02 | 0.54 | 0.12 | 1.01 | 0.21 | 0.35 | 0.17 | 0.06 | 0.22 | 0.50 | 0.12 | 0.35 | 0.08 | 0.22 |
| -0.01 | 0.25 | 0.01 | 0.38 | -0.03 | 0.33 | 0.01 | 0.34 | 0.06 | 0.29 | 0.37 | 0.72 | 0.23 | 1.03 | 0.10 | 0.65 | 0.21 | 0.06 | 0.11 | 0.66 | 0.23 | 0.43 | 0.10 | 0.25 |
| 0.00 | 0.31 | -0.02 | 0.45 | 0.00 | 0.35 | 0.00 | 0.36 | 0.01 | 0.31 | 0.29 | 0.74 | 0.08 | 1.03 | 0.12 | 0.72 | 0.02 | 0.12 | 0.11 | 0.75 | 0.17 | 0.45 | 0.09 | 0.25 |
| -0.03 | 0.32 | -0.04 | 0.39 | -0.02 | 0.34 | -0.03 | 0.42 | -0.08 | 0.27 | 0.11 | 0.78 | -0.23 | 1.08 | 0.14 | 0.76 | 0.32 | 0.31 | 0.17 | 0.74 | 0.10 | 0.46 | 0.02 | 0.21 |
| 0.21 | 0.54 | 0.22 | 0.74 | 0.24 | 0.43 | 0.22 | 0.51 | 0.22 | 0.41 | 0.04 | 0.72 | 0.25 | 0.85 | 0.48 | 0.86 | 0.30 | 0.40 | 0.40 | 0.75 | 0.56 | 0.62 | 0.18 | 0.23 |
| -0.02 | 0.62 | 0.01 | 0.74 | 0.16 | 0.52 | 0.21 | 0.59 | 0.14 | 0.45 | 0.17 | 0.73 | 0.13 | 0.94 | 0.19 | 0.81 | 0.15 | 0.44 | 0.27 | 0.77 | 0.36 | 0.68 | 0.08 | 0.27 |

Pi = Ponding Index  I = Individual  C = Cumulative

Series 1 Ponding Index Data [ L = Whole Basin (dx=20) ]

| Pi data (dip-oriented) | | | | | | | | | | Proximal | | Pi data (strike-oriented) | | | | | | | | | | Distal | |
|---|---|---|---|---|---|---|---|---|---|---|---|---|---|---|---|---|---|---|---|---|---|---|---|
| d160 | | d180 | | d220 | | d260 | | d280 | | x240 | | x300 | | x340 | | x360 | | x400 | | x450 | | x500 | |
| I | C | I | C | I | C | I | C | I | C | I | C | I | C | I | C | I | C | I | C | I | C | I | C |
| -0.04 | -0.04 | -0.08 | -0.08 | 0.02 | 0.02 | 0.00 | 0.00 | 0.01 | 0.01 | 0.04 | 0.04 | -0.39 | -0.39 | 0.19 | 0.19 | 0.12 | 0.12 | 0.10 | 0.10 | 0.06 | 0.06 | 0.03 | 0.03 |
| 0.04 | -0.05 | 0.00 | -0.10 | 0.02 | 0.05 | -0.02 | 0.04 | -0.01 | -0.03 | 0.06 | -0.01 | -0.05 | -0.44 | 0.07 | 0.23 | 0.07 | 0.08 | 0.04 | 0.14 | 0.05 | 0.08 | -0.01 | 0.03 |
| 0.00 | -0.08 | -0.05 | -0.03 | 0.03 | 0.12 | 0.07 | 0.10 | 0.03 | 0.04 | 0.53 | 0.14 | 0.19 | -0.04 | 0.08 | 0.39 | 0.13 | 0.10 | 0.08 | 0.22 | 0.21 | 0.24 | 0.07 | 0.11 |
| -0.01 | -0.09 | -0.02 | -0.03 | 0.00 | 0.13 | 0.00 | 0.11 | 0.01 | 0.03 | 0.09 | 0.18 | 0.08 | -0.03 | 0.06 | 0.43 | 0.03 | 0.12 | 0.05 | 0.27 | 0.00 | 0.26 | 0.03 | 0.11 |
| 0.07 | -0.03 | 0.05 | -0.02 | 0.04 | 0.20 | 0.06 | 0.20 | 0.01 | 0.03 | 0.33 | 0.25 | 0.67 | 0.56 | 0.14 | 0.37 | 0.03 | 0.00 | 0.04 | 0.35 | 0.06 | 0.29 | 0.05 | 0.12 |
| -0.03 | 0.10 | -0.02 | 0.00 | -0.03 | 0.25 | 0.01 | 0.21 | 0.08 | 0.16 | 0.29 | 0.36 | 0.59 | 0.62 | -0.14 | 0.31 | -0.01 | -0.31 | 0.03 | 0.46 | 0.06 | 0.36 | 0.04 | 0.16 |
| -0.02 | 0.09 | 0.02 | 0.01 | -0.05 | 0.27 | 0.03 | 0.24 | -0.06 | 0.21 | 0.48 | 0.41 | 0.13 | 0.87 | -0.04 | 0.31 | 0.00 | -0.43 | 0.03 | 0.50 | 0.08 | 0.35 | 0.07 | 0.20 |
| 0.00 | 0.00 | 0.05 | 0.13 | 0.03 | 0.26 | -0.08 | 0.31 | 0.02 | 0.24 | 0.30 | 0.49 | -0.22 | 1.01 | -0.02 | 0.16 | 0.02 | -0.45 | 0.24 | 0.59 | 0.10 | 0.37 | 0.00 | 0.18 |
| 0.00 | -0.03 | -0.03 | 0.10 | 0.02 | 0.26 | -0.01 | 0.32 | -0.02 | 0.24 | 0.15 | 0.50 | -0.09 | 0.96 | 0.05 | 0.15 | 0.02 | -0.59 | 0.06 | 0.62 | 0.08 | 0.37 | 0.03 | 0.18 |
| -0.01 | 0.15 | -0.02 | 0.15 | -0.02 | 0.24 | 0.00 | 0.34 | -0.05 | 0.26 | 0.02 | 0.52 | 0.10 | 1.04 | -0.02 | 0.23 | 0.03 | -0.67 | 0.03 | 0.58 | 0.11 | 0.38 | 0.05 | 0.21 |
| 0.13 | 0.20 | 0.12 | 0.40 | 0.05 | 0.14 | 0.03 | 0.37 | 0.00 | 0.31 | -0.08 | 0.51 | 0.29 | 1.11 | 0.20 | 0.31 | 0.03 | -0.05 | 0.22 | 0.68 | 0.17 | 0.39 | 0.07 | 0.25 |
| -0.05 | 0.40 | 0.01 | 0.45 | 0.01 | 0.12 | 0.01 | 0.39 | 0.02 | 0.36 | 0.23 | 0.58 | 0.27 | 1.05 | 0.09 | 0.33 | 0.11 | 0.07 | 0.14 | 0.81 | 0.12 | 0.44 | 0.07 | 0.26 |
| 0.04 | 0.51 | 0.00 | 0.51 | 0.01 | 0.13 | 0.01 | 0.42 | -0.02 | 0.35 | 0.23 | 0.71 | 0.10 | 1.06 | 0.10 | 0.43 | 0.13 | 0.12 | 0.10 | 0.88 | 0.11 | 0.48 | 0.08 | 0.25 |
| -0.03 | 0.50 | -0.08 | 0.49 | -0.02 | 0.11 | -0.01 | 0.48 | -0.06 | 0.32 | -0.11 | 0.81 | 0.39 | 1.14 | 0.15 | 0.46 | 0.08 | -0.01 | 0.12 | 0.81 | 0.13 | 0.49 | -0.02 | 0.23 |
| 0.21 | 0.81 | 0.19 | 0.72 | 0.23 | 0.28 | 0.25 | 0.57 | 0.29 | 0.44 | 0.06 | 0.73 | 0.18 | 0.82 | 0.37 | 0.88 | 0.29 | 0.24 | 0.41 | 0.76 | 0.56 | 0.62 | 0.14 | 0.24 |
| -0.02 | 0.90 | 0.00 | 0.65 | 0.13 | 0.30 | 0.22 | 0.67 | 0.21 | 0.47 | 0.12 | 0.75 | -0.11 | 0.94 | 0.06 | 0.94 | 0.09 | 0.32 | 0.29 | 0.75 | 0.38 | 0.76 | 0.06 | 0.26 |

Pi = Ponding Index I = Individual C = Cumulative

Series 1 Ponding Index Data [ L = Whole Basin (dx=50) ]

| Pi data (dip-oriented) | | | | | | | | | | Proximal | | Pi data (strike-oriented) | | | | | | | | | | Distal | |
|---|---|---|---|---|---|---|---|---|---|---|---|---|---|---|---|---|---|---|---|---|---|---|---|
| d160 | | d180 | | d220 | | d260 | | d280 | | x240 | | x300 | | x340 | | x360 | | x400 | | x450 | | x500 | |
| I | C | I | C | I | C | I | C | I | C | I | C | I | C | I | C | I | C | I | C | I | C | I | C |
| -0.02 | -0.02 | -0.16 | -0.16 | 0.03 | 0.03 | -0.03 | -0.03 | 0.02 | 0.02 | 0.01 | 0.01 | -0.30 | -0.30 | 0.22 | 0.22 | 0.07 | 0.07 | 0.03 | 0.03 | 0.02 | 0.02 | 0.00 | 0.00 |
| 0.02 | -0.01 | 0.03 | -0.20 | 0.02 | 0.05 | -0.01 | -0.05 | 0.02 | 0.03 | 0.01 | 0.00 | 0.05 | -0.33 | -0.05 | 0.25 | 0.03 | 0.15 | 0.02 | 0.05 | 0.01 | 0.03 | 0.01 | -0.01 |
| -0.06 | 0.01 | 0.00 | -0.17 | 0.00 | 0.07 | 0.12 | 0.00 | 0.01 | 0.05 | 0.20 | 0.14 | 0.14 | -0.03 | 0.04 | 0.37 | 0.05 | 0.19 | 0.03 | 0.06 | 0.12 | 0.14 | 0.00 | 0.01 |
| 0.00 | 0.01 | 0.00 | -0.17 | -0.03 | 0.08 | 0.01 | 0.00 | 0.01 | 0.04 | 0.00 | 0.15 | 0.05 | 0.01 | 0.01 | 0.41 | 0.03 | 0.20 | 0.02 | 0.07 | 0.03 | 0.15 | 0.01 | -0.01 |
| -0.03 | 0.04 | 0.06 | -0.14 | 0.18 | 0.02 | 0.06 | 0.01 | 0.00 | 0.06 | 0.41 | 0.32 | 0.36 | 0.22 | -0.16 | 0.60 | -0.10 | 0.18 | 0.09 | 0.11 | 0.04 | 0.17 | 0.05 | 0.03 |
| -0.01 | 0.07 | -0.05 | -0.06 | -0.10 | 0.06 | -0.13 | 0.00 | 0.08 | 0.16 | 0.29 | 0.40 | 0.58 | 0.70 | 0.00 | 0.74 | -0.03 | 0.17 | 0.10 | 0.19 | 0.07 | 0.22 | 0.04 | 0.08 |
| -0.03 | 0.06 | -0.12 | -0.05 | -0.01 | 0.04 | 0.00 | 0.00 | 0.03 | 0.20 | 0.04 | 0.55 | -0.59 | 1.00 | -0.06 | 0.85 | -0.02 | 0.18 | 0.07 | 0.23 | 0.05 | 0.24 | 0.03 | 0.10 |
| 0.00 | 0.02 | -0.03 | 0.03 | -0.01 | 0.04 | -0.03 | -0.01 | -0.02 | 0.25 | 0.07 | 0.60 | -0.22 | 1.19 | 0.16 | 0.90 | -0.05 | 0.15 | 0.04 | 0.26 | 0.10 | 0.29 | -0.06 | 0.11 |
| -0.01 | 0.03 | -0.02 | 0.05 | 0.01 | 0.03 | 0.00 | -0.01 | 0.00 | 0.27 | 0.17 | 0.61 | -0.10 | 1.26 | -0.04 | 0.99 | 0.01 | 0.14 | 0.07 | 0.28 | 0.04 | 0.30 | 0.03 | 0.13 |
| -0.03 | 0.10 | 0.00 | 0.08 | 0.03 | 0.04 | 0.00 | -0.02 | 0.00 | 0.29 | 0.15 | 0.70 | 0.08 | 1.35 | 0.00 | 1.06 | 0.00 | 0.15 | 0.06 | 0.33 | 0.04 | 0.32 | 0.05 | 0.16 |
| 0.07 | 0.16 | 0.16 | 0.27 | 0.42 | -0.13 | 0.00 | -0.01 | 0.01 | 0.30 | -0.33 | 0.74 | 0.17 | 1.34 | 0.12 | 0.75 | 0.05 | 0.26 | 0.27 | 0.47 | 0.12 | 0.37 | 0.05 | 0.18 |
| 0.03 | 0.23 | 0.06 | 0.33 | 0.03 | -0.16 | 0.01 | -0.03 | 0.01 | 0.31 | 0.07 | 0.77 | 0.26 | 1.29 | 0.38 | 0.34 | 0.11 | 0.32 | 0.07 | 0.54 | 0.07 | 0.40 | 0.07 | 0.23 |
| 0.03 | 0.28 | 0.02 | 0.41 | 0.01 | -0.18 | 0.01 | -0.02 | 0.02 | 0.33 | 0.12 | 0.88 | 0.06 | 1.32 | -0.01 | 0.32 | 0.08 | 0.33 | 0.09 | 0.60 | 0.00 | 0.42 | 0.06 | 0.27 |
| 0.00 | 0.29 | 0.26 | 0.27 | 0.01 | -0.26 | 0.00 | -0.02 | -0.05 | 0.39 | -0.28 | 1.00 | -0.25 | 1.45 | 0.08 | 0.22 | -0.01 | 0.47 | 0.05 | 0.60 | 0.12 | 0.44 | -0.04 | 0.24 |
| 0.04 | 0.36 | 0.22 | 0.18 | 0.18 | -0.05 | 0.22 | 0.06 | 0.21 | 0.53 | 0.16 | 0.97 | 0.31 | 1.25 | 0.38 | 0.35 | 0.16 | 0.39 | 0.51 | 0.63 | 0.34 | 0.60 | 0.08 | 0.28 |
| -0.01 | 0.38 | 0.02 | 0.10 | 0.14 | -0.06 | 0.22 | 0.09 | 0.18 | 0.60 | -0.09 | 1.02 | -0.03 | 1.20 | -0.11 | 0.44 | 0.06 | 0.34 | 0.03 | 0.72 | 0.43 | 0.73 | 0.06 | 0.31 |

Pi = Ponding Index  I = Individual  C = Cumulative

Series 1 Ponding Index Data [ L = Whole Basin (dx=100) ]

| Pi data (dip-oriented) | | | | | | | | | | Proximal | | Pi data (strike-oriented) | | | | | | | | | | Distal | |
|---|---|---|---|---|---|---|---|---|---|---|---|---|---|---|---|---|---|---|---|---|---|---|---|
| d160 | | d180 | | d220 | | d260 | | d280 | | x240 | | x300 | | x340 | | x360 | | x400 | | x450 | | x500 | |
| I | C | I | C | I | C | I | C | I | C | I | C | I | C | I | C | I | C | I | C | I | C | I | C |
| -0.04 | -0.04 | 0.15 | 0.15 | -0.09 | -0.09 | -0.04 | -0.04 | -0.05 | -0.05 | 0.04 | 0.04 | -0.09 | -0.09 | -0.09 | -0.09 | -0.03 | -0.03 | 0.03 | 0.03 | 0.02 | 0.02 | 0.04 | 0.04 |
| -0.02 | -0.05 | 0.04 | 0.17 | -0.01 | -0.09 | -0.01 | -0.06 | -0.01 | -0.06 | 0.03 | 0.08 | 0.03 | -0.07 | 0.04 | -0.08 | 0.00 | -0.06 | 0.01 | 0.04 | 0.00 | 0.02 | 0.03 | 0.08 |
| -0.02 | -0.07 | 0.00 | 0.19 | -0.07 | -0.25 | 0.02 | -0.04 | -0.01 | -0.07 | 0.04 | 0.12 | 0.15 | 0.12 | 0.00 | 0.01 | 0.07 | -0.06 | 0.04 | 0.09 | 0.13 | 0.15 | 0.04 | 0.12 |
| -0.02 | -0.08 | -0.01 | 0.21 | -0.01 | -0.28 | 0.01 | -0.05 | 0.00 | -0.07 | 0.02 | 0.15 | 0.04 | 0.15 | -0.04 | 0.04 | 0.00 | -0.02 | 0.02 | 0.10 | 0.01 | 0.15 | 0.02 | 0.15 |
| -0.01 | -0.09 | 0.14 | 0.27 | -0.06 | -0.64 | -0.04 | -0.07 | 0.01 | -0.09 | 0.05 | 0.17 | 0.27 | 0.38 | 0.05 | 0.19 | -0.08 | -0.09 | 0.06 | 0.14 | 0.03 | 0.17 | 0.05 | 0.17 |
| -0.02 | -0.13 | -0.10 | 0.37 | -0.02 | -1.04 | 0.00 | -0.11 | 0.00 | -0.13 | 0.06 | 0.23 | 0.77 | 0.60 | -0.07 | 0.17 | -0.01 | -0.05 | 0.22 | 0.21 | 0.06 | 0.22 | 0.06 | 0.23 |
| 0.00 | -0.15 | -0.04 | 0.47 | -0.01 | -1.31 | 0.01 | -0.13 | 0.02 | -0.15 | 0.03 | 0.26 | -0.27 | 0.67 | -0.14 | 0.14 | 0.01 | -0.03 | 0.06 | 0.25 | 0.04 | 0.25 | 0.03 | 0.26 |
| 0.01 | -0.15 | -0.01 | 0.53 | 0.00 | -1.51 | 0.00 | -0.18 | 0.01 | -0.17 | 0.03 | 0.25 | -0.21 | 0.71 | 0.05 | 0.37 | 0.01 | -0.18 | 0.05 | 0.27 | 0.05 | 0.27 | 0.03 | 0.25 |
| -0.01 | -0.17 | -0.01 | 0.56 | 0.01 | -1.64 | 0.00 | -0.18 | 0.00 | -0.19 | 0.04 | 0.29 | 0.01 | 0.81 | 0.01 | 0.46 | 0.00 | -0.15 | 0.03 | 0.29 | 0.02 | 0.29 | 0.04 | 0.29 |
| -0.01 | -0.20 | 0.01 | 0.61 | 0.01 | -1.81 | 0.01 | -0.21 | 0.01 | -0.20 | 0.02 | 0.33 | 0.02 | 0.97 | 0.09 | 0.71 | -0.03 | -0.13 | 0.11 | 0.33 | 0.04 | 0.31 | 0.02 | 0.33 |
| 0.10 | -0.16 | 0.02 | 0.72 | 0.01 | -1.74 | 0.03 | -0.21 | 0.01 | -0.20 | 0.05 | 0.36 | 0.03 | 1.01 | -0.02 | 0.93 | 0.05 | -0.03 | 0.28 | 0.32 | 0.06 | 0.33 | 0.05 | 0.36 |
| 0.03 | -0.21 | 0.00 | 0.78 | 0.03 | -1.78 | 0.01 | -0.24 | 0.02 | -0.25 | 0.03 | 0.41 | 0.08 | 1.14 | 0.12 | 1.10 | 0.04 | -0.01 | 0.14 | 0.35 | 0.08 | 0.37 | 0.03 | 0.41 |
| 0.01 | -0.23 | 0.01 | 0.85 | 0.02 | -1.80 | 0.02 | -0.25 | 0.01 | -0.26 | 0.04 | 0.47 | 0.00 | 1.22 | -0.11 | 1.19 | 0.12 | 0.07 | 0.12 | 0.38 | 0.04 | 0.39 | 0.04 | 0.47 |
| -0.01 | -0.23 | -0.01 | 0.96 | 0.00 | -1.91 | 0.00 | -0.30 | -0.01 | -0.49 | -0.04 | 0.41 | -0.09 | 1.29 | 0.06 | 1.09 | 0.31 | 0.26 | -0.11 | 0.35 | 0.07 | 0.41 | -0.04 | 0.41 |
| 0.01 | -0.24 | 0.13 | 1.05 | 0.20 | -1.74 | 0.21 | -0.22 | 0.19 | -0.34 | 0.06 | 0.48 | 0.25 | 1.09 | 0.29 | 0.83 | -0.04 | 0.37 | 0.32 | 0.43 | 0.49 | 0.58 | 0.06 | 0.48 |
| 0.03 | -0.24 | 0.04 | 1.11 | 0.12 | -1.77 | 0.24 | -0.21 | 0.18 | -0.28 | 0.07 | 0.52 | 0.00 | 1.15 | -0.09 | 0.84 | 0.06 | 0.36 | 0.03 | 0.48 | 0.27 | 0.64 | 0.07 | 0.52 |

Pi = Ponding Index  I = Individual  C = Cumulative

Series 2 - Input Current Properties

| | |
|---|---|
| Input discharge [$m^3s^{-1}$] | 0.002 |
| Channel width [m] | 0.1 |
| L=channel length [m] | 1.5 |
| Input current height [m] | 0.4 |
| Sediment volumetric concentration (%) | 0.023 |
| Hole diameter [m] | 0.015 |
| Hole area [$m^2$] | 0.000176 |
| Number of holes | 3 |
| Total hole area [$m^2$] | 0.0005 |
| Porosity | 0.0132 |
| Reynolds Number | 20000 |
| Input width [m] | 0.05 |
| Input length [m] | 0.15 |
| Input area [$m^2$] | 0.0015 |
| Input velocity [m $s^{-1}$] | 1.33 |
| Integrated hole velocity [m $s^{-1}$] | 3.772 |
| Input discharge [l $s^{-1}$] | 2 |
| Channel area/hole area | 75.45 |
| Reduced input velocity [m $s^{-1}$] | 0.05 |
| Current thickness at L | 0.02 |
| Volumetric discharge, instantaneous [$m^3$ $s^{-1}$] | 0.0003 |
| Channel width [m] | 0.0265 |
| Basin area [$m^2$] | 0.1963 |
| Basin depth [m] | 0.1 |
| Initial basin volume assume cylinder [$m^3$] | 0.0196 |
| Basin width/channel width | 5 |
| Basin depth/current thickness | 0.25 |

Series 2 - Input Discharge Conditions

| Run time (s) | Vol. discharge, instantaneous [m^3/s] | Sed. Vol. conc. (%) | Vol. discharge, total [m^3] | Sed. discharge, total [m^3] | L=channel length [m] | Channel width [m] | Input velocity [m/s] | Basin volume/ Vol. dis | Basin volume/ Vol. sed dis |
|---|---|---|---|---|---|---|---|---|---|
| 60 | 60 | 0.004 | 3600 | 14.4 | 1.5 | 0.05 | 0.04 | 0.164 | 40.9 |
| 120 | 60 | 0.004 | 7200 | 28.8 | 1.5 | 0.05 | 0.04 | 0.082 | 20.5 |
| 180 | 60 | 0.004 | 10800 | 43.2 | 1.5 | 0.05 | 0.04 | 0.055 | 13.6 |
| 240 | 60 | 0.004 | 14400 | 57.6 | 1.5 | 0.05 | 0.04 | 0.041 | 10.2 |
| 300 | 60 | 0.004 | 18000 | 72 | 1.5 | 0.05 | 0.04 | 0.033 | 8.18 |
| 360 | 60 | 0.004 | 21600 | 86.4 | 1.5 | 0.05 | 0.04 | 0.027 | 6.82 |
| 420 | 60 | 0.004 | 25200 | 100.8 | 1.5 | 0.05 | 0.04 | 0.023 | 5.84 |
| 480 | 60 | 0.004 | 28800 | 115.2 | 1.5 | 0.05 | 0.04 | 0.020 | 5.11 |
| 540 | 60 | 0.004 | 32400 | 129.6 | 1.5 | 0.05 | 0.04 | 0.018 | 4.55 |
| 600 | 60 | 0.004 | 36000 | 144 | 1.5 | 0.05 | 0.04 | 0.016 | 4.09 |
| 660 | 60 | 0.004 | 39600 | 158.4 | 1.5 | 0.05 | 0.04 | 0.015 | 3.72 |
| 720 | 60 | 0.004 | 43200 | 172.8 | 1.5 | 0.05 | 0.04 | 0.014 | 3.41 |
| 780 | 60 | 0.004 | 46800 | 187.2 | 1.5 | 0.05 | 0.04 | 0.013 | 3.15 |
| 840 | 60 | 0.004 | 50400 | 201.6 | 1.5 | 0.05 | 0.04 | 0.012 | 2.92 |
| 900 | 60 | 0.004 | 54000 | 216 | 1.5 | 0.05 | 0.04 | 0.011 | 2.73 |
| 960 | 60 | 0.004 | 57600 | 230.4 | 1.5 | 0.05 | 0.04 | 0.010 | 2.56 |
| 1020 | 60 | 0.004 | 61200 | 244.8 | 1.5 | 0.05 | 0.04 | 0.010 | 2.41 |
| 1080 | 60 | 0.004 | 64800 | 259.2 | 1.5 | 0.05 | 0.04 | 0.009 | 2.27 |
| 1140 | 60 | 0.004 | 68400 | 273.6 | 1.5 | 0.05 | 0.04 | 0.009 | 2.15 |
| 1200 | 60 | 0.004 | 72000 | 288 | 1.5 | 0.05 | 0.04 | 0.008 | 2.05 |

Series 2 - Basin and Sediment Volume Data (Configuration 1)

| Event ID | Initial volume (cm^3) | Final volume (cm^3) | Trapped sed vol. (cm^3) | Cumulative trapped sed vol. (cm^3) | Total sediment supply (cm^3) | Current duration (seconds) | Total sed supply/ Current duration | Initial basin vol./ Final basin vol. | Final basin vol./ Initial basin vol. | Trapped sed vol./ Initial basin vol. | Initial basin vol./ Trapped sed vol. | Cumul. trapped sed vol./ First basin vol. | Trapped sed vol./ Total sed vol. | Total sed vol./ Initial basin vol. |
|---|---|---|---|---|---|---|---|---|---|---|---|---|---|---|
| 1 | 2784 | 2716 | 68 | 68 | 4868 | 900 | 5.41 | 1.02 | 0.9756 | 2.44% | 41.03 | 0.02 | 1.39% | 1.75 |
| 2 | 2716 | 2667 | 49 | 117 | 3457 | 930 | 3.72 | 1.02 | 0.9819 | 1.81% | 55.35 | 0.04 | 1.42% | 1.27 |
| 3 | 2667 | 2635 | 32 | 149 | 2204 | 990 | 2.23 | 1.01 | 0.9881 | 1.19% | 84.24 | 0.05 | 1.44% | 0.83 |
| 4 | 2635 | 2592 | 44 | 192 | 2990 | 960 | 3.11 | 1.02 | 0.9834 | 1.66% | 60.33 | 0.07 | 1.46% | 1.13 |
| 5 | 2592 | 2561 | 31 | 223 | 2076 | 960 | 2.16 | 1.01 | 0.9882 | 1.18% | 84.48 | 0.08 | 1.48% | 0.80 |

Series 2 - Basin and Sediment Volume Data (Configuration 2)

| Event ID | Initial volume (cm^3) | Final volume (cm^3) | Trapped sed vol. (cm^3) | Cumulative trapped sed vol. (cm^3) | Total sediment supply (cm^3) | Current duration (seconds) | Total sed supply/ Current duration | Initial basin vol./ Final basin vol. | Final basin vol./ Initial basin vol. | Trapped sed vol./ Initial basin vol. | Initial basin vol./ Trapped sed vol. | Cumul. trapped sed vol./ First basin vol. | Trapped sed vol./ Total sed vol. | Total sed vol./ Initial basin vol. |
|---|---|---|---|---|---|---|---|---|---|---|---|---|---|---|
| 6 | 6232 | 6206 | 26 | 26 | 4853 | 930 | 5.22 | 1.00 | 0.9959 | 0.41% | 240.99 | 0.00 | 0.53% | 0.78 |
| 7 | 6206 | 6221 | -15 | 11 | 5105 | 930 | 5.49 | 1.00 | 1.0024 | -0.24% | -421.61 | 0.00 | -0.29% | 0.82 |
| 8 | 6221 | 6208 | 13 | 24 | 4139 | 930 | 4.45 | 1.00 | 0.9980 | 0.20% | 488.68 | 0.00 | 0.31% | 0.67 |
| 9 | 6208 | 6195 | 13 | 37 | 15807 | 3600 | 4.39 | 1.00 | 0.9979 | 0.21% | 485.01 | 0.01 | 0.08% | 2.55 |
| 10 | 6195 | 6057 | 138 | 175 | 21484 | 3600 | 5.97 | 1.02 | 0.9777 | 2.23% | 44.74 | 0.03 | 0.64% | 3.47 |
| 11 | 6057 | 5860 | 197 | 372 | 29112 | 3600 | 8.09 | 1.03 | 0.9675 | 3.25% | 30.80 | 0.06 | 0.68% | 4.81 |
| 12 | 5860 | 5975 | -115 | 257 | 20869 | 3600 | 5.80 | 0.98 | 1.0196 | -1.96% | -51.11 | 0.04 | -0.55% | 3.56 |
| 13 | 5975 | 5813 | 162 | 419 | 34560 | 3600 | 9.60 | 1.03 | 0.9729 | 2.71% | 36.96 | 0.07 | 0.47% | 5.78 |
| 14 | 5813 | 5603 | 210 | 629 | 28528 | 3600 | 7.92 | 1.04 | 0.9639 | 3.61% | 27.67 | 0.10 | 0.74% | 4.91 |

Series 2 - Basin and Sediment Volume Data (Configuration 3)

| Event ID | Initial volume (cm^3) | Final volume (cm^3) | Trapped sed vol. (cm^3) | Cumulative trapped sed vol. (cm^3) | Total sediment supply (cm^3) | Current duration (seconds) | Total sed supply/ Current duration | Initial basin vol./ Final basin vol. | Final basin vol./ Initial basin vol. | Trapped sed vol./ Initial basin vol. | Initial basin vol./ Trapped sed vol. | Cumul. trapped sed vol./ First basin vol. | Trapped sed vol./ Total sed vol. | Total sed vol./ Initial basin vol. |
|---|---|---|---|---|---|---|---|---|---|---|---|---|---|---|
| 15 | 10738 | 10467 | 271 | 271 | 36913 | 3600 | 2.16 | 1.03 | 0.9748 | 2.52% | 39.63 | 0.03 | 0.73% | 1.75 |
| 16 | 10467 | 10230 | 237 | 508 | 34560 | 3600 | 2.16 | 1.02 | 0.9774 | 2.26% | 44.16 | 0.05 | 0.69% | 2.75 |
| 17 | 10230 | 9995 | 235 | 743 | 37625 | 3600 | 2.16 | 1.02 | 0.9770 | 2.30% | 43.49 | 0.07 | 0.63% | 3.75 |
| 18 | 9995 | 9746 | 249 | 992 | 32650 | 3600 | 2.16 | 1.03 | 0.9751 | 2.49% | 40.17 | 0.09 | 0.76% | 4.75 |
| 20 | N | O | | D | A | T | A | | S | A | M | P | L | E |
| 21 | 8620 | 8136 | 484 | 1476 | 81124 | 7200 | 2.16 | 1.06 | 0.9439 | 5.61% | 17.81 | 0.14 | 0.60% | 5.75 |
| 22a | 8136 | 8124 | 12 | 1488 | 1902 | 240 | 2.16 | 1.00 | 0.9985 | 0.15% | 671.84 | 0.14 | 0.64% | 6.75 |
| 22b | 8124 | 8106 | 18 | 1506 | 1902 | 240 | 2.16 | 1.00 | 0.9978 | 0.22% | 451.83 | 0.14 | 0.95% | 7.75 |
| 23 | 8106 | 7574 | 532 | 2038 | 71500 | 7200 | 2.16 | 1.07 | 0.9344 | 6.56% | 15.24 | 0.19 | 0.74% | 8.75 |
| 24 | 7574 | 7382 | 192 | 2230 | 67063 | 7200 | 2.16 | 1.03 | 0.9746 | 2.54% | 39.38 | 0.21 | 0.29% | 9.75 |
| 25 | 7382 | 6811 | 571 | 2802 | 52810 | 7200 | 2.16 | 1.08 | 0.9226 | 7.74% | 12.93 | 0.26 | 1.08% | 10.75 |
| 26 | 6811 | 6602 | 209 | 3010 | 30681 | 3600 | 2.16 | 1.03 | 0.9693 | 3.07% | 32.60 | 0.28 | 0.68% | 11.75 |
| 27 | 6602 | 6390 | 212 | 3222 | 30681 | 3600 | 2.16 | 1.03 | 0.9679 | 3.21% | 31.15 | 0.30 | 0.69% | 12.75 |

Series 2 Ponding Index Data [ L = Configuration 1 Basin (dx=2) ]

| | Pi data (dip-oriented) | | | | | | | | | | Proximal | | | Pi data (strike-oriented) | | | Distal | |
|---|---|---|---|---|---|---|---|---|---|---|---|---|---|---|---|---|---|---|
| Event ID | d160 | | d175 | | d190 | | d205 | | d230 | | x230 | | | x255 | | | x280 | |
| | I | C | I | C | I | C | I | C | I | C | I | C | | I | C | | I | C |
| 1 | 0.37 | 0.37 | 0.23 | 0.23 | 0.13 | 0.13 | 0.18 | 0.18 | 0.05 | 0.05 | 0.24 | 0.24 | | 0.28 | 0.28 | | 0.14 | 0.14 |
| 2 | 0.21 | 0.29 | 0.09 | 0.16 | 0.05 | 0.19 | 0.09 | 0.28 | 0.04 | 0.10 | 0.38 | 0.43 | | 0.23 | 0.37 | | 0.35 | 0.19 |
| 3 | 0.17 | 0.35 | 0.08 | 0.25 | 0.02 | 0.19 | 0.06 | 0.32 | 0.18 | 0.12 | 0.21 | 0.41 | | 0.21 | 0.26 | | 0.19 | 0.19 |
| 4 | 0.19 | 0.39 | 0.09 | 0.26 | 0.03 | 0.15 | 0.02 | 0.36 | 0.22 | 0.18 | 0.42 | 0.37 | | 0.26 | 0.34 | | 0.20 | 0.23 |
| 5 | 0.18 | 0.41 | 0.14 | 0.25 | 0.06 | 0.22 | 0.00 | 0.38 | 0.16 | 0.13 | 0.20 | 0.35 | | 0.24 | 0.35 | | 0.21 | 0.26 |

Pi = Ponding Index

I = Individual

C = Cumulative

Series 2 Ponding Index Data [ L = Configuration 1 Basin (dx=4) ]

| | Pi data (dip-oriented) | | | | | | | | | | Proximal | | | Pi data (strike-oriented) | | | | Distal |
|---|---|---|---|---|---|---|---|---|---|---|---|---|---|---|---|---|---|---|
| Event ID | d160 | | d175 | | d190 | | d205 | | d230 | | x230 | | | x255 | | | x280 | |
| | I | C | I | C | I | C | I | C | I | C | I | C | | I | C | | I | C |
| 1 | 0.11 | 0.11 | 0.01 | 0.01 | 0.16 | 0.16 | 0.03 | 0.03 | -0.05 | -0.05 | -0.05 | -0.05 | | 0.06 | 0.06 | | 0.02 | 0.02 |
| 2 | 0.07 | 0.14 | 0.10 | 0.09 | 0.04 | 0.23 | 0.03 | 0.08 | 0.04 | -0.07 | 0.04 | -0.07 | | 0.08 | 0.06 | | 0.05 | -0.02 |
| 3 | 0.05 | 0.16 | 0.07 | 0.10 | -0.05 | 0.24 | -0.01 | 0.09 | -0.02 | -0.06 | -0.02 | -0.06 | | 0.07 | 0.08 | | 0.11 | 0.10 |
| 4 | 0.12 | 0.17 | 0.04 | 0.11 | 0.04 | 0.24 | -0.01 | 0.11 | 0.04 | -0.02 | 0.04 | -0.02 | | 0.08 | 0.13 | | 0.02 | 0.07 |
| 5 | 0.10 | 0.15 | 0.05 | 0.12 | -0.01 | 0.30 | 0.01 | 0.11 | 0.04 | 0.00 | 0.04 | 0.00 | | 0.03 | 0.18 | | 0.05 | 0.03 |

Pi = Ponding Index

I = Individual

C = Cumulative

Series 2 Ponding Index Data [ L = Configuration 1 Basin (dx=10) ]

| | Pi data (dip-oriented) | | | | | | | | | | Proximal | | | Pi data (strike-oriented) | | | Distal | |
|---|---|---|---|---|---|---|---|---|---|---|---|---|---|---|---|---|---|---|
| Event ID | d160 | | d175 | | d190 | | d205 | | d230 | | x230 | | | x255 | | | x280 | |
| | I | C | I | C | I | C | I | C | I | C | I | C | | I | C | | I | C |
| 1 | -0.04 | -0.04 | 0.21 | 0.21 | 0.01 | 0.01 | -0.12 | -0.12 | 0.00 | 0.00 | 0.01 | 0.01 | | 0.02 | 0.02 | | -0.04 | -0.04 |
| 2 | 0.05 | 0.03 | 0.06 | 0.27 | -0.04 | 0.06 | 0.00 | -0.12 | 0.01 | -0.01 | 0.06 | 0.04 | | 0.00 | -0.02 | | -0.02 | -0.05 |
| 3 | 0.02 | 0.03 | -0.03 | 0.26 | 0.00 | 0.09 | 0.03 | -0.13 | -0.01 | -0.02 | 0.01 | 0.09 | | 0.03 | 0.04 | | -0.01 | -0.01 |
| 4 | 0.04 | 0.05 | 0.04 | 0.31 | 0.02 | 0.12 | 0.00 | -0.13 | -0.03 | -0.02 | 0.04 | 0.12 | | 0.04 | 0.05 | | 0.00 | 0.02 |
| 5 | 0.03 | 0.06 | 0.02 | 0.35 | -0.01 | 0.11 | 0.01 | -0.12 | 0.02 | -0.01 | 0.08 | 0.13 | | 0.04 | 0.07 | | -0.01 | 0.01 |

Pi = Ponding Index

I = Individual

C = Cumulative

Series 2 Ponding Index Data [ L = Configuration 2 Basin (dx=20) ]

| | Pi data (dip-oriented) | | | | | | | | | | Proximal | | | Pi data (strike-oriented) | | | Distal | |
|---|---|---|---|---|---|---|---|---|---|---|---|---|---|---|---|---|---|---|
| Event ID | d160 | | d175 | | d190 | | d205 | | d230 | | x230 | | | x255 | | | x280 | |
| | I | C | I | C | I | C | I | C | I | C | I | C | | I | C | | I | C |
| 1 | 0.12 | 0.12 | 0.23 | 0.23 | 0.06 | 0.06 | -0.16 | -0.16 | 0.02 | 0.02 | 0.04 | 0.04 | | 0.01 | 0.01 | | -0.03 | -0.03 |
| 2 | 0.07 | 0.08 | 0.05 | 0.32 | 0.00 | 0.10 | -0.01 | -0.18 | 0.01 | 0.04 | 0.00 | 0.08 | | 0.03 | 0.04 | | 0.00 | -0.02 |
| 3 | 0.06 | 0.09 | -0.01 | 0.34 | -0.01 | 0.11 | -0.01 | -0.13 | 0.02 | 0.04 | 0.03 | 0.09 | | 0.01 | 0.06 | | 0.01 | 0.02 |
| 4 | 0.05 | 0.13 | 0.04 | 0.39 | 0.02 | 0.14 | 0.00 | -0.17 | 0.03 | 0.05 | -0.01 | 0.12 | | 0.02 | 0.07 | | 0.00 | 0.04 |
| 5 | 0.04 | 0.12 | 0.00 | 0.40 | 0.01 | 0.16 | 0.01 | -0.16 | 0.00 | 0.05 | 0.04 | 0.13 | | 0.03 | 0.08 | | 0.01 | 0.06 |

Pi = Ponding Index

I = Individual

C = Cumulative

Series 2 Ponding Index Data [ L = Configuration 1 Basin (dx=50) ]

| | Pi data (dip-oriented) | | | | | | | | | | Proximal | | | Pi data (strike-oriented) | | | | Distal |
|---|---|---|---|---|---|---|---|---|---|---|---|---|---|---|---|---|---|---|
| Event ID | d160 | | d175 | | d190 | | d205 | | d230 | | x230 | | | x255 | | | x280 | |
| | I | C | I | C | I | C | I | C | I | C | I | C | | I | C | | I | C |
| 1 | 0.06 | 0.06 | 0.02 | 0.02 | 0.18 | 0.18 | 0.03 | 0.03 | 0.02 | 0.02 | 0.03 | 0.03 | | 0.00 | 0.00 | | -0.04 | -0.04 |
| 2 | 0.02 | 0.05 | 0.02 | 0.04 | 0.04 | 0.24 | 0.05 | 0.05 | -0.01 | 0.02 | 0.05 | 0.05 | | 0.00 | 0.02 | | 0.01 | -0.03 |
| 3 | 0.00 | 0.04 | 0.02 | 0.05 | 0.01 | 0.26 | 0.00 | 0.06 | 0.01 | 0.03 | 0.03 | 0.06 | | 0.01 | 0.04 | | 0.03 | -0.02 |
| 4 | 0.03 | 0.07 | 0.03 | 0.05 | 0.05 | 0.32 | 0.03 | 0.09 | 0.01 | 0.04 | 0.03 | 0.08 | | 0.04 | 0.05 | | 0.02 | 0.01 |
| 5 | 0.00 | 0.06 | 0.00 | 0.05 | 0.00 | 0.34 | 0.00 | 0.09 | 0.00 | 0.04 | 0.03 | 0.10 | | 0.02 | 0.06 | | 0.01 | 0.01 |

Pi = Ponding Index

I = Individual

C = Cumulative

Series 2 Ponding Index Data [ L = Configuration 1 Basin (dx=100) ]

| | Pi data (dip-oriented) | | | | | | | | | | Proximal | | | Pi data (strike-oriented) | | | | Distal |
|---|---|---|---|---|---|---|---|---|---|---|---|---|---|---|---|---|---|---|
| Event ID | d160 | | d175 | | d190 | | d205 | | d230 | | x230 | | | x255 | | | x280 | |
| | I | C | I | C | I | C | I | C | I | C | I | C | | I | C | | I | C |
| 1 | -0.03 | -0.03 | 0.00 | 0.00 | 0.05 | 0.05 | 0.05 | 0.05 | 0.02 | 0.02 | 0.06 | 0.06 | | 0.18 | 0.18 | | 0.00 | 0.00 |
| 2 | -0.01 | -0.02 | 0.02 | 0.03 | 0.00 | 0.07 | -0.03 | 0.07 | 0.02 | 0.04 | 0.02 | 0.09 | | 0.11 | 0.23 | | 0.02 | 0.01 |
| 3 | 0.00 | -0.01 | 0.00 | 0.03 | -0.01 | 0.08 | 0.00 | 0.08 | 0.01 | 0.04 | 0.02 | 0.11 | | 0.02 | 0.25 | | 0.01 | 0.02 |
| 4 | 0.05 | 0.01 | -0.01 | 0.04 | 0.01 | 0.09 | 0.05 | 0.10 | 0.01 | 0.06 | 0.01 | 0.13 | | 0.07 | 0.30 | | 0.02 | 0.04 |
| 5 | 0.02 | 0.02 | 0.02 | 0.06 | 0.01 | 0.10 | -0.01 | 0.11 | 0.01 | 0.06 | 0.02 | 0.15 | | 0.03 | 0.32 | | 0.02 | 0.05 |

Pi = Ponding Index

I = Individual

C = Cumulative

Series 2 Ponding Index Data [ L = Configuration 2 Basin (dx=2) ]

| | Pi data (dip-oriented) | | | | | | | | | | Proximal | | Pi data (strike-oriented) | | | | | | | Distal |
|---|---|---|---|---|---|---|---|---|---|---|---|---|---|---|---|---|---|---|---|---|
| Event ID | d150 | | d180 | | d190 | | d210 | | d230 | | x210 | | x235 | | x260 | | x285 | | x310 | |
| | I | C | I | C | I | C | I | C | I | C | I | C | I | C | I | C | I | C | I | C |
| 6 | 0.09 | 0.09 | 0.03 | 0.03 | 0.07 | 0.07 | 0.11 | 0.11 | -0.03 | -0.03 | 0.07 | 0.07 | 0.10 | 0.10 | 0.03 | 0.03 | 0.13 | 0.13 | -0.01 | -0.01 |
| 7 | 0.08 | 0.03 | 0.04 | 0.00 | 0.15 | 0.13 | 0.16 | 0.10 | 0.05 | 0.02 | 0.09 | 0.04 | 0.08 | 0.06 | 0.06 | 0.07 | 0.15 | 0.01 | -0.01 | -0.04 |
| 8 | -0.02 | 0.05 | 0.12 | 0.00 | 0.06 | 0.12 | 0.16 | 0.21 | 0.04 | 0.01 | 0.06 | 0.07 | 0.09 | 0.02 | 0.10 | 0.13 | 0.19 | 0.00 | 0.04 | 0.04 |
| 9 | 0.03 | 0.12 | 0.16 | -0.08 | 0.21 | 0.09 | 0.13 | 0.03 | 0.12 | -0.03 | 0.13 | 0.08 | 0.16 | 0.13 | 0.04 | 0.05 | 0.19 | 0.06 | -0.02 | 0.06 |
| 10 | 0.01 | 0.09 | 0.13 | -0.01 | 0.22 | 0.14 | 0.20 | 0.07 | 0.17 | 0.01 | 0.21 | 0.11 | 0.07 | 0.13 | 0.13 | 0.14 | 0.20 | 0.13 | 0.27 | 0.09 |
| 11 | 0.02 | 0.14 | 0.20 | 0.16 | 0.29 | 0.31 | 0.25 | 0.20 | 0.24 | 0.15 | 0.19 | 0.19 | 0.19 | 0.25 | 0.32 | 0.27 | 0.32 | 0.12 | 0.26 | 0.16 |
| 12 | 0.07 | 0.11 | 0.35 | 0.27 | 0.44 | 0.40 | 0.34 | 0.31 | 0.17 | 0.18 | 0.11 | 0.17 | 0.25 | 0.24 | 0.34 | 0.29 | 0.32 | 0.17 | 0.23 | 0.08 |
| 13 | 0.12 | 0.17 | 0.31 | 0.26 | 0.29 | 0.32 | 0.37 | 0.34 | 0.26 | 0.20 | 0.18 | 0.21 | 0.26 | 0.31 | 0.36 | 0.36 | 0.31 | 0.20 | 0.32 | 0.23 |
| 14 | 0.07 | 0.16 | 0.30 | 0.32 | 0.23 | 0.36 | 0.28 | 0.30 | 0.24 | 0.24 | 0.24 | 0.23 | 0.28 | 0.27 | 0.35 | 0.30 | 0.37 | 0.25 | 0.36 | 0.26 |

Pi = Ponding Index

I = Individual

C = Cumulative

Series 2 Ponding Index Data [ L = Configuration 2 Basin (dx=4) ]

| | Pi data (dip-oriented) | | | | | | | | | | Proximal | | Pi data (strike-oriented) | | | | | | | Distal |
|---|---|---|---|---|---|---|---|---|---|---|---|---|---|---|---|---|---|---|---|---|
| Event ID | d150 | | d180 | | d190 | | d210 | | d230 | | x210 | | x235 | | x260 | | x285 | | x310 | |
| | I | C | I | C | I | C | I | C | I | C | I | C | I | C | I | C | I | C | I | C |
| 6 | -0.05 | -0.05 | 0.06 | 0.06 | 0.02 | 0.02 | 0.06 | 0.06 | 0.04 | 0.04 | 0.11 | 0.11 | 0.06 | 0.06 | 0.01 | 0.01 | 0.10 | 0.10 | 0.01 | 0.01 |
| 7 | 0.07 | -0.04 | 0.06 | 0.03 | 0.06 | 0.01 | 0.04 | 0.10 | -0.03 | 0.07 | 0.00 | 0.03 | 0.10 | 0.03 | 0.08 | 0.03 | 0.11 | 0.02 | -0.03 | -0.06 |
| 8 | 0.05 | 0.01 | 0.04 | 0.02 | 0.04 | 0.06 | 0.09 | 0.11 | 0.03 | 0.07 | 0.05 | 0.06 | 0.06 | 0.03 | 0.07 | 0.03 | 0.15 | 0.07 | 0.05 | -0.07 |
| 9 | 0.02 | 0.02 | 0.02 | 0.04 | 0.12 | -0.03 | 0.07 | 0.01 | 0.05 | 0.08 | 0.02 | 0.04 | 0.01 | 0.08 | 0.06 | -0.02 | 0.10 | 0.08 | 0.03 | 0.01 |
| 10 | 0.02 | -0.02 | 0.14 | 0.04 | 0.10 | 0.00 | 0.05 | 0.05 | 0.16 | 0.15 | 0.13 | 0.19 | 0.16 | 0.19 | 0.17 | 0.06 | 0.21 | 0.13 | 0.05 | 0.10 |
| 11 | 0.02 | -0.03 | 0.20 | 0.28 | 0.20 | 0.18 | 0.20 | 0.22 | 0.09 | 0.29 | 0.15 | 0.16 | 0.20 | 0.24 | 0.30 | 0.26 | 0.33 | 0.28 | 0.20 | 0.16 |
| 12 | -0.03 | -0.14 | 0.34 | 0.33 | 0.26 | 0.31 | 0.30 | 0.36 | 0.20 | 0.28 | 0.31 | 0.22 | 0.28 | 0.27 | 0.31 | 0.34 | 0.34 | 0.35 | 0.15 | 0.19 |
| 13 | 0.05 | -0.08 | 0.10 | 0.39 | 0.18 | 0.31 | 0.15 | 0.34 | 0.10 | 0.30 | 0.16 | 0.29 | 0.15 | 0.35 | 0.29 | 0.31 | 0.25 | 0.33 | 0.25 | 0.24 |
| 14 | 0.05 | -0.08 | 0.30 | 0.23 | 0.18 | 0.31 | 0.07 | 0.40 | -0.01 | 0.32 | 0.21 | 0.30 | 0.29 | 0.31 | 0.35 | 0.42 | 0.36 | 0.28 | 0.26 | 0.29 |

Pi = Ponding Index

I = Individual

C = Cumulative

Series 2 Ponding Index Data [ L = Configuration 2 Basin (dx=10) ]

| | Pi data (dip-oriented) | | | | | | | | | | Proximal | | Pi data (strike-oriented) | | | | | | | Distal |
|---|---|---|---|---|---|---|---|---|---|---|---|---|---|---|---|---|---|---|---|---|
| Event ID | d150 | | d180 | | d190 | | d210 | | d230 | | x210 | | x235 | | x260 | | x285 | | x310 | |
| | I | C | I | C | I | C | I | C | I | C | I | C | I | C | I | C | I | C | I | C |
| 6 | -0.01 | -0.01 | 0.01 | 0.01 | -0.01 | -0.01 | -0.01 | -0.01 | -0.07 | -0.07 | 0.05 | 0.05 | 0.05 | 0.05 | -0.02 | -0.02 | 0.02 | 0.02 | -0.03 | -0.03 |
| 7 | 0.00 | -0.02 | 0.03 | -0.02 | -0.01 | -0.03 | -0.01 | -0.06 | 0.03 | -0.05 | 0.03 | 0.03 | 0.00 | 0.09 | 0.03 | -0.04 | 0.11 | 0.03 | -0.03 | -0.06 |
| 8 | 0.03 | 0.00 | 0.00 | 0.00 | 0.02 | -0.04 | -0.01 | -0.06 | -0.01 | -0.07 | 0.03 | 0.05 | 0.01 | 0.08 | 0.01 | -0.03 | 0.03 | 0.04 | 0.01 | -0.05 |
| 9 | -0.01 | -0.01 | -0.01 | -0.03 | 0.03 | -0.05 | -0.01 | -0.11 | 0.04 | -0.09 | -0.01 | 0.05 | 0.03 | 0.11 | 0.00 | -0.03 | 0.04 | 0.05 | 0.00 | -0.07 |
| 10 | 0.01 | 0.02 | 0.01 | -0.02 | 0.05 | -0.02 | -0.19 | -0.30 | 0.07 | 0.00 | 0.14 | 0.15 | 0.17 | 0.10 | 0.24 | 0.02 | 0.16 | 0.17 | 0.13 | 0.06 |
| 11 | 0.03 | 0.01 | 0.15 | 0.26 | 0.17 | 0.25 | 0.26 | 0.19 | 0.03 | 0.00 | 0.10 | 0.27 | 0.15 | 0.26 | 0.31 | 0.32 | 0.27 | 0.28 | 0.15 | 0.15 |
| 12 | -0.01 | -0.01 | 0.22 | 0.39 | 0.16 | 0.41 | 0.31 | 0.42 | 0.20 | 0.16 | 0.25 | 0.11 | 0.30 | 0.26 | 0.42 | 0.32 | 0.34 | 0.33 | 0.16 | 0.18 |
| 13 | 0.08 | 0.01 | 0.01 | 0.39 | 0.00 | 0.34 | 0.10 | 0.39 | -0.11 | 0.08 | 0.11 | 0.31 | 0.11 | 0.27 | 0.13 | 0.41 | 0.22 | 0.33 | 0.13 | 0.26 |
| 14 | 0.01 | 0.02 | 0.07 | 0.15 | -0.12 | 0.46 | -0.25 | 0.34 | 0.02 | 0.09 | 0.06 | 0.32 | 0.17 | 0.35 | 0.43 | 0.44 | 0.08 | 0.28 | 0.05 | 0.22 |

Pi = Ponding Index

I = Individual

C = Cumulative

Series 2 Ponding Index Data [ L = Configuration 2 Basin (dx=20) ]

| | Pi data (dip-oriented) | | | | | | | | | | Proximal | | Pi data (strike-oriented) | | | | | | Distal | |
|---|---|---|---|---|---|---|---|---|---|---|---|---|---|---|---|---|---|---|---|---|
| Event ID | d150 | | d180 | | d190 | | d210 | | d230 | | x210 | | x235 | | x260 | | x285 | | x310 | |
| | I | C | I | C | I | C | I | C | I | C | I | C | I | C | I | C | I | C | I | C |
| 6 | -0.02 | -0.02 | 0.00 | 0.00 | -0.03 | -0.03 | 0.01 | 0.01 | -0.08 | -0.08 | -0.01 | -0.01 | -0.02 | -0.02 | -0.02 | -0.02 | 0.08 | 0.08 | -0.01 | -0.01 |
| 7 | 0.01 | 0.00 | 0.00 | -0.04 | 0.00 | -0.04 | -0.06 | -0.02 | 0.05 | -0.05 | 0.00 | 0.00 | 0.00 | 0.02 | 0.01 | -0.02 | 0.02 | 0.05 | 0.00 | -0.02 |
| 8 | 0.02 | 0.01 | 0.03 | 0.01 | -0.01 | -0.03 | -0.01 | -0.04 | 0.00 | -0.07 | 0.00 | 0.01 | 0.02 | 0.04 | 0.01 | -0.03 | 0.01 | 0.08 | 0.01 | -0.02 |
| 9 | 0.02 | -0.02 | -0.02 | -0.06 | 0.07 | -0.05 | 0.03 | -0.06 | -0.02 | -0.07 | -0.01 | -0.03 | -0.01 | -0.03 | 0.02 | -0.03 | 0.07 | 0.05 | 0.00 | -0.03 |
| 10 | 0.04 | 0.03 | -0.06 | -0.10 | -0.01 | 0.08 | -0.18 | -0.26 | 0.09 | 0.23 | 0.12 | 0.10 | 0.08 | 0.11 | 0.25 | 0.23 | 0.15 | 0.14 | 0.13 | 0.11 |
| 11 | 0.04 | 0.05 | 0.18 | 0.17 | 0.22 | 0.29 | 0.28 | 0.25 | 0.07 | 0.18 | 0.09 | 0.29 | 0.17 | 0.25 | 0.34 | 0.30 | 0.27 | 0.30 | 0.17 | 0.21 |
| 12 | 0.08 | 0.06 | 0.24 | 0.35 | 0.11 | 0.48 | 0.32 | 0.47 | 0.20 | 0.21 | 0.51 | 0.18 | 0.23 | 0.21 | 0.29 | 0.46 | 0.35 | 0.41 | 0.10 | 0.24 |
| 13 | 0.03 | 0.05 | -0.05 | 0.31 | -0.06 | 0.40 | -0.03 | 0.49 | -0.08 | 0.24 | 0.12 | 0.29 | 0.02 | 0.31 | 0.06 | 0.54 | 0.27 | 0.39 | 0.06 | 0.31 |
| 14 | 0.01 | 0.08 | -0.32 | -0.01 | -0.25 | 0.52 | -0.17 | 0.39 | 0.00 | 0.25 | 0.08 | 0.27 | 0.15 | 0.35 | 0.79 | 0.60 | 0.10 | 0.39 | 0.01 | 0.31 |

Pi = Ponding Index

I = Individual

C = Cumulative

Series 2 Ponding Index Data [ L = Configuration 2 Basin (dx=50) ]

| | Pi data (dip-oriented) | | | | | | | | | | Proximal | | Pi data (strike-oriented) | | | | | | | Distal |
|---|---|---|---|---|---|---|---|---|---|---|---|---|---|---|---|---|---|---|---|---|
| Event ID | d150 | | d180 | | d190 | | d210 | | d230 | | x210 | | x235 | | x260 | | x285 | | x310 | |
| | I | C | I | C | I | C | I | C | I | C | I | C | I | C | I | C | I | C | I | C |
| 6 | 0.01 | 0.01 | -0.01 | -0.01 | -0.04 | -0.04 | 0.00 | 0.00 | 0.02 | 0.02 | 0.01 | 0.01 | 0.00 | 0.00 | -0.02 | -0.02 | 0.00 | 0.00 | 0.02 | 0.02 |
| 7 | 0.00 | 0.00 | -0.01 | 0.00 | 0.00 | -0.04 | -0.03 | -0.03 | -0.02 | -0.01 | 0.07 | 0.03 | -0.06 | -0.03 | -0.01 | -0.01 | 0.00 | 0.02 | -0.02 | 0.02 |
| 8 | 0.01 | 0.01 | 0.00 | -0.02 | 0.02 | -0.02 | -0.02 | -0.05 | 0.00 | 0.01 | -0.01 | 0.03 | 0.00 | -0.02 | 0.00 | -0.02 | -0.02 | -0.01 | 0.00 | 0.01 |
| 9 | -0.01 | 0.01 | -0.04 | -0.05 | -0.05 | -0.03 | 0.00 | -0.06 | 0.00 | -0.01 | 0.03 | 0.03 | -0.02 | -0.06 | -0.01 | -0.02 | 0.02 | 0.01 | -0.01 | -0.02 |
| 10 | 0.01 | 0.04 | 0.02 | -0.04 | 0.06 | 0.01 | -0.06 | -0.11 | 0.26 | 0.08 | 0.07 | 0.09 | 0.01 | -0.02 | 0.21 | 0.06 | 0.06 | 0.07 | 0.08 | 0.17 |
| 11 | 0.01 | 0.05 | 0.16 | 0.19 | 0.21 | 0.25 | 0.23 | 0.18 | 0.09 | 0.17 | -0.01 | 0.05 | 0.19 | 0.15 | 0.29 | 0.29 | 0.24 | 0.26 | 0.16 | 0.24 |
| 12 | 0.03 | 0.07 | 0.16 | 0.32 | 0.20 | 0.41 | 0.32 | 0.39 | 0.18 | 0.24 | 0.01 | 0.14 | 0.23 | 0.09 | 0.36 | 0.38 | 0.24 | 0.35 | 0.08 | 0.30 |
| 13 | 0.00 | 0.08 | 0.04 | 0.25 | -0.07 | 0.38 | -0.11 | 0.35 | -0.06 | 0.25 | -0.03 | 0.19 | 0.20 | 0.22 | 0.00 | 0.42 | 0.13 | 0.32 | 0.10 | 0.36 |
| 14 | 0.00 | 0.07 | -0.16 | 0.27 | -0.14 | 0.43 | -0.05 | 0.32 | -0.02 | 0.26 | -0.03 | 0.20 | 0.02 | 0.35 | -0.34 | 0.36 | 0.05 | 0.34 | -0.10 | 0.38 |

Pi = Ponding Index

I = Individual

C = Cumulative

Series 2 Ponding Index Data [ L = Configuration 2 Basin (dx=100) ]

| | Pi data (dip-oriented) | | | | | | | | | | Proximal | | Pi data (strike-oriented) | | | | | | Distal | |
|---|---|---|---|---|---|---|---|---|---|---|---|---|---|---|---|---|---|---|---|---|
| Event ID | d150 | | d180 | | d190 | | d210 | | d230 | | x210 | | x235 | | x260 | | x285 | | x310 | |
| | I | C | I | C | I | C | I | C | I | C | I | C | I | C | I | C | I | C | I | C |
| 6 | 0.00 | 0.00 | -0.01 | -0.01 | -0.02 | -0.02 | -0.01 | -0.01 | 0.00 | 0.00 | 0.01 | 0.01 | 0.00 | 0.00 | 0.00 | 0.00 | -0.01 | -0.01 | 0.01 | 0.01 |
| 7 | -0.01 | -0.01 | 0.01 | -0.01 | -0.02 | -0.04 | -0.01 | -0.04 | 0.02 | 0.02 | -0.01 | -0.02 | 0.01 | 0.00 | 0.02 | 0.00 | 0.00 | -0.01 | -0.01 | 0.00 |
| 8 | 0.00 | 0.00 | 0.00 | -0.01 | -0.02 | -0.07 | -0.01 | -0.04 | -0.01 | 0.02 | 0.00 | -0.02 | 0.00 | 0.01 | 0.00 | 0.00 | 0.01 | -0.01 | 0.00 | 0.01 |
| 9 | 0.00 | 0.00 | -0.01 | -0.03 | -0.01 | -0.09 | -0.03 | -0.07 | 0.00 | -0.01 | 0.01 | -0.02 | 0.01 | 0.01 | -0.01 | -0.01 | -0.01 | -0.02 | 0.01 | 0.00 |
| 10 | 0.02 | 0.01 | 0.08 | 0.07 | 0.11 | 0.03 | 0.03 | -0.04 | 0.01 | 0.00 | -0.02 | -0.02 | 0.04 | 0.09 | 0.08 | 0.05 | 0.05 | 0.09 | 0.06 | 0.02 |
| 11 | 0.04 | 0.03 | 0.24 | 0.25 | 0.20 | 0.14 | 0.09 | 0.17 | 0.06 | 0.02 | -0.02 | -0.07 | 0.01 | 0.22 | 0.22 | 0.25 | 0.20 | 0.23 | 0.13 | 0.11 |
| 12 | -0.03 | 0.03 | 0.17 | 0.37 | 0.20 | 0.26 | 0.22 | 0.32 | 0.14 | 0.21 | -0.10 | -0.18 | 0.06 | 0.28 | 0.08 | 0.32 | 0.17 | 0.33 | 0.01 | 0.13 |
| 13 | 0.02 | 0.05 | 0.01 | 0.39 | -0.12 | 0.25 | -0.20 | 0.31 | 0.02 | 0.17 | 0.05 | -0.16 | 0.04 | 0.28 | -0.06 | 0.33 | 0.10 | 0.34 | 0.16 | 0.22 |
| 14 | 0.01 | 0.07 | -0.04 | 0.40 | -0.07 | 0.17 | -0.08 | 0.24 | -0.03 | 0.16 | -0.04 | -0.14 | 0.01 | 0.40 | 0.07 | 0.36 | -0.13 | 0.33 | 0.12 | 0.31 |

Pi = Ponding Index

I = Individual

C = Cumulative

Series 2 Ponding Index Data [ L = Configuration 3 Basin (dx=2) ]

| | Pi data (dip-oriented) | | | | | | | | | | Proximal | | Pi data (strike-oriented) | | | | | | Distal | |
|---|---|---|---|---|---|---|---|---|---|---|---|---|---|---|---|---|---|---|---|---|
| Event ID | d130 | | d160 | | d190 | | d220 | | d250 | | x150 | | x200 | | x250 | | x300 | | x350 | |
| | I | C | I | C | I | C | I | C | I | C | I | C | I | C | I | C | I | C | I | C |
| 15 | 0.04 | 0.04 | 0.15 | 0.15 | 0.05 | 0.05 | 0.21 | 0.21 | 0.24 | 0.24 | N/A | N/A | 0.10 | 0.10 | 0.11 | 0.11 | 0.14 | 0.14 | 0.22 | 0.22 |
| 16 | 0.11 | 0.10 | 0.07 | 0.17 | 0.10 | 0.05 | 0.16 | 0.24 | 0.15 | 0.28 | N/A | 0.24 | 0.16 | 0.11 | 0.24 | 0.16 | 0.09 | 0.13 | 0.20 | 0.24 |
| 17 | 0.07 | 0.06 | 0.11 | 0.20 | 0.15 | 0.03 | 0.28 | 0.31 | 0.19 | 0.31 | 0.17 | 0.26 | 0.19 | 0.21 | 0.15 | 0.15 | 0.21 | 0.13 | 0.36 | 0.32 |
| 18 | 0.11 | 0.09 | 0.12 | 0.22 | 0.01 | 0.08 | 0.12 | 0.34 | 0.14 | 0.35 | N/A | N/A | 0.16 | 0.22 | 0.20 | 0.17 | 0.24 | 0.21 | 0.24 | 0.36 |
| 20 | 0.24 | 0.19 | 0.29 | 0.42 | 0.36 | 0.28 | 0.44 | 0.11 | 0.22 | 0.34 | N/A | 0.26 | 0.23 | 0.35 | 0.32 | 0.30 | 0.37 | 0.34 | 0.36 | 0.30 |
| 21 | 0.27 | 0.18 | 0.25 | 0.37 | 0.19 | 0.37 | 0.17 | 0.29 | 0.17 | 0.39 | 0.23 | 0.30 | 0.26 | 0.37 | 0.34 | 0.41 | 0.27 | 0.32 | 0.44 | 0.34 |
| 22a | 0.18 | 0.21 | 0.28 | 0.38 | 0.25 | 0.33 | 0.44 | 0.27 | 0.17 | 0.41 | 0.28 | 0.18 | 0.20 | 0.36 | 0.43 | 0.39 | 0.41 | 0.30 | 0.36 | 0.43 |
| 22b | 0.19 | 0.19 | 0.31 | 0.38 | 0.22 | 0.39 | 0.36 | 0.29 | 0.21 | 0.44 | 0.24 | 0.23 | 0.31 | 0.45 | 0.32 | 0.39 | 0.46 | 0.36 | 0.42 | 0.51 |
| 23 | 0.25 | 0.27 | 0.30 | 0.51 | 0.30 | 0.33 | 0.58 | 0.46 | 0.35 | 0.44 | 0.38 | 0.23 | 0.30 | 0.43 | 0.29 | 0.41 | 0.41 | 0.32 | 0.40 | 0.32 |
| 24 | 0.25 | 0.28 | 0.40 | 0.43 | 0.16 | 0.30 | 0.44 | 0.41 | 0.22 | 0.53 | 0.34 | 0.34 | 0.35 | 0.43 | 0.44 | 0.43 | 0.34 | 0.36 | 0.39 | 0.34 |
| 25 | 0.38 | 0.37 | 0.46 | 0.48 | 0.40 | 0.48 | 0.37 | 0.51 | 0.41 | 0.53 | 0.28 | 0.26 | 0.34 | 0.50 | 0.55 | 0.52 | 0.52 | 0.45 | 0.43 | 0.42 |
| 26 | 0.37 | 0.38 | 0.36 | 0.52 | 0.31 | 0.46 | 0.75 | 0.46 | 0.46 | 0.53 | 0.17 | 0.21 | 0.31 | 0.48 | 0.38 | 0.51 | 0.50 | 0.47 | 0.26 | 0.37 |
| 27 | 0.34 | 0.44 | 0.40 | 0.54 | 0.35 | 0.53 | 0.35 | 0.43 | 0.48 | 0.57 | 0.21 | 0.24 | 0.21 | 0.39 | 0.42 | 0.55 | 0.48 | 0.46 | 0.37 | 0.36 |

Pi = Ponding Index

I = Individual

C = Cumulative

Series 2 Ponding Index Data [ L = Configuration 3 Basin (dx=4) ]

| | Pi data (dip-oriented) | | | | | | | | | | Proximal | | Pi data (strike-oriented) | | | | | | | Distal |
|---|---|---|---|---|---|---|---|---|---|---|---|---|---|---|---|---|---|---|---|---|
| Event ID | d130 | | d160 | | d190 | | d220 | | d250 | | x150 | | x200 | | x250 | | x300 | | x350 | |
| | I | C | I | C | I | C | I | C | I | C | I | C | I | C | I | C | I | C | I | C |
| 15 | 0.07 | 0.07 | 0.10 | 0.10 | 0.07 | 0.07 | -0.01 | -0.01 | 0.17 | 0.17 | N/A | N/A | 0.19 | 0.19 | 0.07 | 0.07 | 0.07 | 0.07 | 0.15 | 0.15 |
| 16 | 0.11 | 0.16 | 0.08 | 0.19 | 0.09 | 0.05 | 0.08 | 0.07 | 0.16 | 0.26 | N/A | 0.08 | 0.23 | 0.20 | 0.15 | 0.09 | 0.11 | -0.01 | 0.19 | 0.11 |
| 17 | 0.17 | 0.12 | 0.05 | 0.23 | 0.14 | 0.07 | 0.08 | 0.14 | 0.17 | 0.31 | 0.11 | 0.16 | 0.19 | 0.29 | 0.05 | 0.11 | 0.09 | 0.03 | 0.12 | 0.17 |
| 18 | 0.14 | 0.20 | 0.06 | 0.20 | -0.01 | 0.13 | 0.04 | 0.13 | 0.13 | 0.35 | N/A | N/A | 0.14 | 0.31 | 0.16 | 0.17 | 0.17 | 0.15 | 0.15 | 0.20 |
| 20 | 0.24 | 0.30 | 0.31 | 0.45 | 0.30 | 0.31 | 0.38 | 0.47 | 0.12 | 0.44 | N/A | 0.28 | 0.32 | 0.29 | 0.32 | 0.35 | 0.29 | 0.28 | 0.04 | 0.25 |
| 21 | 0.27 | 0.35 | 0.10 | 0.41 | 0.07 | 0.48 | 0.17 | 0.47 | 0.25 | 0.51 | 0.16 | 0.26 | 0.20 | 0.29 | 0.28 | 0.47 | 0.20 | 0.33 | 0.05 | 0.12 |
| 22a | 0.06 | 0.40 | 0.08 | 0.43 | 0.26 | 0.44 | 0.28 | 0.46 | 0.15 | 0.51 | 0.13 | 0.20 | 0.20 | 0.35 | 0.22 | 0.43 | 0.18 | 0.26 | 0.08 | 0.11 |
| 22b | 0.07 | 0.38 | 0.17 | 0.45 | 0.23 | 0.43 | 0.34 | 0.47 | 0.13 | 0.48 | 0.06 | 0.24 | 0.18 | 0.32 | 0.17 | 0.42 | 0.28 | 0.35 | 0.16 | 0.16 |
| 23 | 0.25 | 0.44 | 0.23 | 0.48 | 0.33 | 0.51 | 0.30 | 0.48 | 0.24 | 0.50 | 0.28 | 0.33 | 0.18 | 0.43 | 0.26 | 0.42 | 0.25 | 0.31 | 0.15 | 0.07 |
| 24 | 0.07 | 0.43 | 0.19 | 0.43 | 0.17 | 0.61 | 0.35 | 0.46 | 0.10 | 0.48 | 0.21 | 0.23 | 0.29 | 0.45 | 0.15 | 0.38 | 0.25 | 0.32 | 0.26 | 0.09 |
| 25 | 0.31 | 0.44 | 0.34 | 0.56 | 0.40 | 0.50 | 0.43 | 0.57 | 0.35 | 0.55 | 0.17 | 0.13 | 0.36 | 0.42 | 0.39 | 0.53 | 0.40 | 0.47 | 0.25 | 0.15 |
| 26 | 0.24 | 0.47 | 0.25 | 0.56 | 0.21 | 0.56 | 0.30 | 0.56 | 0.25 | 0.50 | 0.10 | 0.15 | 0.24 | 0.47 | 0.31 | 0.55 | 0.36 | 0.46 | 0.11 | 0.15 |
| 27 | 0.27 | 0.46 | 0.26 | 0.53 | 0.19 | 0.58 | 0.24 | 0.58 | 0.28 | 0.59 | 0.08 | 0.17 | 0.24 | 0.41 | 0.22 | 0.48 | 0.34 | 0.46 | 0.14 | 0.18 |

Pi = Ponding Index

I = Individual

C = Cumulative

Series 2 Ponding Index Data [ L = Configuration 3 Basin (dx=10) ]

| | Pi data (dip-oriented) | | | | | | | | | | Proximal | | Pi data (strike-oriented) | | | | | | | Distal |
|---|---|---|---|---|---|---|---|---|---|---|---|---|---|---|---|---|---|---|---|---|
| Event ID | d130 | | d160 | | d190 | | d220 | | d250 | | x150 | | x200 | | x250 | | x300 | | x350 | |
| | I | C | I | C | I | C | I | C | I | C | I | C | I | C | I | C | I | C | I | C |
| 15 | -0.01 | -0.01 | 0.10 | 0.10 | 0.04 | 0.04 | -0.15 | -0.15 | 0.10 | 0.10 | N/A | N/A | 0.09 | 0.09 | 0.11 | 0.11 | 0.04 | 0.04 | -0.01 | -0.01 |
| 16 | 0.05 | 0.09 | 0.04 | 0.17 | 0.04 | -0.12 | 0.00 | -0.06 | 0.22 | 0.19 | N/A | 0.06 | 0.01 | 0.19 | 0.19 | 0.08 | 0.04 | -0.01 | 0.09 | -0.01 |
| 17 | 0.02 | 0.20 | -0.01 | 0.19 | 0.01 | -0.05 | -0.03 | -0.08 | 0.12 | 0.26 | 0.15 | 0.06 | 0.17 | 0.35 | 0.09 | 0.07 | 0.06 | 0.02 | 0.03 | -0.02 |
| 18 | 0.16 | 0.23 | 0.05 | 0.21 | 0.06 | -0.01 | -0.01 | -0.03 | 0.11 | 0.26 | N/A | N/A | 0.09 | 0.37 | 0.15 | 0.13 | 0.05 | -0.01 | 0.05 | -0.01 |
| 20 | 0.25 | 0.28 | 0.26 | 0.54 | 0.40 | 0.28 | 0.39 | 0.32 | 0.18 | 0.36 | N/A | 0.02 | 0.28 | 0.33 | 0.37 | 0.41 | 0.24 | 0.30 | 0.04 | -0.05 |
| 21 | 0.14 | 0.42 | -0.03 | 0.52 | -0.02 | 0.22 | 0.39 | 0.28 | 0.12 | 0.35 | 0.15 | -0.02 | 0.20 | 0.44 | 0.22 | 0.43 | 0.06 | 0.30 | -0.01 | -0.13 |
| 22a | 0.02 | 0.43 | 0.02 | 0.53 | 0.12 | 0.17 | 0.12 | 0.31 | 0.01 | 0.33 | 0.06 | -0.02 | 0.10 | 0.44 | 0.10 | 0.38 | 0.13 | 0.33 | 0.05 | -0.10 |
| 22b | 0.00 | 0.44 | 0.05 | 0.53 | 0.12 | 0.22 | 0.11 | 0.32 | -0.01 | 0.36 | 0.05 | -0.01 | 0.06 | 0.36 | 0.05 | 0.39 | 0.10 | 0.28 | 0.01 | -0.13 |
| 23 | 0.08 | 0.44 | 0.15 | 0.48 | 0.01 | 0.41 | 0.07 | 0.32 | 0.07 | 0.42 | 0.46 | 0.40 | 0.15 | 0.49 | 0.13 | 0.42 | 0.22 | 0.28 | 0.12 | -0.26 |
| 24 | 0.03 | 0.45 | 0.01 | 0.46 | 0.00 | 0.44 | -0.02 | 0.31 | 0.02 | 0.43 | 0.21 | 0.48 | 0.13 | 0.53 | 0.01 | 0.34 | 0.04 | 0.27 | 0.01 | -0.19 |
| 25 | 0.29 | 0.49 | 0.23 | 0.60 | 0.37 | 0.52 | 0.41 | 0.48 | 0.26 | 0.51 | 0.01 | 0.47 | 0.35 | 0.44 | 0.31 | 0.53 | 0.39 | 0.42 | 0.02 | -0.14 |
| 26 | 0.01 | 0.52 | 0.08 | 0.57 | 0.08 | 0.52 | 0.14 | 0.48 | 0.09 | 0.52 | 0.02 | 0.56 | 0.17 | 0.47 | 0.02 | 0.48 | 0.15 | 0.41 | 0.01 | -0.18 |
| 27 | 0.10 | 0.48 | 0.05 | 0.55 | 0.07 | 0.45 | 0.13 | 0.49 | 0.09 | 0.57 | 0.06 | 0.63 | 0.21 | 0.51 | 0.00 | 0.49 | 0.11 | 0.41 | -0.04 | -0.14 |

Pi = Ponding Index

I = Individual

C = Cumulative

Series 2 Ponding Index Data [ L = Configuration 3 Basin (dx=20) ]

| | Pi data (dip-oriented) | | | | | | | | | | Proximal | | Pi data (strike-oriented) | | | | | | Distal | |
|---|---|---|---|---|---|---|---|---|---|---|---|---|---|---|---|---|---|---|---|---|
| Event ID | d130 | | d160 | | d190 | | d220 | | d250 | | x150 | | x200 | | x250 | | x300 | | x350 | |
| | I | C | I | C | I | C | I | C | I | C | I | C | I | C | I | C | I | C | I | C |
| 15 | 0.05 | 0.05 | 0.14 | 0.14 | 0.00 | 0.00 | -0.05 | -0.05 | 0.02 | 0.02 | N/A | N/A | 0.21 | 0.21 | 0.13 | 0.13 | -0.03 | -0.03 | 0.00 | 0.00 |
| 16 | 0.08 | 0.07 | 0.00 | 0.24 | -0.03 | -0.03 | -0.02 | -0.04 | 0.17 | 0.07 | N/A | 0.25 | 0.12 | 0.33 | 0.17 | 0.09 | -0.08 | -0.04 | -0.02 | -0.06 |
| 17 | -0.02 | 0.11 | 0.01 | 0.28 | -0.10 | 0.00 | 0.00 | -0.05 | 0.08 | 0.10 | 0.00 | 0.27 | 0.24 | 0.45 | 0.06 | 0.10 | 0.00 | -0.03 | -0.01 | -0.06 |
| 18 | 0.02 | 0.12 | 0.08 | 0.30 | 0.00 | 0.07 | 0.02 | -0.08 | -0.07 | 0.18 | N/A | N/A | -0.04 | 0.49 | 0.20 | 0.19 | 0.10 | 0.05 | 0.03 | -0.08 |
| 20 | 0.21 | 0.22 | 0.26 | 0.63 | 0.32 | 0.50 | 0.39 | 0.48 | 0.13 | 0.22 | N/A | 0.30 | 0.25 | 0.57 | 0.37 | 0.40 | 0.26 | 0.27 | 0.01 | -0.12 |
| 21 | -0.09 | 0.27 | -0.09 | 0.61 | -0.02 | 0.42 | -0.02 | 0.42 | 0.06 | 0.12 | N/A | 0.38 | 0.11 | 0.66 | 0.44 | 0.46 | 0.04 | 0.29 | -0.02 | -0.19 |
| 22a | 0.04 | 0.26 | -0.02 | 0.62 | -0.02 | 0.40 | 0.08 | 0.45 | -0.04 | 0.10 | 0.05 | 0.36 | 0.04 | 0.66 | 0.03 | 0.45 | 0.03 | 0.31 | 0.03 | -0.14 |
| 22b | 0.04 | 0.26 | -0.03 | 0.62 | 0.06 | 0.41 | 0.06 | 0.43 | -0.01 | 0.08 | 0.04 | 0.36 | 0.02 | 0.66 | -0.02 | 0.43 | 0.02 | 0.33 | -0.04 | -0.18 |
| 23 | -0.07 | 0.31 | 0.14 | 0.56 | 0.15 | 0.47 | 0.20 | 0.43 | 0.02 | 0.20 | -0.03 | 0.45 | 0.16 | 0.74 | -0.03 | 0.42 | 0.29 | 0.23 | 0.10 | -0.14 |
| 24 | 0.01 | 0.31 | -0.01 | 0.55 | -0.15 | 0.55 | 0.02 | 0.42 | -0.01 | 0.21 | 0.06 | 0.54 | 0.08 | 0.78 | -0.05 | 0.41 | -0.08 | 0.17 | 0.03 | -0.08 |
| 25 | 0.27 | 0.44 | 0.22 | 0.65 | 0.34 | 0.58 | 0.41 | 0.62 | 0.29 | 0.49 | -0.07 | 0.54 | 0.40 | 0.57 | 0.34 | 0.53 | 0.32 | 0.40 | 0.01 | -0.06 |
| 26 | 0.07 | 0.46 | -0.01 | 0.63 | 0.03 | 0.62 | 0.13 | 0.60 | 0.07 | 0.49 | -0.03 | 0.67 | 0.13 | 0.68 | -0.04 | 0.53 | -0.06 | 0.40 | -0.02 | -0.10 |
| 27 | 0.08 | 0.46 | 0.03 | 0.61 | -0.17 | 0.71 | 0.13 | 0.61 | 0.03 | 0.53 | 0.00 | 0.79 | 0.04 | 0.71 | -0.03 | 0.51 | -0.01 | 0.41 | 0.05 | -0.07 |

Pi = Ponding Index

I = Individual

C = Cumulative

Series 2 Ponding Index Data [ L = Configuration 3 Basin (dx=50) ]

| | Pi data (dip-oriented) | | | | | | | | | | Proximal | | Pi data (strike-oriented) | | | | | | | Distal |
|---|---|---|---|---|---|---|---|---|---|---|---|---|---|---|---|---|---|---|---|---|
| Event ID | d130 | | d160 | | d190 | | d220 | | d250 | | x150 | | x200 | | x250 | | x300 | | x350 | |
| | I | C | I | C | I | C | I | C | I | C | I | C | I | C | I | C | I | C | I | C |
| 15 | 0.01 | 0.01 | -0.02 | -0.02 | 0.00 | 0.00 | -0.02 | -0.02 | 0.07 | 0.07 | N/A | N/A | 0.12 | 0.12 | 0.09 | 0.09 | 0.05 | 0.05 | -0.02 | -0.02 |
| 16 | 0.04 | 0.03 | 0.09 | 0.05 | -0.02 | 0.03 | -0.02 | -0.03 | -0.02 | 0.14 | N/A | 0.11 | 0.09 | 0.22 | -0.02 | 0.11 | -0.03 | 0.02 | -0.03 | -0.06 |
| 17 | 0.08 | 0.08 | 0.01 | 0.04 | -0.06 | 0.04 | 0.02 | -0.05 | 0.01 | 0.18 | 0.03 | 0.20 | 0.05 | 0.29 | 0.04 | 0.12 | 0.02 | 0.05 | 0.00 | -0.08 |
| 18 | 0.06 | 0.09 | -0.01 | 0.07 | 0.02 | 0.13 | 0.07 | -0.08 | 0.02 | 0.23 | N/A | N/A | -0.01 | 0.37 | 0.12 | 0.17 | 0.06 | 0.10 | 0.00 | -0.07 |
| 20 | 0.18 | 0.19 | 0.34 | 0.40 | 0.35 | 0.49 | 0.39 | 0.37 | 0.15 | 0.38 | N/A | 0.41 | 0.26 | 0.53 | 0.37 | 0.41 | 0.24 | 0.35 | -0.03 | -0.07 |
| 21 | -0.04 | 0.25 | -0.06 | 0.38 | 0.04 | 0.51 | -0.23 | 0.30 | 0.04 | 0.42 | -0.07 | 0.41 | -0.17 | 0.58 | 0.22 | 0.44 | 0.08 | 0.37 | 0.00 | -0.05 |
| 22a | 0.00 | 0.23 | -0.01 | 0.36 | 0.01 | 0.53 | 0.01 | 0.30 | 0.01 | 0.42 | 0.01 | 0.42 | 0.00 | 0.57 | 0.04 | 0.45 | 0.01 | 0.38 | 0.00 | -0.05 |
| 22b | 0.02 | 0.25 | 0.02 | 0.38 | 0.05 | 0.51 | 0.02 | 0.28 | 0.00 | 0.42 | 0.07 | 0.43 | 0.00 | 0.58 | -0.01 | 0.44 | 0.06 | 0.39 | 0.02 | -0.04 |
| 23 | 0.01 | 0.29 | 0.16 | 0.36 | -0.02 | 0.52 | -0.02 | 0.33 | 0.13 | 0.50 | -0.24 | 1.01 | 0.12 | 0.59 | -0.11 | 0.49 | 0.06 | 0.37 | 0.07 | -0.05 |
| 24 | 0.01 | 0.30 | 0.00 | 0.36 | 0.09 | 0.59 | -0.01 | 0.33 | 0.03 | 0.51 | -0.04 | 1.14 | 0.02 | 0.60 | -0.15 | 0.54 | -0.06 | 0.38 | 0.03 | -0.04 |
| 25 | 0.33 | 0.43 | 0.30 | 0.51 | 0.40 | 0.62 | 0.33 | 0.54 | 0.29 | 0.52 | 0.04 | 1.20 | 0.30 | 0.54 | 0.31 | 0.52 | 0.32 | 0.56 | 0.00 | -0.03 |
| 26 | 0.03 | 0.43 | -0.01 | 0.50 | -0.06 | 0.64 | 0.08 | 0.54 | 0.07 | 0.53 | 0.02 | 1.42 | 0.13 | 0.55 | -0.05 | 0.53 | -0.11 | 0.55 | 0.02 | -0.03 |
| 27 | 0.06 | 0.44 | -0.05 | 0.49 | 0.06 | 0.71 | 0.06 | 0.55 | 0.04 | 0.56 | 0.05 | 1.63 | 0.12 | 0.56 | 0.02 | 0.54 | -0.03 | 0.54 | 0.07 | -0.01 |

Pi = Ponding Index

I = Individual

C = Cumulative

Series 2 Ponding Index Data [ L = Configuration 3 Basin (dx=100) ]

| | Pi data (dip-oriented) | | | | | | | | | | Proximal | | Pi data (strike-oriented) | | | | | | | Distal |
|---|---|---|---|---|---|---|---|---|---|---|---|---|---|---|---|---|---|---|---|---|
| Event ID | d130 | | d160 | | d190 | | d220 | | d250 | | x150 | | x200 | | x250 | | x300 | | x350 | |
| | I | C | I | C | I | C | I | C | I | C | I | C | I | C | I | C | I | C | I | C |
| 15 | -0.05 | -0.05 | 0.00 | 0.00 | 0.06 | 0.06 | 0.00 | 0.00 | -0.10 | -0.10 | N/A | N/A | 0.09 | 0.09 | 0.05 | 0.05 | 0.03 | 0.03 | -0.01 | -0.01 |
| 16 | 0.00 | -0.05 | 0.06 | 0.07 | -0.01 | 0.08 | 0.03 | -0.02 | 0.02 | -0.11 | N/A | -0.10 | 0.08 | 0.16 | 0.02 | 0.09 | 0.02 | 0.05 | -0.03 | -0.07 |
| 17 | 0.03 | 0.02 | 0.02 | 0.08 | 0.07 | 0.14 | 0.02 | -0.02 | 0.01 | -0.08 | 0.02 | -0.06 | 0.22 | 0.23 | 0.04 | 0.11 | 0.03 | 0.07 | 0.00 | -0.07 |
| 18 | 0.04 | 0.11 | 0.03 | 0.09 | 0.08 | 0.21 | 0.01 | -0.01 | 0.02 | -0.07 | N/A | N/A | 0.03 | 0.30 | 0.07 | 0.18 | 0.04 | 0.11 | 0.00 | -0.07 |
| 20 | 0.10 | 0.19 | 0.41 | 0.41 | 0.30 | 0.53 | 0.34 | 0.35 | 0.09 | 0.08 | N/A | 0.09 | 0.11 | 0.40 | 0.32 | 0.39 | 0.22 | 0.30 | 0.01 | -0.09 |
| 21 | 0.04 | 0.33 | -0.04 | 0.41 | 0.03 | 0.57 | -0.11 | 0.29 | 0.09 | 0.15 | 0.06 | 0.21 | 0.05 | 0.46 | 0.08 | 0.40 | 0.00 | 0.31 | -0.03 | -0.14 |
| 22a | 0.02 | 0.32 | -0.05 | 0.40 | 0.00 | 0.58 | 0.01 | 0.30 | 0.01 | 0.15 | 0.01 | 0.20 | 0.01 | 0.46 | 0.09 | 0.41 | 0.02 | 0.30 | 0.00 | -0.15 |
| 22b | 0.01 | 0.32 | 0.01 | 0.40 | 0.00 | 0.58 | 0.00 | 0.29 | 0.02 | 0.14 | 0.02 | 0.21 | -0.01 | 0.46 | 0.06 | 0.41 | 0.02 | 0.31 | 0.02 | -0.12 |
| 23 | 0.03 | 0.36 | 0.15 | 0.40 | -0.09 | 0.59 | 0.10 | 0.33 | 0.05 | 0.27 | 0.30 | -0.01 | 0.11 | 0.50 | 0.23 | 0.42 | 0.05 | 0.35 | 0.01 | -0.13 |
| 24 | 0.02 | 0.38 | -0.02 | 0.40 | -0.04 | 0.57 | 0.02 | 0.32 | 0.01 | 0.26 | 0.03 | 0.08 | 0.01 | 0.53 | 0.07 | 0.43 | 0.01 | 0.34 | 0.03 | -0.15 |
| 25 | 0.27 | 0.39 | 0.26 | 0.53 | 0.31 | 0.64 | 0.44 | 0.50 | 0.29 | 0.48 | 0.05 | 0.12 | 0.17 | 0.51 | 0.26 | 0.52 | 0.29 | 0.49 | 0.00 | -0.15 |
| 26 | 0.03 | 0.40 | -0.01 | 0.52 | -0.04 | 0.65 | 0.01 | 0.51 | 0.04 | 0.49 | 0.04 | 0.20 | 0.00 | 0.54 | 0.02 | 0.52 | -0.08 | 0.49 | 0.01 | -0.16 |
| 27 | 0.03 | 0.43 | -0.02 | 0.51 | -0.08 | 0.64 | 0.04 | 0.51 | 0.09 | 0.50 | -0.21 | 0.25 | 0.10 | 0.54 | 0.00 | 0.54 | -0.02 | 0.48 | 0.02 | -0.21 |

Pi = Ponding Index

I = Individual

C = Cumulative

Series 2 - Near-bed Velocity Data for Run 1

| Raw Data | | | | | | | Rotated (bed-normal) Data | | |
|---|---|---|---|---|---|---|---|---|---|
| Xlocation (mm) | Ylocation (mm) | X Node | Y Node | u (m/s) | v (m/s) | w (m/s) | $u_{corr}$ (m/s) | $v_{corr}$ (m/s) | $w_{corr}$ (m/s) |
| 2050 | 1820 | 76 | 184 | 0.049 | 0.00E+00 | -9.00E-03 | 0.050 | 3.11E-04 | -7.00E-03 |
| 2150 | 1820 | 126 | 184 | 0.059 | 1.00E-03 | -1.00E-02 | 0.059 | 1.44E-03 | -5.07E-03 |
| 2250 | 1820 | 176 | 184 | 0.072 | 2.00E-03 | -1.70E-02 | 0.073 | 3.64E-03 | -1.41E-02 |
| 2350 | 1820 | 226 | 184 | 0.076 | 0.00E+00 | -2.50E-02 | 0.079 | 1.80E-03 | 1.21E-02 |
| 2450 | 1820 | 276 | 184 | 0.063 | -5.00E-03 | 1.90E-02 | 0.062 | -7.94E-03 | 2.16E-02 |
| 2550 | 1820 | 326 | 184 | 0.051 | -8.00E-03 | 2.00E-03 | 0.045 | -4.67E-03 | 2.52E-02 |
| 2650 | 1820 | 376 | 184 | 0.042 | 2.00E-03 | -6.00E-03 | 0.042 | 1.88E-03 | -4.95E-03 |
| 2750 | 1820 | 426 | 184 | 0.036 | 3.00E-03 | -7.00E-03 | 0.036 | 3.43E-03 | -2.38E-03 |

Series 2 -Near-bed Velocity Data for Run 2

| Raw Data | | | | | | | Rotated (bed-normal) Data | | |
|---|---|---|---|---|---|---|---|---|---|
| Xlocation (mm) | Ylocation (mm) | X Node | Y Node | u (m/s) | v (m/s) | w (m/s) | $u_{corr}$ (m/s) | $v_{corr}$ (m/s) | $w_{corr}$ (m/s) |
| 2050 | 1820 | 76 | 184 | 0.026 | -1.56E-03 | -4.79E-03 | 0.027 | -1.31E-03 | -3.86E-03 |
| 2150 | 1820 | 126 | 184 | 0.070 | 6.12E-04 | -1.16E-02 | 0.071 | 1.53E-03 | -5.33E-03 |
| 2250 | 1820 | 176 | 184 | 0.078 | 1.21E-03 | -1.63E-02 | 0.078 | 2.94E-03 | -1.31E-02 |
| 2350 | 1820 | 226 | 184 | 0.078 | -2.66E-05 | -2.89E-02 | 0.083 | 2.38E-03 | 1.00E-02 |
| 2450 | 1820 | 276 | 184 | 0.077 | -8.91E-03 | 2.19E-02 | 0.075 | -1.25E-02 | 2.41E-02 |
| 2550 | 1820 | 326 | 184 | 0.053 | -9.49E-03 | 7.22E-03 | 0.044 | -5.31E-03 | 3.12E-02 |
| 2650 | 1820 | 376 | 184 | 0.052 | -4.26E-03 | -6.15E-03 | 0.052 | -4.06E-03 | -5.43E-03 |
| 2750 | 1820 | 426 | 184 | 0.041 | 1.83E-03 | -5.83E-03 | 0.041 | 2.27E-03 | -1.31E-03 |

Series 2 -Near-bed Velocity Data for Run 3

| Raw Data | | | | | | | Rotated (bed-normal) Data | | |
|---|---|---|---|---|---|---|---|---|---|
| Xlocation (mm) | Ylocation (mm) | X Node | Y Node | u (m/s) | v (m/s) | w (m/s) | $u_{corr}$ (m/s) | $v_{corr}$ (m/s) | $w_{corr}$ (m/s) |
| 2050 | 1820 | 76 | 184 | 0.048 | -1.92E-03 | -9.14E-03 | 0.048 | -1.60E-03 | -8.55E-03 |
| 2150 | 1820 | 126 | 184 | 0.075 | -8.41E-04 | -1.23E-02 | 0.076 | 1.20E-04 | -5.50E-03 |
| 2250 | 1820 | 176 | 184 | 0.082 | -9.99E-04 | -1.74E-02 | 0.083 | 9.51E-04 | -1.34E-02 |
| 2350 | 1820 | 226 | 184 | 0.025 | -1.58E-02 | -5.42E-03 | 0.026 | -1.49E-02 | -4.06E-03 |
| 2450 | 1820 | 276 | 184 | 0.060 | -9.23E-03 | 1.90E-02 | 0.056 | -1.61E-02 | 2.59E-02 |
| 2550 | 1820 | 326 | 184 | 0.055 | -1.44E-02 | 6.68E-03 | 0.046 | -9.78E-03 | 3.32E-02 |
| 2650 | 1820 | 376 | 184 | 0.046 | -6.23E-03 | -2.49E-03 | 0.046 | -6.17E-03 | -2.20E-03 |
| 2750 | 1820 | 426 | 184 | 0.045 | -9.92E-03 | -6.12E-03 | 0.046 | -9.49E-03 | -1.17E-03 |

Series 2 - Near-bed Velocity Data for Run 5

| Raw Data | | | | | | | Rotated (bed-normal) Data | | |
|---|---|---|---|---|---|---|---|---|---|
| Xlocation (mm) | Ylocation (mm) | X Node | Y Node | u (m/s) | v (m/s) | w (m/s) | $u_{corr}$ (m/s) | $v_{corr}$ (m/s) | $w_{corr}$ (m/s) |
| 2050 | 1820 | 76 | 184 | 0.044 | -1.33E-03 | -9.20E-03 | 0.044 | -1.17E-03 | -9.06E-03 |
| 2150 | 1820 | 126 | 184 | 0.061 | -8.14E-04 | -1.03E-02 | 0.061 | -1.66E-05 | -4.93E-03 |
| 2250 | 1820 | 176 | 184 | 0.072 | -1.07E-03 | -1.50E-02 | 0.073 | 8.59E-04 | -8.12E-03 |
| 2350 | 1820 | 226 | 184 | 0.072 | -1.32E-03 | -2.61E-02 | 0.074 | 1.92E-03 | -2.00E-02 |
| 2450 | 1820 | 276 | 184 | 0.068 | -9.22E-03 | 2.01E-02 | 0.063 | -1.70E-02 | 2.96E-02 |
| 2550 | 1820 | 326 | 184 | 0.058 | -7.71E-03 | 4.33E-03 | 0.051 | -3.59E-03 | 2.99E-02 |
| 2650 | 1820 | 376 | 184 | 0.048 | -4.21E-03 | -6.31E-03 | 0.048 | -3.96E-03 | -5.19E-03 |
| 2750 | 1820 | 426 | 184 | 0.040 | 1.27E-03 | -5.66E-03 | 0.040 | 1.59E-03 | -9.11E-05 |

Series 2 - Near-bed Velocity Data for Run 6

| Raw Data | | | | | | | Rotated (bed-normal) Data | | |
|---|---|---|---|---|---|---|---|---|---|
| Xlocation (mm) | Ylocation (mm) | X Node | Y Node | u (m/s) | v (m/s) | w (m/s) | $u_{corr}$ (m/s) | $v_{corr}$ (m/s) | $w_{corr}$ (m/s) |
| 1950 | 1820 | 1 | 184 | 0.049 | -8.72E-04 | -2.63E-03 | 0.042 | -2.49E-03 | 2.67E-02 |
| 2050 | 1820 | 76 | 184 | 0.034 | -8.79E-04 | -9.84E-03 | 0.034 | -6.47E-04 | -9.61E-03 |
| 2150 | 1820 | 126 | 184 | 0.065 | 8.58E-05 | -2.75E-02 | 0.067 | 2.67E-03 | -2.18E-02 |
| 2250 | 1820 | 176 | 184 | 0.072 | -1.05E-03 | -3.60E-02 | 0.077 | 4.41E-03 | -2.30E-02 |
| 2350 | 1820 | 226 | 184 | 0.064 | -3.07E-03 | -2.13E-03 | 0.064 | -3.10E-03 | 2.55E-03 |
| 2450 | 1820 | 276 | 184 | 0.051 | -4.36E-03 | 2.04E-02 | 0.045 | -1.20E-02 | 2.86E-02 |
| 2550 | 1820 | 326 | 184 | 0.028 | -5.40E-03 | 6.92E-03 | 0.022 | -2.37E-03 | 1.91E-02 |
| 2650 | 1820 | 376 | 184 | 0.029 | -2.50E-03 | -4.23E-03 | 0.029 | -2.38E-03 | -3.82E-03 |
| 2750 | 1820 | 426 | 184 | 0.028 | -2.24E-03 | -5.56E-03 | 0.028 | -1.79E-03 | -2.36E-03 |
| 2850 | 1820 | 476 | 184 | 0.026 | -2.09E-03 | -4.44E-03 | 0.025 | -2.09E-03 | 7.59E-03 |

Series 2 - Near-bed Velocity Data for Run 7

| Raw Data | | | | | | | Rotated (bed-normal) Data | | |
|---|---|---|---|---|---|---|---|---|---|
| Xlocation (mm) | Ylocation (mm) | X Node | Y Node | u (m/s) | v (m/s) | w (m/s) | $u_{corr}$ (m/s) | $v_{corr}$ (m/s) | $w_{corr}$ (m/s) |
| 1950 | 1820 | 1 | 184 | 0.052 | 7.01E-04 | -3.03E-03 | 0.045 | -8.12E-04 | 2.70E-02 |
| 2050 | 1820 | 76 | 184 | 0.002 | -1.40E-03 | -3.32E-03 | 0.002 | -1.43E-03 | -3.29E-03 |
| 2150 | 1820 | 126 | 184 | 0.066 | 9.76E-04 | -2.69E-02 | 0.070 | 2.07E-03 | -1.53E-02 |
| 2250 | 1820 | 176 | 184 | 0.076 | 4.14E-03 | -3.83E-02 | 0.082 | 5.19E-03 | 2.46E-02 |
| 2350 | 1820 | 226 | 184 | 0.073 | 2.87E-03 | -2.12E-03 | 0.064 | 4.01E-03 | 3.44E-02 |
| 2450 | 1820 | 276 | 184 | 0.064 | -8.58E-05 | 2.31E-02 | 0.062 | -1.75E-04 | 2.80E-02 |
| 2550 | 1820 | 326 | 184 | 0.053 | -7.37E-03 | 1.73E-02 | 0.029 | 5.95E-04 | 4.80E-02 |
| 2650 | 1820 | 376 | 184 | 0.017 | -2.06E-03 | -3.95E-03 | 0.017 | -2.26E-03 | -8.38E-04 |
| 2750 | 1820 | 426 | 184 | 0.013 | -3.19E-03 | -3.76E-03 | 0.014 | -2.91E-03 | -1.68E-03 |

Series 2 - Near-bed Velocity Data for Run 8

| Raw Data | | | | | | | Rotated (bed-normal) Data | | |
|---|---|---|---|---|---|---|---|---|---|
| Xlocation (mm) | Ylocation (mm) | X Node | Y Node | u (m/s) | v (m/s) | w (m/s) | $u_{corr}$ (m/s) | $v_{corr}$ (m/s) | $w_{corr}$ (m/s) |
| 1950 | 1820 | 1 | 184 | 0.042 | -2.07E-03 | -2.78E-03 | 0.036 | -3.43E-03 | 2.11E-02 |
| 2050 | 1820 | 76 | 184 | 0.037 | -1.82E-03 | -1.10E-02 | 0.038 | -2.07E-03 | -9.43E-03 |
| 2150 | 1820 | 126 | 184 | 0.050 | -1.79E-03 | -2.38E-02 | 0.053 | -8.82E-04 | -1.44E-02 |
| 2250 | 1820 | 176 | 184 | 0.057 | -1.53E-03 | -2.80E-02 | 0.061 | -8.80E-04 | 1.74E-02 |
| 2350 | 1820 | 226 | 184 | 0.055 | -4.35E-03 | -1.37E-03 | 0.048 | -3.78E-03 | 2.85E-02 |
| 2450 | 1820 | 276 | 184 | 0.048 | -8.42E-03 | 2.07E-02 | 0.046 | -8.14E-03 | 2.46E-02 |
| 2550 | 1820 | 326 | 184 | 0.030 | -5.66E-03 | 3.39E-03 | 0.021 | -2.38E-03 | 2.25E-02 |
| 2650 | 1820 | 376 | 184 | 0.023 | -1.68E-03 | -4.10E-03 | 0.023 | -1.86E-03 | 1.02E-04 |
| 2750 | 1820 | 426 | 184 | 0.022 | -3.35E-03 | -5.70E-03 | 0.022 | -2.89E-03 | -2.83E-03 |
| 2850 | 1820 | 476 | 184 | 0.013 | -2.33E-03 | -4.13E-03 | 0.013 | -2.33E-03 | 2.13E-03 |

Series 2 - Near-bed Velocity Data for Run 9

| Raw Data | | | | | | | Rotated (bed-normal) Data | | |
|---|---|---|---|---|---|---|---|---|---|
| Xlocation (mm) | Ylocation (mm) | X Node | Y Node | u (m/s) | v (m/s) | w (m/s) | $u_{corr}$ (m/s) | $v_{corr}$ (m/s) | $w_{corr}$ (m/s) |
| 1950 | 1820 | 1 | 184 | 0.042 | -5.24E-04 | -2.80E-03 | 0.036 | -1.81E-03 | 2.06E-02 |
| 2050 | 1820 | 76 | 184 | 0.029 | -1.36E-03 | -9.01E-03 | 0.030 | -1.36E-03 | -7.55E-03 |
| 2150 | 1820 | 126 | 184 | 0.047 | -3.98E-04 | -2.14E-02 | 0.051 | 5.21E-04 | -1.05E-02 |
| 2250 | 1820 | 176 | 184 | 0.057 | -2.21E-04 | -2.91E-02 | 0.062 | 8.78E-04 | 1.45E-02 |
| 2350 | 1820 | 226 | 184 | 0.044 | -1.67E-03 | -2.22E-03 | 0.037 | -1.37E-03 | 2.28E-02 |
| 2450 | 1820 | 276 | 184 | 0.043 | -6.32E-03 | 1.83E-02 | 0.041 | -5.67E-03 | 2.16E-02 |
| 2550 | 1820 | 326 | 184 | 0.022 | -2.83E-03 | 3.47E-03 | 0.015 | -1.34E-04 | 1.72E-02 |
| 2650 | 1820 | 376 | 184 | 0.018 | -2.13E-03 | -3.23E-03 | 0.018 | -2.27E-03 | 1.99E-04 |
| 2750 | 1820 | 426 | 184 | 0.018 | -2.06E-03 | -4.14E-03 | 0.018 | -1.73E-03 | -1.67E-03 |
| 2850 | 1820 | 476 | 184 | 0.012 | -2.64E-03 | -3.38E-03 | 0.012 | -2.64E-03 | 2.44E-03 |
| 2350 | 2120 | 226 | 244 | 0.002 | 9.16E-04 | -4.38E-03 | 0.003 | -6.48E-04 | -3.76E-03 |
| 2350 | 2020 | 226 | 224 | -0.004 | -4.78E-03 | -7.56E-03 | -0.003 | -7.04E-03 | -6.26E-03 |
| 2350 | 1920 | 226 | 204 | -0.013 | 8.22E-03 | -3.70E-03 | -0.009 | 8.91E-03 | -8.83E-03 |
| 2350 | 1720 | 226 | 164 | -0.006 | -4.63E-03 | -4.12E-03 | -0.003 | -2.54E-03 | -7.21E-03 |
| 2350 | 1620 | 226 | 144 | 0.000 | -8.16E-04 | -2.62E-04 | 0.000 | -6.63E-04 | -5.80E-04 |
| 2350 | 1520 | 226 | 124 | 0.001 | -8.25E-04 | -4.06E-04 | 0.001 | -7.16E-04 | -5.44E-04 |

Series 2 - Near-bed Velocity Data for Run 10

| Raw Data | | | | | | | Rotated (bed-normal) Data | | |
|---|---|---|---|---|---|---|---|---|---|
| Xlocation (mm) | Ylocation (mm) | X Node | Y Node | u (m/s) | v (m/s) | w (m/s) | $u_{corr}$ (m/s) | $v_{corr}$ (m/s) | $w_{corr}$ (m/s) |
| 1950 | 1895 | 1 | 186 | 0.056 | -1.12E-03 | -3.08E-03 | 0.049 | -2.33E-03 | 2.88E-02 |
| 2050 | 1895 | 76 | 186 | 0.037 | -2.04E-03 | -9.82E-03 | 0.037 | -1.72E-03 | -7.71E-03 |
| 2150 | 1895 | 126 | 186 | 0.068 | -7.74E-04 | -3.01E-02 | 0.073 | 1.75E-03 | -1.29E-02 |
| 2250 | 1895 | 176 | 186 | 0.074 | -2.07E-04 | -3.65E-02 | 0.080 | 8.37E-04 | 2.18E-02 |
| 2350 | 1895 | 226 | 186 | 0.065 | -3.36E-04 | -2.21E-03 | 0.055 | 4.25E-04 | 3.52E-02 |
| 2450 | 1895 | 276 | 186 | 0.053 | -2.42E-03 | 2.14E-02 | 0.051 | -2.26E-03 | 2.48E-02 |
| 2550 | 1895 | 326 | 186 | 0.033 | -3.94E-03 | 5.41E-03 | 0.021 | -1.38E-03 | 2.62E-02 |
| 2650 | 1895 | 376 | 186 | 0.032 | -3.21E-03 | -5.43E-03 | 0.032 | -3.46E-03 | 4.44E-04 |
| 2750 | 1895 | 426 | 186 | 0.022 | -5.58E-03 | -5.22E-03 | 0.022 | -5.00E-03 | -2.83E-03 |
| 2850 | 1895 | 475 | 186 | 0.019 | -2.39E-03 | -3.90E-03 | 0.019 | -2.39E-03 | 5.10E-03 |
| 2255 | 2095 | 176 | 286 | 0.000 | -3.45E-04 | -2.07E-04 | 0.000 | -3.95E-04 | -1.75E-04 |
| 2255 | 1995 | 176 | 236 | -0.005 | -2.76E-03 | -1.45E-03 | -0.002 | -3.27E-03 | -4.13E-03 |
| 2255 | 1895 | 176 | 186 | 0.081 | 2.35E-03 | -3.62E-02 | 0.084 | 3.02E-03 | 2.67E-02 |
| 2255 | 1795 | 176 | 136 | 0.001 | -1.21E-04 | -2.31E-03 | 0.002 | 1.64E-04 | -1.13E-03 |
| 2255 | 1695 | 176 | 86 | 0.007 | -1.26E-05 | -4.94E-03 | 0.008 | 8.94E-04 | -3.55E-03 |
| 2300 | 2195 | 201 | 326 | -0.002 | -3.37E-03 | -4.52E-03 | -0.001 | -3.33E-03 | -4.81E-03 |
| 2300 | 2095 | 201 | 286 | 0.002 | -1.13E-03 | -3.08E-03 | 0.002 | -1.61E-03 | -2.76E-03 |
| 2300 | 1995 | 201 | 236 | 0.002 | -4.03E-03 | -1.17E-03 | 0.002 | -4.03E-03 | 1.20E-03 |
| 2300 | 1895 | 201 | 186 | 0.074 | 1.96E-03 | -1.43E-02 | 0.060 | 2.25E-03 | 4.57E-02 |
| 2300 | 1795 | 201 | 136 | -0.002 | -2.58E-03 | -2.57E-03 | -0.001 | -1.30E-03 | -3.87E-03 |
| 2300 | 1695 | 201 | 86 | 0.000 | -5.55E-04 | -2.45E-04 | 0.000 | -4.74E-04 | -4.24E-04 |
| 2350 | 2195 | 226 | 326 | 0.000 | -4.03E-04 | -1.91E-04 | 0.000 | -4.14E-04 | -1.42E-04 |
| 2350 | 2095 | 226 | 286 | -0.003 | 1.05E-04 | -1.13E-04 | -0.003 | 4.00E-05 | -4.65E-04 |
| 2350 | 1995 | 226 | 236 | -0.014 | 1.94E-02 | -3.08E-03 | -0.011 | 1.53E-02 | -1.52E-02 |

Series 2 - Near-bed Velocity Data for Run 10 Cont'd

| | | | | | | | | | |
|---|---|---|---|---|---|---|---|---|---|
| 2350 | 1795 | 226 | 136 | -0.003 | -5.96E-03 | -3.23E-03 | -0.003 | -4.91E-03 | -4.92E-03 |
| 2350 | 1695 | 226 | 86 | 0.001 | 2.01E-03 | -2.31E-03 | 0.001 | 2.38E-03 | -1.80E-03 |
| 2350 | 1595 | 226 | 36 | 0.001 | 1.59E-03 | -6.72E-03 | 0.001 | 2.07E-03 | -6.54E-03 |
| 2400 | 2195 | 251 | 326 | 0.004 | 9.87E-04 | -6.89E-03 | 0.006 | 5.81E-04 | -5.76E-03 |
| 2400 | 1995 | 251 | 236 | -0.021 | 3.87E-03 | -3.07E-03 | -0.017 | 4.84E-04 | -1.21E-02 |
| 2400 | 1895 | 251 | 186 | 0.060 | 2.42E-03 | 1.11E-02 | 0.057 | 1.62E-03 | 2.13E-02 |
| 2400 | 1795 | 251 | 136 | -0.009 | -3.10E-03 | -3.05E-03 | -0.009 | -2.10E-03 | -4.46E-03 |
| 2400 | 1695 | 251 | 86 | -0.001 | 1.54E-03 | -2.32E-03 | -0.001 | 1.93E-03 | -2.08E-03 |
| 2400 | 1595 | 251 | 36 | -0.001 | -4.58E-04 | -7.83E-03 | -0.001 | -1.41E-05 | -7.88E-03 |

Series 2 - Near-bed Velocity Data for Run 11

| Raw Data | | | | | | | Rotated (bed-normal) Data | | |
|---|---|---|---|---|---|---|---|---|---|
| Xlocation (mm) | Ylocation (mm) | X Node | Y Node | u (m/s) | v (m/s) | w (m/s) | $u_{corr}$ (m/s) | $v_{corr}$ (m/s) | $w_{corr}$ (m/s) |
| 1950 | 1895 | 1 | 186 | 0.077 | -2.87E-03 | -3.98E-03 | 0.063 | -4.57E-03 | 4.36E-02 |
| 2050 | 1895 | 76 | 186 | 0.070 | -3.53E-03 | -1.99E-02 | 0.072 | -2.95E-03 | -9.73E-03 |
| 2150 | 1895 | 126 | 186 | 0.083 | -1.14E-03 | -3.62E-02 | 0.091 | 2.14E-04 | -1.45E-03 |
| 2200 | 1895 | 151 | 186 | 0.085 | -1.93E-03 | -4.30E-02 | 0.094 | 5.92E-04 | 1.58E-02 |
| 2250 | 1895 | 176 | 186 | 0.092 | -1.00E-03 | -4.29E-02 | 0.097 | -5.41E-04 | 2.92E-02 |
| 2300 | 1895 | 201 | 186 | 0.087 | -2.37E-03 | -1.75E-02 | 0.070 | -1.56E-03 | 5.35E-02 |
| 2350 | 1895 | 226 | 186 | 0.075 | -9.12E-04 | -2.01E-03 | 0.064 | -3.90E-03 | 3.92E-02 |
| 2450 | 1895 | 276 | 186 | 0.061 | -2.73E-03 | 2.61E-02 | 0.056 | -1.31E-03 | 3.57E-02 |
| 2550 | 1895 | 326 | 186 | 0.043 | -3.20E-03 | 9.55E-03 | 0.028 | 4.43E-04 | 3.45E-02 |
| 2650 | 1895 | 376 | 186 | 0.040 | -4.83E-03 | -5.72E-03 | 0.040 | -5.00E-03 | 2.20E-03 |
| 2750 | 1895 | 426 | 186 | 0.033 | -2.47E-03 | -5.78E-03 | 0.033 | -2.03E-03 | -9.24E-04 |
| 2255 | 1995 | 176 | 236 | 0.001 | -5.92E-04 | -3.96E-03 | 0.004 | -9.84E-04 | -1.73E-03 |
| 2255 | 1795 | 176 | 136 | -0.001 | -1.31E-03 | -3.93E-03 | 0.002 | -1.19E-03 | -3.34E-03 |
| 2350 | 2195 | 226 | 326 | 0.008 | 3.83E-03 | -4.49E-03 | 0.009 | 3.59E-03 | -3.32E-03 |
| 2350 | 2095 | 226 | 286 | 0.000 | -1.11E-03 | -2.75E-03 | 0.000 | -1.69E-03 | -2.45E-03 |
| 2350 | 1995 | 226 | 236 | -0.005 | 1.15E-02 | -2.76E-03 | -0.003 | 9.05E-03 | -8.44E-03 |
| 2350 | 1795 | 226 | 136 | 0.000 | -1.10E-03 | -3.56E-03 | 0.001 | -1.51E-04 | -3.68E-03 |
| 2350 | 1695 | 226 | 86 | -0.001 | 3.80E-04 | -2.82E-04 | -0.001 | 4.15E-04 | -2.60E-04 |
| 2450 | 2195 | 276 | 326 | 0.002 | -1.15E-03 | -2.16E-03 | 0.003 | -1.13E-03 | -1.56E-03 |
| 2450 | 2095 | 276 | 286 | -0.007 | -7.49E-03 | -8.51E-04 | -0.007 | -7.56E-03 | 5.26E-05 |
| 2450 | 1995 | 276 | 236 | -0.002 | -9.73E-03 | -2.11E-04 | -0.002 | -9.68E-03 | 1.02E-03 |
| 2450 | 1795 | 276 | 136 | 0.007 | 3.97E-03 | 1.47E-03 | 0.007 | 3.99E-03 | 1.41E-03 |

| | | | | | | | | | |
|---|---|---|---|---|---|---|---|---|---|
| 2450 | 1695 | 276 | 86 | -0.001 | 2.24E-03 | -1.44E-03 | -0.001 | 2.25E-03 | -1.42E-03 |
| 2450 | 1595 | 276 | 36 | 0.000 | -9.75E-04 | -2.11E-03 | 0.000 | -6.61E-04 | -2.21E-03 |

Series 2 - Near-bed Velocity Data for Run 11 Cont'd

| | | | | | | | | | |
|---|---|---|---|---|---|---|---|---|---|
| 2550 | 2195 | 326 | 326 | -0.001 | -3.62E-03 | -2.32E-03 | -0.001 | -3.51E-03 | -2.53E-03 |
| 2550 | 2095 | 326 | 276 | 0.002 | -5.07E-03 | -2.28E-03 | 0.002 | -4.48E-03 | -3.18E-03 |
| 2550 | 1995 | 326 | 236 | 0.011 | -1.92E-02 | -2.42E-03 | 0.012 | -1.90E-02 | 9.70E-04 |
| 2550 | 1795 | 326 | 136 | 0.028 | 1.16E-02 | -9.41E-04 | 0.025 | 1.36E-02 | 1.09E-02 |
| 2550 | 1695 | 326 | 86 | 0.008 | 1.01E-02 | -2.68E-03 | 0.008 | 1.02E-02 | -2.05E-03 |
| 2550 | 1595 | 326 | 36 | 0.003 | 5.25E-03 | -1.86E-03 | 0.003 | 5.27E-03 | -1.37E-03 |
| 2650 | 2195 | 376 | 326 | -0.004 | -6.28E-03 | -4.33E-03 | -0.003 | -5.82E-03 | -5.47E-03 |
| 2650 | 2095 | 376 | 286 | 0.006 | -1.09E-02 | -3.23E-03 | 0.006 | -1.09E-02 | -2.36E-03 |
| 2650 | 1995 | 376 | 236 | 0.021 | -1.34E-02 | -5.54E-03 | 0.022 | -1.23E-02 | -4.91E-03 |
| 2650 | 1795 | 376 | 136 | 0.035 | 1.33E-02 | -5.34E-03 | 0.035 | 1.33E-02 | -5.33E-03 |
| 2650 | 1695 | 376 | 86 | 0.014 | 1.49E-02 | -3.25E-03 | 0.014 | 1.49E-02 | -9.32E-04 |
| 2650 | 1595 | 376 | 36 | 0.010 | 1.24E-02 | -3.05E-03 | 0.010 | 1.21E-02 | -2.77E-03 |
| 2750 | 2195 | 426 | 326 | 0.001 | -3.91E-03 | -2.63E-03 | 0.001 | -3.58E-03 | -2.92E-03 |
| 2750 | 2095 | 426 | 286 | 0.004 | -7.86E-03 | -2.93E-03 | 0.005 | -7.80E-03 | -2.48E-03 |
| 2750 | 1995 | 426 | 236 | 0.025 | -1.29E-02 | -5.47E-03 | 0.025 | -1.29E-02 | 4.92E-03 |
| 2750 | 1795 | 426 | 136 | 0.020 | 1.44E-02 | -3.71E-03 | 0.020 | 1.40E-02 | -4.36E-03 |
| 2750 | 1695 | 426 | 86 | 0.020 | 1.44E-02 | -3.71E-03 | 0.020 | 1.42E-02 | -2.88E-03 |
| 2750 | 1595 | 426 | 36 | 0.016 | 1.55E-02 | -4.52E-03 | 0.016 | 1.49E-02 | -4.22E-03 |

Series 2 - Near-bed Velocity Data for Run 12

| Raw Data | | | | | | | Rotated (bed-normal) Data | | |
|---|---|---|---|---|---|---|---|---|---|
| Xlocation (mm) | Ylocation (mm) | X Node | Y Node | u (m/s) | v (m/s) | w (m/s) | $u_{corr}$ (m/s) | $v_{corr}$ (m/s) | $w_{corr}$ (m/s) |
| 1950 | 1895 | 1 | 186 | 0.055 | -6.85E-04 | -2.91E-03 | 0.047 | -7.79E-04 | 2.91E-02 |
| 2050 | 1895 | 76 | 186 | 0.056 | -7.96E-04 | -1.84E-02 | 0.057 | -7.11E-04 | -1.48E-02 |
| 2150 | 1895 | 126 | 186 | 0.055 | -2.12E-04 | -2.42E-02 | 0.060 | -3.82E-06 | -4.98E-04 |
| 2250 | 1895 | 176 | 186 | 0.063 | 2.33E-03 | -2.61E-02 | 0.063 | 2.41E-03 | 2.51E-02 |
| 2350 | 1895 | 226 | 186 | 0.037 | 5.71E-03 | -1.80E-03 | 0.032 | 4.49E-03 | 1.84E-02 |
| 2450 | 1895 | 276 | 186 | 0.029 | 1.21E-04 | 1.21E-02 | 0.029 | -7.12E-05 | 1.26E-02 |
| 2550 | 1895 | 326 | 186 | 0.021 | -2.31E-03 | 9.32E-04 | 0.016 | -1.25E-03 | 1.47E-02 |
| 2650 | 1895 | 376 | 186 | 0.017 | -5.36E-03 | -3.87E-03 | 0.018 | -5.56E-03 | -5.29E-04 |
| 2750 | 1895 | 426 | 186 | 0.009 | -2.67E-03 | -4.28E-03 | 0.009 | -2.18E-03 | -3.18E-03 |
| 2255 | 1995 | 176 | 236 | 0.000 | -9.90E-04 | -2.17E-03 | 0.001 | -1.26E-03 | -1.54E-03 |
| 2255 | 1795 | 176 | 136 | 0.001 | -6.40E-04 | -3.28E-03 | 0.003 | -8.02E-04 | -1.72E-03 |
| 2350 | 2095 | 226 | 286 | 0.000 | 1.02E-03 | -2.86E-03 | 0.000 | 3.74E-04 | -3.01E-03 |
| 2350 | 1995 | 226 | 236 | -0.017 | 1.60E-02 | -7.01E-04 | -0.015 | 1.35E-02 | -1.14E-02 |
| 2350 | 1795 | 226 | 136 | -0.003 | -4.16E-03 | -3.03E-03 | -0.003 | -3.20E-03 | -4.30E-03 |
| 2350 | 1695 | 226 | 86 | 0.002 | -2.18E-03 | -5.35E-03 | 0.002 | -1.44E-03 | -5.47E-03 |
| 2450 | 2095 | 276 | 286 | -0.005 | -5.89E-03 | -1.41E-03 | -0.005 | -6.05E-03 | -6.86E-04 |
| 2450 | 1995 | 276 | 236 | -0.010 | -1.10E-02 | -1.04E-03 | -0.010 | -1.10E-02 | -2.97E-04 |
| 2450 | 1795 | 276 | 136 | -0.001 | 4.28E-03 | -1.03E-03 | -0.001 | 4.26E-03 | -1.12E-03 |
| 2450 | 1695 | 276 | 86 | -0.001 | -6.04E-04 | -1.78E-03 | -0.001 | -6.13E-04 | -1.78E-03 |
| 2450 | 1595 | 276 | 36 | 0.015 | -9.13E-03 | -2.27E-02 | 0.019 | -6.02E-03 | -2.09E-02 |
| 2550 | 2195 | 326 | 326 | 0.002 | -4.82E-03 | -2.39E-03 | 0.002 | -4.76E-03 | -2.39E-03 |
| 2550 | 2095 | 326 | 276 | 0.002 | -5.17E-03 | -1.93E-03 | 0.002 | -4.63E-03 | -2.91E-03 |

| | | | | | | | | | |
|---|---|---|---|---|---|---|---|---|---|
| 2550 | 1995 | 326 | 236 | 0.008 | -1.67E-02 | -1.32E-04 | 0.008 | -1.66E-02 | -3.29E-04 |
| 2550 | 1795 | 326 | 136 | 0.011 | 1.04E-02 | -1.30E-03 | 0.010 | 1.05E-02 | 1.48E-03 |

Series 2 - Near-bed Velocity Data for Run 12 Cont'd

| | | | | | | | | | |
|---|---|---|---|---|---|---|---|---|---|
| 2550 | 1695 | 326 | 86 | 0.002 | 3.81E-03 | -1.64E-03 | 0.002 | 3.89E-03 | -1.40E-03 |
| 2550 | 1595 | 326 | 36 | 0.001 | 5.67E-03 | -5.75E-04 | 0.001 | 5.67E-03 | -5.07E-04 |
| 2650 | 2195 | 376 | 326 | 0.003 | -5.67E-03 | -2.80E-03 | 0.003 | -5.39E-03 | -2.89E-03 |
| 2650 | 2095 | 376 | 286 | 0.001 | -5.98E-03 | -3.98E-03 | 0.002 | -6.05E-03 | -3.69E-03 |
| 2650 | 1995 | 376 | 236 | 0.007 | -8.28E-03 | -2.84E-03 | 0.008 | -7.72E-03 | -3.29E-03 |
| 2650 | 1795 | 376 | 136 | 0.017 | 9.83E-03 | -3.67E-03 | 0.017 | 9.84E-03 | -3.56E-03 |
| 2650 | 1695 | 376 | 86 | 0.009 | 8.25E-03 | -2.67E-03 | 0.010 | 8.23E-03 | -1.13E-03 |
| 2650 | 1595 | 376 | 36 | 0.005 | 4.75E-03 | -2.19E-03 | 0.005 | 4.59E-03 | -1.86E-03 |
| 2750 | 2195 | 426 | 326 | 0.001 | -3.79E-03 | -3.13E-03 | 0.002 | -3.38E-03 | -3.31E-03 |
| 2750 | 2095 | 426 | 286 | 0.003 | -4.72E-03 | -3.83E-03 | 0.004 | -4.57E-03 | -3.45E-03 |
| 2750 | 1995 | 426 | 236 | 0.006 | -6.18E-03 | -3.42E-03 | 0.007 | -6.12E-03 | -9.62E-04 |
| 2750 | 1795 | 426 | 136 | 0.017 | 6.73E-03 | -4.38E-03 | 0.017 | 6.34E-03 | -4.43E-03 |
| 2750 | 1695 | 426 | 86 | 0.008 | 5.45E-03 | -2.87E-03 | 0.008 | 5.29E-03 | -2.39E-03 |
| 2750 | 1595 | 426 | 36 | 0.010 | 8.46E-03 | -3.41E-03 | 0.010 | 8.04E-03 | -2.87E-03 |

Series 2 - Near-bed Velocity Data for Run 13

| Raw Data | | | | | | | Rotated (bed-normal) Data | | |
|---|---|---|---|---|---|---|---|---|---|
| Xlocation (mm) | Ylocation (mm) | X Node | Y Node | u (m/s) | v (m/s) | w (m/s) | $u_{corr}$ (m/s) | $v_{corr}$ (m/s) | $w_{corr}$ (m/s) |
| 1950 | 1895 | 1 | 186 | 0.035 | -1.06E-03 | -4.11E-03 | 0.031 | -1.11E-03 | 1.65E-02 |
| 2050 | 1895 | 76 | 186 | 0.040 | -1.05E-03 | -1.23E-02 | 0.041 | -9.93E-04 | -9.67E-03 |
| 2150 | 1895 | 126 | 186 | 0.041 | -5.05E-04 | -1.87E-02 | 0.045 | -3.40E-04 | -8.61E-04 |
| 2250 | 1895 | 176 | 186 | 0.032 | -1.13E-03 | -1.43E-02 | 0.033 | -9.08E-04 | 1.14E-02 |
| 2350 | 1895 | 226 | 186 | 0.022 | 4.10E-03 | 1.86E-03 | 0.018 | 2.95E-03 | 1.37E-02 |
| 2450 | 1895 | 276 | 186 | 0.035 | 1.11E-03 | 1.10E-02 | 0.035 | 9.33E-04 | 1.16E-02 |
| 2550 | 1895 | 326 | 186 | 0.044 | 1.43E-03 | 1.31E-02 | 0.026 | 4.94E-03 | 3.81E-02 |
| 2650 | 1895 | 376 | 186 | 0.022 | 1.69E-03 | -7.16E-03 | 0.023 | 1.20E-03 | -3.63E-03 |
| 2750 | 1895 | 426 | 186 | 0.010 | -1.07E-03 | -4.07E-03 | 0.010 | -6.32E-04 | -2.61E-03 |
| 2255 | 1995 | 176 | 236 | 0.001 | -1.38E-03 | -3.75E-03 | 0.004 | -1.75E-03 | -1.34E-03 |
| 2255 | 1795 | 176 | 136 | 0.004 | 1.78E-03 | -5.83E-03 | 0.007 | 1.53E-03 | -1.82E-03 |
| 2350 | 2095 | 226 | 286 | -0.002 | -1.79E-03 | -7.98E-03 | -0.001 | -3.49E-03 | -7.55E-03 |
| 2350 | 1995 | 226 | 236 | -0.009 | 1.29E-02 | -1.63E-03 | -0.008 | 1.07E-02 | -9.02E-03 |
| 2350 | 1795 | 226 | 136 | -0.003 | -3.91E-03 | -2.47E-03 | -0.003 | -3.11E-03 | -3.67E-03 |
| 2450 | 2095 | 276 | 286 | 0.006 | 7.09E-03 | -6.00E-03 | 0.006 | 6.11E-03 | -6.76E-03 |
| 2450 | 1995 | 276 | 236 | 0.004 | -6.11E-03 | 4.22E-04 | 0.004 | -6.06E-03 | 9.02E-04 |
| 2450 | 1795 | 276 | 136 | 0.003 | 1.00E-02 | 1.86E-03 | 0.003 | 1.01E-02 | 1.65E-03 |
| 2450 | 1695 | 276 | 86 | -0.003 | -4.69E-03 | -2.30E-03 | -0.003 | -4.70E-03 | -2.28E-03 |
| 2550 | 1995 | 326 | 236 | 0.004 | -5.57E-03 | -3.18E-03 | 0.006 | -4.83E-03 | -1.74E-03 |
| 2550 | 1795 | 326 | 136 | -0.001 | 1.32E-03 | -2.67E-03 | 0.001 | 9.90E-05 | -3.01E-03 |
| 2550 | 1695 | 326 | 86 | -0.003 | -3.01E-03 | -3.22E-03 | -0.002 | -2.85E-03 | -3.42E-03 |
| 2650 | 1995 | 376 | 236 | 0.007 | -5.97E-03 | -3.98E-03 | 0.007 | -5.24E-03 | -4.07E-03 |

Series 2 - Near-bed Velocity Data for Run 13 Cont'd

| | | | | | | | | | |
|---|---|---|---|---|---|---|---|---|---|
| 2650 | 1795 | 376 | 136 | 0.008 | 6.79E-03 | -2.60E-03 | 0.008 | 6.80E-03 | -2.54E-03 |
| 2750 | 2095 | 426 | 286 | -0.004 | -1.04E-03 | -3.41E-03 | -0.003 | -8.89E-04 | -3.98E-03 |
| 2750 | 1995 | 426 | 236 | 0.005 | -4.55E-03 | -5.01E-03 | 0.007 | -4.44E-03 | -2.75E-03 |
| 2750 | 1795 | 426 | 136 | 0.002 | 3.62E-03 | -3.95E-03 | 0.002 | 3.25E-03 | -4.20E-03 |

Series 2 - Near-bed Velocity Data for Run 15

| Raw Data | | | | | | | Rotated (bed-normal) Data | | |
|---|---|---|---|---|---|---|---|---|---|
| Xlocation (mm) | Ylocation (mm) | X Node | Y Node | u (m/s) | v (m/s) | w (m/s) | $u_{corr}$ (m/s) | $v_{corr}$ (m/s) | $w_{corr}$ (m/s) |
| 1950 | 1895 | 1 | 186 | 0.097 | -2.12E-03 | -1.06E-02 | 0.086 | -6.19E-04 | 4.68E-02 |
| 2050 | 1895 | 76 | 186 | 0.088 | 3.20E-04 | -5.31E-02 | 0.103 | -2.20E-03 | -2.50E-06 |
| 2150 | 1895 | 126 | 186 | 0.103 | -3.43E-03 | -4.84E-02 | 0.113 | -4.88E-03 | 9.67E-03 |
| 2250 | 1895 | 176 | 186 | 0.078 | -2.67E-03 | -2.15E-02 | 0.072 | -3.71E-03 | 3.62E-02 |
| 2350 | 1895 | 226 | 186 | 0.065 | -1.47E-03 | 1.83E-03 | 0.060 | -2.04E-03 | 2.53E-02 |
| 2450 | 1895 | 276 | 186 | 0.047 | -1.22E-03 | 1.78E-02 | 0.046 | -1.54E-03 | 2.02E-02 |
| 2550 | 1895 | 326 | 186 | 0.008 | -4.86E-03 | 1.49E-03 | 0.005 | -4.18E-03 | 6.74E-03 |
| 2650 | 1895 | 376 | 186 | 0.024 | -1.93E-03 | -4.48E-03 | 0.025 | -2.13E-03 | -2.43E-04 |
| 2750 | 1895 | 426 | 186 | 0.025 | 3.22E-03 | -5.75E-03 | 0.025 | 3.66E-03 | -1.74E-03 |
| 2255 | 2095 | 176 | 286 | 0.000 | -8.44E-04 | -4.30E-03 | 0.001 | -1.96E-03 | -3.69E-03 |
| 2255 | 1995 | 176 | 236 | -0.001 | -8.44E-04 | -3.16E-03 | 0.002 | -1.17E-03 | -2.45E-03 |
| 2255 | 1795 | 176 | 136 | 0.001 | 3.44E-04 | -3.11E-03 | 0.003 | 8.68E-04 | -1.72E-03 |
| 2255 | 1695 | 176 | 86 | -0.003 | -3.07E-03 | -3.44E-03 | -0.002 | -2.25E-03 | -4.43E-03 |
| 2350 | 2195 | 226 | 326 | 0.000 | 8.05E-04 | -3.31E-03 | 0.000 | 5.24E-04 | -3.34E-03 |
| 2350 | 2095 | 226 | 286 | -0.011 | 6.72E-03 | -1.16E-03 | -0.011 | 6.17E-03 | -3.66E-03 |
| 2350 | 1995 | 226 | 236 | -0.006 | 7.02E-03 | -3.58E-03 | -0.005 | 4.75E-03 | -7.49E-03 |
| 2350 | 1795 | 226 | 136 | -0.009 | 1.28E-04 | -8.93E-04 | -0.009 | 4.61E-04 | -1.74E-03 |
| 2350 | 1695 | 226 | 86 | -0.010 | -2.56E-03 | -1.54E-03 | -0.010 | -2.32E-03 | -2.31E-03 |
| 2350 | 1595 | 226 | 36 | 0.000 | -1.16E-03 | 4.02E-04 | 0.000 | -1.19E-03 | 3.12E-04 |
| 2450 | 2195 | 276 | 326 | -0.002 | -1.09E-02 | -2.43E-03 | -0.001 | -1.08E-02 | -2.88E-03 |
| 2450 | 2095 | 276 | 286 | -0.013 | -9.27E-03 | -5.77E-04 | -0.013 | -9.29E-03 | 2.23E-04 |
| 2450 | 1995 | 276 | 236 | 0.010 | -1.07E-02 | 1.73E-03 | 0.010 | -1.07E-02 | 1.33E-03 |

Series 2 - Near-bed Velocity Data for Run 15 Cont'd

| | | | | | | | | | |
|---|---|---|---|---|---|---|---|---|---|
| 2450 | 1795 | 276 | 136 | -0.004 | 2.93E-03 | -1.85E-03 | -0.004 | 2.95E-03 | -1.82E-03 |
| 2450 | 1695 | 276 | 86 | -0.008 | 3.34E-03 | -1.82E-03 | -0.008 | 3.31E-03 | -1.89E-03 |
| 2450 | 1595 | 276 | 36 | 0.001 | 3.96E-03 | -2.42E-03 | 0.001 | 4.24E-03 | -1.75E-03 |
| 2550 | 2195 | 326 | 326 | 0.005 | -1.51E-02 | -3.82E-03 | 0.005 | -1.50E-02 | -4.16E-03 |
| 2550 | 2095 | 326 | 276 | 0.005 | -1.60E-02 | -1.75E-03 | 0.005 | -1.51E-02 | -5.26E-03 |
| 2550 | 1995 | 326 | 236 | 0.011 | -1.26E-02 | 5.67E-03 | 0.008 | -1.44E-02 | 6.36E-03 |
| 2550 | 1795 | 326 | 136 | 0.005 | 1.10E-02 | -6.04E-04 | 0.006 | 1.04E-02 | -2.24E-03 |
| 2550 | 1695 | 326 | 86 | 0.005 | 1.18E-02 | -1.55E-03 | 0.005 | 1.18E-02 | -1.09E-03 |
| 2550 | 1595 | 326 | 36 | 0.007 | 1.25E-02 | -2.45E-03 | 0.008 | 1.25E-02 | -1.69E-03 |
| 2650 | 2195 | 376 | 326 | 0.015 | -2.30E-02 | -6.30E-03 | 0.016 | -2.23E-02 | -6.66E-03 |
| 2650 | 2095 | 376 | 286 | 0.019 | -1.82E-02 | -5.71E-03 | 0.020 | -1.82E-02 | -3.27E-03 |
| 2650 | 1995 | 376 | 236 | 0.023 | -1.32E-02 | -5.04E-03 | 0.023 | -1.24E-02 | -4.26E-03 |
| 2650 | 1795 | 376 | 136 | 0.019 | 1.64E-02 | -3.60E-03 | 0.019 | 1.64E-02 | -3.47E-03 |
| 2650 | 1695 | 376 | 86 | 0.015 | 1.42E-02 | -3.26E-03 | 0.015 | 1.41E-02 | -1.58E-03 |
| 2650 | 1595 | 376 | 36 | 0.009 | 7.58E-03 | -3.06E-03 | 0.010 | 7.33E-03 | -2.35E-03 |
| 2750 | 2195 | 426 | 326 | 0.011 | -1.28E-02 | -4.52E-03 | 0.011 | -1.23E-02 | -4.09E-03 |
| 2750 | 2095 | 426 | 286 | 0.022 | -1.55E-02 | -5.12E-03 | 0.022 | -1.54E-02 | -1.59E-03 |
| 2750 | 1995 | 426 | 236 | 0.029 | -1.10E-02 | -6.05E-03 | 0.029 | -1.10E-02 | 5.79E-03 |
| 2750 | 1795 | 426 | 136 | 0.021 | 1.10E-02 | -5.36E-03 | 0.021 | 1.06E-02 | -5.70E-03 |
| 2750 | 1695 | 426 | 86 | 0.018 | 1.24E-02 | -3.22E-03 | 0.018 | 1.22E-02 | -2.65E-03 |
| 2750 | 1595 | 426 | 36 | 0.015 | 1.13E-02 | -3.99E-03 | 0.015 | 1.08E-02 | -3.10E-03 |

Series 2 - Near-bed Velocity Data for Run 16

| Raw Data | | | | | | | Rotated (bed-normal) Data | | |
|---|---|---|---|---|---|---|---|---|---|
| Xlocation (mm) | Ylocation (mm) | X Node | Y Node | u (m/s) | v (m/s) | w (m/s) | $u_{corr}$ (m/s) | $v_{corr}$ (m/s) | $w_{corr}$ (m/s) |
| 1950 | 1895 | 1 | 186 | 0.091 | -5.19E-03 | -1.15E-02 | 0.081 | -3.81E-03 | 4.30E-02 |
| 2050 | 1895 | 76 | 186 | 0.090 | 1.11E-02 | 6.85E-04 | 0.088 | -4.24E-04 | 2.19E-02 |
| 2150 | 1895 | 126 | 186 | 0.085 | -7.82E-03 | -4.70E-02 | 0.088 | -4.24E-04 | 2.19E-02 |
| 2250 | 1895 | 176 | 186 | 0.088 | -5.21E-03 | -2.10E-02 | 0.097 | -7.36E-03 | 3.62E-03 |
| 2350 | 1895 | 226 | 186 | 0.057 | -9.24E-03 | 5.94E-04 | 0.080 | -7.06E-03 | 4.35E-02 |
| 2450 | 1895 | 276 | 186 | 0.035 | -3.56E-03 | 1.36E-02 | 0.055 | -7.89E-03 | 1.57E-02 |
| 2550 | 1895 | 326 | 186 | 0.005 | -8.13E-04 | -2.65E-03 | 0.033 | -3.00E-03 | 1.71E-02 |
| 2650 | 1895 | 376 | 186 | 0.015 | -1.39E-03 | -3.00E-03 | 0.006 | -9.67E-04 | 8.24E-04 |
| 2750 | 1895 | 426 | 186 | 0.018 | -1.67E-03 | -4.97E-03 | 0.015 | -1.54E-03 | -8.42E-04 |
| 2150 | 1995 | 126 | 236 | 0.001 | -1.98E-03 | -4.09E-03 | 0.019 | -1.27E-03 | -2.46E-03 |
| 2150 | 1795 | 126 | 136 | 0.001 | -2.19E-03 | -3.91E-03 | 0.002 | -2.49E-03 | -3.22E-03 |
| 2255 | 2195 | 176 | 326 | 0.000 | 1.83E-04 | -1.20E-04 | 0.003 | -2.37E-03 | -2.94E-03 |
| 2255 | 2095 | 176 | 286 | -0.001 | -2.68E-03 | -3.75E-03 | 0.000 | 1.68E-04 | -1.63E-04 |
| 2255 | 1995 | 176 | 236 | 0.002 | 1.59E-03 | -3.10E-03 | 0.000 | -3.62E-03 | -2.87E-03 |
| 2255 | 1795 | 176 | 136 | 0.000 | -8.73E-04 | -2.49E-03 | 0.004 | 1.35E-03 | -8.90E-04 |
| 2255 | 1695 | 176 | 86 | 0.000 | -8.96E-04 | -3.46E-03 | 0.002 | -4.19E-04 | -1.81E-03 |
| 2255 | 1595 | 176 | 36 | 0.000 | -1.05E-03 | -1.05E-02 | 0.000 | -1.83E-04 | -3.56E-03 |
| 2350 | 2195 | 226 | 326 | 0.000 | -1.59E-03 | -3.12E-03 | 0.002 | 8.10E-05 | -1.04E-02 |
| 2350 | 2095 | 226 | 286 | -0.007 | 6.32E-03 | -4.15E-03 | 0.000 | -1.86E-03 | -2.96E-03 |
| 2350 | 1995 | 226 | 236 | -0.024 | 1.64E-02 | -4.56E-03 | -0.007 | 5.30E-03 | -5.88E-03 |
| 2350 | 1795 | 226 | 136 | -0.018 | -6.57E-03 | -3.45E-03 | -0.022 | 1.24E-02 | -1.57E-02 |
| 2350 | 1695 | 226 | 86 | -0.011 | -4.64E-03 | -3.41E-03 | -0.018 | -5.38E-03 | -6.55E-03 |
| 2350 | 1595 | 226 | 36 | 0.000 | 9.49E-05 | -2.56E-04 | -0.011 | -4.15E-03 | -4.45E-03 |
| 2450 | 2195 | 276 | 326 | 0.001 | -7.54E-03 | -2.46E-03 | 0.000 | 1.18E-04 | -2.56E-04 |

Series 2 - Near-bed Velocity Data for Run 16 Cont'd

| | | | | | | | | | |
|---|---|---|---|---|---|---|---|---|---|
| 2450 | 2095 | 276 | 286 | -0.011 | -7.56E-03 | -1.46E-03 | 0.002 | -7.51E-03 | -2.18E-03 |
| 2450 | 1995 | 276 | 236 | -0.014 | -1.28E-02 | -1.55E-03 | -0.011 | -7.69E-03 | -8.57E-04 |
| 2450 | 1795 | 276 | 136 | -0.012 | 1.04E-02 | -2.32E-03 | -0.014 | -1.29E-02 | -1.07E-03 |
| 2450 | 1695 | 276 | 86 | -0.005 | 6.24E-03 | -2.63E-04 | -0.012 | 1.05E-02 | -2.14E-03 |
| 2450 | 1595 | 276 | 36 | NaN | NaN | NaN | -0.005 | 6.23E-03 | -4.14E-04 |
| 2550 | 2195 | 326 | 326 | 0.005 | -1.14E-02 | -3.20E-03 | 0.005 | -1.12E-02 | -3.55E-03 |
| 2550 | 2095 | 326 | 276 | 0.005 | -1.41E-02 | -1.94E-03 | 0.005 | -1.32E-02 | -4.90E-03 |
| 2550 | 1995 | 326 | 236 | 0.010 | -1.55E-02 | 4.92E-04 | 0.009 | -1.58E-02 | 2.14E-03 |
| 2550 | 1795 | 326 | 136 | 0.009 | 9.94E-03 | -3.30E-04 | 0.009 | 9.90E-03 | 1.26E-04 |
| 2550 | 1695 | 326 | 86 | 0.011 | 1.22E-02 | -2.33E-03 | 0.011 | 1.22E-02 | -2.14E-03 |
| 2550 | 1595 | 326 | 36 | 0.008 | 9.82E-03 | -2.17E-03 | 0.008 | 9.82E-03 | -1.18E-03 |
| 2650 | 2195 | 376 | 326 | 0.009 | -1.37E-02 | -5.50E-03 | 0.010 | -1.30E-02 | -5.51E-03 |
| 2650 | 2095 | 376 | 286 | 0.012 | -1.33E-02 | -4.80E-03 | 0.013 | -1.33E-02 | -3.40E-03 |
| 2650 | 1995 | 376 | 236 | 0.024 | -1.07E-02 | -5.05E-03 | 0.024 | -9.96E-03 | -3.28E-03 |
| 2650 | 1795 | 376 | 136 | 0.020 | 5.05E-03 | -3.23E-03 | 0.020 | 5.05E-03 | -3.23E-03 |
| 2650 | 1695 | 376 | 86 | 0.017 | 8.93E-03 | -3.81E-03 | 0.018 | 8.81E-03 | -1.11E-03 |
| 2650 | 1595 | 376 | 36 | 0.013 | 9.73E-03 | -3.31E-03 | 0.013 | 9.43E-03 | -2.94E-03 |
| 2750 | 2195 | 426 | 326 | 0.005 | -8.67E-03 | -6.47E-03 | 0.006 | -7.83E-03 | -6.57E-03 |
| 2750 | 2095 | 426 | 286 | 0.013 | -8.40E-03 | -4.45E-03 | 0.013 | -8.22E-03 | -2.25E-03 |
| 2750 | 1995 | 426 | 236 | 0.015 | -5.05E-03 | -3.80E-03 | 0.015 | -5.00E-03 | 1.89E-03 |
| 2750 | 1795 | 426 | 136 | 0.017 | 4.16E-03 | -4.50E-03 | 0.017 | 3.71E-03 | -4.09E-03 |
| 2750 | 1695 | 426 | 86 | 0.017 | 6.56E-03 | -3.26E-03 | 0.017 | 6.35E-03 | -2.13E-03 |
| 2750 | 1595 | 426 | 36 | 0.015 | 8.75E-03 | -4.11E-03 | 0.015 | 8.27E-03 | -2.83E-03 |

Series 2 - Near-bed Velocity Data for Run 17

| Raw Data | | | | | | | Rotated (bed-normal) Data | | |
|---|---|---|---|---|---|---|---|---|---|
| Xlocation (mm) | Ylocation (mm) | X Node | Y Node | u (m/s) | v (m/s) | w (m/s) | $u_{corr}$ (m/s) | $v_{corr}$ (m/s) | $w_{corr}$ (m/s) |
| 1950 | 1895 | 1 | 186 | 0.099 | -4.70E-03 | -1.18E-02 | 0.088 | -3.64E-03 | 4.71E-02 |
| 2050 | 1895 | 76 | 186 | 0.095 | 3.79E-03 | -5.22E-04 | -0.015 | 3.79E-03 | -4.67E-03 |
| 2150 | 1895 | 126 | 186 | 0.092 | -6.33E-03 | -4.75E-02 | 0.097 | -7.25E-03 | 3.71E-02 |
| 2250 | 1895 | 176 | 186 | 0.093 | -5.18E-03 | -1.93E-02 | 0.081 | -4.60E-03 | 5.05E-02 |
| 2350 | 1895 | 226 | 186 | 0.071 | -3.37E-03 | 4.33E-03 | 0.067 | -4.02E-03 | 2.39E-02 |
| 2450 | 1895 | 276 | 186 | 0.053 | -4.70E-03 | 1.86E-02 | 0.048 | -8.05E-03 | 2.91E-02 |
| 2550 | 1895 | 326 | 186 | 0.004 | -5.26E-04 | -5.71E-04 | 0.003 | -5.12E-04 | 2.42E-03 |
| 2650 | 1895 | 376 | 186 | 0.031 | 2.47E-03 | -4.14E-03 | 0.030 | 2.52E-03 | 7.02E-03 |
| 2750 | 1895 | 426 | 186 | 0.031 | 3.85E-03 | -5.63E-03 | 0.031 | 4.19E-03 | -9.50E-04 |
| 2150 | 1995 | 126 | 236 | 0.001 | 3.63E-04 | -4.98E-03 | 0.004 | -5.00E-05 | -2.47E-03 |
| 2150 | 1795 | 126 | 136 | 0.000 | -2.23E-03 | -4.41E-03 | 0.003 | -9.16E-04 | -3.64E-03 |
| 2255 | 2195 | 176 | 326 | 0.002 | -4.29E-04 | -7.01E-03 | 0.003 | -1.50E-03 | -6.30E-03 |
| 2255 | 2095 | 176 | 286 | -0.001 | -3.26E-04 | -4.84E-03 | -0.001 | -1.19E-03 | -4.72E-03 |
| 2255 | 1995 | 176 | 236 | -0.002 | -6.36E-04 | -2.54E-03 | 0.000 | -7.84E-04 | -3.23E-03 |
| 2255 | 1795 | 176 | 136 | -0.001 | 4.47E-03 | 1.30E-03 | -0.003 | 3.89E-03 | 1.35E-03 |
| 2255 | 1695 | 176 | 86 | -0.002 | -1.65E-03 | -3.57E-03 | -0.001 | -5.90E-04 | -4.17E-03 |
| 2255 | 1595 | 176 | 36 | -0.002 | -6.83E-03 | -3.08E-03 | 0.000 | -5.47E-03 | -5.44E-03 |
| 2350 | 2195 | 226 | 326 | -0.001 | -2.20E-03 | -2.67E-03 | 0.000 | -2.50E-03 | -2.43E-03 |
| 2350 | 2095 | 226 | 286 | -0.008 | 7.67E-03 | -3.21E-03 | -0.007 | 8.85E-03 | -1.65E-03 |
| 2350 | 1995 | 226 | 236 | -0.027 | 9.45E-03 | -2.13E-03 | -0.027 | 9.04E-03 | -3.86E-03 |
| 2350 | 1795 | 226 | 136 | -0.017 | -4.27E-03 | -3.84E-03 | -0.017 | -4.30E-03 | -3.81E-03 |
| 2350 | 1695 | 226 | 86 | -0.012 | -5.33E-03 | -3.55E-03 | -0.012 | -4.74E-03 | -4.69E-03 |
| 2350 | 1595 | 226 | 36 | 0.000 | -1.48E-03 | -2.52E-03 | 0.000 | -1.13E-03 | -2.68E-03 |
| 2450 | 2195 | 276 | 326 | 0.002 | -5.54E-03 | -3.28E-03 | 0.002 | -5.83E-03 | -2.52E-03 |

Series 2 - Near-bed Velocity Data for Run 17 Cont'd

| | | | | | | | | | |
|---|---|---|---|---|---|---|---|---|---|
| 2450 | 2095 | 276 | 286 | -0.014 | -7.61E-03 | -9.88E-04 | -0.014 | -7.71E-03 | 8.29E-05 |
| 2450 | 1995 | 276 | 236 | -0.010 | -1.41E-02 | -8.65E-04 | -0.009 | -1.39E-02 | -3.02E-03 |
| 2450 | 1795 | 276 | 136 | -0.020 | 1.20E-02 | -5.32E-03 | -0.020 | 1.21E-02 | -5.04E-03 |
| 2450 | 1695 | 276 | 86 | -0.008 | 7.88E-03 | -5.93E-04 | -0.007 | 6.36E-03 | -5.82E-03 |
| 2450 | 1595 | 276 | 36 | 0.003 | 7.79E-03 | -1.43E-03 | 0.003 | 7.86E-03 | -9.63E-04 |
| 2550 | 2195 | 326 | 326 | 0.007 | -1.70E-02 | -4.16E-03 | 0.007 | -1.67E-02 | -5.07E-03 |
| 2550 | 2095 | 326 | 276 | 0.005 | -2.15E-02 | -1.61E-03 | 0.006 | -1.81E-02 | -1.10E-02 |
| 2550 | 1995 | 326 | 236 | 0.018 | -1.97E-02 | 4.20E-03 | 0.013 | -2.13E-02 | 9.68E-03 |
| 2550 | 1795 | 326 | 136 | 0.007 | 1.29E-02 | -1.02E-03 | 0.008 | 1.25E-02 | -7.76E-04 |
| 2550 | 1695 | 326 | 86 | 0.008 | 1.43E-02 | -1.84E-03 | 0.009 | 1.35E-02 | -4.37E-03 |
| 2550 | 1595 | 326 | 36 | 0.010 | 1.24E-02 | -2.45E-03 | 0.010 | 1.23E-02 | -2.15E-03 |
| 2650 | 2195 | 376 | 326 | 0.012 | -1.62E-02 | -5.29E-03 | 0.013 | -1.56E-02 | -5.26E-03 |
| 2650 | 2095 | 376 | 286 | 0.020 | -1.92E-02 | -5.82E-03 | 0.021 | -1.91E-02 | -3.81E-03 |
| 2650 | 1995 | 376 | 236 | 0.030 | -1.27E-02 | -4.73E-03 | 0.030 | -1.22E-02 | -2.75E-04 |
| 2650 | 1795 | 376 | 136 | 0.019 | 9.28E-03 | -2.90E-03 | 0.019 | 9.19E-03 | -7.09E-05 |
| 2650 | 1695 | 376 | 86 | 0.015 | 8.99E-03 | -3.26E-03 | 0.015 | 8.93E-03 | -1.42E-03 |
| 2650 | 1595 | 376 | 36 | 0.014 | 1.31E-02 | -3.49E-03 | 0.015 | 1.28E-02 | -3.32E-03 |
| 2750 | 2195 | 426 | 326 | 0.016 | -1.36E-02 | -4.43E-03 | 0.017 | -1.31E-02 | -3.47E-03 |
| 2750 | 2095 | 426 | 286 | 0.025 | -1.42E-02 | -5.05E-03 | 0.025 | -1.40E-02 | -8.21E-04 |
| 2750 | 1995 | 426 | 236 | 0.026 | -7.07E-03 | -5.62E-03 | 0.027 | -7.05E-03 | 4.91E-03 |
| 2750 | 1795 | 426 | 136 | 0.022 | 1.11E-02 | -5.35E-03 | 0.022 | 1.05E-02 | -5.41E-03 |
| 2750 | 1695 | 426 | 86 | 0.021 | 1.15E-02 | -3.19E-03 | 0.021 | 1.13E-02 | -1.95E-03 |
| 2750 | 1595 | 426 | 36 | 0.016 | 1.11E-02 | -4.09E-03 | 0.016 | 1.05E-02 | -3.54E-03 |

Series 2 - Near-bed Velocity Data for Run 18

| Raw Data | | | | | | | Rotated (bed-normal) Data | | |
|---|---|---|---|---|---|---|---|---|---|
| Xlocation (mm) | Ylocation (mm) | X Node | Y Node | u (m/s) | v (m/s) | w (m/s) | $u_{corr}$ (m/s) | $v_{corr}$ (m/s) | $w_{corr}$ (m/s) |
| 1950 | 1895 | 1 | 186 | 0.086 | -2.33E-03 | -1.15E-02 | 0.076 | -1.06E-03 | 4.14E-02 |
| 2050 | 1895 | 76 | 186 | 0.087 | -1.50E-02 | -5.33E-03 | -0.005 | -1.50E-02 | -7.00E-03 |
| 2150 | 1895 | 126 | 186 | 0.081 | -1.92E-02 | -1.27E-02 | 0.003 | -1.95E-02 | -1.43E-02 |
| 2250 | 1895 | 176 | 186 | 0.090 | -1.12E-03 | -4.42E-02 | 0.095 | -2.15E-03 | 3.11E-02 |
| 2350 | 1895 | 226 | 186 | 0.073 | -2.34E-03 | 4.67E-03 | 0.067 | -4.14E-03 | 2.95E-02 |
| 2450 | 1895 | 276 | 186 | 0.053 | -3.49E-03 | 1.86E-02 | 0.048 | -5.77E-03 | 2.82E-02 |
| 2550 | 1895 | 326 | 186 | 0.016 | -6.47E-04 | 3.98E-03 | 0.009 | -8.35E-04 | 1.41E-02 |
| 2650 | 1895 | 376 | 186 | 0.028 | 5.19E-03 | -3.62E-03 | 0.027 | 5.24E-03 | 6.48E-03 |
| 2750 | 1895 | 426 | 186 | 0.036 | 1.56E-03 | -6.86E-03 | 0.037 | 2.01E-03 | -2.31E-03 |
| 2150 | 1995 | 126 | 236 | -0.003 | -2.05E-03 | -1.63E-03 | -0.001 | -2.26E-03 | -2.92E-03 |
| 2150 | 1795 | 126 | 136 | 0.003 | -7.19E-04 | -5.33E-03 | 0.006 | 4.42E-04 | -1.87E-03 |
| 2255 | 2195 | 176 | 326 | 0.000 | -5.33E-04 | -2.23E-04 | 0.000 | -5.64E-04 | -1.59E-04 |
| 2255 | 2095 | 176 | 286 | -0.001 | -2.70E-03 | -4.22E-03 | -0.001 | -3.35E-03 | -3.75E-03 |
| 2255 | 1995 | 176 | 236 | 0.002 | -2.05E-04 | -3.87E-03 | 0.004 | -7.34E-04 | -1.43E-03 |
| 2255 | 1795 | 176 | 136 | -0.009 | -4.88E-04 | -3.27E-03 | -0.004 | 2.12E-03 | -8.90E-03 |
| 2255 | 1695 | 176 | 86 | -0.005 | -4.48E-03 | -3.67E-03 | -0.004 | -3.25E-03 | -5.60E-03 |
| 2255 | 1595 | 176 | 36 | -0.001 | -3.21E-03 | -4.70E-03 | 0.000 | -1.55E-03 | -5.59E-03 |
| 2350 | 2195 | 226 | 326 | 0.000 | -1.14E-03 | -3.01E-03 | 0.000 | -1.42E-03 | -2.90E-03 |
| 2350 | 2095 | 226 | 286 | -0.003 | 2.57E-03 | -3.68E-03 | -0.002 | 4.12E-03 | -2.85E-03 |
| 2350 | 1995 | 226 | 236 | -0.023 | 1.13E-02 | -2.17E-03 | -0.023 | 1.08E-02 | -4.10E-03 |
| 2350 | 1795 | 226 | 136 | -0.029 | -9.85E-03 | -3.12E-03 | -0.029 | -9.65E-03 | -3.75E-03 |
| 2350 | 1695 | 226 | 86 | -0.012 | -5.40E-03 | -3.90E-03 | -0.011 | -4.75E-03 | -5.07E-03 |
| 2350 | 1595 | 226 | 36 | -0.001 | -1.64E-03 | -2.74E-03 | -0.001 | -1.22E-03 | -3.05E-03 |
| 2450 | 2195 | 276 | 326 | -0.001 | -1.14E-02 | -2.56E-03 | -0.001 | -1.16E-02 | -1.62E-03 |

Series 2 - Near-bed Velocity Data for Run 18 Cont'd

| | | | | | | | | | |
|---|---|---|---|---|---|---|---|---|---|
| 2450 | 2095 | 276 | 286 | -0.012 | -7.80E-03 | -1.08E-03 | -0.012 | -7.91E-03 | 1.57E-04 |
| 2450 | 1995 | 276 | 236 | -0.009 | -2.09E-02 | 1.88E-03 | -0.009 | -2.09E-02 | -2.53E-03 |
| 2450 | 1795 | 276 | 136 | -0.022 | 1.27E-02 | -5.54E-03 | -0.022 | 1.22E-02 | -6.73E-03 |
| 2450 | 1695 | 276 | 86 | -0.009 | 8.21E-03 | 1.64E-04 | -0.009 | 6.99E-03 | -5.43E-03 |
| 2450 | 1595 | 276 | 36 | 0.002 | 4.87E-03 | -1.63E-03 | 0.002 | 4.93E-03 | -1.42E-03 |
| 2550 | 2195 | 326 | 326 | 0.005 | -1.32E-02 | -3.30E-03 | 0.006 | -1.29E-02 | -4.03E-03 |
| 2550 | 2095 | 326 | 276 | 0.004 | -1.81E-02 | -1.85E-03 | 0.006 | -1.50E-02 | -9.62E-03 |
| 2550 | 1995 | 326 | 236 | 0.013 | -1.98E-02 | 2.62E-03 | 0.010 | -2.07E-02 | 5.85E-03 |
| 2550 | 1795 | 326 | 136 | 0.008 | 1.64E-02 | -5.38E-04 | 0.009 | 1.60E-02 | -1.74E-03 |
| 2550 | 1695 | 326 | 86 | 0.009 | 1.32E-02 | -2.17E-03 | 0.010 | 1.23E-02 | -4.28E-03 |
| 2550 | 1595 | 326 | 36 | 0.008 | 1.28E-02 | -2.49E-03 | 0.008 | 1.27E-02 | -2.41E-03 |
| 2650 | 2195 | 376 | 326 | 0.012 | -1.59E-02 | -5.12E-03 | 0.012 | -1.52E-02 | -5.22E-03 |
| 2650 | 2095 | 376 | 286 | 0.019 | -1.57E-02 | -5.81E-03 | 0.019 | -1.56E-02 | -4.22E-03 |
| 2650 | 1995 | 376 | 236 | 0.030 | -1.02E-02 | -5.44E-03 | 0.031 | -9.72E-03 | -5.17E-04 |
| 2650 | 1795 | 376 | 136 | 0.021 | 1.21E-02 | -3.36E-03 | 0.021 | 1.19E-02 | -4.49E-04 |
| 2650 | 1695 | 376 | 86 | 0.018 | 1.47E-02 | -4.10E-03 | 0.018 | 1.47E-02 | -2.01E-03 |
| 2650 | 1595 | 376 | 36 | 0.011 | 1.05E-02 | -3.72E-03 | 0.011 | 1.01E-02 | -3.52E-03 |
| 2750 | 2195 | 426 | 326 | 0.012 | -1.37E-02 | -5.27E-03 | 0.013 | -1.30E-02 | -4.64E-03 |
| 2750 | 2095 | 426 | 286 | 0.025 | -1.54E-02 | -5.41E-03 | 0.026 | -1.52E-02 | -7.12E-04 |
| 2750 | 1995 | 426 | 236 | 0.029 | -9.80E-03 | -6.30E-03 | 0.029 | -9.76E-03 | 4.69E-03 |
| 2750 | 1795 | 426 | 136 | 0.025 | 1.02E-02 | -6.19E-03 | 0.025 | 9.58E-03 | -6.12E-03 |
| 2750 | 1695 | 426 | 86 | 0.018 | 8.87E-03 | -3.28E-03 | 0.018 | 8.68E-03 | -2.02E-03 |
| 2750 | 1595 | 426 | 36 | 0.015 | 1.06E-02 | -4.46E-03 | 0.016 | 9.95E-03 | -3.85E-03 |

Series 2 – Near-bed Velocity Data for Run 21

| Raw Data | | | | | | | Rotated (bed-normal) Data | | |
|---|---|---|---|---|---|---|---|---|---|
| Xlocation (mm) | Ylocation (mm) | X Node | Y Node | u (m/s) | v (m/s) | w (m/s) | $u_{corr}$ (m/s) | $v_{corr}$ (m/s) | $w_{corr}$ (m/s) |
| 1950 | 1895 | 1 | 186 | 0.107 | -6.18E-03 | -2.10E-02 | 0.099 | -5.56E-03 | 4.56E-02 |
| 2050 | 1895 | 76 | 186 | 0.031 | -2.66E-03 | -4.90E-02 | 0.045 | -4.70E-03 | -3.62E-02 |
| 2150 | 1895 | 126 | 186 | 0.120 | -5.74E-03 | -5.03E-02 | 0.120 | -5.78E-03 | 5.15E-02 |
| 2250 | 1895 | 176 | 186 | 0.128 | -1.89E-03 | -1.37E-02 | 0.106 | 3.33E-03 | 7.38E-02 |
| 2350 | 1895 | 226 | 186 | 0.098 | -2.36E-03 | -1.57E-03 | 0.094 | -3.03E-03 | 2.69E-02 |
| 2450 | 1895 | 276 | 186 | 0.066 | -3.09E-04 | 1.09E-02 | 0.064 | -1.24E-03 | 1.88E-02 |
| 2550 | 1895 | 326 | 186 | 0.024 | 1.42E-03 | 8.90E-03 | 0.011 | 9.91E-04 | 2.32E-02 |
| 2650 | 1895 | 376 | 186 | 0.042 | -3.08E-03 | -5.64E-03 | 0.041 | -2.97E-03 | 1.07E-02 |
| 2750 | 1895 | 426 | 186 | 0.043 | -4.38E-03 | -7.95E-03 | 0.044 | -3.88E-03 | -2.84E-03 |
| 2150 | 1995 | 126 | 236 | 0.011 | -1.07E-02 | -1.37E-03 | 0.008 | -1.04E-02 | 8.33E-03 |
| 2150 | 1795 | 126 | 136 | 0.000 | -2.43E-03 | -4.10E-03 | 0.003 | -1.16E-03 | -3.55E-03 |
| 2255 | 2195 | 176 | 326 | 0.001 | -4.95E-04 | -1.90E-03 | 0.001 | -7.83E-04 | -1.59E-03 |
| 2255 | 2095 | 176 | 286 | -0.013 | 1.23E-02 | -4.54E-03 | -0.013 | 1.13E-02 | -6.89E-03 |
| 2255 | 1995 | 176 | 236 | 0.028 | -5.02E-03 | 2.93E-03 | 0.018 | -2.71E-03 | 2.25E-02 |
| 2255 | 1795 | 176 | 136 | 0.005 | -3.25E-03 | -2.44E-04 | 0.004 | -3.69E-03 | 2.23E-03 |
| 2255 | 1695 | 176 | 86 | -0.005 | -6.82E-03 | -3.94E-03 | -0.004 | -5.46E-03 | -6.55E-03 |
| 2255 | 1595 | 176 | 36 | 0.000 | -3.04E-04 | -3.11E-03 | 0.001 | 6.48E-04 | -3.04E-03 |
| 2350 | 2195 | 226 | 326 | -0.002 | -1.56E-03 | -2.56E-03 | -0.002 | -1.81E-03 | -2.48E-03 |
| 2350 | 2095 | 226 | 286 | -0.017 | 1.38E-02 | -2.09E-03 | -0.017 | 1.44E-02 | -7.03E-04 |
| 2350 | 1995 | 226 | 236 | -0.004 | 7.56E-03 | -2.55E-03 | -0.003 | 6.85E-03 | -4.26E-03 |
| 2350 | 1795 | 226 | 136 | -0.015 | -9.44E-03 | -1.82E-03 | -0.015 | -9.27E-03 | -2.61E-03 |
| 2350 | 1695 | 226 | 86 | -0.020 | -5.94E-03 | -4.25E-03 | -0.020 | -5.23E-03 | -5.76E-03 |
| 2350 | 1595 | 226 | 36 | -0.003 | 5.46E-04 | -2.32E-03 | -0.003 | 8.90E-04 | -2.43E-03 |
| 2450 | 2195 | 276 | 326 | -0.003 | -8.76E-03 | -2.00E-03 | -0.003 | -8.91E-03 | -1.39E-03 |

Series 2 - Near-bed Velocity Data for Run 21 Cont'd

| | | | | | | | | | |
|---|---|---|---|---|---|---|---|---|---|
| 2450 | 2095 | 276 | 286 | -0.017 | -5.98E-03 | -2.91E-03 | -0.017 | -6.60E-03 | -2.34E-03 |
| 2450 | 1995 | 276 | 236 | 0.001 | -1.05E-02 | -6.12E-05 | 0.001 | -1.03E-02 | -1.77E-03 |
| 2450 | 1795 | 276 | 136 | -0.008 | 1.27E-02 | -8.40E-04 | -0.008 | 1.27E-02 | -1.26E-03 |
| 2450 | 1695 | 276 | 86 | -0.013 | 1.33E-02 | -1.73E-04 | -0.012 | 1.13E-02 | -8.75E-03 |
| 2450 | 1595 | 276 | 36 | -0.001 | 9.93E-03 | -1.55E-03 | -0.001 | 9.99E-03 | -1.09E-03 |
| 2550 | 2195 | 326 | 326 | 0.003 | -1.58E-02 | -3.41E-03 | 0.004 | -1.54E-02 | -4.50E-03 |
| 2550 | 2095 | 326 | 276 | 0.002 | -1.82E-02 | -1.92E-03 | 0.004 | -1.48E-02 | -1.02E-02 |
| 2550 | 1995 | 326 | 236 | 0.011 | -1.62E-02 | 3.35E-03 | 0.008 | -1.72E-02 | 5.45E-03 |
| 2550 | 1795 | 326 | 136 | 0.027 | 2.11E-02 | 2.12E-03 | 0.023 | 2.34E-02 | 9.29E-03 |
| 2550 | 1695 | 326 | 86 | 0.007 | 2.18E-02 | -2.78E-03 | 0.008 | 2.05E-02 | -7.24E-03 |
| 2550 | 1595 | 326 | 36 | 0.007 | 2.07E-02 | -2.83E-03 | 0.007 | 2.07E-02 | -3.03E-03 |
| 2650 | 2195 | 376 | 326 | 0.012 | -2.03E-02 | -5.25E-03 | 0.013 | -1.97E-02 | -5.99E-03 |
| 2650 | 2095 | 376 | 286 | 0.022 | -2.38E-02 | -6.09E-03 | 0.022 | -2.37E-02 | -4.59E-03 |
| 2650 | 1995 | 376 | 236 | 0.032 | -1.88E-02 | -6.68E-03 | 0.033 | -1.80E-02 | -2.82E-03 |
| 2650 | 1795 | 376 | 136 | 0.038 | 1.83E-02 | -5.02E-03 | 0.038 | 1.82E-02 | 1.14E-03 |
| 2650 | 1695 | 376 | 86 | 0.023 | 2.22E-02 | -4.89E-03 | 0.024 | 2.21E-02 | -2.88E-03 |
| 2650 | 1595 | 376 | 36 | 0.016 | 2.00E-02 | -3.98E-03 | 0.017 | 1.96E-02 | -3.99E-03 |
| 2750 | 2195 | 426 | 326 | 0.014 | -1.33E-02 | -4.51E-03 | 0.015 | -1.27E-02 | -3.76E-03 |
| 2750 | 2095 | 426 | 286 | 0.026 | -2.01E-02 | -5.79E-03 | 0.027 | -1.99E-02 | -3.00E-04 |
| 2750 | 1995 | 426 | 236 | 0.036 | -1.77E-02 | -7.05E-03 | 0.036 | -1.77E-02 | 5.58E-03 |
| 2750 | 1795 | 426 | 136 | 0.044 | 1.47E-02 | -9.36E-03 | 0.044 | 1.37E-02 | -8.19E-03 |
| 2750 | 1695 | 426 | 86 | 0.032 | 2.13E-02 | -5.06E-03 | 0.033 | 2.09E-02 | -3.26E-03 |
| 2750 | 1595 | 426 | 36 | 0.020 | 2.04E-02 | -5.81E-03 | 0.021 | 1.95E-02 | -5.67E-03 |

Series 2 – PADV Profiler Data for Run 23

| X Location (mm) | Y Location (mm) | Bed Elevation (mm) | X-node | Y-node | Profile Sample Elevation From Bed (mm) | u (m/s) | v (m/s) | w (m/s) | $u_{corr}$ (m/s) | $v_{corr}$ (m/s) | $w_{corr}$ (m/s) |
|---|---|---|---|---|---|---|---|---|---|---|---|
| 1950 | 1895 | -1403.8 | 1 | 186 | 49 | 0.0000 | 0.0000 | 0.0000 | 0.0000 | 0.0000 | 0.0000 |
| 1950 | 1895 | -1403.8 | 1 | 186 | 29 | 0.0176 | -0.0004 | -0.0059 | 0.0176 | -0.0004 | -0.0059 |
| 1950 | 1895 | -1403.8 | 1 | 186 | 9 | 0.0677 | -0.0009 | -0.0145 | 0.0677 | -0.0009 | -0.0145 |
| 2050 | 1895 | -1424.3 | 1 | 76 | 49 | 0.0000 | 0.0000 | 0.0000 | 0.0000 | 0.0000 | 0.0000 |
| 2050 | 1895 | -1424.3 | 1 | 76 | 29 | 0.0226 | 0.0002 | -0.0219 | 0.0226 | 0.0002 | -0.0219 |
| 2050 | 1895 | -1424.3 | 1 | 76 | 9 | -0.0883 | 0.0068 | 0.0058 | -0.0883 | 0.0068 | 0.0058 |
| 2150 | 1895 | -1482.8 | 126 | 186 | 49 | 0.0000 | 0.0000 | 0.0000 | 0.0000 | 0.0000 | 0.0000 |
| 2150 | 1895 | -1482.8 | 126 | 186 | 29 | 0.0121 | -0.0006 | -0.0079 | 0.0121 | -0.0006 | -0.0079 |
| 2150 | 1895 | -1482.8 | 126 | 186 | 9 | 0.0085 | -0.0068 | -0.0046 | 0.0085 | -0.0068 | -0.0046 |
| 2250 | 1895 | -1522.9 | 176 | 186 | 49 | 0.0000 | 0.0000 | 0.0000 | 0.0000 | 0.0000 | 0.0000 |
| 2250 | 1895 | -1522.9 | 176 | 186 | 29 | 0.0199 | 0.0075 | 0.0008 | 0.0199 | 0.0075 | 0.0008 |
| 2250 | 1895 | -1522.9 | 176 | 186 | 9 | 0.0645 | 0.0065 | -0.0041 | 0.0645 | 0.0065 | -0.0041 |
| 2350 | 1895 | -1546.0 | 226 | 186 | 49 | 0.0048 | 0.0000 | -0.0008 | 0.0048 | 0.0000 | -0.0008 |
| 2350 | 1895 | -1546.0 | 226 | 186 | 29 | 0.0304 | 0.0028 | 0.0003 | 0.0304 | 0.0028 | 0.0003 |
| 2350 | 1895 | -1546.0 | 226 | 186 | 9 | 0.0635 | 0.0023 | 0.0024 | 0.0635 | 0.0023 | 0.0024 |
| 2450 | 1895 | -1551.2 | 276 | 186 | 49 | 0.0192 | 0.0001 | 0.0000 | 0.0192 | 0.0001 | 0.0000 |
| 2450 | 1895 | -1551.2 | 276 | 186 | 29 | 0.0474 | 0.0026 | 0.0083 | 0.0474 | 0.0026 | 0.0083 |
| 2450 | 1895 | -1551.2 | 276 | 186 | 9 | 0.0384 | -0.0002 | 0.0101 | 0.0384 | -0.0002 | 0.0101 |
| 2550 | 1895 | -1543.6 | 326 | 186 | 49 | 0.0000 | 0.0000 | -0.0029 | 0.0000 | 0.0000 | -0.0029 |
| 2550 | 1895 | -1543.6 | 326 | 186 | 29 | 0.0056 | -0.0011 | -0.0027 | 0.0056 | -0.0011 | -0.0027 |
| 2550 | 1895 | -1543.6 | 326 | 186 | 9 | 0.0460 | -0.0034 | 0.0024 | 0.0460 | -0.0034 | 0.0024 |
| 2650 | 1895 | -1496.5 | 376 | 186 | 49 | 0.0000 | 0.0000 | 0.0000 | 0.0000 | 0.0000 | 0.0000 |
| 2650 | 1895 | -1496.5 | 376 | 186 | 29 | -0.0024 | -0.0001 | -0.0087 | -0.0024 | -0.0001 | -0.0087 |
| 2650 | 1895 | -1496.5 | 376 | 186 | 9 | 0.0161 | 0.0023 | -0.0027 | 0.0161 | 0.0023 | -0.0027 |
| 2750 | 1895 | -1495.6 | 426 | 186 | 49 | 0.0000 | 0.0000 | 0.0000 | 0.0000 | 0.0000 | 0.0000 |

Series 2 – PADV Profiler Data for Run 23 Cont'd

| | | | | | | | | | | | |
|---|---|---|---|---|---|---|---|---|---|---|---|
| 2750 | 1895 | -1495.6 | 426 | 186 | 29 | -0.0003 | 0.0024 | -0.0099 | -0.0003 | 0.0024 | -0.0099 |
| 2750 | 1895 | -1495.6 | 426 | 186 | 9 | 0.0137 | -0.0025 | -0.0036 | 0.0137 | -0.0025 | -0.0036 |
| 2350 | 2195 | -1483.3 | 226 | 326 | 49 | 0.0000 | 0.0000 | 0.0000 | 0.0000 | 0.0000 | 0.0000 |
| 2350 | 2195 | -1483.3 | 226 | 326 | 29 | -0.0030 | 0.0013 | -0.0045 | -0.0030 | 0.0013 | -0.0045 |
| 2350 | 2195 | -1483.3 | 226 | 326 | 9 | -0.0035 | -0.0034 | -0.0043 | -0.0035 | -0.0034 | -0.0043 |
| 2350 | 2095 | -1507.3 | 226 | 286 | 49 | 0.0000 | 0.0000 | 0.0000 | 0.0000 | 0.0000 | 0.0000 |
| 2350 | 2095 | -1507.3 | 226 | 286 | 29 | -0.0049 | 0.0014 | -0.0033 | -0.0049 | 0.0014 | -0.0033 |
| 2350 | 2095 | -1507.3 | 226 | 286 | 9 | -0.0118 | -0.0053 | -0.0005 | -0.0118 | -0.0053 | -0.0005 |
| 2350 | 1995 | -1547.1 | 226 | 236 | 49 | 0.0000 | 0.0000 | 0.0000 | 0.0000 | 0.0000 | 0.0000 |
| 2350 | 1995 | -1547.1 | 226 | 236 | 29 | -0.0017 | 0.0009 | -0.0021 | -0.0017 | 0.0009 | -0.0021 |
| 2350 | 1995 | -1547.1 | 226 | 236 | 9 | -0.0046 | 0.0021 | -0.0011 | -0.0046 | 0.0021 | -0.0011 |
| 2350 | 1795 | -1544.1 | 226 | 136 | 49 | 0.0000 | 0.0000 | 0.0000 | 0.0000 | 0.0000 | 0.0000 |
| 2350 | 1795 | -1544.1 | 226 | 136 | 29 | -0.0034 | 0.0001 | -0.0026 | -0.0034 | 0.0001 | -0.0026 |
| 2350 | 1795 | -1544.1 | 226 | 136 | 9 | -0.0163 | 0.0005 | -0.0007 | -0.0163 | 0.0005 | -0.0007 |
| 2350 | 1695 | -1498.5 | 226 | 86 | 49 | 0.0000 | 0.0000 | 0.0000 | 0.0000 | 0.0000 | 0.0000 |
| 2350 | 1695 | -1498.5 | 226 | 86 | 29 | -0.0053 | 0.0006 | -0.0036 | -0.0053 | 0.0006 | -0.0036 |
| 2350 | 1695 | -1498.5 | 226 | 86 | 9 | -0.0052 | -0.0022 | -0.0018 | -0.0052 | -0.0022 | -0.0018 |
| 2350 | 1595 | -1481.5 | 226 | 36 | 49 | 0.0000 | 0.0000 | 0.0000 | 0.0000 | 0.0000 | 0.0000 |
| 2350 | 1595 | -1481.5 | 226 | 36 | 29 | -0.0026 | -0.0004 | -0.0054 | -0.0026 | -0.0004 | -0.0054 |
| 2350 | 1595 | -1481.5 | 226 | 36 | 9 | 0.0100 | 0.0028 | -0.0036 | 0.0100 | 0.0028 | -0.0036 |

Series 2 - PADV Profiler Data for Run 24

| X Location (mm) | Y Location (mm) | Bed Elevation (mm) | X-node | Y-node | Profile Sample Elevation From Bed (mm) | u (m/s) | v (m/s) | w (m/s) | $u_{corr}$ (m/s) | $v_{corr}$ (m/s) | $w_{corr}$ (m/s) |
|---|---|---|---|---|---|---|---|---|---|---|---|
| 1950 | 1895 | -1397.8 | 1 | 186 | 49 | 0.0000 | 0.0000 | 0.0000 | 0.0000 | 0.0000 | 0.0000 |
| 1950 | 1895 | -1397.8 | 1 | 186 | 29 | -0.0039 | 0.0042 | -0.0047 | -0.0039 | 0.0042 | -0.0047 |
| 1950 | 1895 | -1397.8 | 1 | 186 | 9 | 0.0580 | -0.0028 | -0.0145 | 0.0580 | -0.0028 | -0.0145 |
| 2050 | 1895 | -1419.4 | 76 | 186 | 49 | 0.0000 | 0.0000 | 0.0000 | 0.0000 | 0.0000 | 0.0000 |
| 2050 | 1895 | -1419.4 | 76 | 186 | 29 | 0.0045 | -0.0004 | -0.0075 | 0.0045 | -0.0004 | -0.0075 |
| 2050 | 1895 | -1419.4 | 76 | 186 | 9 | 0.0053 | -0.0039 | -0.0236 | 0.0053 | -0.0039 | -0.0236 |
| 2150 | 1895 | -1477.6 | 126 | 186 | 49 | 0.0000 | 0.0000 | 0.0000 | 0.0000 | 0.0000 | 0.0000 |
| 2150 | 1895 | -1477.6 | 126 | 186 | 29 | 0.0137 | -0.0006 | -0.0073 | 0.0137 | -0.0006 | -0.0073 |
| 2150 | 1895 | -1477.6 | 126 | 186 | 9 | 0.0390 | -0.0013 | -0.0162 | 0.0390 | -0.0013 | -0.0162 |
| 2250 | 1895 | -1517.8 | 176 | 186 | 49 | 0.0000 | 0.0000 | 0.0000 | 0.0000 | 0.0000 | 0.0000 |
| 2250 | 1895 | -1517.8 | 176 | 186 | 29 | 0.0214 | 0.0046 | -0.0068 | 0.0214 | 0.0046 | -0.0068 |
| 2250 | 1895 | -1517.8 | 176 | 186 | 9 | 0.0493 | -0.0008 | -0.0035 | 0.0493 | -0.0008 | -0.0035 |
| 2350 | 1895 | -1540.7 | 226 | 186 | 49 | -0.0004 | 0.0001 | -0.0015 | -0.0004 | 0.0001 | -0.0015 |
| 2350 | 1895 | -1540.7 | 226 | 186 | 29 | 0.0231 | 0.0030 | -0.0008 | 0.0231 | 0.0030 | -0.0008 |
| 2350 | 1895 | -1540.7 | 226 | 186 | 9 | 0.0449 | -0.0012 | -0.0012 | 0.0449 | -0.0012 | -0.0012 |
| 2450 | 1895 | -1546.5 | 276 | 186 | 49 | 0.0092 | -0.0015 | -0.0037 | 0.0092 | -0.0015 | -0.0037 |
| 2450 | 1895 | -1546.5 | 276 | 186 | 29 | 0.0317 | 0.0001 | 0.0064 | 0.0317 | 0.0001 | 0.0064 |
| 2450 | 1895 | -1546.5 | 276 | 186 | 9 | 0.0331 | -0.0018 | 0.0076 | 0.0331 | -0.0018 | 0.0076 |
| 2550 | 1895 | -1539.5 | 326 | 186 | 49 | 0.0000 | 0.0000 | 0.0000 | 0.0000 | 0.0000 | 0.0000 |
| 2550 | 1895 | -1539.5 | 326 | 186 | 29 | 0.0026 | -0.0023 | -0.0024 | 0.0026 | -0.0023 | -0.0024 |
| 2550 | 1895 | -1539.5 | 326 | 186 | 9 | 0.0337 | -0.0015 | 0.0075 | 0.0337 | -0.0015 | 0.0075 |
| 2650 | 1895 | -1494.5 | 376 | 186 | 49 | 0.0000 | 0.0000 | 0.0000 | 0.0000 | 0.0000 | 0.0000 |
| 2650 | 1895 | -1494.5 | 376 | 186 | 29 | 0.0021 | -0.0009 | -0.0087 | 0.0021 | -0.0009 | -0.0087 |

Series 2 - PADV Profiler Data for Run 24 Cont'd

| | | | | | | | | | | | |
|---|---|---|---|---|---|---|---|---|---|---|---|
| 2650 | 1895 | -1494.5 | 376 | 186 | 9 | 0.0207 | -0.0014 | -0.0040 | 0.0207 | -0.0014 | -0.0040 |
| 2750 | 1895 | -1493.6 | 426 | 186 | 49 | 0.0000 | 0.0000 | 0.0000 | 0.0000 | 0.0000 | 0.0000 |
| 2750 | 1895 | -1493.6 | 426 | 186 | 29 | 0.0027 | -0.0009 | -0.0068 | 0.0027 | -0.0009 | -0.0068 |
| 2750 | 1895 | -1493.6 | 426 | 186 | 9 | 0.0145 | 0.0004 | -0.0036 | 0.0145 | 0.0004 | -0.0036 |
| 2150 | 1995 | -1483.2 | 126 | 236 | 49 | 0.0000 | 0.0000 | 0.0000 | 0.0000 | 0.0000 | 0.0000 |
| 2150 | 1995 | -1483.2 | 126 | 236 | 29 | -0.0020 | 0.0001 | -0.0032 | -0.0020 | 0.0001 | -0.0032 |
| 2150 | 1995 | -1483.2 | 126 | 236 | 9 | -0.0004 | -0.0007 | -0.0012 | -0.0004 | -0.0007 | -0.0012 |
| 2150 | 1795 | -1477.2 | 126 | 136 | 49 | 0.0000 | 0.0000 | 0.0000 | 0.0000 | 0.0000 | 0.0000 |
| 2150 | 1795 | -1475.6 | 126 | 136 | 29 | -0.0020 | -0.0001 | -0.0032 | -0.0020 | -0.0001 | -0.0032 |
| 2150 | 1795 | -1475.6 | 126 | 136 | 9 | -0.0004 | 0.0007 | -0.0012 | -0.0004 | 0.0007 | -0.0012 |
| 2250 | 2195 | -1472.4 | 176 | 326 | 49 | 0.0000 | 0.0000 | 0.0000 | 0.0000 | 0.0000 | 0.0000 |
| 2250 | 2195 | -1472.4 | 176 | 326 | 29 | -0.0040 | 0.0052 | -0.0038 | -0.0040 | 0.0052 | -0.0038 |
| 2250 | 2195 | -1472.4 | 176 | 326 | 9 | 0.0065 | -0.0121 | -0.0049 | 0.0065 | -0.0121 | -0.0049 |
| 2250 | 2095 | -1498.1 | 176 | 286 | 49 | 0.0000 | 0.0000 | 0.0000 | 0.0000 | 0.0000 | 0.0000 |
| 2250 | 2095 | -1498.1 | 176 | 286 | 29 | -0.0016 | -0.0025 | -0.0024 | -0.0016 | -0.0025 | -0.0024 |
| 2250 | 2095 | -1498.1 | 176 | 286 | 9 | -0.0035 | 0.0011 | -0.0027 | -0.0035 | 0.0011 | -0.0027 |
| 2250 | 1995 | -1526.2 | 176 | 236 | 49 | 0.0000 | 0.0000 | 0.0000 | 0.0000 | 0.0000 | 0.0000 |
| 2250 | 1995 | -1526.2 | 176 | 236 | 29 | -0.0035 | 0.0032 | -0.0009 | -0.0035 | 0.0032 | -0.0009 |
| 2250 | 1995 | -1526.2 | 176 | 236 | 9 | -0.0063 | 0.0025 | -0.0009 | -0.0063 | 0.0025 | -0.0009 |
| 2250 | 1795 | -1519.4 | 176 | 136 | 49 | 0.0000 | 0.0000 | 0.0000 | 0.0000 | 0.0000 | 0.0000 |
| 2250 | 1795 | -1519.4 | 176 | 136 | 29 | -0.0053 | -0.0036 | -0.0018 | -0.0053 | -0.0036 | -0.0018 |
| 2250 | 1795 | -1519.4 | 176 | 136 | 9 | -0.0075 | 0.0002 | -0.0016 | -0.0075 | 0.0002 | -0.0016 |
| 2250 | 1695 | -1489.7 | 176 | 86 | 49 | 0.0000 | 0.0000 | 0.0000 | 0.0000 | 0.0000 | 0.0000 |
| 2250 | 1695 | -1489.7 | 176 | 86 | 29 | -0.0042 | -0.0023 | -0.0029 | -0.0042 | -0.0023 | -0.0029 |
| 2250 | 1695 | -1489.7 | 176 | 86 | 9 | 0.0012 | 0.0007 | -0.0018 | 0.0012 | 0.0007 | -0.0018 |
| 2250 | 1595 | -1469.4 | 176 | 36 | 49 | 0.0000 | 0.0000 | 0.0000 | 0.0000 | 0.0000 | 0.0000 |
| 2250 | 1595 | -1469.4 | 176 | 36 | 29 | -0.0008 | -0.0032 | -0.0052 | -0.0008 | -0.0032 | -0.0052 |
| 2250 | 1595 | -1469.4 | 176 | 36 | 9 | -0.0017 | 0.0091 | -0.0017 | -0.0017 | 0.0091 | -0.0017 |
| 2350 | 2195 | -1483.3 | 226 | 326 | 49 | 0.0000 | 0.0000 | 0.0000 | 0.0000 | 0.0000 | 0.0000 |
| 2350 | 2195 | -1483.3 | 226 | 326 | 29 | -0.0001 | 0.0058 | -0.0027 | -0.0001 | 0.0058 | -0.0027 |

Series 2 - PADV Profiler Data for Run 24 Cont'd

| | | | | | | | | | | | |
|---|---|---|---|---|---|---|---|---|---|---|---|
| 2350 | 2195 | -1483.3 | 226 | 326 | 9 | -0.0016 | -0.0101 | -0.0044 | -0.0016 | -0.0101 | -0.0044 |
| 2350 | 2095 | -1506.4 | 226 | 286 | 49 | 0.0000 | 0.0000 | 0.0000 | 0.0000 | 0.0000 | 0.0000 |
| 2350 | 2095 | -1506.4 | 226 | 286 | 29 | -0.0008 | 0.0052 | -0.0040 | -0.0008 | 0.0052 | -0.0040 |
| 2350 | 2095 | -1506.4 | 226 | 286 | 9 | -0.0112 | -0.0003 | -0.0012 | -0.0112 | -0.0003 | -0.0012 |
| 2350 | 1995 | -1542.1 | 226 | 236 | 49 | 0.0000 | 0.0000 | 0.0000 | 0.0000 | 0.0000 | 0.0000 |
| 2350 | 1995 | -1542.1 | 226 | 236 | 29 | -0.0054 | 0.0016 | -0.0022 | -0.0054 | 0.0016 | -0.0022 |
| 2350 | 1995 | -1542.1 | 226 | 236 | 9 | -0.0091 | 0.0014 | -0.0010 | -0.0091 | 0.0014 | -0.0010 |
| 2350 | 1795 | -1539.9 | 226 | 136 | 49 | 0.0000 | 0.0000 | 0.0000 | 0.0000 | 0.0000 | 0.0000 |
| 2350 | 1795 | -1539.9 | 226 | 136 | 29 | -0.0020 | 0.0010 | -0.0037 | -0.0020 | 0.0010 | -0.0037 |
| 2350 | 1795 | -1539.9 | 226 | 136 | 9 | -0.0064 | -0.0040 | -0.0018 | -0.0064 | -0.0040 | -0.0018 |
| 2350 | 1695 | -1498.1 | 226 | 86 | 49 | 0.0000 | 0.0000 | 0.0000 | 0.0000 | 0.0000 | 0.0000 |
| 2350 | 1695 | -1498.1 | 226 | 86 | 29 | -0.0007 | -0.0043 | -0.0044 | -0.0007 | -0.0043 | -0.0044 |
| 2350 | 1695 | -1498.1 | 226 | 86 | 9 | -0.0053 | -0.0014 | -0.0023 | -0.0053 | -0.0014 | -0.0023 |
| 2350 | 1595 | -1481.6 | 226 | 36 | 49 | 0.0000 | 0.0000 | 0.0000 | 0.0000 | 0.0000 | 0.0000 |
| 2350 | 1595 | -1481.6 | 226 | 36 | 29 | 0.0003 | -0.0037 | -0.0042 | 0.0003 | -0.0037 | -0.0042 |
| 2350 | 1595 | -1481.6 | 226 | 36 | 9 | -0.0045 | 0.0089 | -0.0048 | -0.0045 | 0.0089 | -0.0048 |
| 2450 | 2195 | -1487.1 | 276 | 326 | 49 | 0.0000 | 0.0000 | 0.0000 | 0.0000 | 0.0000 | 0.0000 |
| 2450 | 2195 | -1487.1 | 276 | 326 | 29 | 0.0005 | 0.0012 | -0.0101 | 0.0005 | 0.0012 | -0.0101 |
| 2450 | 2195 | -1487.1 | 276 | 326 | 9 | 0.0012 | -0.0069 | -0.0039 | 0.0012 | -0.0069 | -0.0039 |
| 2450 | 2095 | -1515.9 | 276 | 286 | 49 | 0.0000 | 0.0000 | 0.0000 | 0.0000 | 0.0000 | 0.0000 |
| 2450 | 2095 | -1515.9 | 276 | 286 | 29 | -0.0023 | 0.0003 | -0.0054 | -0.0023 | 0.0003 | -0.0054 |
| 2450 | 2095 | -1515.9 | 276 | 286 | 9 | -0.0053 | -0.0059 | -0.0024 | -0.0053 | -0.0059 | -0.0024 |
| 2450 | 1995 | -1544.3 | 276 | 236 | 49 | 0.0000 | 0.0000 | 0.0000 | 0.0000 | 0.0000 | 0.0000 |
| 2450 | 1995 | -1544.3 | 276 | 236 | 29 | -0.0066 | -0.0109 | -0.0031 | -0.0066 | -0.0109 | -0.0031 |
| 2450 | 1995 | -1544.3 | 276 | 236 | 9 | -0.0102 | -0.0163 | -0.0024 | -0.0102 | -0.0163 | -0.0024 |
| 2450 | 1795 | -1543.1 | 276 | 136 | 49 | 0.0000 | 0.0000 | 0.0000 | 0.0000 | 0.0000 | 0.0000 |
| 2450 | 1795 | -1543.1 | 276 | 136 | 29 | 0.0059 | 0.0032 | 0.0010 | 0.0059 | 0.0032 | 0.0010 |
| 2450 | 1795 | -1543.1 | 276 | 136 | 9 | -0.0002 | 0.0128 | 0.0015 | -0.0002 | 0.0128 | 0.0015 |
| 2450 | 1695 | -1500.8 | 276 | 86 | 49 | 0.0000 | 0.0000 | 0.0000 | 0.0000 | 0.0000 | 0.0000 |
| 2450 | 1695 | -1500.8 | 276 | 86 | 29 | -0.0031 | -0.0002 | -0.0040 | -0.0031 | -0.0002 | -0.0040 |

Series 2 - PADV Profiler Data for Run 24 Cont'd

| | | | | | | | | | | | |
|---|---|---|---|---|---|---|---|---|---|---|---|
| 2450 | 1695 | -1500.8 | 276 | 86 | 9 | -0.0081 | 0.0048 | -0.0011 | -0.0081 | 0.0048 | -0.0011 |
| 2450 | 1595 | -1484.8 | 276 | 36 | 49 | 0.0000 | 0.0000 | 0.0000 | 0.0000 | 0.0000 | 0.0000 |
| 2450 | 1595 | -1484.8 | 276 | 36 | 29 | 0.0003 | -0.0003 | -0.0039 | 0.0003 | -0.0003 | -0.0039 |
| 2450 | 1595 | -1484.8 | 276 | 36 | 9 | -0.0010 | 0.0064 | -0.0006 | -0.0010 | 0.0064 | -0.0006 |
| 2540 | 2135 | -1488.8 | 321 | 297 | 49 | 0.0003 | 0.0000 | 0.0000 | 0.0003 | 0.0000 | 0.0000 |
| 2550 | 2195 | -1489.2 | 326 | 326 | 29 | 0.0007 | 0.0014 | -0.0047 | 0.0007 | 0.0014 | -0.0047 |
| 2550 | 2195 | -1489.2 | 326 | 326 | 9 | 0.0005 | -0.0104 | -0.0020 | 0.0005 | -0.0104 | -0.0020 |
| 2550 | 2095 | -1502.2 | 326 | 286 | 49 | 0.0000 | 0.0000 | 0.0000 | 0.0000 | 0.0000 | 0.0000 |
| 2550 | 2095 | -1502.2 | 326 | 286 | 29 | 0.0001 | 0.0015 | -0.0045 | 0.0001 | 0.0015 | -0.0045 |
| 2550 | 2095 | -1502.2 | 326 | 286 | 9 | 0.0026 | -0.0071 | -0.0019 | 0.0026 | -0.0071 | -0.0019 |
| 2550 | 1995 | -1537.6 | 326 | 236 | 49 | 0.0000 | 0.0000 | 0.0000 | 0.0000 | 0.0000 | 0.0000 |
| 2550 | 1995 | -1537.6 | 326 | 236 | 29 | 0.0007 | 0.0006 | -0.0032 | 0.0007 | 0.0006 | -0.0032 |
| 2550 | 1995 | -1537.6 | 326 | 236 | 9 | 0.0032 | -0.0118 | -0.0015 | 0.0032 | -0.0118 | -0.0015 |
| 2550 | 1795 | -1533.6 | 326 | 136 | 49 | 0.0000 | 0.0000 | 0.0000 | 0.0000 | 0.0000 | 0.0000 |
| 2550 | 1795 | -1533.6 | 326 | 136 | 29 | -0.0004 | 0.0051 | -0.0045 | -0.0004 | 0.0051 | -0.0045 |
| 2550 | 1795 | -1533.6 | 326 | 136 | 9 | 0.0121 | 0.0165 | -0.0007 | 0.0121 | 0.0165 | -0.0007 |
| 2550 | 1695 | -1496.4 | 326 | 86 | 49 | 0.0000 | 0.0000 | 0.0000 | 0.0000 | 0.0000 | 0.0000 |
| 2550 | 1695 | -1496.4 | 326 | 86 | 29 | 0.0024 | 0.0018 | -0.0036 | 0.0024 | 0.0018 | -0.0036 |
| 2550 | 1695 | -1496.4 | 326 | 86 | 9 | 0.0048 | 0.0101 | -0.0014 | 0.0048 | 0.0101 | -0.0014 |
| 2550 | 1595 | -1489.5 | 326 | 36 | 49 | 0.0000 | 0.0000 | 0.0000 | 0.0000 | 0.0000 | 0.0000 |
| 2550 | 1595 | -1489.5 | 326 | 36 | 29 | -0.0028 | 0.0008 | -0.0047 | -0.0028 | 0.0008 | -0.0047 |
| 2550 | 1595 | -1489.5 | 326 | 36 | 9 | 0.0016 | 0.0088 | -0.0009 | 0.0016 | 0.0088 | -0.0009 |
| 2650 | 2195 | -1494.1 | 376 | 326 | 49 | 0.0000 | 0.0000 | 0.0000 | 0.0000 | 0.0000 | 0.0000 |
| 2650 | 2195 | -1494.1 | 376 | 326 | 29 | 0.0000 | 0.0000 | 0.0000 | 0.0000 | 0.0000 | 0.0000 |
| 2650 | 2195 | -1494.1 | 376 | 326 | 9 | 0.0000 | 0.0000 | 0.0000 | 0.0000 | 0.0000 | 0.0000 |
| 2650 | 2095 | -1489.5 | 376 | 286 | 49 | 0.0000 | 0.0000 | 0.0000 | 0.0000 | 0.0000 | 0.0000 |
| 2650 | 2095 | -1489.5 | 376 | 286 | 29 | 0.0003 | -0.0006 | -0.0034 | 0.0003 | -0.0006 | -0.0034 |
| 2650 | 2095 | -1489.5 | 376 | 286 | 9 | 0.0055 | -0.0056 | -0.0027 | 0.0055 | -0.0056 | -0.0027 |
| 2650 | 1995 | -1494.4 | 376 | 236 | 49 | 0.0000 | 0.0000 | 0.0000 | 0.0000 | 0.0000 | 0.0000 |
| 2650 | 1995 | -1494.4 | 376 | 236 | 29 | -0.0001 | 0.0019 | -0.0059 | -0.0001 | 0.0019 | -0.0059 |

Series 2 - PADV Profiler Data for Run 24 Cont'd

| | | | | | | | | | | | |
|---|---|---|---|---|---|---|---|---|---|---|---|
| 2650 | 1995 | -1494.4 | 376 | 236 | 9 | 0.0131 | -0.0072 | -0.0040 | 0.0131 | -0.0072 | -0.0040 |
| 2650 | 1795 | -1493.1 | 376 | 136 | 49 | 0.0000 | 0.0000 | 0.0000 | 0.0000 | 0.0000 | 0.0000 |
| 2650 | 1795 | -1493.1 | 376 | 136 | 29 | -0.0021 | 0.0019 | -0.0055 | -0.0021 | 0.0019 | -0.0055 |
| 2650 | 1795 | -1493.1 | 376 | 136 | 9 | 0.0165 | 0.0096 | -0.0024 | 0.0165 | 0.0096 | -0.0024 |
| 2650 | 1695 | -1492.0 | 376 | 86 | 49 | 0.0000 | 0.0000 | 0.0000 | 0.0000 | 0.0000 | 0.0000 |
| 2650 | 1695 | -1492.0 | 376 | 86 | 29 | -0.0023 | 0.0017 | -0.0060 | -0.0023 | 0.0017 | -0.0060 |
| 2650 | 1695 | -1492.0 | 376 | 86 | 9 | 0.0055 | 0.0026 | -0.0026 | 0.0055 | 0.0026 | -0.0026 |
| 2650 | 1595 | -1497.4 | 376 | 36 | 49 | 0.0000 | 0.0000 | 0.0000 | 0.0000 | 0.0000 | 0.0000 |
| 2650 | 1595 | -1497.4 | 376 | 36 | 29 | -0.0003 | 0.0010 | -0.0094 | -0.0003 | 0.0010 | -0.0094 |
| 2650 | 1595 | -1497.4 | 376 | 36 | 9 | 0.0040 | 0.0010 | -0.0039 | 0.0040 | 0.0010 | -0.0039 |
| 2750 | 2195 | -1503.8 | 426 | 326 | 49 | 0.0000 | 0.0000 | 0.0000 | 0.0000 | 0.0000 | 0.0000 |
| 2750 | 2195 | -1503.8 | 426 | 326 | 29 | 0.0024 | -0.0009 | -0.0036 | 0.0024 | -0.0009 | -0.0036 |
| 2750 | 2195 | -1503.8 | 426 | 326 | 9 | 0.0076 | -0.0021 | -0.0027 | 0.0076 | -0.0021 | -0.0027 |
| 2750 | 2095 | -1498.0 | 426 | 286 | 48.8 | 0.0000 | 0.0000 | 0.0000 | 0.0000 | 0.0000 | 0.0000 |
| 2750 | 2095 | -1498.0 | 426 | 286 | 29 | 0.0018 | 0.0011 | -0.0085 | 0.0018 | 0.0011 | -0.0085 |
| 2750 | 2095 | -1498.0 | 426 | 286 | 9 | 0.0077 | -0.0120 | -0.0037 | 0.0077 | -0.0120 | -0.0037 |
| 2750 | 1995 | -1494.0 | 426 | 236 | 49 | 0.0000 | 0.0000 | 0.0000 | 0.0000 | 0.0000 | 0.0000 |
| 2750 | 1995 | -1494.0 | 426 | 236 | 29 | 0.0002 | 0.0014 | -0.0084 | 0.0002 | 0.0014 | -0.0084 |
| 2750 | 1995 | -1494.0 | 426 | 236 | 9 | 0.0095 | -0.0083 | -0.0036 | 0.0095 | -0.0083 | -0.0036 |
| 2750 | 1795 | -1496.4 | 426 | 136 | 49 | 0.0000 | 0.0000 | 0.0000 | 0.0000 | 0.0000 | 0.0000 |
| 2750 | 1795 | -1496.4 | 426 | 136 | 29 | 0.0009 | 0.0022 | -0.0082 | 0.0009 | 0.0022 | -0.0082 |
| 2750 | 1795 | -1496.4 | 426 | 136 | 9 | 0.0137 | 0.0036 | -0.0033 | 0.0137 | 0.0036 | -0.0033 |
| 2750 | 1695 | -1500.2 | 426 | 86 | 49 | 0.0000 | 0.0000 | 0.0000 | 0.0000 | 0.0000 | 0.0000 |
| 2750 | 1695 | -1500.2 | 426 | 86 | 29 | -0.0007 | 0.0014 | -0.0073 | -0.0007 | 0.0014 | -0.0073 |
| 2750 | 1695 | -1500.2 | 426 | 86 | 9 | 0.0074 | 0.0026 | -0.0030 | 0.0074 | 0.0026 | -0.0030 |
| 2750 | 1595 | -1505.6 | 426 | 36 | 49 | 0.0000 | 0.0000 | 0.0000 | 0.0000 | 0.0000 | 0.0000 |
| 2750 | 1595 | -1505.6 | 426 | 36 | 29 | 0.0004 | 0.0022 | -0.0056 | 0.0004 | 0.0022 | -0.0056 |
| 2750 | 1595 | -1505.6 | 426 | 36 | 9 | 0.0014 | 0.0026 | -0.0041 | 0.0014 | 0.0026 | -0.0041 |

Series 2 - PADV Profiler Data for Run 25

| X Location (mm) | Y Location (mm) | Bed Elevation (mm) | X-node | Y-node | Profile Sample Elevation From Bed (mm) | u (m/s) | v (m/s) | w (m/s) | $u_{corr}$ (m/s) | $v_{corr}$ (m/s) | $w_{corr}$ (m/s) |
|---|---|---|---|---|---|---|---|---|---|---|---|
| 1950 | 1895 | -1395.7 | 1950 | 1895 | 49 | 0.0000 | 0.0000 | 0.0000 | 0.0000 | 0.0000 | 0.0000 |
| 1950 | 1895 | -1395.7 | 1950 | 1895 | 29 | -0.0002 | 0.0017 | -0.0033 | -0.0002 | 0.0017 | -0.0033 |
| 1950 | 1895 | -1395.7 | 1950 | 1895 | 9 | 0.0391 | 0.0006 | -0.0088 | 0.0391 | 0.0006 | -0.0088 |
| 2050 | 1895 | -1418.2 | 2050 | 1895 | 49 | 0.0000 | 0.0000 | 0.0000 | 0.0000 | 0.0000 | 0.0000 |
| 2050 | 1895 | -1418.2 | 2050 | 1895 | 29 | 0.0001 | -0.0002 | -0.0040 | 0.0001 | -0.0002 | -0.0040 |
| 2050 | 1895 | -1418.2 | 2050 | 1895 | 9 | 0.0058 | 0.0006 | -0.0035 | 0.0058 | 0.0006 | -0.0035 |
| 2150 | 1895 | -1477.2 | 2150 | 1895 | 49 | 0.0000 | 0.0000 | 0.0000 | 0.0000 | 0.0000 | 0.0000 |
| 2150 | 1895 | -1477.2 | 2150 | 1895 | 29 | -0.0028 | 0.0001 | -0.0029 | -0.0028 | 0.0001 | -0.0029 |
| 2150 | 1895 | -1477.2 | 2150 | 1895 | 9 | 0.0459 | 0.0025 | -0.0179 | 0.0459 | 0.0025 | -0.0179 |
| 2250 | 1895 | -1516.6 | 2250 | 1895 | 49 | 0.0000 | 0.0000 | 0.0000 | 0.0000 | 0.0000 | 0.0000 |
| 2250 | 1895 | -1516.6 | 2250 | 1895 | 29 | 0.0228 | 0.0048 | 0.0103 | 0.0228 | 0.0048 | 0.0103 |
| 2250 | 1895 | -1516.6 | 2250 | 1895 | 9 | 0.0524 | -0.0019 | -0.0020 | 0.0524 | -0.0019 | -0.0020 |
| 2350 | 1895 | -1539.7 | 2350 | 1895 | 49 | 0.0000 | 0.0000 | 0.0000 | 0.0000 | 0.0000 | 0.0000 |
| 2350 | 1895 | -1539.7 | 2350 | 1895 | 29 | 0.0268 | 0.0053 | 0.0036 | 0.0268 | 0.0053 | 0.0036 |
| 2350 | 1895 | -1539.7 | 2350 | 1895 | 9 | 0.0515 | 0.0068 | 0.0040 | 0.0515 | 0.0068 | 0.0040 |
| 2450 | 1895 | -1544.9 | 2450 | 1895 | 49 | 0.0000 | 0.0000 | 0.0000 | 0.0000 | 0.0000 | 0.0000 |
| 2450 | 1895 | -1544.9 | 2450 | 1895 | 29 | 0.0314 | 0.0034 | 0.0053 | 0.0314 | 0.0034 | 0.0053 |
| 2450 | 1895 | -1544.9 | 2450 | 1895 | 9 | 0.0348 | 0.0029 | 0.0075 | 0.0348 | 0.0029 | 0.0075 |
| 2550 | 1895 | -1538.1 | 2550 | 1895 | 49 | 0.0000 | 0.0000 | 0.0000 | 0.0000 | 0.0000 | 0.0000 |
| 2550 | 1895 | -1538.1 | 2550 | 1895 | 29 | 0.0070 | 0.0006 | -0.0038 | 0.0070 | 0.0006 | -0.0038 |
| 2550 | 1895 | -1538.1 | 2550 | 1895 | 9 | 0.0280 | -0.0015 | 0.0055 | 0.0280 | -0.0015 | 0.0055 |
| 2650 | 1895 | -1493.7 | 2650 | 1895 | 49 | 0.0000 | 0.0000 | 0.0000 | 0.0000 | 0.0000 | 0.0000 |
| 2650 | 1895 | -1493.7 | 2650 | 1895 | 29 | 0.0004 | -0.0003 | -0.0048 | 0.0004 | -0.0003 | -0.0048 |
| 2650 | 1895 | -1493.7 | 2650 | 1895 | 9 | 0.0074 | -0.0016 | -0.0026 | 0.0074 | -0.0016 | -0.0026 |
| 2750 | 1895 | -1492.7 | 2750 | 1895 | 49 | 0.0000 | 0.0000 | 0.0000 | 0.0000 | 0.0000 | 0.0000 |

Series 2 - PADV Profiler Data for Run 25 Cont'd

| | | | | | | | | | | | | |
|---|---|---|---|---|---|---|---|---|---|---|---|---|
| 2750 | 1895 | -1492.7 | 2750 | 1895 | 29 | 0.0009 | 0.0003 | -0.0056 | 0.0009 | 0.0003 | -0.0056 |
| 2750 | 1895 | -1492.7 | 2750 | 1895 | 9 | 0.0054 | -0.0006 | -0.0031 | 0.0054 | -0.0006 | -0.0031 |
| 2150 | 1995 | -1483.2 | 2150 | 1995 | 49 | 0.0000 | 0.0000 | 0.0000 | 0.0000 | 0.0000 | 0.0000 |
| 2150 | 1995 | -1483.2 | 2150 | 1995 | 29 | -0.0019 | 0.0025 | -0.0022 | -0.0019 | 0.0025 | -0.0022 |
| 2150 | 1995 | -1483.2 | 2150 | 1995 | 9 | -0.0034 | 0.0004 | -0.0004 | -0.0034 | 0.0004 | -0.0004 |
| 2150 | 1795 | -1475.6 | 2150 | 1795 | 49 | 0.0000 | 0.0000 | 0.0000 | 0.0000 | 0.0000 | 0.0000 |
| 2150 | 1795 | -1475.6 | 2150 | 1795 | 29 | -0.0022 | -0.0016 | -0.0022 | -0.0022 | -0.0016 | -0.0022 |
| 2150 | 1795 | -1475.6 | 2150 | 1795 | 9 | -0.0028 | -0.0029 | -0.0002 | -0.0028 | -0.0029 | -0.0002 |
| 2250 | 2195 | -1472.2 | 2250 | 2195 | 49 | 0.0000 | 0.0000 | 0.0000 | 0.0000 | 0.0000 | 0.0000 |
| 2250 | 2195 | -1472.2 | 2250 | 2195 | 29 | 0.0002 | 0.0028 | NaN | 0.0002 | 0.0028 | NaN |
| 2250 | 2195 | -1472.2 | 2250 | 2195 | 9 | -0.0078 | -0.0049 | -0.0039 | -0.0078 | -0.0049 | -0.0039 |
| 2250 | 2095 | -1497.7 | 2250 | 2095 | 49 | 0.0000 | 0.0000 | 0.0000 | 0.0000 | 0.0000 | 0.0000 |
| 2250 | 2095 | -1497.7 | 2250 | 2095 | 29 | -0.0035 | -0.0034 | -0.0053 | -0.0035 | -0.0034 | -0.0053 |
| 2250 | 2095 | -1497.7 | 2250 | 2095 | 9 | 0.0009 | 0.0047 | -0.0031 | 0.0009 | 0.0047 | -0.0031 |
| 2250 | 1995 | -1524.8 | 2250 | 1995 | 49 | 0.0000 | 0.0000 | 0.0000 | 0.0000 | 0.0000 | 0.0000 |
| 2250 | 1995 | -1524.8 | 2250 | 1995 | 29 | -0.0005 | 0.0026 | -0.0027 | -0.0005 | 0.0026 | -0.0027 |
| 2250 | 1995 | -1524.8 | 2250 | 1995 | 9 | -0.0064 | 0.0079 | -0.0008 | -0.0064 | 0.0079 | -0.0008 |
| 2250 | 1795 | -1518.7 | 2250 | 1795 | 49 | 0.0000 | 0.0000 | 0.0000 | 0.0000 | 0.0000 | 0.0000 |
| 2250 | 1795 | -1518.7 | 2250 | 1795 | 29 | -0.0050 | -0.0046 | -0.0028 | -0.0050 | -0.0046 | -0.0028 |
| 2250 | 1795 | -1518.7 | 2250 | 1795 | 9 | -0.0095 | -0.0063 | -0.0020 | -0.0095 | -0.0063 | -0.0020 |
| 2250 | 1695 | -1489.6 | 2250 | 1695 | 49 | 0.0000 | 0.0000 | 0.0000 | 0.0000 | 0.0000 | 0.0000 |
| 2250 | 1695 | -1489.6 | 2250 | 1695 | 29 | -0.0013 | 0.0004 | -0.0020 | -0.0013 | 0.0004 | -0.0020 |
| 2250 | 1695 | -1489.6 | 2250 | 1695 | 9 | 0.0018 | -0.0016 | -0.0017 | 0.0018 | -0.0016 | -0.0017 |
| 2250 | 1595 | -1469.5 | 2250 | 1595 | 49 | 0.0000 | 0.0000 | 0.0000 | 0.0000 | 0.0000 | 0.0000 |
| 2250 | 1595 | -1469.5 | 2250 | 1595 | 29 | -0.0007 | -0.0013 | -0.0063 | -0.0007 | -0.0013 | -0.0063 |
| 2250 | 1595 | -1469.5 | 2250 | 1595 | 9 | -0.0005 | 0.0102 | -0.0024 | -0.0005 | 0.0102 | -0.0024 |
| 2350 | 2195 | -1483.6 | 2350 | 2195 | 49 | 0.0000 | 0.0000 | 0.0000 | 0.0000 | 0.0000 | 0.0000 |
| 2350 | 2195 | -1483.6 | 2350 | 2195 | 29 | 0.0007 | 0.0038 | -0.0057 | 0.0007 | 0.0038 | -0.0057 |
| 2350 | 2195 | -1483.6 | 2350 | 2195 | 9 | -0.0066 | -0.0087 | -0.0034 | -0.0066 | -0.0087 | -0.0034 |
| 2350 | 2095 | -1506.5 | 2350 | 2095 | 49 | 0.0000 | 0.0000 | 0.0000 | 0.0000 | 0.0000 | 0.0000 |
| 2350 | 2095 | -1506.5 | 2350 | 2095 | 29 | -0.0016 | 0.0033 | -0.0038 | -0.0016 | 0.0033 | -0.0038 |

Series 2 - PADV Profiler Data for Run 25 Cont'd

| | | | | | | | | | | | |
|---|---|---|---|---|---|---|---|---|---|---|---|
| 2350 | 2095 | -1506.5 | 2350 | 2095 | 9 | -0.0090 | 0.0031 | -0.0012 | -0.0090 | 0.0031 | -0.0012 |
| 2350 | 1995 | -1540.7 | 2350 | 1995 | 49 | 0.0000 | 0.0000 | 0.0000 | 0.0000 | 0.0000 | 0.0000 |
| 2350 | 1995 | -1540.7 | 2350 | 1995 | 29 | -0.0041 | 0.0033 | -0.0026 | -0.0041 | 0.0033 | -0.0026 |
| 2350 | 1995 | -1540.7 | 2350 | 1995 | 9 | -0.0064 | 0.0031 | -0.0003 | -0.0064 | 0.0031 | -0.0003 |
| 2350 | 1795 | -1538.8 | 2350 | 1795 | 49 | 0.0000 | 0.0000 | 0.0000 | 0.0000 | 0.0000 | 0.0000 |
| 2350 | 1795 | -1538.8 | 2350 | 1795 | 29 | -0.0003 | 0.0014 | -0.0025 | -0.0003 | 0.0014 | -0.0025 |
| 2350 | 1795 | -1538.8 | 2350 | 1795 | 9 | -0.0038 | -0.0016 | -0.0006 | -0.0038 | -0.0016 | -0.0006 |
| 2350 | 1695 | -1498.1 | 2350 | 1695 | 49 | 0.0000 | 0.0000 | 0.0000 | 0.0000 | 0.0000 | 0.0000 |
| 2350 | 1695 | -1498.1 | 2350 | 1695 | 29 | -0.0007 | 0.0031 | -0.0047 | -0.0007 | 0.0031 | -0.0047 |
| 2350 | 1695 | -1498.1 | 2350 | 1695 | 9 | 0.0055 | -0.0004 | -0.0016 | 0.0055 | -0.0004 | -0.0016 |
| 2350 | 1595 | -1481.8 | 2350 | 1595 | 49 | 0.0000 | 0.0000 | 0.0000 | 0.0000 | 0.0000 | 0.0000 |
| 2350 | 1595 | -1481.8 | 2350 | 1595 | 29 | -0.0005 | -0.0042 | -0.0023 | -0.0005 | -0.0042 | -0.0023 |
| 2350 | 1595 | -1481.8 | 2350 | 1595 | 9 | -0.0040 | 0.0080 | -0.0045 | -0.0040 | 0.0080 | -0.0045 |
| 2450 | 2195 | -1486.8 | 2450 | 2195 | 49 | 0.0000 | 0.0000 | 0.0000 | 0.0000 | 0.0000 | 0.0000 |
| 2450 | 2195 | -1486.8 | 2450 | 2195 | 29 | -0.0017 | 0.0013 | -0.0050 | -0.0017 | 0.0013 | -0.0050 |
| 2450 | 2195 | -1486.8 | 2450 | 2195 | 9 | 0.0003 | -0.0082 | -0.0019 | 0.0003 | -0.0082 | -0.0019 |
| 2450 | 2095 | -1515.8 | 2450 | 2095 | 49 | 0.0000 | 0.0000 | 0.0000 | 0.0000 | 0.0000 | 0.0000 |
| 2450 | 2095 | -1515.8 | 2450 | 2095 | 29 | 0.0011 | -0.0011 | -0.0030 | 0.0011 | -0.0011 | -0.0030 |
| 2450 | 2095 | -1515.8 | 2450 | 2095 | 9 | -0.0051 | -0.0044 | -0.0019 | -0.0051 | -0.0044 | -0.0019 |
| 2450 | 1995 | -1542.8 | 2450 | 1995 | 49 | 0.0000 | 0.0000 | 0.0000 | 0.0000 | 0.0000 | 0.0000 |
| 2450 | 1995 | -1542.8 | 2450 | 1995 | 29 | 0.0010 | -0.0014 | -0.0025 | 0.0010 | -0.0014 | -0.0025 |
| 2450 | 1995 | -1542.8 | 2450 | 1995 | 9 | -0.0058 | -0.0080 | -0.0004 | -0.0058 | -0.0080 | -0.0004 |
| 2450 | 1795 | -1541.6 | 2450 | 1795 | 49 | 0.0000 | 0.0000 | 0.0000 | 0.0000 | 0.0000 | 0.0000 |
| 2450 | 1795 | -1541.6 | 2450 | 1795 | 29 | 0.0018 | 0.0023 | -0.0026 | 0.0018 | 0.0023 | -0.0026 |
| 2450 | 1795 | -1541.6 | 2450 | 1795 | 9 | -0.0032 | 0.0071 | 0.0001 | -0.0032 | 0.0071 | 0.0001 |
| 2450 | 1695 | -1500.4 | 2450 | 1695 | 49 | 0.0000 | 0.0000 | 0.0000 | 0.0000 | 0.0000 | 0.0000 |
| 2450 | 1695 | -1500.4 | 2450 | 1695 | 29 | -0.0006 | 0.0005 | -0.0045 | -0.0006 | 0.0005 | -0.0045 |
| 2450 | 1695 | -1500.4 | 2450 | 1695 | 9 | -0.0052 | 0.0021 | -0.0011 | -0.0052 | 0.0021 | -0.0011 |
| 2450 | 1595 | -1484.8 | 2450 | 1595 | 49 | 0.0000 | 0.0000 | 0.0000 | 0.0000 | 0.0000 | 0.0000 |
| 2450 | 1595 | -1484.8 | 2450 | 1595 | 29 | -0.0007 | -0.0008 | -0.0089 | -0.0007 | -0.0008 | -0.0089 |

Series 2 - PADV Profiler Data for Run 25 Cont'd

| | | | | | | | | | | | |
|---|---|---|---|---|---|---|---|---|---|---|---|
| 2450 | 1595 | -1484.8 | 2450 | 1595 | 9 | 0.0055 | 0.0003 | -0.0028 | 0.0055 | 0.0003 | -0.0028 |
| 2550 | 2195 | -1488.5 | 2550 | 2195 | 49 | 0.0000 | 0.0000 | 0.0000 | 0.0000 | 0.0000 | 0.0000 |
| 2550 | 2195 | -1488.5 | 2550 | 2195 | 29 | 0.0009 | -0.0022 | -0.0045 | 0.0009 | -0.0022 | -0.0045 |
| 2550 | 2195 | -1488.5 | 2550 | 2195 | 9 | 0.0028 | -0.0034 | -0.0019 | 0.0028 | -0.0034 | -0.0019 |
| 2550 | 2095 | -1502.2 | 2550 | 2095 | 49 | 0.0000 | 0.0000 | 0.0000 | 0.0000 | 0.0000 | 0.0000 |
| 2550 | 2095 | -1502.2 | 2550 | 2095 | 29 | 0.0012 | 0.0006 | -0.0031 | 0.0012 | 0.0006 | -0.0031 |
| 2550 | 2095 | -1502.2 | 2550 | 2095 | 9 | 0.0025 | -0.0039 | -0.0011 | 0.0025 | -0.0039 | -0.0011 |
| 2550 | 1995 | -1536.2 | 2550 | 1995 | 49 | 0.0000 | 0.0000 | 0.0000 | 0.0000 | 0.0000 | 0.0000 |
| 2550 | 1995 | -1536.2 | 2550 | 1995 | 29 | -0.0019 | 0.0006 | -0.0037 | -0.0019 | 0.0006 | -0.0037 |
| 2550 | 1995 | -1536.2 | 2550 | 1995 | 9 | 0.0050 | -0.0119 | -0.0020 | 0.0050 | -0.0119 | -0.0020 |
| 2550 | 1795 | -1532.0 | 2550 | 1795 | 49 | 0.0000 | 0.0000 | 0.0000 | 0.0000 | 0.0000 | 0.0000 |
| 2550 | 1795 | -1532.0 | 2550 | 1795 | 29 | 0.0017 | 0.0010 | -0.0029 | 0.0017 | 0.0010 | -0.0029 |
| 2550 | 1795 | -1532.0 | 2550 | 1795 | 9 | 0.0073 | 0.0106 | -0.0008 | 0.0073 | 0.0106 | -0.0008 |
| 2550 | 1695 | -1495.6 | 2550 | 1695 | 49 | 0.0000 | 0.0000 | 0.0000 | 0.0000 | 0.0000 | 0.0000 |
| 2550 | 1695 | -1495.6 | 2550 | 1695 | 29 | 0.0009 | 0.0010 | -0.0048 | 0.0009 | 0.0010 | -0.0048 |
| 2550 | 1695 | -1495.6 | 2550 | 1695 | 9 | 0.0045 | 0.0104 | -0.0018 | 0.0045 | 0.0104 | -0.0018 |
| 2550 | 1595 | -1488.9 | 2550 | 1595 | 49 | 0.0000 | 0.0000 | 0.0000 | 0.0000 | 0.0000 | 0.0000 |
| 2550 | 1595 | -1488.9 | 2550 | 1595 | 29 | -0.0011 | 0.0044 | -0.0054 | -0.0011 | 0.0044 | -0.0054 |
| 2550 | 1595 | -1488.9 | 2550 | 1595 | 9 | 0.0070 | 0.0015 | -0.0031 | 0.0070 | 0.0015 | -0.0031 |
| 2650 | 2195 | -1493.5 | 2650 | 2195 | 49 | 0.0000 | 0.0000 | 0.0000 | 0.0000 | 0.0000 | 0.0000 |
| 2650 | 2195 | -1493.5 | 2650 | 2195 | 29 | -0.0012 | -0.0019 | -0.0022 | -0.0012 | -0.0019 | -0.0022 |
| 2650 | 2195 | -1493.5 | 2650 | 2195 | 9 | -0.0001 | 0.0066 | -0.0005 | -0.0001 | 0.0066 | -0.0005 |
| 2650 | 2095 | -1488.7 | 2650 | 2095 | 49 | 0.0000 | 0.0000 | 0.0000 | 0.0000 | 0.0000 | 0.0000 |
| 2650 | 2095 | -1488.7 | 2650 | 2095 | 29 | 0.0029 | 0.0000 | -0.0022 | 0.0029 | 0.0000 | -0.0022 |
| 2650 | 2095 | -1488.7 | 2650 | 2095 | 9 | 0.0009 | -0.0006 | -0.0002 | 0.0009 | -0.0006 | -0.0002 |
| 2650 | 1995 | -1493.6 | 2650 | 1995 | 49 | 0.0000 | 0.0000 | 0.0000 | 0.0000 | 0.0000 | 0.0000 |
| 2650 | 1995 | -1493.6 | 2650 | 1995 | 29 | 0.0058 | -0.0007 | -0.0050 | 0.0058 | -0.0007 | -0.0050 |
| 2650 | 1995 | -1493.6 | 2650 | 1995 | 9 | 0.0117 | -0.0050 | -0.0030 | 0.0117 | -0.0050 | -0.0030 |
| 2650 | 1795 | -1492.3 | 2650 | 1795 | 49 | 0.0000 | 0.0000 | 0.0000 | 0.0000 | 0.0000 | 0.0000 |
| 2650 | 1795 | -1492.3 | 2650 | 1795 | 29 | -0.0014 | 0.0019 | -0.0034 | -0.0014 | 0.0019 | -0.0034 |

Series 2 - PADV Profiler Data for Run 25 Cont'd

| | | | | | | | | | | | |
|---|---|---|---|---|---|---|---|---|---|---|---|
| 2650 | 1795 | -1492.3 | 2650 | 1795 | 9 | 0.0108 | 0.0054 | -0.0021 | 0.0108 | 0.0054 | -0.0021 |
| 2650 | 1695 | -1491.1 | 2650 | 1695 | 49 | 0.0000 | 0.0000 | 0.0000 | 0.0000 | 0.0000 | 0.0000 |
| 2650 | 1695 | -1491.1 | 2650 | 1695 | 29 | 0.0027 | -0.0003 | -0.0039 | 0.0027 | -0.0003 | -0.0039 |
| 2650 | 1695 | -1491.1 | 2650 | 1695 | 9 | 0.0072 | 0.0096 | -0.0019 | 0.0072 | 0.0096 | -0.0019 |
| 2650 | 1595 | -1497.0 | 2650 | 1595 | 49 | 0.0000 | 0.0000 | 0.0000 | 0.0000 | 0.0000 | 0.0000 |
| 2650 | 1595 | -1497.0 | 2650 | 1595 | 29 | -0.0012 | -0.0019 | -0.0049 | -0.0012 | -0.0019 | -0.0049 |
| 2650 | 1595 | -1497.0 | 2650 | 1595 | 9 | -0.0014 | 0.0066 | -0.0012 | -0.0014 | 0.0066 | -0.0012 |
| 2750 | 2195 | -1503.2 | 2750 | 2195 | 49 | 0.0000 | 0.0000 | 0.0000 | 0.0000 | 0.0000 | 0.0000 |
| 2750 | 2195 | -1503.2 | 2750 | 2195 | 29 | 0.0012 | 0.0016 | -0.0059 | 0.0012 | 0.0016 | -0.0059 |
| 2750 | 2195 | -1503.2 | 2750 | 2195 | 9 | 0.0031 | -0.0067 | -0.0040 | 0.0031 | -0.0067 | -0.0040 |
| 2750 | 2095 | -1497.6 | 2750 | 2095 | 49 | 0.0000 | 0.0000 | 0.0000 | 0.0000 | 0.0000 | 0.0000 |
| 2750 | 2095 | -1497.6 | 2750 | 2095 | 29 | 0.0025 | 0.0000 | -0.0030 | 0.0025 | 0.0000 | -0.0030 |
| 2750 | 2095 | -1497.6 | 2750 | 2095 | 9 | 0.0007 | -0.0005 | -0.0037 | 0.0007 | -0.0005 | -0.0037 |
| 2750 | 1995 | -1493.3 | 2750 | 1995 | 49 | 0.0000 | 0.0000 | 0.0000 | 0.0000 | 0.0000 | 0.0000 |
| 2750 | 1995 | -1493.3 | 2750 | 1995 | 29 | 0.0005 | 0.0021 | -0.0010 | 0.0005 | 0.0021 | -0.0010 |
| 2750 | 1995 | -1493.3 | 2750 | 1995 | 9 | 0.0081 | -0.0037 | -0.0029 | 0.0081 | -0.0037 | -0.0029 |
| 2750 | 1795 | -1495.9 | 2750 | 1795 | 49 | 0.0000 | 0.0000 | 0.0000 | 0.0000 | 0.0000 | 0.0000 |
| 2750 | 1795 | -1495.9 | 2750 | 1795 | 29 | 0.0015 | -0.0004 | -0.0050 | 0.0015 | -0.0004 | -0.0050 |
| 2750 | 1795 | -1495.9 | 2750 | 1795 | 9 | 0.0084 | 0.0052 | -0.0031 | 0.0084 | 0.0052 | -0.0031 |
| 2750 | 1695 | -1499.7 | 2750 | 1695 | 49 | 0.0000 | 0.0000 | 0.0000 | 0.0000 | 0.0000 | 0.0000 |
| 2750 | 1695 | -1499.7 | 2750 | 1695 | 29 | 0.0006 | 0.0005 | -0.0036 | 0.0006 | 0.0005 | -0.0036 |
| 2750 | 1695 | -1499.7 | 2750 | 1695 | 9 | 0.0068 | 0.0063 | -0.0020 | 0.0068 | 0.0063 | -0.0020 |
| 2750 | 1595 | -1504.9 | 2750 | 1595 | 49 | 0.0000 | 0.0000 | 0.0000 | 0.0000 | 0.0000 | 0.0000 |
| 2750 | 1595 | -1504.9 | 2750 | 1595 | 29 | 0.0030 | 0.0012 | -0.0043 | 0.0030 | 0.0012 | -0.0043 |
| 2750 | 1595 | -1504.9 | 2750 | 1595 | 9 | 0.0033 | 0.0060 | -0.0005 | 0.0033 | 0.0060 | -0.0005 |

Series 2 - PADV Profiler Data for Run 26

| X Location (mm) | Y Location (mm) | Bed Elevation (mm) | X-node | Y-node | Profile Sample Elevation From Bed (mm) | u (m/s) | v (m/s) | w (m/s) | $u_{corr}$ (m/s) | $v_{corr}$ (m/s) | $w_{corr}$ (m/s) |
|---|---|---|---|---|---|---|---|---|---|---|---|
| 1950 | 1895 | -1395.7 | 1 | 186 | 49 | 0.0000 | 0.0000 | 0.0000 | 0.0000 | 0.0000 | 0.0000 |
| 1950 | 1895 | -1395.7 | 1 | 186 | 29 | 0.0038 | 0.0007 | -0.0036 | 0.0038 | 0.0007 | -0.0036 |
| 1950 | 1895 | -1395.7 | 1 | 186 | 9 | 0.0524 | -0.0040 | -0.0144 | 0.0524 | -0.0040 | -0.0144 |
| 2050 | 1895 | -1418.2 | 76 | 186 | 49 | 0.0000 | 0.0000 | 0.0000 | 0.0000 | 0.0000 | 0.0000 |
| 2050 | 1895 | -1418.2 | 76 | 186 | 29 | 0.0097 | -0.0018 | -0.0072 | 0.0097 | -0.0018 | -0.0072 |
| 2050 | 1895 | -1418.2 | 76 | 186 | 9 | 0.0438 | -0.0122 | -0.0272 | 0.0438 | -0.0122 | -0.0272 |
| 2150 | 1895 | -1477.2 | 126 | 186 | 49 | 0.0000 | 0.0000 | 0.0000 | 0.0000 | 0.0000 | 0.0000 |
| 2150 | 1895 | -1477.2 | 126 | 186 | 29 | 0.0040 | -0.0005 | -0.0037 | 0.0040 | -0.0005 | -0.0037 |
| 2150 | 1895 | -1477.2 | 126 | 186 | 9 | 0.0500 | -0.0052 | -0.0204 | 0.0500 | -0.0052 | -0.0204 |
| 2250 | 1895 | -1516.6 | 176 | 186 | 49 | 0.0000 | 0.0000 | 0.0000 | 0.0000 | 0.0000 | 0.0000 |
| 2250 | 1895 | -1516.6 | 176 | 186 | 29 | 0.0123 | 0.0051 | 0.0023 | 0.0123 | 0.0051 | 0.0023 |
| 2250 | 1895 | -1516.6 | 176 | 186 | 9 | 0.0483 | 0.0005 | -0.0014 | 0.0483 | 0.0005 | -0.0014 |
| 2350 | 1895 | -1539.7 | 226 | 186 | 49 | 0.0036 | -0.0028 | -0.0020 | 0.0036 | -0.0028 | -0.0020 |
| 2350 | 1895 | -1539.7 | 226 | 186 | 29 | 0.0221 | -0.0032 | 0.0027 | 0.0221 | -0.0032 | 0.0027 |
| 2350 | 1895 | -1539.7 | 226 | 186 | 9 | 0.0440 | 0.0004 | 0.0013 | 0.0440 | 0.0004 | 0.0013 |
| 2450 | 1895 | -1544.9 | 276 | 186 | 49 | 0.0011 | 0.0004 | -0.0021 | 0.0011 | 0.0004 | -0.0021 |
| 2450 | 1895 | -1544.9 | 276 | 186 | 29 | 0.0370 | -0.0011 | 0.0041 | 0.0370 | -0.0011 | 0.0041 |
| 2450 | 1895 | -1544.9 | 276 | 186 | 9 | 0.0393 | -0.0009 | 0.0060 | 0.0393 | -0.0009 | 0.0060 |
| 2550 | 1895 | -1538.1 | 326 | 186 | 49 | 0.0000 | 0.0000 | 0.0000 | 0.0000 | 0.0000 | 0.0000 |
| 2550 | 1895 | -1538.1 | 326 | 186 | 29 | 0.0120 | -0.0023 | 0.0014 | 0.0120 | -0.0023 | 0.0014 |
| 2550 | 1895 | -1538.1 | 326 | 186 | 9 | 0.0369 | -0.0033 | 0.0092 | 0.0369 | -0.0033 | 0.0092 |
| 2650 | 1895 | -1493.7 | 376 | 186 | 49 | 0.0000 | 0.0000 | 0.0000 | 0.0000 | 0.0000 | 0.0000 |
| 2650 | 1895 | -1493.7 | 376 | 186 | 29 | -0.0008 | -0.0011 | -0.0056 | -0.0008 | -0.0011 | -0.0056 |

Series 2 - PADV Profiler Data for Run 26 Cont'd

| | | | | | | | | | | | |
|---|---|---|---|---|---|---|---|---|---|---|---|
| 2650 | 1895 | -1493.7 | 376 | 186 | 9 | 0.0190 | -0.0034 | -0.0035 | 0.0190 | -0.0034 | -0.0035 |
| 2750 | 1895 | -1492.7 | 426 | 186 | 49 | 0.0000 | 0.0000 | 0.0000 | 0.0000 | 0.0000 | 0.0000 |
| 2750 | 1895 | -1492.7 | 426 | 186 | 29 | 0.0001 | -0.0022 | -0.0067 | 0.0001 | -0.0022 | -0.0067 |
| 2750 | 1895 | -1492.7 | 426 | 186 | 9 | 0.0159 | -0.0025 | -0.0034 | 0.0159 | -0.0025 | -0.0034 |
| 2250 | 1995 | -1524.8 | 176 | 236 | 49 | 0.0000 | 0.0000 | 0.0000 | 0.0000 | 0.0000 | 0.0000 |
| 2250 | 1995 | -1524.8 | 176 | 236 | 29 | -0.0042 | 0.0056 | -0.0010 | -0.0042 | 0.0056 | -0.0010 |
| 2250 | 1995 | -1524.8 | 176 | 236 | 9 | -0.0074 | 0.0077 | 0.0000 | -0.0074 | 0.0077 | 0.0000 |
| 2250 | 1795 | -1518.7 | 176 | 136 | 49 | 0.0000 | 0.0000 | 0.0000 | 0.0000 | 0.0000 | 0.0000 |
| 2250 | 1795 | -1518.7 | 176 | 136 | 29 | -0.0055 | -0.0049 | -0.0018 | -0.0055 | -0.0049 | -0.0018 |
| 2250 | 1795 | -1518.7 | 176 | 136 | 9 | -0.0069 | -0.0064 | -0.0005 | -0.0069 | -0.0064 | -0.0005 |
| 2350 | 2095 | -1506.5 | 226 | 286 | 49 | 0.0000 | 0.0000 | 0.0000 | 0.0000 | 0.0000 | 0.0000 |
| 2350 | 2095 | -1506.5 | 226 | 286 | 29 | -0.0036 | -0.0037 | -0.0058 | -0.0036 | -0.0037 | -0.0058 |
| 2350 | 2095 | -1506.5 | 226 | 286 | 9 | -0.0131 | 0.0036 | -0.0025 | -0.0131 | 0.0036 | -0.0025 |
| 2350 | 1995 | -1540.7 | 226 | 236 | 49 | 0.0000 | 0.0000 | 0.0000 | 0.0000 | 0.0000 | 0.0000 |
| 2350 | 1995 | -1540.7 | 226 | 236 | 29 | -0.0019 | 0.0007 | -0.0009 | -0.0019 | 0.0007 | -0.0009 |
| 2350 | 1995 | -1540.7 | 226 | 236 | 9 | 0.0008 | 0.0018 | -0.0005 | 0.0008 | 0.0018 | -0.0005 |
| 2350 | 1795 | -1538.8 | 226 | 136 | 49 | 0.0000 | 0.0000 | 0.0000 | 0.0000 | 0.0000 | 0.0000 |
| 2350 | 1795 | -1538.8 | 226 | 136 | 29 | -0.0008 | 0.0003 | -0.0034 | -0.0008 | 0.0003 | -0.0034 |
| 2350 | 1795 | -1538.8 | 226 | 136 | 9 | -0.0066 | -0.0041 | -0.0011 | -0.0066 | -0.0041 | -0.0011 |
| 2350 | 1695 | -1498.1 | 226 | 86 | 49 | 0.0000 | 0.0000 | 0.0000 | 0.0000 | 0.0000 | 0.0000 |
| 2350 | 1695 | -1498.1 | 226 | 86 | 29 | -0.0025 | 0.0000 | -0.0056 | -0.0025 | 0.0000 | -0.0056 |
| 2350 | 1695 | -1498.1 | 226 | 86 | 9 | 0.0032 | 0.0042 | -0.0022 | 0.0032 | 0.0042 | -0.0022 |
| 2450 | 2095 | -1515.8 | 276 | 286 | 49 | 0.0000 | 0.0000 | 0.0000 | 0.0000 | 0.0000 | 0.0000 |
| 2450 | 2095 | -1515.8 | 276 | 286 | 29 | 0.0003 | 0.0026 | -0.0050 | 0.0003 | 0.0026 | -0.0050 |
| 2450 | 2095 | -1515.8 | 276 | 286 | 9 | -0.0087 | -0.0061 | -0.0013 | -0.0087 | -0.0061 | -0.0013 |
| 2450 | 1995 | -1542.8 | 276 | 236 | 49 | 0.0000 | 0.0000 | 0.0000 | 0.0000 | 0.0000 | 0.0000 |
| 2450 | 1995 | -1542.8 | 276 | 236 | 29 | 0.0001 | -0.0007 | -0.0009 | 0.0001 | -0.0007 | -0.0009 |
| 2450 | 1995 | -1542.8 | 276 | 236 | 9 | 0.0023 | -0.0112 | -0.0010 | 0.0023 | -0.0112 | -0.0010 |
| 2450 | 1795 | -1541.6 | 276 | 136 | 49 | 0.0000 | 0.0000 | 0.0000 | 0.0000 | 0.0000 | 0.0000 |
| 2450 | 1795 | -1541.6 | 276 | 136 | 29 | 0.0011 | 0.0042 | -0.0025 | 0.0011 | 0.0042 | -0.0025 |

Series 2 - PADV Profiler Data for Run 26 Cont'd

| | | | | | | | | | | | |
|---|---|---|---|---|---|---|---|---|---|---|---|
| 2450 | 1795 | -1541.6 | 276 | 136 | 9 | 0.0082 | 0.0053 | 0.0005 | 0.0082 | 0.0053 | 0.0005 |
| 2450 | 1695 | -1500.4 | 276 | 86 | 49 | 0.0000 | 0.0000 | 0.0000 | 0.0000 | 0.0000 | 0.0000 |
| 2450 | 1695 | -1500.4 | 276 | 86 | 29 | -0.0017 | 0.0005 | -0.0055 | -0.0017 | 0.0005 | -0.0055 |
| 2450 | 1695 | -1500.4 | 276 | 86 | 9 | -0.0023 | -0.0007 | -0.0015 | -0.0023 | -0.0007 | -0.0015 |

Measured properties of basin and deposit dimensions for Series 2 experiments (See following tables):

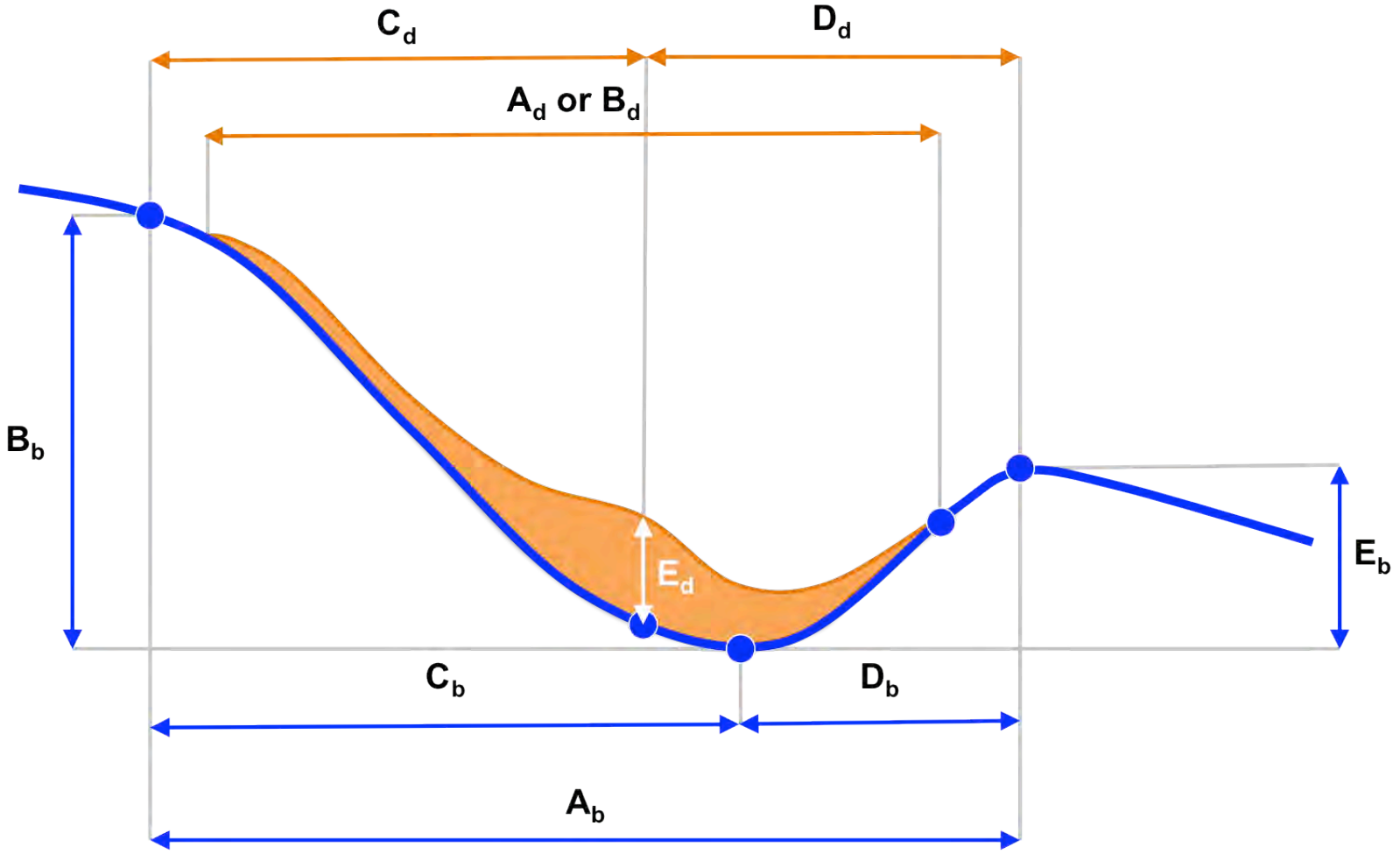

| | | | Basin Dimension Properties (See figure above) | | | | | | | | Deposit Dimension Properties (See figure above) | | | | | |
|---|---|---|---|---|---|---|---|---|---|---|---|---|---|---|---|---|
| | | Run ID | Dip Length *Entrypoint to exit* (mm) | Vertical basin height (mm) | Dip Length *Entrypoint to deepest point of basin* (mm) | Dip length *Deepest point to exit point* (mm) | *Vertical distance from deepest point to spillpoint* (mm) | Strike width (mm) | Deepest Z-value of basin (mm) | Exit point elevation (mm) | Length of deposit (mm) | Dip length Entrypoint to thickest deposit (mm) | Dip Length (Thickest deposit to exit point | Width of Deposit (mm) | Thickest basin deposit (mm) | Deposit Volume (cm3) |
| Configuration 1 | x-datum 236 | | $A_b$ | $B_b$ | $C_b$ | $D_b$ | $E_b$ | | | | $A_d$ | $C_d$ | $D_d$ | $B_d$ | $E_d$ | |
| | z-datum -1464 | 0 | 528 | 75 | 340 | 188 | 36 | 558 | -1539 | -1503 | N/A | N/A | N/A | N/A | N/A | N/A |
| | | 1 | 528 | 73 | 344 | 184 | 34 | 558 | -1537 | -1503 | 204 | 266 | 198 | 202 | 8.91 | 67.85 |
| | | 2 | 536 | 71 | 352 | 184 | 33 | 558 | -1535 | -1502 | 238 | 278 | 202 | 206 | 3.44 | 49.07 |
| | | 3 | 536 | 71 | 354 | 182 | 33 | 558 | -1535 | -1502 | 256 | 302 | 196 | 222 | 1.46 | 31.66 |
| | | 4 | 536 | 70 | 356 | 180 | 32 | 558 | -1534 | -1502 | 240 | 292 | 200 | 238 | 2.39 | 43.68 |
| | | 5 | 536 | 68 | 358 | 178 | 31 | 558 | -1532 | -1501 | 246 | 266 | 198 | 192 | 1.33 | 30.68 |
| Configuration 2 | xdatum 242 | SUBSIDENCE | | | | | | | | | | | | | | |
| | z-datum -1466 | 6 | 562 | 101 | 336 | 226 | 63 | 572 | -1567 | -1504 | 562 | 166 | 252 | 248 | 1.06 | 25.86 |
| | | 7 | 562 | 101 | 336 | 226 | 63 | 572 | -1567 | -1504 | N/A | 186 | 256 | N/A | N/A | -14.72 |
| | | 8 | 562 | 101 | 336 | 226 | 63 | 572 | -1567 | -1504 | N/A | 48 | 254 | N/A | 0.133 | 12.73 |
| | | 9 | 562 | 101 | 336 | 226 | 63 | 572 | -1567 | -1504 | 162 | 194 | 256 | 220 | 0.665 | 12.8 |
| | | 10 | 558 | 101 | 334 | 224 | 63 | 572 | -1567 | -1504 | 474 | 266 | 252 | 222 | 4.39 | 138.46 |
| | | 11 | 546 | 99 | 326 | 220 | 63 | 572 | -1565 | -1502 | 284 | 250 | 246 | 252 | 8.25 | 196.65 |
| | | 12 | 550 | 88 | 370 | 180 | 54 | 572 | -1554 | -1500 | 184 | 302 | 230 | 168 | 4.66 | -114.66 |
| | | 13 | 564 | 86 | 384 | 180 | 53 | 572 | -1552 | -1499 | 382 | 256 | 232 | 244 | 3.59 | 161.64 |
| | | 14 | 566 | 85 | 368 | 198 | 53 | 572 | -1551 | -1498 | 300 | 224 | 224 | 274 | 5.05 | 210.12 |
| Configuration 3 | xdatum 105 | SUBSIDENCE | | | | | | | | | | | | | | |
| | z-datum -1447 | 15 | 590 | 131 | 320 | 270 | 80 | 652 | -1578 | -1498 | 326 | 337 | 197 | 254 | 7.8 | 270.98 |
| | | 16 | 596 | 129 | 326 | 270 | 79 | 652 | -1576 | -1497 | 348 | 241 | 189 | 264 | 4.79 | 237.04 |
| | | 17 | 610 | 127 | 350 | 260 | 78 | 652 | -1574 | -1496 | 338 | 355 | 199 | 260 | 4.26 | 235.24 |
| | | 18 | 622 | 123 | 382 | 240 | 75 | 652 | -1570 | -1495 | 338 | 329 | 207 | 266 | 5.32 | 248.84 |
| | | 19<br>20a<br>20b<br>20c | 630 | 108 | 436 | 194 | 61 | 652 | -1555 | -1494 | 326 | N/A | N/A | 262 | 16.32 | 687.34 |
| | | 21 | 630 | 105 | 412 | 218 | 60 | 652 | -1552 | -1492 | 410 | 265 | 149 | 300 | 8.38 | 484 |

| | | Basin Dimension Properties Cont'd | | | | | | | | Deposit Dimension Properties Cont'd | | | | | |
|---|---|---|---|---|---|---|---|---|---|---|---|---|---|---|---|
| | | 22a | 630 | 105 | 412 | 218 | 60 | 652 | -1552 | -1492 | 416 | N/A | N/A | 372 | 0.5 | 12.11 |
| | | 22b | 636 | 104 | 418 | 218 | 59 | 652 | -1551 | -1492 | 370 | N/A | N/A | 368 | 0.5 | 17.98 |
| | | 23 | 650 | 101 | 430 | 220 | 58 | 660 | -1548 | -1490 | 470 | 325 | 197 | 448 | 8.65 | 531.91 |
| | | 24 | 664 | 100 | 438 | 226 | 58 | 660 | -1547 | -1489 | 412 | 205 | 207 | 276 | 2.93 | 192.34 |
| | | 25 | 680 | 90 | 472 | 208 | 49 | 660 | -1537 | -1488 | 438 | 415 | 221 | 322 | 10.77 | 571.1 |
| | | 26 | 684 | 88 | 468 | 216 | 48 | 660 | -1535 | -1487 | 498 | 291 | 223 | 374 | 2.53 | 208.89 |
| | | 27 | 684 | 87 | 472 | 212 | 47 | 660 | -1534 | -1487 | 496 | 313 | 221 | 304 | 3.19 | 211.92 |

Measured properties of spatial relationships between velocity maxima/ minima and basin features (See following tables):

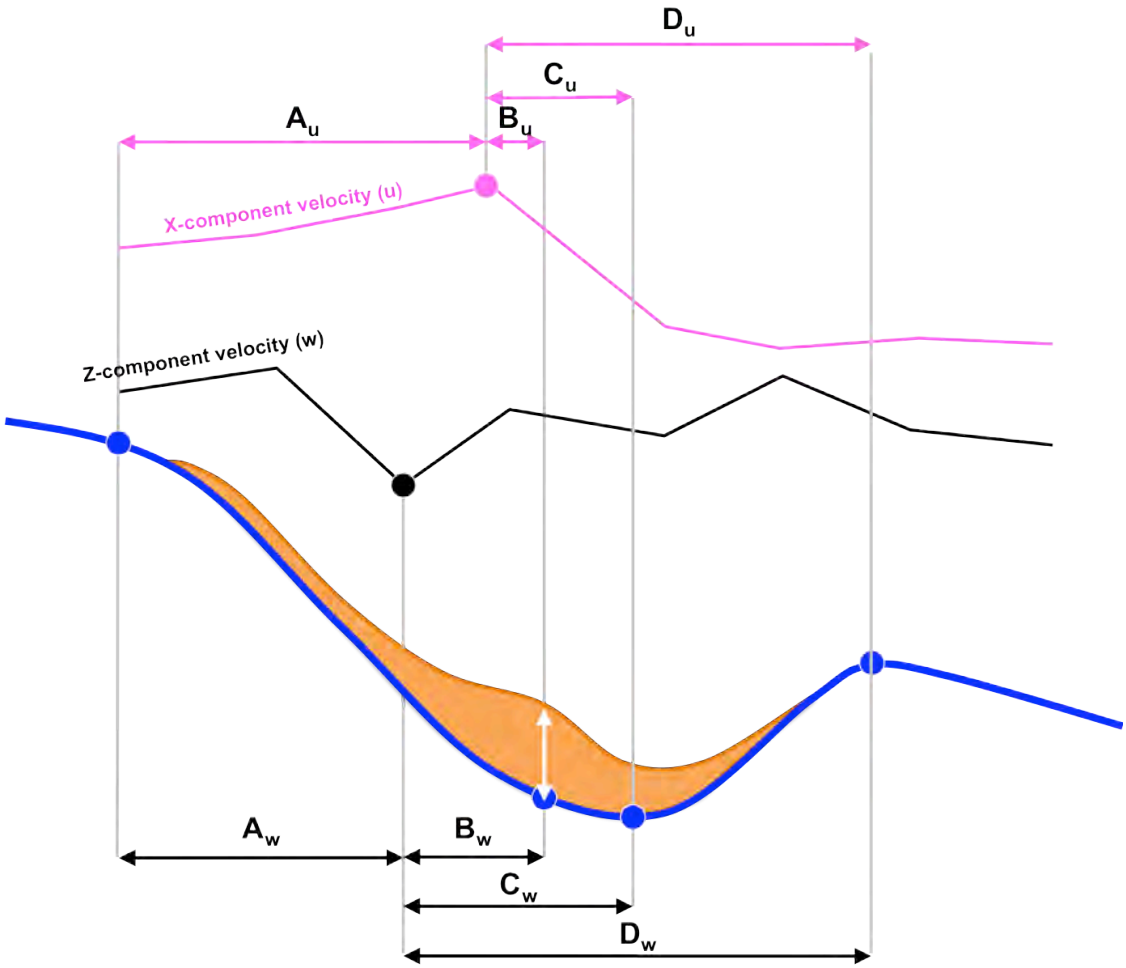

Component Velocity and Basin/Deposit Feature Proximity (See figure above)

| Run ID | x-distance at minimum w (mm) | x-distance at max u (mm) | x-distance at deepest Z of basin (mm) | x-distance at thickest deposit (mm) |
|---|---|---|---|---|
| | | | | |
| 0 | N/A | N/A | N/A | N/A |
| 1 | 352 | 452 | 566 | 502 |
| 2 | 352 | 452 | 570 | 514 |
| 3 | 452 | 452 | 576 | 538 |
| 4 | N/A | N/A | 572 | 528 |
| 5 | 452 | 452 | 574 | 502 |
| SUBSIDENCE | | | | |
| 6 | 452 | 352 | 552 | 408 |
| 7 | 452 | 352 | 548 | 428 |
| 8 | 452 | 352 | 550 | 290 |
| 9 | 452 | 352 | 548 | 436 |
| 10 | 452 | 352 | 548 | 508 |
| 11 | 452 | 352 | 542 | 492 |
| 12 | 452 | 352 | 562 | 544 |
| 13 | 452 | 652 | 574 | 498 |
| 14 | N/A | N/A | 584 | 466 |
| SUBSIDENCE | | | | |
| 15 | 452 | 152 | 498 | 442 |
| 16 | 452 | 252 | 512 | 346 |
| 17 | 352 | 252 | 516 | 460 |
| 18 | 452 | 252 | 520 | 434 |
| 19<br>20a<br>20b<br>20c | N/A | N/A | N/A | N/A |
| 21 | 452 | 352 | 586 | 370 |
| 22a | N/A | N/A | N/A | N/A |
| 22b | N/A | N/A | N/A | N/A |
| 23 | 412 | 412 | 558 | 430 |
| 24 | 212 | 412 | 562 | 310 |
| 25 | 312 | 312 | 564 | 520 |
| 26 | 312 | 412 | 566 | 396 |
| 27 | N/A | N/A | 568 | 418 |

Spatial relationships between Velocity Maxima/ Minima and Basin Features (See figure above).

| | | Dip length *entrypoint to x at max. U* (mm) | Dip Length *x at max. U to x at thickest deposit* (mm) | Dip Length *x at max. U to x at deepest point in basin* (mm) | Dip Length *x at max. U to x at exit point* (mm) | Dip length *entrypoint to w at min. W* (mm) | Dip Length *x at min. W to x at thickest deposit* (mm) | Dip Length *x at min. W to x at deepest point in basin* (mm) | Dip Length *x at min. W to x at exit point* (mm) |
|---|---|---|---|---|---|---|---|---|---|
| | | $A_u$ | $B_u$ | $C_u$ | $D_u$ | $A_w$ | $B_w$ | $C_w$ | $D_w$ |
| Configuration 1 | 1 | 216 | 50 | 114 | 312 | 116 | 150 | 214 | 412 |
| | 2 | 216 | 62 | 118 | 320 | 116 | 162 | 218 | 420 |
| | 3 | 216 | 86 | 124 | 320 | 216 | 86 | 124 | 320 |
| | 4 | N/A | N/A | N/A | N/A | N/A | N/A | N/A | N/A |
| | 5 | 216 | 50 | 122 | 320 | 216 | 50 | 122 | 320 |
| Configuration 2 | SUBSIDENCE | | | | | | | | |
| | 6 | 110 | 56 | 200 | 452 | 210 | -44 | 100 | 352 |
| | 7 | 110 | 76 | 196 | 452 | 210 | -24 | 96 | 352 |
| | 8 | 110 | -62 | 198 | 452 | 210 | -162 | 98 | 352 |
| | 9 | 110 | 84 | 196 | 452 | 210 | -16 | 96 | 352 |
| | 10 | 110 | 156 | 196 | 448 | 210 | 56 | 96 | 348 |
| | 11 | 110 | 140 | 190 | 436 | 210 | 40 | 90 | 336 |
| | 12 | 110 | 192 | 210 | 440 | 210 | 92 | 110 | 340 |
| | 13 | 410 | -154 | -78 | 154 | 210 | 46 | 122 | 354 |
| | 14 | N/A | N/A | N/A | N/A | N/A | N/A | N/A | N/A |
| Configuration 3 | SUBSIDENCE | | | | | | | | |
| | 15 | 47 | -594 | 346 | 543 | 347 | -10 | 46 | 243 |
| | 16 | 147 | -598 | 260 | 449 | 347 | -106 | 60 | 249 |
| | 17 | 147 | -712 | 264 | 463 | 247 | 108 | 164 | 363 |
| | 18 | 147 | -686 | 268 | 475 | 347 | -18 | 68 | 275 |
| | 19 | | | | | | N/A | | |
| | 20a<br>20b<br>20c | N/A | N/A | N/A | N/A | N/A | | N/A | N/A |
| | 21 | 247 | -722 | 234 | 383 | 347 | -82 | 134 | 283 |
| | 22a | N/A | N/A | N/A | N/A | N/A | N/A | N/A | N/A |
| | 22b | N/A | N/A | N/A | N/A | N/A | N/A | N/A | N/A |
| | 23 | 307 | -842 | 146 | 343 | 307 | 18 | 146 | 343 |
| | 24 | 307 | -722 | 150 | 357 | 107 | 98 | 350 | 557 |
| | 25 | 207 | -832 | 252 | 473 | 207 | 208 | 252 | 473 |
| | 26 | 307 | -808 | 154 | 377 | 207 | 84 | 254 | 477 |
| | 27 | N/A | N/A | N/A | N/A | N/A | N/A | N/A | N/A |

## APPENDIX C: STRUCTURAL WELL-LOG CROSS SECTION OF BUL. 1 (MIDDLE PLIOCENE) RESERVOIR INTERVAL WELLS, EWING BANK BLOCK 873, GULF OF MEXICO

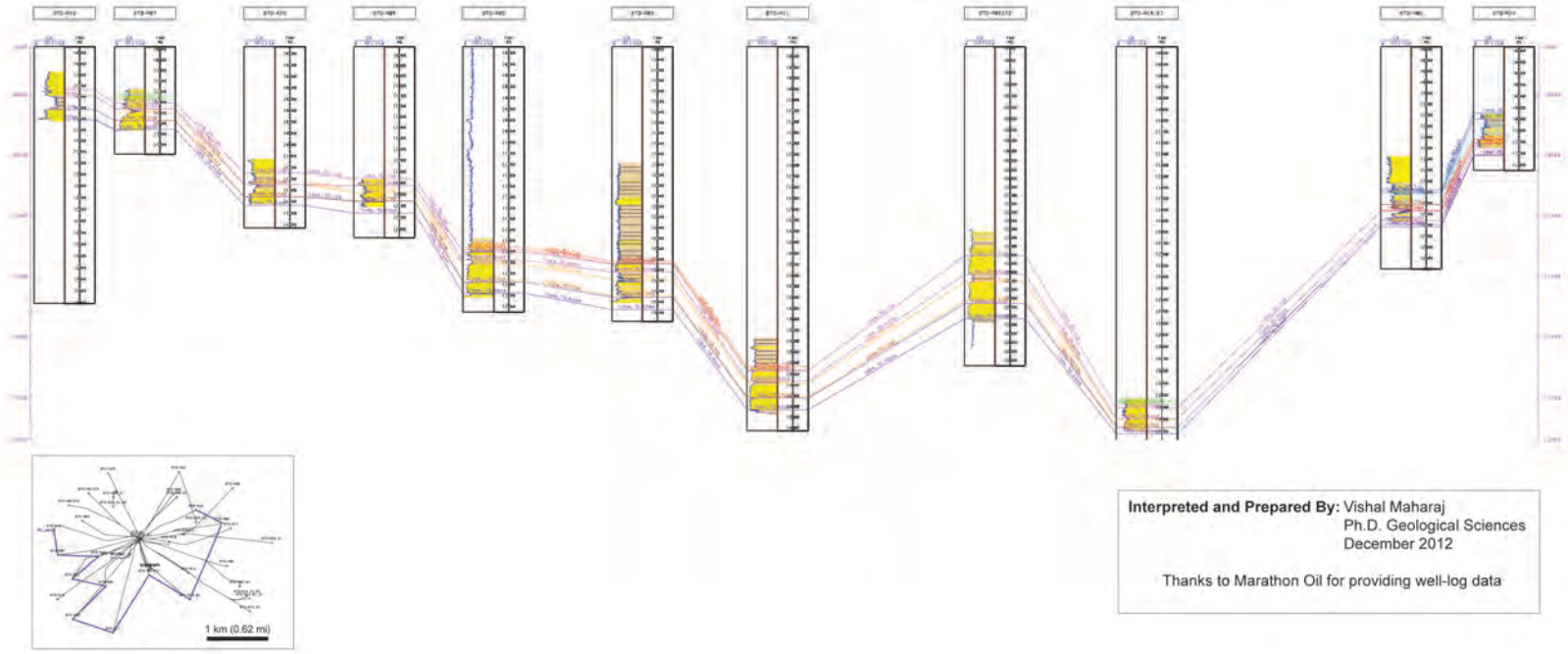

## APPENDIX D: WELL-LOG CROSS SECTION OF BUL. 1 (MIDDLE PLIOCENE) RESERVOIR INTERVAL WELLS, FLATTENED ON BASE LOBE 10 PICK, EWING BANK BLOCK 873, GULF OF MEXICO

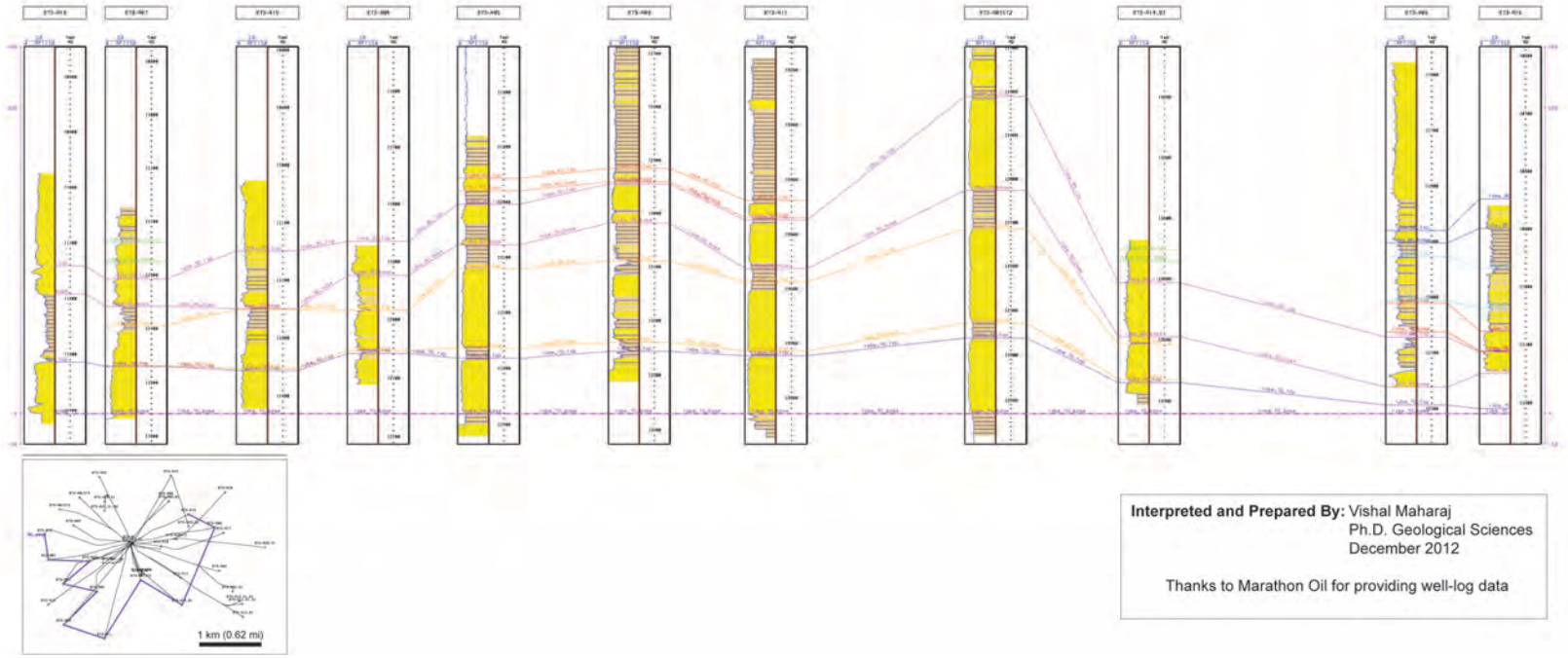

## APPENDIX E: LOBSTER BASIN AND RESERVOIR LOBE COMPLEX MORPHOLOGICAL DATA

| | Lobe Complex ID | Distance to thickest deposit from entry, $C_d$ (km) | Basin length, $A_b$ (km) | $Cd/A_b$ | Average |
|---|---|---|---|---|---|
| LCS1 | S | 6.61 | 12.60 | 0.52 | 0.51 |
| | T | 6.05 | 12.60 | 0.48 | |
| | U | 6.52 | 12.60 | 0.52 | |
| LCS2 | V | 4.32 | 12.60 | 0.34 | 0.34 |
| | W | 4.45 | 12.60 | 0.35 | |
| | X | 4.19 | 12.60 | 0.33 | |
| LCS3 | Y | 4.43 | 12.60 | 0.35 | 0.36 |
| | Z | 4.57 | 12.60 | 0.36 | |
| Total Fill | Total Fill | 4.29 | 12.60 | 0.34 | 0.34 |

| | Lobe Complex ID | Distance to thickest deposit from exit, $D_d$ (km) | Basin length, $A_b$ (km) | $D_d/A_b$ | Average |
|---|---|---|---|---|---|
| LCS1 | S | 4.97 | 12.60 | 0.39 | 0.39 |
| | T | 4.59 | 12.60 | 0.36 | |
| | U | 5.34 | 12.60 | 0.42 | |
| LCS2 | V | 7.17 | 12.60 | 0.57 | 0.58 |
| | W | 7.36 | 12.60 | 0.58 | |
| | X | 7.22 | 12.60 | 0.57 | |
| LCS3 | Y | 7.31 | 12.50 | 0.58 | 0.60 |
| | Z | 7.71 | 12.60 | 0.61 | |
| Total Fill | Total Fill | 7.57 | 12.60 | 0.60 | 0.60 |

| | Lobe Complex ID | Distance to thickest deposit from entry, $C_d$ (km) | Distance to deepest point in basin from entry, $C_b$ (km) | $C_d/C_b$ | Average |
|---|---|---|---|---|---|
| LCS1 | S | 6.61 | 4.29 | 1.54 | 1.49 |
| | T | 6.05 | 4.29 | 1.41 | |
| | U | 6.52 | 4.29 | 1.52 | |
| LCS2 | V | 4.32 | 4.29 | 1.01 | 1.01 |
| | W | 4.45 | 4.29 | 1.04 | |
| | X | 4.19 | 4.29 | 0.98 | |

| | Distance to thickest deposit from exit, $D_d$ (km) | Distance to deepest point in basin from exit, $D_b$ (km) | $D_d/D_b$ | Average | Average |
|---|---|---|---|---|---|
| LCS1 | S | 4.97 | 7.57 | 0.66 | 0.66 |
| | T | 4.59 | 7.57 | 0.61 | |
| | U | 5.34 | 7.57 | 0.70 | |
| LCS2 | V | 7.17 | 7.57 | 0.95 | 0.96 |
| | W | 7.36 | 7.57 | 0.97 | |
| | X | 7.22 | 7.57 | 0.95 | |

Appendix E cont'd

| | | | | | |
|---|---|---|---|---|---|
| LCS3 | Y | 4.43 | 4.29 | 1.03 | 1.05 |
| | Z | 4.57 | 4.29 | 1.06 | |

| | | | | | |
|---|---|---|---|---|---|
| LCS3 | Y | 7.31 | 7.57 | 0.97 | 0.99 |
| | Z | 7.71 | 7.57 | 1.02 | |

| | Lobe Complex ID | Deposit width, $B_d$ (km) | Deposit Length, Ad (km) | $B_d/A_d$ | Average |
|---|---|---|---|---|---|
| LCS1 | S | 2.92 | 5.50 | 0.53 | 0.66 |
| | T | 2.48 | 4.06 | 0.61 | |
| | U | 2.33 | 2.80 | 0.83 | |
| LCS2 | V | 1.59 | 1.25 | 1.28 | 1.01 |
| | W | 1.91 | 1.72 | 1.11 | |
| | X | 1.31 | 2.03 | 0.65 | |
| LCS3 | Y | 1.48 | 3.22 | 0.46 | 0.49 |
| | Z | 1.55 | 2.92 | 0.53 | |

| | Lobe Complex ID | Thickest Deposit thickness, $E_d$ (ft) | Deposit Length, $A_d$ (km) | $Ed/A_d$ | Average |
|---|---|---|---|---|---|
| LCS1 | S | 120.00 | 5.50 | 0.01 | 0.01 |
| | T | 90.00 | 4.06 | 0.01 | |
| | U | 90.00 | 2.80 | 0.01 | |
| LCS2 | V | 80.00 | 1.25 | 0.02 | 0.02 |
| | W | 160.00 | 1.72 | 0.03 | |
| | X | 60.00 | 2.03 | 0.01 | |
| LCS3 | Y | 120.00 | 3.22 | 0.01 | 0.01 |
| | Z | 50.00 | 2.92 | 0.01 | |

# References


Aalto, K. R., 1979, Deep-water sandstone facies and ancient submarine fans; models for exploration for stratigraphic traps; discussion and reply, *in* R. G. Walker, ed., AAPG Bulletin, United States, American Association of Petroleum Geologists : Tulsa, OK, United States, p. 810-811.

Abramowitz, M., and I. A. Stegun, 1964, Handbook of mathematical functions with formulas, graphs, and mathematical tables, Dover Publications, 1076 p.

Al Ja'Aidi, O. S., W. D. McCaffrey, and B. C. Kneller, 2004, Factors influencing the deposit geometry of experimental turbidity currents: implications for sand-body architecture in confined basins: Geological Society, London, Special Publications, v. 222, p. 45-58.

Alabert, F. G., and G. J. Massonnat, 1990, Heterogeneity in a Complex Turbiditic Reservoir: Stochastic Modelling of Facies and Petrophysical Variability, SPE Annual Technical Conference and Exhibition, New Orleans, Louisiana, 1990 Copyright 1990, Society of Petroleum Engineers Inc.

Alabert, F. G., and V. Modot, 1992, Stochastic Models of Reservoir Heterogeneity: Impact on Connectivity and Average Permeabilities, SPE Annual Technical Conference and Exhibition, Washington, D.C., 1992 Copyright 1992, Society of Petroleum Engineers Inc.

Alexander, C. S., L. E. Maley, A. Raposo, and J. Dominey, 2000, The Plutonio discovery, Block 18, Angola; a 3D visualization and multi-attribute approach to exploration success: Annual Meeting Expanded Abstracts - American Association of Petroleum Geologists, v. 2000, p. 4-4.

Alexander, C. S., L. M. Rumelhart, A. Raposo, and J. Dominey, 2001, The Plutonio discovery, Block 18, Angola; a 3-D visualization and multiattribute approach to exploration success: Leading Edge [Tulsa, OK], v. 20, p. 1393.

Alexander, L. L., 1995, Geologic evolution of a Pliocene-Pleistocene salt-withdrawal minibasin; Eugene Island Block 330, offshore Louisiana, *in* P. B. Flemings, ed., AAPG Bulletin, United States, American Association of Petroleum Geologists : Tulsa, OK, United States, p. 1737-1756.

Alexander, L. L., and P. B. Flemings, 1995, Geologic evolution of a Pliocene-Pleistocene salt-withdrawal minibasin; Eugene Island Block 330, offshore Louisiana: AAPG Bulletin, v. 79, p. 1737-1756.

Alves, T. M., J. Cartwright, and R. J. Davies, 2009, Faulting of salt-withdrawal basins during early halokinesis; effects on the Paleogene Rio Doce canyon system (Espirito Santo Basin, Brazil): AAPG Bulletin, v. 93, p. 617-652.

Ambrose, W. A., R. Bouroullec, K. Fouad, R. Jones, E. H. Guevara, E. Garciacaro, A. A. S. Patron, J. P. Ruiz, and J. d. G. C. Lopez, 2005, Deepwater facies architecture and evolution of middle and lower Miocene minibasins in the onshore Salina Basin, southeastern Mexico: Abstracts: Annual Meeting - American Association of Petroleum Geologists, v. 14, p. A5-A5.

Amy, L., B. Kneller, and W. McCaffrey, 2000, Evaluating the links between turbidite characteristics and gross system architecture; upscaling insights from the turbidite sheet-system of Peira Cava, SE France: Program and Abstracts - Society of Economic Paleontologists. Gulf Coast Section. Research Conference, v. 20, p. 1-15.

Amy, L. A., W. D. McCaffrey, and B. C. Kneller, 2004, The influence of a lateral basin-slope on the depositional patterns of natural and experimental turbidity currents: Geological Society Special Publications, v. 221, p. 311-330.

Amy, L. A., W. D. McCaffrey, and P. J. Talling, 2009, Special Issue Introduction: Sediment gravity flows , Recent insights into their dynamic and stratified/composite nature: Marine and Petroleum Geology, v. 26, p. 1897-1899.

Anderton, R., 1995, Sequences, cycles and other nonsense: are submarine fan models any use in reservoir geology?: Geological Society, London, Special Publications, v. 94, p. 5-11.

Anderton, R., 1995, Sequences, cycles and other nonsense: are submarine fan models any use in reservoir geology?: Geological Society, London, Special Publications, v. 94, p. 5-11.

Apps, G. M., F. J. Peel, C. J. Travis, and C. A. Yeilding, 1994, Structural controls on Tertiary deep water deposition in the northern Gulf of Mexico: Papers presented at the Gulf Coast Section, Society of Economic Paleontologists and Mineralogists Foundation Annual Bob F. Perkins Research Conference, v. 15, p. 1-7.

Armentrout, J. M., 2003, Timing of late Pleistocene shelf-margin deltaic depositional and mass-transport events, East Breaks 160-161 shelf-edge minibasin, Gulf of Mexico: Program and Abstracts - Society of Economic Paleontologists. Gulf Coast Section. Research Conference, v. 23, p. 91-114.

Armentrout, J. M., D. H. Suek, D. H. Harrison, P. J. Harrison, D. B. Codding, S. D. Jones, S. Lewis, and S. Graham, 2007, Seismic stratigraphy of a forearc depositional system; shelf-margin deltas to basin floor fans, northern San Joaquin Basin, California: Abstracts: Annual Meeting - American Association of Petroleum Geologists, v. 2007, p. 6-6.

Arya, A. P., 1998, Introduction to classical mechanics: Upper Saddle River, N.J., Prentice Hall.

Aschoff, J. L., 2005, Salt diapir-influenced, shallow-marine sediment dispersal patterns; insights from outcrop analogs, *in* K. A. Giles, ed., AAPG Bulletin, United States,

American Association of Petroleum Geologists : Tulsa, OK, United States, p. 447-469.

Baas, J. H., 2005, The Deep-Water Architecture Knowledge Base; towards an objective comparison of deep-marine sedimentary systems, *in* W. D. McCaffrey, and R. J. Knipe, eds., Petroleum Geoscience, United Kingdom, Geological Society Publishing House for EAGE (European Association of Geoscientists & Engineers : London, United Kingdom, p. 309-320.

Baas, J. H., 2005, Sedimentary gravity flows; recent advances in process and field analysis, Sedimentary Geology, Netherlands, Elsevier : Amsterdam, Netherlands, p. 1-174.

Baas, J. H., W. D. McCaffrey, P. D. W. Haughton, and C. Choux, 2005, Coupling between suspended sediment distribution and turbulence structure in a laboratory turbidity current: J. Geophys. Res., v. 110, p. C11015.

Baas, J. H., W. D. McCaffrey, and R. J. Knipe, 2005, The Deep-Water Architecture Knowledge Base; towards an objective comparison of deep-marine sedimentary systems: Petroleum Geoscience, v. 11, p. 309-320.

Babonneau, N., B. Savoye, M. Cremer, and M. Bez, 2004, Multiple terraces within the deep incised Zaire Valley (ZaiAngo Project): are they confined levees?: Geological Society, London, Special Publications, v. 222, p. 91-114.

Badalini, G., B. Kneller, and C. D. Winker, 1999, Late Pleistocene Trinity-Brazos turbidite system; depositional processes and architectures in a ponded mini-basin system, Gulf of Mexico continental slope: AAPG Bulletin, v. 83, p. 1297-1298.

Badalini, G., B. Kneller, and C. D. Winker, 2000, The late Pleistocene Trinity-Brazos turbidite system; new insights for deep turbidite reservoir interpretation: Annual Meeting Expanded Abstracts - American Association of Petroleum Geologists, v. 2000, p. 8-8.

Badalini, G., B. Kneller, and C. D. Winker, 2000, Architecture and processes in the late Pleistocene Brazos-Trinity turbidite system, Gulf of Mexico continental slope: Program and Abstracts - Society of Economic Paleontologists. Gulf Coast Section. Research Conference, v. 20, p. 16-34.

Badalini, G., B. Kneller, and C. D. Winker, 2001, Basin evolution and depositional processes in a ponded mini-basin system, north western Gulf of Mexico continental slope: ASF Association des Sedimentologistes Francais, v. 36, p. 31-32.

Badalini, G., B. Kneller, and C. D. Winker, 2001, Basin evolution and depositional processes in a ponded mini-basin system, north western Gulf of Mexico continental slope: ASF Association des Sedimentologistes Francais, v. 36, p. 31-32.

Badalini, G., J. Redfern, A. Samuel, R. Heath, S. Burley, N. Steel, and R. Ramadan, 2004, Slope channel evolution; near-surface depositional processes inferred from 3D seismic data, offshore Nile Delta, Egypt: Annual Meeting Expanded Abstracts - American Association of Petroleum Geologists, v. 13, p. 8-8.

Barker, S. P., W. M. McCaffrey, P. D. W. Haughton, J. Baas, and C. Choux, 2005, Turbidity current flow structure linked to vertical textural changes within a 'turbidite' deposit; an experimental approach: Abstracts: Annual Meeting - American Association of Petroleum Geologists, v. 14, p. A11-A11.

Beaubouef, R. T., and V. Abreu, 2006, Basin 4 of the Brazos-Trinity slope system; anatomy of the terminal portion of an intra-slope lowstand systems tract: Transactions - Gulf Coast Association of Geological Societies, v. 56, p. 39-49.

Beaubouef, R. T., V. Abreu, and J. C. Van Wagoner, 2003, Basin 4 of the Brazos-Trinity slope system, western Gulf of Mexico; the terminal portion of a late Pleistocene lowstand systems tract: Program and Abstracts - Society of Economic Paleontologists. Gulf Coast Section. Research Conference, v. 23, p. 45-66.

Beaubouef, R. T., C. Rossen, F. B. Zelt, M. D. Sullivan, D. C. Mohrig, and D. C. Jennette, 1999, Deep-water sandstones,Brushy Canyon Formation, West Texas: Field Guide, AAPG Hedberg Field Research Conference.

Beaubouef, R. T., and S. J. Friedmann, 2000, High resolution seismic/sequence stratigraphic framework for the evolution of Pleistocene intra slope basins, western Gulf of Mexico; depositional models and reservoir analogs: Program and Abstracts - Society of Economic Paleontologists. Gulf Coast Section. Research Conference, v. 20, p. 40-60.

Beaubouef, R. T., and S. J. Friedmann, 2000, High resolution seismic/sequence stratigraphic framework for the evolution of Pleistocene intra slope basins, western Gulf of Mexico; depositional models and reservoir analogs: Program and Abstracts - Society of Economic Paleontologists. Gulf Coast Section. Research Conference, v. 20, p. 40-60.

Beauchamp, W., 1999, Inversion tectonics and the evolution of the High Atlas Mountains, Morocco, based on a geological-geophysical transect, *in* R. W. Allmendinger, M. Barazangi, A. Demnati, M. Alji, and M. Dahmani, eds., Tectonics, United States, American Geophysical Union : Washington, DC, United States, p. 163-184.

Best, J. L., R. A. Kostaschuk, J. Peakall, P. V. Villard, and M. Franklin, 2005, Whole flow field dynamics and velocity pulsing within natural sediment-laden underflows: Geology [Boulder], v. 33, p. 765-768.

Bird, D. E., 2005, Gulf of Mexico tectonic history; hotspot tracks, crustal boundaries, and early salt distribution, *in* K. Burke, S. A. Hall, and J. F. Casey, eds., AAPG

Bulletin, United States, American Association of Petroleum Geologists : Tulsa, OK, United States, p. 311-328.

Bitton, L. F., L. F. Martha, D. Waltham, G. Keevil, and J. Peakall, 2008, Validation of Simplified Mathematical Model for Turbidity Currents.

Bolchert, G., P. Weimer, and B. C. McBride, 2000, Structural and stratigraphic controls on petroleum seeps, Green Canyon and Ewing Bank, northern Gulf of Mexico; implications for petroleum migration: Transactions - Gulf Coast Association of Geological Societies, v. 50, p. 65-74.

Booth, J. R., M. C. Dean, A. E. DuVernay, III, and M. J. Styzen, 2003, Paleo-bathymetric controls on the stratigraphic architecture and reservoir development of confined fans in the Auger Basin; central Gulf of Mexico slope: Marine and Petroleum Geology, v. 20, p. 563-586.

Booth, J. R., A. E. DuVernay, III, D. S. Pfeiffer, and M. J. Styzen, 2000, Sequence stratigraphic framework, depositional models, and stacking patterns of ponded and slope fan systems in the Auger Basin; central Gulf of Mexico slope: Program and Abstracts - Society of Economic Paleontologists. Gulf Coast Section. Research Conference, v. 20, p. 82-103.

Booth, J. R., B. E. Prather, and G. S. Steffens, 2002, Depositional models for ponded and healed-slope accommodation on above-grade slopes; implications for reservoir characterization: Annual Meeting Expanded Abstracts - American Association of Petroleum Geologists, v. 2002, p. 20-21.

Borer, J. M., M. H. Gardner, and N. Mavilla, 2003, Evolution and architecture of base of slope stratigraphic pinch outs, lower Brushy Canyon Formation, Delaware Mountains, West Texas: Annual Meeting Expanded Abstracts - American Association of Petroleum Geologists, v. 12, p. 18-18.

Bouma, A. H., 1962, Sedimentology of some flysch deposits: A graphic approach to facies interpretation: Amsterdam, Elsevier Publishing Company, 168 p.

Bouma, A. H., 1985, Introduction to submarine fans and related turbidite systems Frontiers in sedimentary geology, v. 1: United States, Springer-Verlag : New York, NY, United States, p. 3-5.

Bouma, A. H., 2000, Fine-grained, mud-rich turbidite systems; model and comparison with coarse-grained, sand-rich systems: AAPG Memoir, v. 72, p. 9-20.

Bourrouilh, R., and D. S. Gorsline, 1984, Fine-grained sediments associated with fan lobes: Santa Paula Creek, California: Geological Society, London, Special Publications, v. 15, p. 417-433.

Brami, T. R., C. Pirmez, C. Archie, S. Heeralal, and K. L. Holman, 2000, Late Pleistocene deep-water stratigraphy and depositional processes, offshore Trinidad

and Tobago: Program and Abstracts - Society of Economic Paleontologists. Gulf Coast Section. Research Conference, v. 20, p. 104-115.

Brooke, C. M., T. J. Trimble, and T. A. Mackay, 1995, Mounded shallow gas sands from the Quaternary of the North Sea: analogues for the formation of sand mounds in deep water Tertiary sediments?: Geological Society, London, Special Publications, v. 94, p. 95-101.

Broughton, P., 1993, Hydrocarbon generation in the Essaouira Basin of western Morocco, *in* A. Trepanier, ed., AAPG Bulletin, United States, American Association of Petroleum Geologists : Tulsa, OK, United States, p. 999-1015.

Brown, R. H., 1980, Triassic rocks of Argana Valley, southern Morocco, and their regional structural implications, AAPG Bulletin, United States, American Association of Petroleum Geologists : Tulsa, OK, United States, p. 988-1003.

Bruhn, C. H. L., 1998, Major types of deep-water reservoirs from the eastern Brazilian rift and passive margin basins: AAPG Bulletin, v. 82, p. 1896-1897.

Brunt, R. L., W. D. McCaffrey, and B. C. Kneller, 2004, Experimental modeling of the spatial distribution of grain size developed in a fill-and-spill mini-basin setting: Journal of Sedimentary Research, v. 74, p. 438-446.

Burk, M. K., G. L. Brown, and D. R. Petro, 1998, Evolution of the geological model, Lobster Field (Ewing Bank 873): AAPG Discovery Series, v. 1.

Burk, M. K., G. L. Brown, and D. R. Petro, 1999, Evolution of the geological model, Lobster Field (Ewing Bank 873): Transactions - Gulf Coast Association of Geological Societies, v. 49, p. 154-161.

Campion, K. M., A. R. Sprague, D. Mohrig, R. W. Lovell, P. A. Drzewiecki, M. D. Sullivan, J. A. Ardill, G. N. Jensen, and D. K. Sickafoose, 2003, Outcrop expression of confined channel complexes: Bulletin of the South Texas Geological Society, v. 44, p. 13-36.

Carlson, J., and J. P. Grotzinger, 2001, Submarine fan environment inferred from turbidite thickness distributions: Sedimentology, v. 48, p. 1331-1351.

Catuneanu, O., 2006, Principles of Sequence Stratigraphy: Developments in Sedimentology: Amsterdam, Elsevier.

Choi, S.-u., and M. H. Garcia, 1996, Arbitrary Lagrangian-Eulerian approach for finite element modeling of two-dimensional turbidity currents: Water International, v. 21, p. 175-182.

Chough, S. K., 1984, Fine-grained turbidites and associated mass-flow deposits in the Ulleung (Tsushima) Back-arc Basin, East Sea (Sea of Japan): Geological Society, London, Special Publications, v. 15, p. 185-196.

Choux, C. M. A., 2005, Comparison of spatio-temporal evolution of experimental particulate gravity flows at two different initial concentrations, based on velocity, grain size and density data, *in* J. H. Baas, W. D. McCaffrey, and P. D. W. Haughton, eds., Sedimentary Geology, Netherlands, Elsevier : Amsterdam, Netherlands, p. 49-69.

Choux, C. M. A., J. H. Baas, W. D. McCaffrey, and P. D. W. Haughton, 2005, Comparison of spatio-temporal evolution of experimental particulate gravity flows at two different initial concentrations, based on velocity, grain size and density data: Sedimentary Geology, v. 179, p. 49-69.

Cibin, U., A. Di Giulio, L. Martelli, R. Catanzariti, S. Poccianti, C. Rosselli, and F. Sani, 2004, Factors controlling foredeep turbidite deposition: the case of Northern Apennines (Oligocene-Miocene, Italy): Geological Society, London, Special Publications, v. 222, p. 115-134.

Clark, J. D., 1995, Detailed section across the Ainsa II channel complex, south central Pyrenees, Spain: United Kingdom, Chapman and Hall : London, United Kingdom, 139-144 p.

Clark, J. D., 1996, Architectural elements and growth patterns of submarine channels; application to hydrocarbon exploration, *in* K. T. Pickering, ed., AAPG Bulletin, United States, American Association of Petroleum Geologists : Tulsa, OK, United States, p. 194-221.

Clemenceau, G. R., and J. Colbert, 1999, Levee-overbank turbidite production from Ram/Powell Field, deepwater Gulf of Mexico: AAPG Bulletin, v. 83, p. 1305-1305.

Coe, A. L., D. W. J. Bosence, K. D. Church, S. S. Flint, J. A. Howell, and R. C. L. Wilson, 2003, The sedimentary record of sea-level change: United Kingdom, Cambridge University Press : Cambridge, United Kingdom.

Covault, J. A., 2009, Growth patterns of deep-sea fans revisited; turbidite-system morphology in confined basins, examples from the California Borderland, *in* B. W. Romans, ed., Marine Geology, Netherlands, Elsevier : Amsterdam, Netherlands, p. 51-66.

Covault, J. A., E. Shelef, M. Traer, S. M. Hubbard, B. W. Romans, and A. Fildani, 2012, Deep-water channel run-out length; insights from seafloor geomorphology: Journal of Sedimentary Research, v. 82, p. 25-40.

Crabaugh, J. P., and R. J. Steel, 2004, Basin-floor fans of the Central Tertiary Basin, Spitsbergen: relationship of basin-floor sand-bodies to prograding clinoforms in a structurally active basin: Geological Society, London, Special Publications, v. 222, p. 187-208.

Cronin, B. T., 1995, Structurally-controlled deep sea channel courses: examples from the Miocene of southeast Spain and the Alboran Sea, southwest Mediterranean: Geological Society, London, Special Publications, v. 94, p. 115-135.

Damuth, J. E., R. D. Flood, R. O. Kowsmann, R. H. Belderson, and M. A. Gorini, 1988, Anatomy and growth pattern of Amazon deep-sea fan as revealed by long-range side-scan sonar (GLORIA) and high-resolution seismic studies: AAPG Bulletin, v. 72, p. 885-911.

Davison, I., 2005, Central Atlantic margin basins of northwest Africa; geology and hydrocarbon potential (Morocco to Guinea), Journal of African Earth Sciences, United Kingdom, Elsevier : Oxford, United Kingdom, p. 254-274.

DeVay, J. C., D. Risch, E. D. Scott, and C. Thomas, 2000, A Mississippi-sourced middle Miocene (M4), fine-grained abyssal plain fan complex, northeastern Gulf of Mexico: AAPG Memoir, v. 72, p. 109-118.

Diegel, F. A., J. F. Karlo, D. C. Schuster, R. C. Shoup, and P. R. Tauvers, 1995, Cenozoic structural evolution and tectono-stratigraphic framework of the northern Gulf Coast continental margin: AAPG Memoir, v. 65, p. 109-151.

Donovan, A. D., 2000, Topographic-keyed sequence models; explaining and predicting the development of basin-floor (lowstand) fans within sequences: Annual Meeting Expanded Abstracts - American Association of Petroleum Geologists, v. 2000, p. 40-40.

Dunlap, D. B., L. J. Wood, C. Weisenburger, and H. Jabour, 2010, Seismic geomorphology of offshore Morocco's east margin, Safi Haute Mer area: AAPG Bulletin, v. 94, p. 28.

Edwards, D. A., 1993, Turbidity currents; dynamics, deposits and reversals, Lecture Notes in Earth Sciences, Federal Republic of Germany, Springer-Verlag : Berlin-Heidelberg-New York, Federal Republic of Germany.

Ellison, T. H., and J. S. Turner, 1959, Turbidity entrainment in stratified flows: J. Fluid Mech., v. 6, p. 423-448.

Ellouz, N., 2003, From rifting to Alpine inversion; Mesozoic and Cenozoic subsidence history of some Moroccan basins, *in* M. Patriat, J.-M. Gaulier, R. Bouatmani, and S. Sabounji, eds., Sedimentary Geology, Netherlands, Elsevier : Amsterdam, Netherlands, p. 185-212.

Ercilla, G., 1998, Origin, sedimentary processes and depositional evolution of the Agadir turbidite system, central eastern Atlantic, *in* B. Alonso, F. Perez-Belzuz, F. Estrada, J. Baraza, M. Farran, M. Canals, and D. Masson, eds., Journal of the Geological Society of London, United Kingdom, Geological Society of London : London, United Kingdom, p. 929-939.

Ferrill, D. A., 1997, Geometric considerations of deformation above curved normal faults and salt evacuation surfaces, *in* A. P. Morris, ed., Leading Edge [Tulsa, OK], United States, Society of Exploration Geophysicists : Tulsa, OK, United States, p. 1129-1133.

Fildani, A., and W. R. Normark, 2004, Late Quaternary evolution of channel and lobe complexes of Monterey Fan: Marine Geology, v. 206, p. 199-223.

Galloway, W. E., 2005, Gulf of Mexico basin depositional record of Cenozoic North American drainage basin evolution: Special Publication of the International Association of Sedimentologists, v. 35, p. 409-423.

Galloway, W. E., 2008, Depositional evolution of the Gulf of Mexico sedimentary basin Sedimentary basins of the world, v. 5: Netherlands, Elsevier : Amsterdam, Netherlands, p. 505-549.

Galloway, W. E., R. T. Buffler, X. Li, and P. E. Ganey-Curry, 1998, Gulf of Mexico Basin depositional synthesis; Neogene sequences, depositional systems, and paleogeographic evolution: Transactions - Gulf Coast Association of Geological Societies, v. 48, p. 83-88.

Galloway, W. E., P. E. Ganey-Curry, X. Li, and R. Buffler, 2000, Cenozoic depositional history of the Gulf of Mexico basin: AAPG Bulletin, v. 84, p. 1743-1774.

Galloway, W. E., S. Mentemeier, M. Rowan, and L. M. Gochioco, 2004, Plumbing the depths of the Gulf of Mexico; recent understanding of Cenozoic sand dispersal systems and ultradeep reservoir potential: Leading Edge [Tulsa, OK], v. 23, p. 44-51.

Galloway, W. E., T. L. Whiteaker, and P. Ganey-Curry, 2011, History of Cenozoic North American drainage basin evolution, sediment yield, and accumulation in the Gulf of Mexico Basin: Geosphere, v. 7, p. 938-973.

Gardiner, A. R., 2006, The variability of turbidite sandbody pinchout and its impact on hydrocarbon recovery in stratigraphically trapped fields: Geological Society Special Publications, v. 254, p. 267-287.

Gardner, J. V., R. G. Bohannon, M. E. Field, and D. G. Masson, 1996, The morphology, processes, and evolution of Monterey Fan; a revisit: United Kingdom, Cambridge University Press : Cambridge, United Kingdom, p. 193-220.

Gardner, M. H., and J. M. Borer, 2000, Submarine channel architecture along a slope to basin profile, Brushy Canyon Formation, West Texas: AAPG Memoir, v. 72, p. 195-213.

Gardner, M. H., J. M. Borer, M. Dechesne, and R. Wagerle, 1998, Cut, fill and spill; a new look at the overbank paradigm for sandy deep water systems: Annual Meeting Expanded Abstracts - American Association of Petroleum Geologists, v. 1998.

Gardner, M. H., J. M. Borer, J. J. Melick, N. Mavilla, M. Dechesne, and R. N. Wagerle, 2003, Stratigraphic process-response model for submarine channels and related features from studies of Permian Brushy Canyon outcrops, West Texas: Marine and Petroleum Geology, v. 20, p. 757-787.

Gardner, M. H., J. M. Borer, B. W. Romans, N. Baptista, E. K. Kling, D. Hanggoro, J. J. Melick, R. M. Wagerle, M. Dechesne, M. M. Carr, R. Amerman, and S. Atan, 2008, Stratigraphic models for deep-water sedimentary systems: Papers presented at the Gulf Coast Section, Society of Economic Paleontologists and Mineralogists Foundation Annual Bob F. Perkins Research Conference, v. 28, p. 77-175.

Gaullier, V., 2005, Salt tectonics driven by sediment progradation; Part II, Radial spreading of sedimentary lobes prograding above salt, *in* B. C. Vendeville, ed., AAPG Bulletin, United States, American Association of Petroleum Geologists : Tulsa, OK, United States, p. 1081-1089.

Ge, H., 1997, Kinematics and dynamics of salt tectonics driven by progradation, *in* M. P. A. Jackson, and B. C. Vendeville, eds., AAPG Bulletin, United States, American Association of Petroleum Geologists : Tulsa, OK, United States, p. 398-423.

Ge, H., 1998, Physical modeling of structures formed by salt withdrawal; implications for deformation caused by salt dissolution, *in* M. P. A. Jackson, ed., AAPG Bulletin, United States, American Association of Petroleum Geologists : Tulsa, OK, United States, p. 228-250.

Gervais, A., B. Savoye, T. Mulder, and E. Gonthier, 2006, Sandy modern turbidite lobes; a new insight from high resolution seismic data: Marine and Petroleum Geology, v. 23, p. 485-502.

Gervais, A., B. Savoye, D. J. W. Piper, T. Mulder, M. Cremer, and L. Pichevin, 2004, Present morphology and depositional architecture of a sandy confined submarine system: the Golo turbidite system (eastern margin of Corsica): Geological Society, London, Special Publications, v. 222, p. 59-89.

Gervais, A., B. Savoye, D. J. W. Piper, T. Mulder, M. Cremer, and L. Pichevin, 2004, Present morphology and depositional architecture of a sandy confined submarine system; the Golo turbidite system (eastern margin of Corsica): Geological Society Special Publications, v. 222, p. 59-89.

Gibbs, A. D., 1983, Balanced cross-section construction from seismic sections in areas of extensional tectonics, Journal of Structural Geology, International, Pergamon : Oxford-New York, International, p. 153-160.

Giles, K. A., 2002, Halokinetic sequence stratigraphy adjacent to the El Papalote Diapir, northeastern Mexico, *in* T. F. Lawton, ed., AAPG Bulletin, United States, American Association of Petroleum Geologists : Tulsa, OK, United States, p. 823-840.

Giles, K. A., and T. F. Lawton, 2002, Halokinetic sequence stratigraphy adjacent to the El Papalote Diapir, northeastern Mexico: AAPG Bulletin, v. 86, p. 823-840.

Gladstone, C., J. C. Phillips, and R. S. J. Sparks, 1998, Experiments on bidisperse, constant-volume gravity currents; propagation and sediment deposition: Sedimentology, v. 45, p. 833-843.

Gladstone, C., J. C. Phillips, and R. S. J. Sparks, 1998, Experiments on bidisperse, constant-volume gravity currents; propagation and sediment deposition: Sedimentology, v. 45, p. 833-843.

Gray, T. E., J. Alexander, and M. R. Leeder, 2005, Quantifying velocity and turbulence structure in depositing sustained turbidity currents across breaks in slope: Sedimentology, v. 52, p. 467-488.

Haddou, J., 2007, Subsalt exploration potential of the Moroccan salt basin, *in* G. Tari, ed., Leading Edge [Tulsa, OK], United States, Society of Exploration Geophysicists : Tulsa, OK, United States, p. 1454-1460.

Hafid, M., 1996, Seismic reflection profiles across the on- and offshore Essaouira Basin, Abstracts with Programs - Geological Society of America, United States, Geological Society of America (GSA) : Boulder, CO, United States, p. 17-17.

Hafid, M., 2000, The western termination of the Jebilet-High Atlas system (offshore Essaouira Basin, Morocco), *in* A. Ait Salem, and A. W. Bally, eds., Marine and Petroleum Geology, International, Pergamon : Oxford, International, p. 431-443.

Hafid, M., 2000, Triassic-early Liassic extensional systems and their Tertiary inversion, Essaouira Basin (Morocco), Marine and Petroleum Geology, International, Pergamon : Oxford, International, p. 409-429.

Hafid, M., 2006, Structural styles of the western onshore and offshore termination of the High Atlas, Morocco, *in* M. Zizi, A. W. Bally, and A. Ait Salem, eds., Comptes Rendus - Academie des Sciences. Geoscience, France, Elsevier : Paris, France, p. 50-64.

Hames, W. E., 2003, Geophysical MonographThe Central Atlantic Magmatic Province; insights from fragments of Pangea, *in* J. G. McHone, P. R. Renne, and C. Ruppel, eds., Geophysical Monograph, United States, American Geophysical Union : Washington, DC, United States.

Haq, B. U., J. Hardenbol, and P. R. Vail, 1988, Mesozoic and Cenozoic chronostratigraphy and cycles of sea-level change: Special Publication - Society of Economic Paleontologists and Mineralogists, v. 42, p. 72-108.

Haughton, P., 2000, Debrites and turbidites; strange bedfellows: Irish Journal of Earth Sciences, v. 18, p. 134-134.

Haughton, P., C. Davis, W. McCaffrey, and S. Barker, 2009, Hybrid sediment gravity flow deposits , Classification, origin and significance: Marine and Petroleum Geology, v. 26, p. 1900-1918.

Haughton, P. D. W., 1994, Deposits of deflected and ponded turbidity currents, Sorbas Basin, Southeast Spain: Journal of Sedimentary Research, Section A: Sedimentary Petrology and Processes, v. 64, p. 233-246.

Haughton, P. D. W., 2000, Evolving turbidite systems on a deforming basin floor, Tabernas, SE Spain: Sedimentology, v. 47, p. 497-518.

Hay, A. E., 1987, Turbidity currents and submarine channel formation in Rupert Inlet, British Columbia; 1, Surge observations: Journal of Geophysical Research, v. 92, p. 2875-2881.

Hay, A. E., 1987, Turbidity currents and submarine channel formation in Rupert Inlet, British Columbia; 2, The roles of continuous and surge-type flow: Journal of Geophysical Research, v. 92, p. 2883-2900.

Hedley, R., and J. Warburton, 1999, The structural evolution of the Tafelney Plateau, offshore Morocco: AAPG Bulletin, v. 83, p. 1316.

Heezen, B. C., and W. M. Ewing, 1952, Turbidity currents and submarine slumps, and the 1929 Grand Banks [Newfoundland] earthquake: American Journal of Science, v. 250, p. 849-873.

Heyman, M. A. W., 1989, Tectonic and depositional history of the Moroccan continental margin, AAPG Memoir, United States, American Association of Petroleum Geologists : Tulsa, OK, United States, p. 323-340.

Hickson, T. A., and D. R. Lowe, 2002, Facies architecture of a submarine fan channel-levee complex; the Juniper Ridge Conglomerate, Coalinga, California: Sedimentology, v. 49, p. 335-362.

Hilton, V. C., and K. T. Pickering, 1995, The Montagne de Chalufy turbidite onlap, Eocene-Oligocene turbidite sheet system, Hautes Provence, SE France: United Kingdom, Chapman and Hall : London, United Kingdom, 236-241 p.

Hinz, K., 1981, The continental margin of Morocco; seismic sequences, structural elements and the geological development, *in* H. Dostmann, and J. Fritsch, eds., Oceanologica Acta, France, Gauthier-Villars : Paris, France, p. 21-21.

Hinz, K., H. Dostmann, and J. Fritsch, 1982, The continental margin of Morocco; seismic sequences, structural elements and geological development: Federal Republic of Germany, Springer-Verlag : Berlin, Federal Republic of Germany, 34-60 p.

Hodgson, D. M., and P. D. W. Haughton, 2004, Impact of syndepositional faulting on gravity current behaviour and deep-water stratigraphy; Tabernas-Sorbas Basin, SE Spain: Geological Society Special Publications, v. 222, p. 135-158.

Holman, W. E., and S. S. Robertson, 1995, Field development, depositional model and production performance of the turbiditic 'J' Sands at Prospect Bullwinkle, Green Canyon 65 Field outer-shelf Gulf of Mexico: Annual Meeting Expanded Abstracts - American Association of Petroleum Geologists, v. 4, p. 42.

Huang, H., 2009, The critical densimetric Froude number of subaqueous gravity currents can be non-unity or non-existent, *in* J. Imran, C. Pirmez, Q. Zhang, and G. Chen, eds., Journal of Sedimentary Research, United States, Society for Sedimentary Geology : Tulsa, OK, United States, p. 479-485.

Hudec, M. R., M. P. A. Jackson, and D. D. Schultz-Ela, 2009, The paradox of minibasin subsidence into salt; clues to the evolution of crustal basins: Geological Society of America Bulletin, v. 121, p. 201-221.

Imran, J., G. Parker, and C. Pirmez, 1999, A nonlinear model of flow in meandering submarine and subaerial channels: Journal of Fluid Mechanics, v. 400, p. 295-331.

Jackson, M. P. A., 1992, Initiation of diapirism by regional extension, *in* B. C. Vendeville, ed., Abstracts with Programs - Geological Society of America, United States, Geological Society of America (GSA) : Boulder, CO, United States, p. 279-280.

Jackson, M. P. A., 1994, Salt-related structures in the Gulf of Mexico; a field guide for geophysicists, *in* B. C. Vendeville, and D. D. Schultz-Ela, eds., Geophysics: The Leading Edge of Exploration, United States, Society of Exploration Geophysicists : Tulsa, OK, United States, p. 837-842.

Jackson, M. P. A., 2008, Evolution of the Cretaceous Astrid thrust belt in the ultradeep-water Lower Congo Basin, Gabon, *in* M. R. Hudec, D. C. Jennette, and R. E. Kilby, eds., AAPG Bulletin, United States, American Association of Petroleum Geologists : Tulsa, OK, United States, p. 487-511.

Jervey, M. T., 1988, Quantitative geological modeling of siliciclastic rock sequences and their seismic expression: Special Publication - Society of Economic Paleontologists and Mineralogists, v. 42, p. 47-69.

Joseph, P., and S. A. Lomas, 2004, Deep-water sedimentation in the Alpine foreland basin of SE France; new perspectives on the Gres d'Annot and related systems; an introduction: Geological Society Special Publications, v. 221, p. 1-16.

Kane, I. A., W. D. McCaffrey, J. Peakall, and B. C. Kneller, 2010, Submarine channel levee shape and sediment waves from physical experiments: Sedimentary Geology, v. 223, p. 75-85.

Kane, I. A., D. T. McGee, and Z. R. Jobe, 2012, Halokinetic effects on submarine channel equilibirum profiles and implications for facies architecture: conceptual model illustrated with a case study from Magnolia Field, Gulf of Mexico: Geological Society, London, Special Publications, v. 363, p. 289-3022.

Khan, S. M., and J. Imran, 2008, Numerical investigation of turbidity currents flowing through minibasins on the continental slope: Journal of Sedimentary Research, v. 78, p. 245-257.

Khripounoff, A., A. Vangriesheim, N. Babonneau, P. Crassous, B. Dennielou, and B. Savoye, 2003, Direct observation of intense turbidity current activity in the Zaire submarine valley at 4000 m water depth: Marine Geology, v. 194, p. 151-158.

Klaucke, I., R. Hesse, and W. B. F. Ryan, 1998, Seismic stratigraphy of the Northwest Atlantic Mid-Ocean Channel; growth pattern of a mid-ocean channel-levee complex: Marine and Petroleum Geology, v. 15, p. 575-585.

Kneller, B., 1995, Beyond the turbidite paradigm: physical models for deposition of turbidites and their implications for reservoir prediction: Geological Society, London, Special Publications, v. 94, p. 31-49.

Kneller, B., 1995, Topographic controls on turbidite sandstone reservoirs; facies models with a physical basis: AAPG Bulletin, v. 79, p. 1227-1227.

Kneller, B., 2003, The influence of flow parameters on turbidite slope channel architecture, Marine and Petroleum Geology, United Kingdom, Elsevier : Oxford, United Kingdom, p. 901-910.

Kneller, B., and C. Buckee, 2000, The structure and fluid mechanics of turbidity currents; a review of some recent studies and their geological implications: Sedimentology, v. 47, p. 62-94.

Kneller, B., D. Edwards, W. McCaffrey, and R. Moore, 1991, Oblique reflection of turbidity currents: Geology [Boulder], v. 19, p. 250-252.

Kneller, B., O. J. Martinsen, and B. McCaffrey, 2009, External controls on deep-water depositional systems, Special Publication - Society for Sedimentary Geology, United States, Society for Sedimentary Geology (SEPM) : Tulsa, OK, United States.

Kneller, B., and B. McCaffrey, 2001, Flow parameters and stratigraphic architecture in turbidite systems: Annual Meeting Expanded Abstracts - American Association of Petroleum Geologists, v. 2001, p. 106-107.

Kneller, B., and W. McCaffrey, 1999, Depositional effects of flow nonuniformity and stratification within turbidity currents approaching a bounding slope; deflection, reflection, and facies variation: Journal of Sedimentary Research, v. 69, p. 980-991.

Kneller, B., and W. D. McCaffrey, 1995, Modelling the effects of salt-induced topography on deposition from turbidity currents: Papers presented at the Gulf Coast Section, Society of Economic Paleontologists and Mineralogists Foundation Annual Bob F. Perkins Research Conference, v. 16, p. 137-145.

Kneller, B. C., S. J. Bennett, and W. D. McCaffrey, 1995, Macroturbulence and fluid stresses in experimental gravity currents; implications for sediment transport and deposition in the ocean: Eos, Transactions, American Geophysical Union, v. 76, p. 289-289.

Kneller, B. C., and M. J. Branney, 1995, Sustained high-density turbidity currents and the deposition of thick massive sands: Sedimentology, v. 42, p. 607-616.

Kneller, B. C., and W. D. McCaffrey, 2003, The interpretation of vertical sequences in turbidite beds; the influence of longitudinal flow structure: Journal of Sedimentary Research, v. 73, p. 706-713.

Lamb, M. P., T. Hickson, J. G. Marr, B. Sheets, C. Paola, and G. Parker, 2004, Surging versus continuous turbidity currents; flow dynamics and deposits in an experimental intraslope minibasin: Journal of Sedimentary Research, v. 74, p. 148-155.

Lamb, M. P., B. McElroy, B. Kopriva, J. Shaw, and D. Mohrig, 2010, Linking river-flood dynamics to hyperpycnal-plume deposits; experiments, theory, and geological implications: Geological Society of America Bulletin, v. 122, p. 1389-1400.

Lamb, M. P., H. Toniolo, and G. Parker, 2006, Trapping of sustained turbidity currents by intraslope minibasins: Sedimentology, v. 53, p. 147-160.

Lancelot, Y., 1980, Evolution of the Moroccan oceanic basin and adjacent continental margin; a synthesis, *in* E. L. Winterer, ed., Initial Reports of the Deep Sea Drilling Project, United States, Texas A & M University, Ocean Drilling Program : College Station, TX, United States, p. 801-821.

Lane-Serff, G. F., 2005, Sedimentation from buoyant jets, *in* T. J. Moran, ed., Journal of Hydraulic Engineering, United States, American Society of Civil Engineers : New York, NY, United States, p. 166-174.

Lane-Serff, G. F., L. M. Beal, and T. D. Hadfield, 1995, Gravity current flow over obstacles: J. Fluid Mech., v. 292, p. 39-53.

Laval, A., M. Cremer, P. Beghin, and C. Ravenne, 1988, Density surges; two-dimensional experiments: Sedimentology, v. 35, p. 73-84.

Le Roy, P., 2001, Triassic-Liassic western Moroccan synrift basins in relation to the central Atlantic opening, *in* A. Pique, ed., Marine Geology, Netherlands, Elsevier : Amsterdam, Netherlands, p. 359-381.

Lee, S. E., L. A. Amy, and P. J. Talling, 2004, The character and origin of thick base-of-slope sandstone units of the Peira Cava outlier, SE France: Geological Society Special Publications, v. 221, p. 331-347.

Leeder, M. R., T. E. Gray, and J. Alexander, 2005, Sediment suspension dynamics and a new criterion for the maintenance of turbulent suspensions: Sedimentology, v. 52, p. 683-691.

Lehner, P., 1969, Salt tectonics and Pleistocene stratigraphy on continental slope of northern Gulf of Mexico: American Association of Petroleum Geologists Bulletin, v. 53, p. 2431-2479.

Lehner, P., 1977, Structural history of Atlantic margin of Africa, *in* P. A. C. de Ruiter, ed., AAPG Bulletin, United States, American Association of Petroleum Geologists : Tulsa, OK, United States, p. 961-981.

Link, M. H., and P. Weimer, 1991, Seismic facies and sedimentary processes of submarine fans and turbidite-systems; an overview Frontiers in sedimentary geology: United States, Springer-Verlag : New York, NY, United States, p. 3-7.

Liu, J., Y., and W. R. Bryant, 1999, Seafloor Morphology and Sediment Paths of the Northern Gulf of Mexico Deepwater: Gulf Coast Association of Geological Societies Transactions, v. 49, p. 4.

Liu, J. Y., and W. R. Bryant, 2000, Sea floor morphology and sediment paths of the northern Gulf of Mexico deepwater, *in* A. H. Bouma, and C. G. Stone, eds., Fine-grained turbidite systems, v. 72: Tulsa, OK, United States, American Association of Petroleum Geologists p. 13.

Lomas, S. A., and P. Joseph, 2004, Confined turbidite systems: Geological Society, London, Special Publications, v. 222, p. 1-7.

Lowe, D. R., 1982, Sediment gravity flows; II, Depositional models with special reference to the deposits of high-density turbidity currents: Journal of Sedimentary Petrology, v. 52, p. 279-297.

Luthi, S., 1981, Some new aspects of two-dimensional turbidity currents: Sedimentology, v. 28, p. 97-105.

Luthi, S. a., 1981, Experiments on non-channelized turbidity currents and their deposits: Marine Geology, v. 40, p. M59-M68.

Madof, A. S., and N. Christie-Blick, 2007, The role of gravity-driven sedimentation in the evolution of salt withdrawal intraslope minibasins; insights from north-central Green Canyon, Gulf of Mexico: Abstracts with Programs - Geological Society of America, v. 39, p. 149-150.

Madof, A. S., N. Christie-Blick, and M. A. Anders, 2009, Stratigraphic controls on a salt-withdrawal intraslope minibasin, north-central Green Canyon, Gulf of Mexico: Implications for misinterpreting sea level change: AAPG Bulletin, v. 93, p. 535-561.

Mahaffie, M. J., 1994, Reservoir classification for turbidite intervals at the Mars discovery, Mississippi Canyon 807, Gulf of Mexico: Papers presented at the Gulf Coast Section, Society of Economic Paleontologists and Mineralogists Foundation Annual Bob F. Perkins Research Conference, v. 15, p. 233-244.

Mallarino, G., R. T. Beaubouef, A. W. Droxler, V. Abreu, and L. Labeyrie, 2006, Sea level influence on the nature and timing of a minibasin sedimentary fill (northwestern slope of the Gulf of Mexico): AAPG Bulletin, v. 90, p. 1089-1119.

Masson, D. G., N. H. Kenyon, J. V. Gardner, and M. E. Field, 1995, Monterey Fan; channel and overbank morphology: United Kingdom, Chapman and Hall : London, United Kingdom, 74-79 p.

Mayall, M., 1998, The architecture of turbidite slope channels, *in* I. Stewart, ed., AAPG Bulletin, United States, American Association of Petroleum Geologists : Tulsa, OK, United States, p. 1941-1941.

McCaffrey, W., and B. Kneller, 2001, Process controls on the development of stratigraphic trap potential on the margins of confined turbidite systems and aids to reservoir evaluation: AAPG Bulletin, v. 85, p. 971-988.

McCaffrey, W. D., R. Brunt, and B. C. Kneller, 2001, Predicting spatial trends in grainsize distribution within deep marine clastic systems: Annual Meeting Expanded Abstracts - American Association of Petroleum Geologists, v. 2001, p. 130-130.

McCaffrey, W. D., and B. C. Kneller, 1995, Scale models of unconfined turbidity currents and their deposits: Abstracts with Programs - Geological Society of America, v. 27, p. 127-127.

McCaffrey, W. D., and B. C. Kneller, 2004, Scale effects of non-uniformity on deposition from turbidity currents with reference to the Gres d'Annot of SE France: Geological Society Special Publications, v. 221, p. 301-310.

McCaffrey, W. D., B. C. Kneller, and J. Peakall, Particulate gravity currents: Special Publication of the International Association of Sedimentologists.

McCave, I. N., 1984, Erosion, transport and deposition of fine-grained marine sediments: Geological Society, London, Special Publications, v. 15, p. 35-69.

McGee, D. T., P. W. Bilinski, P. S. Gary, D. S. Pfeiffer, and J. L. Sheiman, 1994, Geologic models and reservoir geometries of Auger field, deepwater Gulf of Mexico: Submarine fans and turbidite systems – sequence stratigraphy, reservoir architecture, and production characteristics: Gulf Coast Section, Society of Economic Paleontologists and Mineralogists, Fifteenth Annual Research Conference, p. 245-256.

Meckel, L. D., III, 2004, Linking shelf-edge deltas to deepwater sheet sand and channel turbidite reservoirs; examples from the Miocene-Pleistocene, Gulf of Mexico: NOGS Log, v. 44, p. 7-7.

Medina, F., 1995, Syn- and postrift evolution of the El Jadida-Agadir Basin (Morocco); constraints for the rifting models of the central Atlantic, Canadian Journal of

Earth Sciences = Revue Canadienne des Sciences de la Terre, Canada, National Research Council of Canada : Ottawa, ON, Canada, p. 1273-1291.

Mehdi, K., 2004, Role de l'halocinese dans l'evolution du bassin d'Essaouira (Sud-Ouest marocain), *in* R. Griboulard, and C. Bobier, eds., Role of halokinesis in the Essaouira Basin evolution, southwestern Morocco, France, Elsevier : Paris, France, p. 587-595.

Meiburg, E., and B. Kneller, 2009, Turbidity currents and their deposits: Annual Review of Fluid Mechanics, v. 42, p. 135-156.

Meiburg, E., B. Kneller, B. Hall, F. Blanchette, V. Birman, M. Strauss, M. E. Glinsky, and C. Lerch, 2008, High-resolution simulations of gravity and turbidity currents: Abstracts: Annual Meeting - American Association of Petroleum Geologists, v. 2008.

Middleton, G. V., 1967, The orientation of concavo-convex particles deposited from experimental turbidity currents: Journal of Sedimentary Petrology, v. 37, p. 229-232.

Middleton, G. V., 1993, Sediment deposition from turbidity currents: Annual Review of Earth and Planetary Sciences, v. 21, p. 89-114.

Middleton, G. V., and M. A. Hampton, 1973, Sediment gravity flows; mechanics of flow and deposition: United States, Soc. Econ. Paleontol. Mineral., Pac. Sect., Los Angeles, p. 1-38.

Middleton, G. V., and M. A. Hampton, 1976, Subaqueous sediment transport and deposition by sediment gravity flows: United States, John Wiley & Sons : New York, N.Y., United States, p. 197-218.

Middleton, G. V., and J. B. Southard, 1984, Mechanics of sediment movement, SEPM Short Course, United States, Society of Sedimentary Geology : Tulsa, OK, United States.

Mitchum, R. M., Jr., 1985, Seismic stratigraphic expression of submarine fans: AAPG Memoir, v. 39, p. 117-136.

Mohrig, D., and J. Buttles, 2007, Deep turbidity currents in shallow channels: Geology [Boulder], v. 35, p. 155-158.

Mohrig, D., A. Elverhoi, and G. Parker, 1999, Experiments on the relative mobility of muddy subaqueous and subaerial debris flows, and their capacity to remobilize antecedent deposits: Marine Geology, v. 154, p. 117-129.

Mohrig, D., and J. G. Marr, 2003, Constraining the efficiency of turbidity current generation from submarine debris flows and slides using laboratory experiments: Marine and Petroleum Geology, v. 20, p. 883-899.

Mohrig, D., K. M. Straub, and J. Buttles, 2008, Turbidity current flow out of channels and its contribution to constructing the continental slope: Abstracts: Annual Meeting - American Association of Petroleum Geologists, v. 2008.

Montoya, P., and M. R. Hudec, 2007, Active salt tectonics and its effect on the internal architecture and connectivity between minibasins near the Sigsbee Escarpment, Gulf of Mexico: Abstracts: Annual Meeting - American Association of Petroleum Geologists, v. 2007, p. 96-96.

Morabet, A. M., 1998, An overview of the petroleum systems of Morocco, *in* R. Bouchta, and H. Jabour, eds., Geological Society Special Publications, United Kingdom, Geological Society of London : London, United Kingdom, p. 283-296.

Morgan, S. R., and K. M. Campion, 1990, Stratification of shelf and basinal turbidites; recognition of deltaic vs. fan deposits: AAPG Bulletin, v. 74, p. 725-725.

Muck, M. T., and M. B. Underwood, 1990, Upslope flow of turbidity currents - A comparison among field observations, theory, and laboratory models: Geology, v. 18, p. 54-57.

Mulder, T., and J. Alexander, 2001, The physical character of subaqueous sedimentary density flows and their deposits: Sedimentology, v. 48, p. 269-299.

Mulder, T., and J. Alexander, 2001, The physical character of subaqueous sedimentary density flows and their deposits: Sedimentology, v. 48, p. 269-299.

Mulder, T., and J. P. M. Syvitski, 1995, Turbidity currents generated at river mouths during exceptional discharges to the world oceans: Journal of Geology, v. 103, p. 285-299.

Mutti, E., 1972, Examples of ancient deep-sea fan deposits from circum-Mediterranean geosynclines: United States, Univ. Wis.-Madison--Natl. Sci. Found., Madison, p. 20-21.

Mutti, E., 1974, Examples of ancient deep-sea fan deposits from Circum-Mediterranean geosynclines: Special Publication - Society of Economic Paleontologists and

Mutti, E., D. Bernoulli, F. Ricci Lucchi, and R. Tinterri, 2009, Turbidites and turbidity currents from Alpine 'flysch' to the exploration of continental margins: Sedimentology, v. 56, p. 267-318.

Mutti, E., and G. Ghibaudo, 1972, Un esempio di torbiditi di conoide sottomarina esterna: le Arenarie di San Salvatore (Formazione di Bobbio, Miocene): Matematiche e Naturali, v. 4, 40 p.

Mutti, E., and W. R. Normark, 1987, Comparing examples of modern and ancient turbidite systems; problems and concepts: United Kingdom, Graham and Trotman : London, United Kingdom, p. 1-38.

Mutti, E., and W. R. Normark, 1991, An integrated approach to the study of turbidite systems Frontiers in sedimentary geology: United States, Springer-Verlag : New York, NY, United States, p. 75-106.

Mutti, E., A. Obrador, and J. Rosell, 1973, Sedimenti deltizii e di piana di marea nel Paleogene della Valle di Ager (provincia di Lerida, Spagna): Paleogene deltaic and nearshore sediments of the Ager Valley, Lerida, Spain, v. 92, p. 517-528.

Mutti, E., G. Orombelli, and R. Pozzi, 1970, Geological studies on the Dodecanese Islands (Aegean Sea); IX, Geological map of the island of Rhodes (Greece); explanatory notes: Annales Geologiques des Pays Helleniques, v. 22, p. 79-226.

Mutti, E., E. Remacha, R. Tinterri, N. Mavilla, S. Angella, and L. Fava, 1999, Facies tracts of highly-efficient turbidity currents in large and elongate foreland basins, and their implications for basin analysis and exploration: Giornale di Geologia, v. 61, Serie 3C, p. 187-190.

Mutti, E., and F. Ricci Lucchi, 1972, Le torbiditi dell'Appennino settentrionale: Introduzione all' analisi di facies: Societa Geologica Italiana, v. 11, p. 161-199.

Nardin, T. R., 1983, Late Quaternary depositional systems and sea level change; Santa Monica and San Pedro basins, California continental borderland: AAPG Bulletin, v. 67, p. 1104-1124.

Natland, M. L., and P. H. Kuenen, 1951, Sedimentary history of the Ventura Basin, California, and the action of turbidity currents: Special Publication - Society of Economic Paleontologists and Mineralogists, v. 2, p. 76-107.

Nelson, C. H., 1984, Modern deep-sea-fan deposional processes and patterns: SEPM Short Course, v. 14, p. 136-169.

Nelson, C. H., 2002, Basic types of turbidite systems based on modern sea floor images: Annual Meeting Expanded Abstracts - American Association of Petroleum Geologists, v. 2002, p. 130-130.

Nelson, C. H., 2002, Basic types of turbidite systems based on modern sea floor images: Annual Meeting Expanded Abstracts - American Association of Petroleum Geologists, v. 2002, p. 130-130.

Nelson, C. H., C. Escutia, J. E. Damuth, and D. C. Twichell, Jr., Interplay of mass-transport and turbidite-system deposits in different active tectonic and passive continental margin settings; external and local controlling factors: Special Publication - Society for Sedimentary Geology, v. 96, p. 39-66.

Nelson, C. H., and T. H. Nilsen, 1974, Depositional trends of modern and ancient deep-sea fans: Special Publication - Society of Economic Paleontologists and Mineralogists, v. 19, p. 69-91.

Nelson, C. H., and T. H. Nilsen, 1976, Depositional trends of modern and ancient deep-sea fans Benchmark papers in geology, v. 24: United States, Dowden, Hutchinson and Ross, Inc. : Stroudsburg, Pa., United States, p. 388-410.

Nichols, R. J., 1995, The liquification and remobilization of sandy sediments: Geological Society, London, Special Publications, v. 94, p. 63-76.

Nilsen, K. T., B. C. Vendeville, and J.-T. Johansen, 1994, An example of salt tectonics controlled by regional tectonics; the Nordkapp Basin, Norway: Annual Meeting Expanded Abstracts - American Association of Petroleum Geologists, v. 1994, p. 225-225.

Nilsen, T. H., 1990, Santonian, Campanian, and Maestrichtian depositional systems, Sacramento Basin, California: Field Trip Guidebook - Pacific Section, Society of Economic Paleontologists and Mineralogists, v. 65, p. 95-132.

Nilsen, T. H., D. P. Imperato, and D. W. Moore, 1994, Reservoir geometry and architecture of productive Upper Cretaceous mud-rich and sand-rich submarine-fan systems, Sacramento Basin, California: Papers presented at the Gulf Coast Section, Society of Economic Paleontologists and Mineralogists Foundation Annual Bob F. Perkins Research Conference, v. 15, p. 269-280.

Nilsen, T. H., R. G. Walker, and W. R. Normark, 1980, Modern and ancient submarine fans; discussion and replies: AAPG Bulletin, v. 64, p. 1094-1112.

Normark, W. R., 1970, Growth patterns of deep-sea fans: American Association of Petroleum Geologists Bulletin, v. 54, p. 2170-2195.

Normark, W. R., 1976, Growth patterns of deep-sea fans Benchmark papers in geology: United States, Dowden, Hutchinson and Ross, Inc. : Stroudsburg, Pa., United States, 220-235 p.

Normark, W. R., 1978, Fan Valleys, channels, and depositional lobes on modern submarine fans; characters for recognition of sandy turbidite environments, AAPG Bulletin, United States, American Association of Petroleum Geologists : Tulsa, OK, United States, p. 912-931.

Normark, W. R., 1978, Fan Valleys, channels, and depositional lobes on modern submarine fans; characters for recognition of sandy turbidite environments: AAPG Bulletin, v. 62, p. 912-931.

Normark, W. R., 1983, Quaternary development of channels, levees, and lobes on middle Laurentian Fan, *in* D. J. W. Piper, and D. A. V. Stow, eds., AAPG Bulletin, United States, American Association of Petroleum Geologists : Tulsa, OK, United States, p. 1400-1409.

Normark, W. R., 1987, Depositional models from modern submarine fans and ancient turbidites; interpretation differences or different animals: SEPM Guidebook, v. 54, p. 25-31.

Normark, W. R., 1989, Observed parameters for turbidity-current flow in channels, Reserve Fan, Lake Superior: Journal of Sedimentary Petrology, v. 59, p. 423-431.

Normark, W. R., N. E. Barnes, and A. H. Bouma, 1985, Comments and new directions for deep-sea fan research Frontiers in sedimentary geology, v. 1: United States, Springer-Verlag : New York, NY, United States, p. 341-343.

Normark, W. R., and G. R. Hess, 1980, Quaternary growth patterns of California submarine fans: Pacific Coast Paleogeography Symposium, p. 201-210.

Normark, W. R., G. R. Hess, and F. N. Spiess, 1978, Mapping of small scale (outcrop-size) sedimentological features on modern submarine fans: Proceedings - Offshore Technology Conference, p. 593-598.

Normark, W. R., and D. J. W. Piper, 1991, Initiation processes and flow evolution of turbidity currents; implications for the depositional record: Special Publication - Society of Economic Paleontologists and Mineralogists, v. 46, p. 207-230.

Normark, W. R., and D. J. W. Piper, 1991, Initiation processes and flow evolution of turbidity currents; implications for the depositional record: Special Publication - Society of Economic Paleontologists and Mineralogists, v. 46, p. 207-230.

Normark, W. R., D. J. W. Piper, and G. R. Hess, 1979, Distributary channels, sand lobes, and mesotopography of Navy submarine fan, California Borderland, with applications to ancient fan sediments: Sedimentology, v. 26, p. 749-774.

Normark, W. R., D. J. W. Piper, and R. N. Hiscott, 1998, Sea level controls on the textural characteristics and depositional architecture of the Hueneme and associated submarine fan systems, Santa Monica Basin, California: Sedimentology, v. 45, p. 53-70.

Normark, W. R., D. J. W. Piper, B. W. Romans, J. A. Covault, P. Dartnell, and R. W. Sliter, 2009, Submarine canyon and fan systems of the California continental borderland: Special Paper - Geological Society of America, v. 454, p. 141-168.

Normark, W. R., H. Posamentier, and E. Mutti, 1993, Turbidite systems; state of the art and future directions: Reviews of Geophysics, v. 31, p. 91-116.

O'Byrne, C. J., 2000, Re-entrant fans and bypass aprons; depositional response to dynamic slope topography: Annual Meeting Expanded Abstracts - American Association of Petroleum Geologists, v. 2000, p. 109-109.

Ouchi, S., F. G. Ethridge, E. W. James, and S. A. Schumm, 1995, Experimental study of subaqueous fan development: Geological Society, London, Special Publications, v. 94, p. 13-29.

Ouchi, S., F. G. Ethridge, E. W. James, and S. A. Schumm, 1995, Experimental study of subaqueous fan development: Geological Society, London, Special Publications, v. 94, p. 13-29.

Pantin, H. M., and M. C. Franklin, Improved experimental evidence for autosuspension: Sedimentary Geology, v. 237, p. 46-54.

Paola, C., J. Mullin, C. Ellis, D. C. Mohrig, J. B. Swenson, G. S. Parker, T. Hickson, P. L. Heller, L. Pratson, J. Syvitski, B. Sheets, and N. Strong, 2001, Experimental stratigraphy: GSA Today, v. 11, p. 4-9.

Parker, G., M. Garcia, Y. Fukushima, and W. Yu, 1987, Experiments on turbidity currents over an erodible bed: Journal of Hydraulic Research = Journal de Recherches Hydrauliques, v. 25, p. 123-147.

Parker, G., C. Paola, K. X. Whipple, and D. Mohrig, 1998, Alluvial fans formed by channelized fluvial and sheet flow; I, Theory: Journal of Hydraulic Engineering, v. 124, p. 985-995.

Parker, G., C. Paola, K. X. Whipple, D. Mohrig, C. M. Toro-Escobar, M. Halverson, and T. W. Skoglund, 1998, Alluvial fans formed by channelized fluvial and sheet flow; II, Application: Journal of Hydraulic Engineering, v. 124, p. 996-1004.

Parker, G., H. Toniolo, J. Marr, C. Paola, and T. Hickson, 2001, Modeling of submarine debris flows and turbidity currents; implications for deepwater stratigraphy: Annual Meeting Expanded Abstracts - American Association of Petroleum Geologists, v. 2001, p. 151-151.

Parker, G., J. Violet, Y. Akamatsu, and R. Beaubouef, 2004, Experiments on the formation of internal deltas in minibasins on the continental slope: International Geological Congress, Abstracts = Congres Geologique International, Resumes, v. 32, Part 2, p. 1376-1376.

Parsons, J. D., C. T. Friedrichs, P. A. Traykovski, D. Mohrig, J. Imran, J. P. M. Syvitski, G. Parker, P. Puig, J. L. Buttles, and M. H. Garcia, 2007, The mechanics of marine sediment gravity flows: Special Publication of the International Association of Sedimentologists, v. 37, p. 275-337.

Parsons, J. D., and M. H. Garcia, 1998, Similarity of gravity current fronts: Physics of Fluids, v. 10, p. 3209-3213.

Peakall, J., K. J. Amos, G. M. Keevil, P. W. Bradbury, and S. Gupta, 2007, Flow processes and sedimentation in submarine channel bends: Marine and Petroleum Geology, v. 24, p. 470-486.

Peakall, J., K. J. Amos, G. M. Keevil, P. William Bradbury, and S. Gupta, 2007, Flow processes and sedimentation in submarine channel bends: Marine and Petroleum Geology, v. 24, p. 470-486.

Peakall, J., M. Felix, B. McCaffrey, and B. C. Kneller, 2001, Particulate gravity currents; perspectives: Special Publication of the International Association of Sedimentologists, v. 31, p. 1-8.

Peakall, J., B. McCaffrey, and B. Kneller, 2001, Sinuous submarine channels; evolution and flow processes: Annual Meeting Expanded Abstracts - American Association of Petroleum Geologists, v. 2001, p. 155-155.

Pickering, K., 1986, A high sinuosity, laterally migrating submarine fan channel-levee-overbank; results from DSDP Leg 96 on the Mississippi Fan, Gulf of Mexico, *in* J. Coleman, M. Cremer, L. Droz, B. Kohl, W. R. Normark, S. O'Connell, D. Stow, and A. A. Meyer-Wright, eds., Marine and Petroleum Geology, United Kingdom, Butterworth [in conjunction with the] Geological Society : Surrey, United Kingdom, p. 3-18.

Pickering, K. T., 1981, Two types of outer fan lobe sequence, from the late Precambrian Kongsfjord Formation submarine fan, Finnmark, North Norway, Journal of Sedimentary Petrology, United States, Society of Economic Paleontologists and Mineralogists : Tulsa, OK, United States, p. 1277-1286.

Pickering, K. T., 1982, Middle-fan deposits from the late Precambrian Kongsfjord Formation submarine fan, Northeast Finnmark, Northern Norway, Sedimentary Geology, Netherlands, Elsevier : Amsterdam, Netherlands, p. 79-110.

Pickering, K. T., 1984, Facies, facies-associations and sediment transport/deposition processes in a late Precambrian upper basin-slope/pro-delta,, Finnmark, N. Norway: Geological Society, London, Special Publications, v. 15, p. 343-362.

Pickering, K. T., 1998, Quantifying deep-water, high-continuity sandy turbidite systems: AAPG Bulletin, v. 82, p. 1951-1952.

Pickering, K. T., J. D. Clark, R. D. A. Smith, R. N. Hiscott, F. Ricci Lucchi, and N. H. Kenyon, 1995, Architectural element analysis of turbidite systems, and selected topical problems for sand-prone deep-water systems: United Kingdom, Chapman and Hall : London, United Kingdom, p. 1-10.

Pickering, K. T., and R. N. Hiscott, 1985, Contained (reflected) turbidity currents from the Middle Ordovician Cloridorme Formation, Quebec, Canada; an alternative to the antidune hypothesis: Sedimentology, v. 32, p. 373-394.

Pickering, K. T., R. N. Hiscott, and F. J. Hein, 1989, Deep marine environments; clastic sedimentation and tectonics: United Kingdom, Unwin Hyman : London, United Kingdom.

Pickering, K. T., R. N. Hiscott, and F. J. Hein, 1989, Deep marine environments; clastic sedimentation and tectonics: United Kingdom, Unwin Hyman : London, United Kingdom.

Pindell, J., and J. F. Dewey, 1982, Permo-Triassic reconstruction of western Pangea and the evolution of the Gulf of Mexico/Caribbean region: Tectonics, v. 1, p. 179-211.

Piper, D. J. W., 1978, Turbidite muds and silts on deep sea fans and abyssal plains, *in* D. J. Stanley, and G. Kelling, eds., Sedimentation in submarine canyons, fans and trenches: Stroudsburg, PA, Dowden, Hutchinson and Ross, p. 163-175.

Piper, D. J. W., 1999, Outcrop-scale acoustic facies analysis and latest Quaternary development of Hueneme and Dume submarine fans, offshore California, *in* R. N. Hiscott, and W. R. Normark, eds., Sedimentology, International, Blackwell : Oxford-Boston, International, p. 47-78.

Piper, D. J. W., 2001, Sandy fans; from Amazon to Hueneme and beyond, *in* W. R. Normark, ed., AAPG Bulletin, United States, American Association of Petroleum Geologists : Tulsa, OK, United States, p. 1407-1438.

Piper, D. J. W., and W. R. Normark, 1983, Turbidite depositional patterns and flow characteristics, Navy submarine fan, California Borderland: Sedimentology, v. 30, p. 681-694.

Pirmez, C., R. T. Beaubouef, S. J. Friedmann, and D. C. Mohrig, 2000, Equilibrium profile and baselevel in submarine channels; examples from late Pleistocene systems and implications for the architecture of deepwater reservoirs: Program and Abstracts - Society of Economic Paleontologists. Gulf Coast Section. Research Conference, v. 20, p. 782-805.

Pirmez, C., B. E. Prather, G. Mallarino, W. W. O'Hayer, and A. W. Droxler, 2012, Chronostratigraphy of the Brazos–Trinity Depositional System, Western Gulf of Mexico: Implications For Deepwater Depositional Models: SEPM Special Publication, v. 99, p. 111-143.

Posamentier, H. W., R. J. Davies, J. A. Cartwright, and L. J. Wood, 2007, Seismic geomorphology; an overview: Geological Society Special Publications, v. 277, p. 1-14.

Posamentier, H. W., M. T. Jervey, and P. R. Vail, 1988, Eustatic controls on clastic deposition; I, Conceptual framework: Special Publication - Society of Economic Paleontologists and Mineralogists, v. 42, p. 109-124.

Posamentier, H. W., and V. Kolla, 2003, Anatomy of a deep-water channel avulsion; example from the basin floor of the Desoto Canyon area, Gulf of Mexico: Annual Meeting Expanded Abstracts - American Association of Petroleum Geologists, v. 12, p. 140-140.

Posamentier, H. W., and V. Kolla, 2003, Seismic geomorphology and stratigraphy of depositional elements in deep-water settings: Journal of Sedimentary Research, v. 73, p. 367-388.

Posamentier, H. W., and P. R. Vail, 1988, Eustatic controls on clastic deposition; II, Sequence and systems tract models: Special Publication - Society of Economic Paleontologists and Mineralogists, v. 42, p. 125-154.

Posamentier, H. W., and R. G. Walker, 2006, Deep-water turbidites and submarine fans: Special Publication - Society for Sedimentary Geology, v. 84, p. 399-520.

Prather, B. E., 1998, Classification, lithologic calibration, and stratigraphic succession of seismic facies of intraslope basins, deep-water Gulf of Mexico; errata, *in* J. R. Booth, G. S. Steffens, and P. A. Craig, eds., AAPG Bulletin, United States, American Association of Petroleum Geologists : Tulsa, OK, United States, p. 707R-707R.

Prather, B. E., 1998, A Gulf of Mexico based depositional process model for above-grade slopes: AAPG Bulletin, v. 82, p. 1953-1953.

Prather, B. E., 2000, Calibration and visualization of depositional process models for above-grade slopes; a case study from the Gulf of Mexico, Marine and Petroleum Geology, United Kingdom, Elsevier : Oxford, United Kingdom, p. 619-638.

Prather, B. E., 2003, Controls on reservoir distribution, architecture and stratigraphic trapping in slope settings, Marine and Petroleum Geology, United Kingdom, Elsevier : Oxford, United Kingdom, p. 529-545.

Prather, B. E., 2003, Controls on reservoir distribution, architecture and stratigraphic trapping in slope settings: Marine and Petroleum Geology, v. 20, p. 529-545.

Prather, B. E., and A, 1998, Classification, lithologic calibration, and stratigraphic succession of seismic facies of intraslope basins, deep-water Gulf of Mexico, *in* J. R. Booth, G. S. Steffens, and P. A. Craig, eds., AAPG Bulletin, United States, American Association of Petroleum Geologists : Tulsa, OK, United States, p. 701-728.

Pratson, L. E., J. Imran, G. Parker, J. P. M. Syvitski, and E. Hutton, 2000, Debris flows vs. turbidity currents; a modeling comparison of their dynamics and deposits: AAPG Memoir, v. 72, p. 57-71.

Pratson, L. F., and W. B. F. Ryan, 1994, Pliocene to Recent infilling and subsidence of intraslope basins offshore Louisiana: AAPG Bulletin, v. 78, p. 1483-1506.

Prélat, A., D. M. Hodgson, and S. S. Flint, 2009, Evolution, architecture and hierarchy of distributary deep-water deposits: a high-resolution outcrop investigation from the Permian Karoo Basin, South Africa: Sedimentology, v. 56, p. 2132-2154.

Price, I., 1980, Gravity tectonics on a passive margin; Deep Sea Drilling Project Site 415 in relation to regional seismic data, Initial Reports of the Deep Sea Drilling Project, United States, Texas A & M University, Ocean Drilling Program : College Station, TX, United States, p. 759-771.

Pyles, D. R., 2008, Multiscale stratigraphic analysis of a structurally confined submarine fan; Carboniferous Ross Sandstone, Ireland: AAPG Bulletin, v. 92, p. 557-587.

Pyles, D. R., and D. C. Jennette, 2009, Geometry and architectural associations of co-genetic debrite-turbidite beds in basin margin strata, Carboniferous Ross

Sandstone (Ireland); applications to reservoirs located on the margins of structurally confined submarine fans: Marine and Petroleum Geology, v. 26, p. 1974-1996.

Pyles, D. R., J. P. M. Syvitski, and R. M. Slatt, 2011, Defining the concept of stratigraphic grade and applying it to stratal (reservoir) architecture and evolution of the slope-to-basin profile: An outcrop perspective: Marine and Petroleum Geology, v. 28, p. 675-697.

Reading, H. G., and M. Richards, 1994, Turbidite systems in deep-water basin margins classified by grain size and feeder system: AAPG Bulletin, v. 78, p. 792-822.

Richards, M., and M. Bowman, 1998, Submarine fans and related depositional systems; II, Variability in reservoir architecture and wireline log character: Marine and Petroleum Geology, v. 15, p. 821-839.

Richards, M., M. Bowman, and H. Reading, 1998, Submarine-fan systems; I, Characterization and stratigraphic prediction: Marine and Petroleum Geology, v. 15, p. 689-717.

Ross, W. C., B. A. Halliwell, J. A. May, D. E. Watts, and J. P. M. Syvitski, 1994, Slope readjustment; a new model for the development of submarine fans and aprons: Geology [Boulder], v. 22, p. 511-514.

Ross, W. C., B. A. Halliwell, J. A. May, D. E. Watts, and J. P. M. Syvitski, 1994, Slope readjustment; a new model for the development of submarine fans and aprons: Geology [Boulder], v. 22, p. 511-514.

Rottman, J. W., J. E. Simpson, J. C. R. Hunt, and R. E. Britter, 1985, Unsteady gravity current flows over obstacles: Some observations and analysis related to the phase II trials: Journal of Hazardous Materials, v. 11, p. 325-340.

Rowan, M. G., 1993, A systematic technique for the sequential restoration of salt structures, Tectonophysics, Netherlands, Elsevier : Amsterdam, Netherlands, p. 331-348.

Rowan, M. G., 1995, Structural styles and evolution of allochthonous salt, central Louisiana outer shelf and upper slope: AAPG Memoir, v. 65, p. 199-228.

Rowan, M. G., 1999, Salt-related fault families and fault welds in the northern Gulf of Mexico, *in* M. P. A. Jackson, and B. D. Trudgill, eds., AAPG Bulletin, United States, American Association of Petroleum Geologists : Tulsa, OK, United States, p. 1454-1484.

Rowan, M. G., 2001, Emplacement and evolution of the Mahogany salt body, central Louisiana outer shelf, northern Gulf of Mexico, *in* R. A. Ratliff, B. D. Trudgill, and J. Barcelo Duarte, eds., AAPG Bulletin, United States, American Association of Petroleum Geologists : Tulsa, OK, United States, p. 947-969.

Rowan, M. G., 2001, Gravity-driven foldbelts on passive margins, *in* F. J. Peel, and B. C. Vendeville, eds., Annual Meeting Expanded Abstracts - American Association of Petroleum Geologists, United States, American Association of Petroleum Geologists and Society of Economic Paleontologists and Mineralogists (AAPG) : Tulsa, OK, United States, p. 174-174.

Rowan, M. G., T. F. Lawton, K. A. Giles, and R. A. Ratliff, 2003, Near-salt deformation in La Popa Basin, Mexico, and the northern Gulf of Mexico; a general model for passive diapirism: AAPG Bulletin, v. 87, p. 733-756.

Rowan, M. G., and P. Weimer, 1998, Salt-sediment interaction, northern Green Canyon and Ewing Bank (offshore Louisiana), northern Gulf of Mexico: AAPG Bulletin, v. 82, p. 1055-1082.

Salaheldin, T. M., J. Imran, M. H. Chaudhry, and C. Reed, 2000, Role of fine-grained sediment in turbidity current flow dynamics and resulting deposits: Marine Geology, v. 171, p. 21-38.

Saller, A., 2008, Characteristics of Pleistocene deep-water fan lobes and their application to an upper Miocene reservoir model, offshore East Kalimantan, Indonesia, *in* K. Werner, F. Sugiaman, A. Cebastiant, R. May, D. Glenn, and C. Barker, eds., AAPG Bulletin, United States, American Association of Petroleum Geologists : Tulsa, OK, United States, p. 919-949.

Salvador, A., 1987, Late Triassic-Jurassic paleogeography and origin of Gulf of Mexico Basin: AAPG Bulletin, v. 71, p. 419-451.

Satterfield, W. M., and E. W. Behrens, 1988, Intraslope basin evolution, Northwest Gulf of Mexico: AAPG Bulletin, v. 72, p. 244-244.

Satterfield, W. M., and E. W. Behrens, 1990, A late Quaternary canyon channel system, Northwest Gulf of Mexico continental slope: Marine Geology, v. 92, p. 51-67.

Scheidegger, A. E., and P. E. Potter, 1971, Downcurrent decline of grain size and thickness of single turbidite beds; a semi-quantitative analysis: Sedimentology, v. 17, p. 41-49.

Seibold, E., and D. Fuetterer, 1982, Sediment dynamics on the Northwest African continental margin: United Kingdom, John Wiley & Sons : Chichester, United Kingdom, 147-163 p.

Seni, S. J., and M. P. A. Jackson, 1983, Evolution of salt structures, East Texas diapir province; Part 1, Sedimentary record of halokinesis: AAPG Bulletin, v. 67, p. 1219-1244.

Sequeiros, O. E., B. Spinewine, R. T. Beaubouef, T. Sun, M. H. Garcia, and G. Parker, 2009, Bedload transport and bed resistance associated with density and turbidity currents: Sedimentology, v. 57, p. 1463-1490.

Sequeiros, O. E., B. Spinewine, M. H. Garcia, R. T. Beaubouef, T. Sun, and G. Parker, 2009, Experiments on wedge-shaped deep sea sedimentary deposits in minibasins and/or on channel levees emplaced by turbidity currents; Part I, Documentation of the flow: Journal of Sedimentary Research, v. 79, p. 593-607.

Shanmugam, G., 1999, Deep-water processes and facies models; a paradigm shift for the 21st century: Program and Abstracts - Society of Economic Paleontologists. Gulf Coast Section. Research Conference, v. 19.

Shanmugam, G., R. J. Moiola, and J. E. Damuth, 1985, Eustatic control of submarine fan development Frontiers in sedimentary geology, v. 1: United States, Springer-Verlag : New York, NY, United States, p. 23-28.

Shoup, R. C., and J. F. Karlo, 1999, Classification of syndepositional structural systems, northern Gulf of Mexico: AAPG Bulletin, v. 83, p. 1339-1340.

Sinclair, H. D., and P. A. Cowie, 2003, Basin-floor topography and the scaling of turbidites: Journal of Geology, v. 111, p. 277-299.

Sinclair, H. D., and M. Tomasso, 2002, Depositional evolution of confined turbidite basins: Journal of Sedimentary Research, v. 72, p. 451-456.

Smith, R., 2004, Silled sub-basins to connected tortuous corridors: sediment distribution systems on topographically complex sub-aqueous slopes: Geological Society, London, Special Publications, v. 222, p. 23-43.

Stacey, M. W., and A. J. Brown, 1988, Vertical structure of density and turbidity currents: Theory and observations: J. Geophys. Res., v. 93, p. 3528-42.

Steffens, G. S., E. K. Biegert, H. S. Sumner, and D. Bird, 2003, Quantitative bathymetric analyses of selected deepwater siliciclastic margins; receiving basin configurations for deepwater fan systems: Marine and Petroleum Geology, v. 20, p. 547-561.

Stow, D. A. V., 1986, Deep Clastic Seas, *in* H. G. Reading, ed., Sedimentary Environments and Facies, Blackwell Scientific Publications, p. 399-444.

Stow, D. A. V., M. Alam, and D. J. W. Piper, 1984, Sedimentology of the Halifax Formation, Nova Scotia: Lower Palaeozoic fine-grained turbidites: Geological Society, London, Special Publications, v. 15, p. 127-144.

Stow, D. A. V., and A. J. Bowen, 1980, A physical model for the transport and sorting of fine-grained sediment by turbidity currents: Sedimentology, v. 27, p. 31-46.

Stow, D. A. V., and A. J. Bowen, 1980, A physical model for the transport and sorting of fine-grained sediment by turbidity currents: Sedimentology, v. 27, p. 31-46.

Stow, D. A. V., M. Cremer, A. W. Meyer, W. R. Normark, S. O'Connell, K. T. Pickering, C. E. Stelting, S. A. Angell, and C. Chaplin, 1986, Facies, composition, and

texture of Mississippi Fan sediments, Deep Sea Drilling Project Leg 96, Gulf of Mexico: Initial Reports of the Deep Sea Drilling Project, v. 96, p. 475-487.

Stow, D. A. V., and D. J. W. Piper, 1984, Deep-water fine-grained sediments: facies models: Geological Society, London, Special Publications, v. 15, p. 611-646.

Stow, D. A. V., and G. Shanmugam, 1980, Sequence of structures in fine-grained turbidites; comparison of Recent deep-sea and ancient flysch sediments: Sedimentary Geology, v. 25, p. 23-42.

Straub, K. M., 2007, Quantifying turbidity current interactions with topography, United States.

Straub, K. M., C. Paola, D. Mohrig, M. A. Wolinsky, and T. George, 2009, Compensational stacking of channelized sedimentary deposits: Journal of Sedimentary Research, v. 79, p. 673-688.

Sullivan, M., G. Jensen, F. Goulding, D. Jennette, L. Foreman, and D. Stern, 2000, Architectural analysis of deepwater outcrops: implications for exploration and production of the Diana sub-basin, western Gulf of Mexico, *in* P. Weimer, R. M. Slatt, J. L. Coleman, N. Rosen, C. H. Nelson, A. H. Bouma, M. Styzen, and D. T. Lawrence, eds., Global Deep-Water Reservoirs: Gulf Coast Section-SEPM Foundation 20th Annual Bob F. Perkins Research Conference, p. 1010-1031.

Sullivan, M.D., Foreman, J.L., Jennette, D.C., Stern, D., Jensen, G.N., and Goulding, F.J., 2004, An integrated approach to characterization and modeling of deepwater reservoirs, Diana field, western Gulf of Mexico, in Grammer, G.M., Harris, P.M., and Eberli, G.P., eds., Integration of outcrop and modern analogs in reservoir modeling: American Association of Petroleum Geologists Memoir 80, p. 215–234.

Sweet, M. L., and L. T. Sumpter, 2007, Genesis Field, Gulf of Mexico; recognizing reservoir compartments on geologic and production time scales in deep-water reservoirs: AAPG Bulletin, v. 91, p. 1701-1729.

Tari, G., 2000, Salt tectonics in the Atlantic margin of Morocco, *in* J. Molnar, P. Ashton, and R. Hedley, eds., Leading Edge [Tulsa, OK], United States, Society of Exploration Geophysicists : Tulsa, OK, United States, p. 1074.

Tari, G. C., 2001, Examples of deep-water salt tectonics from West Africa; are they analogs to the deep-water salt-cored fold belts of the Gulf of Mexico?: Program and Abstracts - Society of Economic Paleontologists. Gulf Coast Section. Research Conference, v. 21, p. 251-270.

Tari, G. C., 2002, Expression of the Atlas inversion tectonics in deep-water offshore Morocco; implications for hydrocarbon exploration, *in* P. R. Ashton, J. S. Molnar, and P. Thompson, eds., Annual Meeting Expanded Abstracts - American Association of Petroleum Geologists, United States, American Association of

Petroleum Geologists and Society of Economic Paleontologists and Mineralogists (AAPG) : Tulsa, OK, United States, p. 174-174.

Tari, G., 2003, Examples of salt tectonics from West Africa; a comparative approach, *in* J. Molnar, and P. Ashton, eds., Geological Society Special Publications, United Kingdom, Geological Society of London : London, United Kingdom, p. 85-104.

Toniolo, H., 2003, Depositional turbidity currents in diapiric minibasins on the continental slope; theory, experiments and numerical simulation, *in* P. Gary, ed., Annual Meeting Expanded Abstracts - American Association of Petroleum Geologists, United States, American Association of Petroleum Geologists and Society of Economic Paleontologists and Mineralogists : Tulsa, OK, United States, p. 171-171.

Toniolo, H., and P. Gary, 2003, Depositional turbidity currents in diapiric minibasins on the continental slope; theory, experiments and numerical simulation: Annual Meeting Expanded Abstracts - American Association of Petroleum Geologists, v. 12, p. 171-171.

Toniolo, H., P. Harff, J. Marr, C. Paola, and G. Parker, 2004, Experiments on reworking by successive unconfined subaqueous and subaerial muddy debris flows: Journal of Hydraulic Engineering, v. 130, p. 38-48.

Toniolo, H., M. Lamb, and G. Parker, 2006, Depositional turbidity currents in diapiric minibasins on the continental slope; formulation and theory: Journal of Sedimentary Research, v. 76, p. 783-797.

Toniolo, H., G. Parker, V. Voller, and R. T. Beaubouef, 2006, Depositional turbidity currents in diapiric minibasins on the continental slope; experiments-numerical simulation and upscaling: Journal of Sedimentary Research, v. 76, p. 798-818.

Toniolo, H. A., 2002, Debris flows and turbidity current deposition in the deep sea and reservoirs, United States.

Vail, P. R., R. M. Mitchum, Jr., and S. Thompson, III, 1977, Seismic stratigraphy and global changes of sea level; Part 3, Relative changes of sea level from coastal onlap: Memoir - American Association of Petroleum Geologists, p. 63-81.

van Andel, T. H., and P. D. Komar, 1969, Ponded sediments of the Mid-Atlantic ridge between 22 degrees and 23 degrees north latitude: Geological Society of America Bulletin, v. 80, p. 1163-1190.

Villamil, T., C. Arango, P. Weimer, A. Waterman, M. G. Rowan, P. Varnai, A. J. Pulham, and J. R. Crews, 1998, Biostratigraphic techniques for analyzing benthic biofacies, stratigraphic condensation, and key surface identification, Pliocene and Pleistocene sediments, northern Green Canyon and Ewing Bank (offshore Louisiana), northern Gulf of Mexico: AAPG Bulletin, v. 82, p. 961-985.

Vincent, E., 1980, Biostratigraphy and depositional history of the Moroccan Basin, eastern North Atlantic, Deep Sea Drilling Project Leg 50, *in* P. Cepek, W. Sliter, M. J. Westberg, and S. Gartner, eds., Initial Reports of the Deep Sea Drilling Project, United States, Texas A & M University, Ocean Drilling Program : College Station, TX, United States, p. 775-800.

Violet, J., B. Sheets, L. Pratson, C. Paola, R. Beaubouef, and G. Parker, 2005, Experiment on turbidity currents and their deposits in a model 3D subsiding minibasin: Journal of Sedimentary Research, v. 75, p. 820-843.

Violet, J. A., B. A. Sheets, C. Paola, L. F. Pratson, and G. Parker, 2002, Filling of a salt-withdrawal minibasin on the continental slope by turbidity currents; further research and results: Eos, Transactions, American Geophysical Union, v. 83, p. F696-F696.

Walker, R. G., 1978, Deep-water sandstone facies and ancient submarine fans; models for exploration for stratigraphic traps, AAPG Bulletin, United States, American Association of Petroleum Geologists : Tulsa, OK, United States, p. 932-966.

Walker, R. G., and E. Mutti, 1973, Turbidite facies and facies associations: United States, Soc. Econ. Paleontol. Mineral., Pac. Sect., Los Angeles, p. 119-157.

Weaver, P. P. E., R. B. Wynn, N. H. Kenyon, and J. Evans, 2000, Continental margin sedimentation, with special reference to the North-east Atlantic margin: Sedimentology, v. 47, Suppl. 1, p. 239-256.

Weimer, P., 1990, Sequence stratigraphy, facies geometries, and depositional history of the Mississippi Fan, Gulf of Mexico: AAPG Bulletin, v. 74, p. 425-453.

Weimer, P., 1991, Seismic facies, characteristics, and variations in channel evolution, Mississippi Fan (Plio-Pleistocene), Gulf of Mexico Frontiers in sedimentary geology: United States, Springer-Verlag : New York, NY, United States, p. 323-347.

Weimer, P., A. H. Bouma, and B. F. Perkins, 1994, Submarine fans and turbidite systems; sequence stratigraphy, reservoir architecture and production characteristics, Gulf of Mexico and international; papers presented at the Gulf Coast Section Society of Economic Paleontologists and Mineral: Papers presented at the Gulf Coast Section, Society of Economic Paleontologists and Mineralogists Foundation Annual Bob F. Perkins Research Conference.

Weimer, P., J. R. Crews, R. S. Crow, and P. Varnai, 1998, Atlas of petroleum fields and discoveries, northern Green Canyon, Ewing Bank, and southern Ship Shoal and South Timbalier areas (offshore Louisiana), northern Gulf of Mexico: AAPG Bulletin, v. 82, p. 878-917.

Weimer, P., and M. H. Link, 1991, Global petroleum occurrences in submarine fans and turbidite systems Frontiers in sedimentary geology: United States, Springer-Verlag : New York, NY, United States, p. 9-67.

Weimer, P., P. Varnai, F. M. Budhijanto, Z. M. Acosta, R. E. Martinez, A. F. Navarro, M. G. Rowan, B. C. McBride, T. Villamil, C. Arango, J. R. Crews, and A. J. Pulham, 1998, Sequence stratigraphy of Pliocene and Pleistocene turbidite systems, northern Green Canyon and Ewing Bank (offshore Louisiana), northern Gulf of Mexico: AAPG Bulletin, v. 82, p. 918-960.

Weisenburger, C. M., 2007, Salt Tectonics, Sedimentation, and Basin Development in Safi Haute Mer, offshore Morocco: M.S. thesis, University of Texas at Austin, Austin, TX, 106 p.

Winker, C. D., 1996, High-resolution seismic stratiraphy of a late Pleistocene submarine fan ponded by salt-withdrawal minibasins on the Gulf of Mexico continental slope: Proceedings - Offshore Technology Conference, v. 28, Vol. 1, p. 619-628.

Winker, C. D., and J. R. Booth, 2000, Sedimentary dynamics of the salt-dominated continental slope, Gulf of Mexico; integration of observations from the seafloor, near-surface, and deep subsurface: Program and Abstracts - Society of Economic Paleontologists. Gulf Coast Section. Research Conference, v. 20, p. 1059-1086.

Wood, L. J., 2007, Quantitative seismic geomorphology of Pliocene and Miocene fluvial systems in the northern Gulf of Mexico, U.S.A: Journal of Sedimentary Research, v. 77, p. 713-730.

Wood, L. J., S. Sullivan, and P. Mann, 2004, Influence of mobile shales in the creation of successful hydrocarbon basins: Program and Abstracts - Society of Economic Paleontologists. Gulf Coast Section. Research Conference, v. 24, p. 38-38.

Wynn, R. B., 2002, Classification and characterisation of deep-water sediment waves, *in* D. A. V. Stow, ed., Marine Geology, Netherlands, Elsevier : Amsterdam, Netherlands, p. 7-22.

Wynn, R. B., 2002, Generation and migration of coarse-grained sediment waves in turbidity current channels and channel-lobe transition zones, *in* D. J. W. Piper, and M. J. R. Gee, eds., Marine Geology, Netherlands, Elsevier : Amsterdam, Netherlands, p. 59-78.

Zuehlke, R., 2004, Quantitative Meso-/Cenozoic development of the eastern central Atlantic continental shelf, western High Atlas, Morocco, *in* M.-S. Bouaouda, B. Ouajhain, T. Bechstaedt, and R. Leinfelder, eds., Marine and Petroleum Geology, United Kingdom, Elsevier : Oxford, United Kingdom, p. 225-276.

# Vita

Vishal Timal Maharaj was born in Trinidad and Tobago. He received his B.S. degree in Geology at the University of the West Indies in Jamaica in 2006 and his M.S. degree in Geological Sciences from the Jackson School of Geosciences at the University of Texas at Austin in 2008. Vishal's B.S. thesis documented his field mapping of the Morne L'Enfer formation in southwest Trinidad, and his M.S. thesis documented results from an integrated subsurface study of the stratigraphy of the Pennsylvanian Atoka Group of north-central Texas. While at the University of Texas at Austin, Vishal was advised by Dr. Lesli Wood who directed the Quantitative Clastics Laboratory at the Bureau of Economic Geology. With the continued support of his research advisor, Vishal researched the effects of confining topography on turbidity current dynamics and deposit architecture for his Ph.D. work. Much of this work has culminated in the results of this dissertation. While at the University of Texas, Vishal completed an internship in the summer of 2008 with ConocoPhillips in Houston, TX. Vishal also completed summer internships with BP Trinidad and Tobago (2005), BHPBilliton Houston (2009) and Marathon Oil Houston (2011). Vishal will be employed in December 2012 with Marathon Oil.

Permanent email: vmaharaj@utexas.edu

This dissertation was typed by Vishal Timal Maharaj.